

**FUNDAMENTAL STUDY OF 1-D SEMICONDUCTOR AND NANOSCALE
ELECTRODE ARCHITECTURES FOR PHOTO-ELECTROCHEMICAL WATER
SPLITTING**

by

Prasad Prakash Patel

B.S. in Chemical Engineering

Institute of Chemical Technology (formerly U.D.C.T.), Mumbai, India, 2012

Submitted to the Graduate Faculty of
Swanson School of Engineering in partial fulfillment
of the requirements for the degree of
Doctor of Philosophy

University of Pittsburgh

2018

UNIVERSITY OF PITTSBURGH
SWANSON SCHOOL OF ENGINEERING

This dissertation was presented

by

Prasad Prakash Patel

It was defended on

January 3, 2018

and approved by

Dr. Robert M. Enick, Covestro Professor & Vice Chair for Research, Department of Chemical
& Petroleum Engineering, University of Pittsburgh

Dr. Judith Yang, Professor, Department of Chemical & Petroleum Engineering, University of
Pittsburgh

Dr. Jung-Kun Lee, Associate Professor, Department of Mechanical Engineering & Materials
Science, University of Pittsburgh

Dissertation Director: Dr. Prashant N. Kumta, Edward. R. Weidlein Chair Professor,
Department of Chemical & Petroleum Engineering, University of Pittsburgh

Copyright © by Prasad Prakash Patel

2018

FUNDAMENTAL STUDY OF 1-D SEMICONDUCTOR AND NANOSCALE ELECTRODE ARCHITECTURES FOR PHOTO-ELECTROCHEMICAL WATER SPLITTING

Prasad Prakash Patel, PhD

University of Pittsburgh, 2018

Photoelectrochemical (PEC) water splitting is a promising technology for the production of clean hydrogen, long identified as a potential energy carrier for the much awaited hydrogen economy. Clean hydrogen is indeed capable of meeting the global energy demand placing minimal stress on the environment compared to hitherto combustion based technologies. Generation of clean hydrogen however, represents major challenges. Identification and development of suitable semiconductor materials as photoanodes exhibiting narrow band gap and superior solar-to-hydrogen efficiency (STH) combined with the desired PEC stability would represent a major breakthrough in the arduous path towards identifying and economically manufacturing commercially viable PEC water splitting systems. In addition to the photoanode, engineering of novel non-noble based cathode electro-catalysts with superior electrochemical activity for hydrogen evolution reaction (HER) compared to expensive state of the art noble metal electro-catalyst (e.g. Pt) will significantly contribute towards further lowering the cost of PEC water splitting cells.

Keeping in line with these goals, a co-doping strategy was adopted in this study for generating photoanodes with systematic band gap engineering. Accordingly, the co-doping strategy was implemented to modify the band gaps of ZnO and SnO₂, which exhibit good electron mobility but possess wide band gaps yielding poor PEC activity. It was demonstrated that by synergistically co-doping Co and N into the ZnO lattice, and Nb and N co-doping into SnO₂ crystalline structure resulted in significantly improved light absorption properties offering 4-5 orders of magnitude higher carrier density contributing to remarkably higher PEC activity with the highest applied bias photon-to-current efficiency (ABPE) (~4.1%) obtained for (Sn_{0.95}Nb_{0.05})O₂:N-600 nanotubes (NTs). The optoelectronic and PEC properties of (Sn_{0.95}Nb_{0.05})O₂:N-600 NTs are further improved by developing novel 1-D bilayer structures of

WO₃ and (Sn_{0.95}Nb_{0.05})O₂:N-600. The novel bilayer composite heterostructures offered improved light absorption, high carrier density and efficient separation of photogenerated carriers leading to long carrier lifetimes. As a result, superior PEC activity and STH (~3.83%) under zero applied bias was achieved, which is the highest STH obtained so far compared to other well-studied materials such as TiO₂, ZnO, α -Fe₂O₃, to the best of our knowledge. The composite bilayer structure also showed superior PEC stability in electrolyte solution under illumination.

Furthermore, ultra-low noble metal containing non-noble metals based Co_{1-x}(Ir_x) (x=0.3, 0.4) and completely noble metal free (Cu_{0.83}Co_{0.17})₃P:x at. %S (x=10, 20, 30) solid solution electro-catalyst systems have been studied as cathode electro-catalyst for HER. The synergistic interaction of Co and Ir as well as Cu, Co, P and S offered excellent electrochemical properties. Accordingly, Co_{1-x}(Ir_x) (x=0.3, 0.4) displayed ~40% and ~93% improved electrocatalytic response compared to Pt/C. On the other hand, (Cu_{0.83}Co_{0.17})₃P:30 at. %S showed HER response similar to that of Pt/C. These results together indeed reflect the significant advances made in the pursuit of non-noble metal electro-catalyst for HER replacing Pt/C, the expensive albeit, the prevalent gold standard HER electrocatalyst.

This thesis provides a detailed account of the fundamental study conducted into the synthesis, materials, characterization, photoelectrochemical and electrochemical response ably supported by first principles theoretical studies as required.

TABLE OF CONTENTS

LIST OF TABLES	XI
LIST OF FIGURES	XIII
1.0 INTRODUCTION.....	1
1.1 HYDROGEN-THE NEXT GENERATION FUEL	1
1.2 HYDROGEN PRODUCTION TECHNOLOGIES.....	3
1.3 WATER SPLITTING	6
2.0 BACKGROUND	8
2.1 SOLAR ENERGY-A PROMISING ENERGY SOURCE.....	8
2.2 SOLAR WATER SPLITTING.....	11
2.2.1 PHOTOCATALYSIS.....	11
2.2.2 PHOTOELECTRO-CATALYSIS	14
2.3 THERMODYNAMICS AND KINETICS.....	17
2.4 REACTION MECHANISMS.....	18
2.5 DESIRED PROPERTIES OF SEMICONDCUTOR MATERIAL (PHOTOANODE).....	20
2.5.1 BAND GAP	20
2.5.2 BAND STRUCTURE	20
2.5.3 ELECTRICAL CONDUCTIVITY	23

2.5.4	RECOMBINATION OF THE PHOTOGENERATED CARRIERS	23
2.5.5	PHOTOELECTROCHEMICAL STABILITY	24
2.6	DESIRED PROPERTIES OF THE CATHODE ELECTRO-CATALYST	25
2.7	SOLAR-TO-HYDROGEN EFFICIENCY	26
2.8	CHALLENGES FOR PEC WATER SPLITTING	27
3.0	MOTIVATION AND SPECIFIC AIMS	32
3.1	MOTIVATION	32
3.1.1	SEMICONDUCTOR MATERIALS FOR PHOTOANODE	32
3.1.2	CATHODE ELECTRO-CATALYSTS FOR HER	40
3.2	SPECIFIC AIMS	47
4.0	EXPERIMENTAL DETAILS	50
4.1	SEMICONDUCTOR NANOMATERIALS PREPARATION FOR PHOTOANODE	50
4.1.1	SYNTHESIS OF $(\text{Zn}_{1-x}\text{Co}_x)\text{O}:\text{N}$ NANOWIRES (NWs) ($x=0.05$)	50
4.1.2	SYNTHESIS OF $(\text{Sn}_{1-x}\text{Nb}_x)\text{O}_2:\text{N}$ NANOTUBES (NTs) ($x=0.05$) USING ZnO NWs AS SACRIFICIAL TEMPLATE	52
4.1.3	SYNTHESIS OF $[\text{WO}_3-(\text{Sn}_{0.95}\text{Nb}_{0.05})\text{O}_2:\text{N}-600]$ BILAYER NANOTUBES (NTs)	53
4.2	ELECTRO-CATALYSTS PREPARATION FOR THE CATHODE	55
4.2.1	SYNTHESIS OF $\text{Co}_{1-x}(\text{Ir}_x)$ ($x=0, 0.2, 0.3, 0.4, 1$) NANOPARTICLES (NPs)	55
4.2.2	SYNTHESIS OF $(\text{Cu}_{0.83}\text{Co}_{0.17})_3\text{P}:\text{x}$ at.% S ($x=10, 20, 30$) NANOPARTICLES (NPs)	57

4.3	STRUCTURAL CHARACTERIZATION.....	58
4.4	PHOTOELECTROCHEMICAL CHARACTERIZATION OF SEMICONDUCTOR NANOMATERIALS FOR PHOTOANODE	60
4.5	ELECTROCHEMICAL CHARACTERIZATION OF HER ELECTRO-CATALYSTS FOR CATHODE	65
5.0	RESULTS AND DISCUSSION	71
5.1	Co AND N Co-DOPED ZnO NANOWIRES (NWs) (PHOTOANODE).....	71
5.1.1	STRUCTURAL ANALYSIS OF ZnO AND (Zn _{0.95} Co _{0.05})O:N NWs.....	71
5.1.2	PHOTOELECTROCHEMICAL CHARACTERIZATION OF ZnO AND (Zn _{0.95} Co _{0.05})O:N NWs	88
5.2	Nb AND N CO-DOPED SnO ₂ NANOTUBES (NTs) (PHOTOANODE) ...	109
5.2.1	STRUCTURAL ANALYSIS OF SnO ₂ AND (Sn _{0.95} Nb _{0.05})O ₂ :N NTs.....	109
5.2.2	PHOTOELECTROCHEMICAL CHARACTERIZATION OF SnO ₂ AND (Sn _{0.95} Nb _{0.05})O ₂ :N NTs.....	123
5.3	[WO ₃ -(SN _{0.95} NB _{0.05})O ₂ :N-600] BILAYER PHOTOANODES.....	145
5.3.1	STRUCTURAL ANALYSIS OF [WO ₃ -(Sn _{0.95} Nb _{0.05})O ₂ :N-600] NANOTUBES (NTs)	145
5.3.2	PHOTOELECTROCHEMICAL CHARACTERIZATION OF [WO ₃ -(Sn _{0.95} Nb _{0.05})O ₂ :N-600] NTs.....	163
5.4	Co(Ir) SOLID SOLUTION HER ELECTRO-CATALYST FOR CATHODE	195
5.4.1	STRUCTURAL ANALYSIS OF Co _{1-x} (Ir _x) (x=0.2, 0.3, 0.4) NANOPARTICLES (NPs)	195

5.4.2	ELECTROCHEMICAL CHARACTERIZATION OF $\text{Co}_{1-x}(\text{Ir}_x)$ FOR H_2 PRODUCTION FROM ELECTROLYTIC WATER SPLITTING	207
5.4.3	ELECTROCHEMICAL CHARACTERIZATION OF $\text{Co}_{1-x}(\text{Ir}_x)$ ($x=0.3, 0.4$) IN PEC WATER SPLITTING CELL	222
5.5	$(\text{Cu}_{0.83}\text{Co}_{0.17})_3\text{P}:\text{S}$ HER ELECTRO-CATALYST FOR CATHODE	228
5.5.1	STRUCTURAL CHARACTERIZATION OF PURE Cu_3P NANOPARTICLES (NPs), $(\text{Cu}_{0.83}\text{Co}_{0.17})_3\text{P}$ NPs AND $(\text{Cu}_{0.83}\text{Co}_{0.17})_3\text{P}:\text{x at.}\%$ S NPs ($X=10, 20, 30$)	228
5.5.2	ELECTROCHEMICAL CHARACTERIZATION OF $(\text{Cu}_{0.83}\text{Co}_{0.17})_3\text{P}$ NPs AND $(\text{Cu}_{0.83}\text{Co}_{0.17})_3\text{P}:\text{x at.}\%$ S NPs ($X=10, 20, 30$) COMPOSITIONS FOR HER IN ELECTROLYTIC WATER SPLITTING	238
5.5.3	ELECTROCHEMICAL CHARACTERIZATION OF $(\text{Cu}_{0.83}\text{Co}_{0.17})_3\text{P}:\text{30S}$ NPs AS HER ELECTRO-CATALYST IN H-TYPE PHOTOELECTROCHEMICAL WATER SPLITTING CELL	258
6.0	SUMMARY	265
6.1	1-D SEMICONDUCTOR PHOTOELECTRO-CATALYSTS FOR PHOTOANODES	267
6.2	NANOSTRUCTURED HER ELECTRO-CATALYSTS	270
APPENDIX A		273
A.1	Co AND N CO-DOPED ZnO NANOWIRES (NWs) (PHOTOANODE).....	273
A.1.1	COMPUTATIONAL METHODOLOGY	273
A.1.2	RESULTS OF THE COMPUTATIONAL STUDY.....	276
A.2	Nb AND N CO-DOPED SnO_2 NANOTUBES (NTs) (PHOTOANODE)	284

A.2.1 COMPUTATIONAL METHODOLOGY	284
A.2.2 RESULTS OF THE COMPUTATIONAL STUDY.....	286
A.3 Co(Ir) SOLID SOLUTION HER ELECTRO-CATALYST FOR CATHODE... 293	
A.3.1 COMPUTATIONAL METHODOLOGY	293
A.3.2 RESULTS OF THE COMPUTATIONAL STUDY.....	296
A.4 (Cu_{0.83}Co_{0.17})₃P:S HER ELECTRO-CATALYST FOR CATHODE.....	303
A.4.1 COMPUTATIONAL METHODOLOGY	303
A.4.2 RESULTS OF THE COMPUTATIONAL STUDY.....	306
APPENDIX B	312
BIBLIOGRAPHY.....	314

LIST OF TABLES

Table 1: The lattice parameter and molar volume for ZnO and (Zn _{0.95} Co _{0.05})O:N NWs, along with N concentration for (Zn _{0.95} Co _{0.05})O:N NWs by EDX	73
Table 2: Results of Tauc analysis, Mott-Schottky analysis and photoelectrochemical characterization of ZnO and (Zn _{0.95} Co _{0.05})O:N NWs of different N concentration	95
Table 3: Efficiency of photoelectrochemical water splitting of various photoanode materials, reported in the literature	96
Table 4: Results of EIS analysis of ZnO and (Zn _{0.95} Co _{0.05})O:N NWs of different N concentration, carried out at 0.79 V (vs RHE) in frequency range of 100 mHz-100 kHz (AC amplitude=10 mV) under illumination (100 mW cm ⁻²) in 0.5 M Na ₂ SO ₄ (pH 7) electrolyte solution	100
Table 5: The lattice parameter and molar volume for SnO ₂ and (Sn _{0.95} Nb _{0.05})O ₂ :N NTs, along with N concentration for (Sn _{0.95} Nb _{0.05})O ₂ :N NTs (obtained from EDX analysis)	111
Table 6: Results of Tauc analysis, Mott-Schottky analysis and photoelectrochemical characterization of SnO ₂ , (Sn _{1-x} Nb _x)O ₂ (x=0.05, 0.1) and (Sn _{0.95} Nb _{0.05})O ₂ :N NTs (performed in 0.5 M H ₂ SO ₄ electrolyte solution under illumination of 100 mW cm ⁻² at 26°C)	129
Table 7: Results of EIS analysis of SnO ₂ and (Sn _{0.95} Nb _{0.05})O ₂ :N NTs performed at 0.75 V (RHE) in 0.5 M H ₂ SO ₄ electrolyte solution in frequency range of 100 mHz-100 kHz under illumination (100 mW cm ⁻²) at 26°C	132
Table 8: Efficiency of photoelectrochemical water splitting of various photoanode materials, reported in the literature	136
Table 9: The lattice parameters and quantitative elemental composition analysis by EDX for (Sn _{0.95} Nb _{0.05})O ₂ :N-600 NTs, [WO ₃ -(Sn _{0.95} Nb _{0.05})O ₂ :N-600]-1 NTs, [WO ₃ -(Sn _{0.95} Nb _{0.05})O ₂ :N-600]-2 NTs and [WO ₃ -(Sn _{0.95} Nb _{0.05})O ₂ :N-600]-3 NTs	149
Table 10: Results of Mott-Schottky analysis, structural and photoelectrochemical characterization of (Sn _{0.95} Nb _{0.05})O ₂ :N-600 NTs, [WO ₃ -(Sn _{0.95} Nb _{0.05})O ₂ :N-600]-1 NTs, [WO ₃ -(Sn _{0.95} Nb _{0.05})O ₂ :N-600]-2 NTs and [WO ₃ -(Sn _{0.95} Nb _{0.05})O ₂ :N-600]-3 NTs	168

Table 11: Efficiency of photoelectrochemical water splitting of various photoanode materials, reported in the literature	170
Table 12: Results of ICP analysis on 0.5 M H ₂ SO ₄ solution after chronoamperometry test of [WO ₃ -(Sn _{0.95} Nb _{0.05})O ₂ :N-600]-2 NTs	188
Table 13: The lattice parameter, molar volume, and composition determined from EDX and XPS analysis of Co _{1-x} (Ir _x) electrocatalyst.....	199
Table 14: Results of electrochemical characterization for HER of Co _{1-x} (Ir _x) and Pt/C in 0.5 M H ₂ SO ₄ at 26°C	208
Table 15: Results of EIS analysis of Co _{1-x} (Ir _x) and Pt/C, carried out at (-0.05 V vs RHE) in frequency range of 100mHz-100kHz in 0.5 M H ₂ SO ₄ at 26°C and Tafel plot analysis	215
Table 16: Results of structural and electrochemical characterization for HER of pure Cu ₃ P NPs (total loading=0.7 mg/cm ²), (Cu _{0.83} Co _{0.17}) ₃ P NPs (total loading=0.7 mg/cm ²), (Cu _{0.83} Co _{0.17}) ₃ P:S NPs (total loading=0.7 mg/cm ²) and Pt/C (Pt loading=0.4 mg _{Pt} /cm ²) in 0.5 M H ₂ SO ₄ electrolyte solution at 26°C	241
Table 17: Comparison of HER performance of (Cu _{0.83} Co _{0.17}) ₃ P:30S NPs with other reported non-noble metals based HER electro-catalysts in acidic media	244
Table 18: Results of ICP analysis on 0.5 M H ₂ SO ₄ solution after chronoamperometry test of (Cu _{0.83} Co _{0.17}) ₃ P:30S NPs	258
Table 19: Calculated and experimental optical band gaps E _{BG} for pure and doped ZnO.....	277
Table 20: Calculated and experimental values of optical band gap (E _{BG}) of pure and doped SnO ₂	289
Table 21: ΔG _{H*} in eV calculated for different materials and different types of the active sites.	298
Table 22: Average and interpolated ΔG _{H*} for various Co-Ir alloys	299
Table 23: Calculated free energy of hydrogen adsorption ΔG _{H*} , the electronic density of states at the Fermi level, and cohesive energy -E _{coh} for all materials considered in the present study	311

LIST OF FIGURES

Figure 1: Current and predicted global energy consumption.....	1
Figure 2: Different ways of production of hydrogen using solar energy ¹³	9
Figure 3: Schematic of photocatalytic water splitting	11
Figure 4: Schematic diagram of PEC water splitting in H-type cell.....	14
Figure 5: Hydrogen fuel economy	16
Figure 6: Energy band diagram for semiconductor material (photoanode) and cathode electro-catalyst.....	21
Figure 7: Effect of Co and N co-doping on the band gap of ZnO	35
Figure 8: Vertical orientation of semiconductor material facilitating charge transport in the material.....	36
Figure 9: Effect of Nb and N co-doping on the band gap of SnO ₂	37
Figure 10: Schematic illustration of bilayer structure, [WO ₃ -(Sn _{0.95} Nb _{0.05})O ₂ :N-600] NTs	40
Figure 11: Schematic of the process for synthesizing of ZnO nanowires (NWs) using liquid phase deposition process	51

Figure 12: Schematic of the synthesis process of $[\text{WO}_3-(\text{Sn}_{0.95}\text{Nb}_{0.05})\text{O}_2:\text{N}-600]$ NTs	54
Figure 13: Schematic of H-type PEC water splitting cell for photoelectrochemical characterization	62
Figure 14: Schematic of three electrode cell for electrochemical characterization of electrocatalysts for HER (in electrolytic water splitting).....	66
Figure 15: The XRD patterns of ZnO and $(\text{Zn}_{0.95}\text{Co}_{0.05})\text{O}:\text{N}$ NWs of different N concentration in wide angle 2θ scan	72
Figure 16: SEM micrograph showing top view, cross-sectional view and EDX spectrum of $(\text{Zn}_{0.95}\text{Co}_{0.05})\text{O}:\text{N}-600$ NWs	74
Figure 17: The bright field TEM image of $(\text{Zn}_{0.95}\text{Co}_{0.05})\text{O}:\text{N}-600$ NWs showing the presence of nanowire with the diameter of ~ 220 nm	75
Figure 18: The HRTEM image of $(\text{Zn}_{0.95}\text{Co}_{0.05})\text{O}:\text{N}-600$ NWs showing lattice fringes with a spacing of ~ 0.264 nm corresponding to (002) crystal plane	76
Figure 19: The XPS spectra of $(\text{Zn}_{0.95}\text{Co}_{0.05})\text{O}:\text{N}$ NWs of different N concentration showing Zn $2p_{3/2}$ peak	78
Figure 20: The XPS spectra of $(\text{Zn}_{0.95}\text{Co}_{0.05})\text{O}:\text{N}$ NWs of different N concentration showing N 1s peak	79
Figure 21: The XPS spectra of $(\text{Zn}_{0.95}\text{Co}_{0.05})\text{O}:\text{N}$ NWs of different N concentration showing Co $2p_{1/2}$ and $2p_{3/2}$ doublet	80
Figure 22: UV-Vis absorption spectra of ZnO, $(\text{Zn}_{0.95}\text{Co}_{0.05})\text{O}$ and $(\text{Zn}_{0.95}\text{Co}_{0.05})\text{O}:\text{N}$ NWs of different N concentration.....	82
Figure 23: Tauc analysis of ZnO and $(\text{Zn}_{0.95}\text{Co}_{0.05})\text{O}:\text{N}$ NWs of different N concentration.....	83

Figure 24: Mott-Schottky plot of ZnO NWs obtained by performing EIS measurements in dark at a frequency of 7.5 kHz with an AC amplitude of 10 mV between voltage window of -0.8 V to 1.2 V (<i>vs</i> NHE) in 0.5 M Na ₂ SO ₄ (pH 7) electrolyte solution at 26°C.....	86
Figure 25: Mott-Schottky plot of (Zn _{0.95} Co _{0.05})O:N NWs of different N concentration obtained by performing EIS measurements in dark at a frequency of 7.5 kHz with an AC amplitude of 10 mV between voltage window of -0.8 V to 1.2 V (<i>vs</i> NHE) in 0.5 M Na ₂ SO ₄ (pH 7) electrolyte solution at 26°C	87
Figure 26: IPCE spectra of ZnO and (Zn _{0.95} Co _{0.05})O:N NWs of different N concentration.....	89
Figure 27: Linear scan voltammogram (LSV) curves for ZnO and (Zn _{0.95} Co _{0.05})O:N NWs of different N concentration in dark and illumination of 100 mW cm ⁻² measured in 0.5 M Na ₂ SO ₄ (pH 7) electrolyte solution at 26°C, before and after <i>i</i> R _Ω correction	92
Figure 28: Applied bias photon-to-current efficiency (ABPE) as a function of applied potential for (Zn _{0.95} Co _{0.05})O:N NWs of different N concentration	93
Figure 29: Applied bias photon-to-current efficiency (ABPE) as a function of applied potential for ZnO NWs.....	94
Figure 30: EIS spectra of ZnO and (Zn _{0.95} Co _{0.05})O:N NWs of different N concentration obtained at 0.79V (<i>vs</i> RHE) in 0.5 M Na ₂ SO ₄ (pH 7) electrolyte solution at 26°C in the frequency range of 100 mHz to 100 kHz (AC amplitude=10 mV) under illumination (100 mW cm ⁻²), with the circuit used for fitting experimental data.....	99
Figure 31: The variation of photocurrent density <i>vs</i> time in the chronoamperometry test of (Zn _{0.95} Co _{0.05})O:N-600 NWs, performed in a 0.5 M Na ₂ SO ₄ (pH 7) electrolyte solution under a constant potential of 0.79V (<i>vs</i> RHE) at 26°C for 24 h.....	103
Figure 32: Linear scan voltammogram (LSV) curves for (Zn _{0.95} Co _{0.05})O:N-600 NWs in dark and illumination of 100 mW cm ⁻² measured in 0.5 M Na ₂ SO ₄ (pH 7) electrolyte solution at 26°C, obtained before and after 24 h of chronoamperometry test.....	104
Figure 33: The variation of photocurrent density <i>vs</i> time in the chronoamperometry test of ZnO NWs, performed in a 0.5 M Na ₂ SO ₄ (pH 7) electrolyte solution under a constant potential of 0.79V (<i>vs</i> RHE) at 26°C for 24 h	105

Figure 34: Theoretical and experimentally measured concentration of H ₂ and O ₂ gases, measured during chronoamperometry test of (Zn _{0.95} Co _{0.05})O:N-600 NWs, performed in 0.5 M Na ₂ SO ₄ (pH 7) electrolyte solution under a constant potential of 0.79V (vs RHE) at 26°C for 24 h	107
Figure 35: The XRD patterns of pure SnO ₂ NTs and (Sn _{0.95} Nb _{0.05})O ₂ :N NTs of different N concentration in wide angle 2θ scan.....	110
Figure 36: SEM micrograph showing top view, cross-sectional view and EDX spectrum of (Sn _{0.95} Nb _{0.05})O ₂ :N-600 NTs	112
Figure 37: The bright field TEM images of (Sn _{0.95} Nb _{0.05})O ₂ :N-600 NTs showing hollow nanotubes of diameter ~180-220 nm.....	113
Figure 38: The XPS spectra of (Sn _{0.95} Nb _{0.05})O ₂ :N NTs showing Sn 3d _{3/2} and 3d _{5/2} doublet.....	115
Figure 39: The XPS spectra of (Sn _{0.95} Nb _{0.05})O ₂ :N NTs showing N 1s peak	116
Figure 40: The XPS spectra of (Sn _{0.95} Nb _{0.05})O ₂ :N NTs showing Nb 3d _{3/2} and 3d _{5/2} doublet.....	117
Figure 41: UV-vis absorption spectra of SnO ₂ NTs and (Sn _{0.95} Nb _{0.05})O ₂ :N NTs of different N concentration	119
Figure 42: Tauc analysis of SnO ₂ NTs and (Sn _{0.95} Nb _{0.05})O ₂ :N NTs of different N concentration	120
Figure 43: Mott-Schottky plots of (Sn _{0.95} Nb _{0.05})O ₂ :N NTs of different N concentration.....	122
Figure 44: Mott-Schottky plot of SnO ₂ NTs.....	123
Figure 45: IPCE spectra of (Sn _{0.95} Nb _{0.05})O ₂ :N NTs of different N concentration measured at potential of ~0V (vs RHE).....	125

Figure 46: The linear scan voltammogram (LSV) curves for SnO₂ NTs in dark and illumination of 100 mW cm⁻² measured in 0.5 M H₂SO₄ at 26°C, before and after iR_Ω correction 127

Figure 47: The linear scan voltammogram (LSV) curves for (Sn_{0.95}Nb_{0.05})O₂:N NTs of different N concentration in dark and illumination of 100 mW cm⁻² measured in 0.5 M H₂SO₄ at 26°C, before and after iR_Ω correction..... 128

Figure 48: EIS spectra of SnO₂ NTs and (Sn_{0.95}Nb_{0.05})O₂:N NTs of different N concentration obtained at 0.75 V (*vs* RHE) in 0.5 M H₂SO₄ at 26°C in the frequency range of 100 mHz to 100 kHz under illumination (100 mW cm⁻²) with the circuit used for fitting experimental data 131

Figure 49: Applied bias photon-to-current efficiency (ABPE) as a function of applied potential for SnO₂ NTs 134

Figure 50: Applied bias photon-to-current efficiency (ABPE) as a function of applied potential for (Sn_{0.95}Nb_{0.05})O₂:N NTs of different N concentration 135

Figure 51: The variation of photocurrent density *vs* time in the chronoamperometry test of (Sn_{0.95}Nb_{0.05})O₂:N-600 NTs, performed in 0.5 M H₂SO₄ solution under a constant potential of 0.75 V (*vs* RHE) at 26°C for 24 h under illumination (100 mW cm⁻²)... 139

Figure 52: The variation of photocurrent density *vs* time in the chronoamperometry test of (Sn_{0.95}Nb_{0.05})O₂:N-600 NTs, performed in 0.5 M H₂SO₄ solution at 26°C under a constant potential of 0.75 V (*vs* RHE) at 100 mW/cm² with 200 sec light ON/OFF cycles for 25 min 140

Figure 53: The linear scan voltammogram (LSV) curve for (Sn_{0.95}Nb_{0.05})O₂:N-600 NTs in dark and under illumination of 100 mW cm⁻² measured in 0.5 M H₂SO₄ at 26°C, obtained before and after 24 h chronoamperometry test..... 141

Figure 54: Theoretical and experimentally measured concentration of H₂ gas and experimentally measured concentration of O₂ gas, measured during 24 h chronoamperometry test of (Sn_{0.95}Nb_{0.05})O₂:N-600 NTs, performed in 0.5 M H₂SO₄ solution under a constant potential of 0.75 V (*vs* RHE) at 26°C for 24 h 143

Figure 55: The XRD patterns of SnO ₂ NTs, (Sn _{0.95} Nb _{0.05})O ₂ :N-600 NTs, [WO ₃ -(Sn _{0.95} Nb _{0.05})O ₂ :N-600]-1 NTs, [WO ₃ -(Sn _{0.95} Nb _{0.05})O ₂ :N-600]-2 NTs and [WO ₃ -(Sn _{0.95} Nb _{0.05})O ₂ :N-600]-3 NTs in wide angle 2θ scan	146
Figure 56: SEM micrograph showing top and cross-sectional view along with EDX spectrum of [WO ₃ -(Sn _{0.95} Nb _{0.05})O ₂ :N-600]-2 NTs	148
Figure 57: The bright field TEM images of (Sn _{0.95} Nb _{0.05})O ₂ :N-600 NT, [WO ₃ -(Sn _{0.95} Nb _{0.05})O ₂ :N-600]-1 NT, [WO ₃ -(Sn _{0.95} Nb _{0.05})O ₂ :N-600]-2 NT and [WO ₃ -(Sn _{0.95} Nb _{0.05})O ₂ :N-600]-3 NT.....	150
Figure 58: The XPS spectra of (a) [WO ₃ -(Sn _{0.95} Nb _{0.05})O ₂ :N-600]-1 NTs, (b) [WO ₃ -(Sn _{0.95} Nb _{0.05})O ₂ :N-600]-2 NTs and (c) [WO ₃ -(Sn _{0.95} Nb _{0.05})O ₂ :N-600]-3 NTs, showing Sn 3d _{3/2} and 3d _{5/2} doublet.....	152
Figure 59: The XPS spectra of (a) [WO ₃ -(Sn _{0.95} Nb _{0.05})O ₂ :N-600]-1 NTs, (b) [WO ₃ -(Sn _{0.95} Nb _{0.05})O ₂ :N-600]-2 NTs and (c) [WO ₃ -(Sn _{0.95} Nb _{0.05})O ₂ :N-600]-3 NTs, showing N 1s peak	153
Figure 60: The XPS spectra of (a) [WO ₃ -(Sn _{0.95} Nb _{0.05})O ₂ :N-600]-1 NTs, (b) [WO ₃ -(Sn _{0.95} Nb _{0.05})O ₂ :N-600]-2 NTs and (c) [WO ₃ -(Sn _{0.95} Nb _{0.05})O ₂ :N-600]-3 NTs, showing Nb 3d _{3/2} and 3d _{5/2} doublet.....	154
Figure 61: The XPS spectra of (a) [WO ₃ -(Sn _{0.95} Nb _{0.05})O ₂ :N-600]-1 NTs, (b) [WO ₃ -(Sn _{0.95} Nb _{0.05})O ₂ :N-600]-2 NTs and (c) [WO ₃ -(Sn _{0.95} Nb _{0.05})O ₂ :N-600]-3 NTs, showing W 4f _{5/2} and 4f _{7/2} doublet.....	155
Figure 62: UV-vis absorption spectra of (Sn _{0.95} Nb _{0.05})O ₂ :N-600 NTs, [WO ₃ -(Sn _{0.95} Nb _{0.05})O ₂ :N-600]-1 NTs, [WO ₃ -(Sn _{0.95} Nb _{0.05})O ₂ :N-600]-2 NTs and [WO ₃ -(Sn _{0.95} Nb _{0.05})O ₂ :N-600]-3 NTs	158
Figure 63: UV-vis absorption spectra of (a) FTO substrate and (b) FTO annealed at 600 ⁰ C in NH ₃ atmosphere	158
Figure 64: Valence band spectra of SnO ₂ , (Sn _{0.95} Nb _{0.05})O ₂ :N-600 and [WO ₃ -(Sn _{0.95} Nb _{0.05})O ₂ :N-600]-2 NTs.....	159

Figure 65: Mott-Schottky plots of $[\text{WO}_3\text{-(Sn}_{0.95}\text{Nb}_{0.05}\text{O}_2\text{:N-600)]-1$ NTs, $[\text{WO}_3\text{-(Sn}_{0.95}\text{Nb}_{0.05}\text{O}_2\text{:N-600)]-2$ NTs and $[\text{WO}_3\text{-(Sn}_{0.95}\text{Nb}_{0.05}\text{O}_2\text{:N-600)]-3$ NTs.....	163
Figure 66: The linear scan voltammogram (LSV) curves of $(\text{Sn}_{0.95}\text{Nb}_{0.05}\text{O}_2\text{:N-600})$ NTs, $[\text{WO}_3\text{-(Sn}_{0.95}\text{Nb}_{0.05}\text{O}_2\text{:N-600)]-1$ NTs, $[\text{WO}_3\text{-(Sn}_{0.95}\text{Nb}_{0.05}\text{O}_2\text{:N-600)]-2$ NTs and $[\text{WO}_3\text{-(Sn}_{0.95}\text{Nb}_{0.05}\text{O}_2\text{:N-600)]-3$ NTs in dark and under illumination of 100 mW/cm^2 measured in $0.5 \text{ M H}_2\text{SO}_4$ at 26°C , before and after iR_Ω correction.....	166
Figure 67: EIS spectra of $(\text{Sn}_{0.95}\text{Nb}_{0.05}\text{O}_2\text{:N-600})$ NTs, $[\text{WO}_3\text{-(Sn}_{0.95}\text{Nb}_{0.05}\text{O}_2\text{:N-600)]-1$ NTs, $[\text{WO}_3\text{-(Sn}_{0.95}\text{Nb}_{0.05}\text{O}_2\text{:N-600)]-2$ NTs and $[\text{WO}_3\text{-(Sn}_{0.95}\text{Nb}_{0.05}\text{O}_2\text{:N-600)]-3$ NTs obtained at $\sim 0.1 \text{ V}$ (<i>vs</i> RHE) in $0.5 \text{ M H}_2\text{SO}_4$ at 26°C in the frequency range of 100 mHz to 100 kHz under illumination (100 mW/cm^2).....	172
Figure 68: IPCE plots for $[\text{WO}_3\text{-(Sn}_{0.95}\text{Nb}_{0.05}\text{O}_2\text{:N-600)]-2$ NTs under no bias and applied 0.6 V (<i>vs</i> RHE) bias.....	175
Figure 69: Schematic of PEC process showing losses without and with $\sim 0.6 \text{ V}$ bias.....	180
Figure 70: Variation of open circuit potential (V_{oc}) under light ON/OFF conditions with time for $(\text{Sn}_{0.95}\text{Nb}_{0.05}\text{O}_2\text{:N-600})$ NTs, $[\text{WO}_3\text{-(Sn}_{0.95}\text{Nb}_{0.05}\text{O}_2\text{:N-600)]-1$ NTs, $[\text{WO}_3\text{-(Sn}_{0.95}\text{Nb}_{0.05}\text{O}_2\text{:N-600)]-2$ NTs and $[\text{WO}_3\text{-(Sn}_{0.95}\text{Nb}_{0.05}\text{O}_2\text{:N-600)]-3$ NTs.....	184
Figure 71: Carrier lifetime (τ) as function of open circuit potential (V_{oc}) for $(\text{Sn}_{0.95}\text{Nb}_{0.05}\text{O}_2\text{:N-600})$ NTs, $[\text{WO}_3\text{-(Sn}_{0.95}\text{Nb}_{0.05}\text{O}_2\text{:N-600)]-1$ NTs, $[\text{WO}_3\text{-(Sn}_{0.95}\text{Nb}_{0.05}\text{O}_2\text{:N-600)]-2$ NTs and $[\text{WO}_3\text{-(Sn}_{0.95}\text{Nb}_{0.05}\text{O}_2\text{:N-600)]-3$ NTs.....	185
Figure 72: The variation of photocurrent density <i>vs</i> irradiation time in the chronoamperometry test of $[\text{WO}_3\text{-(Sn}_{0.95}\text{Nb}_{0.05}\text{O}_2\text{:N-600)]-2$ NT, performed in $0.5 \text{ M H}_2\text{SO}_4$ solution under a constant potential of $\sim 0.6 \text{ V}$ (<i>vs</i> RHE) at 26°C for 24 h under illumination (100 mW/cm^2).....	187
Figure 73: Theoretical and experimentally measured concentration of H_2 gas and experimentally measured concentration of O_2 gas measured under illumination (100 mW/cm^2) with no applied potential for $[\text{WO}_3\text{-(Sn}_{0.95}\text{Nb}_{0.05}\text{O}_2\text{:N-600)]-2$ NT measured in $0.5 \text{ M H}_2\text{SO}_4$ solution at 26°C for 24 h	189

Figure 74: Variation of solar-to-hydrogen efficiency (STH) (determined from concentration of evolved H ₂ gas measured under illumination of 100 mW/cm ² with no applied potential as shown in Figure 73) vs irradiation time for [WO ₃ -(Sn _{0.95} Nb _{0.05})O ₂ :N-600]-2 NTs	191
Figure 75: The XRD patterns of Co _{1-x} (Ir _x) (x=0, 0.2, 0.3, 0.4, 1) nanoparticles in wide angle 2θ scan.....	196
Figure 76: Variation of molar volume of Co _{1-x} (Ir _x) (x=0, 0.2, 0.3, 0.4, 1) with iridium content	197
Figure 77: Co-Ir binary equilibrium phase diagram	198
Figure 78: The bright field TEM image of Co _{0.7} (Ir _{0.3}) shows the presence of fine nanoparticles (~5-9 nm) with HRTEM image showing lattice fringes with a spacing of ~0.213 nm	200
Figure 79: The bright field TEM image of Co _{0.6} (Ir _{0.4}) shows the presence of fine nanoparticles (~4-7 nm).....	201
Figure 80: The HRTEM image of Co _{0.6} (Ir _{0.4}) shows lattice fringes with a spacing of ~0.215 nm	202
Figure 81: SEM micrograph with x-ray maps of Co and Ir and EDX spectrum of Co _{0.6} (Ir _{0.4}) ..	203
Figure 82: The XPS spectra of Co _{1-x} (Ir _x) (x=0.2, 0.3, 0.4, 1) showing (a) Ir 4f _{5/2} and 4f _{7/2} doublet	204
Figure 83: The XPS spectra of Co _{1-x} (Ir _x) (x=0.2, 0.3, 0.4) showing (b) Co 2p _{1/2} and 2p _{3/2} doublet	206
Figure 84: The iR _Ω corrected linear scan voltammogram (LSV) curves for HER of Co _{1-x} (Ir _x) (x=0.2, 0.3, 0.4) and Pt/C, measured in 0.5 M H ₂ SO ₄ at 26 ⁰ C at scan rate of 1 mV/sec	210

Figure 85: EIS spectra of $\text{Co}_{1-x}(\text{Ir}_x)$ ($x=0.2, 0.3, 0.4$), Ir-NPs and Pt/C obtained at (-0.05V vs RHE) in 0.5 M H_2SO_4 at 26 ⁰ C in the frequency range of 100 mHz to 100 kHz.....	213
Figure 86: EIS spectra of pure Co NPs obtained at (-0.05V vs RHE) in 0.5 M H_2SO_4 at 26 ⁰ C in the frequency range of 100 mHz to 100 kHz	214
Figure 87: Tafel plot of $\text{Co}_{1-x}(\text{Ir}_x)$ ($x=0.2, 0.3, 0.4$) and Pt/C, before and after iR_{Ω} correction (in 0.5 M H_2SO_4)	217
Figure 88: Tafel plot of Co-NPs, before and after iR_{Ω} correction (in 0.5 M H_2SO_4).....	219
Figure 89: Tafel plot of Ir-NPs, before and after iR_{Ω} correction (in 0.5 M H_2SO_4).....	220
Figure 90: The variation of current vs time in the chronoamperometry test of $\text{Co}_{1-x}(\text{Ir}_x)$ ($x=0.3, 0.4$) and Pt/C, performed in a 0.5 M H_2SO_4 solution under a constant potential of (-0.05V vs RHE) at 26 ⁰ C for 24 h.....	221
Figure 91: Amount of H_2 evolved as a function of irradiation time for $\text{Co}_{1-x}(\text{Ir}_x)$ ($x=0.3, 0.4$) and Pt/C as cathode electro-catalyst for HER and $(\text{Sn}_{0.95}\text{Nb}_{0.05})\text{O}_2\text{:N-600}$ NTs as photoanode/working electrode, obtained in 0.5 M H_2SO_4 solution at 26 ⁰ C under illumination (100 mW/cm ²).....	223
Figure 92: Applied bias photon-to-current efficiency (ABPE) as a function of irradiation time for $\text{Co}_{1-x}(\text{Ir}_x)$ ($x=0.3, 0.4$) and Pt/C as cathode electro-catalyst for HER and $(\text{Sn}_{0.95}\text{Nb}_{0.05})\text{O}_2\text{:N-600}$ NTs as photoanode/working electrode, obtained in 0.5 M H_2SO_4 solution at 26 ⁰ C under illumination (100 mW/cm ²)	225
Figure 93: The XRD patterns of pure Cu_3P nanoparticiles (NPs), $(\text{Cu}_{0.83}\text{Co}_{0.17})_3\text{P}$ NPs and $(\text{Cu}_{0.83}\text{Co}_{0.17})_3\text{P:S}$ NPs of different S concentration in wide angle 2θ scan	229
Figure 94: The bright field TEM image of $(\text{Cu}_{0.83}\text{Co}_{0.17})_3\text{P:30S}$ NPs	230
Figure 95: SEM micrograph with EDX spectrum of $(\text{Cu}_{0.83}\text{Co}_{0.17})_3\text{P:30S}$ NPs.....	231

Figure 96: Elemental x-ray maps of $(\text{Cu}_{0.83}\text{Co}_{0.17})_3\text{P}:30\text{S}$ NPs.....	232
Figure 97: The XPS spectra of pure Cu_3P NPs and $(\text{Cu}_{0.83}\text{Co}_{0.17})_3\text{P}:30\text{S}$ NPs in the Cu $2p_{3/2}$ region.....	235
Figure 98: The XPS spectra of pure Cu_3P NPs and $(\text{Cu}_{0.83}\text{Co}_{0.17})_3\text{P}:30\text{S}$ NPs in the P 2p region	236
Figure 99: The XPS spectra of pure Cu_3P NPs and $(\text{Cu}_{0.83}\text{Co}_{0.17})_3\text{P}:30\text{S}$ NPs in the Co $2p_{3/2}$ region.....	237
Figure 100: The XPS spectra of pure Cu_3P NPs and $(\text{Cu}_{0.83}\text{Co}_{0.17})_3\text{P}:30\text{S}$ NPs in the S 2p region	238
Figure 101: The iR_{Ω} corrected linear scan voltammogram (LSV) curves for HER of pure Cu_3P NPs (total loading= 0.7 mg/cm^2), $(\text{Cu}_{0.83}\text{Co}_{0.17})_3\text{P}$ NPs (total loading= 0.7 mg/cm^2), $(\text{Cu}_{0.83}\text{Co}_{0.17})_3\text{P}:\text{S}$ NPs of different S concentration (total loading= 0.7 mg/cm^2), Ti foil (current collector) and commercial Pt/C (Pt loading= $0.4 \text{ mg}_{\text{Pt}}/\text{cm}^2$), obtained in 0.5 M H_2SO_4 electrolyte solution at 26°C using scan rate of 1 mV/sec	239
Figure 102: EIS spectra of $(\text{Cu}_{0.83}\text{Co}_{0.17})_3\text{P}$ NPs (total loading= 0.7 mg/cm^2), $(\text{Cu}_{0.83}\text{Co}_{0.17})_3\text{P}:\text{S}$ NPs of different S concentration (total loading= 0.7 mg/cm^2) and commercial Pt/C (Pt loading= $0.4 \text{ mg}_{\text{Pt}}/\text{cm}^2$) obtained at (-0.1 V vs RHE) in 0.5 M H_2SO_4 electrolyte solution at 26°C in the frequency range of 100 mHz to 100 kHz (Amplitude=10 mV)	249
Figure 103: EIS spectrum of Cu_3P NPs (total loading= 0.7 mg/cm^2) obtained at (-0.05 V vs RHE) in 0.5 M H_2SO_4 electrolyte solution at 26°C in the frequency range of 100 mHz to 100 kHz (Amplitude=10 mV)	250
Figure 104: Tafel plot of pure Cu_3P NPs (in 0.5 M H_2SO_4 electrolyte solution)	253
Figure 105: Tafel plot of $(\text{Cu}_{0.83}\text{Co}_{0.17})_3\text{P}$ NPs (in 0.5 M H_2SO_4 electrolyte solution).....	254

Figure 106: Tafel plot of $(\text{Cu}_{0.83}\text{Co}_{0.17})_3\text{P:S}$ NPs of different S concentration (total loading=0.7 mg/cm^2) and commercial Pt/C (Pt loading=0.4 $\text{mg}_{\text{Pt}}/\text{cm}^2$) (in 0.5 M H_2SO_4 electrolyte solution).....	255
Figure 107: The variation of current vs time in the chronoamperometry (CA) test of $(\text{Cu}_{0.83}\text{Co}_{0.17})_3\text{P:30S}$ NPs (total loading=0.7 mg/cm^2) and commercial Pt/C (Pt loading=0.4 $\text{mg}_{\text{Pt}}/\text{cm}^2$), performed in 0.5 M H_2SO_4 electrolyte solution at a constant potential of (-0.05 V vs RHE) at 26 ⁰ C for 24 h.....	256
Figure 108: The iR_{Ω} corrected linear scan voltammogram (LSV) curve for HER of $(\text{Cu}_{0.83}\text{Co}_{0.17})_3\text{P:30S}$ NPs (total loading=0.7 mg/cm^2), obtained in 0.5 M H_2SO_4 electrolyte solution at 26 ⁰ C using scan rate of 1 mV/sec, after 24 h of CA test	257
Figure 109: Amount of H_2 evolved at cathode as a function of irradiation time for $(\text{Cu}_{0.83}\text{Co}_{0.17})_3\text{P:30S}$ NPs (total loading=0.7 mg/cm^2) and Pt/C (Pt loading=0.4 $\text{mg}_{\text{Pt}}/\text{cm}^2$) as cathode electro-catalyst for HER	260
Figure 110: ABPE as a function of irradiation time for $(\text{Cu}_{0.83}\text{Co}_{0.17})_3\text{P:30S}$ NPs (total loading=0.7 mg/cm^2) and Pt/C (Pt loading=0.4 $\text{mg}_{\text{Pt}}/\text{cm}^2$) as cathode electro-catalyst for HER	261
Figure 111: Projected density of states for pure ZnO. Fermi level is set for zero. Fermi level is set for zero	277
Figure 112: Total and projected density of states for ZnO doped with 6.25 at% of Co. Top panel is for spin-up, bottom panel is for spin-down. Fermi level is set for zero	279
Figure 113: Projected density of states for ZnO doped with 6.25 at% of N. Fermi level is set for zero	280
Figure 114: Projected density of states for ZnO doped with 6.25 at% of Co and 6.25 at% of N. Top panel is for spin-up, bottom panel is for spin-down. Fermi level is set for zero	282
Figure 115: Projected density of states for ZnO doped with 6.25 at% of Co and 12.5 at% of N. Top panel is for spin-up, bottom panel is for spin-down. Fermi level is set for zero	283

Figure 116: Projected density of states for pure SnO ₂ , SnO ₂ doped with 6.25 at% of Nb, SnO ₂ doped with 3.125 at% of N. Fermi level is set for zero.....	288
Figure 117: Projected density of states for (Sn _{0.94} Nb _{0.06})(O _{1.97} N _{0.03}), (Sn _{0.94} Nb _{0.06})(O _{1.94} N _{0.06}), (Sn _{0.94} Nb _{0.06})(O _{1.875} N _{0.125}). Fermi level is set for zero	292
Figure 118: (111) fcc surface with [2x3] (solid lines) and [3x3] (extended with dashed lines) unit cell. Yellow balls – the top layer; blue balls – middle layer; light gray balls – the bottom layer. Arrows denote <i>fcc</i> active sites. Numbers 1, 2, and 3 denote sites with different surroundings	295
Figure 119: Experimentally measured exchange current density (<i>i</i> ₀) as a function of calculated Δ <i>G</i> _H * for pure Co, Ir, Pt and Co-Ir alloys.....	301
Figure 120: Surface slab of Cu ₃ P structure doped with Co and S. Red box is the unit cell used in all DFT calculations. Small blue balls – Cu, small green – Co, large yellow – P, large orange – S, the smallest black – hydrogen atoms attached to the surface on active sites. Vectors <i>a</i> , <i>b</i> , and <i>c</i> correspond to the bulk crystal structure lattice parameters	305
Figure 121: Calculated density of electronic states for pure Cu ₃ P, (Co _{0.17} Cu _{0.87}) ₃ P and (Co _{0.17} Cu _{0.87}) ₃ P _{0.5} :S _{0.5} ; Fermi level corresponds to zero energy	310

1.0 INTRODUCTION

1.1 HYDROGEN-THE NEXT GENERATION FUEL

The major challenge that we are facing today is the identification of alternate clean and environmentally benign energy sources, capable of meeting the global energy demand. Currently, the major portion of this global energy demand (14,361 Mtoe) is completely met by the combustion of fossil fuels (**Figure 1**).¹⁻³ However, the excess consumption and thus correspondingly, rapid depletion of fossil fuels has led to deleterious effects on the environment due to increased levels of pollutants (CO₂, NO_x, SO_x, etc.) released into the atmosphere.⁴⁻¹¹

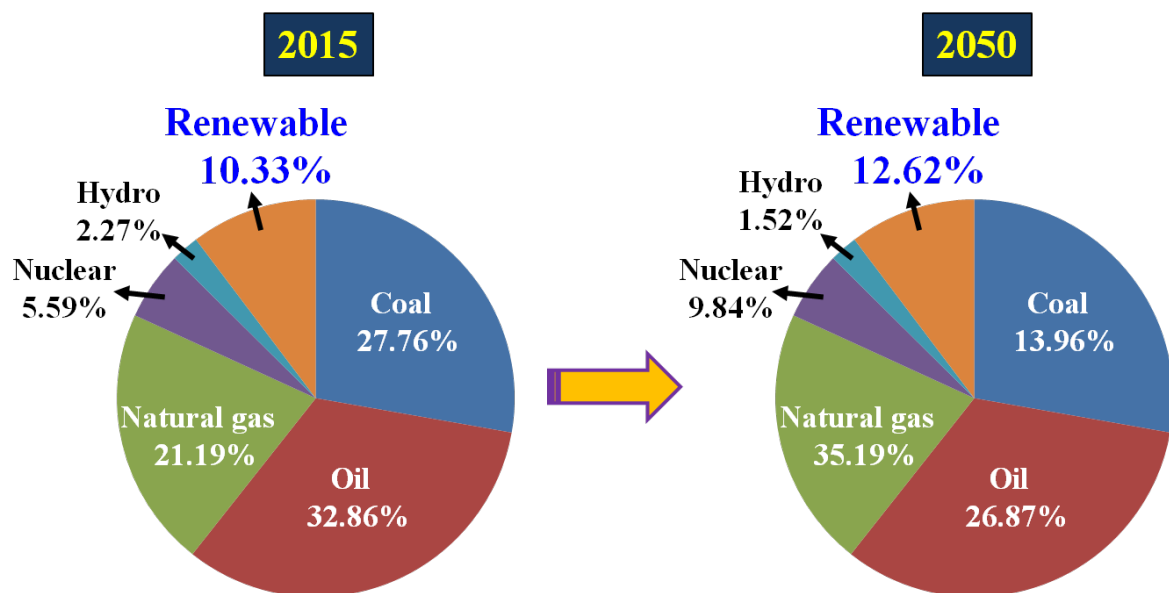


Figure 1: Current and predicted global energy consumption

The current world population is estimated at 7.2 billion.¹⁻³ It is predicted that the world population will rise by ~48% in 2050, which will also lead to further increase in the global energy demand.¹⁻³ Accordingly, the predicted global energy demand in 2050 is 19,679 Mtoe.¹⁻³ If the global energy demand is continued to be met by the combustion of fossil fuels, the projected rise in CO₂ (a major contributor of global greenhouse gas emissions) emissions will increase from ~33 Gt in 2015 to ~55 Gt in 2050.¹⁻³ Despite rising awareness of these serious concerns, the predicted contribution from the renewable energy sources to global energy demand in 2050 is only ~13%, as seen in **Figure 1**.¹⁻³ The best solution to addressing these challenges and minimization of greenhouse gas emissions is the identification of clean (low carbon footprint), reliable, safe and economically producible energy source, which will be easy to store, distribute and capable of meeting the colossal global energy demand. This approach will help to minimize our dependence on fossil fuels and meeting the global energy demand in a sustainable and economic manner.

In this direction, hydrogen has been considered as a promising energy carrier as a replacement of gasoline, due to its high energy density (120 MJ/kg for H₂ higher than 44.4 MJ/kg for Gasoline) and environmentally benign nature.^{6-9, 11-13} Thus, being the most lightweight fuel and having low carbon footprint, it possesses ability in serving as promising energy source and offering clean, efficient, economic and reliable energy supply for meeting the global energy demand with minimum greenhouse gas emissions.^{14, 15} Hydrogen can be used as a fuel in proton exchange membrane fuel cells (PEMFCs) to produce electricity. PEMFCs offer number of advantages. They operate at low temperatures (<120°C) which results in quick start-up, extended durability of system components and low weight and volume due to elimination of additional

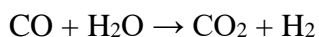
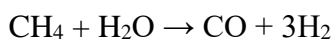
steps of fuel reformation. The simple system design would be reflected in the ease of operation, reduced cost and high reliability.^{5, 16-20} In addition, PEMFCs can be distributed easily without any need of central power generation.

These features of PEMFCs make them promising energy source for portable devices (e.g. Laptops, printers, cameras, etc.), stationary units (e.g. residential power systems, uninterruptible power systems, etc.) and automobile applications. Hence, hydrogen is indeed an attractive alternative to fossil fuels. In addition, H₂ is an important chemical with global production rate of 50 billion kg per year and used in petroleum refining and production of ammonia based fertilizers.²¹ Adopting hydrogen based fuel economy will help in lowering our dependence on fossil fuels and also minimize greenhouse gas emissions. However, the economic production of clean and pure hydrogen, along with cost effective storage and distribution are the roadblocks in the commercialization of hydrogen as a fuel, which need to be addressed.^{22, 23}

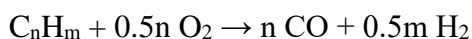
1.2 HYDROGEN PRODUCTION TECHNOLOGIES

Currently, the production of hydrogen on industrial level involves steam reforming of natural gas.^{7, 9} Other widely used methods for hydrogen production are partial oxidation of hydrocarbons and coal gasification. These processes are shown below as:

- Steam reforming of natural gas



- Partial oxidation of hydrocarbons



- Coal gasification



The drawback of these processes are high operating temperature (700°C-1000°C) and production of CO₂-undesired greenhouse pollutant.^{7,9} For these processes to be sustainable in the long time run, their coupling with technology of capture and storage of CO₂ is important. The development of economical and cost-effective CO₂ capture technology is very essential to have an environmental friendly process of production of hydrogen. There are currently a wide range of technologies available for CO₂ capture. These processes have been practiced for a long time in chemical and petrochemical industries.^{24, 25} Existing technologies are based on physical or chemical separation of CO₂, which include absorption, adsorption, cryogenics and membranes.^{24, 25} Absorption techniques use a suitable solvent to absorb CO₂ from flue gas stream. Alkanolamines e.g. monoethanolamine (MEA) and diethanolamine (DMEA) are used in chemical absorption while methanol, dimethylether, polyethylene glycol and sulfolanes are used in physical absorption.^{24, 25} Energy intensive solvent regeneration and equipment corrosion in presence of O₂ are the key challenges in absorption technique which need to be addressed. Additionally, flue gas contaminants like SO_x and NO_x can have negative impact on the process performance.

Adsorption techniques such as pressure swing adsorption (PSA) and temperature swing adsorption (TSA), which utilize solid sorbents e.g. zeolites, alumina and activated carbon, also suffer from energy intensive regeneration.²⁴⁻²⁸ TSA requires long heating and cooling time leading to long cycle time and thus, large adsorbent inventory needs which increases the investment in adsorbent.²⁵ In addition, repeated cycling is responsible for reduced adsorption capacity known as thermal aging for TSA.²⁵ Porous membranes, which work on principle of size

exclusion, have a major drawback of low throughput, requiring multistage operation or stream recycling.²⁴ For the cryogenic distillation, despite the delivery of a highly pure stream of liquid CO₂ for transport and sequestration, the conditions are hard to achieve and maintain, leading to energy intensive operation and thus, high system cost.²⁴ There is ongoing work on developing new process for CO₂ capture, which will offer maximum efficiency with superior CO₂ selectivity and minimum energy requirement.

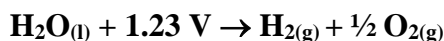
In addition to CO₂ capture and storage, there is a lot of ongoing work on the improvement of catalytic steam reforming of natural gas with focus on thermal energy recovery, process integration and gas purification.²⁹ There is also need for synthesizing new diluents, materials and solvents along with membrane reactors for separation of hydrogen gas from product streams of steam reforming of natural gas, as well as, partial oxidation of hydrocarbons and coal gasification. Hydrogen can also be produced from biomass consisting of agricultural and forest residues, industrial and urban wastes and organic waste materials using different biological processes and thermochemical processes *viz.*, gasification and pyrolysis. These processes have drawbacks of low efficiency, low H₂ output, high energy requirement and high operating cost.

All the above mentioned technologies are energy intensive and do not produce ultra high purity (UHP) hydrogen. Due to high input energy requirements and need of hydrogen separation from product mixtures, these technologies require high capital investments. In addition, these processes primarily depend on fossil fuel reserves. Currently, the global production of hydrogen is 65 million tonnes/year.³⁰ Considering the predicted global energy demand of 30 TW (1800 million tonnes H₂/year) in 2050 and assuming completely adopted or commercialized hydrogen economy for energy production, we will need ~28 times more hydrogen production in 2050,

compared to the current production rate of H₂.³¹⁻³³ Thus, if energy is being produced mainly by combustion of fossil fuels in 2050, ~28 fold more fossil fuels need to be burnt, which is not viable. Hence, alternate technology of hydrogen production need to be identified. This technology should use clean fuel (low carbon footprint), low operating temperature without any greenhouse gas emissions and toxic or corrosive byproducts for sustainable and clean hydrogen production.⁸

1.3 WATER SPLITTING

A promising approach for producing hydrogen is from splitting of water. This process is environmentally benign due to the low carbon footprint of water leading to generation of hydrogen with no greenhouse gas emissions and no toxic byproduct. However, this reaction is an uphill reaction with $\Delta G=237$ kJ/mol (or 1.23 V) and requires external energy to drive this reaction.³⁴ This reaction can be shown as follows:



Thermolysis of water uses high temperature ($\geq 1000^\circ\text{C}$) to overcome this reaction barrier, which results in the question of energy source which will deliver energy for such high operating temperature.^{8, 13} In addition, the back reaction of explosive mixture of H₂ and O₂ gases at high operating temperature is a serious concern, which needs to be addressed for its adaptation on industrial scale.¹³ Another approach for hydrogen production is electricity driven water splitting, known as, water electrolysis. Though this approach seems promising as it does not involve any greenhouse gas emissions and toxic byproducts, the high capital cost of water electrolysis cell

due to use of expensive noble metal electro-catalysts (e.g. IrO₂, RuO₂, Pt), along with use of relatively small and comparatively less efficient systems, combined with the added costs of customized power electronics, and labor intensive fabrication are some of the major challenges that needs to be addressed.^{14, 22, 35-43} However, the use of electricity for splitting of water is very lucrative, if the electricity is produced from sustainable and efficient renewable energy source. This approach will help in overcoming reaction barrier utilizing renewable energy source alone.

2.0 BACKGROUND

2.1 SOLAR ENERGY-A PROMISING ENERGY SOURCE

The solar power is an important sustainable renewable energy source. The sun delivers massive average solar energy of 120,000 TW per year to the surface of the earth alone.⁴⁴ Solar energy is a de-concentrated and a seemingly limitless, vast, environmentally clean natural source of energy, and thus, has long been considered as an attractive approach for solving the global energy crisis. These features of solar energy necessitates its capture and utilization using environmentally benign tools for meeting human energy needs.¹³ The use of solar cells is a promising known technology for production of energy using solar energy. However, the very low efficiency (10-20%) along with the high manufacturing costs are some serious challenges for solar cells that need to be addressed.¹³ Solar energy however, is sporadic, i.e. cloudy weather and night time darkness interrupt the continuous availability of solar energy requiring the use of alternative energy storage and conversion systems to be integrated in tandem. Hence, depending on the locations and the time period when the continuous availability of sunlight is not hindered, it becomes important to store electricity produced from solar cells in secondary devices (e.g. battery) to enable its use at other locations and .¹³ This approach however, involving the production of electricity from solar cells and storage in secondary devices will require coupling of solar cells with secondary devices possibly adding to the already prevalent high system

costs.¹³ Another lucrative approach of efficient utilization of solar energy is the conversion of solar energy to non-carbonaceous fuel, .i.e., hydrogen, which will be stored, distributed and utilized on energy demand. Different pathways of conversion of solar energy into hydrogen are outlined in **Figure 2**.¹³

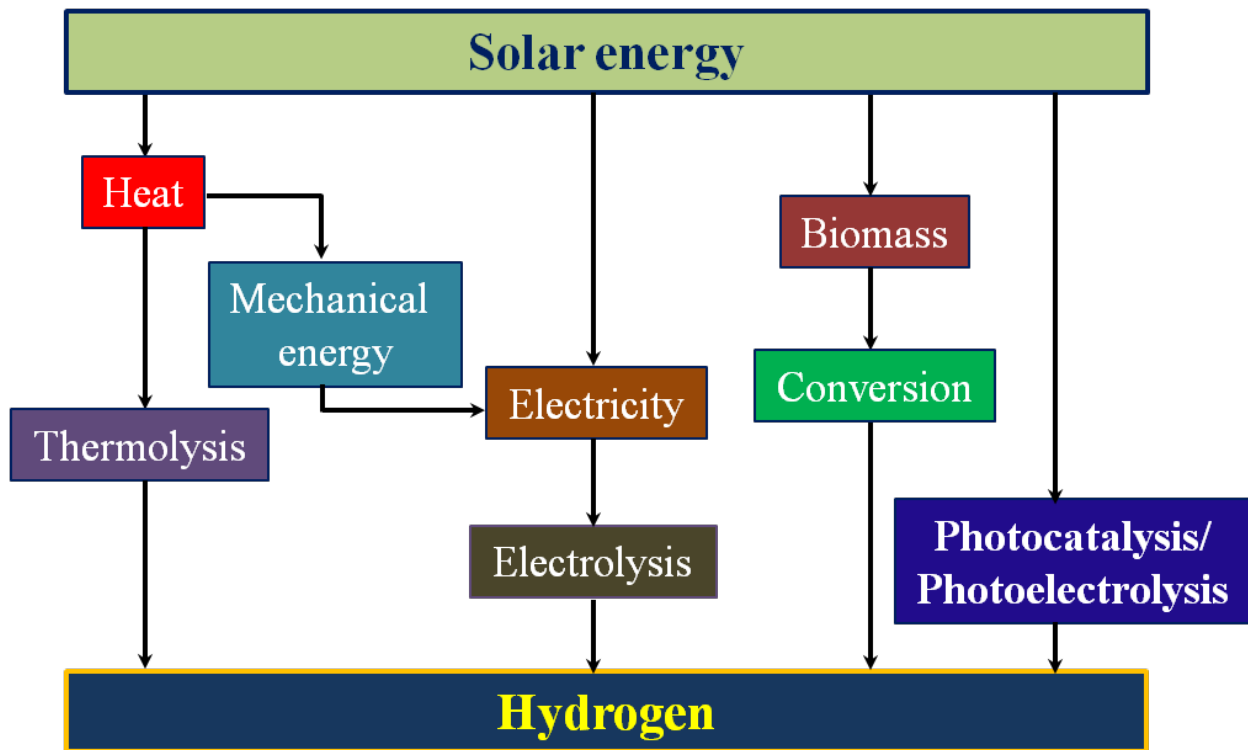


Figure 2: Different ways of production of hydrogen using solar energy¹³

Thermolysis of water produces hydrogen using heat generated from solar panels. This approach needs innovative engineering solutions to avoid back reaction of H₂ and O₂ gases at high operating temperature. The production from electrolysis using electricity produced either from solar cells or from electric generators (which convert mechanical energy produced from the heat generated in solar cells to electricity) is a promising approach. However, this approach has

the drawback of high system cost due to the use of expensive noble metal based electro-catalysts (e.g. IrO_2 , RuO_2 , Pt), along with additional cost contributed due to customized power electronics and labor intensive fabrication, as mentioned earlier in **Section 1.3**. Photobiological hydrogen production uses sunlight and photosynthetic microorganisms for splitting water leading to simultaneous H_2 and O_2 production. This technique faces the challenges of low efficiency, requirement of intense light along with CH_4 emission in the environment and poor long term stability of microorganisms due to the oxygen sensitive nature.⁴⁵

Photocatalytic or photoelectro-catalytic water splitting involves the generation of electricity from the semiconductor material used in the same system for driving hydrogen evolution reaction (HER) which takes place on the surface of the cocatalyst or electro-catalyst. Thus, photocatalytic or photoelectro-catalytic water splitting is a promising approach for production of hydrogen from water, as it combines two promising systems, .i.e., solar cell which produces electricity and water electrolysis which is driven by electricity produced from solar cell. In addition, it does not involve any intense input energy requirements, any greenhouse gas emissions and toxic byproduct. Thus, photocatalytic or photoelectro-catalytic water splitting provides a promising stage for capture of vast and illimitable solar energy, as well as, storing it in form of chemical bonds, .i.e., hydrogen from water splitting reaction using non-carbonaceous and environmentally benign tools.^{8,10}

2.2 SOLAR WATER SPLITTING

Solar water splitting can be carried out using either photocatalysis or photoelectrocatalysis. Though both approaches involve capture of solar energy and converting it to hydrogen, the difference lies in the water splitting cell employed for both approaches. Also, there is difference in the design of materials (Electro-catalyst and semiconductor materials) used for both approaches.

2.2.1 PHOTOCATALYSIS

Photocatalytic water splitting is carried out in a small quartz reactor, in which a photocatalyst is dispersed in water, as shown in **Figure 3**. The photocatalyst consists of a semiconductor material that absorbs the solar energy, along with the cocatalyst/electro-catalyst (e.g. Pt, Pd) for driving the hydrogen evolution reaction (HER). The cocatalyst is dispersed on semiconductor material and used as photocatalyst, as shown in **Figure 3**.^{46, 47}

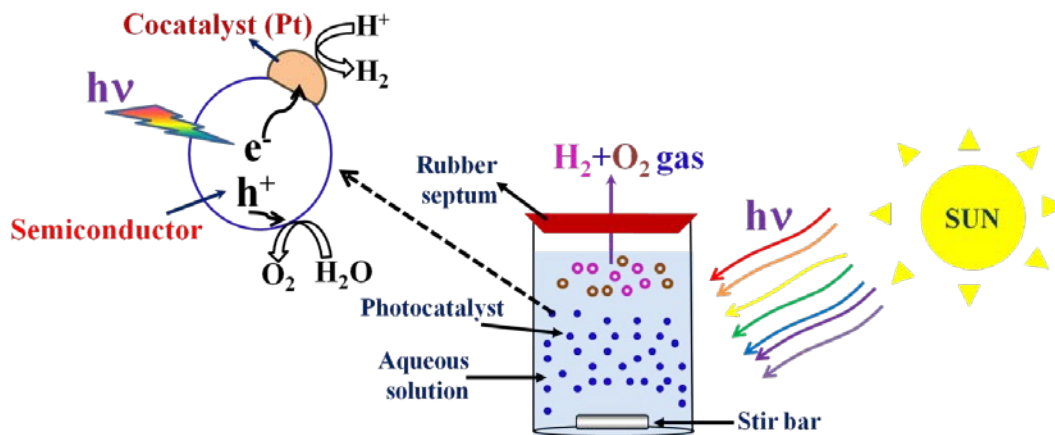


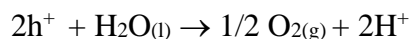
Figure 3: Schematic of photocatalytic water splitting

The steps involved in H₂ generation from photocatalytic water splitting are as follows^{8, 10}:

1. Absorption of solar energy by semiconductor material, which excites electrons from valence band to conduction band leaving behind holes in valence band of semiconductor material
2. Separation of photogenerated electron-hole (e⁻-h⁺) pairs
3. Flow of electrons to the cocatalyst and holes to surface of the semiconductor
4. Hydrogen evolution reaction (HER) at the cocatalyst and oxygen evolution reaction (OER) or oxidation of water at the semiconductor material.

The reaction scheme is shown as^{8, 10}:

At the semiconductor material (OER)



At the cocatalyst (HER)

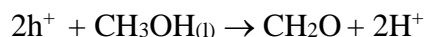


One of the serious challenges for the photocatalytic water splitting is the simultaneous generation and back-reaction of H₂ and O₂ gases. Since, cocatalysts for water splitting reaction are often good catalysts for the back-reaction of H₂ and O₂, if the product gases (H₂ and O₂) are not rapidly removed in photocatalytic water splitting, the photostationary state will be reached where the forward and back reactions will have equal rates and no more net water splitting will occur leading to low efficiency of the process.⁴⁸ Due to the explosive nature of (H₂+O₂) mixture, it is important to separate H₂ from O₂ immediately when formed. Thus, the additional energy

consumed by gas separation assembly for the separation of (H₂+O₂) mixture reduces the overall efficiency of this process.⁴⁸

To avoid water oxidation reaction which produces O₂ gas, sacrificial agents are often mixed with water for photocatalytic water splitting. The sacrificial agents serve as hole scavengers. The oxidation potential of the sacrificial agent is desired to be lower than that of water (1.23 V vs NHE). Due to lower oxidation potential of sacrificial agent, the holes oxidize the sacrificial agent instead of water during the water splitting process.^{49, 50} This avoids the formation of O₂ gas and thus, further required separation of (H₂+O₂) mixture. The most commonly used sacrificial agent is methanol due to its lower oxidation potential (0.02 V vs NHE).^{49, 50} The reaction scheme of the photocatalytic water splitting using sacrificial agent is shown as^{49, 50}:

At the semiconductor material



At the cocatalyst



Though the use of sacrificial agent avoids the generation of O₂ gas, oxidation of sacrificial the agent produces CO₂, an undesired greenhouse gas pollutant. It is therefore, necessary to separate (H₂+CO₂) mixture to generate ultra high purity (UHP) H₂ gas. As described previously in **Section 1.2**, CO₂ separation and storage is an energy intensive operation with requirement of high capital investment. Hence, photocatalytic water splitting with the use of sacrificial agent will lead to high system cost and thereby, reducing overall efficiency of water splitting process.

2.2.2 PHOTOELECTRO-CATALYSIS

Photoelectro-catalytic or photoelectrochemical water splitting involves generation of hydrogen in H-type cell, as shown in **Figure 4**.

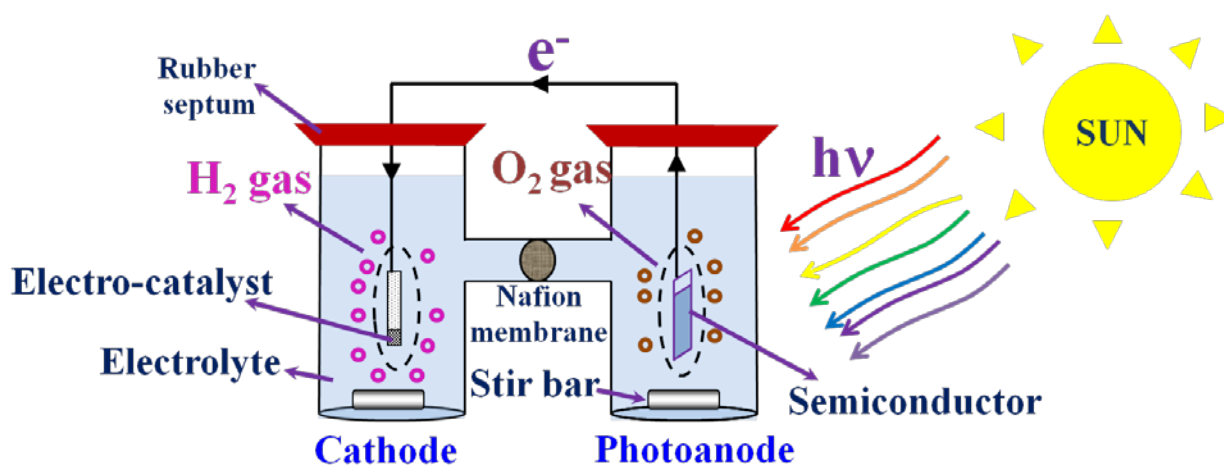


Figure 4: Schematic diagram of PEC water splitting in H-type cell

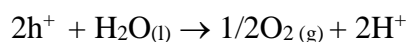
In the H-type cell, the semiconductor material is coated on transparent electrodes (current collector) and placed in one compartment of electrolyte containing cell. This electrode serves photoanode and is involved in water oxidation reaction.⁴⁸ The other compartment consists of electro-catalyst for HER (e.g. Pt) coated on porous titanium foil and this electrode serves as the cathode on which the HER takes place. The photoanode and cathode are separated by Nafion membrane to avoid mixing of H₂ and O₂ gases generated during water splitting process at each electrode.⁵¹

The steps involved in H₂ generation from PEC water splitting are as follows^{8, 10}:

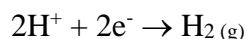
1. Absorption of solar energy by photoanode, which excites electrons from valence band to conduction band leaving behind holes in valence band of semiconductor material
2. Separation of photogenerated electron-hole (e^-h^+) pairs
3. Flow of photogenerated electrons to cathode and holes to surface of semiconductor material
4. Hydrogen evolution reaction (HER) at cathode driven by cathode electro-catalyst and oxygen evolution reaction (OER) or oxidation of water at photoanode.

The reaction scheme is shown as^{8, 10}:

At the photoanode (OER)



At the cathode (HER)



PEC water splitting involves generation of H_2 and O_2 gases in separate compartments of H-type cell (**Figure 4**) and thus, avoids the formation of explosive gaseous mixture. The separate generation of H_2 and O_2 gases avoids their back-reaction. In addition, this process does not require any gas separation assembly and sacrificial agent, as required for photocatalytic water splitting. This offers lower overall cost of the system and also, more efficient process than that of photocatalytic water splitting. Thus, PEC water splitting is a simple, promising and cost-effective approach for hydrogen production using solar energy for splitting of water involving minimum greenhouse gas emissions and no toxic byproduct.⁴⁸ Fujishima and Honda's first pioneer work on PEC water splitting using n-type TiO_2 semiconductor material has placed PEC water splitting using semiconductor material among the frontrunners for economic production of hydrogen in an environmentally friendly manner.^{8, 52} If the challenges for the development of PEC water

splitting (discussed in **Section 2.8**) are successfully addressed, hydrogen fuel economy can be adopted for addressing the global energy demand employing renewable and environmentally benign tools/sources. As mentioned in **Section 1.1**, hydrogen generated from PEC water splitting can be used as a fuel in proton exchange membrane fuel cells (PEMFCs) to produce electricity. PEMFCs can be used as energy sources for portable devices (e.g. Laptops, printers, cameras, etc.), stationary units (e.g. residential power systems, uninterruptible power systems, etc.) and automobile applications. In addition, H₂ can be used in petroleum refining (for processes such as hydrodesulfurization, hydrodenitrogenation, reforming, etc.), production of ammonia based fertilizers and industrially important chemicals like HCl, methanol, etc.²¹

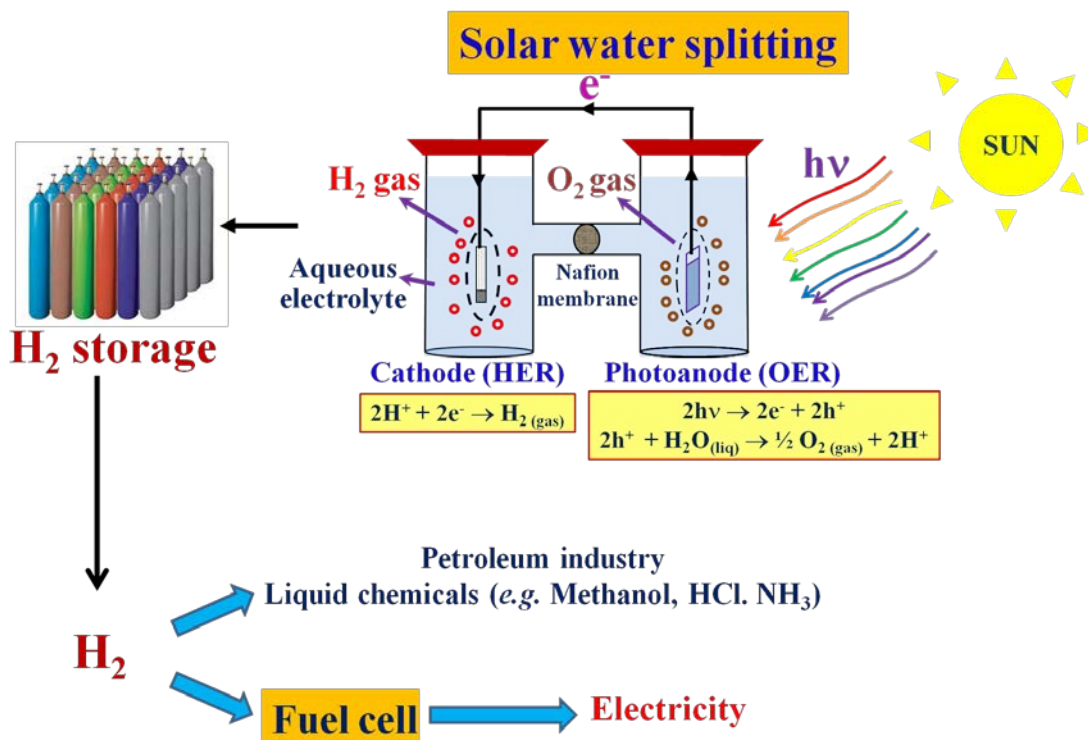


Figure 5: Hydrogen fuel economy

2.3 THERMODYNAMICS AND KINETICS

The energy required for splitting one mole of water into hydrogen and oxygen corresponds to the enthalpy of formation of one mole of water. The Gibbs free energy (ΔG_f) is the minimum amount of the enthalpy of the reaction that needs to be applied *via* solar energy. From the electrochemists' point of view, the minimum reversible cell voltage needed to be applied for splitting of water can be expressed by the equation $V = \Delta G/nF$, where 'n' is the number of electrons per mole of product, .i.e., 2 in the case of water splitting, and F is the Faraday constant (96485 C/mol). At the standard conditions of temperature and pressure *i.e.* T = 25⁰C and P = 1 atm, $\Delta G_f \sim 237$ kJ/mol, $\Delta H_f \sim 285$ kJ/mol and thus, $V \sim 1.23$ V. This potential corresponds to the standard reversible cell potential with respect to water splitting.^{37, 53}

For PEC water splitting where water splitting reaction is driven by solar energy, the semiconductor material (photoanode) must absorb the light with photon energy of 1.23 eV (equal to wavelength of ~ 1000 nm) and convert the energy into H₂ and O₂ at the cathode and photoanode, respectively.^{8, 10} This process must generate two electron-hole pairs per molecule of H₂ (2×1.23 eV = 2.46 eV) or four electron-hole pairs per molecule of O₂ (4×1.23 eV = 4.92 eV).^{8, 10}

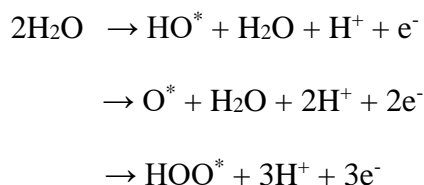
In practice under realistic conditions, the required cell voltage for water splitting reaction is higher than the thermodynamic ideal cell voltage (1.23 V). The cell voltage under practical conditions is the sum of the ideal thermodynamic cell voltage (1.23 V) combined with the voltage drop caused due to ohmic resistance (iR_Ω) at a particular current density ('i') and the

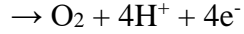
overpotential at both the cathode and anode. The ohmic resistance is contributed mainly by the resistance by electrolyte solution and electrode resistance/contact resistance. The overpotential at the anode and cathode is caused due to the polarization resistance to reaction. The resistance to the reaction pathway occurring as a result of the non-Faradaic sub-steps such as specific adsorption, desorption and re-orientation steps causes ‘reaction polarization’ and contributes to the ‘reaction overpotential’.⁵⁴ The charge transfer occurs at both the anode and cathode via a number of sub-steps and the barrier to such processes is known as ‘activation polarization’.^{54, 55} The activation overpotential is dependent on the rate of exchange of electrons at the electrochemical interface under reversible conditions and on the reaction pathway or mechanism. The catalysts used at the cathode and anode are desired to increase the rate of the reaction at their respective electrodes by lowering reaction overpotential and activation overpotential.

Considering the overpotential due to the voltage drop owing to the ohmic resistance and overpotential for the reaction at the anode and cathode, the required voltage for driving water splitting reaction is >1.23 V and thus, the semiconductor material must absorb light with photon energy of >1.23 eV (wavelength < 1000 nm).^{8, 10}

2.4 REACTION MECHANISMS

The mechanism for oxidation of water or OER at photoanode is given below, where the * represents an active site on the metal oxide surface⁵⁶:



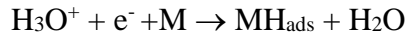


Thus, OER occurs via two electron pathway. In the above mechanism of OER, third reaction is thus the rate determining step of this mechanism and it has been proved theoretically and experimentally in literature.^{22, 57-60}

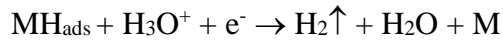
HER can occur on the catalyst surface by two possible mechanisms, .i.e., Volmer-Heyrovsky mechanism or Volmer- Tafel mechanism, each containing two reaction steps^{54, 61}:

(I) Volmer- Heyrovsky HER mechanism:

1. Volmer reaction:



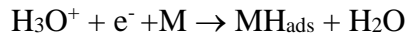
2. Heyrovsky reaction:



or

(II) Volmer- Tafel HER mechanism:

1. Volmer reaction:



2. Tafel reaction:



For state of the art electro-catalyst (Pt), HER occurs via Volmer-Tafel mechanism with Tafel reaction as rate determining step at low overpotential.⁶¹

2.5 DESIRED PROPERTIES OF SEMICONDUCTOR MATERIAL (PHOTOANODE)

2.5.1 BAND GAP

The solar spectrum consists of abundant visible light (~46%) with small amount of incoming solar energy lying in UV region (~4%).^{8, 10} Hence, it is important for photoanode to exhibit superior visible light absorbing properties and thus, generate hydrogen from water splitting driven by visible light. Considering the range of wavelength of visible light (390-700 nm) and also, the required voltage of >1.23 V which also accounts for the different losses due to overpotential as explained in **Section 2.3**, the photoanode must exhibit band gap in the range of ~1.6 eV- 3 eV.^{8, 10} The U.S. Department of Energy has set the target band gap of 2 eV for usable semiconductor band gap in PEC water splitting.⁶²

2.5.2 BAND STRUCTURE

To achieve HER and OER at cathode and photoanode, respectively, with minimum overpotential, it is important to match band gap of semiconductor material with potential of its conduction and valence bands.

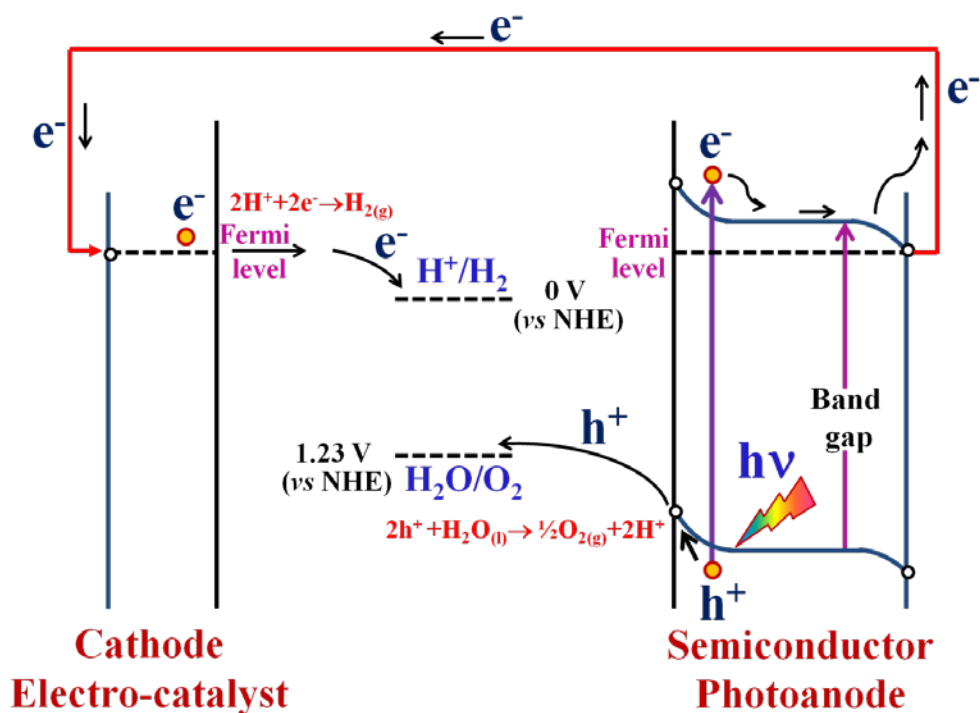


Figure 6: Energy band diagram for semiconductor material (photoanode) and cathode electro-catalyst

As seen in energy band diagram of photoanode material and cathode electro-catalyst in **Figure 6**, when the semiconductor material is illuminated by light, the electrons are excited from the valence band to the conduction band leaving behind holes in the valence band. The free photogenerated electrons in the conduction band of the semiconductor material flow to the cathode, where they are involved in the HER in which the photogenerated electrons react with H^+ ions (present in the electrolyte solution) to generate H_2 gas. Holes present in the valence band of the semiconductor material correspondingly oxidize water and generate O_2 gas by the OER. The reaction scheme of HER and OER is shown in **Section 2.2.2**. The driving force for the flow of photogenerated electrons depends on the difference between the conduction band edge of

semiconductor material and the redox potential of HER (0 V vs NHE).^{8, 10} If the conduction band edge of the semiconductor material is more negative than the standard redox potential of HER, then no external bias is needed to forcibly flow electrons from photoanode to cathode, as seen in **Figure 6**.^{8, 10, 63} In other words, no external bias is needed to match the Fermi level of the semiconductor material with that of the cathode electro-catalyst.^{8, 10}

Similarly, if the valence band of semiconductor material is more positive than standard redox potential of oxidation of water (1.23 V vs NHE), then the holes generated can easily migrate to the surface of the semiconductor material and oxidize water without the need of any external bias.^{8, 10, 63} The driving force for the flow of photogenerated holes to the surface depends on the difference between the valence band edge and redox potential of oxidation of water. Hence, in order to facilitate the flow of photogenerated electrons from the photoanode to the cathode and oxidation of water driven by holes without the any need of external bias, the semiconductor material is desired to exhibit a conduction band edge more negative than 0 V vs NHE and a valence band edge that is more positive than 1.23 V vs NHE . In other words, the semiconductor material should possess an appropriate band structure such that the reduction and oxidation potential of water lie within its band gap.^{8, 10}

Since 1.23 V (vs NHE) is the standard redox potential for driving the water splitting reaction, the semiconductor material is expected to offer a photovoltage of $>1.23\text{ V}$ (considering overpotential losses) for driving the water splitting reaction just by solar energy alone without the need for any external electrical energy, the standard energy bias provided to realize the reaction. If the semiconductor material has the appropriate band structure as explained above, the semiconductor can easily alone offer the desired photovoltage of $>1.23\text{ V}$ for driving the water splitting reaction utilizing solar energy alone without need of any external applied bias.^{8, 10}

2.5.3 ELECTRICAL CONDUCTIVITY

The semiconductor material should have high electrical conductivity which will offer fast charge transport in the semiconductor material. Electrical conductivity is directly proportional to the product of number of carriers or carrier density and electron mobility of the semiconductor material. Thus, the semiconductor material should exhibit high carrier density and electron mobility for achieving superior charge transport. High electron mobility is expected to offer fast movement of the photogenerated electrons from the semiconductor material to the current collector and then to the cathode. In addition to improved electrical conductivity, high carrier density will offer more number of photogenerated carriers (electrons and holes) available for HER and OER at cathode and photoanode, respectively.^{8, 10, 64, 65}

2.5.4 RECOMBINATION OF THE PHOTOGENERATED CARRIERS

As mentioned in **Section 2.2.2**, when the semiconductor material is illuminated with light, the electrons are excited from valence band to conduction band leaving behind holes in the valence band. These photogenerated electrons then flow to cathode, where they participate in HER. Ideally, the lifetime of the photogenerated electrons should be high such that maximum photogenerated electrons flow to the cathode and react with H⁺ ions in the HER process to produce the desired H₂ gas. However, the photogenerated carriers, i.e., electrons and holes, recombine very rapidly (~10 ns) emitting light or generating phonons, due to which very few carriers are available for the reaction at both the electrodes leading to poor efficiency.⁶⁶⁻⁶⁹ The recombination of the photogenerated carriers in the semiconductor material is a deactivation process and includes recombination from both, the surface and the bulk.^{8, 10} The defect sites in

the semiconductor material also act as sites for trapping and recombination of the photogenerated carriers. Hence, the semiconductor material is desired to exhibit high crystallinity or possess very low density of defects to achieve minimum recombination of photogenerated carriers.

The recombination of the photogenerated carriers limits the photovoltage offered by the semiconductor material and thus, reduce the ability of the semiconductor material to drive the water splitting reaction using just solar energy alone without the use of any external bias.¹⁰ Thus, even if the semiconductor material has the appropriate band structure as mentioned in **Section 2.5.2** such that the conduction band edge is more negative than the standard redox potential of HER (0 V *vs* NHE) and the valence band edge is more positive than the standard redox potential of oxidation of water (1.23 V *vs* NHE), recombination of photogenerated carriers lower the photovoltage for water splitting reaction. Hence, it is extremely important to minimize the recombination of photogenerated carriers to achieve the photovoltage of >1.23 V and thus, result in unassisted PEC water splitting.¹⁰

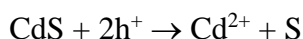
From the above, therefore, it is clear that achieving fast charge transport along with minimum recombination of the photogenerated carriers is of paramount importance in achieving long carrier lifetime and high efficiency of PEC water splitting. The long carrier lifetime will offer more availability of the photogenerated carriers to complete the reactions at both the electrodes leading to high efficiency of the PEC water splitting process.

2.5.5 PHOTOELECTROCHEMICAL STABILITY

The semiconductor material should exhibit superior long term photoelectrochemical stability for continuous H₂ production from PEC water splitting process. Photogenerated holes are mainly responsible for the photocorrosion of the semiconductor material.^{8, 10} Semiconductor

material such as sulfides and selenides have the major drawback of photocorrosion in the electrolyte solution.

e.g. CdS is self-oxidized by the photogenerated holes rather than water in the long term photocatalytic water splitting operation.^{8, 10}



This can be avoided if the carrier transport and thus, the kinetics of water oxidation reaction or OER on the semiconductor material are rapid enough such that the holes are rapidly consumed in OER. As a result, consequently, less holes are available on the surface of the semiconductor material which may possibly cause photocorrosion of the semiconductor material.^{8, 10}

2.6 DESIRED PROPERTIES OF THE CATHODE ELECTRO-CATALYST

The electrochemical activity of the cathode electro-catalyst for HER depends on the binding of the reaction intermediate on the electro-catalyst surface, as per the mechanism of HER shown in **Section 2.4**. To achieve the much desired superior electrochemical activity, there should be optimal adsorption and desorption of H_{ad} on the electro-catalyst surface with neither too strong or too weak binding. The degree of binding of the adsorbed H with the electro-catalyst surface can be described by a parameter, ΔG_{H^*} which is the free energy of H_{ad} on the electro-catalyst surface.^{89, 90} If ΔG_{H^*} is more positive, it will lead to poor binding of H atom with electro-catalyst surface.^{70, 71} On the other hand, more negative ΔG_{H^*} indicates too strong binding of H atoms on the electro-catalyst surface.^{89, 90} For the cathode electro-catalyst, ΔG_{H^*} is desired to be close to 0 eV, which indicates easy adsorption and desorption of hydrogen atoms from the electro-catalyst surface.⁷²⁻⁷⁴ For the state of the art cathode electro-catalyst (Pt), $\Delta G_{\text{H}^*} \sim 0$ eV.^{89, 90}

Based on the above, following are the desired properties for cathode electro-catalyst:

- High electrical conductivity
- Superior electrochemical activity for HER with minimum onset potential
- Facile electron transfer kinetics (low charge transfer resistance)
- Excellent long term electrochemical stability

2.7 SOLAR-TO-HYDROGEN EFFICIENCY

The solar-to-hydrogen efficiency (STH) of the photoanode materials is defined as a term to be used in the absence of bias (for zero applied potential, $V = 0$) and in the presence of bias, the efficiency is considered as the applied bias photon-to-current efficiency (ABPE), which is calculated using the equation⁷⁵⁻⁷⁹:

$$\text{ABPE} = \frac{\Delta G^{\circ} \times n_{\text{H}_2} - V \cdot I}{P \times A} \times 100 = \frac{I \times (1.23 - V)}{P \times A} \times 100 \dots \text{Equation 1}$$

where, n_{H_2} = H_2 evolution rate (mol/sec)

ΔG° = Gibbs free energy for generating one mole of H_2 from water (237130J/mol)

P = Total incident power (W/cm^2)

A = Area irradiated by incident light (cm^2)

I = Photocurrent (A)

V = Bias voltage applied

STH is an important parameter, which relates to the efficiency with which the incident sunlight photons can produce H_2 gas from the water splitting process. Ideally high STH is desirable in PEC water splitting with the input of only solar energy and correspondingly, no

external bias is required. Thus, the onset potential for water splitting process to occur under illumination should be ≤ 0 V. This indicates that hydrogen is produced in the PEC water splitting process via the assistance of only solar energy and no external bias of electrical energy, with the . However, in a specific case, if bias is applied in PEC water splitting process, its contribution (Voltage, (V)).(current, (I)) to STH is subtracted, as shown in **Equation 1**. Envisioning hydrogen production on an industrial scale from PEC water splitting, it is important to achieve a high STH using solar energy alone with no applied external bias indicating the capability of the solar energy in achieving hydrogen production in a large scale from the PEC water splitting process.

Thus, semiconductor material and cathode electro-catalyst exhibiting properties discussed in **Section 2.5** and **Section 2.6** should exhibit superior electrochemical activity with minimum activation and reaction overpotential (**Section 2.3**) to achieve a high STH and good long term stability for robust H₂ production from PEC water splitting. The target set by U.S. DOE for STH is 10% for H₂ production from the PEC water splitting process.⁸⁰

2.8 CHALLENGES FOR PEC WATER SPLITTING

As discussed above, PEC water splitting is a promising approach for the production of hydrogen using solar energy for splitting of water. However, its progress towards commercialization has been stymied by the lack of availability of an ideal semiconductor material for photoanode exhibiting properties mentioned in **Section 2.5**. The development of suitable semiconductor materials exhibiting excellent light absorption properties, high electrical conductivity, superior photoelectrochemical activity and long term photoelectrochemical stability will be a major breakthrough in the field of PEC water splitting.^{8, 10}

In PEC water splitting to date, TiO₂, ZnO and α -Fe₂O₃ have been widely studied as promising semiconductor materials due to their light absorption ability, low cost and ease of availability. Amongst these semiconductor materials, TiO₂ is one of the most promising and widely studied material as a photoanode. TiO₂ offers the advantages of being abundant and is indeed stable in aqueous solutions under irradiation with strong photocatalytic activity under UV light irradiation. However, TiO₂ is still not viable for commercialization of PEC water splitting, mainly due to its low intrinsic electrical conductivity, poor visible light absorption due to its wide band gap (~ 3.2 eV) and significant carrier recombination resulting in poor photoelectrochemical activity.^{65, 81, 82} The photoelectrochemical activity of α -Fe₂O₃ on the other hand, is limited by short diffusion length of photogenerated minority carriers, high resistivity, low electron mobility ($\sim 10^{-2}$ cm² V⁻¹ s⁻¹)⁸³⁻⁸⁶ and high recombination rate of photogenerated carriers.^{48, 87} Also, the conduction (CB) band edge of α -Fe₂O₃ lies 0.2-0.4 eV positive of 0 V (standard redox potential of HER) suggesting the need for an external bias to drive the HER, which reduces the overall efficiency of the water splitting process.⁸⁸ ZnO and α -Fe₂O₃ both, have poor long term photoelectrochemical stability in aqueous electrolyte solution, along with poor visible light absorption properties.^{83-85, 88} Other non-oxide materials such as sulfides and selenides exhibit low band gaps (2.4 eV for CdS and 1.7 eV for CdSe) and hence, superior light absorption properties. However, these systems face the serious problem of photocorrosion in aqueous electrolyte solution under illumination.^{8, 88-90} Hence, non-oxide materials have not been explored in detail so far as photoanodes for PEC water splitting, as compared to the widely studied metal oxide semiconductors which are comparatively stable in the electrolyte solutions. The maximum STH, achieved so far to the best of our knowledge is $\sim 1.7\%$ for Au/TiO₂ nanotubes⁹¹, which is significantly lower than the DOE target of STH of 10%.⁸⁰ This therefore,

warrants further development of semiconductor materials offering excellent optoelectronic properties, superior photoelectrochemical activity and stability.

Another important aspect of PEC water splitting is the cathode electro-catalyst which drives the HER. The HER process to date, mostly relies on the use of state of the art electro-catalyst, Pt/C, which has superior electrochemical activity and excellent electrochemical stability. However, Pt/C being expensive, considerably increases the materials cost of the PEC water splitting cell. Hence, it is important to reduce Pt loading to ultra-low level without compromising the electrochemical activity and stability. Over the years, there has been significant efforts focused at reducing the Pt content by alloying of Pt with transition metals such as Fe, Sn, Ni, Mo⁹²⁻¹⁰¹, which offers reduction in loading of Pt, without compromising the electrochemical performance. High performance of Pt based metal alloy catalyst is attributed to the decrease in the Pt-Pt interatomic distance, well dispersion of Pt over support and modified electronic structure of Pt due to shift in d-band center, which is responsible for high catalytic activity due to reduction in adsorption/dissociation energies for adsorbate.^{96, 97, 102} Though Pt loading is desired to be reduced to ultra-low levels, the ultimate goal is indeed the development of Pt free electro-catalyst with superior electrochemical activity and stability than Pt/C, which will help in reducing materials cost of PEC water splitting cell. There is clearly research work conducted in this area with more activity focused in recent years.

In summary, if the challenges of PEC water splitting discussed above, are indeed addressed by developing novel semiconductor materials with excellent optoelectronic properties, superior photoelectrochemical activity and stability and platinum-free cathode electro-catalyst with superior electrochemical activity for HER and stability than Pt/C, it is conceivable that hydrogen

production from water splitting reaction driven by solar energy on industrial scale could soon be a reality. Such a development will indeed help in addressing the problem of global energy crisis.

Challenges for the development of PEC water splitting

The development of PEC water splitting for economic and efficient hydrogen production has been constrained by the challenges facing both photoanode and cathode materials, which need to be addressed. These limitations are listed below:

Challenges affecting the selection of suitable photoanode systems

- ✘ Wide band gap resulting in poor light absorption ($\sim 2.3-5$ eV)^{81, 82, 103}
- ✘ Low electron mobility ($\sim 0.01-1$ cm² V⁻¹ s⁻¹)^{86, 104}
- ✘ High recombination of the photogenerated carriers ($\sim 50-60\%$ of incident light intensity resulting in poor carrier lifetime of ~ 10 sec at -0.2 V vs RHE which is at near zero applied bias and selected following published reports in the literature)^{65, 105}
- ✘ Poor STH ($\sim 0.11\%-1.63\%$)^{64, 91, 106}
- ✘ Poor long term photoelectrochemical stability in the electrolyte solution under illumination ($\sim 1-6$ h)^{64, 107}

The paucity of an ideal semiconductor material exhibiting properties overcoming the challenges mentioned above is a major impetus for the development of novel materials PEC water splitting. Hence, there is a major need for research to be conducted to identify and develop novel semiconductor materials with unique electronic structure, which will help in achieving superior STH and excellent long term PEC stability. This thesis outlines efforts made to overcome and address some of these issues outlined above.

Challenges for cathode electro-catalysts

As mentioned in the previous section, it is important to identify novel reduced/zero noble metal containing electro-catalyst displaying excellent electrochemical activity and stability, superior than that of expensive Pt/C, which will aid in lowering the cost of PEC water splitting cells. The present thesis also outlines efforts made in this direction to reduce noble metal content in identifying novel electrocatalysts with the ultimate goal of even completely eliminating the presence of any precious or noble metals.

3.0 MOTIVATION AND SPECIFIC AIMS

3.1 MOTIVATION

3.1.1 SEMICONDUCTOR MATERIALS FOR PHOTOANODE

Among all semiconductor materials studied thus far discussed in the earlier chapters, ZnO has shown considerable potential for hydrogen generation from PEC water splitting due to its higher electron mobility ($\sim 155 \text{ cm}^2 \text{ V}^{-1} \text{ s}^{-1}$ for ZnO vs $\sim 10^{-1} \text{ cm}^2 \text{ V}^{-1} \text{ s}^{-1}$ for TiO_2 and $\sim 10^{-2} \text{ cm}^2 \text{ V}^{-1} \text{ s}^{-1}$ for $\alpha\text{-Fe}_2\text{O}_3$).^{83, 86, 108} The high electron mobility helps achieve fast electron transport from the semiconductor material to the current collector due to the superior electrical conductivity (Section 2.5.3).¹⁰⁹ However, poor light absorption arising from the wide band gap ($\sim 3.2 \text{ eV}$) results in poor photoelectrochemical activity, along with inferior long term stability which are the primary key issues for the use of ZnO as the photoanode for PEC water splitting.^{65, 106, 110} This problem has been largely addressed mainly by tailoring the ZnO electronic structure to narrow the band gap by doping the oxide with various metal/non-metal dopants.¹¹¹⁻¹¹³ Thus far, to the best of our knowledge, the maximum applied bias photon-to-current efficiency (ABPE) achieved for ZnO based semiconductor materials is just 0.75% achieved for carbon-doped ZnO porous nanoarchitectures^{110, 114}. The low efficiency thus, will certainly not aid in the commercialization of PEC water splitting cells. Hence, the selection of suitable dopants is

important for ZnO, which necessitates systematic band gap engineering of ZnO to improve its photoelectrochemical activity.

The doping strategy in ZnO is expected to lower the band gap and thus, improve light absorption due to the additional electronic states of dopants introduced into the band gap of ZnO.⁶⁵ In addition to improved light absorption properties, doping of ZnO will offer improved carrier density leading to more photogenerated carriers available for reaction at both the photoanode and cathode.^{64, 106} The improved carrier density will offer improved band bending due to increased Fermi level at the semiconductor-electrolyte interface and thus, more efficient separation of photogenerated carriers, as discussed previously in **Section 2.5.4**. The criterion for the selection of suitable dopants is that the electronic states of dopants should overlap with the states of ZnO to transfer the photogenerated electrons to the cathode electro-catalyst (involved in HER) and correspondingly, transfer the photogenerated holes to active sites on the surface of the semiconductor material of the photoanode (involved in water oxidation reaction) within the electron hole carrier lifetimes.¹¹⁵ The cationic dopants, which give localized d states in the band gap of ZnO, offer recombination sites for photogenerated carriers beyond an optimum concentration. This is also expected to result in poor photoelectrochemical activity of ZnO doped with cationic dopant, beyond an optimum concentration of the cationic dopant.^{115, 116} Hence, identification of suitable dopants and the corresponding effective concentration is important for achieving systematic band gap engineering with the aim of reducing the band gap of ZnO and also, simultaneously improving the photoelectrochemical performance of the oxide.

The computational study of cobalt doping in ZnO by Assadi *et al.* has shown the red shift in light absorption from UV to the visible region due to a reduction in the band gap of ZnO following the introduction of Co-3d states at the bottom of the conduction band of ZnO by cobalt

doping.¹¹⁷ Also, cobalt doping in ZnO offers improved catalytic activity for dye decomposition under UV light illumination, as reported earlier.¹¹⁶ However, cobalt to date has not been explored as a dopant for ZnO for PEC water splitting application, to the best of our knowledge. Also, cobalt doping will have minor influence on the crystal lattice of ZnO, due to the smaller ionic radius of Co^{2+} ($\sim 0.56 \text{ \AA}$) compared to Zn^{2+} ($\sim 0.60 \text{ \AA}$), which will facilitate easy substitution of Zn^{2+} by Co^{2+} with minimum lattice strain.¹¹⁸ Hence, cobalt is selected as a dopant in this study for ZnO.

The study of nitrogen doped TiO_2 by Hoang *et al.* showed that nitrogen is a potential anionic dopant for TiO_2 .¹¹⁹ N-doping in TiO_2 offered significantly improved carrier density and reduced band gap resulting in improved ABPE, compared to pure TiO_2 .¹¹⁹ The improved photo-response following N doping in TiO_2 can be attributed to the introduction of N 2p states near valence band edge of TiO_2 , which helped in lowering the band gap. The N 2p orbital has higher potential energy than the O 2p orbital in ZnO. When N atoms are substituted for O atoms in ZnO, the HOMO (highest occupied molecular orbital) of the material is expected to shift higher without affecting the level of the bottom of the conduction band (i.e., lowest unoccupied molecular orbital, LUMO), which will help in lowering the band gap of ZnO.³⁴ Thus, N as an anionic dopant satisfies the condition for the selection of suitable dopant, as mentioned earlier. Based on the above, Co and N are selected as co-dopants for conducting a systematic band gap engineering study of ZnO in this research proposal as electronic states corresponding to Co and N are expected to be introduced at the bottom of the conduction band and top of the valence band of ZnO, respectively as shown in **Figure 7**.¹¹⁴

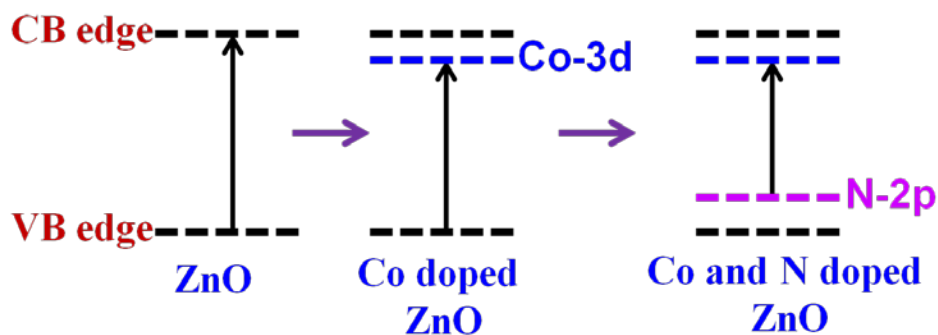


Figure 7: Effect of Co and N co-doping on the band gap of ZnO

The nanowire geometry is also chosen, on the grounds of its advantages which include high surface area providing a large area of electrolyte-electrode contact combined with providing an efficient path for transport of photogenerated carriers in the material thereby offering reduced probability of recombination of the photogenerated carriers as shown in **Figure 8**.¹²⁰⁻¹²² Following this strategy, vertically aligned Co and N co-doped ZnO nanowires (VANWs) are studied as photoanode for PEC water splitting with the aim of achieving improved light absorption properties, superior electronic properties, excellent photoelectrochemical activity and superior long term stability. To the best of our knowledge, a detailed careful assessment of the reported literature that was conducted to date, indicated non-existence of any reports on Co and N co-doped ZnO nanowires synthesized by a simple liquid phase deposition (LPD) approach on fluorine doped tin oxide (FTO) glass slides combined with any reported study of their activity as photoanode for PEC water splitting with consideration of different concentration of dopants. The present thesis therefore describes the detailed research that was conducted in this system.

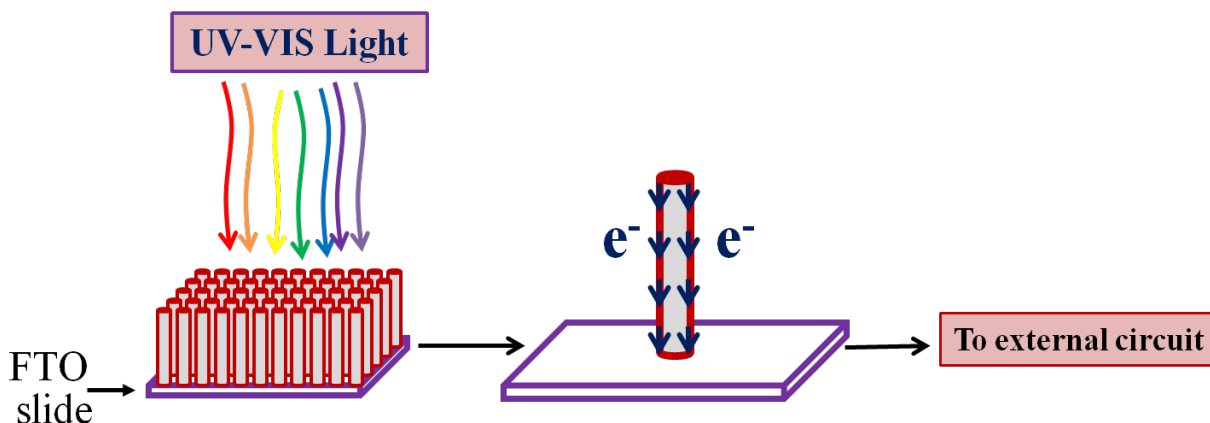


Figure 8: Vertical orientation of semiconductor material facilitating charge transport in the material

Following the work described above, similarly, tin oxide, SnO₂ has also been identified as a promising semiconductor material in dye sensitized solar cells (DSSCs) due to its good electron mobility and in addition, it also exhibits high corrosion resistance in the aqueous electrolyte solution.^{22, 123} The electron mobility of SnO₂ ($\sim 100\text{-}200\text{ cm}^2\text{ V}^{-1}\text{ s}^{-1}$) is orders of magnitude higher than that of TiO₂ ($\sim 10^{-1}\text{ cm}^2\text{ V}^{-1}\text{ s}^{-1}$ and $\sim 10^{-2}\text{ cm}^2\text{ V}^{-1}\text{ s}^{-1}$ for $\alpha\text{-Fe}_2\text{O}_3$).^{108, 109} As mentioned earlier, the high electron mobility will offer fast electron transport from the semiconductor material to the current collector.¹⁰⁹ However, SnO₂ has wide band gap of $\sim 3.5\text{ eV}$ due to which it has not been explored as a photoanode thus far for PEC water splitting, to the best of our knowledge.⁸⁸ Similar to the case for ZnO discussed above, SnO₂ can also be considered promising for PEC water splitting, if its band gap can be lowered significantly, thereby, improving its light absorption properties, which clearly warrants a systematic band gap engineering using suitable dopants for SnO₂. Niobium is clearly, a well-studied dopant for SnO₂ for transparent and conductive oxide thin films (TCO), used mainly to improve the electrical

conductivity of SnO₂.¹²⁴⁻¹²⁶ Niobium is considered as an effective dopant due to its abundant electronic states and minor influence on SnO₂ lattice structure. Further, the lower ionic radii of Nb⁴⁺ (69 pm) than Sn⁴⁺ (71 pm), also contributes to minimum lattice strain.^{127, 128} The doping of Nb into SnO₂ is thus expected to introduce additional electronic states of Nb at the bottom of the conduction band of SnO₂, reducing the band gap of SnO₂ as seen in **Figure 9**.⁶⁰ Further, as mentioned earlier for the case of cobalt doping in ZnO, the position of the electronic states of Nb at the bottom of the conduction band of SnO₂ is advantageous since electronic states introduced by the dopants near the middle of the band gap of SnO₂ can facilitate recombination of photogenerated carriers. Hence, Nb is chosen as a potential dopant for SnO₂ in this study.

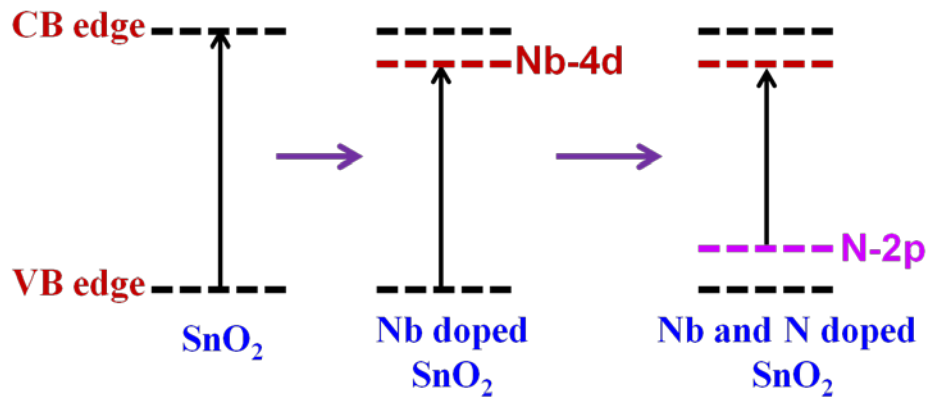


Figure 9: Effect of Nb and N co-doping on the band gap of SnO₂

The wide band gap of SnO₂ is mainly due to the deep position of the valence band position (O 2p orbital) at high potential.³⁴ This issue similar to ZnO can be addressed by systematic upward shift of valence band, without affecting the position of the conduction band, by introduction of suitable dopant into SnO₂ to suitably alter its electronic structure. In the same vein, nitrogen has

also been used in conjunction with niobium as a co-dopant for SnO₂ in this study. Similar to the case of doping in ZnO, N doping is expected to shift the valence band of SnO₂ upwards without affecting the conduction band due to the reasons mentioned before as shown in **Figure 9**. In this research study therefore, vertically aligned Nb and N co-doped SnO₂ nanotubes (VANTs) are studied as photoanode for PEC water splitting. To the best of our evaluation of the widely reported literature, there are no reports to date on the study of photoelectrochemical activity of Nb and N co-doped SnO₂ NTs as photoanode for PEC water splitting justifying the need for a detailed study of this system as planned in the current research.

The research work described in the two specific aims detailed in **Section 5.1** and **Section 5.2**, in the subsequent chapters focus primarily on outlining the experimental work and results of the PEC activity of the two doped nanoscale configurations belonging to ZnO and SnO₂ systems, respectively. The work described in **Section 5.1** and **Section 5.2** primarily address the band gap engineering of the parent materials for improving the photoelectrochemical activity of ZnO and SnO₂. As discussed in **Section 5.2**, accordingly, (Sn_{0.95}Nb_{0.05})O₂:N-600 NTs is considered indeed a promising band gap engineered system exhibiting excellent long term stability and the highest applied bias photon-to-current efficiency (ABPE) of 4.1% obtained using Pt as the HER electrocatalyst (cathode). The ABPE of (Sn_{0.95}Nb_{0.05})O₂:N-600 NTs can be further improved by minimizing the recombination of the photogenerated carriers, which can be achieved by efficiently separating the photogenerated carriers. The photogenerated carriers, i.e. the electrons and holes, recombine very rapidly (~10 ns), due to which very few carriers are available for executing the reactions at both electrodes leading to poor efficiency.⁸⁸ The efficient separation of the photogenerated carriers will significantly aid in minimizing the recombination and thus,

improve the photoelectrochemical activity and consequently help in enhancing the ABPE with minimum applied bias.

This can be achieved by developing a novel bilayer structure. Hence, if $(\text{Sn}_{0.95}\text{Nb}_{0.05})\text{O}_2\text{:N-600}$ NTs is coupled with other semiconductor material whose conduction band is below that of $(\text{Sn}_{0.95}\text{Nb}_{0.05})\text{O}_2\text{:N-600}$ NTs, the photogenerated electrons in the $(\text{Sn}_{0.95}\text{Nb}_{0.05})\text{O}_2\text{:N-600}$ NTs structure can easily flow from the conduction band edge of $(\text{Sn}_{0.95}\text{Nb}_{0.05})\text{O}_2\text{:N-600}$ NTs to that of the other semiconductor material, offering efficient separation of the photogenerated carriers and thus, increase the number of photogenerated electrons available for HER, as shown in **Figure 10**. Hence, a bilayer composite structure of WO_3 coupled with $(\text{Sn}_{0.95}\text{Nb}_{0.05})\text{O}_2\text{:N-600}$ NTs forming a hybrid structure, denoted as, $[\text{WO}_3\text{-(Sn}_{0.95}\text{Nb}_{0.05})\text{O}_2\text{:N-600}]$ NTs has been generated in this research study and studied as the potential semiconductor material for photoanode of PEC water splitting, based on the suitable position of the band edges and the known excellent electrochemical stability of WO_3 in acidic electrolyte solution. Correspondingly, WO_3 NTs have been synthesized and coated with $(\text{Sn}_{0.95}\text{Nb}_{0.05})\text{O}_2\text{:N-600}$ of different thicknesses. The effect of the different thicknesses of $(\text{Sn}_{0.95}\text{Nb}_{0.05})\text{O}_2\text{:N-600}$ layer in $[\text{WO}_3\text{-(Sn}_{0.95}\text{Nb}_{0.05})\text{O}_2\text{:N-600}]$ NTs on the optoelectronic properties and the ensuing photoelectrochemical activity has been correspondingly studied.

To the best of our knowledge, such a detailed study probing the photo-electrochemical activity of vertically aligned $[\text{WO}_3\text{-(Sn}_{0.95}\text{Nb}_{0.05})\text{O}_2\text{:N-600}]$ NTs as a composite bilayer photoanode for PEC water splitting has not been reported. Thus, the present report documents the detailed experimental studies demonstrating the promising photo-electrochemical performance of the novel bilayer composite system, $[\text{WO}_3\text{-(Sn}_{0.95}\text{Nb}_{0.05})\text{O}_2\text{:N-600}]$ NTs of different thicknesses serving as potentially viable photo-anodes for PEC water splitting, which

possibly offers a photovoltage of $\sim 1.45\text{eV}$ [VB of doped SnO_2 - CB of $\text{WO}_3 = 1.5\text{eV} - 0.05\text{eV} = 1.45\text{eV}$ (**Table 10**)]⁸⁸. This potential could likely provide the required driving force for catalyzing the oxygen evolution reaction (OER). Moreover, the study outlines the efficacy of the composite bilayer system for PEC water splitting without the use of any electrical bias. The thesis thus, showcases the effectiveness of this system to efficiently generate hydrogen directly from PEC water splitting without the use of any external electrical bias demonstrating the direct use of solar energy alone to result in water splitting to generate hydrogen.

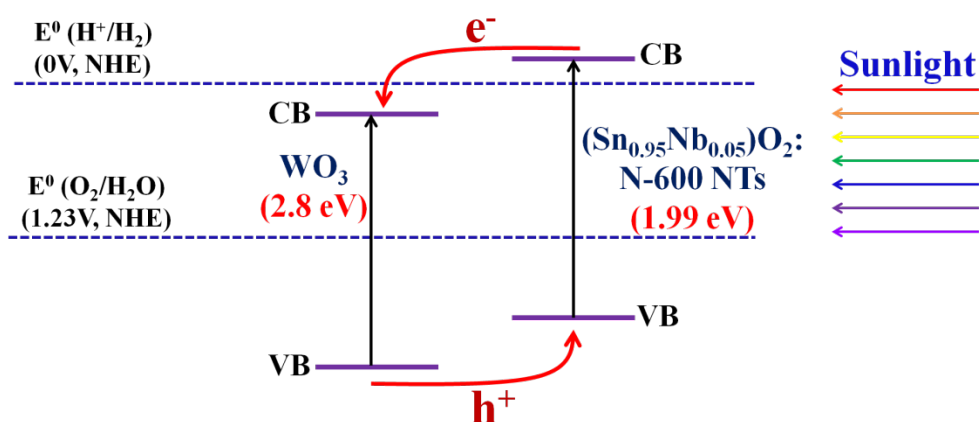


Figure 10: Schematic illustration of bilayer structure, $[\text{WO}_3-(\text{Sn}_{0.95}\text{Nb}_{0.05})\text{O}_2:\text{N-600}]$ NTs

3.1.2 CATHODE ELECTRO-CATALYSTS FOR HER

As mentioned earlier, the highest ABPE of 4.1% was obtained using $(\text{Sn}_{0.95}\text{Nb}_{0.05})\text{O}_2:\text{N-600}$ NTs as the photoanode and Pt as HER electro-catalyst (at cathode). However, Pt being expensive and a precious metal, leads to high overall system cost of the PEC water splitting cell.

Hence, the second part of this research study involves the study focused at developing non-noble metals based electro-catalysts for HER in PEC water splitting. The issue of high capital cost of the water electrolysis configuration using expensive noble metal electrocatalysts can be first addressed by reducing the noble metal content in the prevalent electro-catalysts by developing novel electro-catalysts with reduced noble metal content exhibiting superior electrochemical activity with minimum over-potential and stability compared to the state of the art electro-catalyst (Pt/C) for hydrogen evolution reaction (HER), which constitutes half of the overall water splitting reaction ¹²⁹. Such a system would represent a first step in the ultimate goal of developing completely precious group metal (PGM)-free electro-catalysts for hydrogen generation. Pioneering studies have been reported to date on non-noble metals based transition metal sulfides, transition metal selenides, transition metal nitrides and transition metal phosphides electro-catalysts exhibiting promising performance for HER such as MoS₂ ^{61, 71, 130}, CoSe₂ ¹³¹, Co_{0.6}Mo_{1.4}N₂ ¹³², MoSe₂ ¹³³, NiMoN_x ¹³⁴, WS₂ ¹³⁵, Ni₂P ^{136, 137}, CoP ¹³⁸⁻¹⁴¹, MoP ¹⁴², FeP ^{143, 144}, WP ¹⁴⁵, WP₂ ¹⁴⁶, Ni₅P₄ ¹⁴⁷, W-Mo-O/rGO, CoS₂/rGO¹⁴⁸, Fe-Co-P¹⁴⁹, MoS₂/C¹⁵⁰, Fe-Mo-Rare earth metals¹⁵¹, Ni-CeO₂ ¹⁵², etc. Despite these excellent advances involving recommendable HER electro-catalytic activity and long term stability displayed by these non-noble metals based electro-catalyst materials, there is still a need to achieve practically acceptable and moreover, consistently satisfactory HER performance under the stringest and energetically demanding field level specifications significantly and reproducibly superior to that of Pt/C for practical commercial device applications ¹⁵³.

A widely adapted approach in energy storage systems such as fuel cells to reduce the noble metal content is alloying of noble metal (e.g. Pt) with transition metals such as Fe, Sn, Ni, Mo^{94, 101}, which offers reduction in loading of Pt, without compromising the electrochemical

performance. Platinum based binary alloys have shown good electrochemical performance for fuel cell related devices based on electro-oxidation of different fuels, such as Pt-Sn/C and Pt-Sn-Ir/C ternary alloy for ethanol oxidation, Pt-Co, Pt-Ti/C, Pt-Ni-Cr/C and Pt-CuO/C for methanol oxidation, Pt-Ti/C for oxygen reduction reaction (ORR), Pt-Ni/C and Pt-WO₃-TiO₂/C for hydrogen oxidation reaction (HOR) for PEMFC.^{96, 101, 154-158} As mentioned earlier, superior electrochemical performance of Pt based binary metal alloys is mainly due to the modified electronic structure of Pt resulting in catalytically active phase than pure Pt.^{159, 160} Thus, the alloying approach would offer reduced noble metal loading without compromising electrochemical performance and stability.

In addition to Pt, Ir based electro-catalysts (*e.g.* Ir-Sn) have shown good electrochemical performance for ethanol electro-oxidation in direct ethanol fuel cells.¹⁶¹ Co_{1-x}(Ir_x) (x=0.2, 0.3, 0.4)¹⁵⁹ and (W_{1-x}Ir_x)O_y (x=0.2, 0.3; y=2.7-2.8) for hydrogen oxidation reaction in proton exchange membrane fuel cell (PEMFC) anodes and IrO₂/Ti and Ir-M-O_x (M=Ru, Mo, W, V) binary/ternary oxide catalysts for ORR and OER including solid solution oxide electrocatalysts with and without F doping, Ir_{1-x}M_xO_{2-y}F_y (M=Sn, Nb,) in PEM water electrolysis^{60, 162, 163} are examples of reduced noble metal containing electro-catalysts based on Ir exhibiting superior electrochemical activity and stability. Ir has good stability in acidic media. However, there are limited studies on Ir based electro-catalysts for HER. Hence, herein, solid solution electro-catalyst system Co_{1-x}(Ir_x) (x=0.2, 0.3, 0.4) has been studied for HER in electrolytic water splitting with the aim of achieving superior electrochemical activity and stability than that of Pt/C. The modification of the electronic structure due to the interaction of cobalt with iridium, as indicated by the first principles d-band center studies, can facilitate the reduction in polarization losses as reported earlier.¹⁵⁹ Furthermore, the catalytic activity of the electro-catalyst can be

described by a parameter ΔG_{H^*} , which is the free energy of adsorbed H on the electro-catalyst surface. As discussed in **Section 2.6**, ΔG_{H^*} is desired to be close to 0 eV, which indicates facile adsorption and desorption of hydrogen atoms from the electro-catalyst surface.⁷²⁻⁷⁴ Nanocrystalline solid solution of Co(Ir) is expected to display excellent electrochemical activity for HER compared to pure Co and pure Ir, due to ΔG_{H^*} of $Co_{1-x}(Ir_x)$ ($x=0.2, 0.3, 0.4$) that is expected to lie between that of pure Co and Ir resulting in ease of adsorption and desorption of H^+ from the electro-catalyst surface and thus, reflecting in superior electrochemical activity than pure Co and Ir.⁷⁰ This is mainly due to the possible beneficial interaction of Co and Ir resulting in modified electronic structure exhibiting highly active phase for HER.⁷⁰

In the pursuit of identification and development of cheap, highly electrochemically active and stable electro-catalysts for HER, as mentioned above, there have been pioneering studies reported on non-noble metals based electro-catalysts exhibiting promising performance for HER such as MoS_2 ^{61, 71}, $CoSe_2$ ¹³¹, $Co_{0.6}Mo_{1.4}N_2$ ¹³², $MoSe_2$ ¹³³, $NiMoN_x$ ¹³⁴, WS_2 ¹³⁵, etc. Earth-abundant transition metal phosphides (TMPs) are important materials exhibiting good electrical conductivity and are widely utilized as catalysts in hydrodesulfurization (HDS), and hydrodenitrogenation reactions as well as anode materials for Li ion battery applications.^{141, 144, 164-167} Both HDS and HER rely on reversible binding of hydrogen with the catalyst surface. In HDS, the hydrogen dissociates on the catalyst surface and reacts with sulfur forming H_2S which creates a reactive sulfur vacancy site²¹, while in HER, the protons bind to the electro-catalyst surface promoting HER and generate H_2 gas.¹⁴¹ The presence of metal center (δ^+) and pendant base P (δ^-) in the TMPs provide hydride-acceptor and proton-acceptor sites, respectively, which are known to facilitate HER.¹³⁸ The synergistic interaction of transition metal (Ni, Mo, Co) and non-metal (P) is expected to modify ΔG_{H^*} possibly resulting in optimal adsorption and

desorption of adsorbate on electro-catalyst surface.⁷⁰ Thus, TMPs are also considered as active electro-catalysts for HER. On the basis of this rationale, there have been significant research efforts directed towards the study of TMPs as electro-catalysts for HER such as Ni₂P^{136, 137}, CoP¹³⁸⁻¹⁴¹, MoP¹⁴², FeP^{143, 144}, WP¹⁴⁵, WP₂¹⁴⁶, etc., wherein, these electro-catalysts have shown promising electrochemical activity for HER. Despite these advances, all the above mentioned electro-catalyst materials have still not attained the ubiquitous acceptance standard as that of the state of the art Pt/C electro-catalyst due to the high overpotential for HER (~38-320 V *vs* RHE) in comparison to Pt/C (~10 mV *vs* RHE). Furthermore, the long term electrochemical stability of these materials for continuous long term H₂ production is still considered tenuous needing further study and improvement.^{160, 162, 165}

Based on the above, it is clear that the system necessitates further study and the development of TMPs is very much needed with the aim of reducing the overpotential to achieve onset potentials of ~0 V (*vs* RHE), combined with superior reaction kinetics, excellent electrochemical activity and stability similar or superior to that of Pt/C. With the principle aim targeted at the design and development of cheap non-noble metals based electro-catalysts displaying similar/superior electrochemical activity for HER and stability than that of Pt/C, in this thesis we describe copper phosphide (Cu₃P) based electro-catalyst system that has been studied as a potential electro-catalyst for HER, on the grounds of promising HER performance displayed by self-supported Cu₃P nanowire arrays.¹⁶⁸ However, to modify the system and identify suitable substitutional elements to further improve the electrocatalytic response for HER, in the present study, theoretical first-principles electronic structure calculations were conducted in order to determine the hydrogen binding energy (ΔG_{H^*}) to the surface of specific electro-catalysts. The goal of these calculations were primarily to identify and develop suitable Cu₃P

based electro-catalyst systems exhibiting excellent electrochemical activity for HER similar to that of noble metal electro-catalyst system (Pt). Based on the theoretical calculations, cobalt doped copper phosphosulfide denoted as $(\text{Cu}_{0.83}\text{Co}_{0.17})_3\text{P} \cdot x \text{ at. } \% \text{ S}$ ($x=10, 20, 30$) of different compositions were identified and explored as a suitable electro-catalyst system for HER, for the very first time to the best of our knowledge. Cobalt is selected as the preferred dopant for Cu_3P on the grounds of its ability to offer promotional effect in MoS_2 as reported earlier.^{169, 170} Thus, the incorporation of cobalt in Cu_3P is expected to offer increased number of catalytically active sites (due to a decrease in ΔG_{H^*}) resulting in improved catalytic activity (lower polarization losses) for HER, which is verified by the theoretical first-principles electronic structure calculations reported in this study.¹⁶⁹⁻¹⁷³

The rationale for selection of sulfur is that the most active sites for TMPs in HDS reaction are considered to be the phosphosulfide formed during the reaction. As a result, sulfur is known to play an important role in improving the catalytic activity of metal phosphides for HDS.^{166, 174, 175} Based on these proven observations, it is the hypothesis in this thesis work that incorporation of sulfur in Cu_3P will help achieve electronic and molecular states similar to that seen during HDS operating conditions and thus, translate in achieving excellent electrochemical activity for HER. In addition, incorporation of S into the Cu_3P lattice will offer improved electronic conductivity which will potentially also enable fast charge transfer kinetics. Thus, the simultaneous incorporation of Co and S into the Cu_3P lattice will offer unique opportunity for tailoring the electronic structure, physical, electronic and electro-catalytic properties of Cu_3P to match the noble metal electro-catalyst systems. As a result, the $(\text{Cu}_{0.83}\text{Co}_{0.17})_3\text{P} \cdot x \text{ at. } \% \text{ S}$ ($x=10, 20, \text{ and } 30$) has been explored for the first time, to the best of our knowledge as the universal electro-catalyst system for HER in electrolytic water splitting in acidic media.

Based on the above, it should be further mentioned that $\text{Co}_{1-x}(\text{Ir}_x)$ and $(\text{Cu}_{0.83}\text{Co}_{0.17}\text{Co})_3\text{P}:\text{S}$ systems have also been studied as HER electro-catalysts in PEC water splitting cell using $(\text{Sn}_{0.95}\text{Nb}_{0.05})\text{O}_2:\text{N}-600$ nanotubes (NTs) as the photoanode. The photoelectrochemical characterization as discussed earlier for PEC system has been carried out in H-type cell, in which the cathode (where HER occurs) and photoanode (where the water oxidation reaction is known to occur) are separated by Nafion 115 membrane (DuPont). As discussed in **Section 5.2.2**, which describes the details of this system, a maximum ABPE of $\sim 4.1\%$ is obtained using $(\text{Sn}_{0.95}\text{Nb}_{0.05})\text{O}_2:\text{N}-600$ NTs as the photoanode and Pt/C as the cathode at applied potential of ~ 0.75 V (*vs* RHE), which is the highest ABPE obtained thus far compared to other semiconductor materials studied as photoanode for PEC water splitting such as TiO_2 , ZnO and Fe_2O_3 .^{64, 176-178} However, keeping in line with the desirable ultimate goal of completely replacing Pt with novel non-noble metals based electro-catalyst exhibiting excellent electrochemical activity for HER and stability similar/superior than that of Pt/C, both the $\text{Co}_{1-x}(\text{Ir}_x)$, ($x=0.2, 0.3, 0.4$) and $(\text{Cu}_{0.83}\text{Co}_{0.17}\text{Co})_3\text{P}:\text{S}$ ($x=10, 20, \text{ and } 30$) systems have been studied as HER electro-catalysts to achieve similar/superior ABPE than that of Pt/C. This combined approach will help in progressing towards non-noble metals based electro-catalysis which will result in significant reduction in the capital cost of electrolytic and PEC water splitting system and thus, likely aid in their commercial development for efficient and economic production of hydrogen in an environmentally friendly manner. Realization and successful execution will be extremely relevant and will serve as an important milestone in the overall effort towards realizing the dream of fueling the hydrogen economy for meeting all of the global energy demands which will as outlined in the previous chapters offer massive environmental, economic and technological benefits both, in the short as well as long term.

Thus, the present dissertation documents both, the theoretical and experimental studies on electrochemical performance of nanostructured $\text{Co}_{1-x}(\text{Ir}_x)$ ($x=0.2, 0.3, 0.4$) solid solution and $(\text{Cu}_{0.83}\text{Co}_{0.17}\text{Co})_3\text{P}$: x at. % S ($x=10, 20, \text{ and } 30$) electro-catalyst systems as the cathode electro-catalysts for realizing HER in electrolytic and photoelectrochemical water splitting [using $(\text{Sn}_{0.95}\text{Nb}_{0.05})\text{O}_2$:N-600 NTs as photoanode in the latter]. Accordingly, four specific aims have been proposed in the current dissertation outlined as under.

3.2 SPECIFIC AIMS

Specific aim 1: To improve the fundamental optoelectronic properties (by modification of the electronic structure) of 1-D metal oxide semiconductor nanostructures for photoanode applications in PEC water splitting by systematic band gap engineering (achieved by incorporation of suitable dopants).

This was achieved in two phases as described under:

- a) Synthesis of Co and N co-doped ZnO nanowires denoted as $(\text{Zn}_{0.95}\text{Co}_{0.05})\text{O}$:N NWs and Nb and N co-doped SnO_2 nanotubes denoted as $(\text{Sn}_{0.95}\text{Nb}_{0.05})\text{O}_2$:N NTs on fluorine doped tin oxide (FTO) slide (current collector) by liquid phase deposition (LPD) approach followed by the heat treatment in NH_3 atmosphere at different temperatures (400°C , 500°C , 600°C and 700°C), as photoanodes for PEC water splitting
- b) Study of the optoelectronic properties of the above mentioned materials using UV-vis absorption spectroscopy, T_{auc} analysis and Mott-Schottky analysis

The results of this work has already been published.^{76, 114}

Specific aim 2: To study the nature of the photoelectrochemical behavior in band gap engineered 1-D metal oxide semiconductor nanostructures and to correlate the modification of the optoelectronic properties (achieved by doping) to photoelectrochemical activity of band gap engineered 1-D metal oxide semiconductor nanostructures.

This was achieved by performing photoelectrochemical characterization of the above mentioned materials using linear scan voltammetry, electrochemical impedance spectroscopy (used to study the reaction kinetics of photoelectro-catalysts) and chronoamperometry (CA) under illumination. The results of this work has already been published.^{76, 114}

Specific aim 3: To alter the fundamental photoelectrochemical behavior of band gap engineered 1-D metal oxide semiconductor nanostructures by coating the nanostructures with other metal oxide semiconductor material (bilayer structure).

This was achieved in three stages as detailed under:

- a) Coating WO₃ NTs with different thicknesses of (Sn_{0.95}Nb_{0.05})O₂:N-600
- b) Study the effect of different thicknesses of (Sn_{0.95}Nb_{0.05})O₂:N-600 on the optoelectronic and photoelectrochemical properties of the composite bilayer heterostructures [WO₃-(Sn_{0.95}Nb_{0.05})O₂:N-600] NTs using UV-vis absorption spectroscopy, Tauc analysis, Mott-Schottky analysis, linear scan voltammetry, electrochemical impedance spectroscopy (EIS) (used to study the reaction kinetics on electro-catalysts) and chronoamperometry.
- c) To study the effect of different thicknesss of (Sn_{0.95}Nb_{0.05})O₂:N-600 on the recombination kinetics and carrier lifetime in [WO₃-(Sn_{0.95}Nb_{0.05})O₂:N-600] NTs.

Specific aim 4: To study the combined effects of interaction of metal-metal and metal-non-metal on the fundamental electrochemical properties responsible for the hydrogen evolution reaction (HER).

This was achieved in four phases as outlined below:

- a) Synthesis and structural characterization of nanostructured $\text{Co}_{1-x}(\text{Ir}_x)$ ($x=0.2, 0.3, 0.4$) and $(\text{Cu}_{0.83}\text{Co}_{0.17}\text{Co})_3\text{P}:x$ at.% S ($x=10, 20, 30$) electro-catalysts.
- b) Study of the fundamental electrochemical properties of electro-catalysts for HER using linear scan voltammetry, electrochemical impedance spectroscopy and chronoamperometry.
- c) Study of the electrochemical activity of the cathode electro-catalysts for hydrogen production from PEC water splitting in H-type cell using $(\text{Sn}_{0.95}\text{Nb}_{0.05})\text{O}_2:\text{N}-600$ NTs as the photoanode.

The results of Co(Ir) electro-catalyst system have already been published.¹⁷⁹

4.0 EXPERIMENTAL DETAILS

4.1 SEMICONDUCTOR NANOMATERIALS PREPARATION FOR PHOTOANODE

4.1.1 SYNTHESIS OF $(\text{Zn}_{1-x}\text{Co}_x)\text{O}:\text{N}$ NANOWIRES (NWs) ($x=0.05$)

$(\text{Zn}_{0.95}\text{Co}_{0.05})\text{O}$ NWs were synthesized by simple liquid phase deposition (LPD) method onto a zinc oxide seed layer deposited fluorine-doped tin oxide (FTO) coated glass substrate (**Figure 11**).^{114, 180, 181} Before growing the nanowires, the FTO coated glass substrate (0.5cm×2.5cm, Aldrich) was thoroughly cleaned by ultrasonication in acetone, ethanol and deionized water. 5.5 mM zinc acetate solution in ethanol (anhydrous, 99.5+%, Aldrich) was spin-coated on cleaned FTO substrate (Specialty coating Systems Inc., Model P6712) at 500 rpm for 40 sec and then heated at 125⁰C. This heating step formed zinc acetate layer on the substrate. The spin coating process was repeated a second time followed by heating at 125⁰C. The ZnO seed layer was formed by heat treatment of FTO slide with zinc acetate layer in air at 340⁰C for 20 min.

The seed layer coated FTO substrate was then placed with conductive surface down in a sealed hydrothermal container containing the growth solution of zinc nitrate hexahydrate (0.05 M, Alfa Aesar), stoichiometric amount of cobalt acetate tetrahydrate (Aldrich), hexamethylenetetramine (HMTA, 0.025 M, Alfa Aesar), polyethylenimine (5 mM, end-capped,

molecular weight 800 gmol^{-1} LS, Aldrich) and ammonium hydroxide (0.35 M). Then, the sealed container was placed in water bath, preheated to 90°C for 6 h. The resulting nanowires were thoroughly rinsed with ethanol and D.I. water, purified by the Milli-Q system (18 $\text{M}\Omega\cdot\text{cm}$ deionized water, Milli-Q Academic, Millipore), followed by drying at 50°C for 6 h. To compare results with undoped ZnO, ZnO NWs were also synthesized by following the same procedure, without adding cobalt acetate tetrahydrate in the growth solution. $(\text{Zn}_{0.95}\text{Co}_{0.05})\text{O}$ NWs, grown on FTO substrate following the same procedure as mentioned above, were heat-treated for 1 h at 400°C , 500°C , 600°C and 700°C in anhydrous NH_3 atmosphere (Matheson: 99.99%, flow rate= $100 \text{ cm}^3/\text{min}$) with ramp rate of $10^\circ\text{C}/\text{min}$. The $(\text{Zn}_{0.95}\text{Co}_{0.05})\text{O}$ NWs, heat-treated in NH_3 at 400°C , 500°C , 600°C and 700°C , are denoted as $(\text{Zn}_{0.95}\text{Co}_{0.05})\text{O:N-400}$ NWs, $(\text{Zn}_{0.95}\text{Co}_{0.05})\text{O:N-500}$ NWs, $(\text{Zn}_{0.95}\text{Co}_{0.05})\text{O:N-600}$ NWs and $(\text{Zn}_{0.95}\text{Co}_{0.05})\text{O:N-700}$ NWs, respectively.

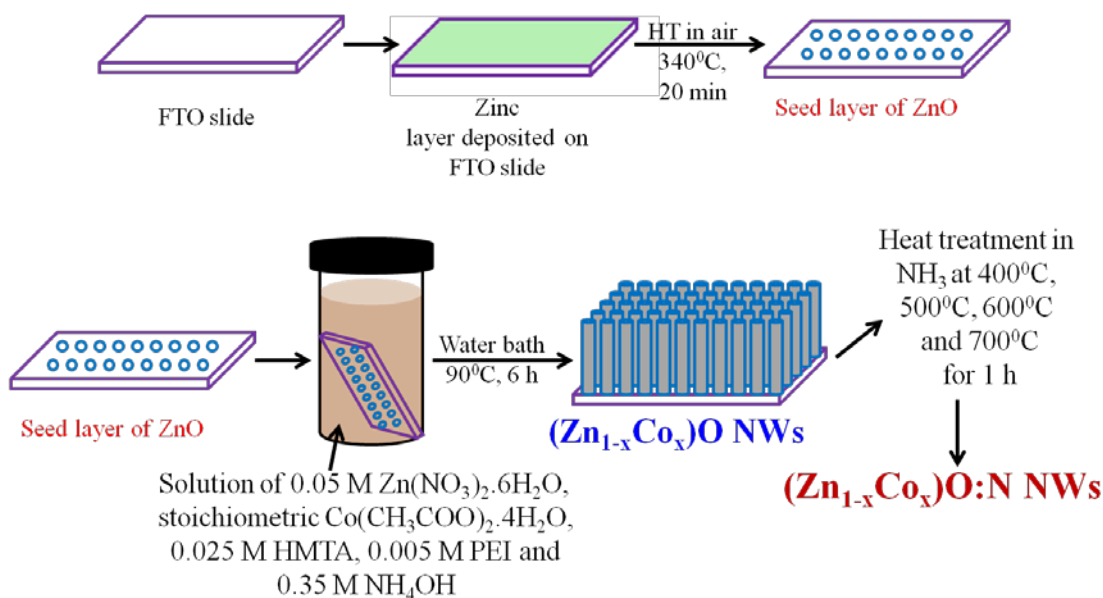


Figure 11: Schematic of the process for synthesizing of ZnO nanowires (NWs) using liquid phase deposition process

4.1.2 SYNTHESIS OF $(\text{Sn}_{1-x}\text{Nb}_x)\text{O}_2\text{:N}$ NANOTUBES (NTs) ($x=0.05$) USING ZnO NWs AS SACRIFICIAL TEMPLATE

ZnO NWs were synthesized on FTO substrate by LPD method, as described previously in **Section 4.1.1.**¹¹⁴ For the synthesis of $(\text{Sn}_{0.95}\text{Nb}_{0.05})\text{O}_2\text{:N}$ NTs, the ZnO NWs were placed in the aqueous solution of 3 ml of 0.15 M ammonium hexafluorostannate (Aldrich), stoichiometric amount of ammonium niobate oxalate hydrate (Aldrich), 1 ml of 0.5 M boric acid (Aldrich) and 1 ml of D.I. water for 30 min. The hydrolysis of precursors resulted in deposition of $(\text{Sn}_{0.95}\text{Nb}_{0.05})\text{O}_2$ on ZnO NWs. The acid¹¹³ formed during the hydrolysis process dissolved the sacrificial template, (ZnO), resulting in the formation of hollow $(\text{Sn}_{0.95}\text{Nb}_{0.05})\text{O}_2$ NTs.^{76, 104, 182, 183} After 30 min, the $(\text{Sn}_{0.95}\text{Nb}_{0.05})\text{O}_2$ NTs were washed with D.I. water and dried at 50°C for 6 h. N doping was carried out by heat treatment of $(\text{Sn}_{0.95}\text{Nb}_{0.05})\text{O}_2$ NTs in anhydrous NH_3 atmosphere (Matheson: 99.99%, flow rate=100cm³/min) at 400°C, 500°C, 600°C and 700°C for 1 h with ramp rate of 10°C/min. The $(\text{Sn}_{0.95}\text{Nb}_{0.05})\text{O}_2$ NTs, heat-treated in NH_3 at 400°C, 500°C, 600°C and 700°C, are denoted as $(\text{Sn}_{0.95}\text{Nb}_{0.05})\text{O}_2\text{:N-400}$ NTs, $(\text{Sn}_{0.95}\text{Nb}_{0.05})\text{O}_2\text{:N-500}$ NTs, $(\text{Sn}_{0.95}\text{Nb}_{0.05})\text{O}_2\text{:N-600}$ NTs and $(\text{Sn}_{0.95}\text{Nb}_{0.05})\text{O}_2\text{:N-700}$ NTs in this study, respectively.

4.1.3 SYNTHESIS OF [WO₃-(Sn_{0.95}Nb_{0.05})O₂:N-600] BILAYER NANOTUBES (NTs)

ZnO nanowires (NWs) were synthesized on fluorine doped tin oxide (FTO) coated glass substrate (0.5cm×2.5cm, Aldrich) using LPD method, as described previously in **Section 4.1.1.**¹¹⁴ WO₃ was deposited on ZnO NWs (**Figure 12**) using wet impregnation method, carried out using ammonium metatungstate (AMT) as tungsten precursor. ZnO NWs prepared using hydrothermal method as mentioned above, were dipped in 50 mM AMT solution for ~1 h. The nanowires were then rinsed with D.I. water and dried at 60°C for 2 h, followed by heat treatment in air at 500°C for 30 min to decompose AMT in WO₃.¹⁸⁴

The synthesized ZnO/WO₃ NWs were placed in an aqueous solution consisting of 3 ml of 0.15 M ammonium hexafluorostannate (AHFS, Aldrich), stoichiometric amount of ammonium niobate oxalate hydrate (ANOH, Aldrich), 1 mL of 0.5 M boric acid (H₃BO₃, Aldrich) and 1 mL of D.I. water at 26°C for 30 min. The hydrolysis of precursors formed the layer of (Sn_{0.95}Nb_{0.05})O₂ deposited on ZnO/WO₃ NWs and ZnO layer was dissolved due to the acid¹¹³ formed during the hydrolysis process, resulting in formation of hollow [WO₃-(Sn_{0.95}Nb_{0.05})O₂]-1.^{76, 104, 182, 183} After 30 min, [WO₃-(Sn_{0.95}Nb_{0.05})O₂]-1 NTs were washed with D.I. water and dried at 60°C for 2 h. N doping was carried out by the heat treatment of [WO₃-(Sn_{0.95}Nb_{0.05})O₂]-1 NTs for 1 h at 600°C in anhydrous NH₃ atmosphere (Matheson: 99.99%, flow rate=100cm³/min) with ramp rate of 10⁰C/min.^{76, 114} This material is denoted as [WO₃-(Sn_{0.95}Nb_{0.05})O₂:N-600]-1 NTs in this study. The schematic of the synthesis process (mentioned above) is shown in **Figure 12**. The thickness of the (Sn_{0.95}Nb_{0.05})O₂:N-600 layer in [WO₃-(Sn_{0.95}Nb_{0.05})O₂:N-600] NTs was increased by increasing the concentration of the precursor solutions and following similar synthesis steps as mentioned above. [WO₃-(Sn_{0.95}Nb_{0.05})O₂:N-600]-2 NTs were synthesized using 3 ml of 0.3 M AHFS solution, stoichiometric amount of ANOH, 1 mL of 1 M H₃BO₃ and 1

mL of D.I. water. The $[\text{WO}_3-(\text{Sn}_{0.95}\text{Nb}_{0.05})\text{O}_2:\text{N}-600]$ -3 NTs were accordingly synthesized using 3 ml of 0.45 M AHFS solution, stoichiometric amount of ANOH, 1 mL of 1.5 M H_3BO_3 and 1 mL of D.I. water.

In order to effectively study the effect of coupling of $(\text{Sn}_{0.95}\text{Nb}_{0.05})\text{O}_2:\text{N}-600$ with WO_3 and thus, compare the optoelectronic properties and photoelectrochemical activity of the resultant bilayer photoanode materials with the parent oxide, namely, $(\text{Sn}_{0.95}\text{Nb}_{0.05})\text{O}_2:\text{N}-600$, $(\text{Sn}_{0.95}\text{Nb}_{0.05})\text{O}_2:\text{N}-600$ NTs were synthesized using the synthesis steps as described previously in Section 4.1.2⁷⁶, using again ZnO NWs as the sacrificial template.

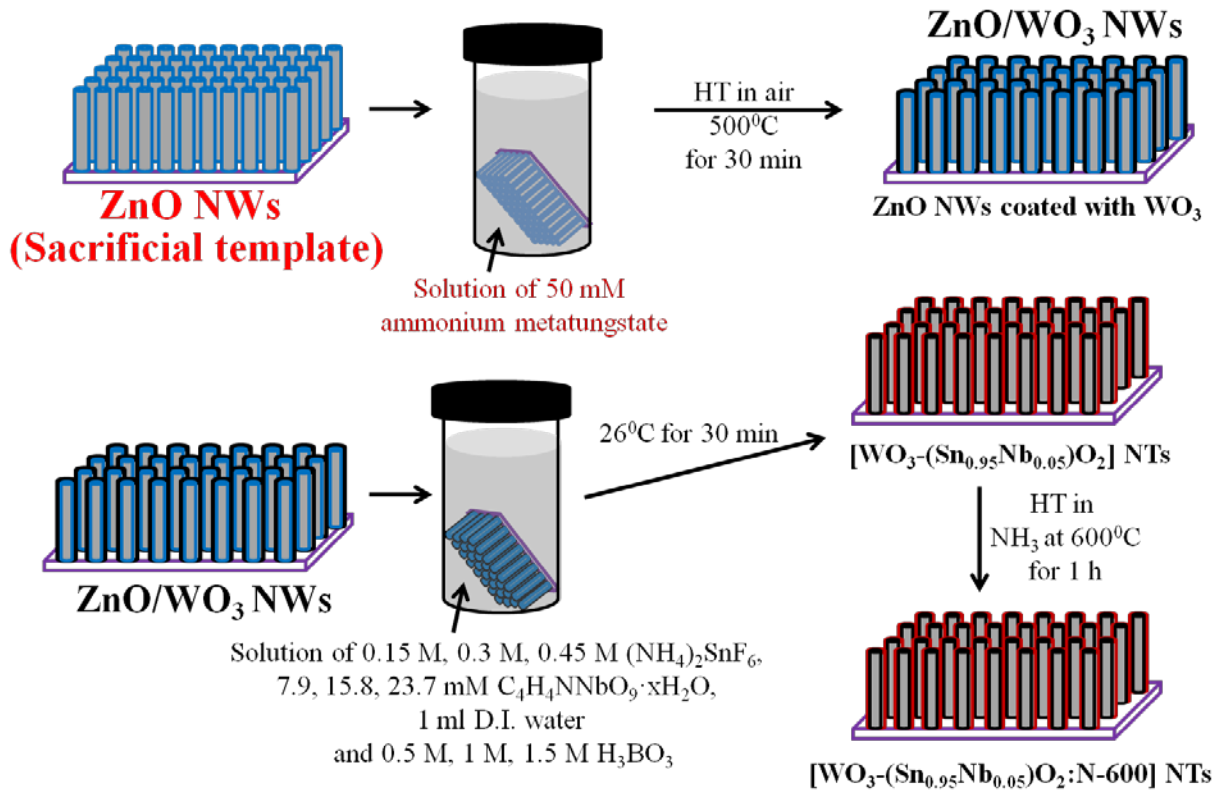


Figure 12: Schematic of the synthesis process of $[\text{WO}_3-(\text{Sn}_{0.95}\text{Nb}_{0.05})\text{O}_2:\text{N}-600]$ NTs

4.2 ELECTRO-CATALYSTS PREPARATION FOR THE CATHODE

4.2.1 SYNTHESIS OF $\text{Co}_{1-x}(\text{Ir}_x)$ ($x=0, 0.2, 0.3, 0.4, 1$) NANOPARTICLES (NPs)

Synthesis of Ir-NPs ($x=1$)

Ir-NPs were synthesized by the reduction of hydrogen hexachloroiridate (IV) hydrate ($\text{H}_2\text{IrCl}_6 \cdot x\text{H}_2\text{O}$, 99.98%, Aldrich) using sodium borohydride (NaBH_4 , 12 wt. % in 14 M NaOH, Aldrich) as the reducing agent.¹⁵⁹ $\text{H}_2\text{IrCl}_6 \cdot x\text{H}_2\text{O}$ was dissolved in ethanol ($\geq 99.5\%$, Aldrich) to which polyvinylpyrrolidone (PVP, Alfa Aesar) was added as a surfactant under stirring. The solution was then adjusted to pH 12 by the addition of NaOH/ethanol solution followed by heating to $65 \pm 5^\circ\text{C}$. After 1 h stirring at $65 \pm 5^\circ\text{C}$, excess NaBH_4 solution was added drop wise under vigorous stirring into the $\text{H}_2\text{IrCl}_6 \cdot x\text{H}_2\text{O}$ solution to form the Ir-NPs by precipitation. The temperature was maintained at $65 \pm 5^\circ\text{C}$ for 1 h. To avoid any deleterious side-reaction with air, the reduction of $\text{H}_2\text{IrCl}_6 \cdot x\text{H}_2\text{O}$ was carried out in high purity N_2 (Matheson; 99.99%, flow rate = $100\text{cm}^3/\text{min}$) atmosphere. The resultant Ir-NPs were centrifuged and washed repeatedly with water purified by the Milli-Q system (18 M Ω cm deionized water, Milli-Q Academic, Millipore) and ethanol followed by drying at 50°C for 6 h. To eliminate any unwanted residue (e.g. PVP), and ensure the complete reduction of any unreacted $\text{H}_2\text{IrCl}_6 \cdot x\text{H}_2\text{O}$ as well, the final Ir-NPs were heat-treated at 200°C in a tube furnace utilizing a mixture of Ar and 6.5% H_2 gas (Matheson; 99.99%, flow rate = $100\text{cm}^3/\text{min}$) for 2 h.¹⁵⁹

Synthesis of Co-NPs ($x=0$)

Co-NPs were synthesized by the chemical reduction of cobalt chloride hexahydrate ($\text{CoCl}_2 \cdot 6\text{H}_2\text{O}$, 98%, Aldrich) using sodium borohydride (NaBH_4 , 12 wt. % in 14 M NaOH, Aldrich) as the reducing agent. $\text{CoCl}_2 \cdot 6\text{H}_2\text{O}$ was dissolved in ethanol ($\geq 99.5\%$, Aldrich) along with polyvinylpyrrolidone (PVP, Alfa Aesar) and then subsequently reduced using NaBH_4 solution to form Co-NPs in a procedure similar to that used to obtain Ir-NPs as explained above. A similar heat-treatment methodology, that was used in the synthesis of Ir-NPs, was employed to obtain residue-free Co-NPs.¹⁵⁹

Synthesis of $\text{Co}_{1-x}(\text{Ir}_x)$ ($x=0.2, 0.3, 0.4$)

Solid solution of $\text{Co}_{1-x}(\text{Ir}_x)$ was synthesized by the reduction of hydrogen hexachloroiridate (IV) hydrate ($\text{H}_2\text{IrCl}_6 \cdot x\text{H}_2\text{O}$, 99.98%, Aldrich) using NaBH_4 in the presence of as-synthesized Co-NPs followed by thermal treatment at 200°C under Ar+6.5% H_2 mixture. In this procedure, the as-synthesized Co-NPs were dispersed in ethanol ($\geq 99.5\%$, Aldrich), to which the PVP as surfactant was added under stirring. To this solution subsequently, stoichiometric amount of $\text{H}_2\text{IrCl}_6 \cdot x\text{H}_2\text{O}$ was added followed by pH adjustment to 12 using NaOH/ethanol solution. The solution was then heated to $65 \pm 5^\circ\text{C}$. After 1 h stirring at $65 \pm 5^\circ\text{C}$, excess NaBH_4 (12 wt. % in 14 M NaOH, Aldrich) solution was added drop wise under the vigorous stirring into the Co-NPs dispersed solution to form Ir-NPs on the surface of the Co-NPs, resulting in the formation of solid solution of $\text{Co}_{1-x}(\text{Ir}_x)$. The temperature was maintained at $65 \pm 5^\circ\text{C}$ for 1 h. To

avoid the oxidation of Co nanoparticles, high purity N₂ (Matheson; 99.99%, flow rate = 100 cm³/min) was kept flowing during the entire synthesis procedure. The resultant electro-catalyst was centrifuged and washed repeatedly with water purified by the Milli-Q system (18 MΩ cm deionized water, Milli-Q Academic, Millipore) and then ethanol, followed by drying at 50°C for 6 h. To ensure complete reaction between Co and Ir and formation of a homogeneous solid solution of Co_{1-x}(Ir_x) as well as remove any unwanted residue from the final product, the final Co_{1-x}(Ir_x) powder was heat-treated at 200°C in a tube furnace using a mixture of Ar and 6.5% H₂ gas (Matheson; 99.99%, flow rate = 100 cm³/min) for 2 h.¹⁵⁹

4.2.2 SYNTHESIS OF (Cu_{0.83}Co_{0.17})₃P:x at.% S (x=10, 20, 30) NANOPARTICLES (NPs)

The mixture of stoichiometric amount of copper chloride dihydrate (CuCl₂.2H₂O, ≥99%, Aldrich), cobalt chloride hexahydrate (CoCl₂.6H₂O, 98%, Aldrich), sodium hypophosphite hydrate (NaH₂PO₂.xH₂O, Aldrich) and sodium thiosulfate pentahydrate (Na₂S₂O₃.5H₂O, ≥99.5%, Aldrich) was mechanically ground using a mortar and pestle. The solid mixture was then heat-treated in ultra-high purity (UHP)-argon atmosphere (Matheson; 99.99%, flow rate = 100 cm³/min) at 250°C for 1 h. After heat treatment, the resultant solid mixture was washed repeatedly with D.I. water purified by the Milli-Q system (18 MΩ cm deionized water, Milli-Q Academic, Millipore) followed by drying at room temperature, forming cobalt-doped copper phosphosulfide NPs. Pure Cu₃P NPs were synthesized following the same procedure as mentioned above, by heat treatment of solid mixture of CuCl₂.2H₂O and NaH₂PO₂.xH₂O in UHP-argon atmosphere (Matheson; 99.99%, flow rate = 100 cm³/min) at 250°C for 1 h, followed by washing with D.I. water and drying at room temperature. (Cu_{0.83}Co_{0.17})₃P NPs were

accordingly also synthesized by heat treatment of stoichiometric mixture of $\text{CuCl}_2 \cdot 2\text{H}_2\text{O}$, $\text{CoCl}_2 \cdot 6\text{H}_2\text{O}$ and $\text{NaH}_2\text{PO}_4 \cdot x\text{H}_2\text{O}$ in UHP-argon atmosphere (Matheson; 99.99%, flow rate = $100\text{cm}^3/\text{min}$) at 250°C for 1 h and further following similar steps as mentioned above. $(\text{Cu}_{0.83}\text{Co}_{0.17})_3\text{P}: x \text{ at.}\% \text{ S}$ ($x=10, 20, 30$) nanoparticles (NPs) of different S concentration are denoted as $(\text{Cu}_{0.83}\text{Co}_{0.17})_3\text{P}:10\text{S}$ NPs, $(\text{Cu}_{0.83}\text{Co}_{0.17})_3\text{P}:20\text{S}$ NPs and $(\text{Cu}_{0.83}\text{Co}_{0.17})_3\text{P}:30\text{S}$ NPs, respectively in this study.

4.3 STRUCTURAL CHARACTERIZATION

X-ray diffraction

Qualitative phase analysis of synthesized nanomaterials was carried out using x-ray diffraction (XRD). Philips XPERT PRO system was used for the XRD analysis, employing CuK_α ($\lambda = 0.15406 \text{ nm}$) radiation at an operating voltage and current of 45 kV and 40 mA, respectively. The XRD peak profile of nanomaterials was analyzed using the Pseudo-Voigt function to determine the Lorentzian and Gaussian contribution of the peak. The integral breadth of the Lorentzian contribution, determined from peak profile analysis using the single line approximation method after eliminating the instrumental broadening and lattice strain contribution, was used in the Scherrer formula to calculate the particle size of the electro-catalysts.¹⁸⁵ The lattice parameter and molar volume of the synthesized nanomaterials have been calculated using the least square refinement techniques.^{76, 114, 159, 160, 179, 186-188}

Microstructure analysis

The microstructure of nanomaterials was studied using scanning electron microscopy (SEM). Energy dispersive x-ray spectroscopy (EDX) analyzer (attached with the SEM machine) was used for quantitative elemental analysis and to ensure homogeneous distribution of elements (by elemental x-ray mapping) within particles of nanomaterials. The elemental and x-ray mapping analysis was carried out using Philips XL-30FEG equipped with an EDX detector system with an ultrathin beryllium window and Si(Li) detector operating at 20 kV. The structure of nanomaterials was studied using transmission electron microscopy using JEOL JEM-2100F.

X-ray photoelectron spectroscopy

The oxidation states of elements in nanomaterials were investigated by conducting x-ray photoelectron spectroscopy (XPS) on the electro-catalysts. A Physical Electronics (PHI) model 32-096 X-ray source control and a 22-040 power supply interfaced to a model 04-548 X-ray source with an Omni Focus III spherical capacitance analyzer (SCA) was used for XPS analysis of electro-catalysts. The system was operated in the pressure range of 10^{-8} to 10^{-9} Torr (1.3×10^{-6} to 1.3×10^{-7} Pa). Calibration of the system was carried out by following the manufacturer's procedures, wherein the photoemission lines, E_b of Cu $2p_{3/2}$ (932.7 eV), E_b of Au $4f_{7/2}$ (84 eV) and E_b of Ag $3d_{5/2}$ (368.3eV) were utilized employing a magnesium anode. The experimentally determined peak areas were correspondingly divided by the instrumental sensitivity factors to determine the desired intensities and these intensity values were reported in this study. The adventitious C 1s peak to 284.8 eV was considered as a reference for the charge correction.

Optical characterization

To study the optical properties of the semiconductor nanomaterials (for photoanode), UV-vis absorption spectra were obtained using the spectrophotometer (DU-600, Beckman). All the spectra were background subtracted. 500 nm is chosen for comparison of the absorbance of semiconductor materials used in this study, as it is close to the wavelength at which maximum solar irradiance is obtained.¹⁸⁹ The Tauc analysis was carried out on the absorption data for determination of the band gap using the following equation^{76, 114, 190}:

$$(\alpha h\nu)^2 = B(h\nu - E_g)$$

where, α is the absorption coefficient, $h\nu$ is the photon energy, B is the constant, E_g is the band gap of the material. The band gap is determined from the x-intercept of $(\alpha h\nu)^2$ vs $h\nu$ plot.

4.4 PHOTOELECTROCHEMICAL CHARACTERIZATION OF SEMICONDUCTOR NANOMATERIALS FOR PHOTOANODE

Photoelectrochemical characterization was conducted in the electrolyte solutions of 0.5 M Na₂SO₄ (pH buffered to 7.0) and 0.5 M H₂SO₄ (pH~0) at 26°C (temperature of the cell maintained using a Fisher Scientific 910 Isotemp refrigerator circulator) employing an electrochemical workstation (VersaSTAT 3, Princeton Applied Research) using a H-type cell (as shown in **Figure 13**) divided into photoanode and cathode compartments separated by Nafion 115 membrane (Dupont).^{76, 114} The photoelectrode was fabricated by affixing a copper wire on the exposed electrically conducting parts of the semiconductor nanomaterials coated on FTO substrates using a silver conductive glue. The substrate was sealed properly on all edges with epoxy resin except the active working areas to provide insulation and ensure strong connection.⁵¹

All the photoelectrochemical measurements were performed using the specific photoelectrode as the working electrode (photoanode), Pt wire (Alfa Aesar, 0.25 mm thick, 99.95%) as the counter electrode, Ag/AgCl (saturated with 4M KCl) as the reference electrode (~ 0.197 V *vs* NHE) for 0.5 M Na₂SO₄ electrolyte solution (pH buffered to 7.0) and Hg/Hg₂SO₄ reference electrode (XR-200, Hach, 0.65 V *vs* NHE) for 0.5 M H₂SO₄ electrolyte solution (pH \sim 0) placed next to the photoanode. Prior to the photoelectrochemical testing, both compartments of the testing cell were purged with ultra-high purity (UHP)-Ar gas for ~ 15 min to expel oxygen present in the electrolyte solution. The photoelectrode was illuminated (100 mW cm⁻²) using a 300 W xenon lamp (Model 6258, Newport) equipped with an AM1.5G filter (Model 81094, Newport) to simulate the solar spectrum and calibrated following the standard manufacturer instructions. To study the effect of modified optical properties on the charge collection and conversion efficiency, the incident photon to current efficiency (IPCE) was recorded under illumination of a monochromatic beam of light from a xenon lamp using different band pass optical filters with center wavelengths at 350, 400, 450, 500, 550 and 600 nm (Newport), respectively.

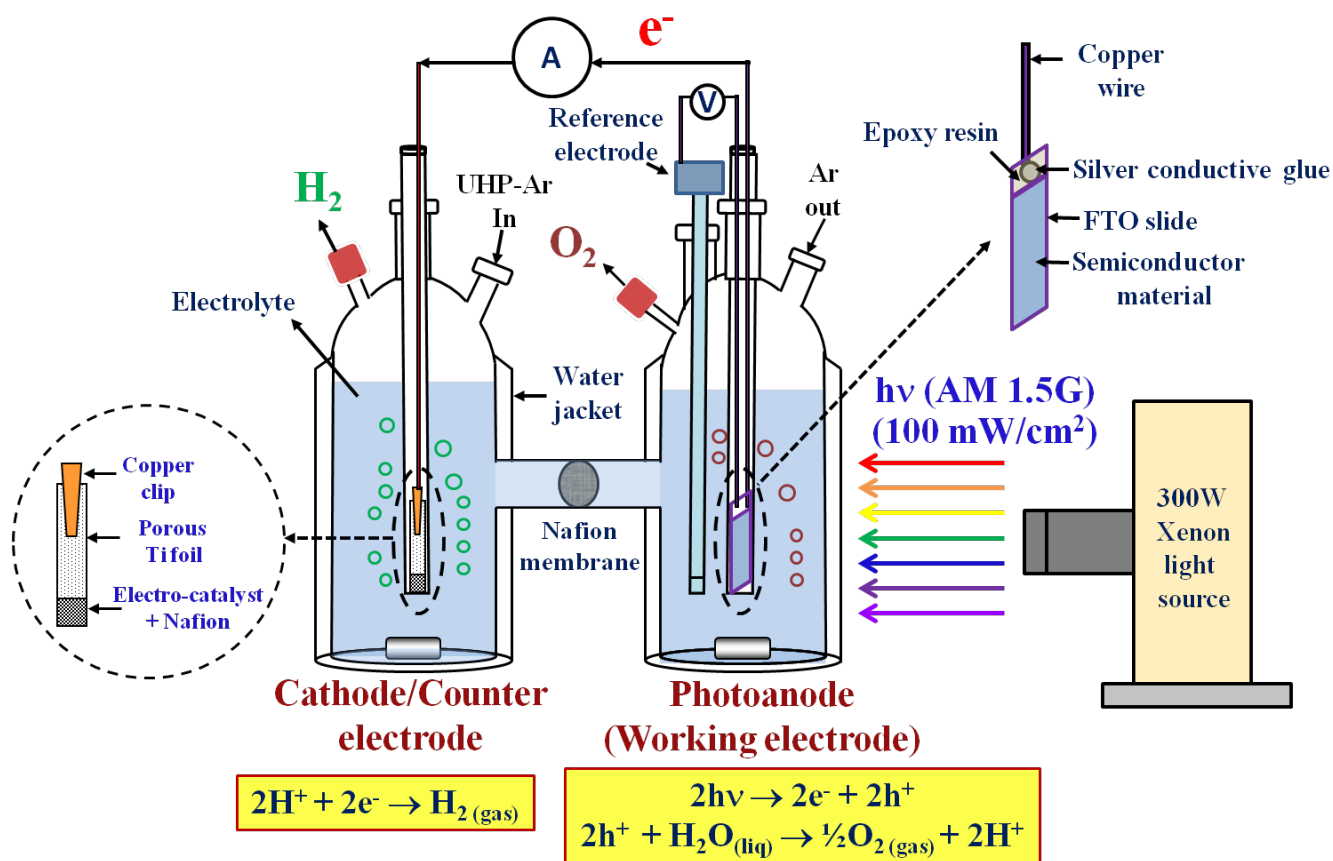


Figure 13: Schematic of H-type PEC water splitting cell for photoelectrochemical characterization

Linear sweep voltammetry

The photoelectrochemical activity of the different photoanode materials has been determined by conducting linear sweep voltammetry (LSV) by scanning the potential using the scan rate of 1 mV sec^{-1} under illumination of 100 mW cm^{-2} . All the reported values of potential in this study are converted to reversible hydrogen electrode (RHE) using the Nernst equation⁷⁶.

114.

$$E_{\text{RHE}} = E_{\text{ref}} + E^{\circ}_{\text{ref}} + 0.059\text{pH}$$

E_{RHE} is the potential versus RHE. E_{ref} is the potential measured against the reference electrode. E°_{ref} is the standard electrode potential of reference electrode. The photocurrent density in iR_{Ω} corrected linear sweep voltammograms (LSVs) obtained under illumination, after subtraction of the current density in the dark was used to compare the photoelectrochemical activity of the different NW materials (R_{Ω} , the ohmic resistance was determined from the electrochemical impedance spectroscopy analysis described in detail below).

Electrochemical impedance spectroscopy (EIS)

EIS has been carried out to determine the ohmic resistance (R_{Ω}), which includes resistance of the various components such as electrolyte solution (R_s) and electrode (R_e).^{76, 114, 159, 160} EIS has been carried out in the frequency range of 100 mHz-100 kHz using the electrochemical work station (VersaSTAT 3, Princeton Applied Research) under illumination (100 mW cm^{-2}) at an amplitude of 10 mV. The experimentally obtained EIS plot was fitted using the ZView software from Scribner Associates with a circuit model $R_s(R_eQ_1)(R_{ct}Q_{dl})$, where R_s is the solution resistance, R_e is the electrode resistance, Q_1 is constant phase element (CPE) and Q_{dl} represents contribution by double layer capacitance.^{76, 114, 159, 160} R_{Ω} was used for ohmic loss correction ($iR_{\Omega}=iR_s + iR_e$) in the LSV curves of the semiconductor materials and the charge transfer resistance (R_{ct}) has been used to study the polarization resistance of the synthesized photoelectro-catalysts. The Mott-Schottky plots of photoanode materials were obtained by performing the EIS measurements at a frequency of 7.5 kHz with an AC amplitude of 10 mV between the voltage window of -0.8 V to 1.2 V (vs NHE).^{76, 114, 191} In addition, hall effect measurement was performed with magnetic field strength of 1.02 T at room temperature (by Van der Pauw method) using the Ecopia 3000 system.

IPCE

To study the effect of light absorption properties on the photoelectrochemical properties, incident photon to current efficiency (IPCE) was determined for semiconductor materials in electrolyte solution at 26°C using different bandpass optical filters with wavelength centered at 350, 400, 450, 500, 550 and 600 nm, similar to earlier reports¹⁹²⁻¹⁹⁵. The IPCE is calculated by the equation¹⁹⁵:

$$\text{IPCE (\%)} = \frac{1240 \times J \times 100}{\lambda \times P}$$

where, J is the measured photocurrent density (mA cm⁻²), P is the incident light intensity (mW cm⁻²) at a specific wavelength (λ , nm).

Photoelectrochemical stability test

To study the photoelectrochemical stability of the photoanode materials, chronoamperometry (CA) (photocurrent density vs time) was performed for 24 h in the electrolyte solution at 26°C, wherein, the photoelectrode was maintained at a constant potential and the loss in photocurrent density was studied. The concentration of the evolved gases (collected in separate chambers of H-type cell consisting of two chambers) was measured during the CA test by using a gas chromatography (GC) system employing Helium as the carrier gas (Agilent 7820A). The amount of elements leached out into the solution from the photoelectrode correlates to the photoelectrochemical stability of the photoelectro-catalyst.^{76, 114, 159, 160} Therefore, accordingly inductively coupled plasma optical emission spectroscopy (ICP-OES, iCAP 6500 duo Thermo Fisher) has been carried out on the electrolyte, collected after 24 h of execution of the CA test, to determine the amount of elements leached out in the electrolyte

solution from the photoanode which relates to photoelectrochemical stability of photoanode materials.^{76, 114, 159, 160}

4.5 ELECTROCHEMICAL CHARACTERIZATION OF HER ELECTRO-CATALYSTS FOR CATHODE

Electrochemical characterization of electro-catalysts for HER (in electrolytic water splitting) was performed at 26⁰C (maintained using a Fisher Scientific 910 Isotemp refrigerator circulator) on a VersaSTAT 3 (Princeton Applied Research) electrochemical workstation using a three electrode cell (**Figure 14**) in the electrolyte solution of 0.5 M sulfuric acid (H₂SO₄) (pH~0). Prior to electrochemical testing, the electrolyte solution was purged with UHP-argon gas for expelling oxygen from the electrolyte solution. The electro-catalyst ink was prepared using 85 wt.% electro-catalyst and 15 wt.% Nafion 117 (5 wt.% solution in lower aliphatic alcohols, Aldrich). The working electrodes were prepared by spreading the electro-catalyst ink on porous Ti foil (Alfa Aesar). The total loading of pure Cu₃P NPs, (Cu_{0.83}Co_{0.17})₃P NPs, and (Cu_{0.83}Co_{0.17})₃P:xS NPs (x=10, 20, 30) was 0.7 mg on 1 cm² area and total loading of 0.4 mg/cm² was used for Co_{1-x}(Ir_x) (x=0, 0.2, 0.3, 0.4, 1). A Pt wire (Alfa Aesar, 0.25 mm thick, 99.95%) was used as the counter electrode and mercury/mercurous sulfate (Hg/Hg₂SO₄) electrode (XR-200, Hach) (0.65 V *vs* NHE) was used as the reference electrode. The electrochemical performance of synthesized non-noble metals based electro-catalysts is compared with state of the art commercial Pt/C electro-catalyst in this study. Hence, the electrochemical performance of commercial 40% Pt/C electro-catalyst (Alfa Aesar) was studied using loading of 0.4 mg of Pt on 1 cm² area under identical operating conditions.

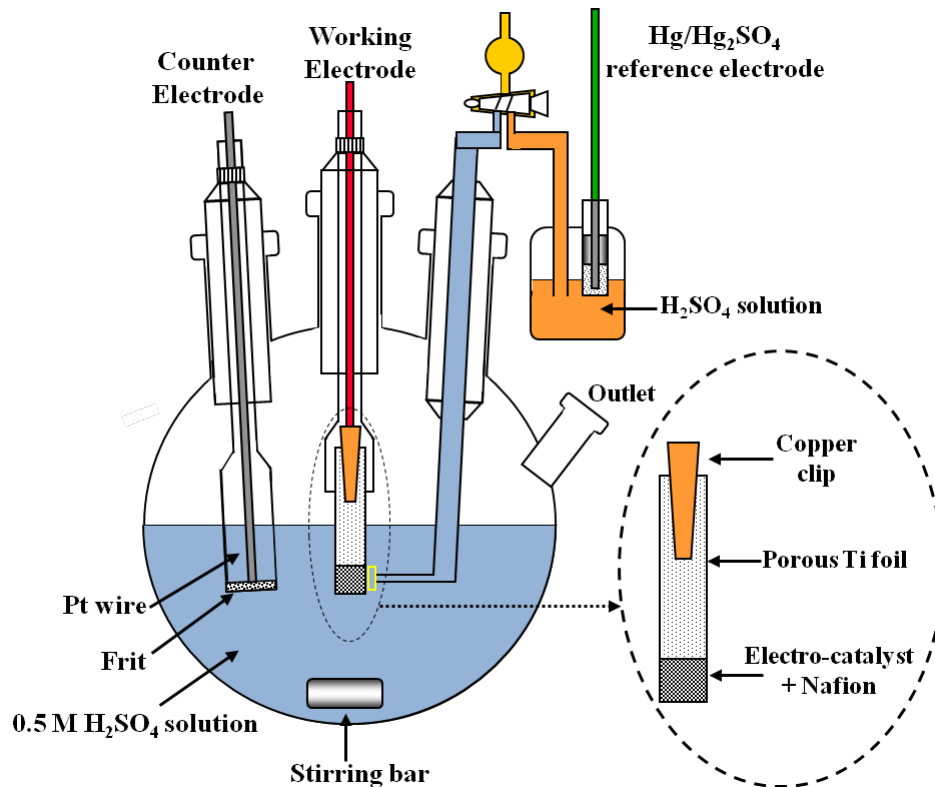


Figure 14: Schematic of three electrode cell for electrochemical characterization of electro-catalysts for HER (in electrolytic water splitting)

Linear scan voltammetry

The electrochemical activity of electro-catalysts for HER was studied by conducting linear scan voltammetry in 0.5 M H₂SO₄ electrolyte solution at 26⁰C using scan rate of 1 mV/sec. Linear scan voltammogram (LSV) curves of different electro-catalysts were iR_{Ω} corrected (R_{Ω} , the ohmic resistance was determined from electrochemical impedance spectroscopy analysis discussed below). The overpotential required for electro-catalysts to reach 10 mA/cm², 20 mA/cm² and 100 mA/cm², as well as, the current density at finite potential near 0V (standard

potential of HER) used to overcome overpotential losses ,i.e., [(-0.05V vs RHE, the standard representative potential selected following literature reports for measuring electrochemical activity for HER^{138, 144, 179, 196-202}] in iR_{Ω} corrected LSV curves were used for comparison of electrochemical activity of different electro-catalysts for HER in this study. The Tafel plot after iR_{Ω} correction given by the equation $\eta = a + b \log i$ (plot of overpotential η vs. log current, log i) was used to determine Tafel slope (b) which was further used to study the reaction kinetics of electro-catalysts for HER.

Electrochemical impedance spectroscopy

The ohmic resistance (R_{Ω}) (which includes resistance from components like electrolyte, electrode) and the charge transfer resistance (R_{ct}) of the electro-catalyst were determined from electrochemical impedance spectroscopy (EIS). The frequency range of 100 mHz-100 kHz at (-0.1 V vs RHE) was used for EIS, which was carried out using the electrochemical work station (VersaSTAT 3, Princeton Applied Research) in 0.5 M H_2SO_4 electrolyte solution (pH~0) at 26⁰C. The experimentally obtained EIS plots of electro-catalysts were fitted using the ZView software from Scribner Associates with a circuit model $R_{\Omega}(R_{ct}Q_1)$ to determine^{76, 114, 159, 160}:

R_{Ω} = Resistance by components like electrolyte, electrode

R_{ct} = Charge transfer resistance (,i.e., polarization resistance)

Q_1 = Constant phase element (represents the capacitance behavior of the electro-catalyst surface)

The ohmic resistance (R_{Ω}) obtained from EIS was used for iR_{Ω} correction in linear scan voltammogram (LSV) curves of electro-catalysts.

Electrochemical stability test

The long term electrochemical stability of electro-catalysts for HER was studied by conducting chronoamperometry (CA) test (current vs time) for 24 h in 0.5 M H₂SO₄ electrolyte solution at 26⁰C, wherein the electrode was maintained at constant voltage of [-0.05 V vs RHE, which is close to standard potential for HER (0V vs RHE)] and the loss in current density (,.i.e., electrochemical activity) for period of 24 h was studied. For comparison, CA test was also performed for commercial Pt/C. The electrolyte (H₂SO₄) solution, collected after 24 h of CA testing of electro-catalyst material, was analyzed using inductively coupled plasma optical emission spectroscopy (ICP-OES, iCAP 6500 duo Thermo Fisher) to determine the composition of elements leached out in the solution from the electrode. This is important as the composition of elements in the solution gives information about the electrochemical stability of electro-catalyst.^{122, 137, 143, 144, 184, 192}

Testing as cathode electro-catalyst for HER in photoelectrochemical water splitting system

Photoelectrochemical characterization has been performed in 0.5 M H₂SO₄ electrolyte solution in H-type cell (**Figure 13**) in an electrochemical workstation (VersaSTAT 3, Princeton Applied Research) at 26⁰C (maintained using a Fisher Scientific 910 Isotemp refrigerator circulator). In H-type cell^{76, 114}, semiconductor material (photoanode) and cathode electro-catalyst were placed in two different compartments, separated by Nafion 115 (Dupont) membrane. The (Sn_{0.95}Nb_{0.05})O₂:N-600 nanotubes (NTs) was used as the photoanode. (Cu_{0.83}Co_{0.17})₃P:S NPs (total loading=0.7 mg/cm²) and Co_{1-x}(Ir_x) NPs (total loading=0.4 mg/cm²) were used as the cathode electro-catalyst for HER. The detailed procedure for fabrication of photoanode has been described previously in **Section 4.4**. (Sn_{0.95}Nb_{0.05})O₂:N-600 NTs was used

as working electrode/photoanode. Hg/Hg₂SO₄ electrode (XR-200, Hach) (potential of +0.65V vs NHE) was used as the reference electrode. Prior to photoelectrochemical testing, both compartments (photoanode and cathode) were purged with UHP-argon gas for ~15 min to expel oxygen present in the electrolyte solution. The photoanode was then illuminated with an intensity of 100 mW/cm² using a 300 W Xe lamp (Model 6258, Newport) equipped with an AM1.5G filter (Model 81094, Newport) to simulate the solar spectrum. The cathode electro-catalyst was coated on porous Ti foil (Alfa Aesar) following the same procedure as described previously. For comparison, Pt/C (Pt loading=0.4 mg_{Pt}/cm²) was also studied as cathode electro-catalyst for HER in PEC water splitting using (Sn_{0.95}Nb_{0.05})O₂:N-600 NTs as photoanode under identical operating conditions.

Maximum ABPE of ~4.1% was obtained using Pt/C as cathode electro-catalyst and (Sn_{0.95}Nb_{0.05})O₂:N-600 NTs as photoanode at applied bias of ~0.75 V (vs RHE) (discussed later in results of photoelectrochemical characterization in **Section 5.2.2**). Hence, chronoamperometry test was conducted using (Cu_{0.83}Co_{0.17})₃P:S NPs and Co_{1-x}(Ir_x) NPs as the cathode electro-catalyst and (Sn_{0.95}Nb_{0.05})O₂:N-600 NTs as working electrode (photoanode) at constant potential of ~0.75 V (vs RHE) for 24 h under illumination (100 mW/cm²). The amount of H₂ gas (evolved at cathode) was measured after each 1 h interval using a gas chromatograph with Helium as the carrier gas (Agilent 7820A). The amount of evolved H₂ gas was used for the determination of ABPE. ABPE was determined using the equation⁷⁵⁻⁷⁹:

$$ABPE = \frac{\Delta G^{\circ} \cdot n_{H_2} - V \cdot I}{P \cdot A} \times 100$$

where, n_{H₂} = H₂ evolution rate (mol/sec)

ΔG° =Gibbs free energy for generating one mole of H₂ from water (237130 J/mol)

P = Total incident power (W/cm²)

A = Area irradiated by incident light (cm²)

I = Photocurrent (A)

V = Bias voltage applied (0.75 V vs RHE) to (Sn_{0.95}Nb_{0.05})O₂:N-600 NTs (photoanode)

5.0 RESULTS AND DISCUSSION

5.1 Co AND N CO-DOPED ZnO NANOWIRES (NWs) (PHOTOANODE)

5.1.1 STRUCTURAL ANALYSIS OF ZnO AND (Zn_{0.95}Co_{0.05})O:N NWs

X-ray diffraction (XRD) study

The XRD patterns of (Zn_{0.95}Co_{0.05})O:N-400 NWs, (Zn_{0.95}Co_{0.05})O:N-500 NWs and (Zn_{0.95}Co_{0.05})O:N-600 NWs (**Figure 15**), show peaks corresponding to ZnO with the wurtzite structure (JCPDS: 01-076-0704) and crystal orientation along (002) plane indicating the c-axis oriented nanowires. The XRD patterns of (Zn_{0.95}Co_{0.05})O:N-400 NWs, (Zn_{0.95}Co_{0.05})O:N-500 NWs and (Zn_{0.95}Co_{0.05})O:N-600 NWs do not show any peaks corresponding to cobalt, cobalt oxide or other Co-containing phases suggesting the formation of single phase Co and N doped ZnO NWs. However, peaks corresponding to pure zinc are seen for (Zn_{0.95}Co_{0.05})O:N-700 NWs, with absence of cobalt, cobalt oxide or other Co-containing phases, suggesting the formation of Co-doped zinc. This can be due to reduction of (Zn_{0.95}Co_{0.05})O NWs due to atomic hydrogen, arising from the decomposition of NH₃ gas.¹⁰⁶ The values of molar volume and lattice parameters of (Zn_{0.95}Co_{0.05})O:N NWs of different N concentration, calculated using the least square refinement technique are shown in **Table 1**. An increase in lattice parameter and molar volume is observed with increase in nitrogen concentration incorporated in the lattice of

(Zn_{0.95}Co_{0.05})O NWs, which indicates lattice expansion upon nitrogen doping, as observed earlier.²⁰³

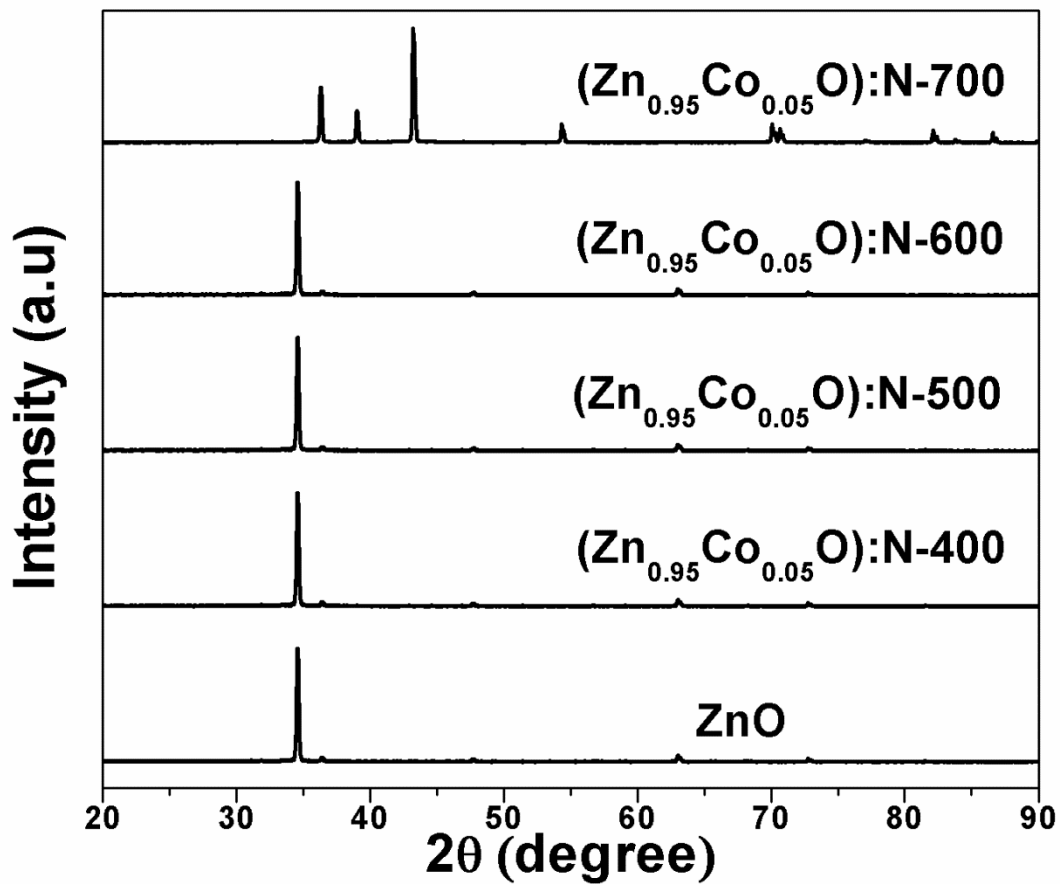


Figure 15: The XRD patterns of ZnO and (Zn_{0.95}Co_{0.05})O:N NWs of different N concentration in wide angle 2θ scan

Table 1: The lattice parameter and molar volume for ZnO and (Zn_{0.95}Co_{0.05})O:N NWs, along with N concentration for (Zn_{0.95}Co_{0.05})O:N NWs by EDX

Composition	Lattice parameter (nm)	Molar volume (cm³/mol)	N concentration by EDX (at. %)
ZnO	a=0.3253 c=0.5213	14.38	-
(Zn _{0.95} Co _{0.05})O:N-400	a=0.3271 c=0.5222	14.57	2.5
(Zn _{0.95} Co _{0.05})O:N-500	a=0.3287 c=0.5232	14.74	6.4
(Zn _{0.95} Co _{0.05})O:N-600	a=0.3309 c=0.5233	14.94	13.2

SEM/EDX study of (Zn_{0.95}Co_{0.05})O:N NWs

Scanning electron microscopy (SEM) has been carried out to study the morphology of the representative composition, (Zn_{0.95}Co_{0.05})O:N-600 NWs. SEM images, showing top view and cross-sectional view, of (Zn_{0.95}Co_{0.05})O:N-600 NWs are shown in **Figure 16**. Cross-sectional view of (Zn_{0.95}Co_{0.05})O:N-600 NWs shows dense and vertically oriented nanowires of diameter of ~180-240 nm and length of ~14 μm. Also, the SEM image of (Zn_{0.95}Co_{0.05})O:N-600 NWs reveals well- spaced/separated nanowires with a clean top surface free of particles at the top and

bottom of nanowires. Energy dispersive x-ray spectroscopy (EDX) is conducted to confirm the presence of elements Zn, Co and N and also, determine concentration of N in $(\text{Zn}_{0.95}\text{Co}_{0.05})\text{O}:\text{N}$ NWs, heat-treated in NH_3 at different temperatures. EDX spectrum of $(\text{Zn}_{0.95}\text{Co}_{0.05})\text{O}:\text{N}$ -600 NWs, shown in **Figure 16**, confirms the presence of elements Zn, Co and N in $(\text{Zn}_{0.95}\text{Co}_{0.05})\text{O}:\text{N}$ -600 NWs. Quantitative elemental composition analysis by EDX is carried out to determine the concentration of nitrogen for $(\text{Zn}_{0.95}\text{Co}_{0.05})\text{O}:\text{N}$ -400, $(\text{Zn}_{0.95}\text{Co}_{0.05})\text{O}:\text{N}$ -500 and $(\text{Zn}_{0.95}\text{Co}_{0.05})\text{O}:\text{N}$ -600 NWs, shown in **Table 1**. The Table clearly shows increase in N concentration with increase in temperature of heat treatment in NH_3 .^{204, 205}

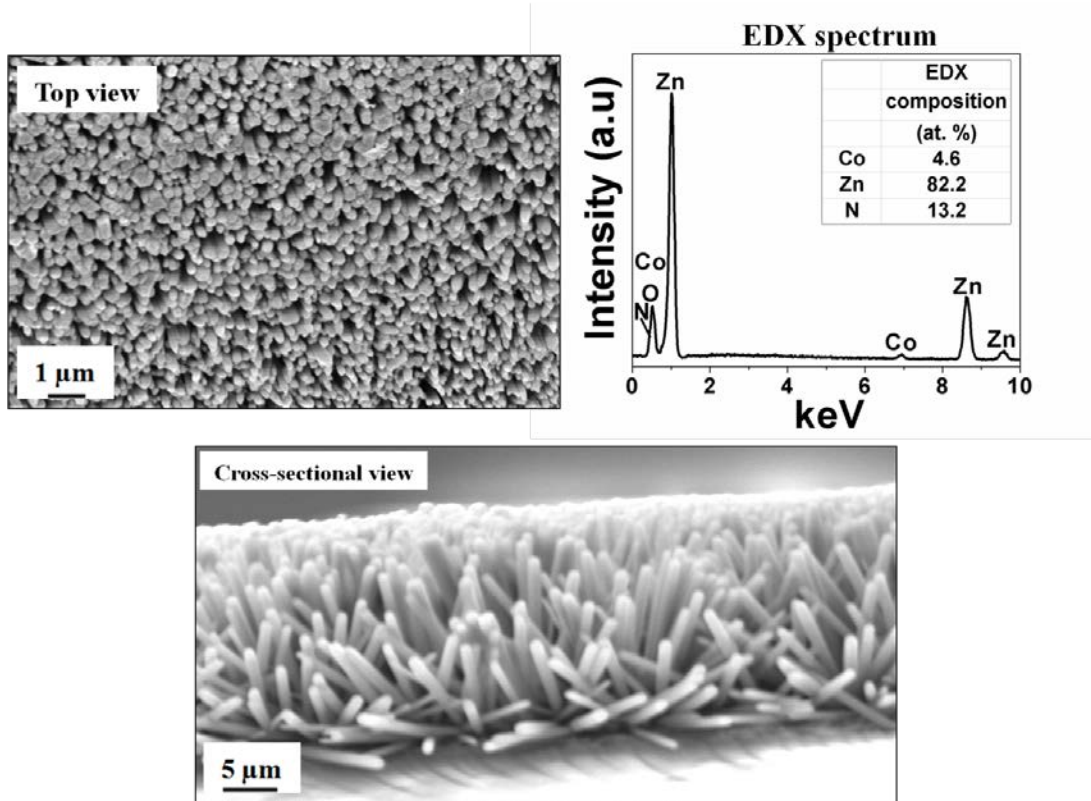


Figure 16: SEM micrograph showing top view, cross-sectional view and EDX spectrum of $(\text{Zn}_{0.95}\text{Co}_{0.05})\text{O}:\text{N}$ -600 NWs

TEM/HRTEM study of $(\text{Zn}_{0.95}\text{Co}_{0.05})\text{O}:\text{N}$ NWs ($x=0.05$)

TEM image of representative composition, $(\text{Zn}_{0.95}\text{Co}_{0.05})\text{O}:\text{N}$ -600 NWs, shown in **Figure 17**, reveals the wire-like geometry with diameter of ~ 220 nm. In **Figure 18**, HRTEM image of $(\text{Zn}_{0.95}\text{Co}_{0.05})\text{O}:\text{N}$ -600 NWs shows lattice fringe with spacing of ~ 0.264 nm, corresponding to (002) plane of ZnO crystal. [slightly larger than the value of d_{111} for ZnO (JCPDS: 01-076-0704, $d_{002} \sim 0.26$ nm) possibly as a result of lattice expansion due to incorporation of N in the lattice of $(\text{Zn}_{0.95}\text{Co}_{0.05})\text{O}$ NWs.

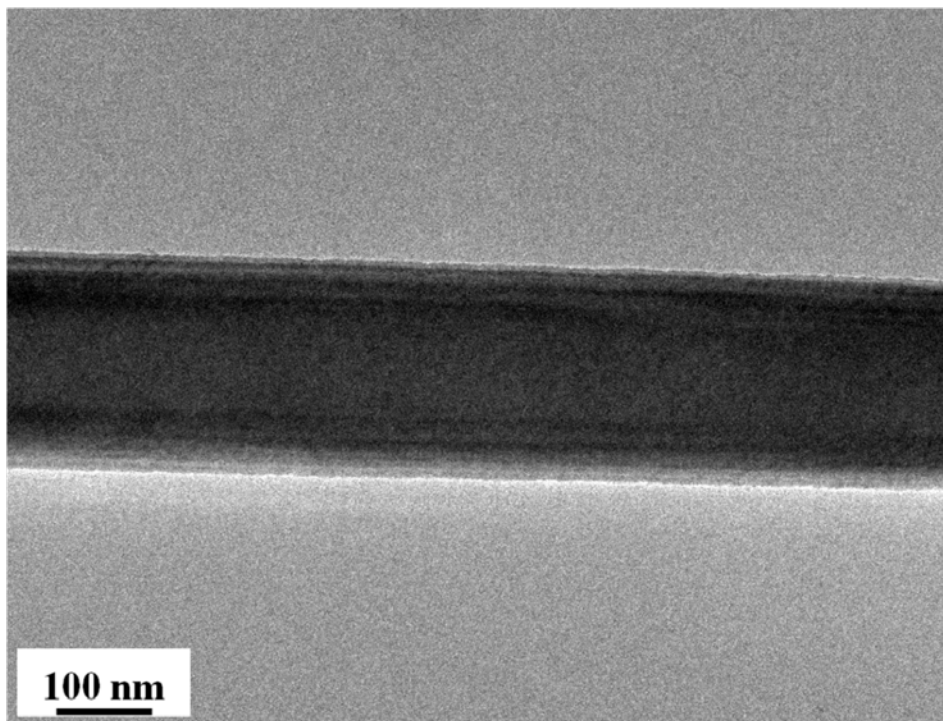


Figure 17: The bright field TEM image of $(\text{Zn}_{0.95}\text{Co}_{0.05})\text{O}:\text{N}$ -600 NWs showing the presence of nanowire with the diameter of ~ 220 nm

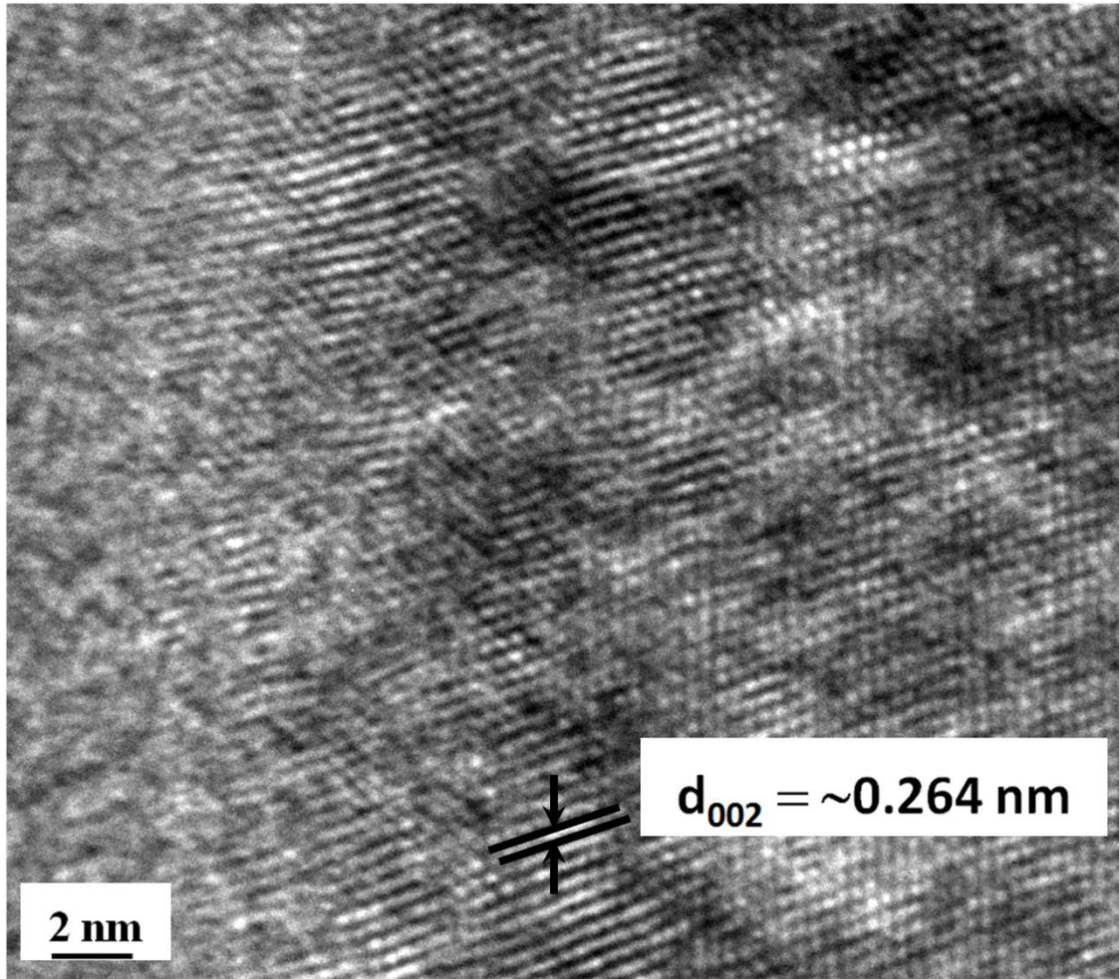


Figure 18: The HRTEM image of $(\text{Zn}_{0.95}\text{Co}_{0.05})\text{O}:\text{N}$ -600 NWs showing lattice fringes with a spacing of $\sim 0.264 \text{ nm}$ corresponding to (002) crystal plane

X-ray photoelectron spectroscopy study of ZnO and $(\text{Zn}_{0.95}\text{Co}_{0.05})\text{O}:\text{N}$ NWs

To determine the oxidation state of Zn, Co and N, X-ray photoelectron spectroscopy (XPS) was carried out on $(\text{Zn}_{0.95}\text{Co}_{0.05})\text{O}:\text{N}$ NWs of different N concentrations and pure ZnO NWs. The XPS spectrum of Zn (**Figure 19**) of pure ZnO shows the presence of Zn $2p_{3/2}$ peak centered at $\sim 1021.6 \text{ eV}$, which shows presence of Zn^{2+} . An increasing negative shift in binding energy is observed with increase in N concentration for Zn $2p_{3/2}$ peak of $(\text{Zn}_{0.95}\text{Co}_{0.05})\text{O}:\text{N}$ NWs,

which is consistent with previously reported results for N-doped TiO₂ nanoparticles.²⁰⁶ In accordance with the previously reported results on N-doped TiO₂ nanoparticles²⁰⁶, the negative shift in Zn 2p_{3/2} peak for (Zn_{0.95}Co_{0.05})O:N NWs can be due to change in electron density around Zn²⁺ due to Co and N co-doping, resulting in modification in the electronic structure of ZnO NWs. The XPS spectrum of N, shown in **Figure 20**, shows the presence of N 1s peak centered at ~398.3 eV for (Zn_{0.95}Co_{0.05})O:N NWs of different N concentration. The N 1s peak at ~398.3 eV for (Zn_{0.95}Co_{0.05})O:N NWs indicates the presence of oxynitride (O-Zn-N or O-Co-N) for (Zn_{0.95}Co_{0.05})O:N NWs.^{106, 207} This shows that heat treatment of (Zn_{0.95}Co_{0.05})O NWs in NH₃ atmosphere favors the substitutional doping of N at O sites in the lattice of (Zn_{0.95}Co_{0.05})O NWs.^{106, 207} The XPS spectrum of Co of (Zn_{0.95}Co_{0.05})O:N NWs, shown in **Figure 21**, shows the presence of Co 2p_{1/2} and Co 2p_{3/2} peaks centered at ~796.3 and ~780.7 eV and satellite peak at ~788.3 eV, corresponding to Co²⁺, with shift in Co 2p_{1/2} and Co 2p_{3/2} peaks to lower binding energy values, compared to bulk CoO by ~0.2 eV.²⁰⁸⁻²¹⁰ The shift of Co 2p_{1/2} and Co 2p_{3/2} peaks to lower binding energy values increases with increase in N concentration similar to the case of Zn, which suggests the presence of oxynitride (O-Co-N) due to substitutional doping of N at O sites.²¹¹ Co-3d are expected to introduce near -0.2eV in the band gap of (Zn_{0.95}Co_{0.05})O NWs [Band gap of (Zn_{0.95}Co_{0.05})O -band gap of ZnO as shown in **Figure 22**, **Figure 23** and **Table 2**]. This suggests the possible compensational and synergistic effect of cobalt substitution combined with the presence of oxygen vacancies created in the material due to the incorporation of nitrogen in the crystal lattice of ZnO resulting in the introduction of electronic states near the CB of ZnO NWs.²¹¹ Fundamental materials characterization is however, further required to gather more in sights into the electronic structure of the material which will be part of future studies.

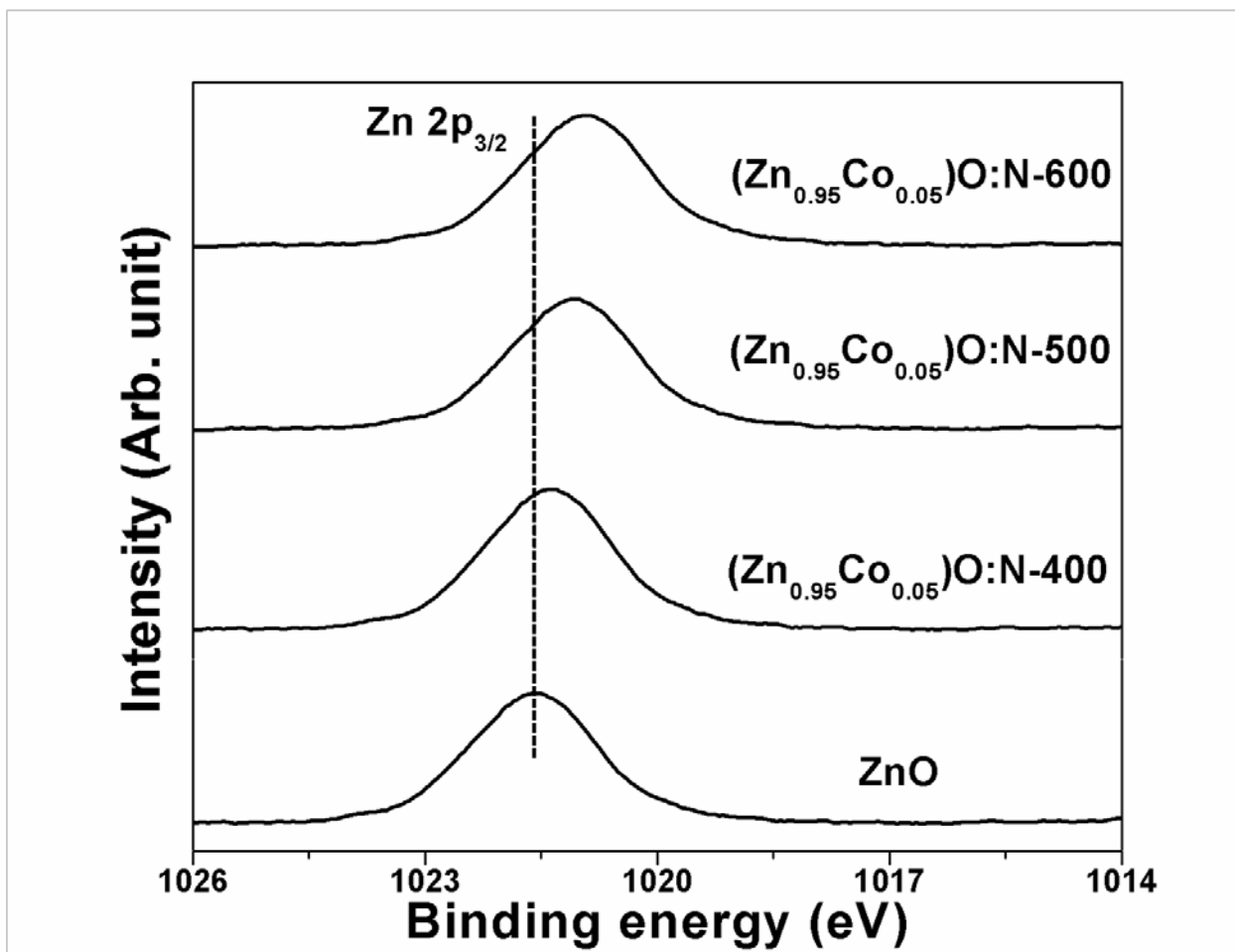


Figure 19: The XPS spectra of (Zn_{0.95}Co_{0.05})O:N NWs of different N concentration showing Zn 2p_{3/2} peak

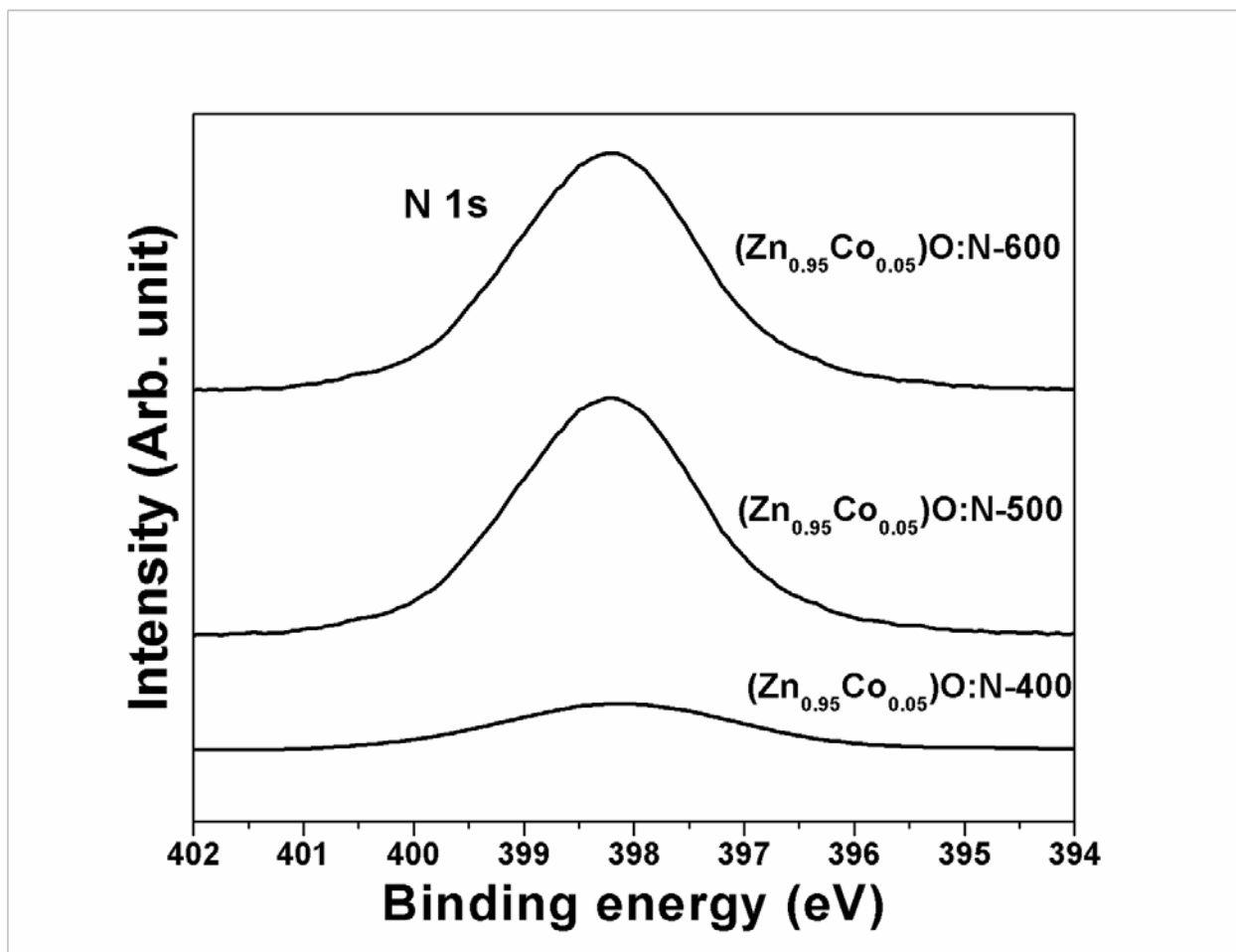


Figure 20: The XPS spectra of $(\text{Zn}_{0.95}\text{Co}_{0.05})\text{O:N}$ NWs of different N concentration showing N 1s peak

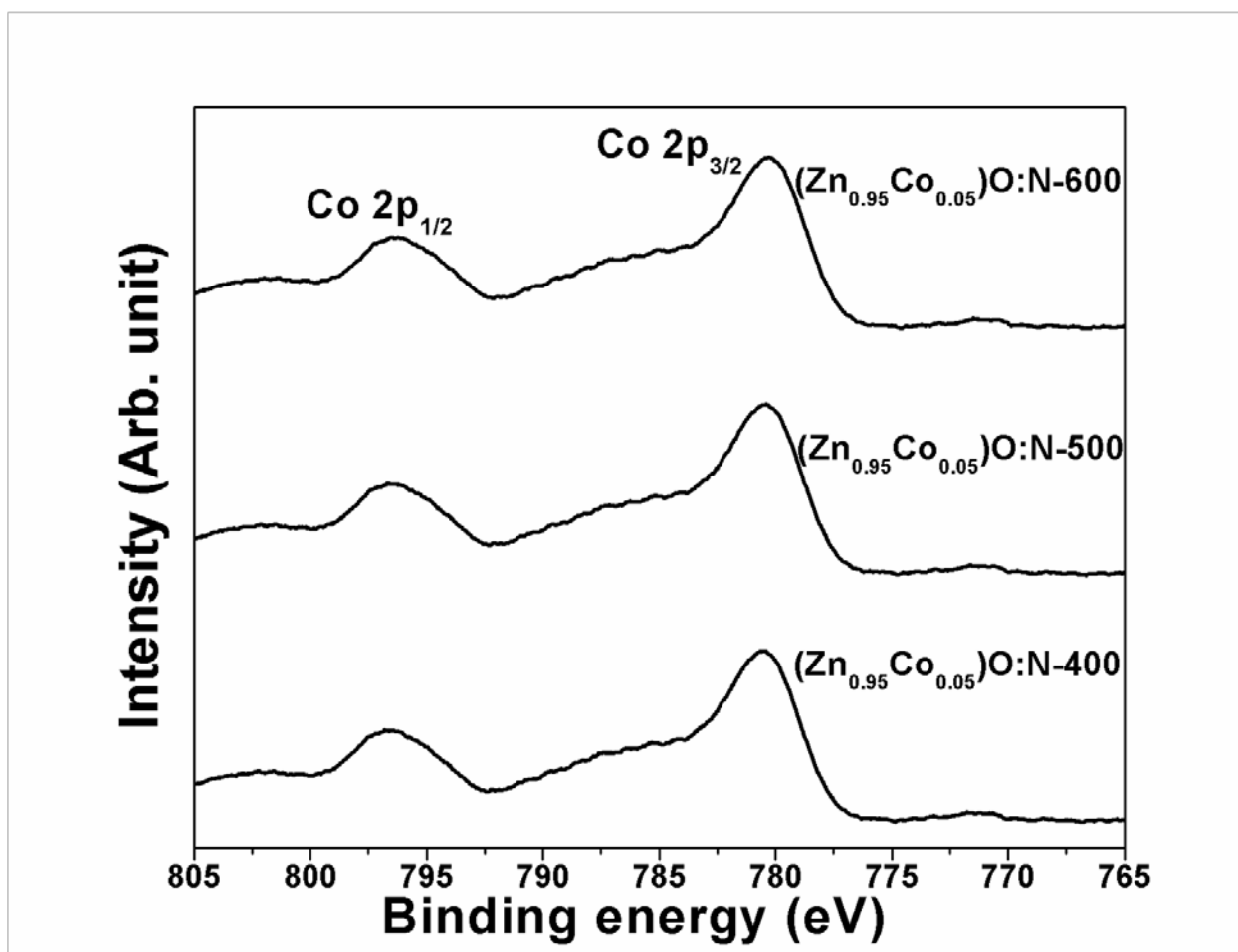


Figure 21: The XPS spectra of (Zn_{0.95}Co_{0.05})O:N NWs of different N concentration showing Co 2p_{1/2} and 2p_{3/2} doublet

UV-Vis absorption spectroscopy and Tauc analysis of ZnO and (Zn_{0.95}Co_{0.05})O:N NWs

The optical properties of ZnO and (Zn_{0.95}Co_{0.05})O:N NWs are studied using UV-Vis absorption spectroscopy. UV-Vis absorption spectra of (Zn_{0.95}Co_{0.05})O:N-400, (Zn_{0.95}Co_{0.05})O:N-500 and (Zn_{0.95}Co_{0.05})O:N-600 NWs are shown in **Figure 22**, along with ZnO NWs for comparison. The onset of light absorption for pure ZnO NWs is seen at ~450 nm, which is similar to that reported earlier.^{82, 116, 212} (Zn_{0.95}Co_{0.05})O:N NWs show excellent light absorption

behavior in the visible region of interest, in comparison to pure ZnO NWs. The absorption peaks for $(\text{Zn}_{0.95}\text{Co}_{0.05})\text{O}:\text{N}$ NWs for different N concentration are red-shifted to higher wavelengths compared to ZnO NWs and the red-shift increases with increase in N concentration. $(\text{Zn}_{0.95}\text{Co}_{0.05})\text{O}:\text{N}-400$, $(\text{Zn}_{0.95}\text{Co}_{0.05})\text{O}:\text{N}-500$ and $(\text{Zn}_{0.95}\text{Co}_{0.05})\text{O}:\text{N}-600$ NWs show ~117%, ~483% and ~598% improved light absorption at 500 nm in comparison to pure ZnO NWs, respectively. 500 nm is chosen for comparison of the absorbance of the semiconductor materials in this study, as it is close to the wavelength at which maximum solar irradiance is obtained.¹⁸⁹ The corresponding Tauc analysis, shown in **Figure 23**, was carried out for estimation of the band gap of $(\text{Zn}_{0.95}\text{Co}_{0.05})\text{O}:\text{N}-400$, $(\text{Zn}_{0.95}\text{Co}_{0.05})\text{O}:\text{N}-500$ and $(\text{Zn}_{0.95}\text{Co}_{0.05})\text{O}:\text{N}-600$ NWs. The values of band gap are determined from the x-intercept of $(\alpha h\nu)^2$ vs $h\nu$ curves. As shown in **Figure 23** and **Table 2**, reduction in band gap with increase in N concentration is seen for $(\text{Zn}_{0.95}\text{Co}_{0.05})\text{O}:\text{N}$ NWs, with the lowest band gap obtained for $(\text{Zn}_{0.95}\text{Co}_{0.05})\text{O}:\text{N}-600$ NWs (~2.16 eV). It is noteworthy that Co and N co-doping helped in significantly reducing the band gap of ZnO from ~3.18 eV to ~2.16 eV for $(\text{Zn}_{0.95}\text{Co}_{0.05})\text{O}:\text{N}-600$ NWs (**Table 2**). The reduction in the band gap of ZnO NWs is important since this facilitates maximum light absorption. This in turn, results in high number of photogenerated electrons available for the reaction, which helps in achieving a marked improvement in the photoelectrochemical performance.

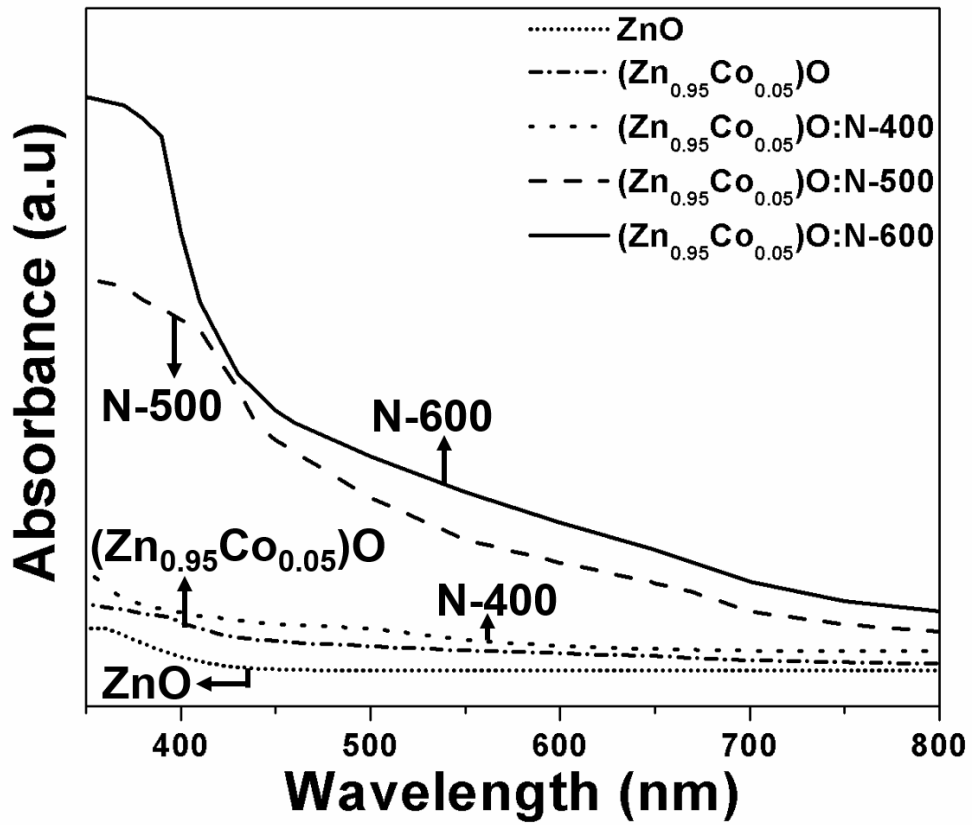


Figure 22: UV-Vis absorption spectra of ZnO, (Zn_{0.95}Co_{0.05})O and (Zn_{0.95}Co_{0.05})O:N NWs of different N concentration

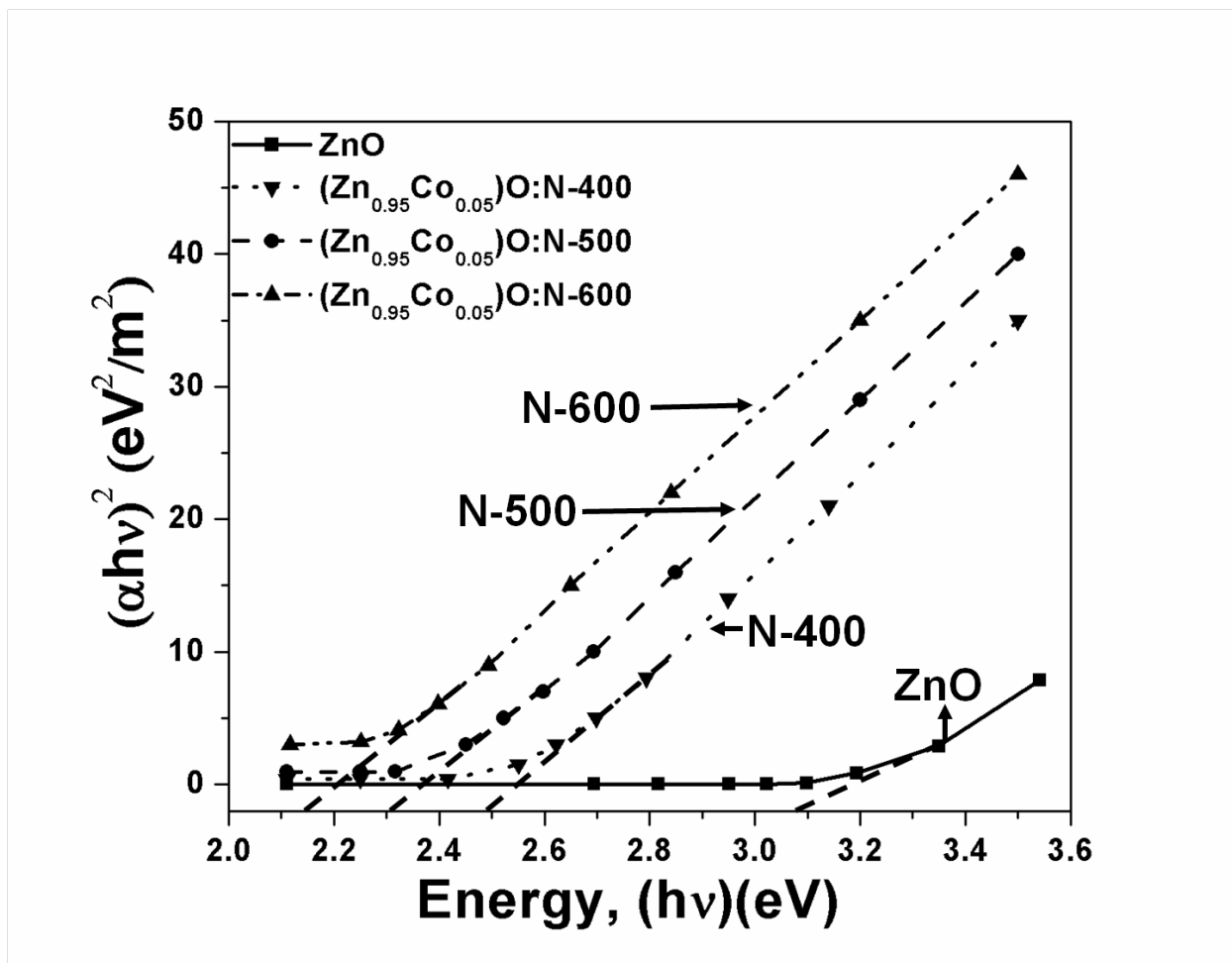


Figure 23: Tauc analysis of ZnO and (Zn_{0.95}Co_{0.05})O:N NWs of different N concentration

Mott-Schottky analysis of ZnO and (Zn_{0.95}Co_{0.05})O:N NWs

The electronic properties of ZnO and (Zn_{0.95}Co_{0.05})O:N NWs were studied by Mott-Schottky analysis, carried out using EIS performed in the dark, shown in **Figure 24** and **Figure 25**. Carrier density in ZnO and (Zn_{1-x}Co_x)O:N NWs as well as flat band potential at the nanowires/electrolyte interface are determined using the Mott-Schottky equation¹⁰⁶:

$$1/C^2 = (2/e_0\epsilon\epsilon_0N_d)[(V-V_{FB})-kT/e_0]$$

where, e_0 is the electron charge, ϵ is the dielectric constant of ZnO (taken as 10)^{106, 213}, ϵ_0 is the permittivity of vacuum, N_d is the carrier density, V is the applied electric potential, V_{FB} is the flat band potential, k is the Boltzmann constant, T is the absolute temperature.

For undoped ZnO NWs, V_{FB} determined from the x-intercept in Mott-Schottky plots ($1/C^2$ vs V), is $\sim(-0.5 \text{ V vs NHE})$, which is closer to the value reported earlier.¹⁰⁶ The flat band potential (V_{FB}) of $(Zn_{0.95}Co_{0.05})O:N-400$ NWs, $(Zn_{0.95}Co_{0.05})O:N-500$ NWs and $(Zn_{0.95}Co_{0.05})O:N-600$ NWs are $\sim(-0.58 \text{ V vs NHE})$, $\sim(-0.59 \text{ V vs NHE})$ and $\sim(-0.66 \text{ V vs NHE})$, respectively. The V_{FB} required for a water splitting reaction to proceed should be more cathodic than the standard reduction potential of hydrogen (E_h), which depends on the value of pH and can be calculated by the equation:

$$E_h = E^0 - 0.059(\text{pH}) = 0 - 0.059(\text{pH})$$

where, E^0 is the standard reduction potential of the water reduction reaction (0V vs NHE). In this study, the electrochemical impedance measurements were conducted at $\text{pH}=7$, which corresponds to $E_h = -0.413 \text{ V (vs NHE)}$. Thus, the values of V_{FB} of ZnO and $(Zn_{0.95}Co_{0.05})O:N$ NWs of different N concentration are more negative (cathodic) than the calculated V_{FB} of $-0.413 \text{ V (vs NHE)}$. This suggests that band edges of ZnO and $(Zn_{0.95}Co_{0.05})O:N$ NWs are more negative than the reduction potential of water (0V vs NHE).

Additionally, n-type behavior is seen for ZnO and $(Zn_{0.95}Co_{0.05})O:N$ NWs, as evidenced by the positive slope obtained in Mott-Schottky plot. The carrier density is calculated from slopes determined from Mott-Schottky plot using the equation^{76, 106, 114}:

$$N_d = (2/e_0\epsilon\epsilon_0)[d(1/C^2)/dV]^{-1}$$

The carrier density of $(Zn_{0.95}Co_{0.05})O:N-400$, $(Zn_{0.95}Co_{0.05})O:N-500$ and $(Zn_{0.95}Co_{0.05})O:N-600$ NWs is $3.1 \times 10^{22} \text{ cm}^{-3}$, $3.98 \times 10^{22} \text{ cm}^{-3}$ and $4.66 \times 10^{22} \text{ cm}^{-3}$ at frequency of 7.5 kHz, which is 4-

orders of magnitude higher than the carrier density determined for pure ZnO NWs ($2.35 \times 10^{18} \text{ cm}^{-3}$ which is almost similar to the earlier reports in the literature¹⁰⁶) (**Table 2**). The carrier density of $4.66 \times 10^{22} \text{ cm}^{-3}$ of $(\text{Zn}_{0.95}\text{Co}_{0.05})\text{O:N-600}$ NWs is the highest carrier density obtained for ZnO based nanostructured photoanodes reported so far, which clearly suggests the profound influence of Co and N co-doping leading to significant improvement in the carrier density of ZnO NWs.^{65, 106, 207} This increment in carrier density is thus important as it offers more photogenerated electrons available for the photoelectrochemical water splitting reaction. In addition, the increased carrier density is expected to shift the Fermi level upwards towards the conduction band, which will distinctly help in achieving improved charge separation at the interface between the $(\text{Zn}_{0.95}\text{Co}_{0.05})\text{O:N}$ NWs and the electrolyte solution, due to an increased degree of band bending.^{64, 214} The improved band bending for $(\text{Zn}_{0.95}\text{Co}_{0.05})\text{O:N}$ NWs is expected to offer large driving force for the photogenerated electrons resulting in improved photocurrent density and thus, expectedly an improved photoelectrochemical performance, compared to pure ZnO NWs.

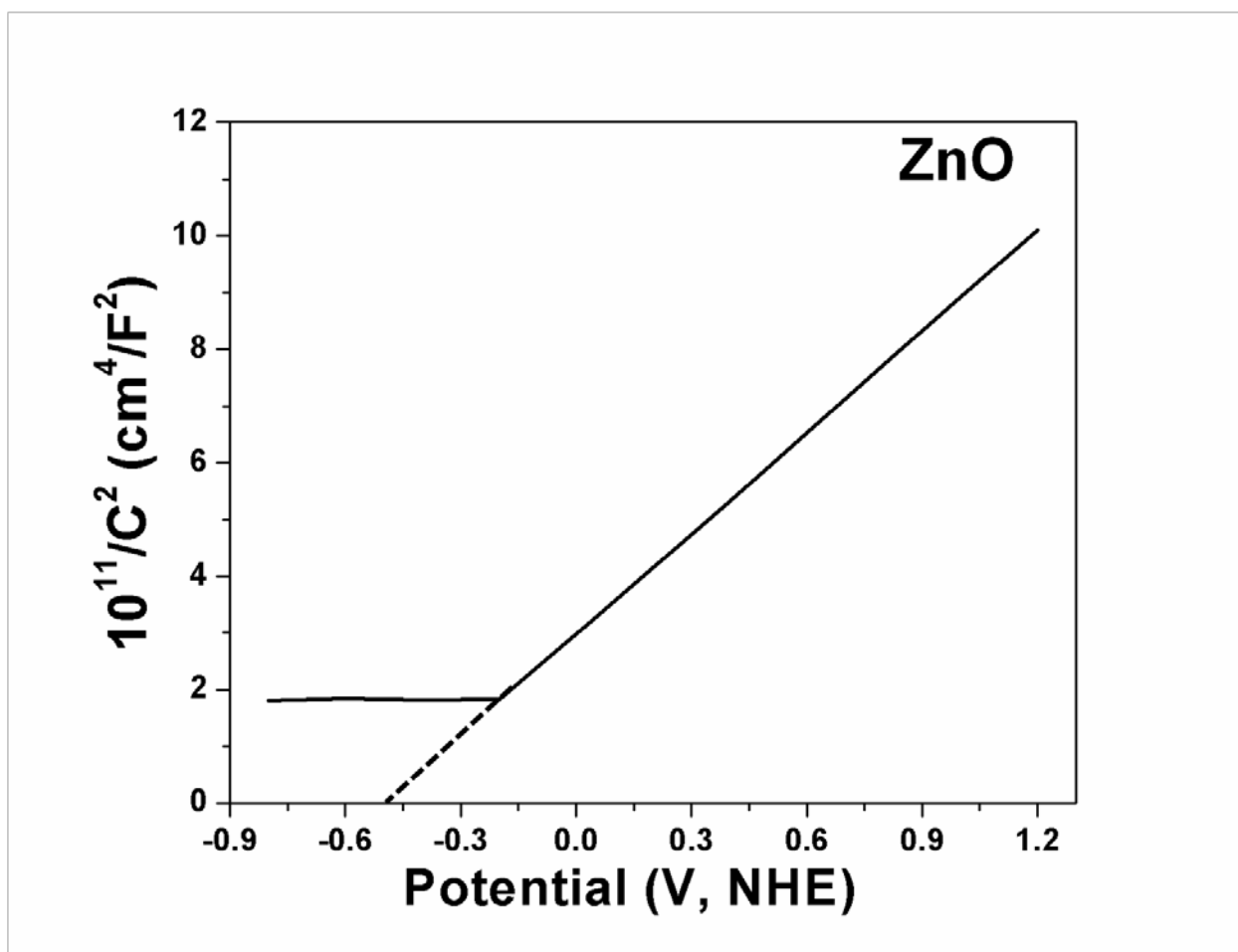


Figure 24: Mott-Schottky plot of ZnO NWs obtained by performing EIS measurements in dark at a frequency of 7.5 kHz with an AC amplitude of 10 mV between voltage window of -0.8 V to 1.2 V (vs NHE) in 0.5 M Na_2SO_4 (pH 7) electrolyte solution at 26°C

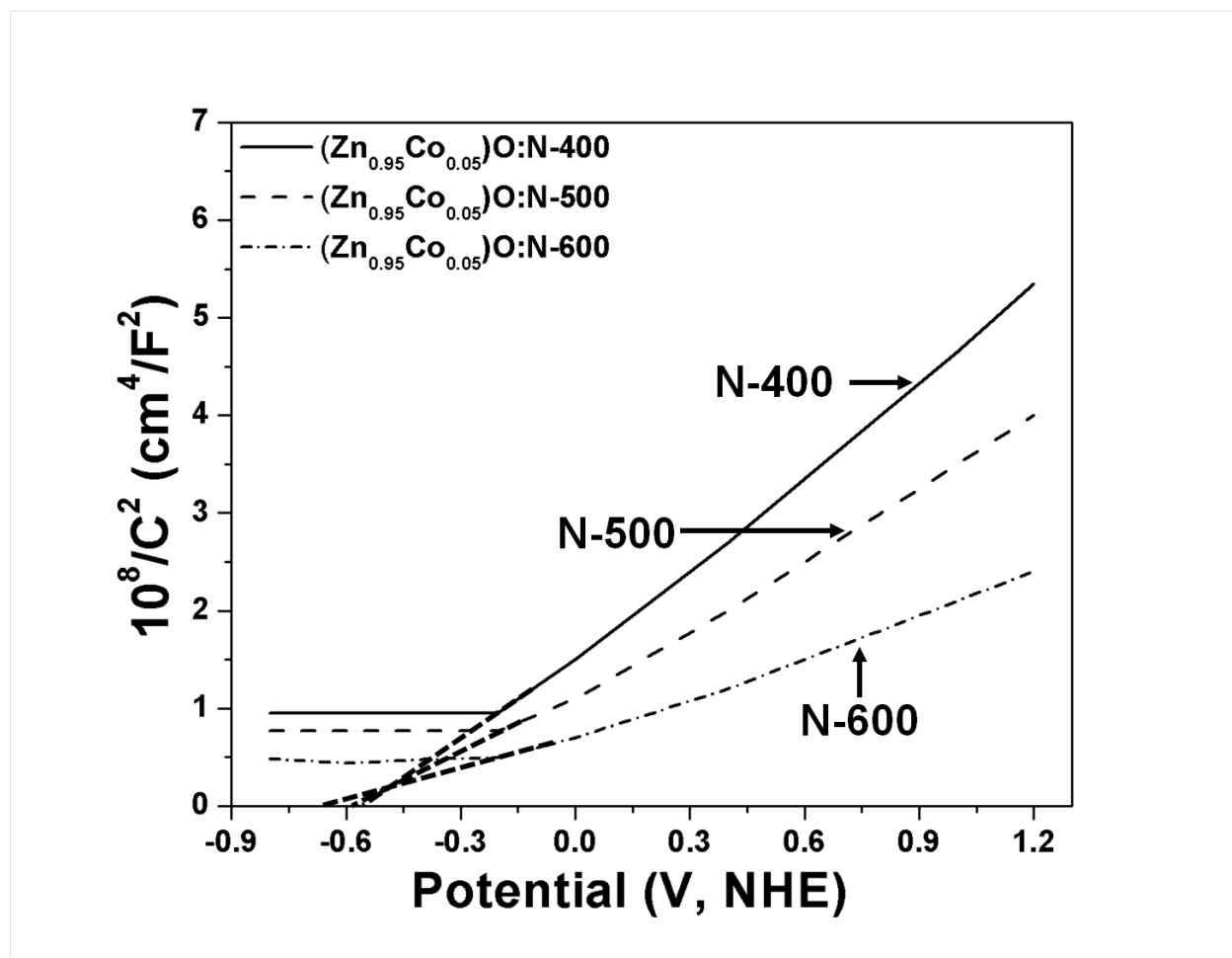


Figure 25: Mott-Schottky plot of $(\text{Zn}_{0.95}\text{Co}_{0.05})\text{O}:\text{N}$ NWs of different N concentration obtained by performing EIS measurements in dark at a frequency of 7.5 kHz with an AC amplitude of 10 mV between voltage window of -0.8 V to 1.2 V (vs NHE) in 0.5 M Na_2SO_4 (pH 7) electrolyte solution at 26°C

5.1.2 PHOTOELECTROCHEMICAL CHARACTERIZATION OF ZnO AND (Zn_{0.95}Co_{0.05})O:N NWs

IPCE of ZnO and (Zn_{0.95}Co_{0.05})O:N NWs

The incident photon to current efficiency (IPCE) was studied using different band pass optical filters to correlate the optical properties with photoelectrochemical properties for the synthesized co-doped (Zn_{0.95}Co_{0.05})O:N-400, (Zn_{0.95}Co_{0.05})O:N-500 and (Zn_{0.95}Co_{0.05})O:N-600 NWs. The IPCE values for (Zn_{0.95}Co_{0.05})O:N-400, (Zn_{0.95}Co_{0.05})O:N-500 and (Zn_{0.95}Co_{0.05})O:N-600 NWs are obtained by measuring the photocurrent density upon light illumination using different band pass optical filters with wavelengths centered at 350, 400, 450, 500, 550 and 600 nm, shown in **Figure 26**. The corresponding IPCE is calculated by the equation^{76, 114, 195}:

$$\text{IPCE (\%)} = \frac{1240 \times J \times 100}{\lambda \times P}$$

where, J is the measured photocurrent density (mA cm⁻²), P is the incident light intensity (mW cm⁻²) at a specific wavelength (λ , nm). An increase in IPCE is observed with increase in N concentration for (Zn_{0.95}Co_{0.05})O:N NWs, which can be attributed to decrease in band gap and significant increase in carrier density which offers enhanced charge separation and improved charge transport (which is confirmed by EIS analysis discussed later) in (Zn_{0.95}Co_{0.05})O:N NWs due to superior band bending as discussed earlier. The corresponding IPCE at the wavelength of 500 nm for (Zn_{0.95}Co_{0.05})O:N-400, (Zn_{0.95}Co_{0.05})O:N-500 and (Zn_{0.95}Co_{0.05})O:N-600 NWs are 1.9%, 3.5% and 15%, respectively. It is noteworthy that the IPCE of (Zn_{0.95}Co_{0.05})O:N NWs is significantly higher than that of pure ZnO NWs (~0% at 500 nm), suggesting the beneficial role of Co and N co-doping in not only lowering the band gap and offering improved light absorption, but also improved charge collection and conversion efficiency in the visible region of

interest.¹⁰⁶ The IPCE for undoped ZnO nanowires (NWs) is 2.5% at 350 nm (which is in UV region) (**Figure 26**) which is similar to that obtained earlier.^{215, 216} The poor IPCE of ZnO NWs under UV light is mainly due to (I) low carrier density (**Table 2**),¹⁸² high charge transfer resistance (R_{ct} , discussed later) leading to poor carrier mobility and superior recombination of photogenerated carriers (**Figure 30** and **Table 4**). The highest IPCE obtained in this study obtained for $(Zn_{0.95}Co_{0.05})O:N-600$ NWs (15% at 500 nm) is the highest IPCE reported so far for ZnO based photoanodes, to the best our knowledge.^{65, 82, 83, 106, 110, 207, 217} This shows that Co and N co-doping is indeed a promising strategy for improving photoelectrochemical response of ZnO.

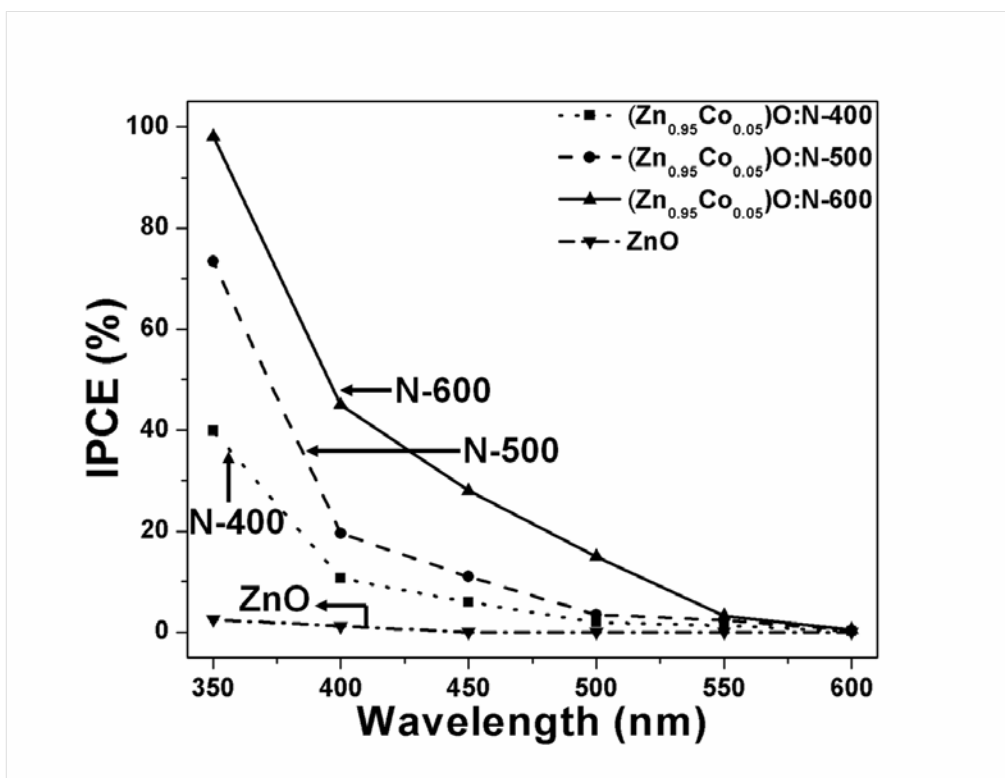


Figure 26: IPCE spectra of ZnO and $(Zn_{0.95}Co_{0.05})O:N$ NWs of different N concentration

Photoelectrochemical activity of ZnO and (Zn_{0.95}Co_{0.05})O:N NWs

The photoelectrochemical activity of (Zn_{0.95}Co_{0.05})O:N NWs is studied using 0.5 M Na₂SO₄ aqueous solution (with pH buffered to ~7.0) as the electrolyte. **Figure 27** shows LSV curves for (Zn_{0.95}Co_{0.05})O:N-400, (Zn_{0.95}Co_{0.05})O:N-500 and (Zn_{0.95}Co_{0.05})O:N-600 NWs, in the dark and with illumination of 100 mW cm⁻², obtained with a scan rate of 1 mV sec⁻¹. Dark scan LSV curves showed a small current density in the range of ~10⁻³ mA cm⁻² for (Zn_{0.95}Co_{0.05})O:N NWs. Under illumination, pronounced photocurrent density is seen for (Zn_{0.95}Co_{0.05})O:N NWs, which increases with increase in potential. The onset of photocurrent density under illumination starts at (0.28 V vs RHE) for ZnO NWs and at (-0.005V vs RHE), (-0.015V vs RHE), (-0.03V vs RHE) for (Zn_{0.95}Co_{0.05})O:N-400, (Zn_{0.95}Co_{0.05})O:N-500 and (Zn_{0.95}Co_{0.05})O:N-600 NWs, respectively (**Table 2**). Thus, the lower onset potential of (Zn_{0.95}Co_{0.05})O:N NWs than that of ZnO suggests lower recombination of photogenerated carriers than ZnO, thereby, resulting in improved photoelectrochemical activity of ZnO upon Co and N co-doping.^{76, 81, 114, 218} The onset potential of (-0.03 V vs RHE) obtained for (Zn_{0.95}Co_{0.05})O:N-400 NWs, (Zn_{0.95}Co_{0.05})O:N-500 NWs and (Zn_{0.95}Co_{0.05})O:N-600 NWs in this study is the lowest onset potential obtained for ZnO based photoanode materials studied so far as shown in Table 3 suggesting excellent photoelectrochemical activity of (Zn_{0.95}Co_{0.05})O:N NWs than other ZnO based materials studied so far.

The photocurrent density at 0.79V (vs RHE) in *iR_Ω* corrected LSV plots for (Zn_{0.95}Co_{0.05})O:N-400, (Zn_{0.95}Co_{0.05})O:N-500 and (Zn_{0.95}Co_{0.05})O:N-600 NWs is 3.56 mA cm⁻², 6.56 mA cm⁻² and 8.78 mA cm⁻², respectively (**Table 2**). This shows that the photoelectrochemical activity increases with increase in N concentration for (Zn_{0.95}Co_{0.05})O:N

NWs. The maximum photocurrent density obtained for $(\text{Zn}_{0.95}\text{Co}_{0.05})\text{O:N-600}$ NWs (8.78 mA cm^{-2}) is $\sim 147\%$ and $\sim 34\%$ higher than that of $(\text{Zn}_{0.95}\text{Co}_{0.05})\text{O:N-400}$ (3.56 mA cm^{-2}) and $(\text{Zn}_{0.95}\text{Co}_{0.05})\text{O:N-500}$ NWs (6.56 mA cm^{-2}), respectively. It is also noteworthy that the photocurrent density of $(\text{Zn}_{0.95}\text{Co}_{0.05})\text{O:N-600}$ NWs (8.78 mA cm^{-2}) is ~ 68 and ~ 275 times higher than that of $(\text{Zn}_{0.95}\text{Co}_{0.05})\text{O}$ NWs (0.13 mA cm^{-2}) and ZnO NWs (0.032 mA cm^{-2}). The excellent photoelectrochemical activity of $(\text{Zn}_{0.95}\text{Co}_{0.05})\text{O:N}$ NWs can be attributed to significantly reduced band gap (**Figure 23** and **Table 2**) resulting in superior light absorption (**Figure 22**), high carrier density (**Figure 25** and **Table 2**), improved charge separation and collection (**Figure 26**) and improved electron transfer (shown by EIS analysis under illumination discussed later) at the interface between the $(\text{Zn}_{0.95}\text{Co}_{0.05})\text{O:N}$ NWs and electrolyte solution.

The variation of ABPE, calculated using **Equation 1**, with the applied potential is shown in **Figure 28** and **Figure 29**. The maximum ABPE, observed for $(\text{Zn}_{0.95}\text{Co}_{0.05})\text{O:N-400}$, $(\text{Zn}_{0.95}\text{Co}_{0.05})\text{O:N-500}$ and $(\text{Zn}_{0.95}\text{Co}_{0.05})\text{O:N-600}$ NWs, is 0.82% , 0.92% and 1.39% at 0.79 V (*vs* RHE), which is ~ 51 , ~ 57 , ~ 87 fold higher than that of ZnO (0.016% at 0.92 V *vs* RHE), respectively (**Table 2**). The superior ABPE obtained at low potential for $(\text{Zn}_{0.95}\text{Co}_{0.05})\text{O:N}$ NWs shows the beneficial role of N as potential dopant in improving the ABPE of $(\text{Zn}_{0.95}\text{Co}_{0.05})\text{O}$ NWs. The maximum ABPE for $(\text{Zn}_{0.95}\text{Co}_{0.05})\text{O:N-600}$ NWs (1.39%) is $\sim 70\%$ and $\sim 51\%$ higher than that of $(\text{Zn}_{0.95}\text{Co}_{0.05})\text{O:N-400}$ (0.82%) and $(\text{Zn}_{0.95}\text{Co}_{0.05})\text{O:N-500}$ NWs (0.92%), respectively. To the best of our knowledge and based on values of ABPE for different ZnO materials studied so far given in **Table 3**, the ABPE of 1.39% for $(\text{Zn}_{0.95}\text{Co}_{0.05})\text{O:N-600}$ NWs is the maximum ABPE, reported thus far, at considerably lower potential (0.79 V *vs* RHE) than the other ZnO based materials studied to date. These results thus suggest the remarkable improvement in photoelectrochemical activity of ZnO by co-doping of Co and N.

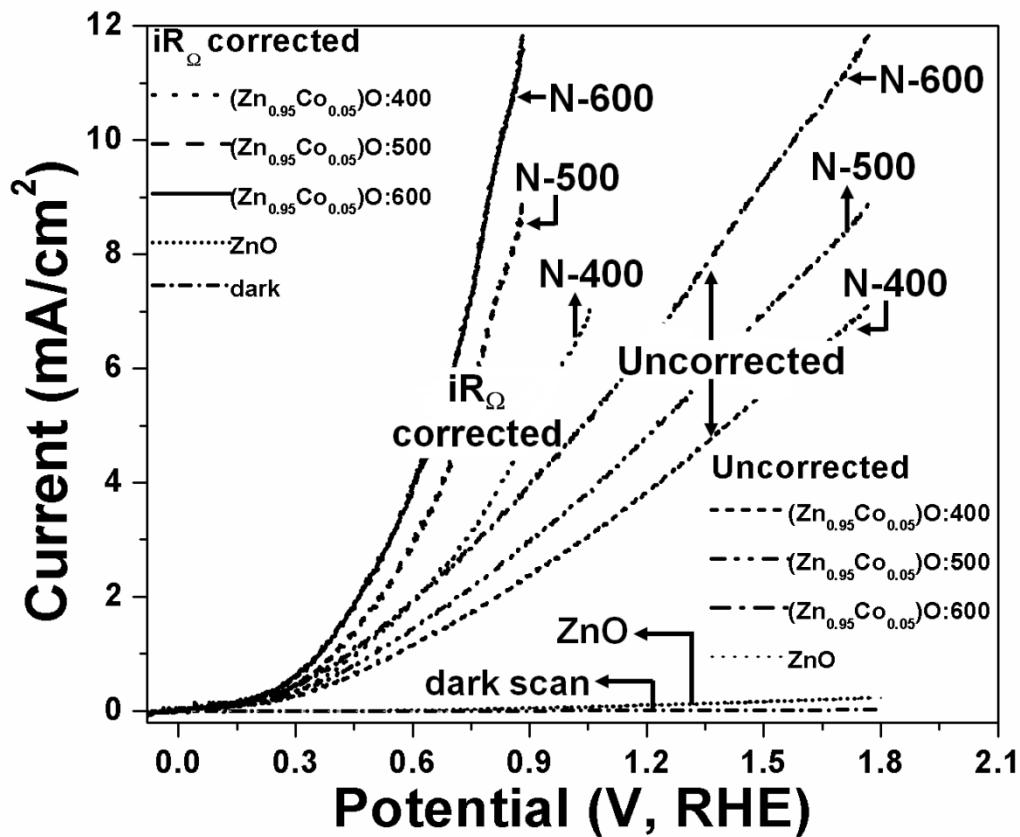


Figure 27: Linear scan voltammogram (LSV) curves for ZnO and (Zn_{0.95}Co_{0.05})O:N NWs of different N concentration in dark and illumination of 100 mW cm⁻² measured in 0.5 M Na₂SO₄ (pH 7) electrolyte solution at 26°C, before and after iR_Ω correction

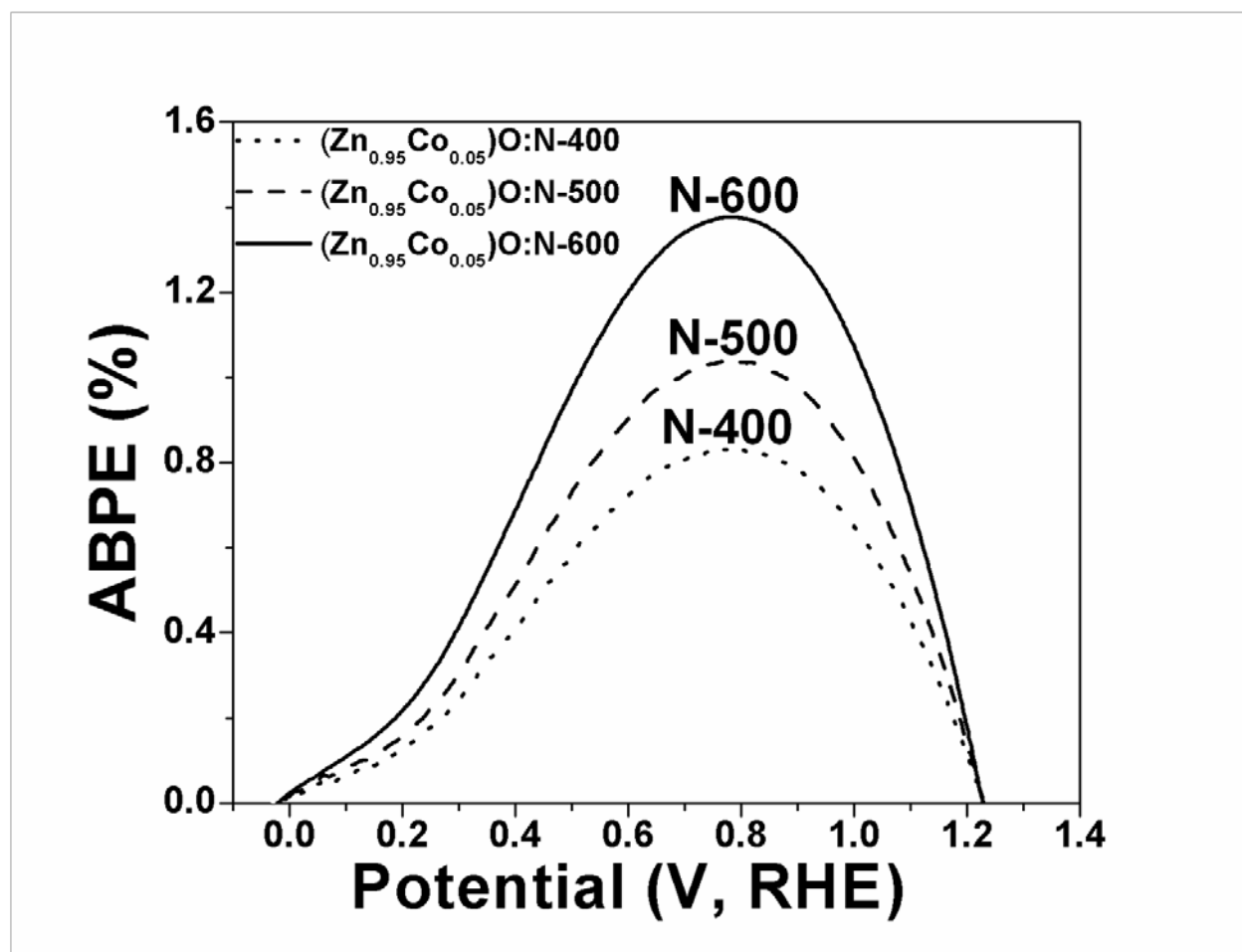


Figure 28: Applied bias photon-to-current efficiency (ABPE) as a function of applied potential for $(\text{Zn}_{0.95}\text{Co}_{0.05})\text{O:N}$ NWs of different N concentration

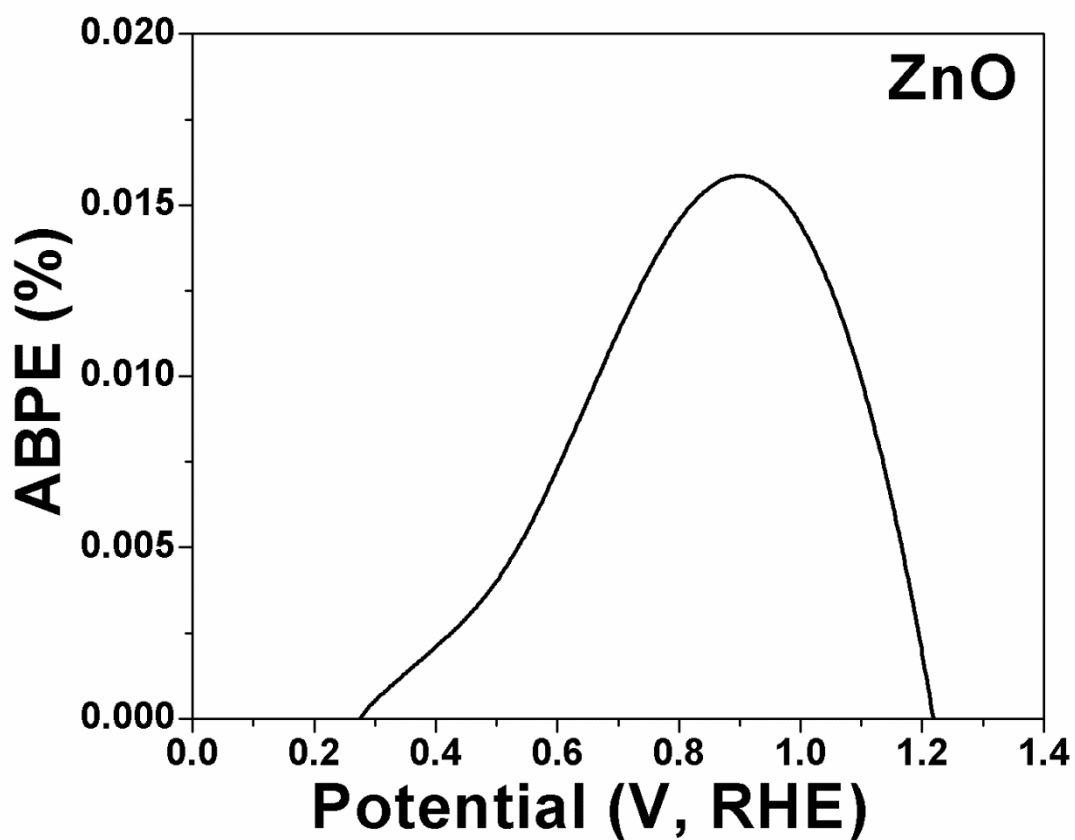


Figure 29: Applied bias photon-to-current efficiency (ABPE) as a function of applied potential for ZnO NWs

Table 2: Results of Tauc analysis, Mott-Schottky analysis and photoelectrochemical characterization of ZnO and (Zn_{0.95}Co_{0.05})O:N NWs of different N concentration

Composition	Band gap (eV)	Carrier density (cm⁻³)	Onset potential (V, RHE)	Photocurrent density at 0.79V (RHE) (mA cm⁻²)	Max. solar to hydrogen efficiency (SHE) (%)	Potential at max. SHE (V, RHE)
ZnO	3.18	2.35×(10 ¹⁸)	0.28	0.032	0.016	0.92
(Zn _{0.95} Co _{0.05})O	2.98	3.98×(10 ¹⁸)	0.15	0.13	0.058	0.82
(Zn _{0.9} Co _{0.1})O	2.92	5.02×(10 ¹⁸)	0.15	0.075	0.034	0.82
(Zn _{0.95} Co _{0.05})O:N-400	2.49	3.1×(10 ²²)	-0.005	3.56	0.82	0.79
(Zn _{0.95} Co _{0.05})O:N-500	2.31	3.98×(10 ²²)	-0.015	6.56	0.92	0.79
(Zn _{0.95} Co _{0.05})O:N-600	2.16	4.6×(10 ²²)	-0.03	8.78	1.39	0.79

Table 3: Efficiency of photoelectrochemical water splitting of various photoanode materials, reported in the literature

Photoanode material	Max. ABPE, %	Potential at max. ABPE (V, RHE)	Onset potential (V, RHE)	Ref
N-doped ZnO nanowire arrays	0.15	1.11	0.21	¹⁰⁶
N-doped ZnO nanotetrapods	0.31	0.92	0.41	²⁰⁷
TiO ₂ :Al nanorod array thin film	0.02	0.5 (vs Ag/AgCl)	0.61	²¹⁹
Bent ZnO nanorod photoanode	0.08	0.69	-	²²⁰
Si/ZnO core/shell nanowire arrays	0.38	0.65 (vs Ag/AgCl)	0.11	²²¹
Hierarchical Fe ₂ O ₃ /WO _x nanowires	0.2	0.25	0.01	²²²
C-doped ZnO porous nanoarchitectures	0.75	0.91	0.31	¹¹⁰
Si/TiO ₂ core/shell nanowire arrays	0.035	1.15	0.36	²²³

Table 3 (continued)				
Fe ₂ O ₃ :Cu nanostructured film	0.28	0.6 (vs Ag/AgCl)	1.44	⁸³
ZnFe ₂ O ₄ /ZnO system	0.15	1.21	0.51	²¹⁷
TiO ₂ -ZnS core-shell	0.38	0.81	0.26	⁶⁵
Au coated 3D ZnO nanowires	0.52	0.75	0.3	⁸²
<u>(Zn_{0.95}Co_{0.05})O:N-600 NWs</u>	<u>1.39</u>	<u>0.79</u>	<u>-0.03</u>	<u>Present work</u>

Electrochemical impedance spectroscopy of ZnO and (Zn_{0.95}Co_{0.05})O:N NWs under illumination

In addition to the optoelectronic and photoelectrochemical properties discussed above, electron transfer properties are also of considerable importance in understanding the photoelectrochemical processes operational for the facile hydrogen production from PEC water splitting. Higher ABPE obtained for (Zn_{0.95}Co_{0.05})O:N-600 NWs compared to (Zn_{0.95}Co_{0.05})O:N-400 and (Zn_{0.95}Co_{0.05})O:N-500 NWs could possibility indicate improved electrochemical reaction kinetics in addition to increased light absorption (**Figure 22**), carrier density (**Figure 25** and **Table 2**) and charge collection and conversion efficiency or IPCE (**Figure 26**) for (Zn_{0.95}Co_{0.05})O:N-600 NWs than (Zn_{0.95}Co_{0.05})O:N-400 and (Zn_{0.95}Co_{0.05})O:N-500 NWs. Hence, to understand the reaction kinetics for (Zn_{0.95}Co_{0.05})O:N NWs, electrochemical impedance spectroscopy (EIS) was carried out to study the charge transfer resistance (R_{ct}) at the photoelectro-catalyst/electrolyte interface. R_{ct} for (Zn_{0.95}Co_{0.05})O:N NWs decreases with increase

in N concentration with the lowest R_{ct} for $(Zn_{0.95}Co_{0.05})O:N-600$ NWs ($16 \Omega.cm^2$), indicating the improved reaction kinetics for $(Zn_{0.95}Co_{0.05})O:N$ NWs with increase in N concentration (**Figure 30** and **Table 4**). Also, it should be noted that the R_{ct} for $(Zn_{0.95}Co_{0.05})O:N-600$ NWs ($16 \Omega.cm^2$) is almost six-fold lower than pure ZnO ($90 \Omega.cm^2$).

These results thus show that the electrochemical reaction kinetics and thus, photoelectrochemical activity is superior for $(Zn_{0.95}Co_{0.05})O:N-600$ NWs in comparison to ZnO NWs, $(Zn_{0.95}Co_{0.05})O:N-400$ NWs and $(Zn_{0.95}Co_{0.05})O:N-500$ NWs, which compounded together aid in achieving the maximum ABPE of 1.39% for $(Zn_{0.95}Co_{0.05})O:N-600$ NWs. The lower R_{ct} for $(Zn_{0.95}Co_{0.05})O:N-600$ NWs could possibly be attributed to the efficient separation and thus, minimum recombination of the photogenerated carriers, as seen in IPCE analysis (**Figure 26**).^{76, 114, 224, 225} The facile nature of the reaction kinetics in addition to improved optoelectronic characteristics renders $(Zn_{0.95}Co_{0.05})O:N-600$ NWs a very promising material in comparison to other semiconductor materials hitherto under study.

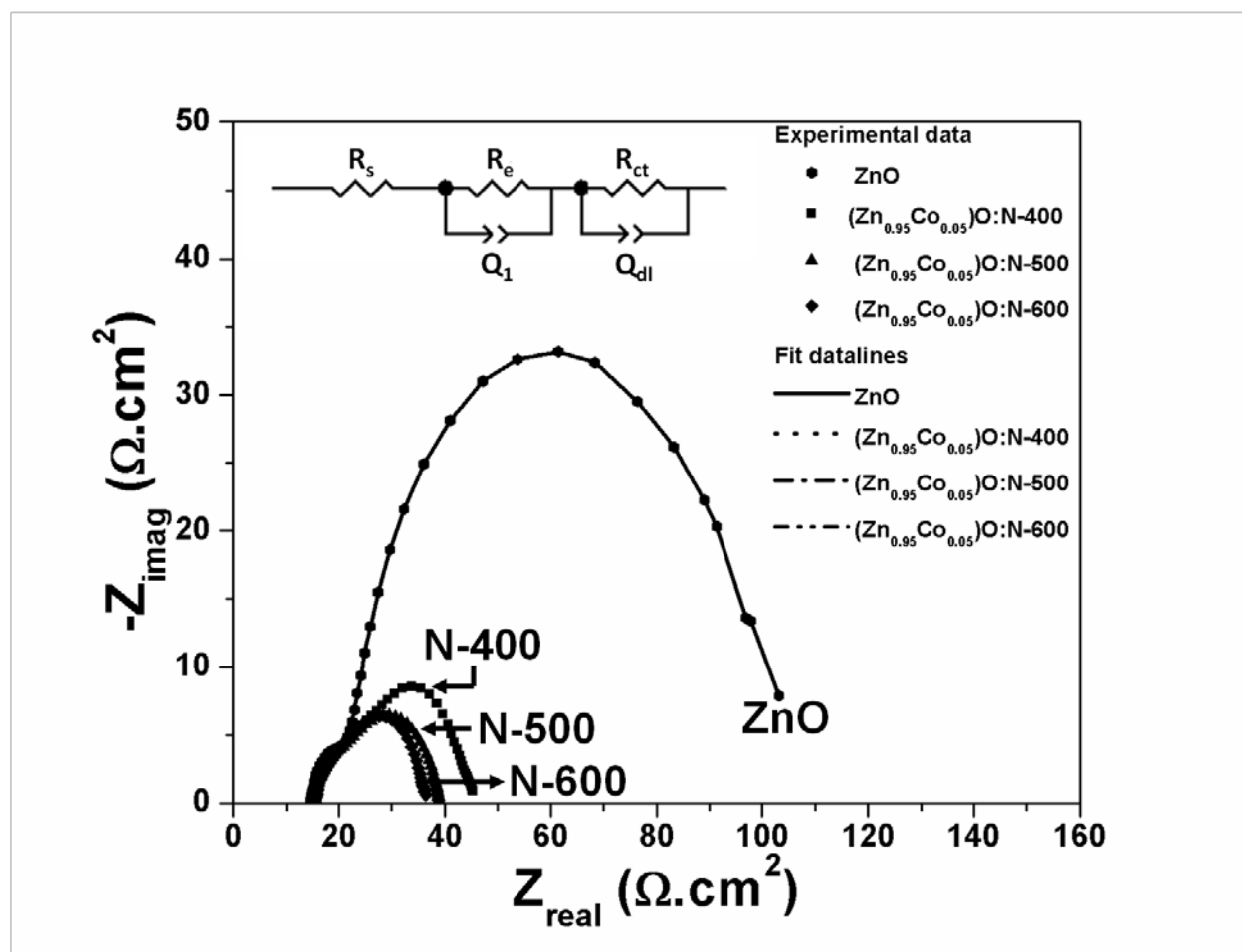


Figure 30: EIS spectra of ZnO and $(\text{Zn}_{0.95}\text{Co}_{0.05})\text{O}$:N NWs of different N concentration obtained at 0.79V (vs RHE) in 0.5 M Na_2SO_4 (pH 7) electrolyte solution at 26°C in the frequency range of 100 mHz to 100 kHz (AC amplitude=10 mV) under illumination (100 mW cm^{-2}), with the circuit used for fitting experimental data

Table 4: Results of EIS analysis of ZnO and (Zn_{0.95}Co_{0.05})O:N NWs of different N concentration, carried out at 0.79 V (vs RHE) in frequency range of 100 mHz-100 kHz (AC amplitude=10 mV) under illumination (100 mW cm⁻²) in 0.5 M Na₂SO₄ (pH 7) electrolyte solution

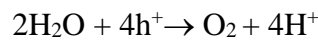
Composition	R _s (Ωcm ²)	R _e (Ωcm ²)	R _{ct} (Ωcm ²)
ZnO	15.2	5.8	90
(Zn _{0.95} Co _{0.05})O:N-400	15.21	5.7	25
(Zn _{0.95} Co _{0.05})O:N-500	15.2	5.65	20
(Zn _{0.95} Co _{0.05})O:N-600	15.21	5.5	16

Photoelectrochemical stability of ZnO and (Zn_{0.95}Co_{0.05})O:N NWs

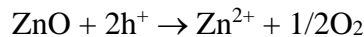
The photoelectrochemical stability of semiconductor material (photoanode) is important for long term operation of PEC water splitting system for hydrogen generation. Hence, to study the photoelectrochemical stability of (Zn_{0.95}Co_{0.05})O:N-600 NWs, chronoamperometry (CA) test is carried out at 0.79 V (vs RHE) (at which max. ABPE of 1.39% is obtained for (Zn_{0.95}Co_{0.05})O:N-600 NWs) under illumination for 24 h in the 0.5 M Na₂SO₄ electrolyte solution (with pH buffered to ~7.0). The CA curve for (Zn_{0.95}Co_{0.05})O:N-600 NWs is shown in **Figure 31**. The very minimal loss in photocurrent density is seen for (Zn_{0.95}Co_{0.05})O:N-600 NWs indicating excellent photoelectrochemical stability of (Zn_{0.95}Co_{0.05})O:N-600 NWs. Also following the 24 h CA test, LSV is carried out to ensure that (Zn_{0.95}Co_{0.05})O:N-600 NWs displays no degradation and is exhibiting similar photoelectrochemical activity, prior to the start of the CA test. The LSV curve after 24 h CA test shown in **Figure 32**, indeed shows negligible loss in photoelectrochemical activity for (Zn_{0.95}Co_{0.05})O:N-600 NWs. ICP analysis conducted on the

electrolyte solution, collected after the CA test does not show the presence of Zn and Co for (Zn_{0.95}Co_{0.05})O:N-600 NWs. To compare the photoelectrochemical stability of (Zn_{0.95}Co_{0.05})O:N-600 NWs with ZnO NWs, CA test is also carried out for pure ZnO NWs under similar conditions as that used for (Zn_{0.95}Co_{0.05})O:N-600 NWs. The CA curve for pure ZnO (**Figure 33**) shows steady drop in photocurrent density, indicating poor photoelectrochemical stability of ZnO NWs. These results clearly show the superior photoelectrochemical stability of (Zn_{0.95}Co_{0.05})O:N-600 NWs under illumination in the electrolyte 0.5 M Na₂SO₄ (pH 7) electrolyte solution over extended period of time compared to that of pure ZnO NWs.

ZnO is known to undergo photocorrosion²²⁶ resulting in the fade behavior as observed in **Figure 33**. The gradual deactivation of ZnO occurs as a result of production of electron-hole pairs in the presence of light wherein the electrons are separated to the cathode where they react with H⁺ ions to generate hydrogen gas. The holes on the other hand, on the surface of ZnO oxidize water to generate oxygen gas. Two factors play a role in photo-corrosion of ZnO-(a) rate of electron-hole generation (b) rate of electrochemical consumption of holes by the reaction¹⁰:



In the event that the rate of the electrochemical reaction is very sluggish, an excess of holes is created on the ZnO surface resulting in photocorrosion by reaction²²⁶:



This is the case with the undoped ZnO NWs observed in this study. The six-fold lower R_{ct} than ZnO NWs (**Figure 30** and **Table 4**) along with significantly higher IPCE for (Zn_{0.95}Co_{0.05})O:N-600 NWs (**Figure 26**) indicates far more expeditious carrier generation, transport and conversion for (Zn_{0.95}Co_{0.05})O:N-600 NWs than undoped ZnO NWs due to increased carrier density (offered by Co and N co-doping) resulting in improved band bending at the semiconductor-electrolyte

interface (as discussed earlier). Thus, this suggests that photogenerated carriers are rapidly consumed in the water oxidation process for $(\text{Zn}_{0.95}\text{Co}_{0.05})\text{O}:\text{N}$ -600 NWs due to superior reaction kinetics (**Figure 30** and **Table 4**) offered by Co and N co-doping, compared to that for the undoped ZnO NWs. In addition, ICP analysis of electrolyte solution collected after the CA test does not show the presence of Zn and Co for $(\text{Zn}_{0.95}\text{Co}_{0.05})\text{O}:\text{N}$ -600 NWs. Thus, the deactivation process of the semiconductor material by holes is minimal for doped ZnO, .i.e., $(\text{Zn}_{0.95}\text{Co}_{0.05})\text{O}:\text{N}$ -600 NWs resulting in superior long term photoelectrochemical stability as seen in the CA curve and minimal loss in photoelectrochemical activity after 24 h of CA test conducted under illumination (**Figure 31** and **Figure 32**). However, significantly higher R_{ct} (**Figure 30** and **Table 4**) values observed for undoped ZnO NWs indicates poor water oxidation reaction kinetics. Hence, excess holes can possibly deactivate ZnO NWs (by reaction mentioned above) resulting in a steady drop in the photocurrent density as seen in the CA curve (**Figure 33**).

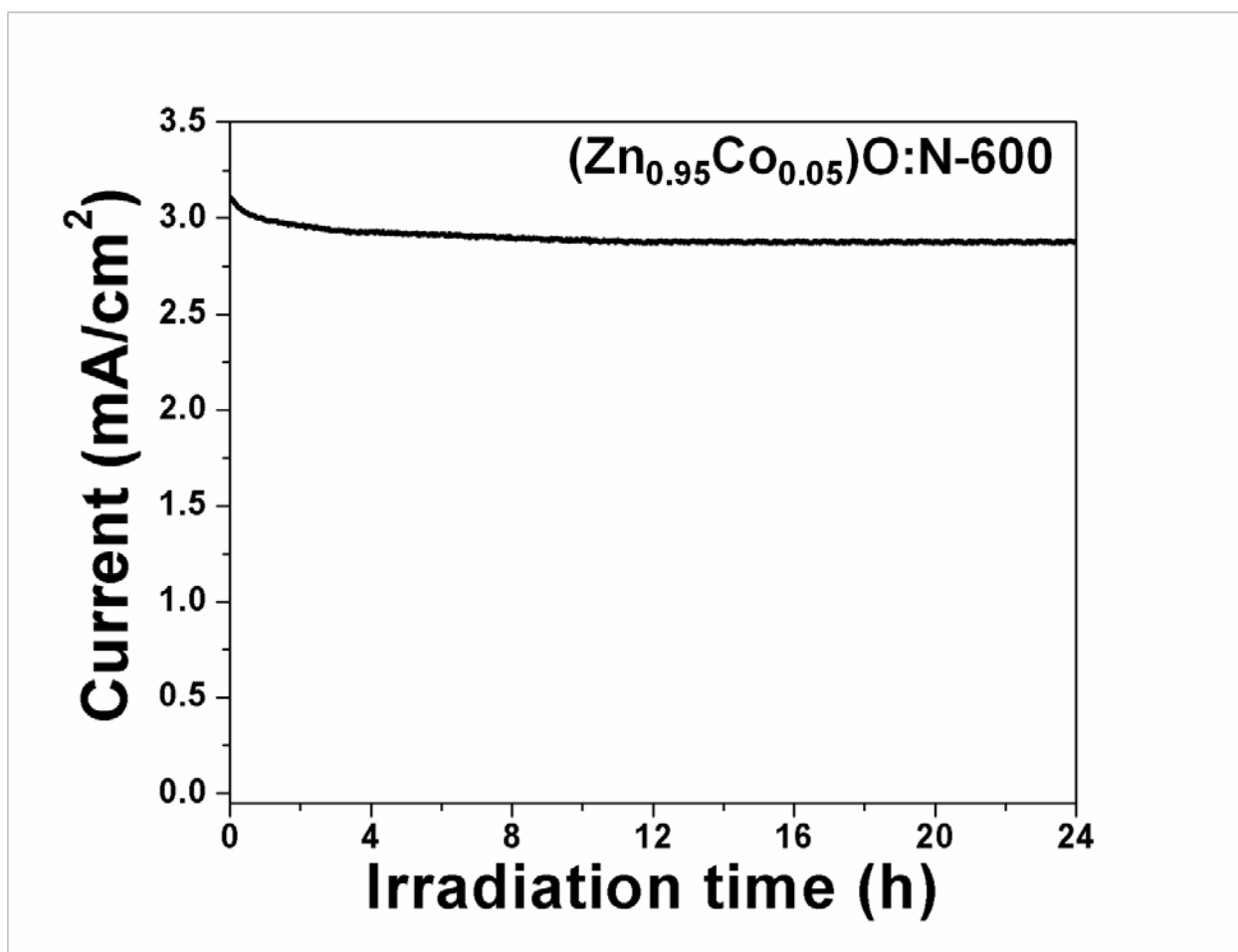


Figure 31: The variation of photocurrent density *vs* time in the chronoamperometry test of $(\text{Zn}_{0.95}\text{Co}_{0.05})\text{O:N-600}$ NWs, performed in a 0.5 M Na_2SO_4 (pH 7) electrolyte solution under a constant potential of 0.79V (*vs* RHE) at 26°C for 24 h

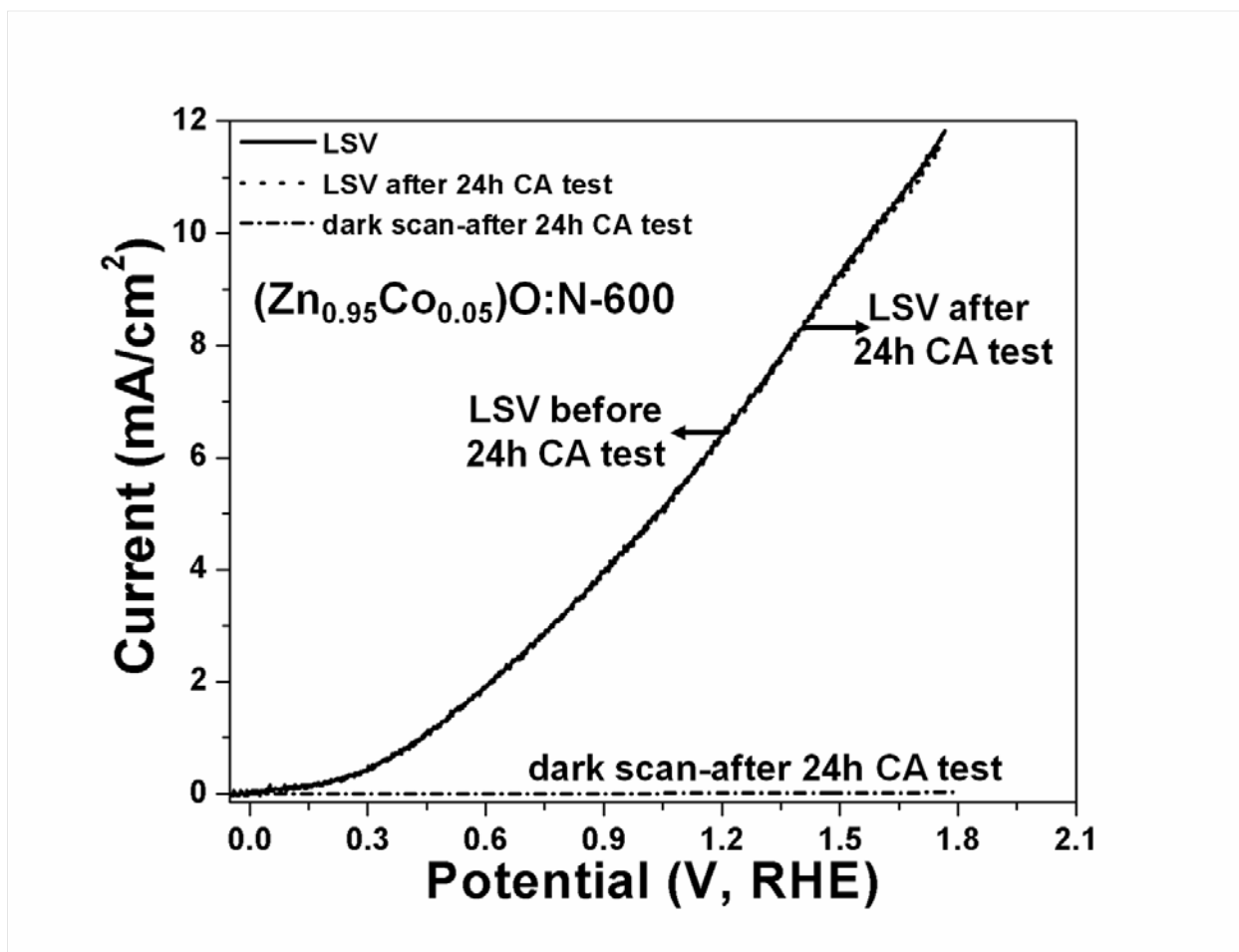


Figure 32: Linear scan voltammogram (LSV) curves for $(\text{Zn}_{0.95}\text{Co}_{0.05})\text{O:N-600}$ NWs in dark and illumination of 100 mW cm^{-2} measured in $0.5 \text{ M Na}_2\text{SO}_4$ (pH 7) electrolyte solution at 26°C , obtained before and after 24 h of chronoamperometry test

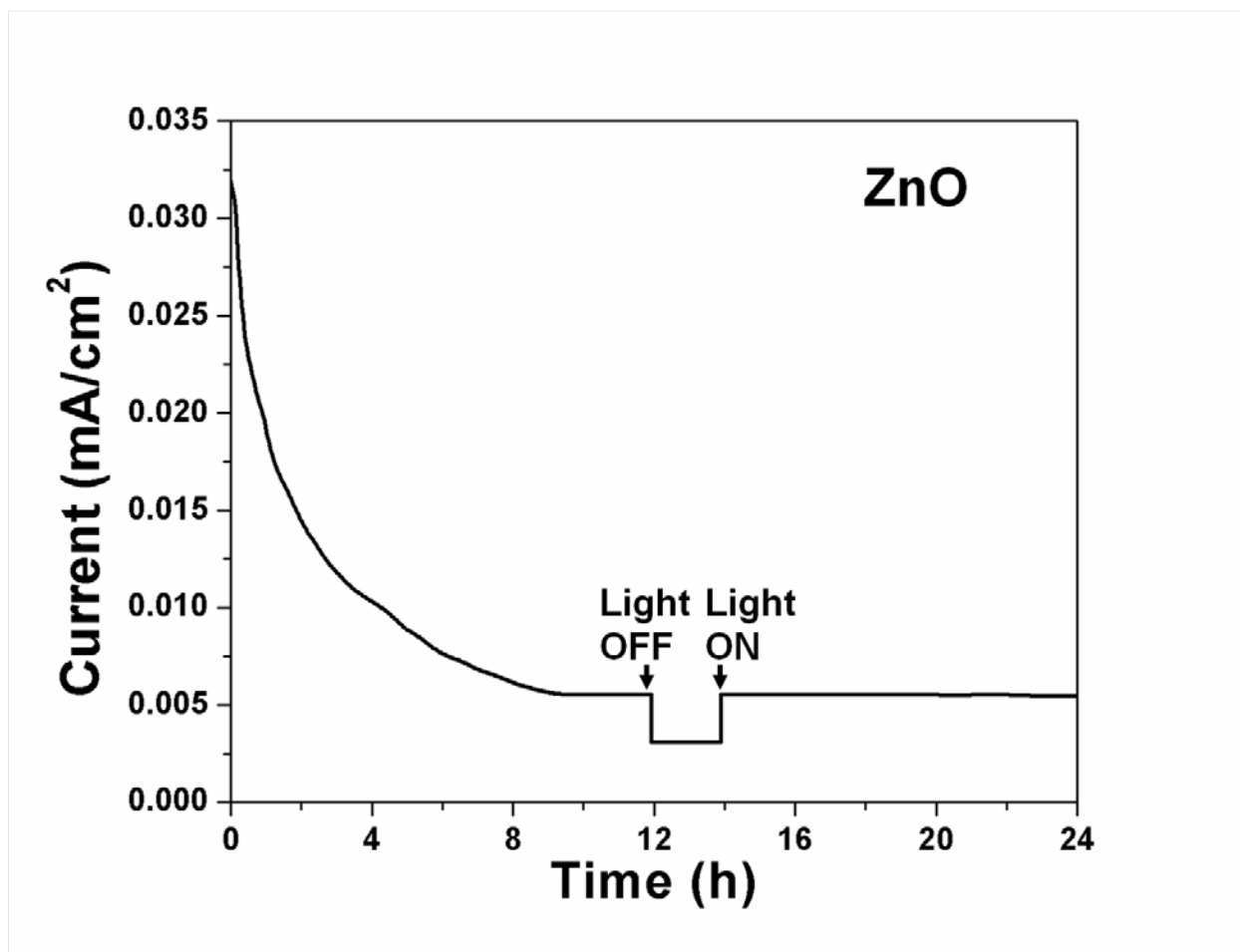


Figure 33: The variation of photocurrent density vs time in the chronoamperometry test of ZnO NWs, performed in a 0.5 M Na₂SO₄ (pH 7) electrolyte solution under a constant potential of 0.79V (vs RHE) at 26°C for 24 h

Measurement of H₂ and O₂ gases under illumination

It is important to measure the concentration of H₂ and O₂ gases generated at the cathode and photoanode, respectively, to ensure that the photocurrent density is arising from the water splitting reaction and that no current density is resulting from any adventitious unwanted side reactions. Hence, during the CA test of (Zn_{0.95}Co_{0.05})O:N-600 NWs at constant potential of 0.79 V (vs RHE), the concentration of gases evolved was measured at 1 h intervals by gas

chromatography (helium used as the carrier gas). Also, the theoretical concentration of H₂ gas is calculated from the measured photocurrent density using the Faraday's law given as:¹⁹⁵

$$\text{No. of moles of H}_2 = \frac{Q}{2F} = \frac{It}{2F} = \frac{\int_0^t I \cdot dt}{2F}$$

where, I is the photocurrent density, t is time, F is the Faraday constant (96484.34 C/mole) and Q is the quantity of charge in coulomb. The concentration of theoretical and experimentally measured H₂ gas and O₂ gases measured during the CA test for (Zn_{0.95}Co_{0.05})O:N-600 NWs are shown in **Figure 34**. The measured amount of evolved H₂ gas is closer or comparable to the theoretical amount of H₂ indicating ~100% Faradaic efficiency for hydrogen generation. In addition, the ratio of concentration of generated H₂ and O₂ gases is ~2 and also, no change is observed in the pH of the electrolyte solution (~7) before and after water splitting reaction, suggesting that there is stoichiometric decomposition of water to H₂ and O₂ occurring in the present study for (Zn_{0.95}Co_{0.05})O:N-600 NWs. These results therefore show the excellent long term photoelectrochemical stability of (Zn_{0.95}Co_{0.05})O:N-600 NWs for hydrogen generation under illumination, which is of paramount importance for the potential commercialization of the PEC water splitting cell system.

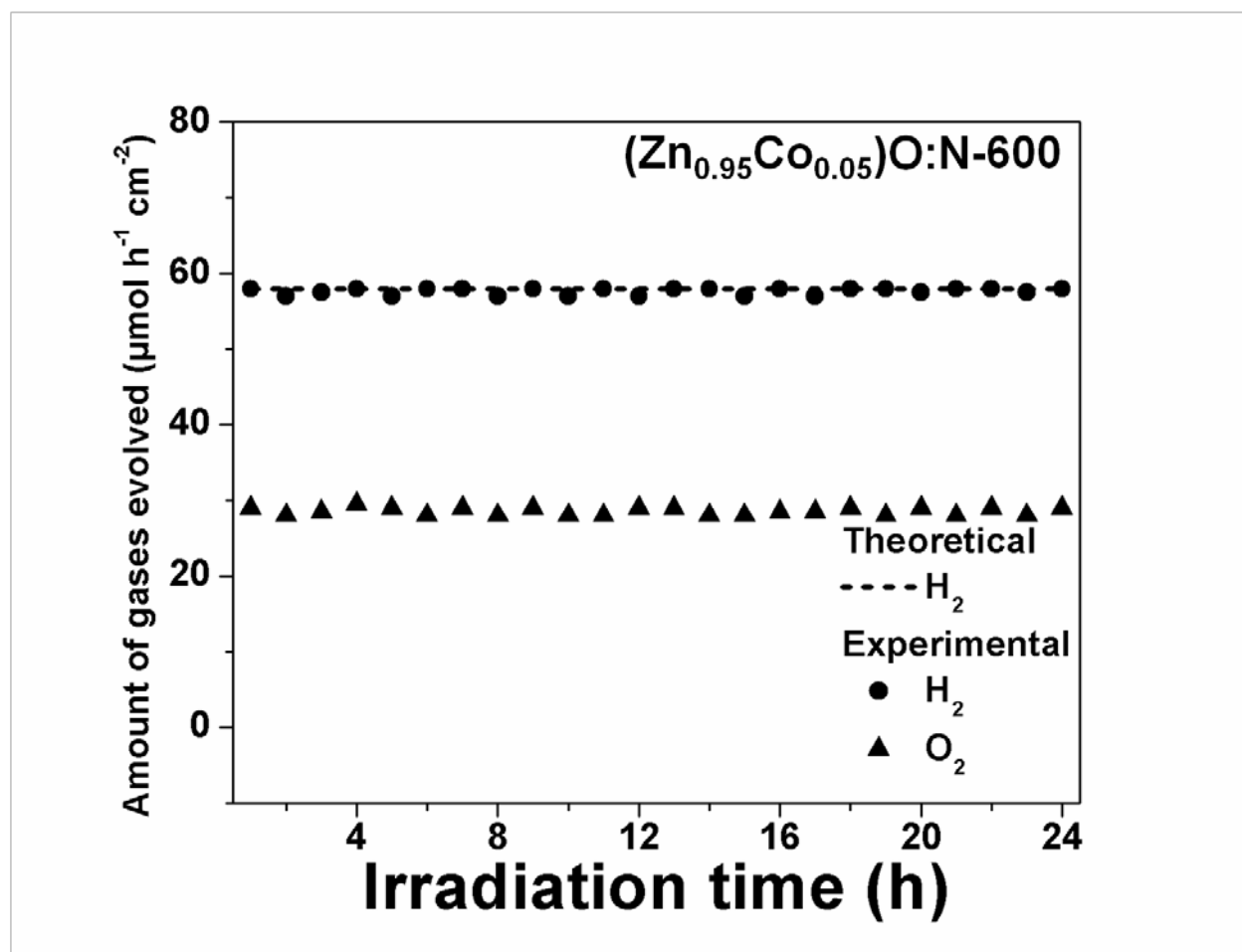


Figure 34: Theoretical and experimentally measured concentration of H₂ and O₂ gases, measured during chronoamperometry test of (Zn_{0.95}Co_{0.05})O:N-600 NWs, performed in 0.5 M Na₂SO₄ (pH 7) electrolyte solution under a constant potential of 0.79V (*vs* RHE) at 26°C for 24 h

Conclusions:

The present study explores (Zn_{0.95}Co_{0.05})O:N NWs as a potential photoanode for photoelectrochemical water splitting. The nanowires were grown on FTO slide by a simple hydrothermal route, followed by heat treatment in NH₃ atmosphere. The above results demonstrate cobalt and nitrogen as potential dopants for reducing the band gap of ZnO from 3.18

eV for pure ZnO NWs to 2.16 eV for $(\text{Zn}_{0.95}\text{Co}_{0.05})\text{O:N-600}$ NWs. The results of this study also establishes the effectiveness of co-doping using Co and N in ZnO NWs, which yields a four orders of magnitude improved carrier density, improved carrier separation, transport and collection efficiency, combined with superior photoelectrochemical activity with negative onset potential of (-0.02 V *vs* RHE), and excellent ABPE. The optimal ABPE of 1.39% obtained for $(\text{Zn}_{0.95}\text{Co}_{0.05})\text{O:N-600}$ NWs at 0.79V *vs* RHE (or 0.18 V *vs* Ag/AgCl) is the highest ABPE reported so far for ZnO nanostructured photoanodes. Additionally, long-term life test for 24 h showed excellent photoelectrochemical stability of $(\text{Zn}_{0.95}\text{Co}_{0.05})\text{O:N-600}$ NWs in the electrolyte solution under illumination, compared to pure ZnO NWs. The co-doping strategy reported here has thus been seen to result in an improvement in photoelectrochemical performance through a conjunction of (a) improved light absorption (b) increased carrier density and (c) faster electrochemical charge transfer. Hence, it is envisaged that this work will be important in the search for semiconductor materials or photoanodes with high photoelectrochemical activity and stability in the electrolyte solution for long term operation, portending well with the overall aim of achieving efficient and economical hydrogen generation via water splitting by effective utilization of solar energy.

5.2 Nb AND N CO-DOPED SnO₂ NANOTUBES (NTs) (PHOTOANODE)

5.2.1 STRUCTURAL ANALYSIS OF SnO₂ AND (Sn_{0.95}Nb_{0.05})O₂:N NTs

X-ray diffraction (XRD) study

The XRD patterns of SnO₂ NTs, (Sn_{0.95}Nb_{0.05})O₂:N-400 NTs, (Sn_{0.95}Nb_{0.05})O₂:N-500 NTs, (Sn_{0.95}Nb_{0.05})O₂:N-600 NTs, shown in **Figure 35**, show peaks corresponding to tetragonal SnO₂ (PDF code: 01-041-1445) without any peaks corresponding to Sn or Nb containing phase, suggesting the formation of doped SnO₂ NTs.⁷⁶ The values of molar volume and lattice parameters of SnO₂ and (Sn_{0.95}Nb_{0.05})O₂:N NTs, calculated using the least square refinement technique, are shown in **Table 5**. The lattice parameter and molar volume of pure SnO₂ NTs is a=b=4.738Å, c=3.187Å and 21.54 cm³ mol⁻¹, respectively, which is similar to that reported earlier.²²⁷ The increase in lattice parameter and molar volume is observed with increase in the temperature of heat treatment in NH₃ for (Sn_{0.95}Nb_{0.05})O₂:N-400 NTs, (Sn_{0.95}Nb_{0.05})O₂:N-500 NTs and (Sn_{0.95}Nb_{0.05})O₂:N-600 NTs, suggesting incorporation of nitrogen into the (Sn_{0.95}Nb_{0.05})O₂ NTs and also lattice expansion upon nitrogen doping.^{114, 203} However, the XRD pattern of (Sn_{0.95}Nb_{0.05})O₂:N-700 NTs shows peaks corresponding to Sn and Nb, suggesting the reduction of (Sn_{0.95}Nb_{0.05})O₂ NTs possibly by the atomic hydrogen originating from the decomposition of NH₃.¹⁰⁶ Hence, 600°C was used as the optimal temperature for ammonolysis.

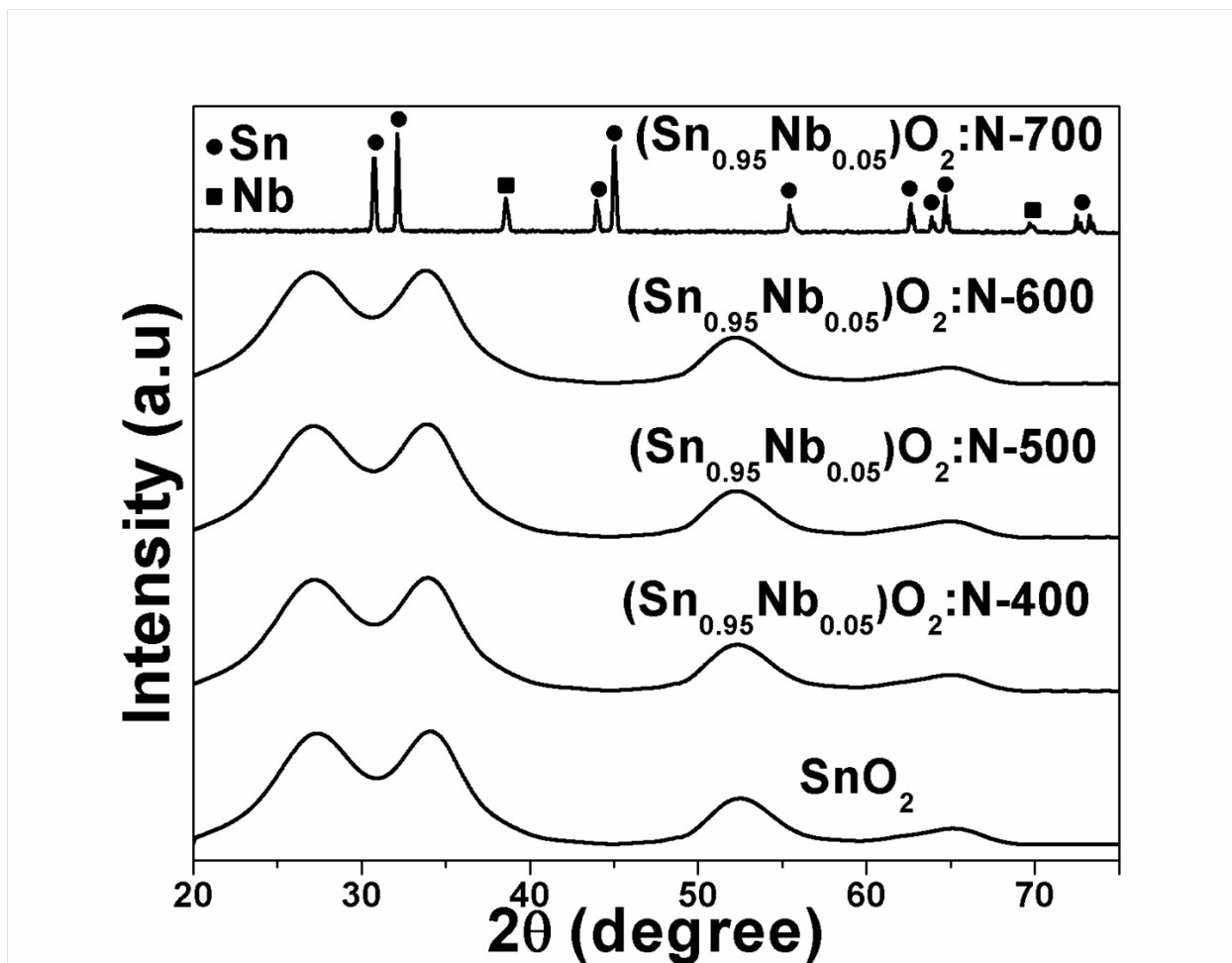


Figure 35: The XRD patterns of pure SnO_2 NTs and $(\text{Sn}_{0.95}\text{Nb}_{0.05})\text{O}_2$:N NTs of different N concentration in wide angle 2θ scan

Table 5: The lattice parameter and molar volume for SnO₂ and (Sn_{0.95}Nb_{0.05})O₂:N NTs, along with N concentration for (Sn_{0.95}Nb_{0.05})O₂:N NTs (obtained from EDX analysis)

Composition	Lattice parameter (nm)	Molar volume (cm³ mol⁻¹)	N concentration from EDX analysis (at. %)
SnO ₂	a=b=0.4738 c=0.3187	21.54	-
(Sn _{0.95} Nb _{0.05})O ₂ :N-400	a=b=0.4741 c=0.3190	21.58	3.02
(Sn _{0.95} Nb _{0.05})O ₂ :N-500	a=b=0.4743 c=0.3193	21.62	7.1
(Sn _{0.95} Nb _{0.05})O ₂ :N-600	a=b=0.4748 c=0.3196	21.69	14.01

SEM/EDX and TEM study of (Sn_{0.95}Nb_{0.05})O₂:N-600 NTs

Scanning electron microscopy (SEM) has been carried out to study the morphology of the representative composition, (Sn_{0.95}Nb_{0.05})O₂:N-600 NTs. SEM image showing top view and cross-sectional view of (Sn_{0.95}Nb_{0.05})O₂:N-600 NTs is shown in **Figure 36**, respectively. Cross-sectional view of (Sn_{0.95}Nb_{0.05})O₂:N-600 NTs show dense and vertically oriented nanotubes of diameter of 180-240 nm and length of ~14μm. The SEM image of (Sn_{0.95}Nb_{0.05})O₂:N-600 NTs reveals well-spaced nanotubes with clean surface and without any particles at the top and bottom

of nanotubes. Energy dispersive x-ray spectroscopy (EDX) is conducted to confirm the presence of elements Sn, Nb and N and also, determine concentration of N in the $(\text{Sn}_{0.95}\text{Nb}_{0.05})\text{O}_2:\text{N}$ NTs, heat-treated in NH_3 at different temperatures.^{114, 228, 229} EDX spectrum of representative composition, $(\text{Sn}_{0.95}\text{Nb}_{0.05})\text{O}_2:\text{N}$ -600 NTs, shown in **Figure 36**, confirms the presence of elements Sn, Nb and N. Quantitative elemental composition analysis by EDX of $(\text{Sn}_{0.95}\text{Nb}_{0.05})\text{O}_2:\text{N}$ -400 NTs, $(\text{Sn}_{0.95}\text{Nb}_{0.05})\text{O}_2:\text{N}$ -500 NTs and $(\text{Sn}_{0.95}\text{Nb}_{0.05})\text{O}_2:\text{N}$ -600 NTs, shown in **Table 5**, shows increase in N concentration incorporated in $(\text{Sn}_{0.95}\text{Nb}_{0.05})\text{O}_2$ NTs with increase in temperature of heat treatment in NH_3 .^{114, 204, 205} TEM images of representative composition, $(\text{Sn}_{0.95}\text{Nb}_{0.05})\text{O}_2:\text{N}$ -600 NTs, shown in **Figure 37** reveals the geometry of hollow nanotube with diameter of $\sim 180\text{-}220$ nm.

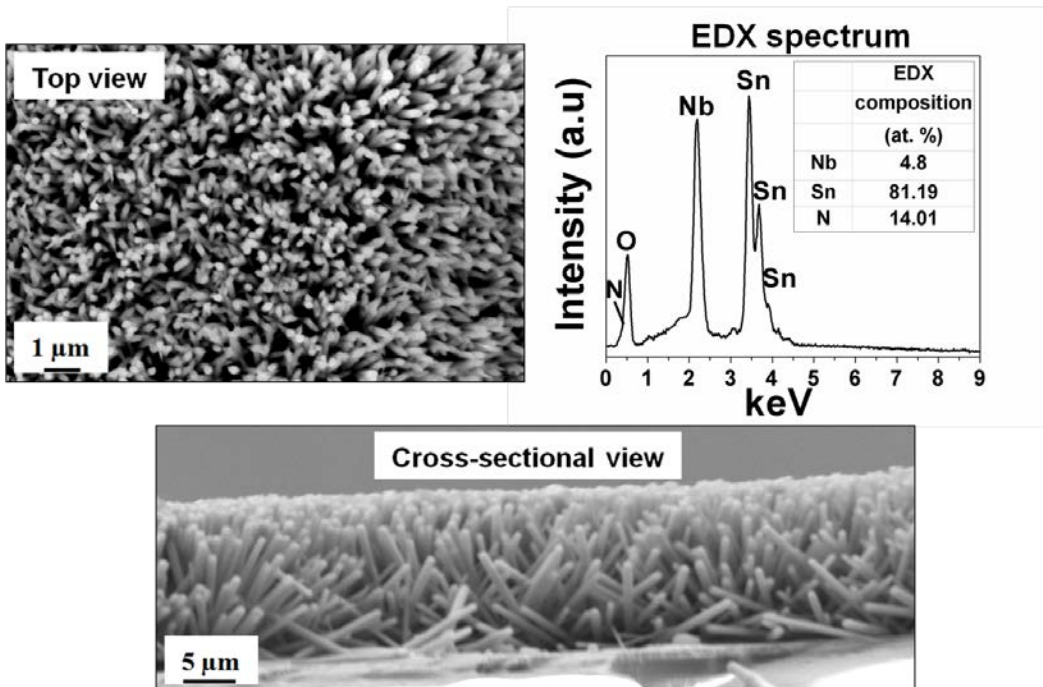


Figure 36: SEM micrograph showing top view, cross-sectional view and EDX spectrum of $(\text{Sn}_{0.95}\text{Nb}_{0.05})\text{O}_2:\text{N}$ -600 NTs

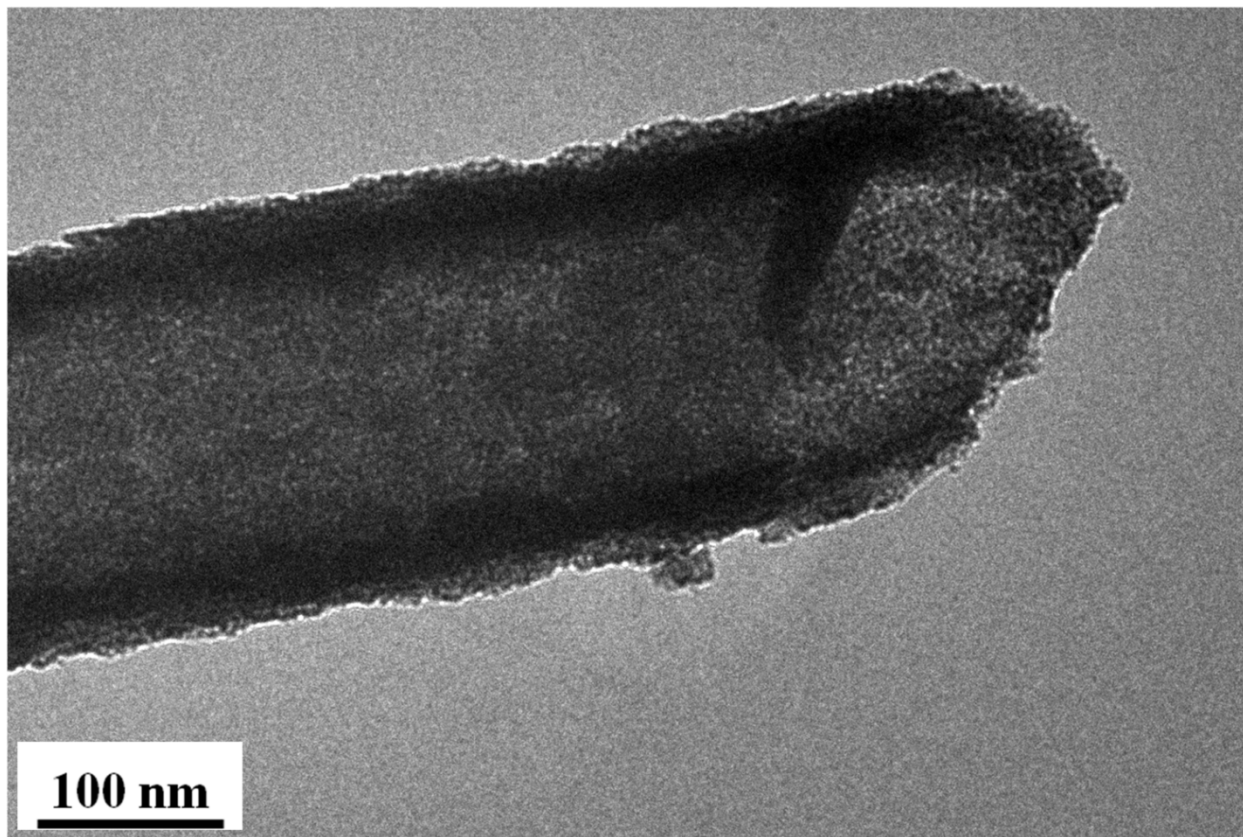


Figure 37: The bright field TEM images of $(\text{Sn}_{0.95}\text{Nb}_{0.05})\text{O}_2:\text{N}$ -600 NTs showing hollow nanotubes of diameter $\sim 180\text{-}220$ nm

X-ray photoelectron spectroscopy study of SnO_2 and $(\text{Sn}_{0.95}\text{Nb}_{0.05})\text{O}_2:\text{N}$ NTs

To determine the oxidation state of Sn, Nb and N, x-ray photoelectron spectroscopy (XPS) was carried out on $(\text{Sn}_{0.95}\text{Nb}_{0.05})\text{O}_2:\text{N}$ NTs of different N concentration and pure SnO_2 NTs. The XPS spectrum of Sn (**Figure 38**) of pure SnO_2 shows the presence of Sn $3d_{3/2}$ and $3d_{5/2}$ doublet centered at ~ 495.37 eV and ~ 486.95 eV, corresponding to Sn^{4+} .²³⁰ The negative shift in binding energy of Sn $3d_{3/2}$ and $3d_{5/2}$ doublet is observed for $(\text{Sn}_{0.95}\text{Nb}_{0.05})\text{O}_2:\text{N}$ NTs, which

increases with increase in N concentration, which is consistent with previously reported results for N-doped TiO₂ nanoparticles.²⁰⁶ In accordance with the previously reported results on N-doped TiO₂ nanoparticles²⁰⁶, the negative shift in Sn 3d_{3/2} and 3d_{5/2} doublet for (Sn_{0.95}Nb_{0.05})O₂:N NTs can be assigned to change in electron density around Sn⁴⁺ due to Nb and N co-doping and thus, indicates modification in the electronic structure of SnO₂ NTs by Nb and N co-doping.^{114, 206}

The XPS spectrum of N, shown in **Figure 39**, shows the presence of N 1s peak centered at ~398.3 eV for (Sn_{0.95}Nb_{0.05})O₂:N NTs of different N concentration. The N 1s peak at ~398.3 eV indicates the presence of oxynitride (O-Sn-N or O-Nb-N) for (Sn_{0.95}Nb_{0.05})O₂:N NTs.^{114, 231, 232} This shows substitutional doping of N at O sites in the lattice of (Sn_{0.95}Nb_{0.05})O₂:N NTs.^{106, 114} Furthermore, the N composition (determined by XPS) is ~14% for (Sn_{0.95}Nb_{0.05})O₂:N-600 NTs, which is similar to that obtained from EDX analysis. The XPS spectrum of Nb of (Sn_{0.95}Nb_{0.05})O₂:N NTs, shown in **Figure 40**, shows the presence of Nb 3d_{3/2} and Nb 3d_{5/2} doublet centered at ~210.4 and ~207.6 for (Sn_{0.95}Nb_{0.05})O₂:N-400 NTs, corresponding to Nb⁴⁺, respectively.^{233, 234} The shift of Nb 3d_{3/2} and Nb 3d_{5/2} doublet to lower binding energy value by ~0.1 eV and ~0.2 eV is observed for both (Sn_{0.95}Nb_{0.05})O₂:N-500 NTs and (Sn_{0.95}Nb_{0.05})O₂:N-600 NTs, which suggests the presence of oxynitride (O-Nb-N) due to substitutional doping of N at the O sites.^{114, 231}

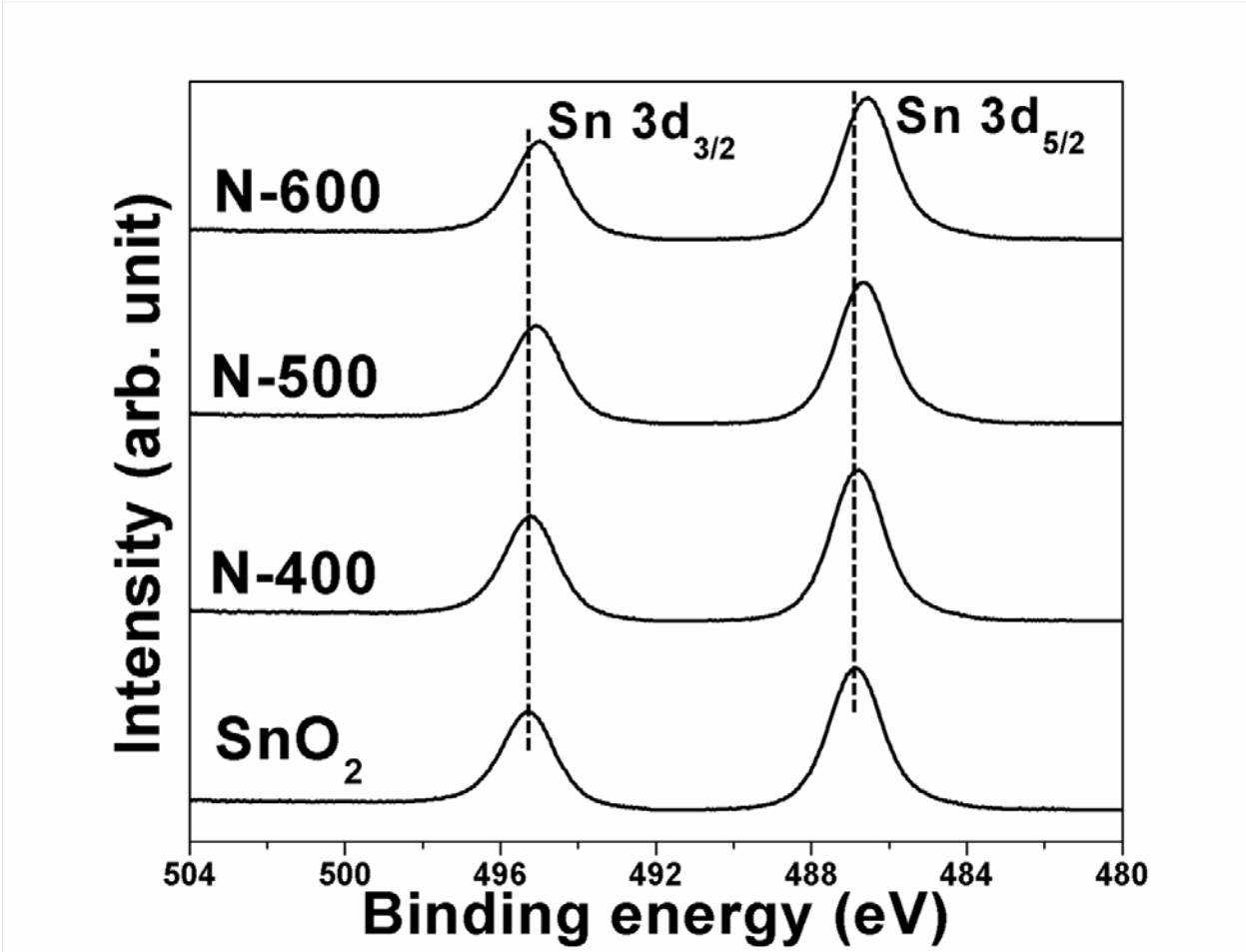


Figure 38: The XPS spectra of (Sn_{0.95}Nb_{0.05})O₂:N NTs showing Sn 3d_{3/2} and 3d_{5/2} doublet

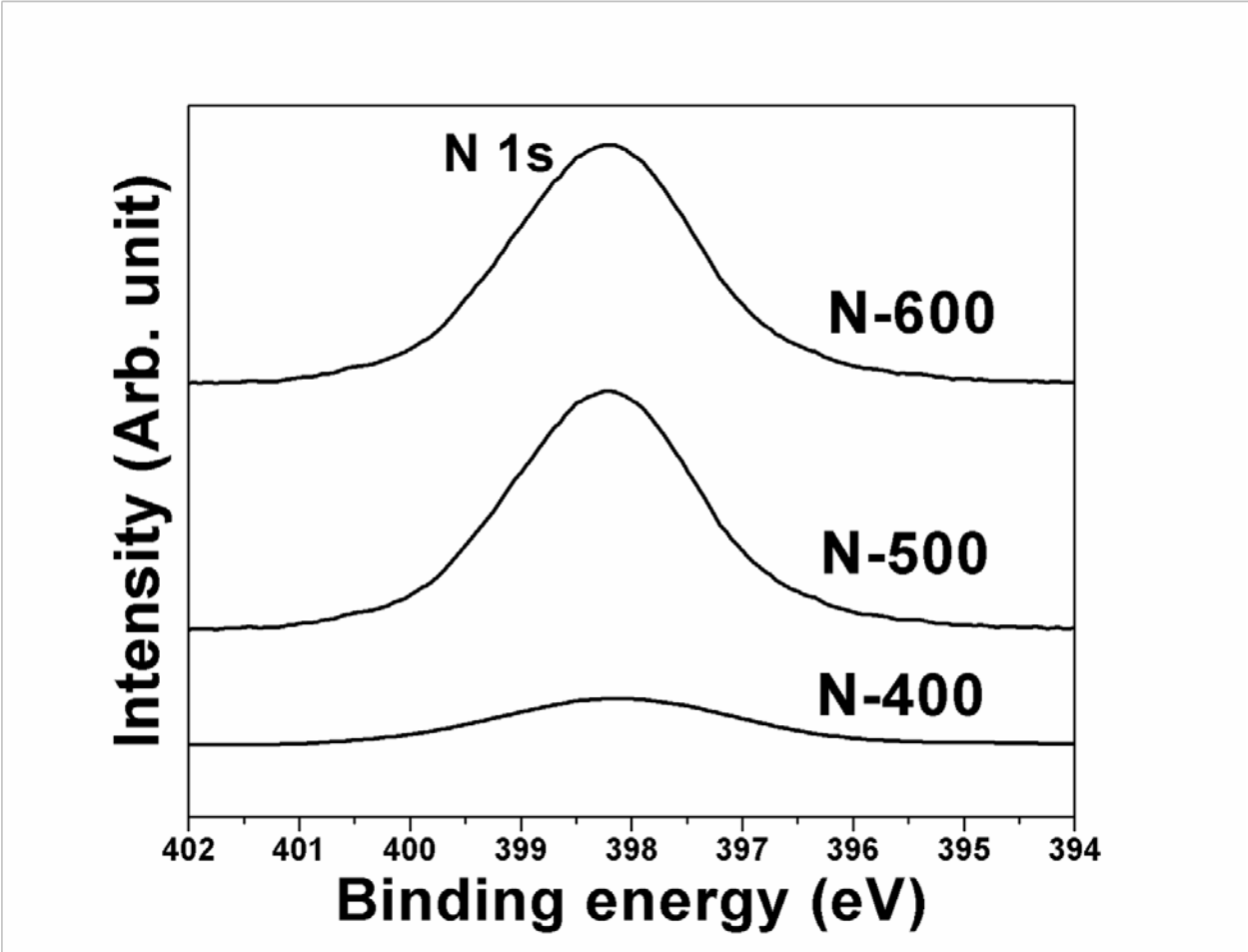


Figure 39: The XPS spectra of (Sn_{0.95}Nb_{0.05})O₂:N NTs showing N 1s peak

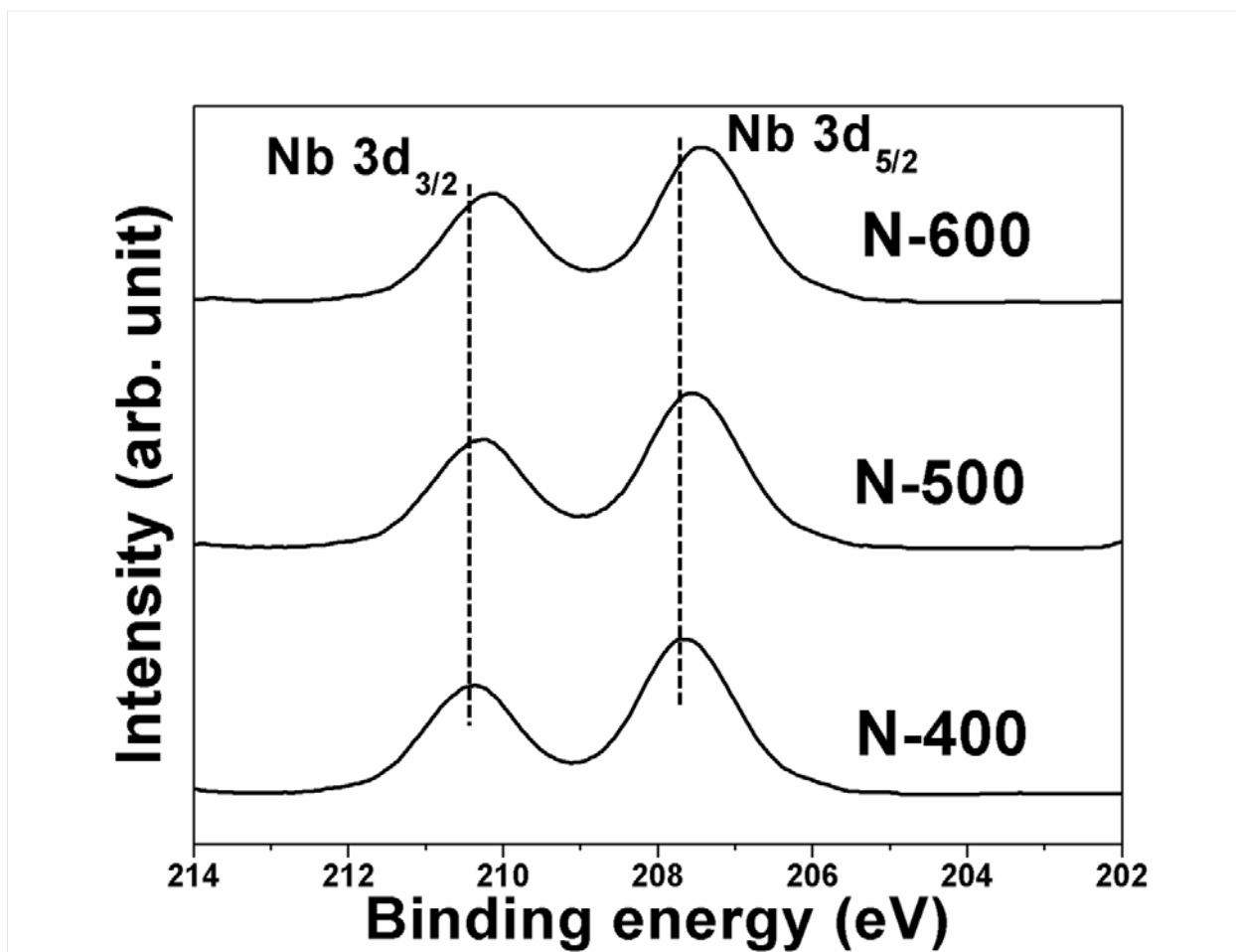


Figure 40: The XPS spectra of (Sn_{0.95}Nb_{0.05})O₂:N NTs showing Nb 3d_{3/2} and 3d_{5/2} doublet

UV-Vis absorption study and Tauc analysis of SnO₂ and (Sn_{0.95}Nb_{0.05})O₂:N NTs

The light absorption property of SnO₂ and (Sn_{0.95}Nb_{0.05})O₂:N NTs corresponding to different N concentration is studied from the UV-Vis absorption spectra, shown in **Figure 41**. The UV-Vis absorption spectrum of pure SnO₂ NTs shows the onset of light absorption at ~350 nm, which is similar to that reported earlier.^{235, 236} The UV-Vis absorption spectra show excellent light absorption for (Sn_{0.95}Nb_{0.05})O₂:N NTs, compared to pure SnO₂ NTs. (Sn_{0.95}Nb_{0.05})O₂:N-400 NTs, (Sn_{0.95}Nb_{0.05})O₂:N-500 NTs and (Sn_{0.95}Nb_{0.05})O₂:N-600 NTs show superior light absorption

than that of both pure SnO₂ NTs at 500 nm. 500 nm is chosen for comparison of the absorbance of semiconductor materials in this study, as it is closest to the wavelength at which maximum solar irradiance is reportedly obtained.¹⁸⁹ The light absorption in the visible region increases with increase in N concentration for (Sn_{0.95}Nb_{0.05})O₂:N NTs, suggesting the reduction in the band gap due to N incorporation in (Sn_{0.95}Nb_{0.05})O₂ NTs.

Tauc analysis as conducted earlier for the non-nitrogen doped system is accordingly conducted to determine the band gap for (Sn_{0.95}Nb_{0.05})O₂:N NTs. The values of the band gap determined from the x-intercept of $(\alpha hv)^2$ vs hv curves of Tauc analysis (**Figure 42**) are given in **Table 6**. As can be seen, reduction in the band gap is obtained with increase in N concentration for (Sn_{0.95}Nb_{0.05})O₂:N NTs, as indicated in **Table 6**. Also, the band gap of (Sn_{0.95}Nb_{0.05})O₂:N NTs is lower than that of pure SnO₂ NTs (~3.53 eV which is similar to that reported earlier²³⁷⁻²³⁹). It is thus noteworthy that the lowest band gap of 1.99 eV is achieved for (Sn_{0.95}Nb_{0.05})O₂:N-600 NTs, which is significantly lower than non-nitrogen containing SnO₂ NTs (3.53 eV), suggesting the beneficial role of Nb and N co-doping facilitating the reduction in the wide band gap of SnO₂. This observed narrowing of the band gap is mainly attributed to the hybridization of the substitutional N 2p states with O 2p states, which is expected to shift the valence band upwards, without affecting the conduction band thereby, reducing the band gap and improving the light absorption in the visible region of interest.^{34, 114} The reduction in the band gap is important since it offers improved light absorption in the visible wavelength regime of use and thus creates the appropriate conditions providing more photogenerated carriers for HER.

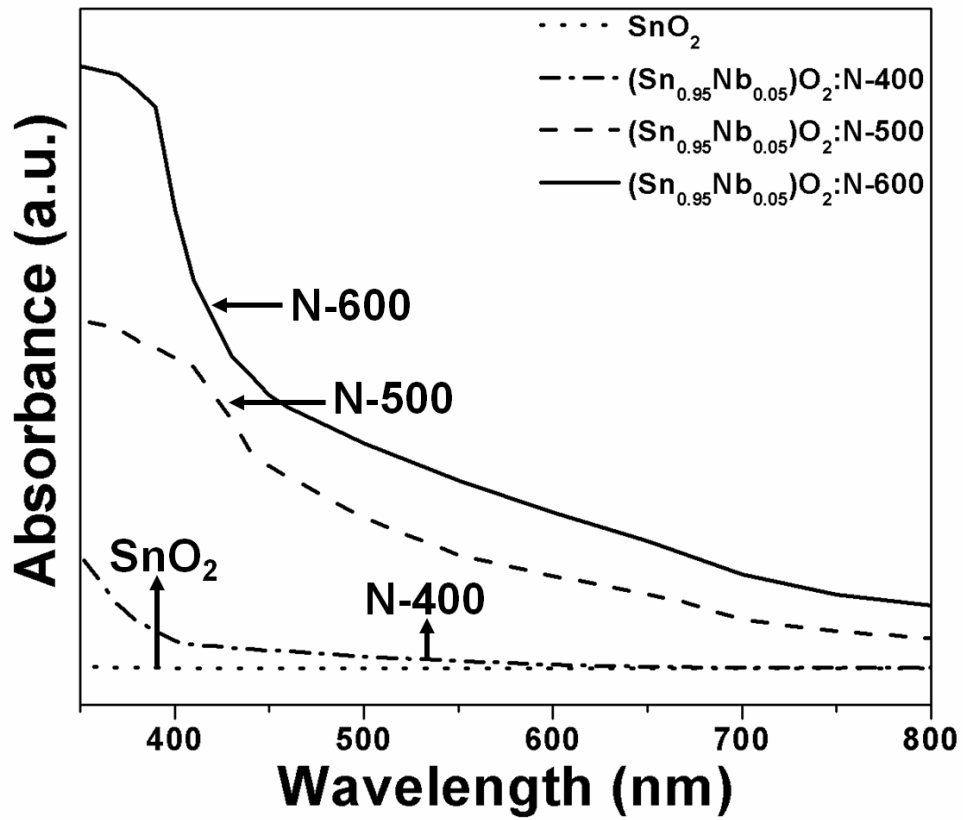


Figure 41: UV-vis absorption spectra of SnO₂ NTs and (Sn_{0.95}Nb_{0.05})O₂:N NTs of different N concentration

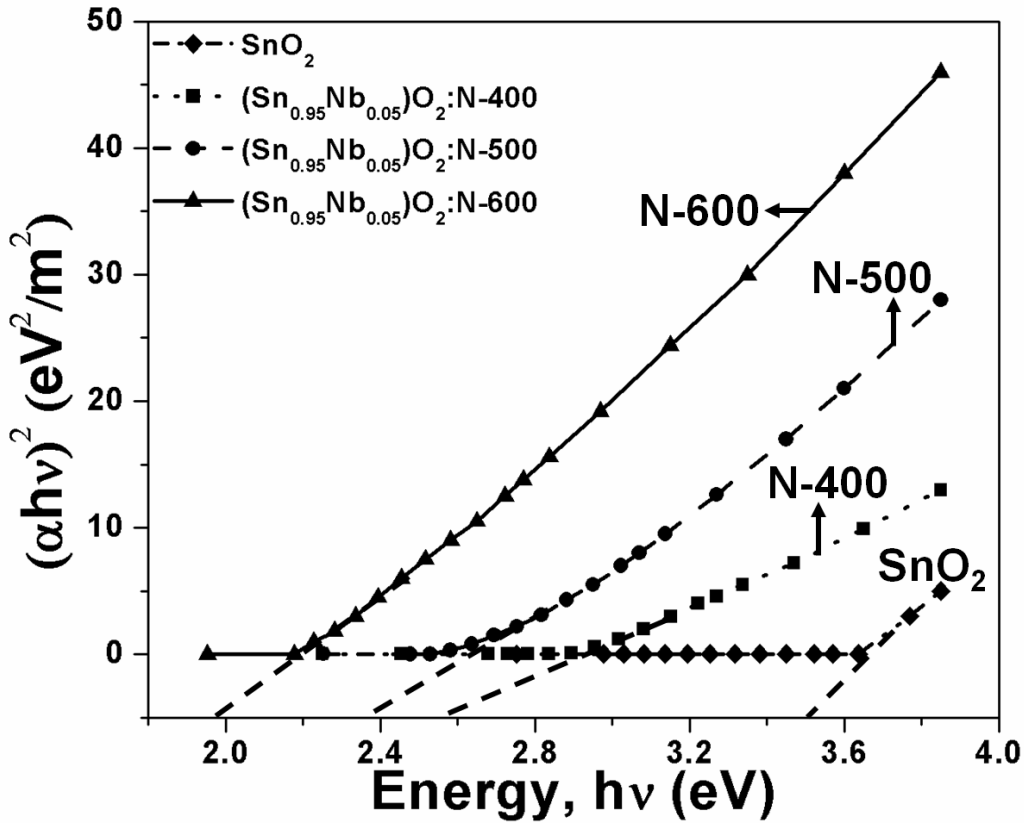


Figure 42: Tauc analysis of SnO₂ NTs and (Sn_{0.95}Nb_{0.05})O₂:N NTs of different N concentration

Mott-Schottky analysis of SnO₂ and (Sn_{0.95}Nb_{0.05})O₂:N NTs

The positive effect of Nb and N incorporation in the lattice of SnO₂ NTs on the electronic properties is studied by Mott-Schottky analysis by performing EIS in the dark in 0.5 M H₂SO₄ electrolyte solution at 26°C. The carrier density and flat band potential at the nanotubes/electrolyte interface are determined by the Mott-Schottky equation¹⁰⁶:

$$1/C^2 = (2/e_0\epsilon_0\epsilon N_d)[(V-V_{FB})-kT/e_0]$$

where, e_0 is the electron charge, ϵ is the dielectric constant of SnO₂ (taken as 13)^{240, 241} ϵ_0 is the permittivity of vacuum, N_d is the dopant/carrier density, V is the applied electric potential, V_{FB} is the flat band potential, k is the Boltzmann constant, T is the absolute temperature (299 K).

The Mott-Schottky plots of (Sn_{0.95}Nb_{0.05})O₂:N NTs for different N concentration and SnO₂ NTs are shown in **Figure 43** and **Figure 44**. The flat band potential (V_{FB}) of pure and doped SnO₂ NTs is found from the x-intercept in Mott-Schottky plots ($1/C^2$ vs V). For undoped SnO₂ NTs, V_{FB} is ~ 0.05 V (vs RHE), while V_{FB} for (Sn_{0.95}Nb_{0.05})O₂:N-400 NTs, (Sn_{0.95}Nb_{0.05})O₂:N-500 NTs and (Sn_{0.95}Nb_{0.05})O₂:N-600 NTs are $\sim (-0.2$ V), $\sim (-0.28$ V) and $\sim (-0.33$ V) (vs RHE), respectively. Thus, the values of V_{FB} of (Sn_{0.95}Nb_{0.05})O₂:N NTs for the different N concentration are more negative than the standard reduction potential of water (0 V vs NHE), indicating more negative band edge position for (Sn_{0.95}Nb_{0.05})O₂:N NTs than standard reduction potential of water. A more negative V_{FB} is thus expected to offer efficient separation of the photogenerated carriers at the semiconductor-electrolyte interface due to improved band bending at the semiconductor surface.^{64, 81, 214} This is expected to offer a large driving force to the photogenerated electrons resulting in improved photocurrent density.^{64, 81, 214} The carrier density is calculated from the slope determined from the Mott-Schottky plot using the following equation:

$$N_d = (2/e_0\epsilon\epsilon_0)[d(1/C^2)/dV]^{-1}$$

The positive slope obtained in the Mott-Schottky plots indicate n-type behavior for SnO₂ and (Sn_{0.95}Nb_{0.05})O₂:N NTs. The carrier density of (Sn_{0.95}Nb_{0.05})O₂:N-400 NTs, (Sn_{0.95}Nb_{0.05})O₂:N-500 NTs and (Sn_{0.95}Nb_{0.05})O₂:N-600 NTs is 3.3×10^{22} cm⁻³, 4.05×10^{22} cm⁻³ and 4.7×10^{22} cm⁻³, which is 4 orders of magnitude higher than that of SnO₂ NTs (2.42×10^{18} cm⁻³) (**Table 6**). These results therefore clearly demonstrate the potential of Nb and N doping in SnO₂

NTs contributing to significantly enhancing the carrier density which is vital since this implies that a higher number of photogenerated electrons are available for HER (at cathode).

The increased carrier density for $(\text{Sn}_{0.95}\text{Nb}_{0.05})\text{O}_2:\text{N}$ NTs with increase in N concentration is expected to shift the Fermi level upwards towards the conduction band resulting in negative shift in V_{FB} with increase in N concentration and thus resulting in increased degree of band bending with increase in N concentration.^{64, 106, 114, 207, 214, 218, 242-246} This is expected to result in improved separation of photogenerated carriers at the interface between the $(\text{Sn}_{0.95}\text{Nb}_{0.05})\text{O}_2:\text{N}$ NTs and the electrolyte solution, leading to improved photocurrent density and thus, superior ABPE for $(\text{Sn}_{0.95}\text{Nb}_{0.05})\text{O}_2:\text{N}$ NTs, compared to pure SnO_2 NTs.^{64, 106, 114, 207, 214, 218, 242-246}

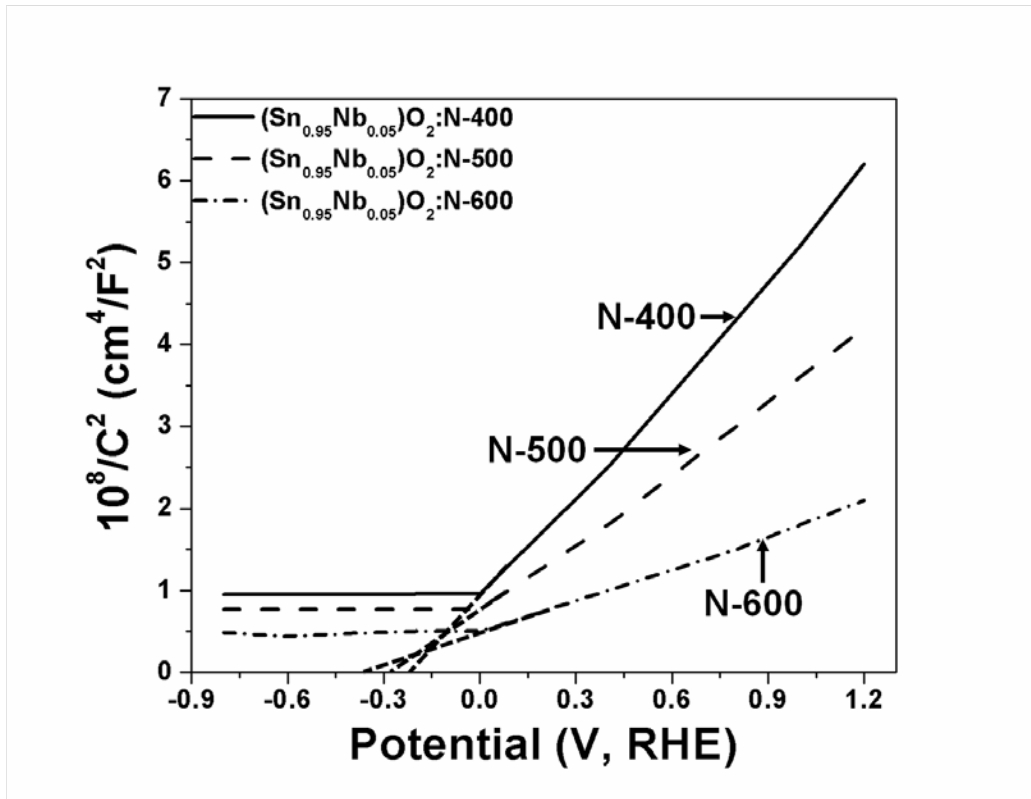


Figure 43: Mott-Schottky plots of $(\text{Sn}_{0.95}\text{Nb}_{0.05})\text{O}_2:\text{N}$ NTs of different N concentration

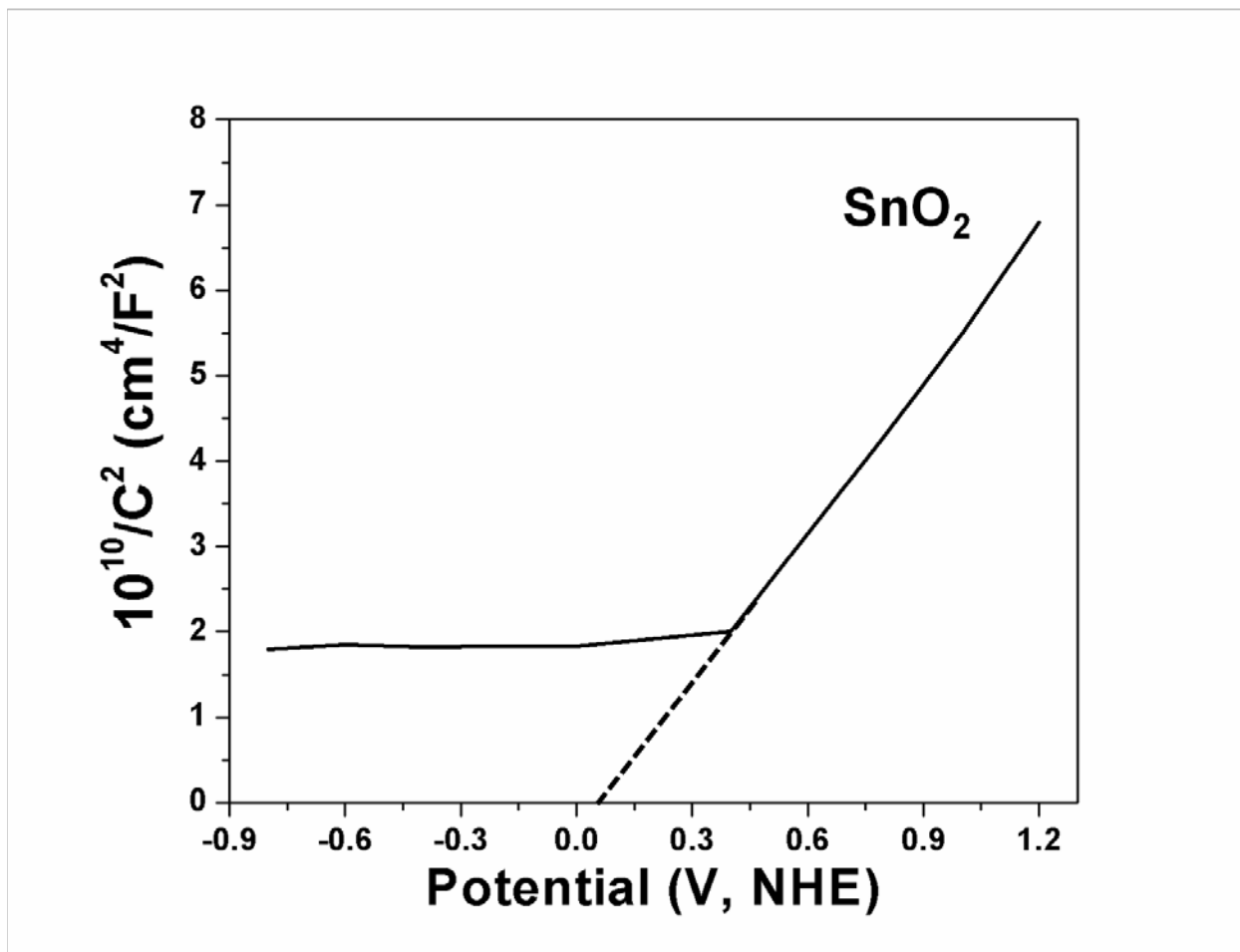


Figure 44: Mott-Schottky plot of SnO₂ NTs

5.2.2 PHOTOELECTROCHEMICAL CHARACTERIZATION OF SnO₂ AND (Sn_{0.95}Nb_{0.05})O₂:N NTs

IPCE of (Sn_{0.95}Nb_{0.05})O₂:N NTs

To study the effect of light absorption properties on the photoelectrochemical properties, incident photon to current efficiency (IPCE) was determined for (Sn_{0.95}Nb_{0.05})O₂:N NTs using

different bandpass optical filters with wavelength centered at 350, 370, 400, 420, 450, 470, 500, 520, 550, 570 and 600 nm. The IPCE is calculated by the equation¹⁹⁵:

$$\text{IPCE (\%)} = \frac{1240 \times J \times 100}{\lambda \times P}$$

where, J is the measured photocurrent density (mA cm^{-2}), P is the incident light intensity (mW cm^{-2}) at a specific wavelength (λ , nm). As shown in **Figure 45**, the IPCE value is observed to increase for $(\text{Sn}_{0.95}\text{Nb}_{0.05})\text{O}_2\text{:N}$ NTs with increase in N concentration with the highest value obtained for $(\text{Sn}_{0.95}\text{Nb}_{0.05})\text{O}_2\text{:N-600}$ NTs at all the wavelengths considered. At 500 nm in fact, IPCE for $(\text{Sn}_{0.95}\text{Nb}_{0.05})\text{O}_2\text{:N-400}$ NTs, $(\text{Sn}_{0.95}\text{Nb}_{0.05})\text{O}_2\text{:N-500}$ NTs and $(\text{Sn}_{0.95}\text{Nb}_{0.05})\text{O}_2\text{:N-600}$ NTs is 2%, 7% and 10%, respectively. This relatively large increase in IPCE with increase in N concentration for $(\text{Sn}_{0.95}\text{Nb}_{0.05})\text{O}_2\text{:N}$ NTs can be attributed to the lowering of the optical band gap which in turn leads to improved visible light absorption and increase in carrier density, thereby, resulting in enhanced charge separation, collection as well as conversion efficiency in the visible region of interest. Once again, it should be mentioned that the IPCE value of 10% obtained in this study for $(\text{Sn}_{0.95}\text{Nb}_{0.05})\text{O}_2\text{:N-600}$ NTs at 500 nm is indeed the highest IPCE value obtained for semiconductor materials explored so far for PEC water splitting to the best of our reported understanding.^{64, 65, 91, 106} The analyses conducted thus far indeed shows that Nb and N co-doping together is a promising strategy for improving the photoelectrochemical activity of SnO_2 NT based systems.

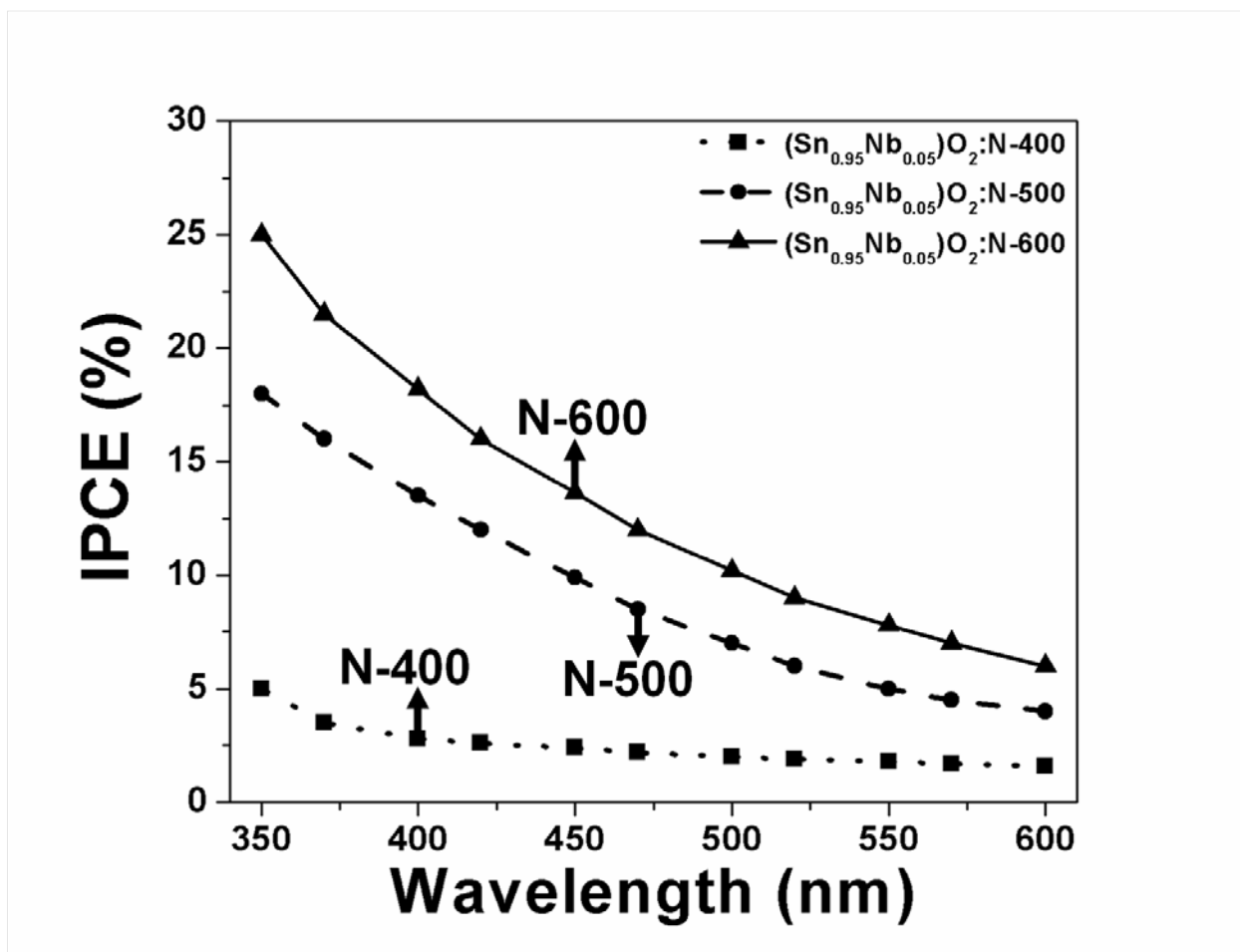


Figure 45: IPCE spectra of $(\text{Sn}_{0.95}\text{Nb}_{0.05})\text{O}_2:\text{N}$ NTs of different N concentration measured at potential of $\sim 0\text{V}$ (vs RHE)

Photoelectrochemical activity of SnO_2 and $(\text{Sn}_{0.95}\text{Nb}_{0.05})\text{O}_2:\text{N}$ NTs

The photoelectrochemical activity of SnO_2 and $(\text{Sn}_{0.95}\text{Nb}_{0.05})\text{O}_2:\text{N}$ NTs of different N concentration is studied in 0.5 M H_2SO_4 as the electrolyte solution using a 300 W xenon lamp (Model 6258, Newport) equipped with an AM1.5G filter (Model 81094, Newport) used to simulate the solar spectrum. **Figure 46** and **Figure 47** shows the uncorrected and iR_Ω (R_Ω , the ohmic resistance was determined from EIS analysis discussed in detail later) corrected linear

scan voltammogram (LSV) curves of SnO₂ NTs and (Sn_{0.95}Nb_{0.05})O₂:N NTs collected in the dark and with illumination of 100 mW cm⁻² obtained at a scan rate of 1 mV sec⁻¹. The LSV curves generated in the dark showed a small current in the range of ~10⁻³ mA cm⁻² for SnO₂ and (Sn_{0.95}Nb_{0.05})O₂:N NTs. Pure SnO₂ NTs showed poor photoelectrochemical activity with onset potential of 0.28 V (*vs* RHE) and photocurrent density of ~0 mA cm⁻² at 0.75 V mainly due to its wide band gap (3.53 eV as shown in **Table 6**). In comparison to pure SnO₂ NTs, an enhanced photocurrent density is observed for (Sn_{0.95}Nb_{0.05})O₂:N NTs under illumination with onset potential of (-0.01V), (-0.04V) and (-0.14V) (*vs* RHE) for (Sn_{0.95}Nb_{0.05})O₂:N-400 NTs, (Sn_{0.95}Nb_{0.05})O₂:N-500 NTs and (Sn_{0.95}Nb_{0.05})O₂:N-600 NTs, respectively (**Table 6**). The onset potential for (Sn_{0.95}Nb_{0.05})O₂:N NTs is lower than SnO₂ (0.28 V *vs* RHE) (**Table 6**), indicating improvement in photoelectrochemical activity due to Nb and N doping in SnO₂ NTs. Also, the decrease in the onset potential with increase in N concentration for (Sn_{0.95}Nb_{0.05})O₂:N NTs suggests the beneficial role of N in improving the photoelectrochemical activity. It is also again noteworthy to point out that the negative onset potential of (Sn_{0.95}Nb_{0.05})O₂:N NTs of (-0.14V *vs* RHE) obtained in this study for (Sn_{0.95}Nb_{0.05})O₂:N-600 NTs suggests that a very minimal bias would be required in converting solar energy to photocurrent density indicating superior utilization of solar energy in the production of hydrogen from water, an important aspect to be considered for commercialization of this novel system. The wide band gap of SnO₂ usually does not allow for such low onset potentials for water splitting under photo-chemical conditions. The tailoring of the band gap of SnO₂ by co-doping of Nb and N in this study thus results in this remarkable and highly attractive photo-electrochemical behavior.

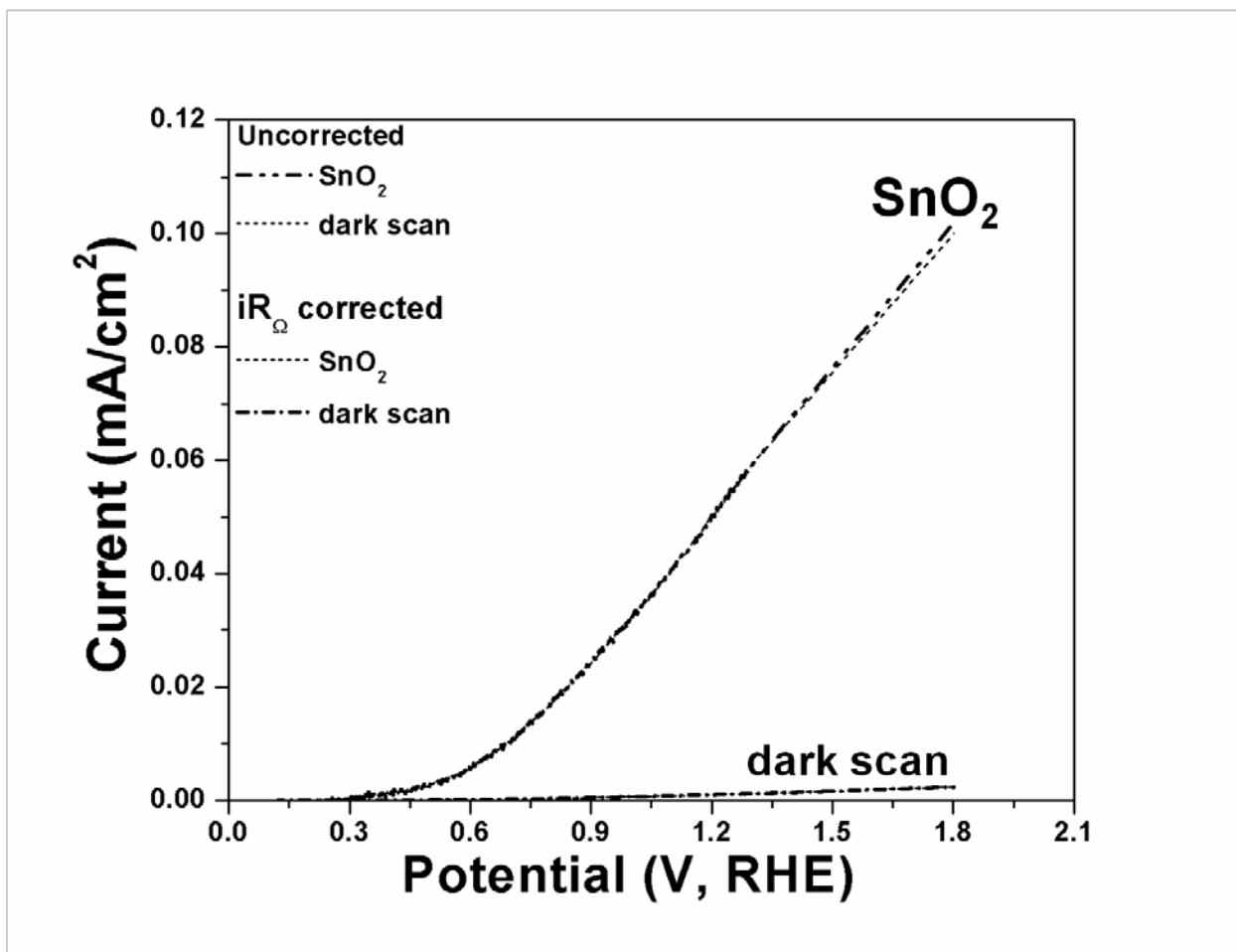


Figure 46: The linear scan voltammogram (LSV) curves for SnO₂ NTs in dark and illumination of 100 mW cm⁻² measured in 0.5 M H₂SO₄ at 26°C, before and after iR_{Ω} correction

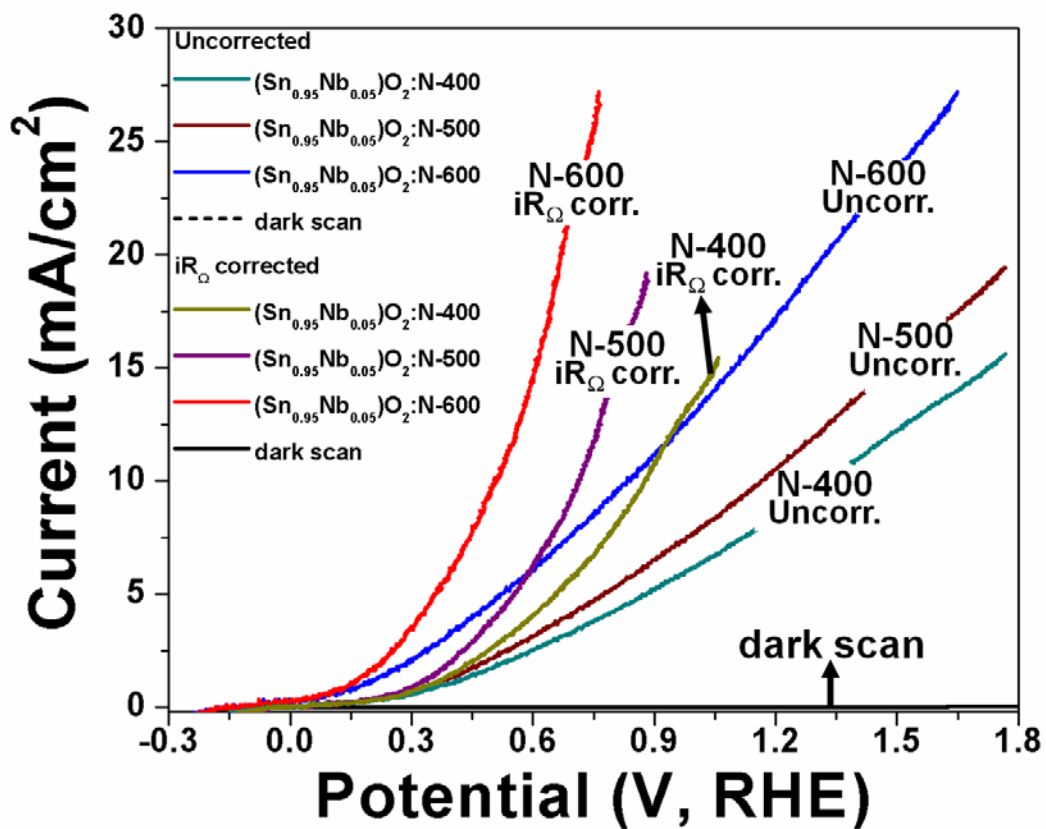


Figure 47: The linear scan voltammogram (LSV) curves for $(\text{Sn}_{0.95}\text{Nb}_{0.05})\text{O}_2:\text{N}$ NTs of different N concentration in dark and illumination of 100 mW cm^{-2} measured in $0.5 \text{ M H}_2\text{SO}_4$ at 26°C , before and after iR_Ω correction

Table 6: Results of Tauc analysis, Mott-Schottky analysis and photoelectrochemical characterization of SnO₂, (Sn_{1-x}Nb_x)O₂ (x=0.05, 0.1) and (Sn_{0.95}Nb_{0.05})O₂:N NTs (performed in 0.5 M H₂SO₄ electrolyte solution under illumination of 100 mW cm⁻² at 26°C)

Composition	Band gap (eV)	Carrier density (cm ⁻³)	Onset potential (V, RHE)	Photocurrent density at 0.75 V (vs RHE) (mA cm ⁻²)	Max. ABPE (%)	Potential corresponding to max. ABPE (V vs RHE)
SnO ₂	3.53	2.42×(10 ¹⁸)	0.28	~0	0.008	0.9
(Sn _{0.95} Nb _{0.05})O ₂ :N-400 NTs	2.58	3.3×(10 ²²)	(-0.01)	6.76	1.83	0.8
(Sn _{0.95} Nb _{0.05})O ₂ :N-500 NTs	2.38	4.05×(10 ²²)	(-0.04)	11.74	2.29	0.78
(Sn _{0.95} Nb _{0.05})O ₂ :N-600 NTs	1.99	4.7×(10 ²²)	(-0.14)	25.39	4.1	0.75

The photocurrent density at 0.75 V [chosen since the max. ABPE of 4.1% is obtained for (Sn_{0.95}Nb_{0.05})O₂:N-600 NTs at 0.75 V discussed later] in the *iR_Ω* corrected LSV plot (**Figure 47**) for (Sn_{0.95}Nb_{0.05})O₂:N-400 NTs, (Sn_{0.95}Nb_{0.05})O₂:N-500 NTs and (Sn_{0.95}Nb_{0.05})O₂:N-600 NTs is 6.76 mA cm⁻², 11.74 mA cm⁻² and 25.39 mA cm⁻², respectively (**Table 6**). Thus, the photocurrent density at 0.75 V increases with progressive increase in N concentration for (Sn_{0.95}Nb_{0.05})O₂:N NTs, with the maximum value obtained for (Sn_{0.95}Nb_{0.05})O₂:N-600 NTs

(25.39 mA cm⁻²), which is ~275% and ~116% higher than that obtained for (Sn_{0.95}Nb_{0.05})O₂:N-400 NTs (6.76 mA cm⁻²) and (Sn_{0.95}Nb_{0.05})O₂:N-500 NTs (11.74 mA cm⁻²), respectively. This indicates the observed improved reaction kinetics and thus, photoelectrochemical activity with increase in N concentration for (Sn_{0.95}Nb_{0.05})O₂:N NTs. Hence, the reaction kinetics is further studied by determining charge transfer resistance (R_{ct}) from EIS of (Sn_{0.95}Nb_{0.05})O₂:N NTs. R_{ct} is determined from the diameter of the low frequency semicircle and is shown in **Table 7**. As seen in **Figure 48**, R_{ct} for (Sn_{0.95}Nb_{0.05})O₂:N NTs decreases with increase in N concentration with the lowest R_{ct} obtained for (Sn_{0.95}Nb_{0.05})O₂:N-600 NTs composition (15.3 Ω.cm²), indicating improved reaction kinetics with increase in N concentration. Also, R_{ct} for (Sn_{0.95}Nb_{0.05})O₂:N-600 NTs (15.3 Ω.cm²) is almost six-fold lower than pure SnO₂ (92 Ω.cm²) (**Table 7**). These results concomitantly show the excellent reaction kinetics and thus expectedly improved photoelectrochemical activity for (Sn_{0.95}Nb_{0.05})O₂:N-600 NTs, in comparison to SnO₂ NTs, (Sn_{0.95}Nb_{0.05})O₂:N-400 NTs and (Sn_{0.95}Nb_{0.05})O₂:N-500 NTs. The lower R_{ct} obtained for (Sn_{0.95}Nb_{0.05})O₂:N-600 NTs can be attributed to the efficient charge separation and thus, minimum recombination of photogenerated carriers, as seen in the IPCE analysis (**Figure 45**)²²⁴,²²⁵. Interestingly, there was no saturation seen in photocurrent density at higher potential under illumination, possibly due to efficient separation of photogenerated carriers (**Figure 47**).^{106, 114,}

207, 218, 224, 225

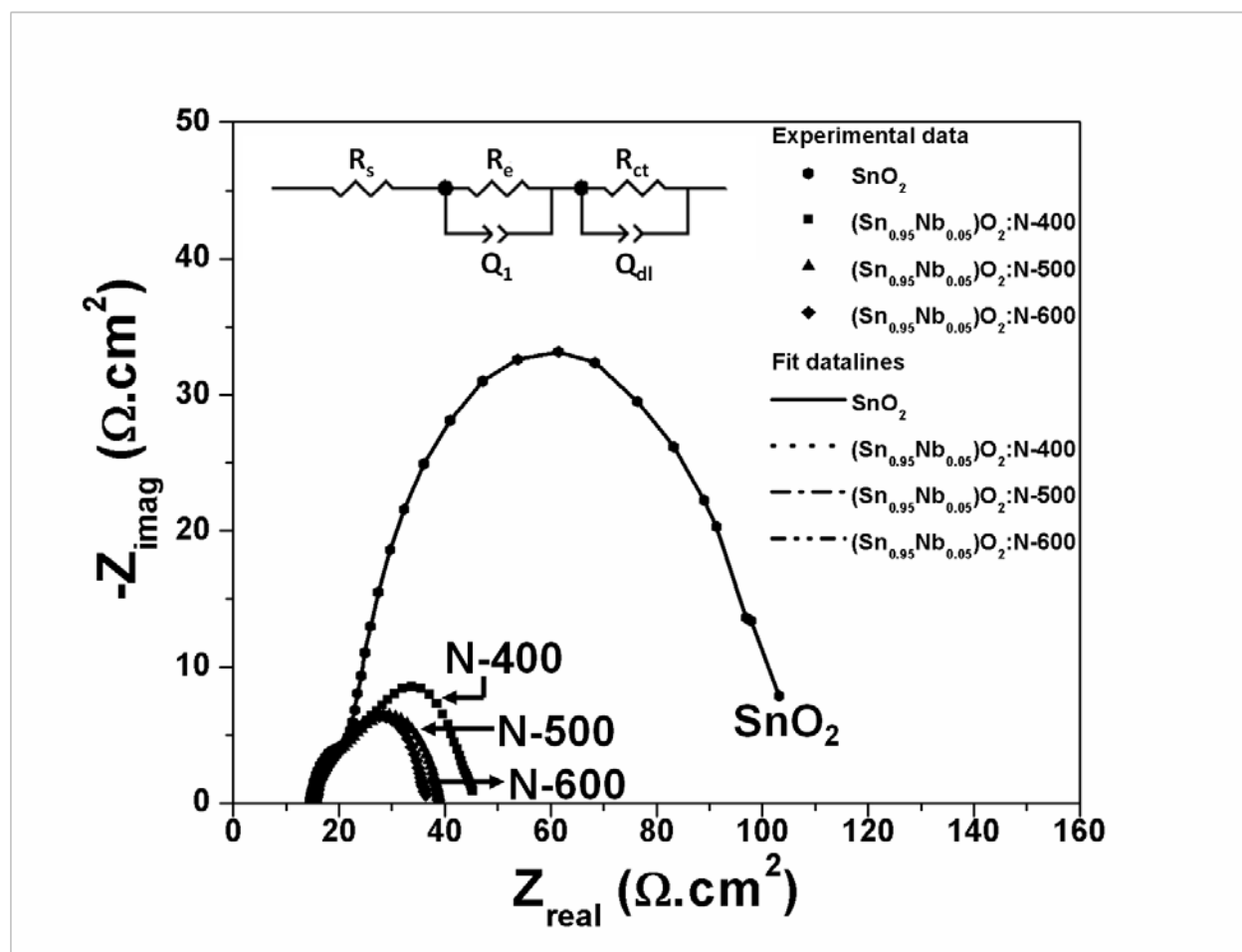


Figure 48: EIS spectra of SnO_2 NTs and $(\text{Sn}_{0.95}\text{Nb}_{0.05})\text{O}_2:\text{N}$ NTs of different N concentration obtained at 0.75 V (*vs* RHE) in 0.5 M H_2SO_4 at 26°C in the frequency range of 100 mHz to 100 kHz under illumination (100 mW cm^{-2}) with the circuit used for fitting experimental data

Table 7: Results of EIS analysis of SnO₂ and (Sn_{0.95}Nb_{0.05})O₂:N NTs performed at 0.75 V (RHE) in 0.5 M H₂SO₄ electrolyte solution in frequency range of 100 mHz-100 kHz under illumination (100 mW cm⁻²) at 26°C

Composition	R_s (Ω.cm²)	R_e (Ω.cm²)	R_{ct} (Ω.cm²)
SnO ₂	15.16	6.49	92
(Sn _{0.95} Nb _{0.05})O ₂ :N- 400 NTs	15.17	6.43	24.6
(Sn _{0.95} Nb _{0.05})O ₂ :N- 500 NTs	15.16	6.41	19.2
(Sn _{0.95} Nb _{0.05})O ₂ :N- 600 NTs	15.17	6.38	15.3

The photocurrent density at 0.75 V in iR_{Ω} corrected LSV plot (**Figure 47**) for (Sn_{0.95}Nb_{0.05})O₂:N NTs is significantly higher than that of pure SnO₂ NTs (~0 mA cm⁻²) (**Figure 46**), suggesting remarkably improved photoelectrochemical activity of (Sn_{0.95}Nb_{0.05})O₂:N NTs after Nb and N doping. Thus the excellent photoelectrochemical activity of (Sn_{0.95}Nb_{0.05})O₂:N NTs which increases with increase in N concentration with maximum value obtained for (Sn_{0.95}Nb_{0.05})O₂:N-600 NTs can be attributed to the decrease in the band gap (as seen in the Tauc analysis in **Figure 42** and **Table 6**) and thus, improved light absorption (as seen in the UV-vis absorption spectra in **Figure 41**), increase in carrier density (as perceived in the Mott-Schottky analysis in **Figure 43** and **Table 6**), improved charge separation, transport and collection (as observed in the IPCE analysis in **Figure 45**) and improved electrochemical charge transfer (as

witnessed in the EIS plots obtained under illumination in **Figure 48** and **Table 7**) with increase in N concentration.¹¹⁴

The variation of applied bias photon-to-current efficiency (ABPE) for SnO₂ NTs and (Sn_{0.95}Nb_{0.05})O₂:N NTs, calculated using **Equation 1** with applied potential is shown in **Figure 49** and **Figure 50**. The maximum ABPE observed for (Sn_{0.95}Nb_{0.05})O₂:N-400 NTs, (Sn_{0.95}Nb_{0.05})O₂:N-500 NTs and (Sn_{0.95}Nb_{0.05})O₂:N-600 NTs is 1.83%, 2.29% and 4.1% at 0.8 V, 0.78 V and 0.75 V (*vs* RHE), respectively. These results indicate that the ABPE obtained for (Sn_{0.95}Nb_{0.05})O₂:N NTs is 100-1000 order of magnitude higher than that for SnO₂ NTs (0.008% at 0.9 V) clearly pointing towards the beneficial role of Nb and N co-doping simultaneously leading to significant improvement in the ABPE of SnO₂ NTs. The impressive progression seen here can be gauged from the fact that the highest ABPE obtained in this study for (Sn_{0.95}Nb_{0.05})O₂:N-600 NTs (4.1% at 0.75 V) is correspondingly ~124% and ~79% higher than that of (Sn_{0.95}Nb_{0.05})O₂:N-400 NTs (1.83% at 0.8V) and (Sn_{0.95}Nb_{0.05})O₂:N-500 NTs (2.29% at 0.78V), respectively. These results therefore validate the implementation of Nb and N as a potential dopant in improving the photoelectrochemical activity of SnO₂ NTs.

It is also important to note that the ABPE of 4.1% obtained in this study for (Sn_{0.95}Nb_{0.05})O₂:N-600 NTs (at 0.75 V) is the highest ABPE obtained so far compared to other semiconductor materials studied as photoanode for PEC water splitting such as TiO₂, ZnO and Fe₂O₃, to the best of our assessment of the widely reported literature to date (**Table 8**).^{64, 114, 176-178} These excellent and unprecedented results clearly show the potential of Nb and N co-doping leading to significantly improving the photoelectrochemical activity and ABPE of SnO₂ NTs, as evidenced in above studies.

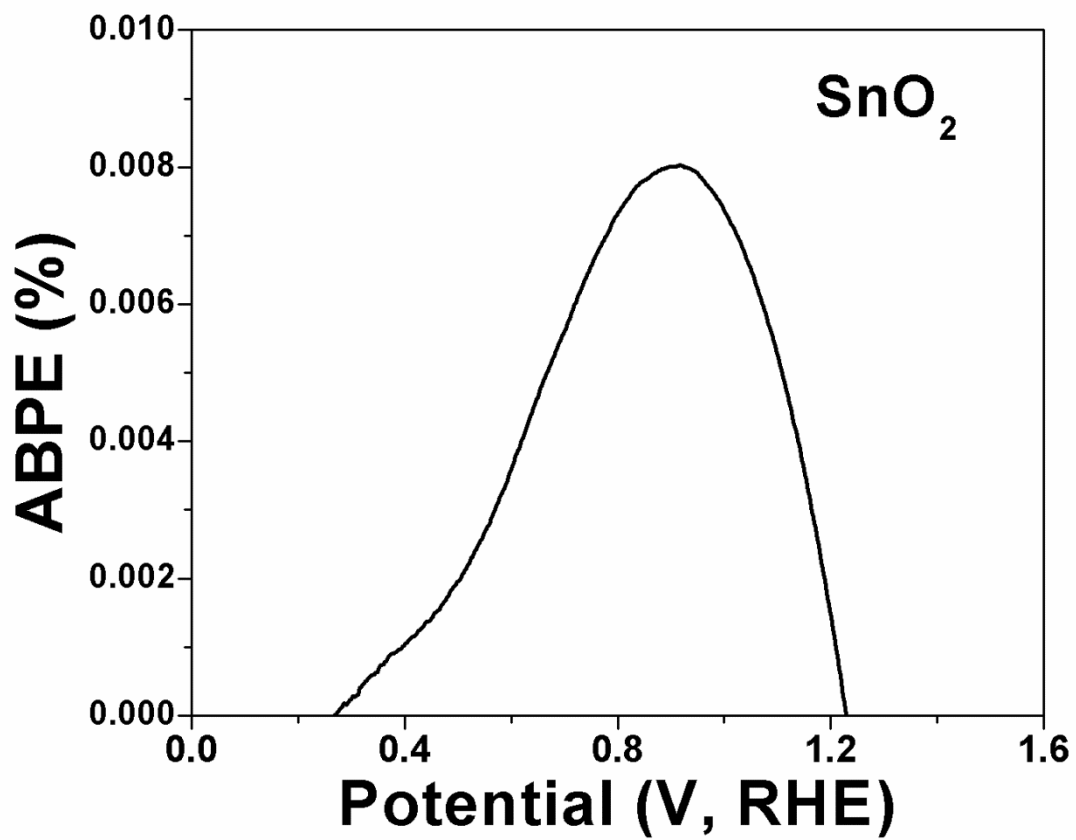


Figure 49: Applied bias photon-to-current efficiency (ABPE) as a function of applied potential for SnO₂ NTs

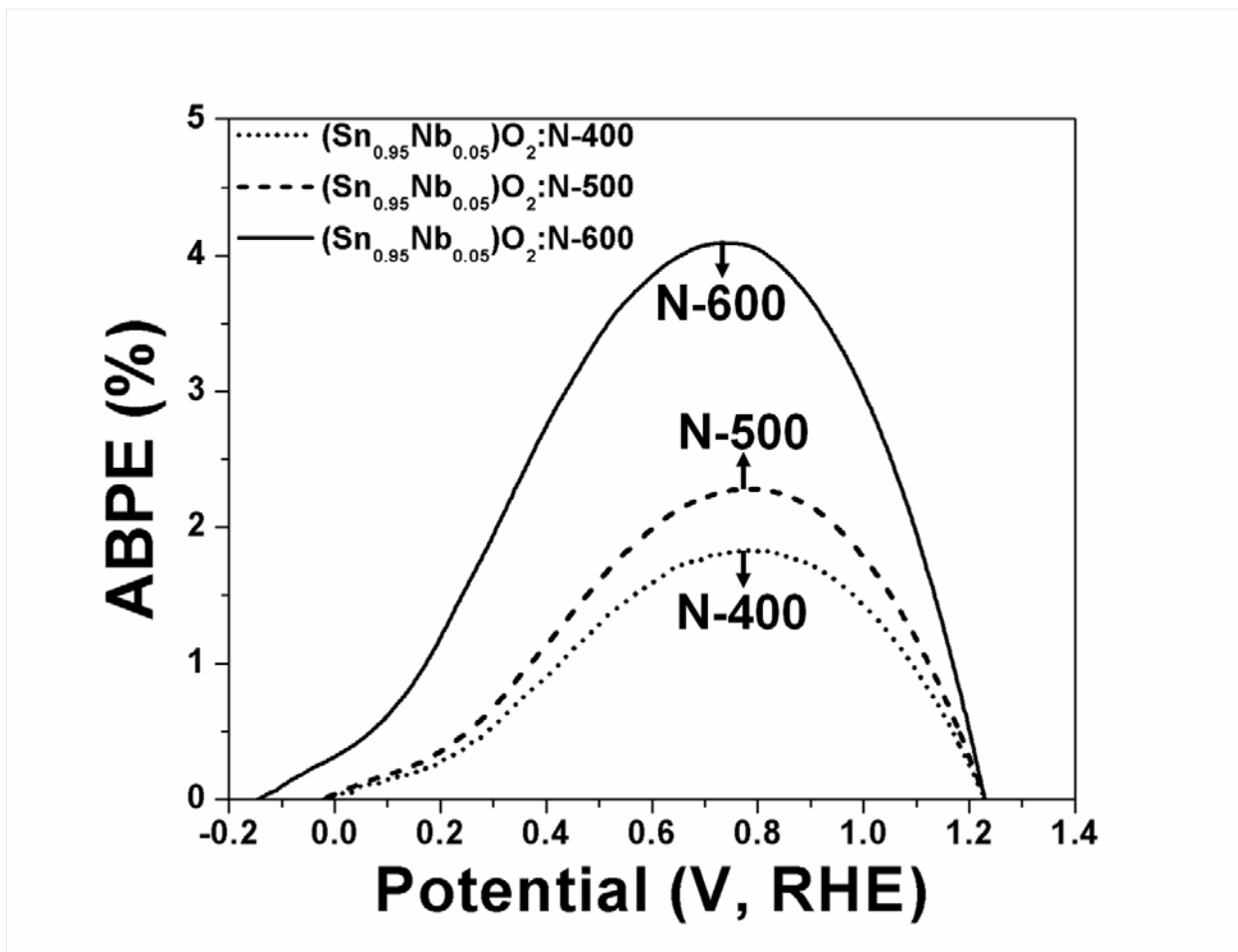


Figure 50: Applied bias photon-to-current efficiency (ABPE) as a function of applied potential for $(\text{Sn}_{0.95}\text{Nb}_{0.05})\text{O}_2:\text{N}$ NTs of different N concentration

Table 8: Efficiency of photoelectrochemical water splitting of various photoanode materials, reported in the literature

Photoanode material	Max. ABPE, %	Potential at max. ABPE (V, RHE)	Onset potential (V, RHE)	Ref
N-doped ZnO nanowire arrays	0.15	1.11	0.21	¹⁰⁶
N-doped ZnO nanotetrapods	0.31	0.92	0.41	²⁰⁷
TiO ₂ :Al nanorod array thin film	0.02	0.5 (vs Ag/AgCl)	0.61	²¹⁹
Bent ZnO nanorod photoanode	0.08	0.69	-	²²⁰
Si/ZnO core/shell nanowire arrays	0.38	0.65 (vs Ag/AgCl)	0.11	²²¹
Hierarchical Fe ₂ O ₃ /WO _x nanowires	0.2	0.25	0.01	²²²
C-doped ZnO porous nanoarchitectures	0.75	0.91	0.31	¹¹⁰
Si/TiO ₂ core/shell nanowire arrays	0.035	1.15	0.36	²²³

Table 8 (continued)				
Fe ₂ O ₃ :Cu nanostructured film	0.28	0.6 (vs Ag/AgCl)	1.44	⁸³
ZnFe ₂ O ₄ /ZnO system	0.15	1.21	0.51	²¹⁷
TiO ₂ -ZnS core-shell	0.38	0.81	0.26	⁶⁵
Au coated 3D ZnO nanowires	0.52	0.75	0.3	⁸²
<u>(Sn_{0.95}Nb_{0.05})O₂:N-600 NTs</u>	<u>4.1</u>	<u>0.75</u>	<u>-0.14</u>	<u>Present work</u>

Photoelectrochemical stability of (Sn_{0.95}Nb_{0.05})O₂:N NTs

It is important that in addition to the excellent photoelectrochemical activity discussed above, the semiconductor materials need to also exhibit adequate and acceptable long term photoelectrochemical stability for use of these systems in PEC water splitting cell. Hence, accordingly, chronoamperometry (CA) test has been carried out for 24 h to study the long term photoelectrochemical stability of (Sn_{0.95}Nb_{0.05})O₂:N-600 NTs under illumination in the electrolyte solution. The CA test is carried out at a constant potential of 0.75 V (at which the max. ABPE is obtained, as shown in **Figure 50** and **Table 6**) in 0.5 M H₂SO₄ solution by illuminating the photoanode for 24 h. The corresponding CA curve of (Sn_{0.95}Nb_{0.05})O₂:N-600 NTs is shown in **Figure 51**. A very minimal loss in photocurrent density is observed for (Sn_{0.95}Nb_{0.05})O₂:N-600 NTs indicating excellent photoelectrochemical stability of the co-doped system. In addition, the CA curve obtained under light ON/OFF cycles shows instantaneous

photoresponse of $(\text{Sn}_{0.95}\text{Nb}_{0.05})\text{O}_2\text{:N-600}$ NTs under illumination and also, displays superior photoelectrochemical stability with negligible loss in photocurrent density (**Figure 52**). After 24 h CA test, LSV is carried out (**Figure 53**) to study and determine any potential loss in photoelectrochemical activity of $(\text{Sn}_{0.95}\text{Nb}_{0.05})\text{O}_2\text{:N-600}$ NTs and accordingly, ensure that the system undergoes no degradation and exhibits similar photoelectrochemical activity prior to the start of the CA test. Accordingly, LSV collected after 24 h CA test shows negligible loss in photoelectrochemical activity of $(\text{Sn}_{0.95}\text{Nb}_{0.05})\text{O}_2\text{:N-600}$ NTs, suggesting the excellent photoelectrochemical stability of the co-doped system obtained following ammonolysis at 600°C . The ICP analysis conducted on the electrolyte solution collected after CA test does not show the presence of Sn and Nb for the $(\text{Sn}_{0.95}\text{Nb}_{0.05})\text{O}_2\text{:N-600}$ NTs. This result is a further testimonial affirming the excellent photoelectrochemical stability of $(\text{Sn}_{0.95}\text{Nb}_{0.05})\text{O}_2\text{:N-600}$ NTs in the electrolyte solution under illumination of 100 mW cm^{-2} indicating the ability of the system to be deployed for long term operation in PEC water splitting cell.

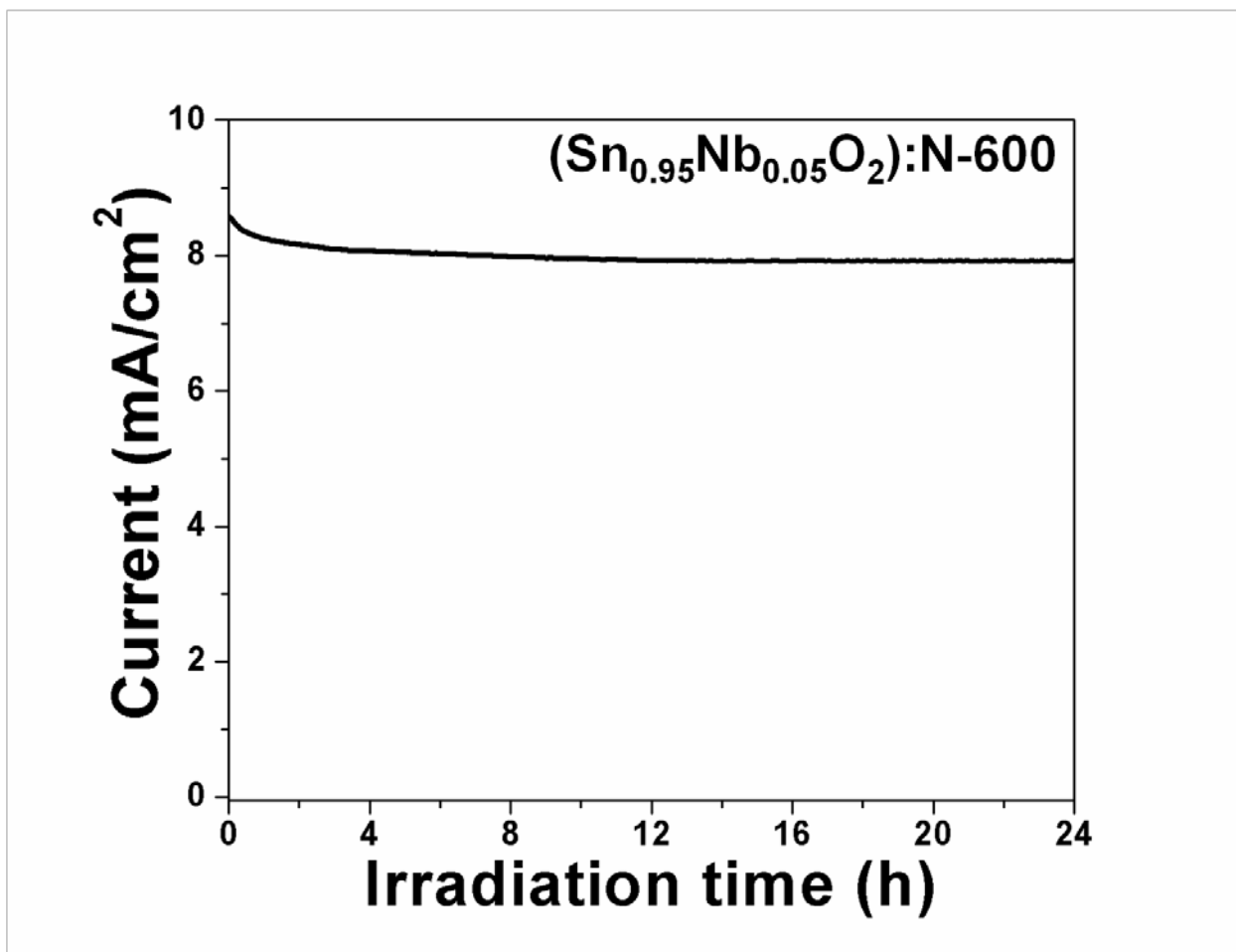


Figure 51: The variation of photocurrent density *vs* time in the chronoamperometry test of $(\text{Sn}_{0.95}\text{Nb}_{0.05})\text{O}_2:\text{N}-600$ NTs, performed in 0.5 M H_2SO_4 solution under a constant potential of 0.75 V (*vs* RHE) at 26°C for 24 h under illumination (100 mW cm^{-2})

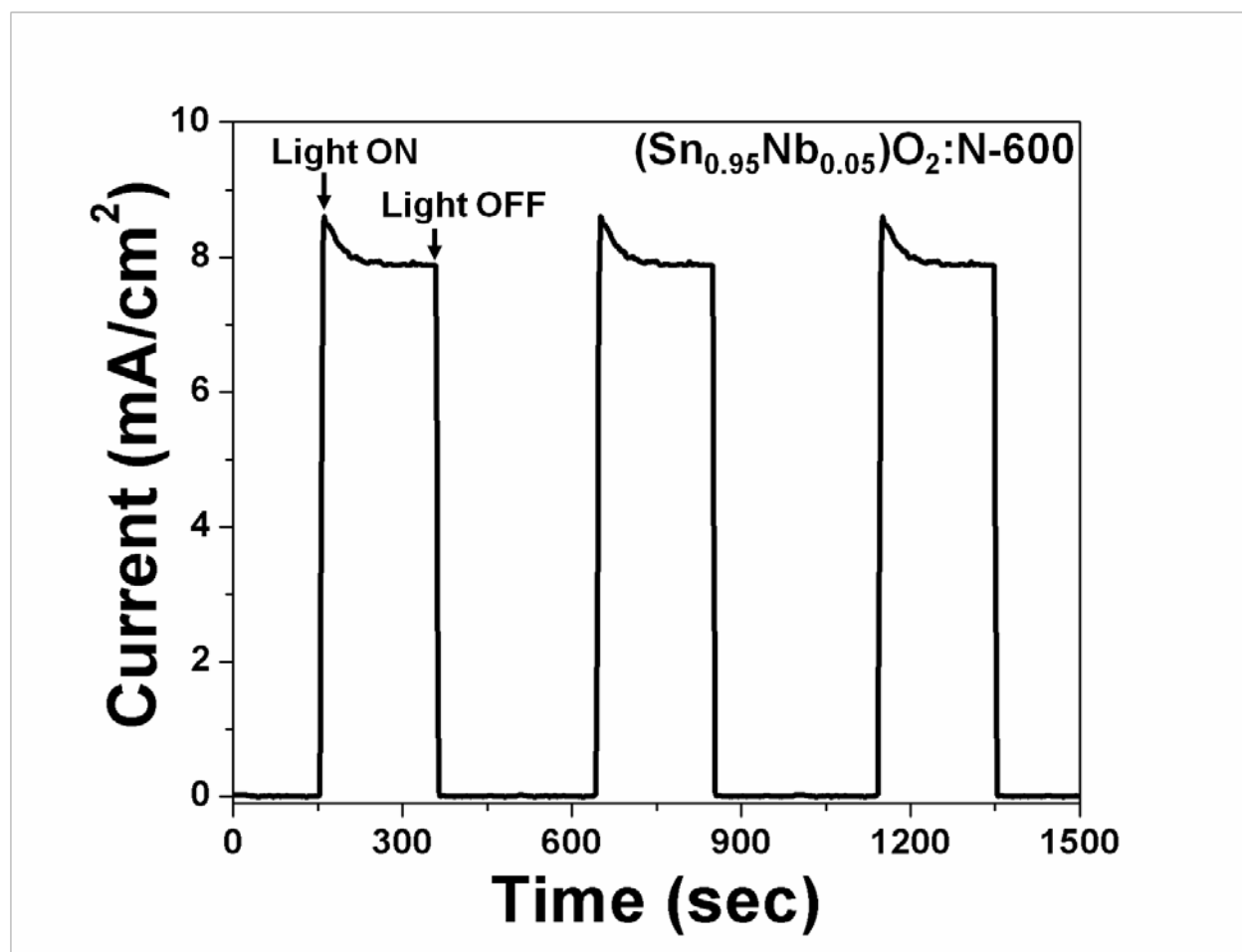


Figure 52: The variation of photocurrent density *vs* time in the chronoamperometry test of $(\text{Sn}_{0.95}\text{Nb}_{0.05})\text{O}_2:\text{N}-600$ NTs, performed in 0.5 M H_2SO_4 solution at 26⁰C under a constant potential of 0.75 V (*vs* RHE) at 100 mW/cm² with 200 sec light ON/OFF cycles for 25 min

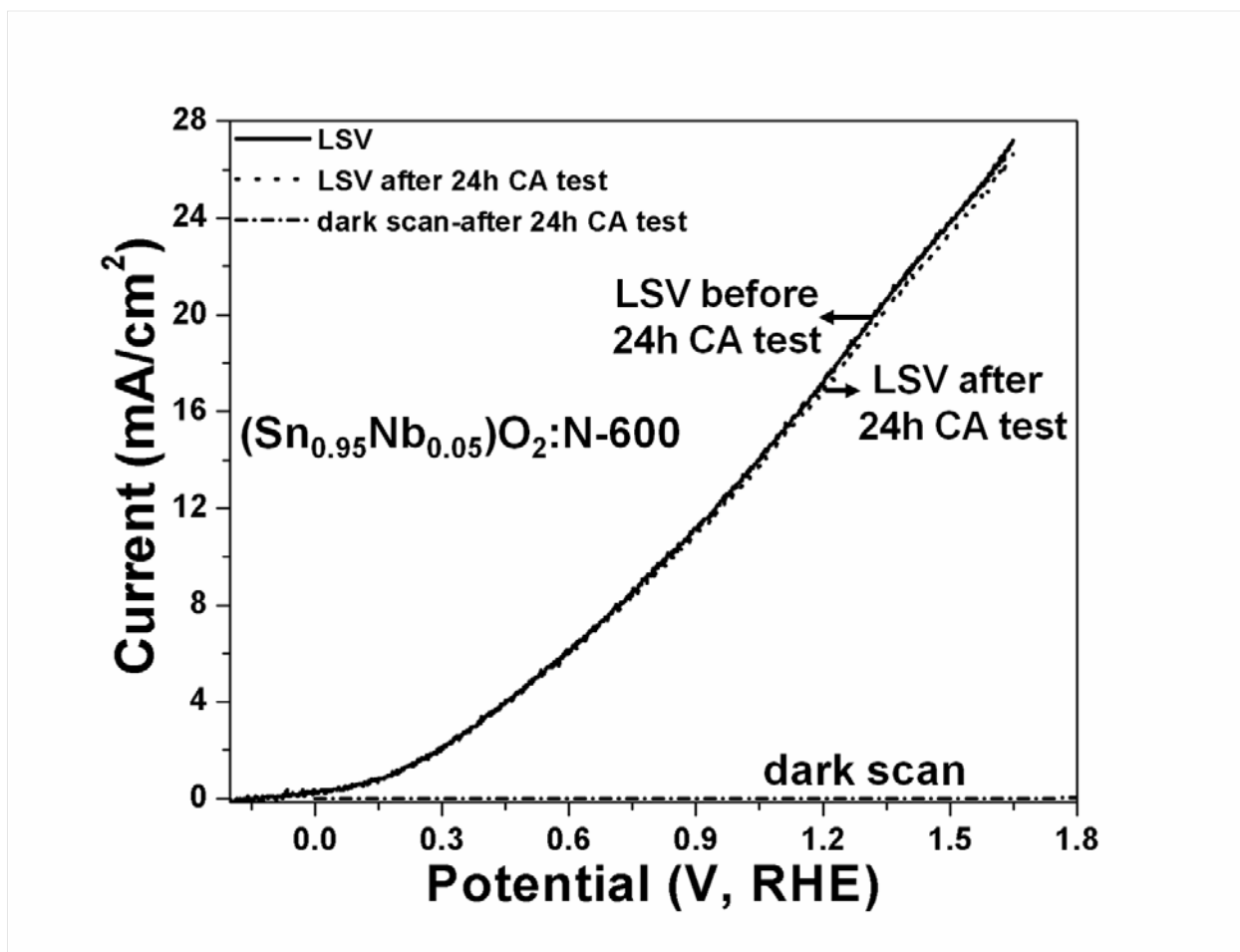


Figure 53: The linear scan voltammogram (LSV) curve for $(\text{Sn}_{0.95}\text{Nb}_{0.05})\text{O}_2\text{:N-600}$ NTs in dark and under illumination of 100 mW cm^{-2} measured in $0.5 \text{ M H}_2\text{SO}_4$ at 26°C , obtained before and after 24 h chronoamperometry test

Measurement of H_2 and O_2 gases under illumination

Measurement of the concentration of H_2 and O_2 gases generated at the cathode and photoanode, respectively serves as a measure of the efficiency of the system and is thus carried out to ensure that the photocurrent is indeed arising from water splitting. Hence, during CA test of $(\text{Sn}_{0.95}\text{Nb}_{0.05})\text{O}_2\text{:N-600}$ NTs at constant potential of 0.75 V , the concentration of the gases generated were measured after 1 h intervals by gas chromatography. Additionally, the theoretical

concentration of H₂ gas is calculated from the measured photocurrent using the Faraday's law as under¹⁹⁵:

$$\text{No. of moles of H}_2 = \frac{Q}{2F} = \frac{It}{2F} = \frac{\int_0^t I \cdot dt}{2F}$$

where, I is the photocurrent density, t is time, F is the Faraday constant (96484.34 C mol⁻¹) and Q is the quantity of charge in coulomb. The concentration of H₂ and O₂ gases evolved is correspondingly shown in **Figure 54**. As shown in **Figure 54**, the theoretical amount of evolved H₂ gas is closer or comparable to the measured amount of H₂, suggesting ~100% Faradaic efficiency. If the decomposition of water is non-stoichiometric, there will be change in concentration of either H⁺ or OH⁻ ions. However, in this study, the ratio of concentration of generated H₂ and O₂ gases is ~2, as seen in **Figure 54** and also, there was no change observed in the pH of the electrolyte solution (~0) before and after water splitting reaction, an extremely important aspect further confirming the efficiency of the novel system. This result thus shows the expected stoichiometric decomposition of water into H₂ and O₂ in the present study for (Sn_{0.95}Nb_{0.05})O₂:N-600 NTs serving to demonstrate the promise of this uniquely engineered system.

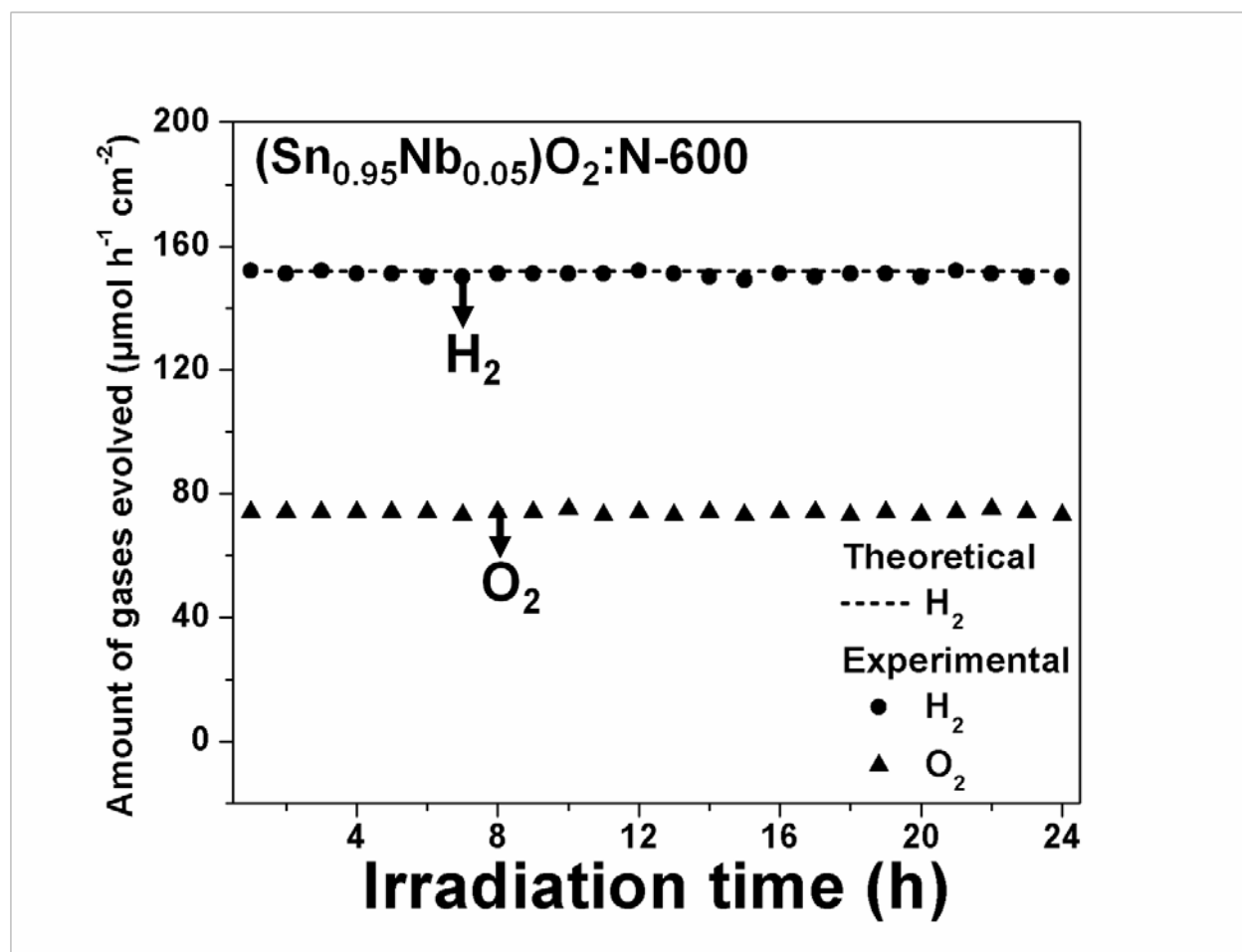


Figure 54: Theoretical and experimentally measured concentration of H₂ gas and experimentally measured concentration of O₂ gas, measured during 24 h chronoamperometry test of (Sn_{0.95}Nb_{0.05})O₂:N-600 NTs, performed in 0.5 M H₂SO₄ solution under a constant potential of 0.75 V (vs RHE) at 26°C for 24 h

Conclusions:

The photoelectrochemical activity of a carefully engineered and band gap tailored system (Sn_{0.95}Nb_{0.05})O₂:N NTs is reported in this study. The nanotubes were synthesized using ZnO NWs as sacrificial template followed by systematic heat treatment in NH₃ atmosphere. This work clearly demonstrates the potential of Nb and N co-doping to significantly reduce the optical band

gap of SnO₂ NTs from 3.53 eV to 1.99 eV for (Sn_{0.95}Nb_{0.05})O₂:N-600 NTs leading to excellent light absorption characteristics. Accordingly, Nb and N co-doping results in 4-orders of magnitude improved carrier density, improved carrier separation and transport and collection efficiency as well as outstanding ABPE, along with negative onset potential (-0.01 V to -0.14 V) indicating superior photoelectrochemical activity. The optical band gap of (Sn_{0.95}Nb_{0.05})O₂:N-600 NTs is indeed the lowest reported for SnO₂ based materials combined with significantly improved carrier density which together opens up new ground for this material to be explored for different solar energy based applications.

The ABPE of 4.1% obtained for (Sn_{0.95}Nb_{0.05})O₂:N-600 NTs at 0.75 V (*vs* RHE) is indeed the highest ABPE reported so far following careful assessment of the reports available in the literature to date compared to other well-known materials, ZnO, Fe₂O₃ and TiO₂. Furthermore, (Sn_{0.95}Nb_{0.05})O₂:N-600 NTs exhibit excellent long term photoelectrochemical stability in the electrolyte solution under illumination. The Nb and N co-doping strategy for SnO₂ thus results in excellent photoelectrochemical performance for (Sn_{0.95}Nb_{0.05})O₂:N-600 NTs mainly due to (a) excellent light absorption properties, (b) increased carrier density, and (c) facile electrochemical charge transfer. This work will therefore be important in the pursuit of photoelectrochemically active and stable semiconductor materials for efficient and economical hydrogen generation from PEC water splitting.

5.3 [WO₃-(Sn_{0.95}Nb_{0.05})O₂:N-600] BILAYER PHOTOANODES

5.3.1 STRUCTURAL ANALYSIS OF [WO₃-(Sn_{0.95}Nb_{0.05})O₂:N-600] NANOTUBES (NTs)

X-ray diffraction (XRD) study

The XRD patterns of (Sn_{0.95}Nb_{0.05})O₂:N-600 NTs, [WO₃-(Sn_{0.95}Nb_{0.05})O₂:N-600]-1 NTs, [WO₃-(Sn_{0.95}Nb_{0.05})O₂:N-600]-2 NTs and [WO₃-(Sn_{0.95}Nb_{0.05})O₂:N-600]-3 NTs are shown in **Figure 55**. The peaks of (Sn_{0.95}Nb_{0.05})O₂:N-600 NTs (**Figure 55**) correspond to that of pure SnO₂ with the tetragonal structure (PDF code: 01-041-1445)⁷⁶, displaying no additional peaks corresponding to other Sn and Nb-containing phases indicating co-doping of Nb and N in the SnO₂ lattice, and also no reduction of the FTO substrate due to heat treatment at 600°C similar to that reported earlier and also verified by the UV-Vis absorption spectra of the FTO substrate as discussed later.^{76, 106} Annealing in NH₃ atmosphere was not performed at temperature higher than 600°C since the reduction of (Sn_{0.95}Nb_{0.05})O₂ NTs likely due to the atomic hydrogen originating from the decomposition of NH₃ was observed (at 700°C) as reported earlier as well.^{76, 106} The XRD patterns of the bilayer materials clearly reveal presence of both WO₃ with the monoclinic structure (PDF code: 01-083-0950)¹⁸⁶ and (Sn_{0.95}Nb_{0.05})O₂:N-600 NTs with the tetragonal structure (**Figure 55**). The lattice parameters of WO₃-(Sn_{0.95}Nb_{0.05})O₂:N-600 are slightly lower than that of (Sn_{0.95}Nb_{0.05})O₂:N-600 (**Table 9**) suggesting presence of lattice strain due to lattice mismatch between WO₃ and (Sn_{0.95}Nb_{0.05})O₂:N-600. The lattice parameters decrease from [WO₃-(Sn_{0.95}Nb_{0.05})O₂:N-600]-1 NTs to [WO₃-(Sn_{0.95}Nb_{0.05})O₂:N-600]-3 NTs (**Table 9**) suggesting slight lattice contraction, which possibly contributes to the modification in the optoelectronic properties and PEC response as discussed later.

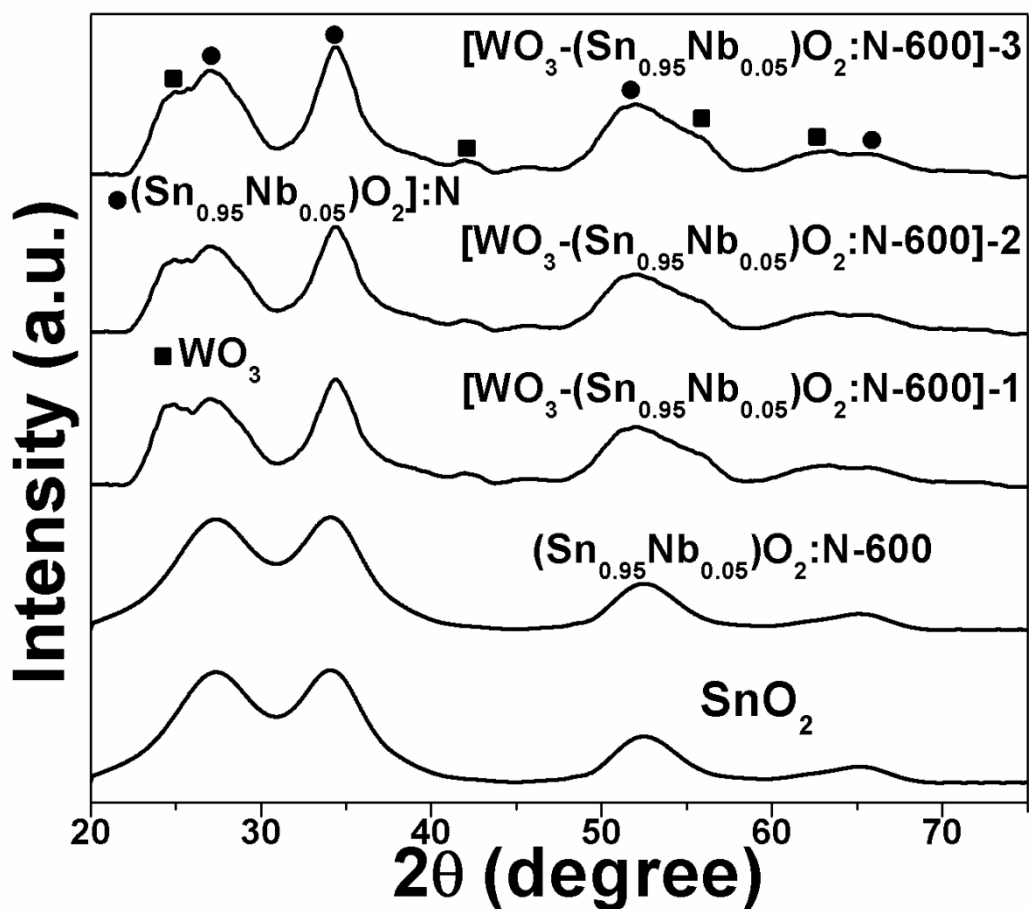


Figure 55: The XRD patterns of SnO₂ NTs, (Sn_{0.95}Nb_{0.05})O₂:N-600 NTs, [WO₃-(Sn_{0.95}Nb_{0.05})O₂:N-600]-1 NTs, [WO₃-(Sn_{0.95}Nb_{0.05})O₂:N-600]-2 NTs and [WO₃-(Sn_{0.95}Nb_{0.05})O₂:N-600]-3 NTs in wide angle 2θ scan

SEM/EDX and TEM study

Scanning electron microscopy (SEM) has been carried out to study the morphology of the representative composition, [WO₃-(Sn_{0.95}Nb_{0.05})O₂:N-600]-2 NTs. SEM images showing the top view and cross-sectional view of [WO₃-(Sn_{0.95}Nb_{0.05})O₂:N-600]-2 NTs are shown in **Figure 56**.

The cross-sectional view of $[\text{WO}_3-(\text{Sn}_{0.95}\text{Nb}_{0.05})\text{O}_2:\text{N}-600]-2$ NTs shows $\sim 12-14 \mu\text{m}$ long well-spaced nanotubes. The nanotubes exhibit clean surface with no presence of any particle at the top or at the bottom of the nanotubes. Quantitative elemental analysis of $[\text{WO}_3-(\text{Sn}_{0.95}\text{Nb}_{0.05})\text{O}_2:\text{N}-600]-2$ NTs has been carried out by energy dispersive x-ray spectroscopy (EDX). The EDX spectrum of $[\text{WO}_3-(\text{Sn}_{0.95}\text{Nb}_{0.05})\text{O}_2:\text{N}-600]-2$ NTs, shown in **Figure 56**, shows the presence of elements Sn, Nb, W and N. Quantitative elemental composition analysis by EDX of $(\text{Sn}_{0.95}\text{Nb}_{0.05})\text{O}_2:\text{N}-600$ NTs, $[\text{WO}_3-(\text{Sn}_{0.95}\text{Nb}_{0.05})\text{O}_2:\text{N}-600]-1$ NTs, $[\text{WO}_3-(\text{Sn}_{0.95}\text{Nb}_{0.05})\text{O}_2:\text{N}-600]-2$ NTs and $[\text{WO}_3-(\text{Sn}_{0.95}\text{Nb}_{0.05})\text{O}_2:\text{N}-600]-3$ NTs is shown in **Table 9**. The increase in the concentration of Sn, Nb and N combined with the decrease in concentration of W can likely be due to the increase in the thickness of the $(\text{Sn}_{0.95}\text{Nb}_{0.05})\text{O}_2:\text{N}-600$ NTs layer which is coated on the WO_3 layer.

TEM images of the single and composite bilayer architectures, $(\text{Sn}_{0.95}\text{Nb}_{0.05})\text{O}_2:\text{N}-600$ NT, $[\text{WO}_3-(\text{Sn}_{0.95}\text{Nb}_{0.05})\text{O}_2:\text{N}-600]-1$ NT, $[\text{WO}_3-(\text{Sn}_{0.95}\text{Nb}_{0.05})\text{O}_2:\text{N}-600]-2$ NT and $[\text{WO}_3-(\text{Sn}_{0.95}\text{Nb}_{0.05})\text{O}_2:\text{N}-600]-3$ NT, displayed in **Figure 57**, reveals clearly the presence of the hollow nanotube with diameter of $\sim 220 \text{ nm}$, $\sim 240 \text{ nm}$, $\sim 270 \text{ nm}$ and $\sim 290 \text{ nm}$, respectively. The larger diameter of $[\text{WO}_3-(\text{Sn}_{0.95}\text{Nb}_{0.05})\text{O}_2:\text{N}-600]-1$ NT compared to that of $(\text{Sn}_{0.95}\text{Nb}_{0.05})\text{O}_2:\text{N}-600$ NT can be attributed to the layer of WO_3 on which $(\text{Sn}_{0.95}\text{Nb}_{0.05})\text{O}_2:\text{N}-600$ layer is coated. The gradual monotonic increase in the diameter of the composite bilayer photoanode materials from $[\text{WO}_3-(\text{Sn}_{0.95}\text{Nb}_{0.05})\text{O}_2:\text{N}-600]-1$ NT to $[\text{WO}_3-(\text{Sn}_{0.95}\text{Nb}_{0.05})\text{O}_2:\text{N}-600]-3$ NT is likely due to the increase in the thickness of the $(\text{Sn}_{0.95}\text{Nb}_{0.05})\text{O}_2:\text{N}-600$ layer due to an increase in the molar concentration of the precursor solutions (AHFS , ANO and H_3BO_3) used for creating the Nb doped tin oxide NTs, as described in the experimental section of this study (**Section 4.1.3**).

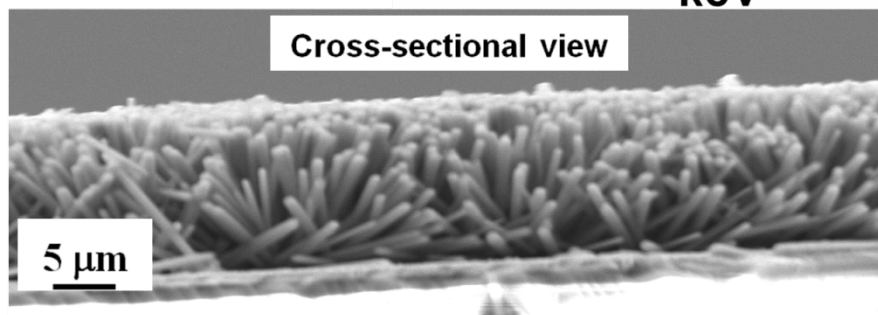
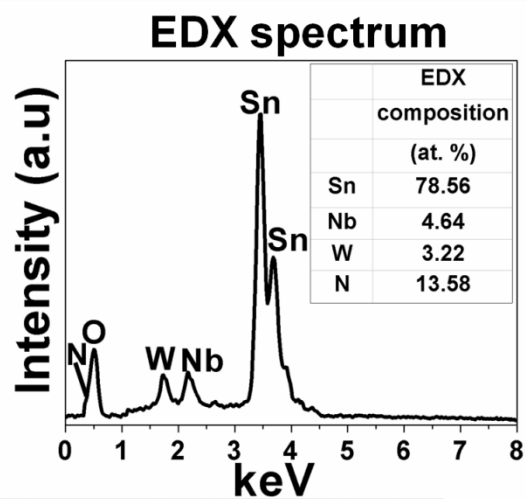
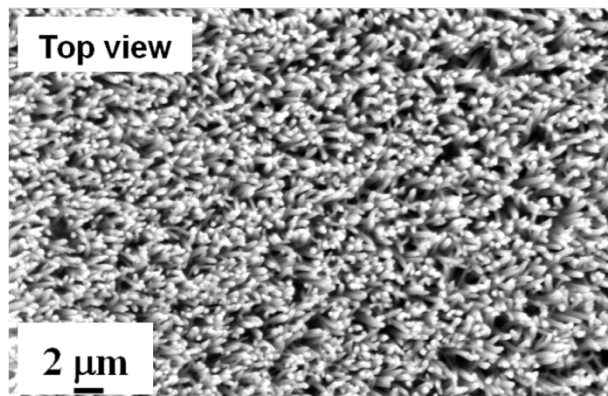


Figure 56: SEM micrograph showing top and cross-sectional view along with EDX spectrum of $[\text{WO}_3-(\text{Sn}_{0.95}\text{Nb}_{0.05})\text{O}_2:\text{N}-600]-2$ NTs

Table 9: The lattice parameters and quantitative elemental composition analysis by EDX

for (Sn_{0.95}Nb_{0.05})O₂:N-600 NTs, [WO₃-(Sn_{0.95}Nb_{0.05})O₂:N-600]-1 NTs, [WO₃-(Sn_{0.95}Nb_{0.05})O₂:N-600]-2 NTs and [WO₃-(Sn_{0.95}Nb_{0.05})O₂:N-600]-3 NTs

Composition	Lattice parameter (nm)	EDX composition			
		Sn (at. %)	Nb (at. %)	N (at. %)	W (at. %)
(Sn _{0.95} Nb _{0.05})O ₂ : N-600 NTs	a=b=0.4748±0.001, c=0.3196±0.002;	81.19	4.8	14.01	-
[WO ₃ - (Sn _{0.95} Nb _{0.05})O ₂ : N-600]-1 NTs	a=b=0.4746±0.01, c=0.3195±0.001	75.95	4.49	13.1	6.45
[WO ₃ - (Sn _{0.95} Nb _{0.05})O ₂ : N-600]-2 NTs	a=b=0.4745±0.002, c=0.3194±0.01	78.56	4.64	13.58	3.22
[WO ₃ - (Sn _{0.95} Nb _{0.05})O ₂ : N-600]-3 NTs	a=b=0.4744±0.001, c=0.3192±0.01	81.17	4.79	14.00	0.03

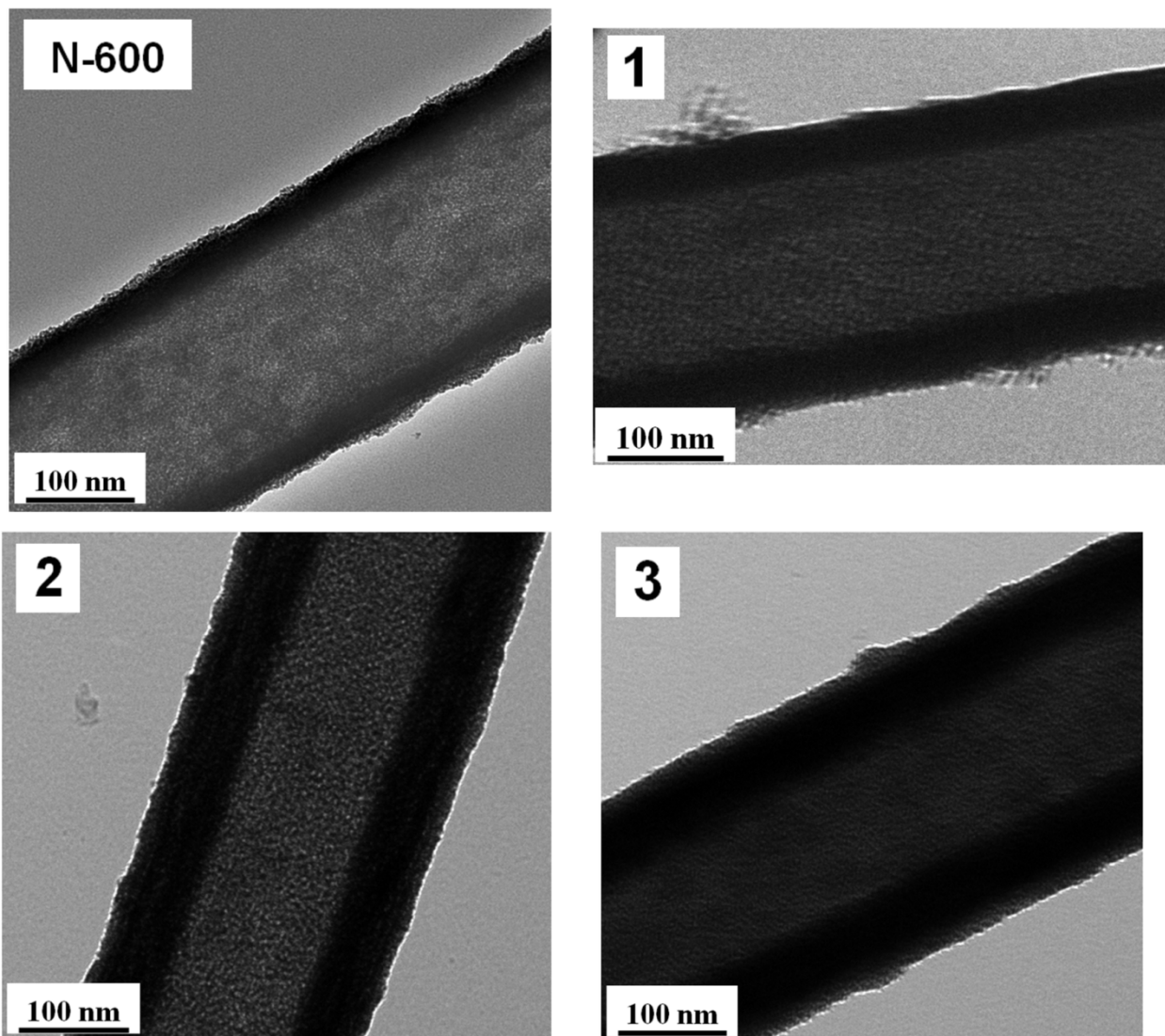


Figure 57: The bright field TEM images of $(\text{Sn}_{0.95}\text{Nb}_{0.05})\text{O}_2\text{:N-600}$ NT, $[\text{WO}_3-(\text{Sn}_{0.95}\text{Nb}_{0.05})\text{O}_2\text{:N-600}]\text{-1}$ NT, $[\text{WO}_3-(\text{Sn}_{0.95}\text{Nb}_{0.05})\text{O}_2\text{:N-600}]\text{-2}$ NT and $[\text{WO}_3-(\text{Sn}_{0.95}\text{Nb}_{0.05})\text{O}_2\text{:N-600}]\text{-3}$ NT

X-ray photoelectron spectroscopy study

The oxidation states of the corresponding elements, Sn, Nb, W and N in the composite bilayer oxide has been determined by performing x-ray photoelectron spectroscopy (XPS) on the respective bilayer composites, $[\text{WO}_3-(\text{Sn}_{0.95}\text{Nb}_{0.05})\text{O}_2\text{:N-600}]\text{-1}$ NTs, $[\text{WO}_3-(\text{Sn}_{0.95}\text{Nb}_{0.05})\text{O}_2\text{:N-}$

600]-2 NTs and [WO₃-(Sn_{0.95}Nb_{0.05})O₂:N-600]-3 NTs. The XPS spectrum of Sn (**Figure 58**) of [WO₃-(Sn_{0.95}Nb_{0.05})O₂:N-600] NTs of different thicknesses shows the presence of Sn 3d_{3/2} and 3d_{5/2} doublet centered at ~495.27 eV and ~486.8 eV, corresponding to Sn⁴⁺.^{76, 230} Thus, the negative shift of ~0.1-0.15 eV is observed in the Sn 3d_{3/2} and 3d_{5/2} doublets in comparison to that of pure SnO₂.⁷⁶ This can be due to a change in the electron density around the Sn⁴⁺ ions due to the introduction of Nb and N co-dopants resulting in modification of the electronic structure of SnO₂ (as reported by us earlier).^{76, 206} The XPS spectrum of N, shown in **Figure 59**, shows the presence of N 1s peak centered at ~398.3 eV for [WO₃-(Sn_{0.95}Nb_{0.05})O₂:N-600] NTs of different thicknesses indicating the presence of the oxynitride (O-Sn-N or O-Nb-N) and thus resulting in the substitutional doping of N at O sites in the lattice of (Sn_{0.95}Nb_{0.05})O₂:N NTs as reported earlier.^{76, 106, 114, 231, 232} The XPS spectrum of Nb shown in **Figure 60** shows the presence of Nb 3d_{3/2} and 3d_{5/2} doublet centered at ~210.3 and ~207.5 for (Sn_{0.95}Nb_{0.05})O₂:N-600 NTs, corresponding to Nb⁴⁺, respectively as observed earlier.^{76, 233, 234} Thus, the negative shift of ~0.1 eV is observed in the Nb 3d_{3/2} and 3d_{5/2} doublets in comparison to that of NbO_x.²⁴⁷ indicates the presence of oxynitride (O-Nb-N) due to the substitutional doping of N at the O sites in the composite bilayer which is similar to that reported by us earlier.^{76, 114} The XPS spectrum of W, shown in **Figure 61**, shows the W 4f_{7/2} and W 4f_{5/2} doublets centered at ~35.7 eV and ~37.9 eV, respectively consistent with bulk WO₃.¹⁸⁶ The increase in the intensities of the Sn 3d doublets, Nb 3d doublets, N 1s peak along with the corresponding decrease in the intensity of the W 4f doublets is observed as the peak intensities are compared arising from [WO₃-(Sn_{0.95}Nb_{0.05})O₂:N-600]-1 NTs to [WO₃-(Sn_{0.95}Nb_{0.05})O₂:N-600]-3 NTs bilayer composite samples clearly reflecting the increase in concentration of Sn, Nb and N and decrease in concentration of W on the surface of bilayer photoanode materials, which is likely due to an increase in the thickness of the

($\text{Sn}_{0.95}\text{Nb}_{0.05}\text{O}_2\text{:N-600}$) NT layer which is coated on the WO_3 NT layer (**Figure 58**, **Figure 59**, **Figure 60** and **Figure 61**).

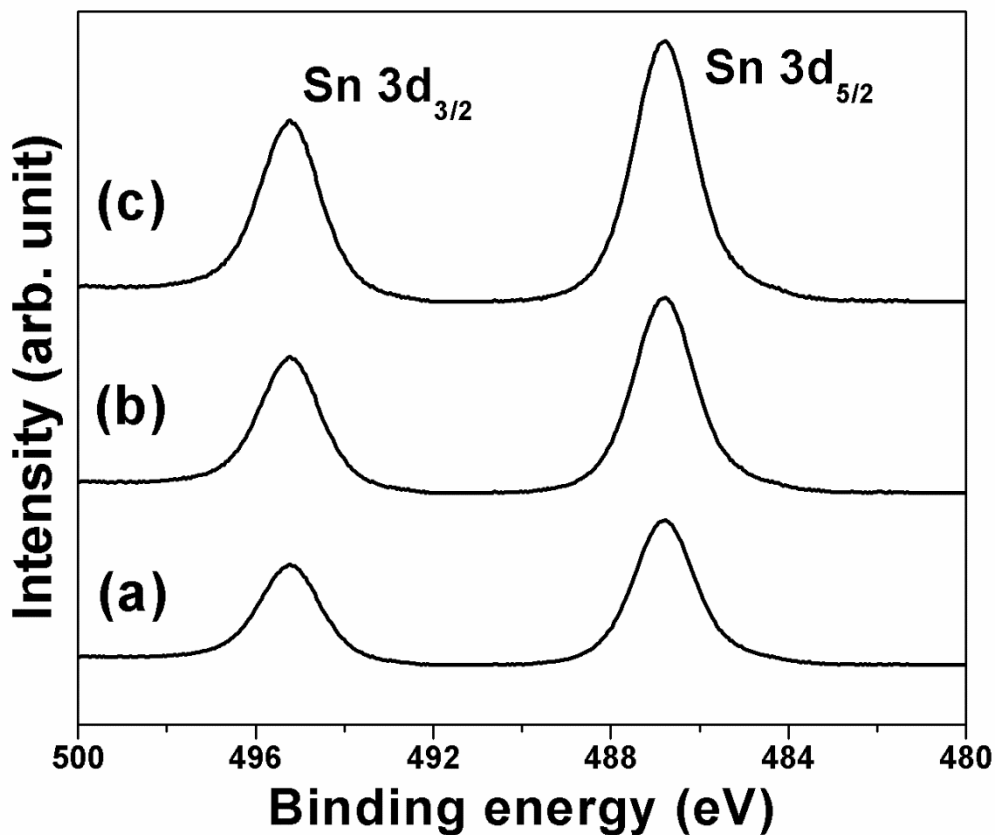


Figure 58: The XPS spectra of (a) [WO₃-(Sn_{0.95}Nb_{0.05}O₂:N-600)]-1 NTs, (b) [WO₃-(Sn_{0.95}Nb_{0.05}O₂:N-600)]-2 NTs and (c) [WO₃-(Sn_{0.95}Nb_{0.05}O₂:N-600)]-3 NTs, showing Sn 3d_{3/2} and 3d_{5/2} doublet

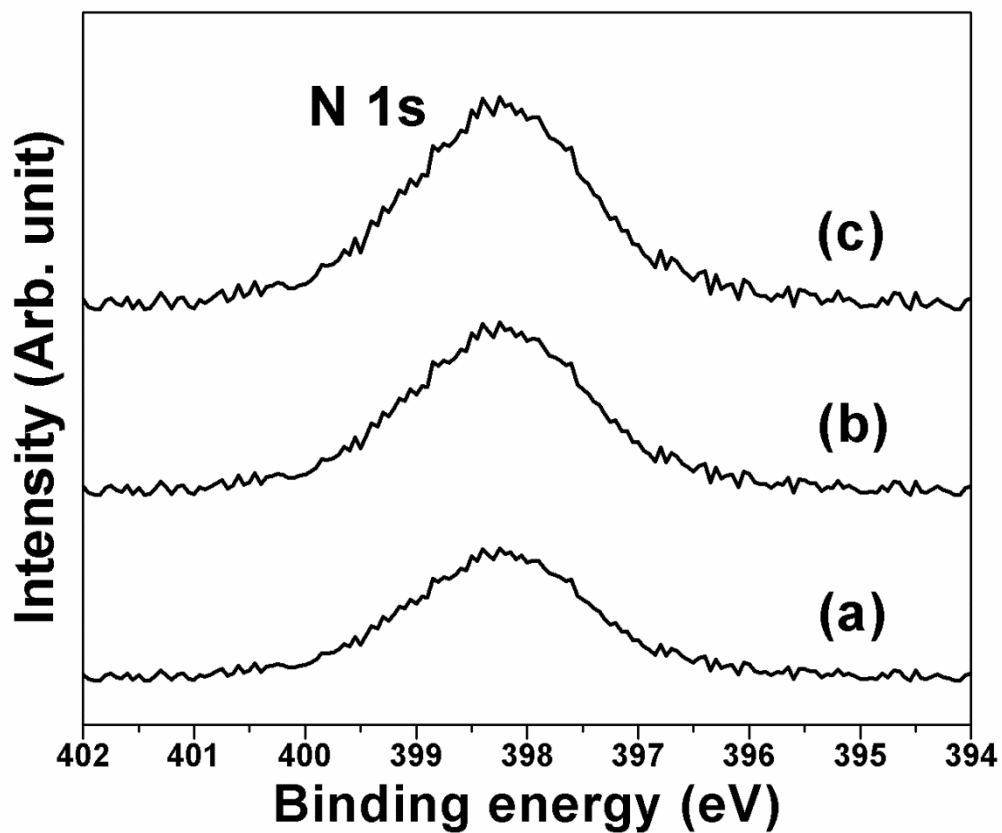


Figure 59: The XPS spectra of (a) $[\text{WO}_3-(\text{Sn}_{0.95}\text{Nb}_{0.05})\text{O}_2:\text{N}-600]-1$ NTs, (b) $[\text{WO}_3-(\text{Sn}_{0.95}\text{Nb}_{0.05})\text{O}_2:\text{N}-600]-2$ NTs and (c) $[\text{WO}_3-(\text{Sn}_{0.95}\text{Nb}_{0.05})\text{O}_2:\text{N}-600]-3$ NTs, showing N 1s peak

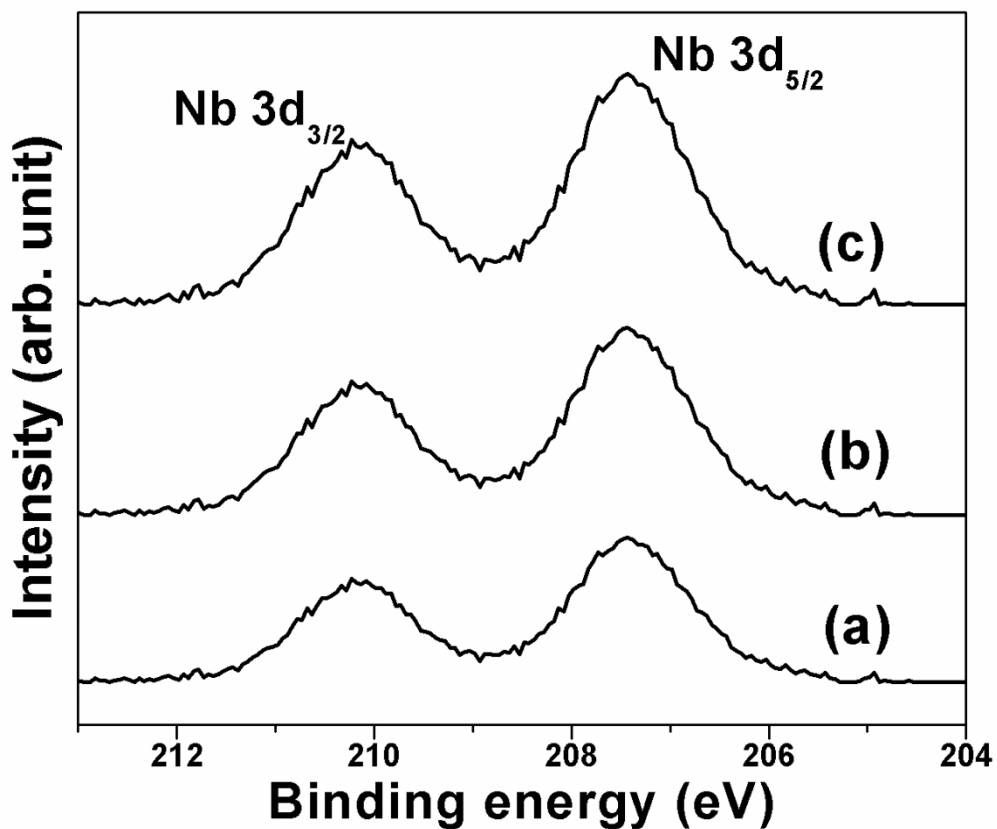


Figure 60: The XPS spectra of (a) [WO₃-(Sn_{0.95}Nb_{0.05})O₂:N-600]-1 NTs, (b) [WO₃-(Sn_{0.95}Nb_{0.05})O₂:N-600]-2 NTs and (c) [WO₃-(Sn_{0.95}Nb_{0.05})O₂:N-600]-3 NTs, showing Nb 3d_{3/2} and 3d_{5/2} doublet

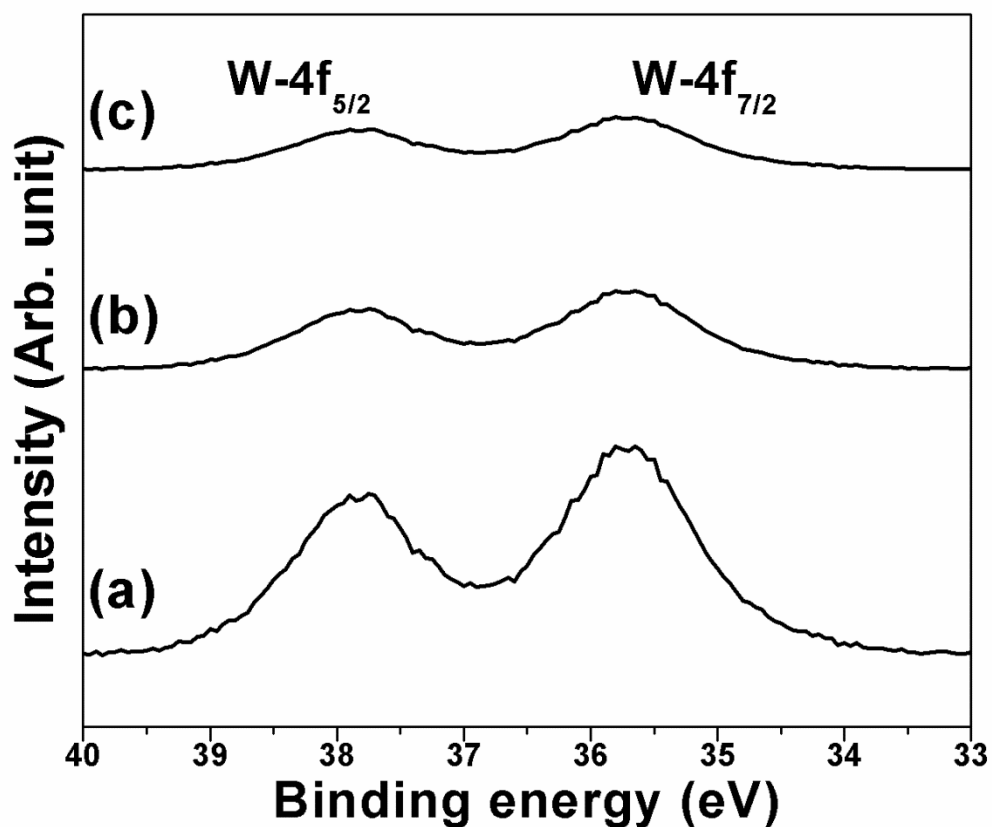


Figure 61: The XPS spectra of (a) [WO₃-(Sn_{0.95}Nb_{0.05})O₂:N-600]-1 NTs, (b) [WO₃-(Sn_{0.95}Nb_{0.05})O₂:N-600]-2 NTs and (c) [WO₃-(Sn_{0.95}Nb_{0.05})O₂:N-600]-3 NTs, showing W 4f_{5/2} and 4f_{7/2} doublet

UV-Vis absorption study

The light absorption characteristics of the three nanotubular bilayer composite architectures, [WO₃-(Sn_{0.95}Nb_{0.05})O₂:N-600]-1 NTs, [WO₃-(Sn_{0.95}Nb_{0.05})O₂:N-600]-2 NTs and [WO₃-(Sn_{0.95}Nb_{0.05})O₂:N-600]-3 NTs are studied from the UV-vis absorption spectra, shown in **Figure 62**. The UV-vis absorption spectrum of (Sn_{0.95}Nb_{0.05})O₂:N-600 NTs is also shown for comparison in **Figure 62**, in order to study the effect of coupling of the two semiconductor

materials, i.e., WO_3 and $(\text{Sn}_{0.95}\text{Nb}_{0.05})\text{O}_2\text{:N-600}$ on the resulting light absorption characteristics. As seen in **Figure 62**, the UV-vis absorption spectrum of $(\text{Sn}_{0.95}\text{Nb}_{0.05})\text{O}_2\text{:N-600}$ NTs show superior light absorption in the visible region indicating red shift in light absorption from the UV region (for pure SnO_2 which is UV active due to wide band gap of ~ 3.5 eV) to the visible region, a consequence of the reduction in the band gap due to Nb and N co-doping in SnO_2 , as reported by us earlier.⁷⁶ Also, as mentioned earlier, this can be attributed to electronic states of Nb introduced in the band gap of SnO_2 , along with the appearance of N 2p states at top of the valence band which hybridize with O 2p states resulting in the shift in the valence band (i.e., highest occupied molecular orbital, HOMO) upwards, without affecting the conduction band (i.e., lowest unoccupied molecular orbital, LUMO), thereby, reducing the band gap.^{34, 76, 115, 119, 248, 249}

The bilayer photoanode materials, i.e., $[\text{WO}_3-(\text{Sn}_{0.95}\text{Nb}_{0.05})\text{O}_2\text{:N-600}]$ NTs corresponding to the different thicknesses show superior light absorption characteristics compared to that of the pristine $(\text{Sn}_{0.95}\text{Nb}_{0.05})\text{O}_2\text{:N-600}$ NTs in both the UV and visible regions, suggesting a further reduction in the band gap (**Table 10**) due to coupling of the WO_3 layer and $(\text{Sn}_{0.95}\text{Nb}_{0.05})\text{O}_2\text{:N-600}$. This can be due to: (I) a redesign of the band gap at the interface of WO_3 and $(\text{Sn}_{0.95}\text{Nb}_{0.05})\text{O}_2\text{:N-600}$ (which are expected to form bilayer structure with staggered type II band alignment).^{65, 88, 250} The lattice strain is expected to exist at the interface due to a lattice mismatch between WO_3 and $(\text{Sn}_{0.95}\text{Nb}_{0.05})\text{O}_2\text{:N-600}$.^{65, 88, 250} The possible relaxation of the crystal structure can introduce delocalization levels in the band gap resulting in a reduction in the band gap.^{65, 88, 250} (II) a combined effect of both WO_3 (band gap of ~ 2.8 eV)⁸⁸ and lower band gap $(\text{Sn}_{0.95}\text{Nb}_{0.05})\text{O}_2\text{:N-600}$ (band gap of ~ 1.99 eV)⁷⁶ on the light absorption.⁸¹ Also, it can be seen that the light absorption monotonically increases for the bilayer photoanode materials from

[WO₃-(Sn_{0.95}Nb_{0.05})O₂:N-600]-1 NTs to [WO₃-(Sn_{0.95}Nb_{0.05})O₂:N-600]-3 NTs, which is likely due to the increase in the thickness of the layer of (Sn_{0.95}Nb_{0.05})O₂:N-600 of relatively small band gap (~1.99 eV) and superior light absorption properties⁷⁶ which is coated on WO₃ layer (having band gap of ~2.8 eV⁸⁸).^{65, 81} This reduction in the band gap is important, which offers improved light absorption and thus, provides more number of photo-generated carriers to induce the desired reactions at both the cathode and the photoanode, respectively. It is important to note that similar UV-Vis spectra of FTO substrate and FTO substrate annealed at 600°C in NH₃ atmosphere indicate no reduction of the FTO substrate phase (see **Figure 63**). The valence band spectra of SnO₂, (Sn_{0.95}Nb_{0.05})O₂:N-600 and [WO₃-(Sn_{0.95}Nb_{0.05})O₂:N-600]-2 NTs were used to study the electronic structure. The top of the valence band measured at the rising edge (**Figure 64**) is ~3.5 eV below the Fermi level for pure SnO₂ which is similar to earlier report.²⁵¹ The top of the valence band however, shifts to the lower position (~1.66 eV) for (Sn_{0.95}Nb_{0.05})O₂:N-600 compared to SnO₂ and further negatively shifts (to ~1.5 eV) lower for [WO₃-(Sn_{0.95}Nb_{0.05})O₂:N-600]-2 compared to SnO₂ and (Sn_{0.95}Nb_{0.05})O₂:N-600. This negative shift at the top of the valence band to lower potential corresponds well with the decrease in the band gap (as seen in **Figure 62**) and negative shift in V_{FB} (**Figure 65**) also discussed below.⁸¹

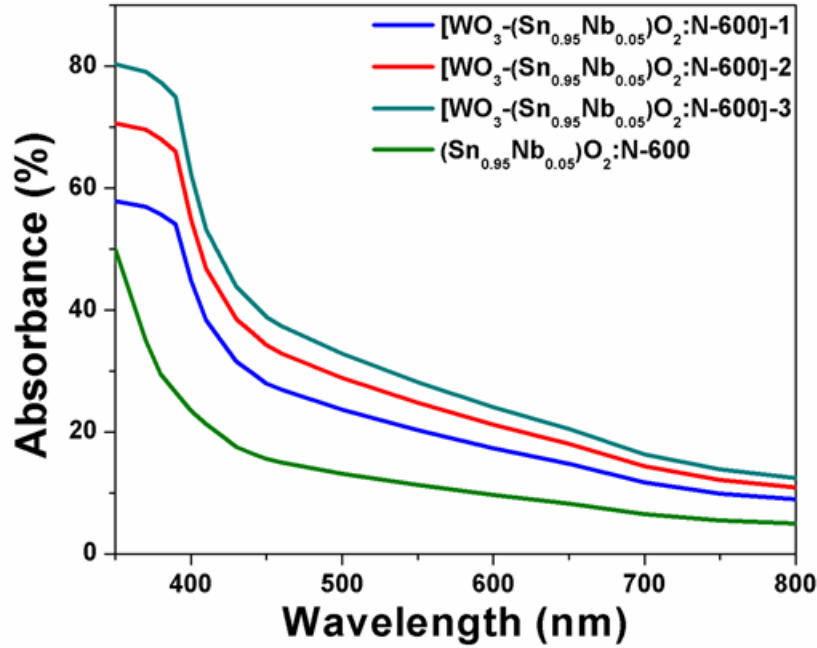


Figure 62: UV-vis absorption spectra of $(\text{Sn}_{0.95}\text{Nb}_{0.05})\text{O}_2:\text{N}-600$ NTs, $[\text{WO}_3-(\text{Sn}_{0.95}\text{Nb}_{0.05})\text{O}_2:\text{N}-600]-1$ NTs, $[\text{WO}_3-(\text{Sn}_{0.95}\text{Nb}_{0.05})\text{O}_2:\text{N}-600]-2$ NTs and $[\text{WO}_3-(\text{Sn}_{0.95}\text{Nb}_{0.05})\text{O}_2:\text{N}-600]-3$ NTs

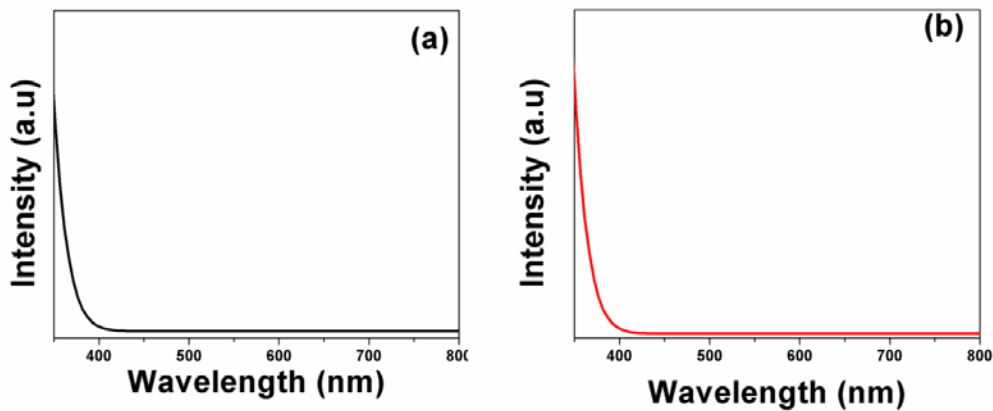


Figure 63: UV-vis absorption spectra of (a) FTO substrate and (b) FTO annealed at 600°C in NH_3 atmosphere

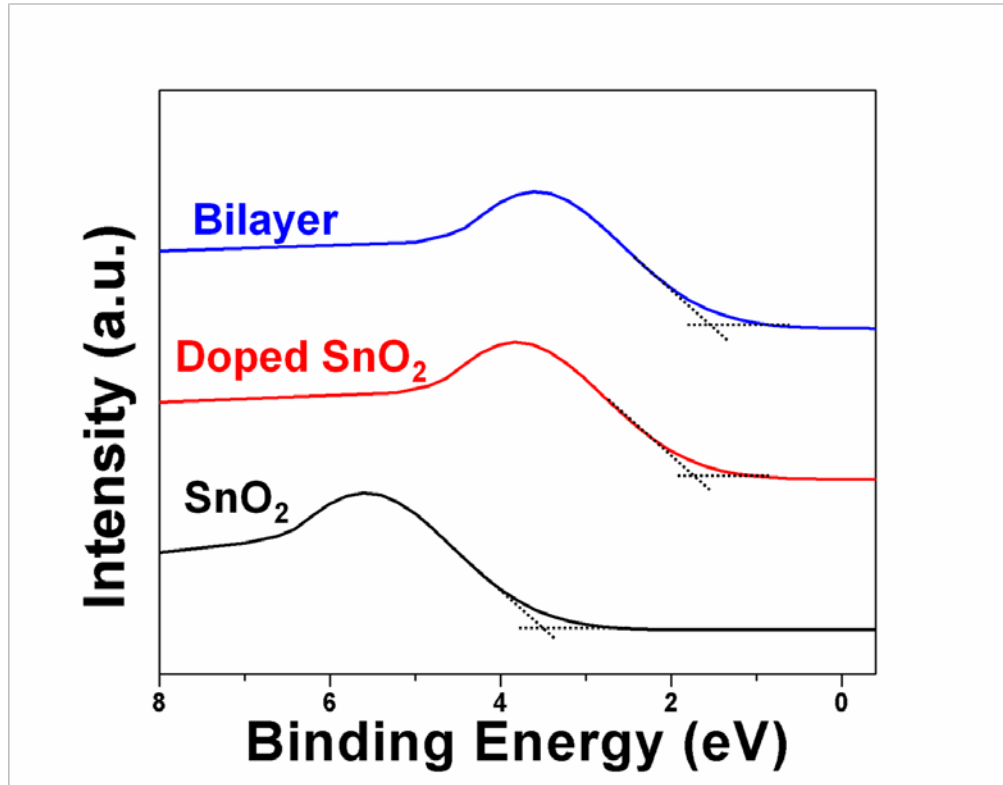


Figure 64: Valence band spectra of SnO₂, (Sn_{0.95}Nb_{0.05})O₂:N-600 and [WO₃-(Sn_{0.95}Nb_{0.05})O₂:N-600]-2 NTs

Mott-Schottky analysis

The effect of coupling of WO₃ and (Sn_{0.95}Nb_{0.05})O₂:N-600 NTs on the electronic properties is studied following the Mott-Schottky analysis. Following this analysis, the capacitance at the electrode is measured by performing electrochemical impedance spectroscopy (EIS) in the dark in 0.5 M H₂SO₄ electrolyte solution at 26°C. The carrier density for the photoanode material is then determined using the Mott-Schottky equation^{114, 218}:

$$1/C^2 = (2/e_0\epsilon\epsilon_0N_d)[(V-V_{FB})-kT/e_0]$$

where, e_0 is the electron charge, ε is the dielectric constant, ε_0 is the permittivity of vacuum, N_d is the carrier density, V is the applied potential, V_{FB} is the flat band potential, k is the Boltzmann constant, T is the absolute temperature (299 K). The Mott-Schottky plot ($1/C^2$ vs V) is plotted for all the three bilayer composite systems namely, for $[\text{WO}_3-(\text{Sn}_{0.95}\text{Nb}_{0.05})\text{O}_2:\text{N}-600]$ -1 NTs, $[\text{WO}_3-(\text{Sn}_{0.95}\text{Nb}_{0.05})\text{O}_2:\text{N}-600]$ -2 NTs and $[\text{WO}_3-(\text{Sn}_{0.95}\text{Nb}_{0.05})\text{O}_2:\text{N}-600]$ -3 NTs and is shown in **Figure 65**. The flat band potential (V_{fb}), determined from the x-intercept of the linear region of the Mott-Schottky plot for $[\text{WO}_3-(\text{Sn}_{0.95}\text{Nb}_{0.05})\text{O}_2:\text{N}-600]$ -1 NTs, $[\text{WO}_3-(\text{Sn}_{0.95}\text{Nb}_{0.05})\text{O}_2:\text{N}-600]$ -2 NTs and $[\text{WO}_3-(\text{Sn}_{0.95}\text{Nb}_{0.05})\text{O}_2:\text{N}-600]$ -3 NTs is $\sim(-0.57 \text{ V vs RHE})$, $\sim(-0.61 \text{ V vs RHE})$ and $\sim(-0.63 \text{ V vs RHE})$, respectively (comparable to that reported earlier^{81, 106}). Thus, the V_{FB} of $[\text{WO}_3-(\text{Sn}_{0.95}\text{Nb}_{0.05})\text{O}_2:\text{N}-600]$ -1 NTs, $[\text{WO}_3-(\text{Sn}_{0.95}\text{Nb}_{0.05})\text{O}_2:\text{N}-600]$ -2 NTs and $[\text{WO}_3-(\text{Sn}_{0.95}\text{Nb}_{0.05})\text{O}_2:\text{N}-600]$ -3 NTs is more negative than the standard redox potential for water reduction reaction (i.e. hydrogen evolution reaction, HER) (0 V vs NHE), indicative of the more negative position of the conduction band than the standard redox potential of HER.^{76, 81, 114, 218} The decrease in V_{fb} for $[\text{WO}_3-(\text{Sn}_{0.95}\text{Nb}_{0.05})\text{O}_2:\text{N}-600]$ -1 NTs, $[\text{WO}_3-(\text{Sn}_{0.95}\text{Nb}_{0.05})\text{O}_2:\text{N}-600]$ -2 NTs and $[\text{WO}_3-(\text{Sn}_{0.95}\text{Nb}_{0.05})\text{O}_2:\text{N}-600]$ -3 NTs suggests an increase in the shift of the conduction band of the bilayer composite material to higher energy.^{64, 76, 81, 106, 114, 207, 214, 218, 242-246} This is expected to result in increase in the driving force for electrons which is important for achieving superior photocurrent density.^{64, 81, 106, 114, 207, 214, 218, 242-246} V_{fb} of $[\text{WO}_3-(\text{Sn}_{0.95}\text{Nb}_{0.05})\text{O}_2:\text{N}-600]$ -1 NTs, $[\text{WO}_3-(\text{Sn}_{0.95}\text{Nb}_{0.05})\text{O}_2:\text{N}-600]$ -2 NTs and $[\text{WO}_3-(\text{Sn}_{0.95}\text{Nb}_{0.05})\text{O}_2:\text{N}-600]$ -3 NTs is more negative than that of $(\text{Sn}_{0.95}\text{Nb}_{0.05})\text{O}_2:\text{N}-600$ NTs which showed a V_{fb} of $\sim(-0.33 \text{ V})$ ⁷⁶ (**Figure 43**), indicating that the position of the conduction band of the composite bilayer photoanode materials is at a higher energy than that of $(\text{Sn}_{0.95}\text{Nb}_{0.05})\text{O}_2:\text{N}-600$ NTs.^{64, 76, 81, 106, 114, 207, 214, 218, 242-246}

The positive slope obtained in the Mott-Schottky plots indicate n-type behavior for (Sn_{0.95}Nb_{0.05})O₂:N-600 NTs, [WO₃-(Sn_{0.95}Nb_{0.05})O₂:N-600]-1 NTs, [WO₃-(Sn_{0.95}Nb_{0.05})O₂:N-600]-2 NTs and [WO₃-(Sn_{0.95}Nb_{0.05})O₂:N-600]-3 NTs. The carrier density is then calculated from the slopes determined from the Mott-Schottky plot using the equation^{76, 106, 114}:

$$N_d = (2/e_0\epsilon\epsilon_0)[d(1/C^2)/dV]^{-1}$$

The carrier density of the three bilayer composite structures namely, [WO₃-(Sn_{0.95}Nb_{0.05})O₂:N-600]-1 NTs, [WO₃-(Sn_{0.95}Nb_{0.05})O₂:N-600]-2 NTs and [WO₃-(Sn_{0.95}Nb_{0.05})O₂:N-600]-3 NTs is determined to be $\sim 4.95 \times 10^{22} \text{ cm}^{-3}$, $\sim 5.6 \times 10^{22} \text{ cm}^{-3}$ and $\sim 6.05 \times 10^{22} \text{ cm}^{-3}$, respectively, which is higher than that of (Sn_{0.95}Nb_{0.05})O₂:N-600 NTs ($\sim 4.7 \times 10^{22} \text{ cm}^{-3}$) (**Table 10**). The carrier density was also measured using the Hall measurement system for three bilayer composites, [WO₃-(Sn_{0.95}Nb_{0.05})O₂:N-600]-1 NTs, [WO₃-(Sn_{0.95}Nb_{0.05})O₂:N-600]-2 NTs and [WO₃-(Sn_{0.95}Nb_{0.05})O₂:N-600]-3 NTs to be $\sim 2.7 \times 10^{22} \text{ cm}^{-3}$, $\sim 4.5 \times 10^{22} \text{ cm}^{-3}$ and $\sim 6.2 \times 10^{22} \text{ cm}^{-3}$, respectively, which is also higher than that of (Sn_{0.95}Nb_{0.05})O₂:N-600 NTs ($\sim 1.9 \times 10^{22} \text{ cm}^{-3}$).

The higher carrier density of the bilayer photoanode materials contrasted to that of the pristine, (Sn_{0.95}Nb_{0.05})O₂:N-600 NTs can be due to coupling of (Sn_{0.95}Nb_{0.05})O₂:N-600 NTs with the WO₃ resulting in better transfer of electrons from the conduction band of (Sn_{0.95}Nb_{0.05})O₂:N-600 NTs to the conduction band of WO₃ (**Figure 10**) leading to a higher density of electrons in WO₃ and thus, resulting in a higher carrier concentration for the bilayer materials similar to that reported earlier.^{65, 218} Also, the monotonic increase in carrier density measured for [WO₃-(Sn_{0.95}Nb_{0.05})O₂:N-600]-1 NTs to [WO₃-(Sn_{0.95}Nb_{0.05})O₂:N-600]-3 NTs can be likely due to the systematic increase in the thickness of (Sn_{0.95}Nb_{0.05})O₂:N-600 layer [which exhibits high carrier density ($\sim 4.7 \times 10^{22} \text{ cm}^{-3}$) (as reported by us earlier⁷⁶) on the WO₃ layer. It should be noted that

the highest carrier density of ($\sim 6.05 \times 10^{22} \text{ cm}^{-3}$) obtained in this study for $[\text{WO}_3-(\text{Sn}_{0.95}\text{Nb}_{0.05})\text{O}_2:\text{N}-600]$ -3 NTs is in the range of that of the hydrogen-treated TiO_2 nanowires ($\sim 2.1 \times 10^{22} \text{ cm}^{-3}$)⁶⁴ which showed excellent photo-electrochemical activity with photo-conversion efficiency of $\sim 1.63\%$ (at applied bias of $\sim 0.42 \text{ V vs RHE}$) and WO_3 films with superior photo-electrochemical performance ($\sim 2.5 \times 10^{22} \text{ cm}^{-3}$)^{252, 253}. These results are very important as high carrier density is expected to offer more number of carriers available for the reactions occurring at both the cathode and photoanode, respectively. The increased carrier density for the bilayer photoanode materials from $[\text{WO}_3-(\text{Sn}_{0.95}\text{Nb}_{0.05})\text{O}_2:\text{N}-600]$ -1 NTs to $[\text{WO}_3-(\text{Sn}_{0.95}\text{Nb}_{0.05})\text{O}_2:\text{N}-600]$ -3 NTs is expected to shift the Fermi level upwards towards the conduction band resulting in negative shift in V_{FB} (as discussed earlier) and thus, this is expected to result in increased degree of band bending from $[\text{WO}_3-(\text{Sn}_{0.95}\text{Nb}_{0.05})\text{O}_2:\text{N}-600]$ -1 NTs to $[\text{WO}_3-(\text{Sn}_{0.95}\text{Nb}_{0.05})\text{O}_2:\text{N}-600]$ -3 NTs.^{64, 76, 106, 114, 207, 214, 218, 242-246} This will offer improved separation of the photo-generated carriers at the interface between the semiconductor material and the electrolyte, leading to improved photo-electrochemical activity.^{64, 76, 106, 114, 207, 214, 218, 242-246} The valence band spectra of SnO_2 , $(\text{Sn}_{0.95}\text{Nb}_{0.05})\text{O}_2:\text{N}-600$ and $[\text{WO}_3-(\text{Sn}_{0.95}\text{Nb}_{0.05})\text{O}_2:\text{N}-600]$ -2 NTs were used to study the electronic structure.

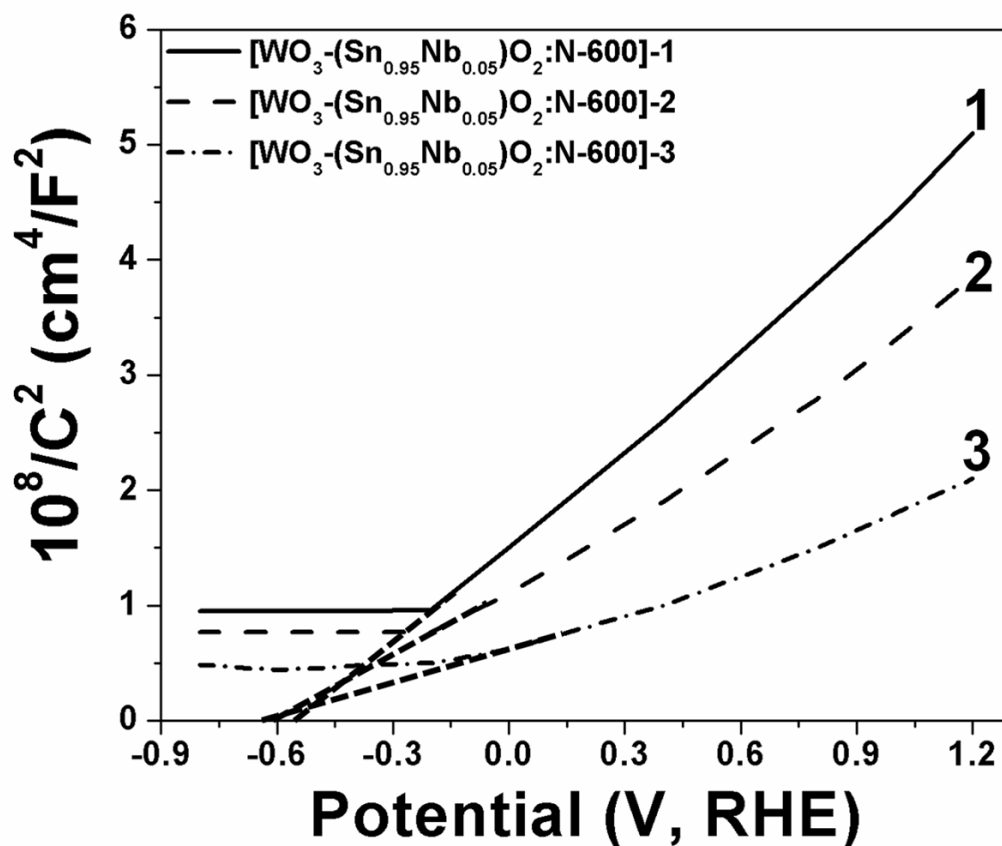


Figure 65: Mott-Schottky plots of [WO₃-(Sn_{0.95}Nb_{0.05})O₂:N-600]-1 NTs, [WO₃-(Sn_{0.95}Nb_{0.05})O₂:N-600]-2 NTs and [WO₃-(Sn_{0.95}Nb_{0.05})O₂:N-600]-3 NTs

5.3.2 PHOTOELECTROCHEMICAL CHARACTERIZATION OF [WO₃-(Sn_{0.95}Nb_{0.05})O₂:N-600] NTs

Photoelectrochemical activity

The photo-electrochemical activity of different photoanode materials is studied in 0.5 M H₂SO₄ electrolyte solution. **Figure 66** shows linear scan voltammogram (LSV) curves of

(Sn_{0.95}Nb_{0.05})O₂:N NTs, [WO₃-(Sn_{0.95}Nb_{0.05})O₂:N-600]-1 NTs, [WO₃-(Sn_{0.95}Nb_{0.05})O₂:N-600]-2 NTs and [WO₃-(Sn_{0.95}Nb_{0.05})O₂:N-600]-3 NTs in dark and under illumination of 100mW cm⁻², obtained using scan rate of 1 mV sec⁻¹. LSV curves obtained in dark showed a small current in the range of ~10⁻³ mA cm⁻² for all the semiconductor materials. However, under illumination, enhanced photocurrent density is observed for all the semiconductor materials. For (Sn_{0.95}Nb_{0.05})O₂:N NTs, the onset of photocurrent density begins at ~(-0.14 V vs RHE) which is noteworthy as it suggests the need for very minimal external potential in generating the desired photocurrent density from the semiconductor material with superior utilization of the solar energy alone, as reported earlier.⁷⁶ The values of the onset potential for all the semiconductor materials studied and presented herein are given in **Table 10**. The onset of photocurrent density for [WO₃-(Sn_{0.95}Nb_{0.05})O₂:N-600]-1 NTs, [WO₃-(Sn_{0.95}Nb_{0.05})O₂:N-600]-2 NTs and [WO₃-(Sn_{0.95}Nb_{0.05})O₂:N-600]-3 NTs starts at ~(-0.4 V vs RHE), ~(-0.55 V vs RHE) and ~(-0.08 vs RHE), respectively. The lower onset potential of [WO₃-(Sn_{0.95}Nb_{0.05})O₂:N-600]-2 NTs than (Sn_{0.95}Nb_{0.05})O₂:N NTs and [WO₃-(Sn_{0.95}Nb_{0.05})O₂:N-600]-1 NTs indicates superior photoelectrochemical activity of [WO₃-(Sn_{0.95}Nb_{0.05})O₂:N-600]-2 NTs than that of (Sn_{0.95}Nb_{0.05})O₂:N NTs and [WO₃-(Sn_{0.95}Nb_{0.05})O₂:N-600]-1 NTs. This can be attributed to: (I) more negative flat band potential and high carrier density (**Figure 65** and **Table 10**) of [WO₃-(Sn_{0.95}Nb_{0.05})O₂:N-600]-2 NTs leading to more negative position of the Fermi level (and thus, conduction band) resulting in more driving force for generating photo-generated electrons^{81, 218} and (II) efficient separation of the photo-generated carriers with minimum recombination leading to long carrier lifetime (discussed later) for [WO₃-(Sn_{0.95}Nb_{0.05})O₂:N-600]-2 NTs.^{81, 218}

However, the higher onset potential of [WO₃-(Sn_{0.95}Nb_{0.05})O₂:N-600]-3 NTs than that of the (Sn_{0.95}Nb_{0.05})O₂:N NTs, [WO₃-(Sn_{0.95}Nb_{0.05})O₂:N-600]-1 NTs and [WO₃-(Sn_{0.95}Nb_{0.05})O₂:N-

600]-2 NTs suggests poor photo-electrochemical activity for $[\text{WO}_3-(\text{Sn}_{0.95}\text{Nb}_{0.05})\text{O}_2:\text{N}-600]-3$ NTs which can be due to a higher recombination of the photo-generated carriers resulting in relatively lower carrier lifetime (discussed later). It is noteworthy that the negative onset potential of $[\text{WO}_3-(\text{Sn}_{0.95}\text{Nb}_{0.05})\text{O}_2:\text{N}-600]-2$ NTs [$\sim(-0.55 \text{ V vs RHE})$] suggests that the solar energy alone can be used in generating the desired photocurrent density which is then consumed for generation of hydrogen from water without the need for any external electrical bias or potential. In addition, the more negative onset potential of $[\text{WO}_3-(\text{Sn}_{0.95}\text{Nb}_{0.05})\text{O}_2:\text{N}-600]-2$ NTs than that of $(\text{Sn}_{0.95}\text{Nb}_{0.05})\text{O}_2:\text{N}$ NTs [$\sim(-0.14 \text{ V vs RHE})$] indicates that the bilayer strategy is indeed a promising and effective strategy in improve the photo-electrochemical activity of $(\text{Sn}_{0.95}\text{Nb}_{0.05})\text{O}_2:\text{N}$ NTs. The wide band gap of SnO_2 along with the recombination of the photo-generated carriers usually does not allow for achieving such low onset potentials for PEC water splitting. The tailoring of the band gap of SnO_2 by co-doping with Nb and N and then coupling of the Nb and N co-doped SnO_2 with WO_3 thus, results in this remarkable photo-electrochemical behavior as described herein.

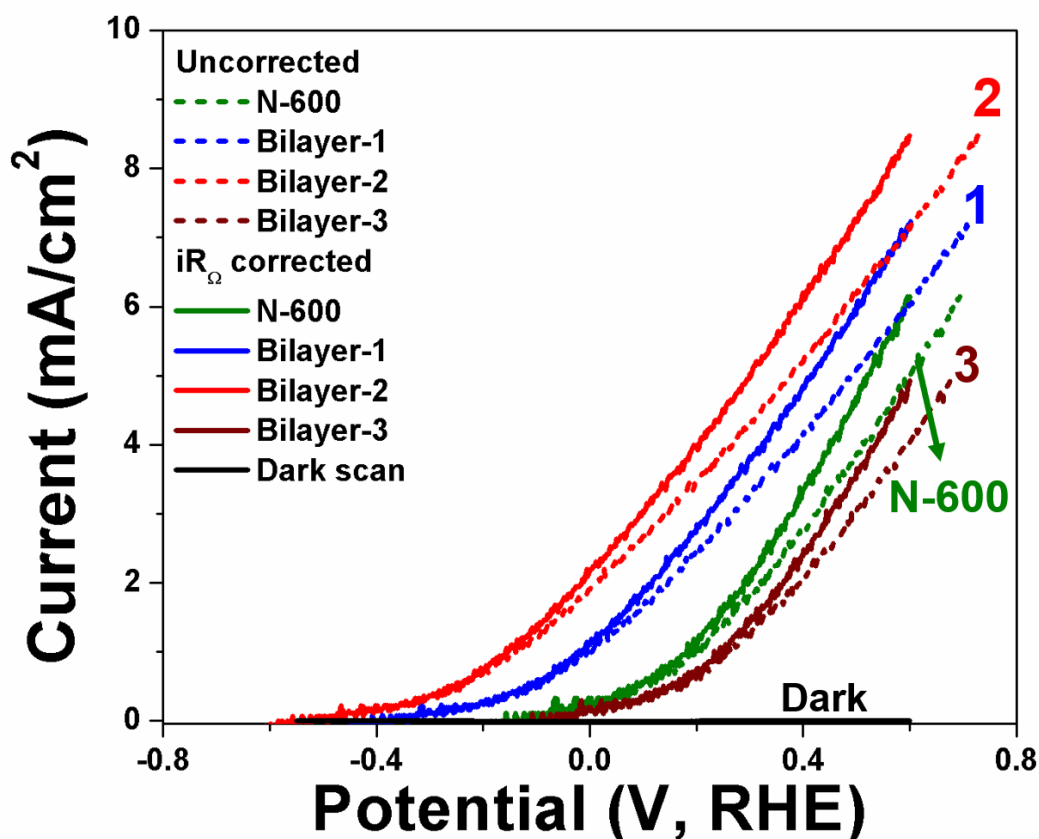


Figure 66: The linear scan voltammogram (LSV) curves of $(\text{Sn}_{0.95}\text{Nb}_{0.05})\text{O}_2\text{:N-600}$ NTs, $[\text{WO}_3-(\text{Sn}_{0.95}\text{Nb}_{0.05})\text{O}_2\text{:N-600}]\text{-1}$ NTs, $[\text{WO}_3-(\text{Sn}_{0.95}\text{Nb}_{0.05})\text{O}_2\text{:N-600}]\text{-2}$ NTs and $[\text{WO}_3-(\text{Sn}_{0.95}\text{Nb}_{0.05})\text{O}_2\text{:N-600}]\text{-3}$ NTs in dark and under illumination of 100 mW/cm^2 measured in $0.5 \text{ M H}_2\text{SO}_4$ at 26°C , before and after iR_Ω correction

The photocurrent density at a finite potential (to overcome over-potential losses) close to zero bias, i.e., $\sim 0.1 \text{ V}$ (vs RHE) in LSV plot (**Figure 66**) is used for comparison of the photoelectrochemical activity of all the semiconductor materials considered in this study. The photocurrent density of $(\text{Sn}_{0.95}\text{Nb}_{0.05})\text{O}_2\text{:N-600}$ NTs, $[\text{WO}_3-(\text{Sn}_{0.95}\text{Nb}_{0.05})\text{O}_2\text{:N-600}]\text{-1}$ NTs,

[WO₃-(Sn_{0.95}Nb_{0.05})O₂:N-600]-2 NTs and [WO₃-(Sn_{0.95}Nb_{0.05})O₂:N-600]-3 NTs at ~0.1 V (vs RHE) in the LSV plot is ~0.56 mA cm⁻², ~1.93 mA cm⁻², ~3.1 mA cm⁻² and ~0.35 mA cm⁻² (**Table 10**). It can be seen that superior photocurrent density is obtained for [WO₃-(Sn_{0.95}Nb_{0.05})O₂:N-600]-1 NTs and [WO₃-(Sn_{0.95}Nb_{0.05})O₂:N-600]-2 NTs with the highest current density, obtained for [WO₃-(Sn_{0.95}Nb_{0.05})O₂:N-600]-2 NTs (comparable to earlier reports^{254, 255}) (**Table 10**) than (Sn_{0.95}Nb_{0.05})O₂:N NTs, which is mainly due to the improved light absorption properties (see **Figure 62** and **Table 10**), superior carrier density (**Figure 65** and **Table 10**), superior reaction kinetics (discussed later) and efficient separation of photo-generated carriers resulting in long carrier lifetime (discussed later). The lower photocurrent density of [WO₃-(Sn_{0.95}Nb_{0.05})O₂:N-600]-3 NTs than that of [WO₃-(Sn_{0.95}Nb_{0.05})O₂:N-600]-2 NTs can be due to poor reaction kinetics (discussed later) of [WO₃-(Sn_{0.95}Nb_{0.05})O₂:N-600]-3 NTs than that of [WO₃-(Sn_{0.95}Nb_{0.05})O₂:N-600]-2 NTs despite having higher carrier densities as discussed earlier.

Table 10: Results of Mott-Schottky analysis, structural and photoelectrochemical characterization of (Sn_{0.95}Nb_{0.05})O₂:N-600 NTs, [WO₃-(Sn_{0.95}Nb_{0.05})O₂:N-600]-1 NTs, [WO₃-(Sn_{0.95}Nb_{0.05})O₂:N-600]-2 NTs and [WO₃-(Sn_{0.95}Nb_{0.05})O₂:N-600]-3 NTs

Composition	Carrier density (cm⁻³)	VB edge (eV)	Band gap (eV)	Onset potential (V vs RHE)	Photocurrent density (mA cm⁻²) at ~0.1 V (vs RHE)	R_{ct} (Ω.cm²)	ABPE (%) at ~0.6 V(vs RHE)	Solar to hydrogen efficiency (STH) (%)
(Sn _{0.95} Nb _{0.05})O ₂ :N-600 NTs	4.7×(10 ²²)	1.66	1.99	-0.14	0.56	15.3	3.84	-
[WO ₃ -(Sn _{0.95} Nb _{0.05})O ₂ :N-600]-1 NTs	4.95×(10 ²²)	-	1.95	-0.4	1.93	11.25	4.53	-
[WO ₃ -(Sn _{0.95} Nb _{0.05})O ₂ :N-600]-2 NTs	5.6×(10 ²²)	1.5	1.93	-0.55	3.1	8.05	5.1	3.83
[WO ₃ -(Sn _{0.95} Nb _{0.05})O ₂ :N-600]-3 NTs	6.05×(10 ²²)	-	1.9	-0.08	0.35	24.9	3.21	-

The highest photocurrent density obtained in this study for [WO₃-(Sn_{0.95}Nb_{0.05})O₂:N-600]-2 NTs (~3.1 mA cm⁻²) is ~5 fold, ~1.55 fold and ~8 fold higher than that of (Sn_{0.95}Nb_{0.05})O₂:N NTs (~0.56 mA cm⁻²), [WO₃-(Sn_{0.95}Nb_{0.05})O₂:N-600]-1 NTs (~1.93 mA cm⁻²) and [WO₃-(Sn_{0.95}Nb_{0.05})O₂:N-600]-3 NTs (~0.35 mA cm⁻²), respectively. It will be useful to additionally compare the performance of the composite bilayer system in absence of electrical bias in the presence of an electric potential. As is known, the applied bias photon-to-current efficiency (ABPE) for the semiconductor materials is calculated using the equation¹¹⁴:

$$\text{ABPE} = \mathbf{I(1.23-V) \times 100 / J_{\text{light}}}$$

wherein, I is the photocurrent density at the measured potential, V is the applied potential and J_{light} is the illumination intensity of 100 mW cm⁻². The ABPE is typically evaluated under harsh operating conditions at the applied potential of ~0.6V (*vs* RHE, which is the typical potential at which highest ABPE is obtained for semiconductor systems reported date based on TiO₂, ZnO, Fe₂O₃, etc.^{64, 76, 114, 176-178}). Under the applied bias, the highest ABPE (at ~0.6V *vs* RHE) of ~5.1% is obtained for [WO₃-(Sn_{0.95}Nb_{0.05})O₂:N-600]-2 NTs which is ~25%, ~11.2% and ~38% higher than that of (Sn_{0.95}Nb_{0.05})O₂:N NTs (~3.84%), [WO₃-(Sn_{0.95}Nb_{0.05})O₂:N-600]-1 NTs (~4.53%) and [WO₃-(Sn_{0.95}Nb_{0.05})O₂:N-600]-3 NTs (~3.21%), respectively (**Table 11**). It should be noted that the ABPE of ~5.1% for [WO₃-(Sn_{0.95}Nb_{0.05})O₂:N-600]-2 NTs (at ~0.6 V *vs* RHE) is the highest ABPE obtained thus far compared to the other semiconductor materials studied for PEC water splitting based on TiO₂, ZnO and Fe₂O₃ reported in the open literature to the best of our assessment of the widely reported literature to date.^{64, 76, 114, 176-178} This higher current density and the ABPE achieved is indeed a reflection of the superior electrochemical charge transfer (improved reaction kinetics) characteristics displayed by the bilayer composite

architecture, $[\text{WO}_3-(\text{Sn}_{0.95}\text{Nb}_{0.05})\text{O}_2:\text{N}-600]$ -2 NTs in comparison to all other materials used in this study.

Table 11: Efficiency of photoelectrochemical water splitting of various photoanode materials, reported in the literature

Photoanode material	Max. ABPE, %	Potential at max. ABPE (V, RHE)	Onset potential (V, RHE)	Ref
N-doped ZnO nanowire arrays	0.15	1.11	0.21	106
N-doped ZnO nanotetrapods	0.31	0.92	0.41	207
TiO ₂ :Al nanorod array thin film	0.02	0.5 (vs Ag/AgCl)	0.61	219
Bent ZnO nanorod photoanode	0.08	0.69	-	220
Si/ZnO core/shell nanowire arrays	0.38	0.65 (vs Ag/AgCl)	0.11	221
Hierarchical Fe ₂ O ₃ /WO _x nanowires	0.2	0.25	0.01	222

Table 11 (continued)				
C-doped ZnO porous nanoarchitectures	0.75	0.91	0.31	110
Si/TiO ₂ core/shell nanowire arrays	0.035	1.15	0.36	223
Fe ₂ O ₃ :Cu nanostructured film	0.28	0.6 (vs Ag/AgCl)	1.44	83
ZnFe ₂ O ₄ /ZnO system	0.15	1.21	0.51	217
TiO ₂ -ZnS core-shell	0.38	0.81	0.26	65
Au coated 3D ZnO nanowires	0.52	0.75	0.3	82
<u>WO₃-</u> <u>(Sn_{0.95}Nb_{0.05})O₂:N-600</u> <u>NTs</u>	<u>5.1</u>	<u>0.6</u>	<u>-0.55</u>	<u>Present</u> <u>work</u>

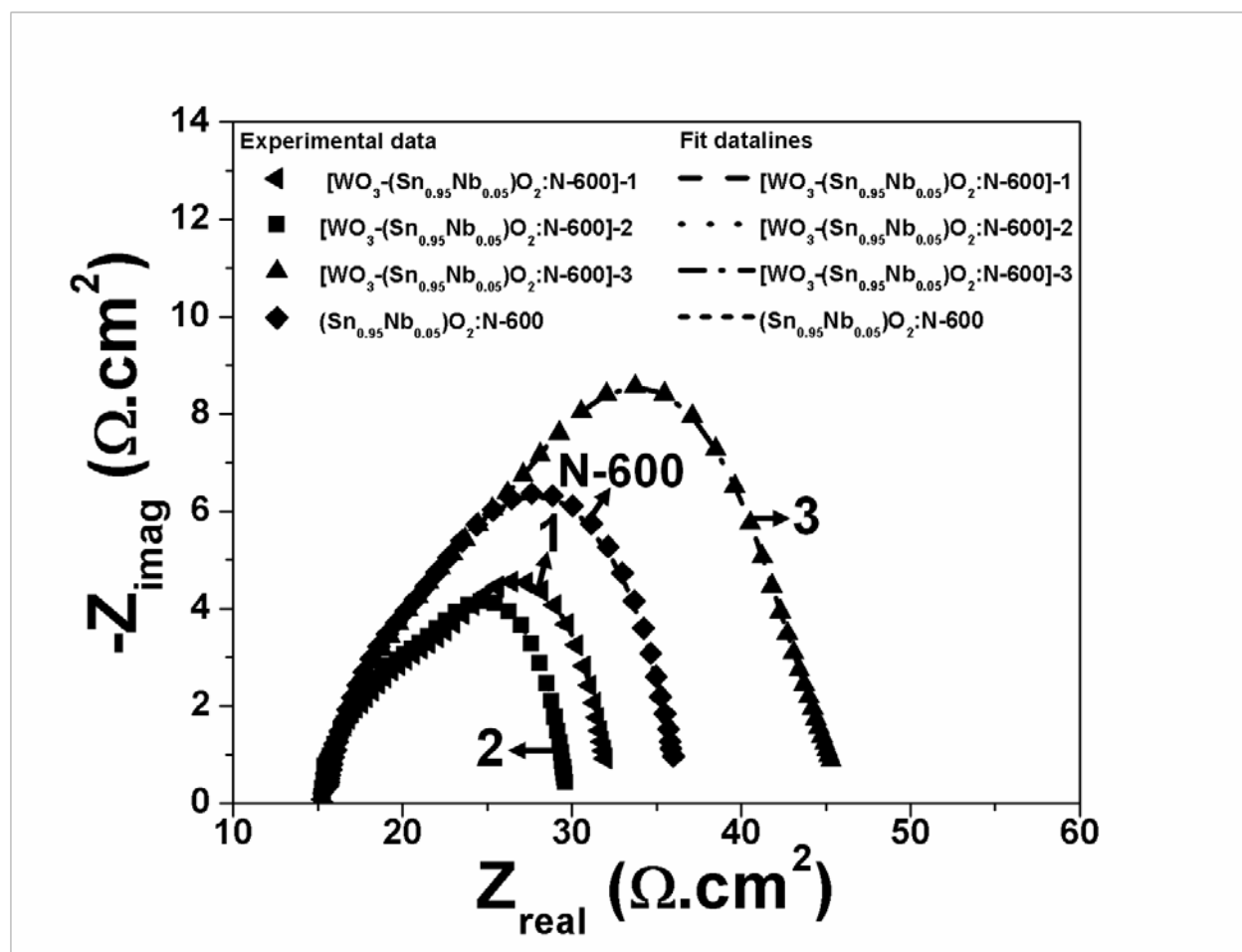


Figure 67: EIS spectra of $(\text{Sn}_{0.95}\text{Nb}_{0.05})\text{O}_2:\text{N-600}$ NTs, $[\text{WO}_3-(\text{Sn}_{0.95}\text{Nb}_{0.05})\text{O}_2:\text{N-600}]-1$ NTs, $[\text{WO}_3-(\text{Sn}_{0.95}\text{Nb}_{0.05})\text{O}_2:\text{N-600}]-2$ NTs and $[\text{WO}_3-(\text{Sn}_{0.95}\text{Nb}_{0.05})\text{O}_2:\text{N-600}]-3$ NTs obtained at ~ 0.1 V (vs RHE) in 0.5 M H_2SO_4 at 26°C in the frequency range of 100 mHz to 100 kHz under illumination ($100 \text{ mW}/\text{cm}^2$)

Electrochemical impedance spectroscopy (EIS) was hence, carried out to determine the charge transfer resistance (R_{ct}) and thus, to study the reaction kinetics for all the materials considered herein in this study. R_{ct} is determined from the diameter of the low frequency semicircle and is tabulated in **Table 10**. As seen in **Figure 67**, $[\text{WO}_3-(\text{Sn}_{0.95}\text{Nb}_{0.05})\text{O}_2:\text{N-600}]-1$ NTs ($\sim 11.25 \Omega \cdot \text{cm}^2$) and $[\text{WO}_3-(\text{Sn}_{0.95}\text{Nb}_{0.05})\text{O}_2:\text{N-600}]-2$ NTs ($\sim 8.05 \Omega \cdot \text{cm}^2$) exhibit lower R_{ct}

than the pristine $(\text{Sn}_{0.95}\text{Nb}_{0.05})\text{O}_2:\text{N}$ NTs ($\sim 15.3 \text{ } \Omega \cdot \text{cm}^2$) and $[\text{WO}_3-(\text{Sn}_{0.95}\text{Nb}_{0.05})\text{O}_2:\text{N}-600]-3$ NTs ($\sim 24.9 \text{ } \Omega \cdot \text{cm}^2$) which is likely due to the efficient separation of the photo-generated carriers with minimum recombination resulting in fast interfacial charge transfer and longer carrier lifetime (discussed later) for the composite bilayer, $[\text{WO}_3-(\text{Sn}_{0.95}\text{Nb}_{0.05})\text{O}_2:\text{N}-600]-1$ NTs and $[\text{WO}_3-(\text{Sn}_{0.95}\text{Nb}_{0.05})\text{O}_2:\text{N}-600]-2$ NTs in comparison to $(\text{Sn}_{0.95}\text{Nb}_{0.05})\text{O}_2:\text{N}$ NTs and $[\text{WO}_3-(\text{Sn}_{0.95}\text{Nb}_{0.05})\text{O}_2:\text{N}-600]-3$ NTs.^{114, 218, 224, 225}

The lower R_{ct} for $[\text{WO}_3-(\text{Sn}_{0.95}\text{Nb}_{0.05})\text{O}_2:\text{N}-600]-2$ NTs ($\sim 8.05 \text{ } \Omega \cdot \text{cm}^2$) contrasted with $[\text{WO}_3-(\text{Sn}_{0.95}\text{Nb}_{0.05})\text{O}_2:\text{N}-600]-1$ NTs ($\sim 11.25 \text{ } \Omega \cdot \text{cm}^2$) can be due to the more efficient separation and minimum recombination of the photo-generated carriers resulting in longer carrier lifetime (discussed later) for the $[\text{WO}_3-(\text{Sn}_{0.95}\text{Nb}_{0.05})\text{O}_2:\text{N}-600]-2$ NTs than $[\text{WO}_3-(\text{Sn}_{0.95}\text{Nb}_{0.05})\text{O}_2:\text{N}-600]-1$ NTs.^{76, 114, 218, 224, 225} However, $[\text{WO}_3-(\text{Sn}_{0.95}\text{Nb}_{0.05})\text{O}_2:\text{N}-600]-3$ NTs ($\sim 24.9 \text{ } \Omega \cdot \text{cm}^2$) shows higher R_{ct} than $[\text{WO}_3-(\text{Sn}_{0.95}\text{Nb}_{0.05})\text{O}_2:\text{N}-600]-1$ NTs ($\sim 11.25 \text{ } \Omega \cdot \text{cm}^2$), $[\text{WO}_3-(\text{Sn}_{0.95}\text{Nb}_{0.05})\text{O}_2:\text{N}-600]-2$ NTs ($\sim 8.05 \text{ } \Omega \cdot \text{cm}^2$) and $(\text{Sn}_{0.95}\text{Nb}_{0.05})\text{O}_2:\text{N}$ NTs ($\sim 15.3 \text{ } \Omega \cdot \text{cm}^2$), which can be due to a higher recombination of the photo-generated carriers resulting in lower carrier lifetime (discussed later) for the composite bilayer, $[\text{WO}_3-(\text{Sn}_{0.95}\text{Nb}_{0.05})\text{O}_2:\text{N}-600]-3$ NTs than all the other materials described and considered in this study.^{76, 114, 218, 224, 225} These excellent results show the potential of coupling WO_3 and $(\text{Sn}_{0.95}\text{Nb}_{0.05})\text{O}_2:\text{N}-600$ in achieving the observed superior photo-electrochemical activity, as evidenced and reported in the results herein.

It is also important to identify the critical losses occurring that limit the attainment of high PEC performance and thus, achieving a high solar to hydrogen (STH) efficiency, which will also aid in choosing a viable approach in engineering novel semiconductor materials in the future. In this study, an incident light of 0.1 W cm^{-2} is incident on the bilayer composite heterostructure. An incident photon conversion efficiency (IPCE) of $\sim 20\%$ is obtained for $[\text{WO}_3-$

($\text{Sn}_{0.95}\text{Nb}_{0.05}\text{O}_2\text{:N-600}$]-2 NTs (**Figure 68**) at 500 nm (as it is typically the accepted wavelength at which maximum solar irradiance is obtained¹⁸⁹). Hence, the contribution of energy from the excited carriers for [$\text{WO}_3\text{-(Sn}_{0.95}\text{Nb}_{0.05}\text{O}_2\text{:N-600}$]-2 NTs is $\sim 5.6 \text{ mW cm}^{-2}$ (absorbed light at $\sim 500 \text{ nm} \times \text{IPCE} = 28 \text{ mW cm}^{-2} \times 20\%$) (**Figure 62** and **Figure 68**) and thus, the energy that is lost in recombination (absorbed light - IPCE) is $\sim 22.4 \text{ mW cm}^{-2}$. Thus, the contribution of energy from excited carriers is $\sim 5.6\%$ (of incident light intensity, $\sim 100 \text{ mW cm}^{-2}$) and $\sim 22.4\%$ energy is lost in the recombination process. The energy used for overcoming ohmic transfer at photoanode/electrolyte interface (I^2R_{Ω}) is $\sim 0.146 \text{ mW cm}^{-2}$. Energy used for overcoming activation polarization at the photoanode/electrolyte interface (I^2R_{ct}) is $\sim 0.077 \text{ mW cm}^{-2}$. Similarly, the energy used for overcoming ohmic transfer at the cathode/electrolyte interface (HER) is $\sim 0.9 \text{ mW cm}^{-2}$. Energy used for activation polarization at cathode/electrolyte interface (HER) is $\sim 0.64 \text{ mW cm}^{-2}$. If overall losses are considered here, $\sim 72\%$ of incident light energy is contributing to light absorption losses at 500 nm (**Figure 62**). Out of $\sim 28\%$ incident light energy absorbed (**Figure 62**), $\sim 5.6 \text{ mW cm}^{-2}$ energy, i.e. with IPCE of 20%, ($\sim 5.6\%$) is available for excited carriers to produce hydrogen gas at the cathode in the PEC cell. Remaining $\sim 22.4\%$ absorbed energy is essentially lost in the recombination losses at the defect/trap sites in the bilayer-2 material. Out of $\sim 5.6 \text{ mW cm}^{-2}$ energy available for the PEC process, 1.046 mW cm^{-2} is getting lost in ohmic polarization and 0.72 mW cm^{-2} is getting utilized to overcome the activation polarization (i.e., charge transfer) at the electrode/electrolyte interfaces for both cathode and photoanode, respectively. The remaining energy ($\sim 3.83 \text{ mW cm}^{-2}$) is thus getting used to convert the incident light energy to hydrogen gas with an efficiency of $\sim 3.83\%$ (**Figure 74**).

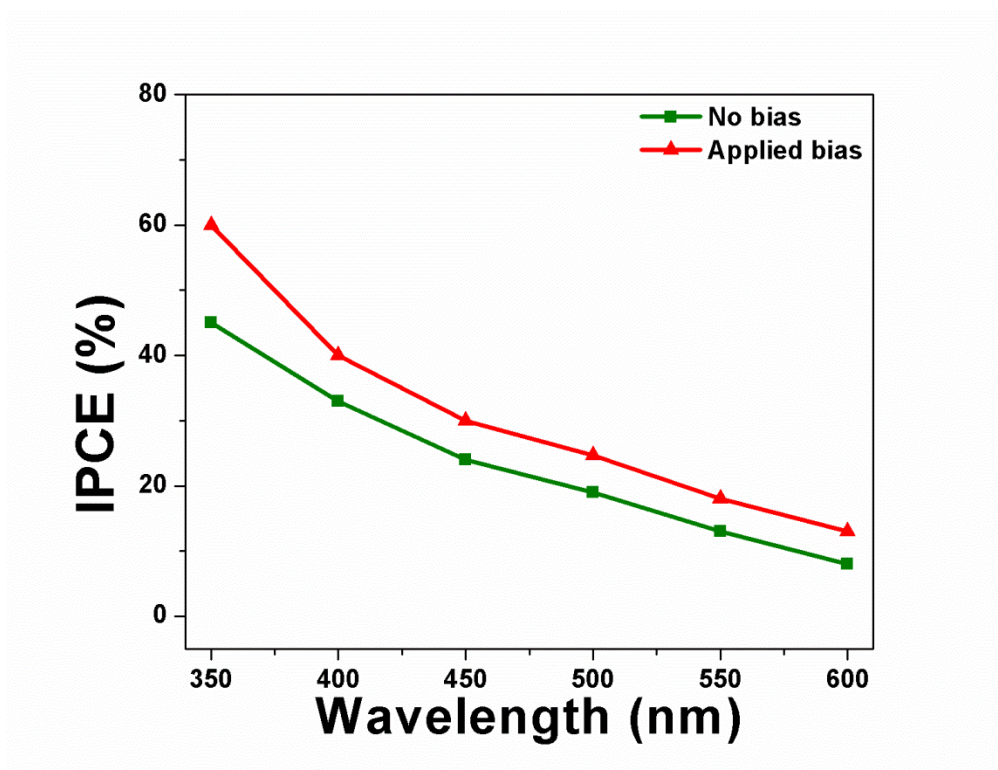


Figure 68: IPCE plots for [WO₃-(Sn_{0.95}Nb_{0.05})O₂:N-600]-2 NTs under no bias and applied 0.6V (vs RHE) bias

Calculated losses limiting PEC performance in the absence of electrical bias for [WO₃-(Sn_{0.95}Nb_{0.05})O₂:N-600]-2 NTs at ~0V:

- Incident light energy=100 mW cm⁻²
- Absorbed light (at ~500 nm which is close to the wavelength at which maximum solar irradiance is obtained¹⁸⁹) (**Figure 62**) = Light absorption×Incident light energy

$$= 28\% \times 100 \text{ mW cm}^{-2} = 28 \text{ mW cm}^{-2}$$
- IPCE at ~500 nm = 20% (**Figure 68**)

— Energy contribution from excited carriers = IPCE × Absorbed light energy = 20% × 28 mW cm⁻² = 5.6 mW cm⁻²

— Energy lost in recombination process = Absorbed light energy - energy of excited carriers
 = 28 mW cm⁻² - 5.6 mW cm⁻²
 = 22.4 mW cm⁻²

— **Photoanode/electrolyte interface:**

The photocurrent density (3.1 mA cm⁻²) at a finite potential (to overcome overpotential losses) close to zero bias, i.e., ~0.1 V (vs RHE) in LSV plot (**Figure 66** and **Table 10**) is used for the following calculations.

Energy used for ohmic transfer = I²R_Ω = (3.1 mA cm⁻²)² × 15.2 Ω.cm² (**Figure 66**, **Figure 67** and **Table 10**)

$$= 0.146 \text{ mW cm}^{-2}$$

Energy used for charge transfer (activation polarization loss) = I²R_{ct} = (3.1 mA cm⁻²)² × 8.05 Ω.cm² = 0.077 mW cm⁻² (**Figure 66**, **Figure 67** and **Table 10**)

— **Cathode/electrolyte interface:**

The current density (7.7 mA cm⁻²) at a finite potential of ~30 mV (vs RHE, to overcome the overpotential losses) close to 0V (standard potential for HER) in HER polarization plot is used for following calculations (see ¹⁷⁹ for electrochemical data of Pt).

Energy used for ohmic transfer = I²R_Ω = (7.7 mA cm⁻²)² × 15.25 Ω.cm² (see ¹⁷⁹ for electrochemical data of Pt)

$$= 0.9 \text{ mW cm}^{-2}$$

Energy used for charge transfer (activation polarization loss) = $I^2R_{ct} = (7.7 \text{ mA cm}^{-2})^2 \times 10.8 \text{ } \Omega \cdot \text{cm}^2 = 0.64 \text{ mW cm}^{-2}$ (see ¹⁷⁹)

Energy contributed from free carriers – Total energy used

$$= 5.6 \text{ mW cm}^{-2} - (0.146 + 0.077 + 0.9 + 0.64) \text{ mW cm}^{-2}$$

$$= 3.837 \text{ mW cm}^{-2} \text{ (close to experimental STH of } \sim 3.83\%)$$

It should be noted that though the goal is to achieve superior STH at zero applied bias, it is important to study the effect of applied bias on the above mentioned losses which limit the PEC performance. The losses are studied at the applied potential of $\sim 0.6 \text{ V}$ (*vs* RHE), which is the typical potential at which highest ABPE is obtained for semiconductor systems based on TiO_2 , ZnO , Fe_2O_3 , etc. ^{64, 76, 114, 176-178}S. Under the applied bias of $\sim 0.6 \text{ V}$, incident energy is $\sim 100 \text{ mW cm}^{-2}$ coming from incident light and $\sim 4.86 \text{ mW cm}^{-2}$ contributed by applied bias (Bias = 0.6 V , $I = \sim 8.1 \text{ mA cm}^{-2}$ shown in **Figure 72**). Thus, the contribution of energy from excited carriers for $[\text{WO}_3-(\text{Sn}_{0.95}\text{Nb}_{0.05})\text{O}_2:\text{N}-600]-2 \text{ NTs}$ is $\sim 8.11 \text{ mW cm}^{-2}$ [(absorbed light at $\sim 500 \text{ nm} +$ energy from applied bias) \times IPCE = $(28 \text{ mW cm}^{-2} + 4.86 \text{ mW cm}^{-2}) \times 24.7\%$] (**Figure 62** and **Figure 68**) and thus, the energy that is lost in recombination (absorbed light at $\sim 500 \text{ nm} -$ energy from excited carriers) is $\sim 19.88 \text{ mW cm}^{-2}$. Energy used for overcoming ohmic transfer at photoanode/electrolyte interface (I^2R_{Ω}) is $\sim 0.997 \text{ mW cm}^{-2}$. Similarly energy used for overcoming activation polarization at the photoanode/electrolyte interface (I^2R_{ct}) is $\sim 0.528 \text{ mW cm}^{-2}$. The energy used for ohmic transfer at the cathode/electrolyte interface (HER) is $\sim 0.9 \text{ mW cm}^{-2}$. Energy used for activation polarization at cathode/electrolyte interface (HER) is $\sim 0.64 \text{ mW cm}^{-2}$. If overall losses are considered under applied bias, $\sim 72\%$ of incident light energy is contributing to light absorption losses at 500 nm (**Figure 62**). Out of $\sim 28\%$ incident light energy

absorbed coupled with input power of 4.86 mW cm^{-2} arising from the applied bias of 0.6V (**Figure 62**), $\sim 8.12 \text{ mW cm}^{-2}$ energy, considering the IPCE of 24.7% , ($\sim 8.12\%$) is available for the excited carriers to produce hydrogen gas at cathode in the PEC cell. Remaining $\sim 19.88\%$ absorbed energy is getting lost in recombination losses in the bilayer-2 material. Out of $\sim 8.12 \text{ mW cm}^{-2}$ energy available for PEC process, 1.897 mW cm^{-2} is getting lost in ohmic polarization and 1.168 mW cm^{-2} is getting utilized to overcome activation polarization (i.e., charge transfer) at the electrode/electrolyte interfaces at cathode and photoanode. Remaining energy ($\sim 5.1 \text{ mW cm}^{-2}$) is thus getting used to convert incident light energy to hydrogen gas with an efficiency of $\sim 5.1\%$ (**Table 10**). The recombination losses decrease by a commendable $\sim 12\%$ under applied bias compared to the case with no applied bias for bilayer-2 system, suggesting the promise of bilayer-2 system. The study also suggest that possible further electronic structural modification in the bilayer-2 system configuration could likely minimize the losses with no electrical bias further offering excellent PEC response. **Figure 69** shows a schematic summarizing the various processes outlined above.

Losses limiting PEC performance for $[\text{WO}_3-(\text{Sn}_{0.95}\text{Nb}_{0.05})\text{O}_2:\text{N}-600]-2$ NTs under applied bias ($\sim 0.6\text{V}$ vs RHE):

- Incident light energy = 100 mW cm^{-2}
- Absorbed light (at $\sim 500 \text{ nm}$ which is close to the wavelength at which maximum solar irradiance is obtained¹⁸⁹) (**Figure 62**) = Light absorption \times Incident light energy

$$= 28\% \times 100 \text{ mW cm}^{-2} = 28 \text{ mW cm}^{-2}$$
- IPCE at $\sim 500 \text{ nm}$ = 24.7% (**Figure 68**)
- Input power (due to applied bias; see **Figure 72**) = $V \times I = 0.6 \text{ V} \times 8.1 \text{ mA cm}^{-2} = 4.86 \text{ mW cm}^{-2}$

— Energy contribution from excited carriers = (Absorbed light energy+Input power)×IPCE=
 $[(28 \text{ mW cm}^{-2}) + (4.86 \text{ mW cm}^{-2})] \times 24.7\% = 8.12 \text{ mW cm}^{-2}$

— Energy lost in recombination process = Absorbed light energy - energy of excited carriers
 $= 28 \text{ mW cm}^{-2} - 8.12 \text{ mW cm}^{-2}$
 $= 19.88 \text{ mW cm}^{-2}$

— **Photoanode/electrolyte interface:**

The photocurrent density (8.1 mA cm^{-2}) at $\sim 0.6\text{V}$ (*vs* RHE) in LSV plot (**Figure 66**) is used for the following calculations.

Energy used for ohmic transfer $= I^2 R_{\Omega} = (8.1 \text{ mA cm}^{-2})^2 \times 15.2 \text{ } \Omega \cdot \text{cm}^2$ (**Figure 66, Figure 67** and **Table 10**)

$$= 0.997 \text{ mW cm}^{-2}$$

Energy used for charge transfer (activation polarization loss) $= I^2 R_{ct} = (8.1 \text{ mA cm}^{-2})^2 \times 8.05 \text{ } \Omega \cdot \text{cm}^2 =$
 0.528 mW cm^{-2} (**Figure 66, Figure 67** and **Table 10**)

— **Cathode/electrolyte interface:**

The current density at a finite potential of $\sim 30 \text{ mV}$ (*vs* RHE, to overcome overpotential losses) close to 0V (standard HER potential) in HER polarization plot is used for following calculations (see ¹⁷⁹ for electrochemical data of Pt).

Energy used for ohmic transfer $= I^2 R_{\Omega} = (7.7 \text{ mA cm}^{-2})^2 \times 15.25 \text{ } \Omega \cdot \text{cm}^2$ (see ¹⁷⁹ for electrochemical data of Pt)

$$= 0.9 \text{ mW cm}^{-2}$$

Energy used for charge transfer (activation polarization loss) $= I^2 R_{ct} = (7.7 \text{ mA cm}^{-2})^2 \times 10.8 \text{ } \Omega \cdot \text{cm}^2 = 0.64 \text{ mW cm}^{-2}$ (see ¹⁷⁹)

Energy contributed from free carriers – Total energy used

$$= 8.12 \text{ mW cm}^{-2} - (0.997 + 0.528 + 0.9 + 0.64) \text{ mW cm}^{-2}$$

$$= 5.1 \text{ mW cm}^{-2} \text{ (close to experimental ABPE of } \sim 5.16\%)$$

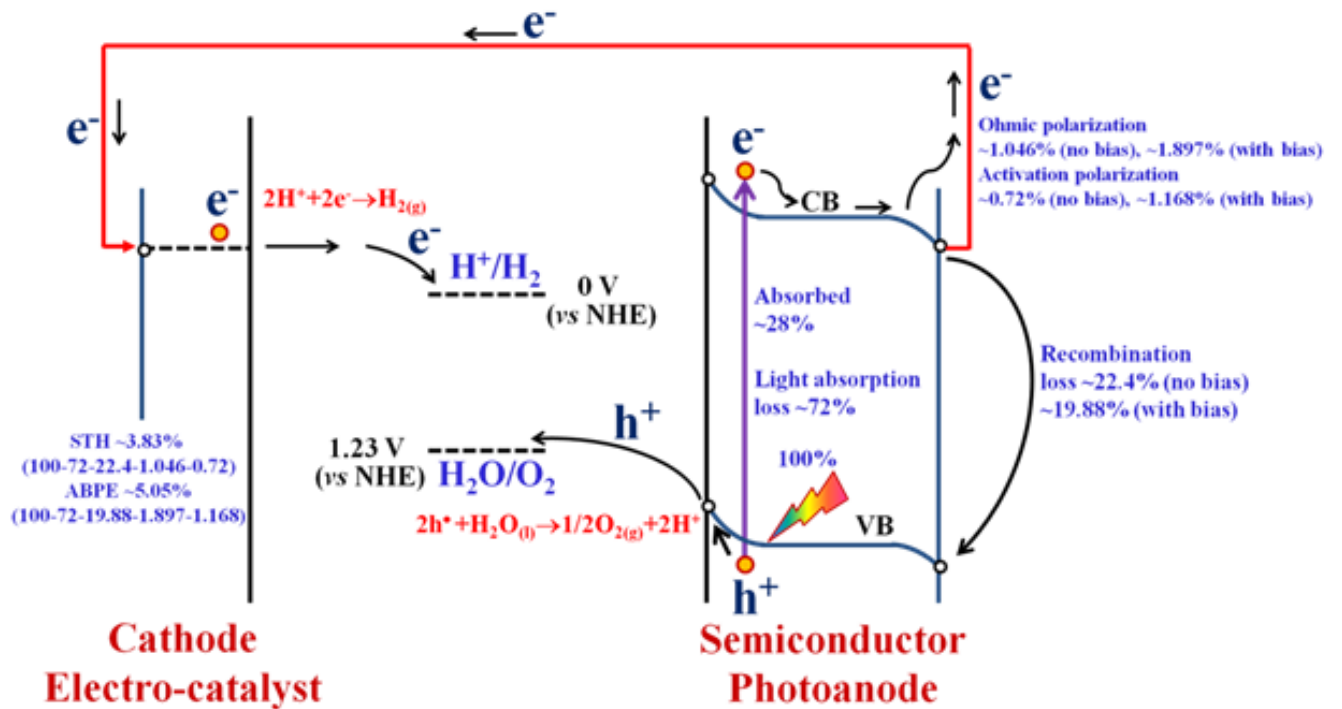


Figure 69: Schematic of PEC process showing losses without and with ~0.6V bias

It is important to decrease the light absorption losses (~72%), the recombination losses (~22.4% at zero bias and ~19.88% under 0.6V bias) and the consequent polarization losses (~1.76% at zero bias and ~3% under 0.6V bias) to achieve high STH (at zero applied bias) and ABPE for bilayer-2 system configuration (**Figure 69**). Hence, it is critical to change the band edge levels in the bilayer 2 material configuration considered herein further which will offer improved light absorption and also superior band bending at the electrode/electrolyte interface aiding the facile transport of the excited carriers through the material. Such facile transport of carriers through the bilayer-2 material will offer lower recombination losses and superior PEC response with need of minimal or even zero applied bias, resulting in lower recombination and polarization losses. This strategy discussed herein can indeed lead to engineering of novel semiconductor materials for PEC process which can be likely achieved by the introduction of suitable acceptor/donor levels in the band gap of the semiconductor material. These strategies can be indeed pursued in the near future.

Study of carrier lifetime

To understand the charge transport properties of the bilayer photoanode materials in detail, recombination kinetics of the photo-generated carriers is studied by measuring the open circuit potential as a function of time under light OFF conditions. When the semiconductor material is illuminated with the solar light, the apparent Fermi level shifts to negative potential due to the accumulation of photo-generated electrons in the semiconductor material (under open circuit conditions).^{65, 105} When the illumination is turned off, the accumulated electrons are discharged in the electrolyte solution as they are scavenged by the redox species in the electrolyte solution.^{65, 105} The recombination of photo-generated carriers is mainly responsible

for the sharp decay of the photo-generated electrons.^{65, 105} The decay in the open circuit potential (V_{oc}) gives information about the rate of recombination of the photo-generated carriers in the semiconductor material.^{65, 105} The decay in V_{oc} as function of time is shown in **Figure 70**. The decay was calculated from the slope by considering different points in the corresponding rising and saturated segments of the curve, similar to earlier reports^{65, 105, 218, 256-260}. As seen in **Figure 70**, [WO₃-(Sn_{0.95}Nb_{0.05})O₂:N-600]-1 NTs (~8.4 mV sec⁻¹) and [WO₃-(Sn_{0.95}Nb_{0.05})O₂:N-600]-2 NTs (~7.7 mV sec⁻¹) exhibit slower V_{oc} decay rate than (Sn_{0.95}Nb_{0.05})O₂:N-600 NTs (~9.6 mV sec⁻¹), suggesting lower recombination of photo-generated carriers in bilayer materials. On the other hand, [WO₃-(Sn_{0.95}Nb_{0.05})O₂:N-600]-3 NTs (~12.6 mV sec⁻¹) has a much higher V_{oc} decay rate than (Sn_{0.95}Nb_{0.05})O₂:N-600 NTs, [WO₃-(Sn_{0.95}Nb_{0.05})O₂:N-600]-1 NTs and [WO₃-(Sn_{0.95}Nb_{0.05})O₂:N-600]-2 NTs, which can be due to the higher thickness of (Sn_{0.95}Nb_{0.05})O₂:N-600 NTs layer coated on WO₃ layer resulting in long transport distance to be traversed by the photo-generated carriers resulting in more recombination of the photo-generated carriers, which is similar to earlier reports^{218, 258}. The carrier lifetime (τ), which is the average time for which photo-generated carriers exist before recombining, is determined using the equation^{29, 85}:

$$\tau = -(k_B T / e) (dV_{oc} / dt)^{-1}$$

where, k_B is Boltzmann constant, T is the absolute temperature (299 K), e is electron charge. The variation of τ with V_{oc} , shown in **Figure 71**, shows significantly longer carrier lifetime for [WO₃-(Sn_{0.95}Nb_{0.05})O₂:N-600]-1 NTs and [WO₃-(Sn_{0.95}Nb_{0.05})O₂:N-600]-2 NTs with the highest lifetime seen for [WO₃-(Sn_{0.95}Nb_{0.05})O₂:N-600]-2 NTs than that of (Sn_{0.95}Nb_{0.05})O₂:N-600 NTs due to a relatively lower recombination rate of photo-generated carriers for the bilayer materials (as discussed before) (**Figure 70**).

However, lower carrier lifetime for $[\text{WO}_3-(\text{Sn}_{0.95}\text{Nb}_{0.05})\text{O}_2:\text{N}-600]$ -3 NTs than the other materials considered in this study can be due to higher recombination kinetics of the photo-generated carriers due to the larger thickness of $(\text{Sn}_{0.95}\text{Nb}_{0.05})\text{O}_2:\text{N}-600$ NTs layer coated on WO_3 layer offering long transport distance to be covered by the photo-generated carriers, which is similar to earlier reports^{218, 258}. The largest carrier lifetime (~ 140 sec) at (-0.2 V *vs* RHE which is near zero bias and selected following the earlier reports in the literature^{65, 105, 218, 256-260}) obtained in this study for $[\text{WO}_3-(\text{Sn}_{0.95}\text{Nb}_{0.05})\text{O}_2:\text{N}-600]$ -2 NTs plays an important role in achieving the superior photo-electrochemical activity, as seen in **Figure 66**. These results clearly suggest the beneficial role of the optimal bilayer structure, i.e., coupling of $(\text{Sn}_{0.95}\text{Nb}_{0.05})\text{O}_2:\text{N}-600$ NTs with WO_3 in increasing the carrier lifetime ~ 20 fold higher (at -0.2 V *vs* RHE) obtained for $[\text{WO}_3-(\text{Sn}_{0.95}\text{Nb}_{0.05})\text{O}_2:\text{N}-600]$ -2 NTs compared to $(\text{Sn}_{0.95}\text{Nb}_{0.05})\text{O}_2:\text{N}-600$ NTs (~ 7 sec at -0.2 V *vs* RHE) and thus, minimizing the recombination of the photo-generated carriers. This is very important in the aim to achieve superior photo-electrochemical performance and thus, yield an efficient PEC water splitting process resulting in effective generation of hydrogen.

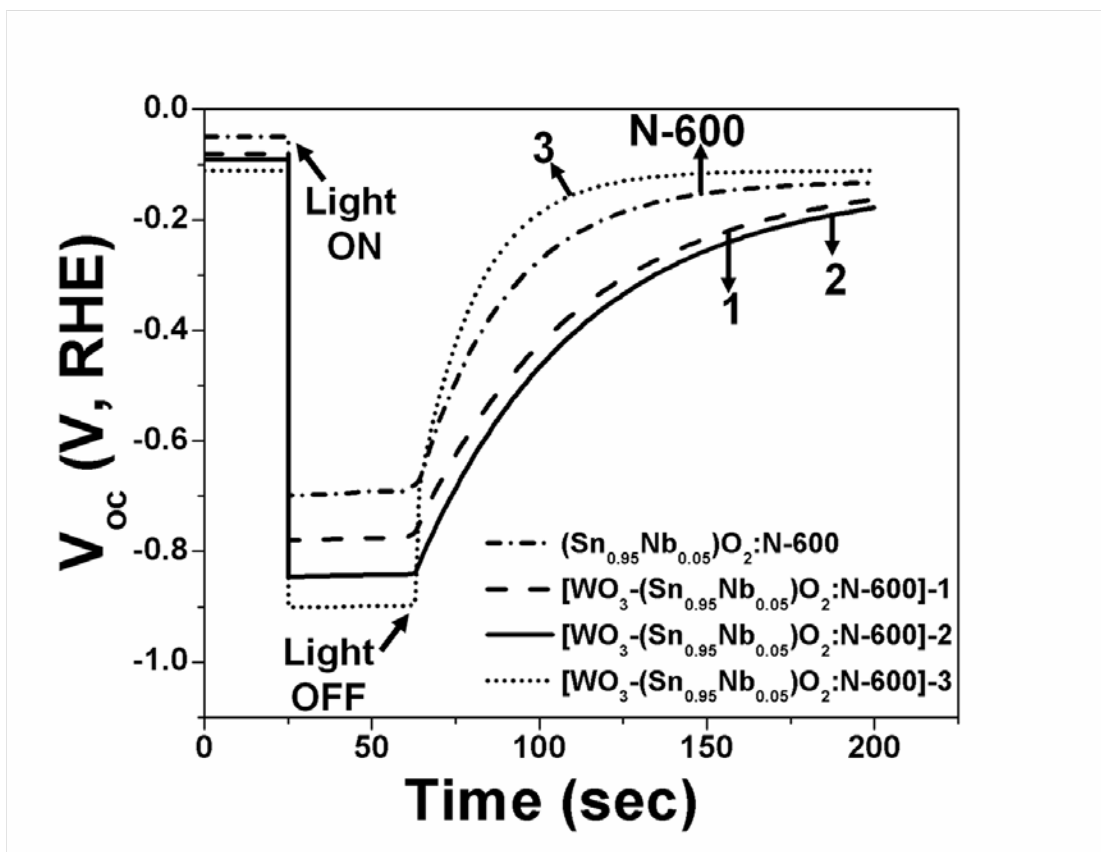


Figure 70: Variation of open circuit potential (V_{oc}) under light ON/OFF conditions with time for $(\text{Sn}_{0.95}\text{Nb}_{0.05})\text{O}_2:\text{N-600}$ NTs, $[\text{WO}_3-(\text{Sn}_{0.95}\text{Nb}_{0.05})\text{O}_2:\text{N-600}]-1$ NTs, $[\text{WO}_3-(\text{Sn}_{0.95}\text{Nb}_{0.05})\text{O}_2:\text{N-600}]-2$ NTs and $[\text{WO}_3-(\text{Sn}_{0.95}\text{Nb}_{0.05})\text{O}_2:\text{N-600}]-3$ NTs

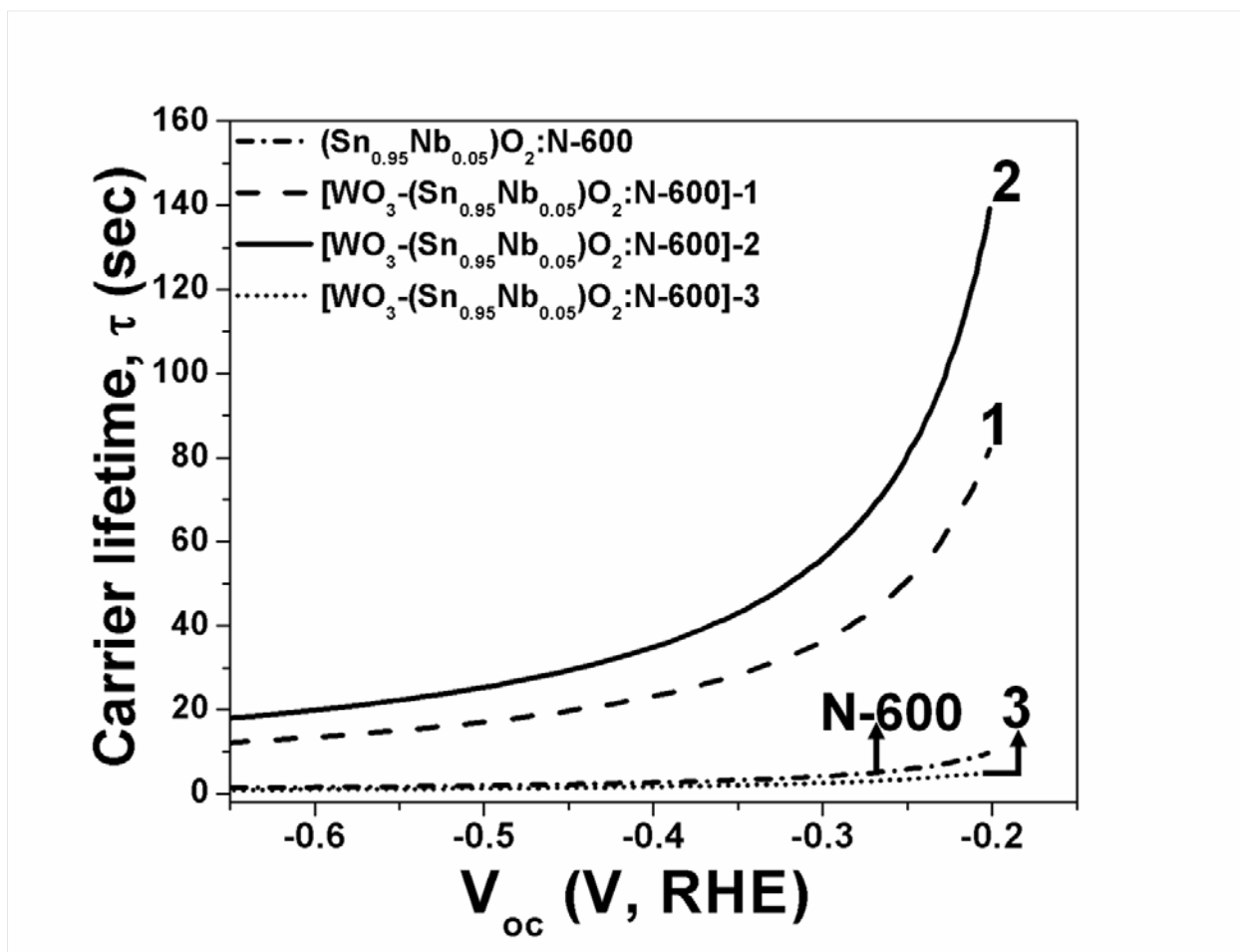


Figure 71: Carrier lifetime (τ) as function of open circuit potential (V_{oc}) for $(\text{Sn}_{0.95}\text{Nb}_{0.05})\text{O}_2\text{:N-600}$ NTs, $[\text{WO}_3-(\text{Sn}_{0.95}\text{Nb}_{0.05})\text{O}_2\text{:N-600}]\text{-1}$ NTs, $[\text{WO}_3-(\text{Sn}_{0.95}\text{Nb}_{0.05})\text{O}_2\text{:N-600}]\text{-2}$ NTs and $[\text{WO}_3-(\text{Sn}_{0.95}\text{Nb}_{0.05})\text{O}_2\text{:N-600}]\text{-3}$ NTs

Photoelectrochemical stability of $[\text{WO}_3-(\text{Sn}_{0.95}\text{Nb}_{0.05})\text{O}_2\text{:N-600}]\text{-2}$ NTs

It is important that the semiconductor material exhibits excellent long term photoelectrochemical stability for achieving continuous, durable and efficient PEC water splitting. In order to demonstrate the durability and stability of the semiconductor material, chronoamperometry (CA) test has been carried out for 24 h to study the long term photo-

electrochemical stability of the optimal bilayer composite architecture, $[\text{WO}_3-(\text{Sn}_{0.95}\text{Nb}_{0.05})\text{O}_2:\text{N}-600]-2$ NTs under constant illumination in the electrolyte solution. The CA test is thus carried out in harsh operating conditions at a constant potential of ~ 0.6 V (*vs* RHE, similar to earlier reports^{114, 261, 262}) in 0.5 M H_2SO_4 solution by illuminating the photoanode (100 mW cm^{-2}) for 24 h. The CA curve of $[\text{WO}_3-(\text{Sn}_{0.95}\text{Nb}_{0.05})\text{O}_2:\text{N}-600]-2$ NTs is shown in **Figure 72**. The very minimal loss in photocurrent density ($\sim 1\%$) is seen for $[\text{WO}_3-(\text{Sn}_{0.95}\text{Nb}_{0.05})\text{O}_2:\text{N}-600]-2$ NTs indicating the excellent long term photo-electrochemical stability of this composite bilayer system. Inductively coupled plasma optical emission spectroscopy (ICP-OES) analysis conducted on the electrolyte solution, collected after CA test, did not show presence (~ 0 ppm) of Sn, Nb and W for $[\text{WO}_3-(\text{Sn}_{0.95}\text{Nb}_{0.05})\text{O}_2:\text{N}-600]-2$ NTs (see **Table 12**). This result essentially demonstrates the potential of the $[\text{WO}_3-(\text{Sn}_{0.95}\text{Nb}_{0.05})\text{O}_2:\text{N}-600]-2$ NTs system to display excellent photo-electrochemical stability in the electrolyte solution under illumination thus validating its long term operation in a PEC water splitting cell. The result thus confirms the stable and long term use of this system under actual field scale PEC operating conditions.

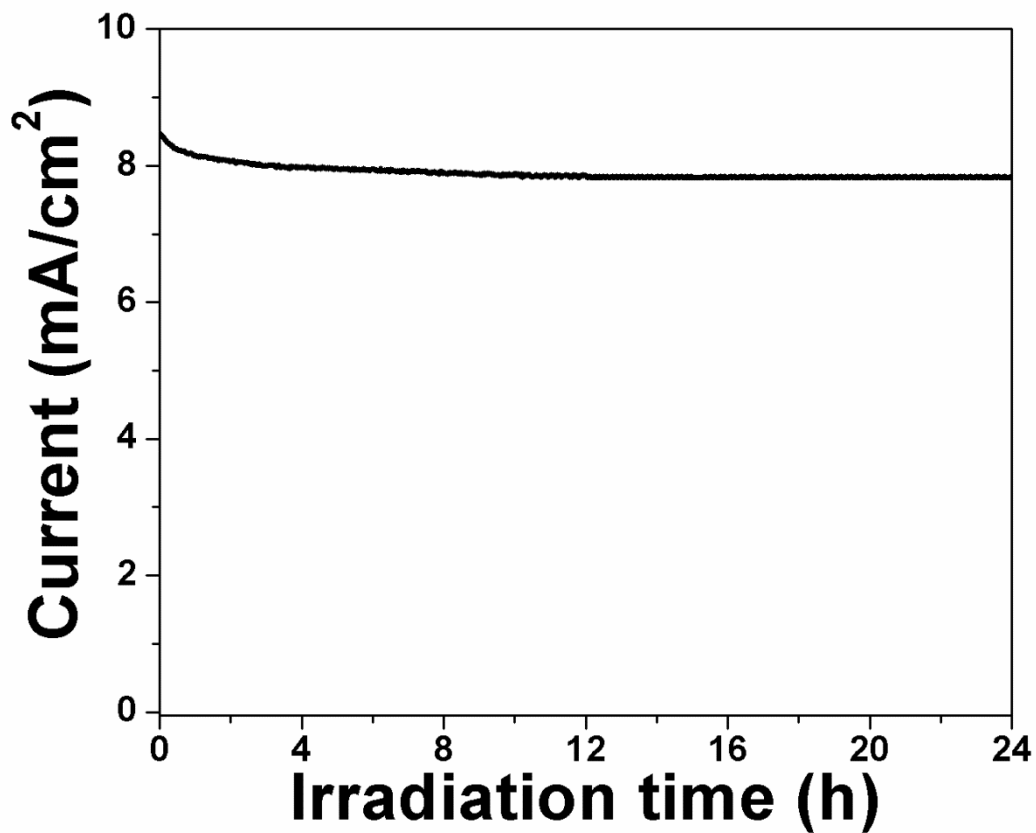


Figure 72: The variation of photocurrent density *vs* irradiation time in the chronoamperometry test of [WO₃-(Sn_{0.95}Nb_{0.05})O₂:N-600]-2 NT, performed in 0.5 M H₂SO₄ solution under a constant potential of ~0.6 V (*vs* RHE) at 26⁰C for 24 h under illumination (100 mW/cm²)

Table 12: Results of ICP analysis on 0.5 M H₂SO₄ solution after chronoamperometry test of [WO₃-(Sn_{0.95}Nb_{0.05})O₂:N-600]-2 NTs

Elements	<u>Concentration (ppm)</u>
Sn	$5.1 \times 10^{-3} \pm 0.001$
Nb	$4.2 \times 10^{-3} \pm 0.002$
W	$6.6 \times 10^{-3} \pm 0.001$

Measurement of evolved H₂ and O₂ gases under illumination for [WO₃-(Sn_{0.95}Nb_{0.05})O₂:N-600]-2 NTs

As mentioned earlier, it is important to achieve efficient hydrogen generation from PEC water splitting with utilization of only solar energy without any applied external potential. Hence, the optimal configuration of the bilayer composite photoanode of [WO₃-(Sn_{0.95}Nb_{0.05})O₂:N-600]-2 NTs was illuminated for 24 h without any application of external potential. The concentration of the resulting H₂ and O₂ gases evolved during the PEC water splitting process at the cathode and photoanode compartments, respectively, has been measured after each 1 h time interval. Also, the theoretical concentration of H₂ gas is calculated from the measured photocurrent by Faraday's law as^{76, 114}:

$$\text{No. of moles of H}_2 = \frac{Q}{2F} = \frac{It}{2F} = \frac{\int_0^t I \cdot dt}{2F}$$

where, I is the photocurrent density, t is time, F is the Faraday constant (96484.34 C mol⁻¹) and Q is the quantity of charge in coulomb. The concentration of evolved H₂ and O₂ gases, shown in **Figure 73**, shows the measured amount of evolved H₂ gas which is closer or comparable to the theoretical amount of H₂, suggesting ~100% Faradaic efficiency. If the decomposition of water

were to occur in a non-stoichiometric fashion, there will be change in concentration of either H^+ or OH^- ions. However, in this study, the ratio of concentration of generated H_2 and O_2 gases is ~ 2 , as seen in **Figure 74** and there was no change observed in the pH of the electrolyte solution (~ 0) before and after water the splitting reaction. This result thus, shows stoichiometric decomposition of water into H_2 and O_2 is achieved in the present study for $[WO_3-(Sn_{0.95}Nb_{0.05})O_2:N-600]-2$ NTs.

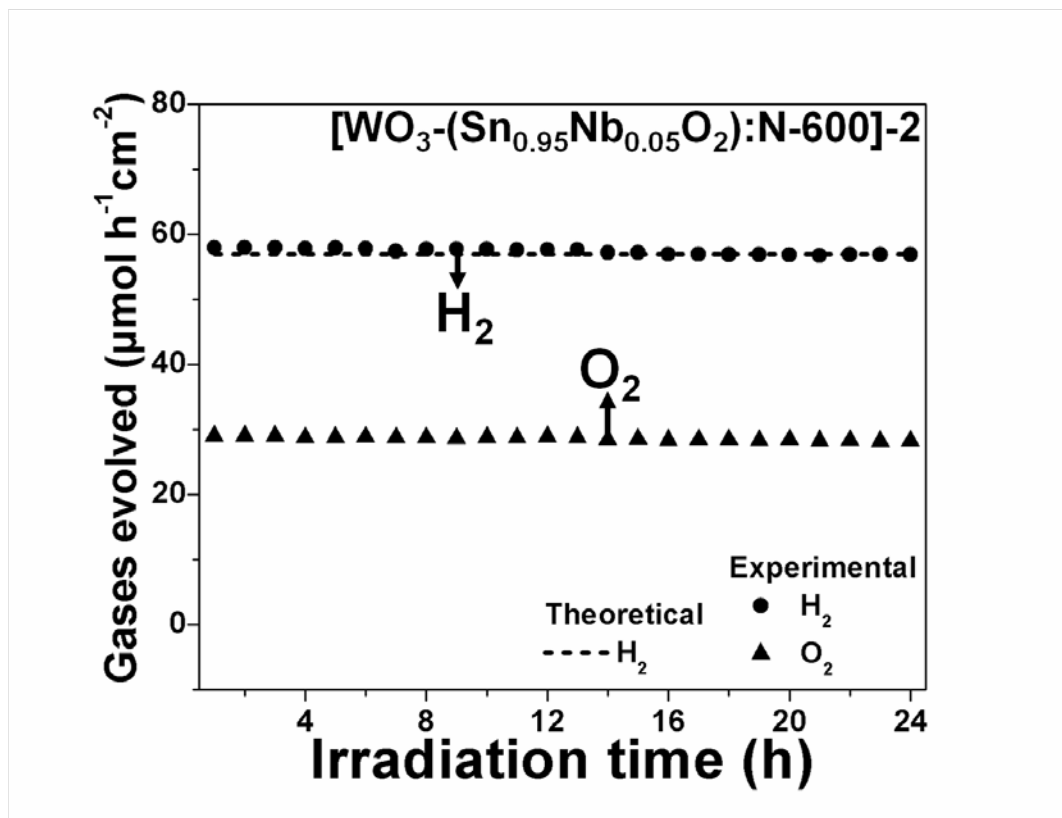


Figure 73: Theoretical and experimentally measured concentration of H_2 gas and experimentally measured concentration of O_2 gas measured under illumination (100 mW/cm^2) with no applied potential for $[WO_3-(Sn_{0.95}Nb_{0.05})O_2:N-600]-2$ NT measured in $0.5 \text{ M H}_2\text{SO}_4$ solution at 26°C for 24 h

The ensuing solar-to-hydrogen efficiency (STH) is determined from the measured concentration of H₂ gas for [WO₃-(Sn_{0.95}Nb_{0.05})O₂:N-600]-2 NTs using the equation⁷⁵⁻⁷⁹:

$$\text{STH} = \frac{\Delta G^{\circ} \times n_{\text{H}_2}}{P \times A} \times 100$$

where, n_{H_2} = H₂ evolution rate (mol sec⁻¹)

ΔG° =Gibbs free energy for generating one mole of H₂ from water (237130 J mol⁻¹)

P = Total incident power (W cm⁻²)

A = Area irradiated by incident light (cm²)

The plot of STH vs irradiation time is shown in **Figure 74**. At the end of 24 h, a minimal loss of (~1%) is seen in the STH for [WO₃-(Sn_{0.95}Nb_{0.05})O₂:N-600]-2 NTs indicating the excellent long term photo-electrochemical stability for continuous hydrogen generation from PEC water splitting under acidic conditions. It is noteworthy to mention herein that the STH of ~3.83% for [WO₃-(Sn_{0.95}Nb_{0.05})O₂:N-600]-2 NTs (with zero applied potential) achieved in the current study for the optimal bilayer composite configuration is the highest STH obtained so far compared to other semiconductor materials studied as photoanode and reported for PEC water splitting to the best of our knowledge. These include systems such as TiO₂, ZnO and Fe₂O₃ to the best of our assessment of the widely reported literature to date.^{64, 76, 114, 176-178} Moreover, the efficiency achieved herein is also comparable to the efficiency achieved with artificial leaf based on the integration of three junction solar cells and optimized hydrogen- and oxygen-evolution catalysts.²⁶³ The input power for [WO₃-(Sn_{0.95}Nb_{0.05})O₂:N-600]-2 NTs and thus, for H₂ production is ~100 mW/cm². The measured H₂ concentration is ~60 μmol/h/cm²; 1.2×10⁻⁷ kg/h/cm²) (**Figure 74**). Thus, required input power for generation of 1 kg H₂ is ~833 kWh/kg

(for 1 cm² area), which is higher than DOE target of <43 kWh/kg. Thus, albeit the electricity cost (~\$0.031/kWh) for the current system (\$25.83/kg) is ~20 fold higher than that of DOE target (~\$ 1.33/kg), it is still lower than other semiconductor materials (TiO₂, ZnO and Fe₂O₃) studied for PEC water splitting process reported in the literature thus far. There is clearly still much research needed but the bilayer system studied herein nevertheless, indeed holds promise on the grounds of recommendable PEC performance showing STH of ~3.83% (at zero applied bias) and ABPE of ~5.1% (at 0.6V vs RHE) higher than other semiconductor materials (TiO₂, ZnO and Fe₂O₃) studied reported in the literature for PEC water splitting process.

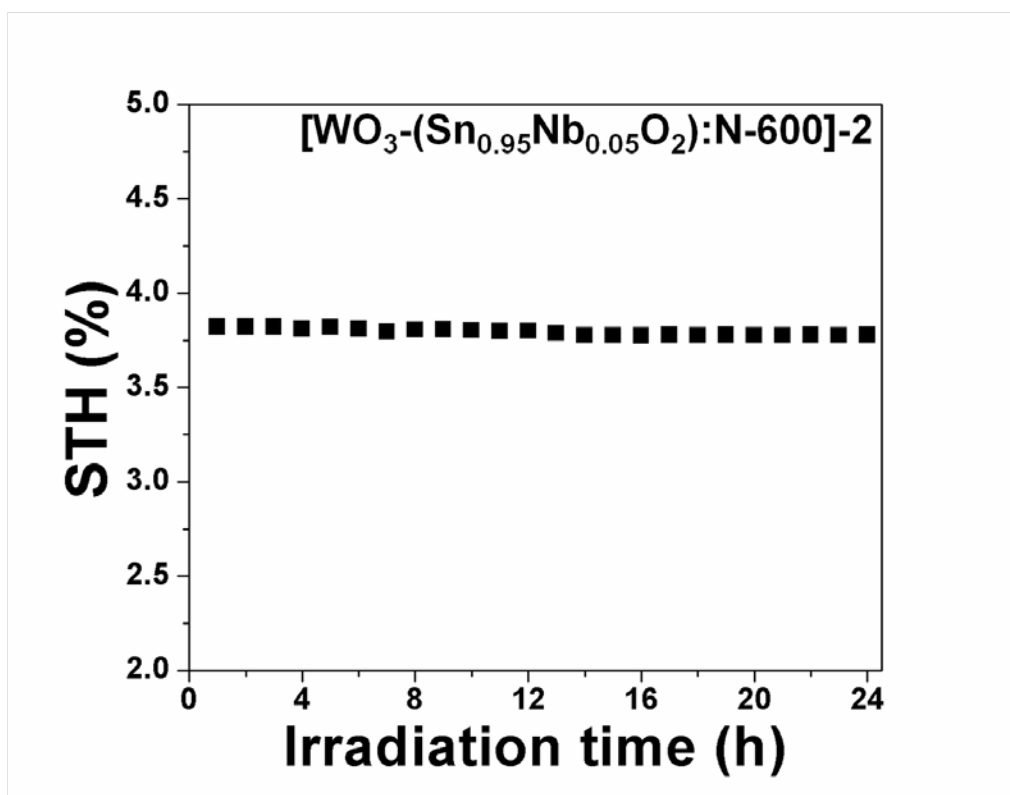


Figure 74: Variation of solar-to-hydrogen efficiency (STH) (determined from concentration of evolved H₂ gas measured under illumination of 100 mW/cm² with no applied potential as shown in Figure 73) vs irradiation time for [WO₃-(Sn_{0.95}Nb_{0.05}O₂):N-600]-2 NTs

The present study clearly demonstrates the superior photo-electrochemical performance of the optimal bilayer composite configuration, $[\text{WO}_3-(\text{Sn}_{0.95}\text{Nb}_{0.05})\text{O}_2:\text{N}-600]-2$ NTs exhibiting excellent solar to hydrogen efficiency (STH) of $\sim 3.83\%$ (with no external potential applied) and ABPE of $\sim 5.1\%$ (at 0.6V vs RHE). As discussed earlier, light absorption losses, recombination losses and polarization losses mainly limit STH/ABPE and electricity cost for the bilayer system (**Figure 69**). As discussed earlier, recombination losses decrease by a commendable $\sim 12\%$ for $[\text{WO}_3-(\text{Sn}_{0.95}\text{Nb}_{0.05})\text{O}_2:\text{N}-600]-2$ NTs under the applied bias of $\sim 0.6\text{V}$ (vs RHE) compared to the no bias condition, suggesting promise of the composite bilayer-2 system. Despite these losses, $[\text{WO}_3-(\text{Sn}_{0.95}\text{Nb}_{0.05})\text{O}_2:\text{N}-600]-2$ NTs show excellent PEC performance under applied bias with recommendable ABPE of $\sim 5.1\%$ (at $\sim 0.6\text{V}$ vs RHE) and STH of $\sim 3.83\%$ (under no bias). Hence, $[\text{WO}_3-(\text{Sn}_{0.95}\text{Nb}_{0.05})\text{O}_2:\text{N}-600]-2$ NTs bilayer system is indeed promising and further electronic structural modification of bilayer system by changing band edge positions, which can be achieved by introduction of suitable acceptor/donor levels (in the band gap), will help in lowering the above mentioned losses and thus, likely contribute to achieving high STH (at zero applied bias) and superior ABPE (under minimal applied bias) as well as lowering electricity cost than DOE target. The superior PEC performance for $[\text{WO}_3-(\text{Sn}_{0.95}\text{Nb}_{0.05})\text{O}_2:\text{N}-600]-2$ NTs can be attributed to significantly improved light absorption characteristics and superior carrier density than $(\text{Sn}_{0.95}\text{Nb}_{0.05})\text{O}_2:\text{N}-600$ NTs and $[\text{WO}_3-(\text{Sn}_{0.95}\text{Nb}_{0.05})\text{O}_2:\text{N}-600]-1$ NTs (**Figure 62**, **Figure 65** and **Table 10**). In addition, the excellent photo-electrochemical performance obtained for $[\text{WO}_3-(\text{Sn}_{0.95}\text{Nb}_{0.05})\text{O}_2:\text{N}-600]-2$ NTs compared to other materials studied herein can be attributed to improved electrochemical charge transfer kinetics (**Figure 67**) and minimum recombination of photo-generated carriers resulting in longer carrier lifetime (~ 20 fold higher

than $(\text{Sn}_{0.95}\text{Nb}_{0.05})\text{O}_2\text{:N-600}$) (**Figure 70** and **Figure 71**). $[\text{WO}_3-(\text{Sn}_{0.95}\text{Nb}_{0.05})\text{O}_2\text{:N-600}]$ -2 NTs displayed excellent long term photo-electrochemical stability, as seen in the CA test carried out under illumination in acidic electrolyte solution for 24 h (**Figure 72**). The above results thus, clearly show that $[\text{WO}_3-(\text{Sn}_{0.95}\text{Nb}_{0.05})\text{O}_2\text{:N-600}]$ -2 NTs is indeed a promising semiconductor material with excellent photo-electrochemical performance and stability displaying a STH of $\sim 3.83\%$ reflective of its promise. Further research into this system and overcoming the losses discussed earlier could also lead to further improvements in the resultant STH efficiencies. The results of the studies described herein are clearly transformational in efficiently producing hydrogen by direct utilization of solar energy in an environment friendly manner. Taken together, the results clearly represent a major milestone in solving the global energy demand with the generation of minimum greenhouse gas emissions.

Conclusions:

The photoelectrochemical activity of the composite bilayer photoanode $[\text{WO}_3-(\text{Sn}_{0.95}\text{Nb}_{0.05})\text{O}_2\text{:N-600}]$ NTs is studied in the present work with consideration of different thicknesses of $(\text{Sn}_{0.95}\text{Nb}_{0.05})\text{O}_2\text{:N-600}$. The work clearly demonstrates the potential of coupling WO_3 with $(\text{Sn}_{0.95}\text{Nb}_{0.05})\text{O}_2\text{:N-600}$, which offers excellent optoelectronic properties, improved charge transport and longer carrier lifetime with minimum recombination of photogenerated carriers (~ 20 fold higher carrier lifetime for $[\text{WO}_3-(\text{Sn}_{0.95}\text{Nb}_{0.05})\text{O}_2\text{:N-600}]$ -2 NTs than $(\text{Sn}_{0.95}\text{Nb}_{0.05})\text{O}_2\text{:N-600}$). This results in excellent photoelectrochemical activity and STH of $\sim 3.83\%$ and ABPE of $\sim 5.1\%$ (at $\sim 0.6\text{V}$ vs RHE), along with negative onset potential for the optimal bilayer materials with the lowest (-0.55 V vs RHE) obtained for $[\text{WO}_3-(\text{Sn}_{0.95}\text{Nb}_{0.05})\text{O}_2\text{:N-600}]$ -2 NTs. The superior light absorption properties along with significantly

improved carrier density ($\sim 5.6 \times 10^{22} \text{ cm}^{-3}$) for $[\text{WO}_3-(\text{Sn}_{0.95}\text{Nb}_{0.05})\text{O}_2:\text{N}-600]-2$ NTs opens up a new territory for this material for different solar energy based applications. An excellent STH of $\sim 3.83\%$ (with no external potential applied) and ABPE of $\sim 5.1\%$ (at $\sim 0.6\text{V}$ vs RHE) is obtained for $[\text{WO}_3-(\text{Sn}_{0.95}\text{Nb}_{0.05})\text{O}_2:\text{N}-600]-2$ NTs, which is the highest reported so far compared to other photoanode materials like ZnO, Fe_2O_3 and TiO_2 , to the best of our knowledge. Accordingly, the composite bilayer, $[\text{WO}_3-(\text{Sn}_{0.95}\text{Nb}_{0.05})\text{O}_2:\text{N}-600]-2$ NTs exhibited excellent long term photoelectrochemical stability with very minimal loss in photocurrent density ($\sim 1\%$) in the acidic electrolyte solution under illumination. Hence, this work will be important for developing photoelectrochemically active and stable semiconductor materials for efficient and economic hydrogen generation from PEC water splitting.

5.4 Co(Ir) SOLID SOLUTION HER ELECTRO-CATALYST FOR CATHODE

5.4.1 STRUCTURAL ANALYSIS OF $\text{Co}_{1-x}(\text{Ir}_x)$ ($x=0.2, 0.3, 0.4$) NANOPARTICLES (NPs)

X-ray diffraction (XRD) study

The XRD patterns of the chemically synthesized $\text{Co}_{1-x}(\text{Ir}_x)$ ($x = 0, 0.2, 0.3, 0.4, 1$) solid solutions are shown in **Figure 75**. The XRD pattern of pure Co ($x=0$) shows the expected hcp structure of lattice parameters, $a= 0.2505$ nm, $c=0.4071$ nm with a molar volume ~ 6.66 cm³/mol, which is in good agreement with the reported literature value.¹¹⁸ The XRD pattern of the pure Ir-NPs synthesized by the reduction of $\text{H}_2\text{IrCl}_6 \cdot x\text{H}_2\text{O}$, displayed in **Figure 75**, shows a face centered cubic structure (fcc) with a lattice parameter $a= 0.3834$ nm and a molar volume (V_m) ~ 8.49 cm³/mol, which is in good agreement with the literature value.²⁶⁴ On the other hand, prevalence of a single phase crystalline fcc solid solution structure is observed for $\text{Co}_{1-x}(\text{Ir}_x)$ of $x=0.3$ and 0.4 , whereas a two-phase mixture of fcc and hcp crystal structure is detected for $\text{Co}_{1-x}(\text{Ir}_x)$ ($x=0.2$) (**Figure 75**Figure 75). The variation of molar volume of fcc- $\text{Co}_{1-x}(\text{Ir}_x)$ with Ir content, shown in **Figure 76** and **Table 13**, shows a linear increase in molar volume with Ir content following the Vegard's law suggesting the formation of a solid solution of Ir and Co with fcc structure. This linear rise in molar volume of $\text{Co}_{1-x}(\text{Ir}_x)$ following increase in Ir content can be explained as occurring due to the higher atomic radius of Ir (~ 180 pm) compared to Co (~ 152 pm).¹¹⁸

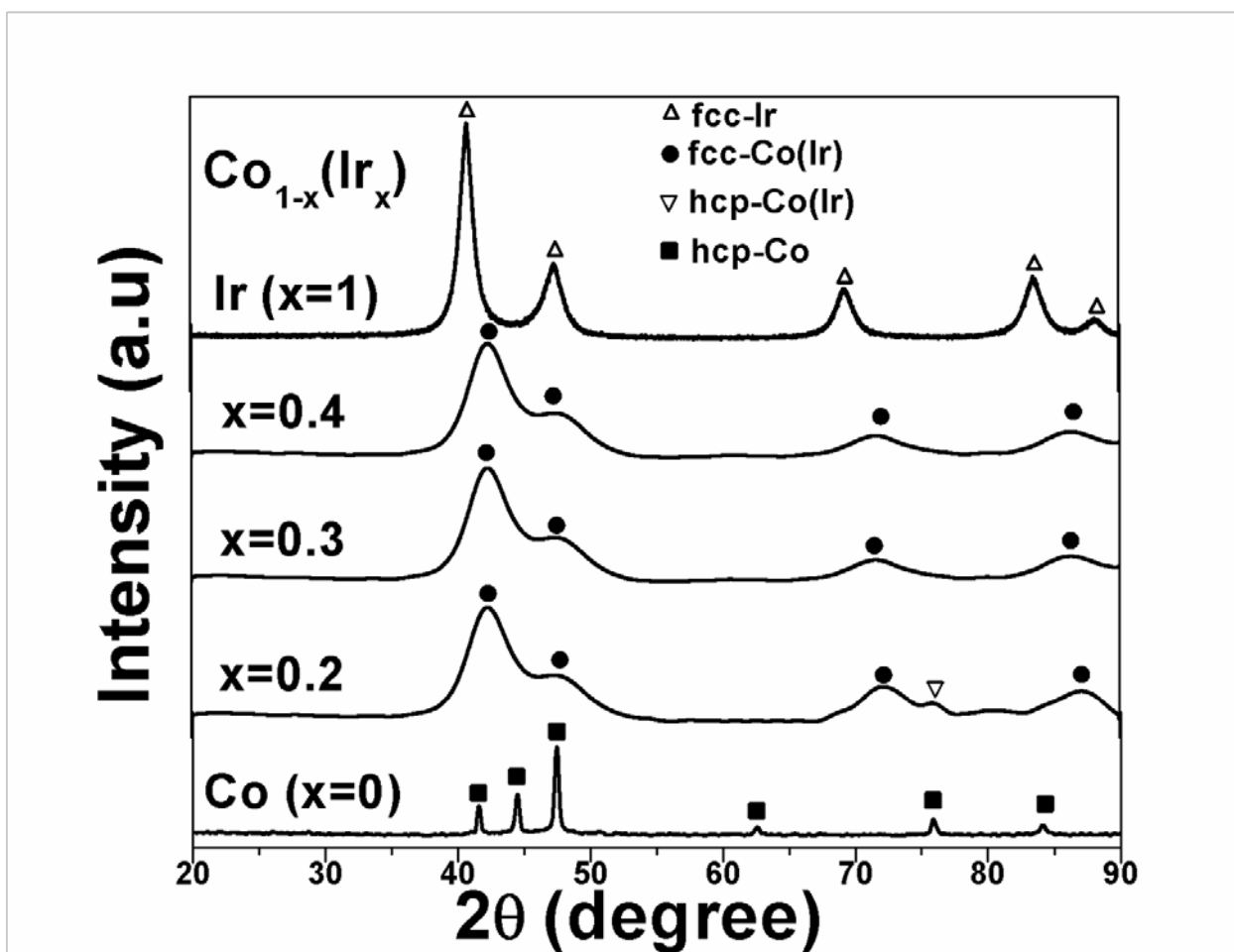


Figure 75: The XRD patterns of $\text{Co}_{1-x}(\text{Ir}_x)$ ($x=0, 0.2, 0.3, 0.4, 1$) nanoparticles in wide angle 2θ scan

It must also be mentioned here that the synthesized $\text{Co}_{1-x}(\text{Ir}_x)$ solid solution is stable exhibiting the fcc crystal structure in contrast to the expected thermodynamically stable equilibrium hcp phase, as evidenced in the Co-Ir binary alloy phase diagram (Figure 77). This preponderant stability of the fcc structure over the hcp structure can be explained by the allotropic transformation occurring during the refinement of the particle size below a critical value, which is mainly governed by the significant contribution of interfacial/surface energy on

the total free energy of the nanocrystalline material.^{265, 266} The particle size of $\text{Co}_{1-x}(\text{Ir}_x)$, with $x=0.3$ and 0.4 , is ~ 4 nm (**Figure 78** and **Figure 79**), which is expected to be below the critical particle size, wherein the fcc cobalt is known to be stable over the normal equilibrium hcp structure due to significant contribution of the interfacial energy thus validating the observed experimental result.^{265, 266}

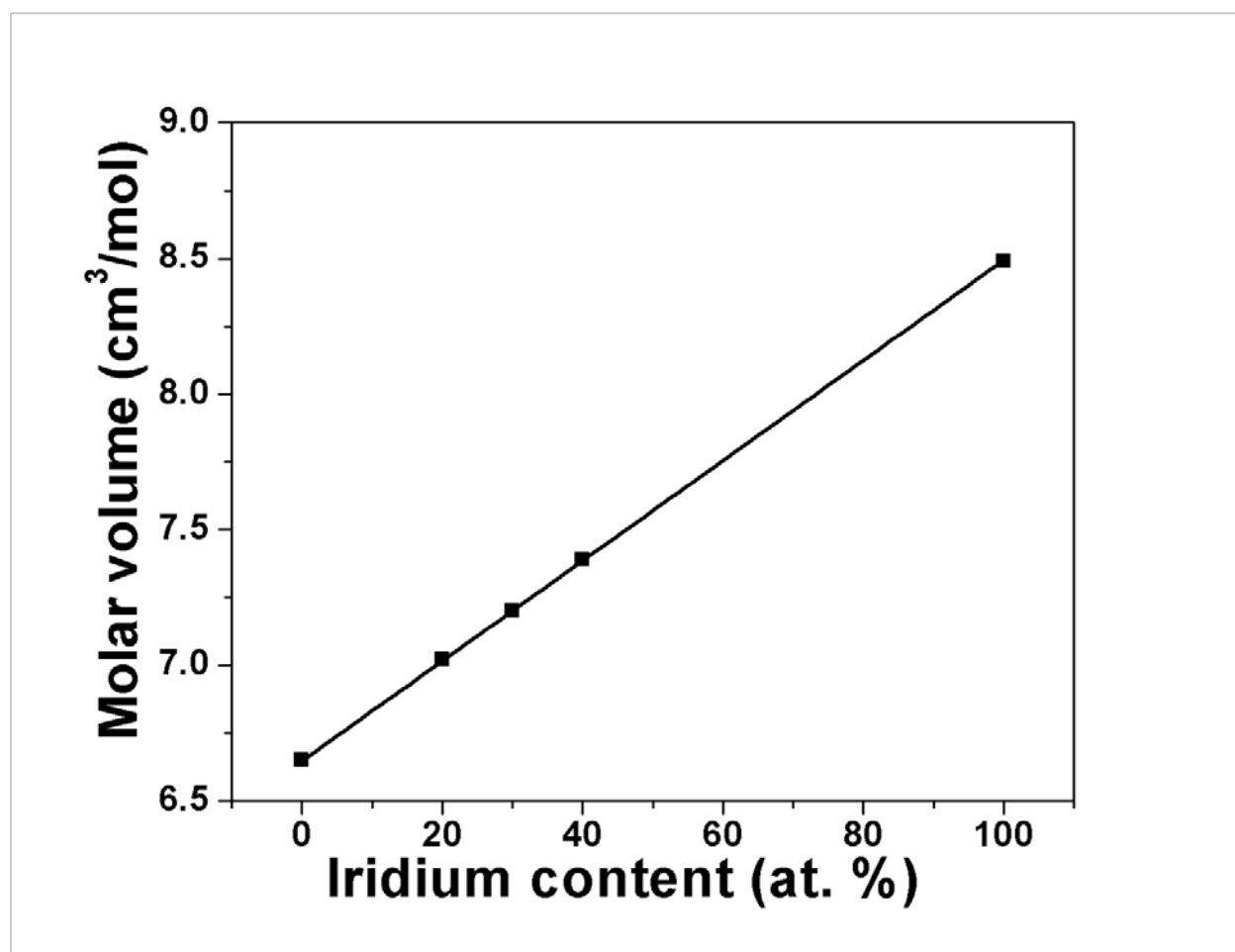


Figure 76: Variation of molar volume of $\text{Co}_{1-x}(\text{Ir}_x)$ ($x=0, 0.2, 0.3, 0.4, 1$) with iridium content

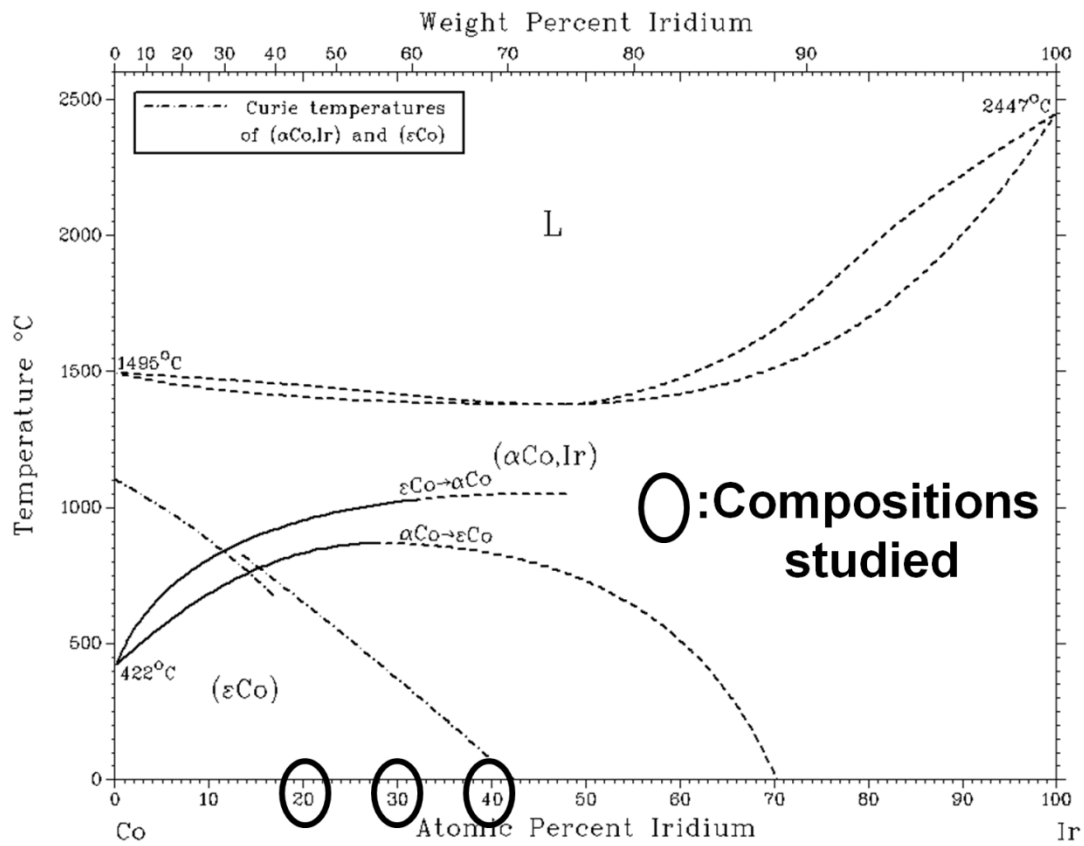


Figure 77: Co-Ir binary equilibrium phase diagram

Table 13: The lattice parameter, molar volume, and composition determined from EDX and XPS analysis of Co_{1-x}(Ir_x) electrocatalyst

Compositions (x)	Lattice parameter (nm)	Molar volume (cm ³ /mol)	Bulk and surface composition by	
			EDAX (bulk)	XPS (surface)
0.0	a=0.2505 c=0.4071	6.66	-	-
0.2	0.3671	7.02	82.1 at.% Co- 17.9 at.% Ir-	61.1 at.% Ir- 38.9 at.% Co
0.3	0.3692	7.22	71.4 at.% Co- 28.6 at.% Ir	66.1 at.% Ir- 33.9 at.% Co
0.4	0.3712	7.42	62.2 at.% Co- 37.8 at.% Ir	68.75 at.% Ir- 31.25 at.% Co
1.0	0.3834	8.49	-	-

TEM/HR-TEM study

The TEM/HRTEM images of Co_{0.7}(Ir_{0.3}), shown in **Figure 78**, also confirms the formation of nanometer sized Co(Ir) particles in the ~5-9 nm range with a lattice spacing of ~0.213 nm also corresponding to the (111) inter-planar spacing of the fcc Co(Ir) alloy. Similarly, the TEM bright field image along with particle size distribution of Co_{0.6}(Ir_{0.4}), displayed in **Figure 79**, shows nanometer sized particles of the solid solution in the size range ~4-7 nm. The

HRTEM image of $\text{Co}_{0.6}(\text{Ir}_{0.4})$, shown in **Figure 80**Figure 80, shows lattice fringes with a spacing of ~ 0.215 nm which corresponds well with the (111) inter-planer spacing of fcc $\text{Co}(\text{Ir})$.

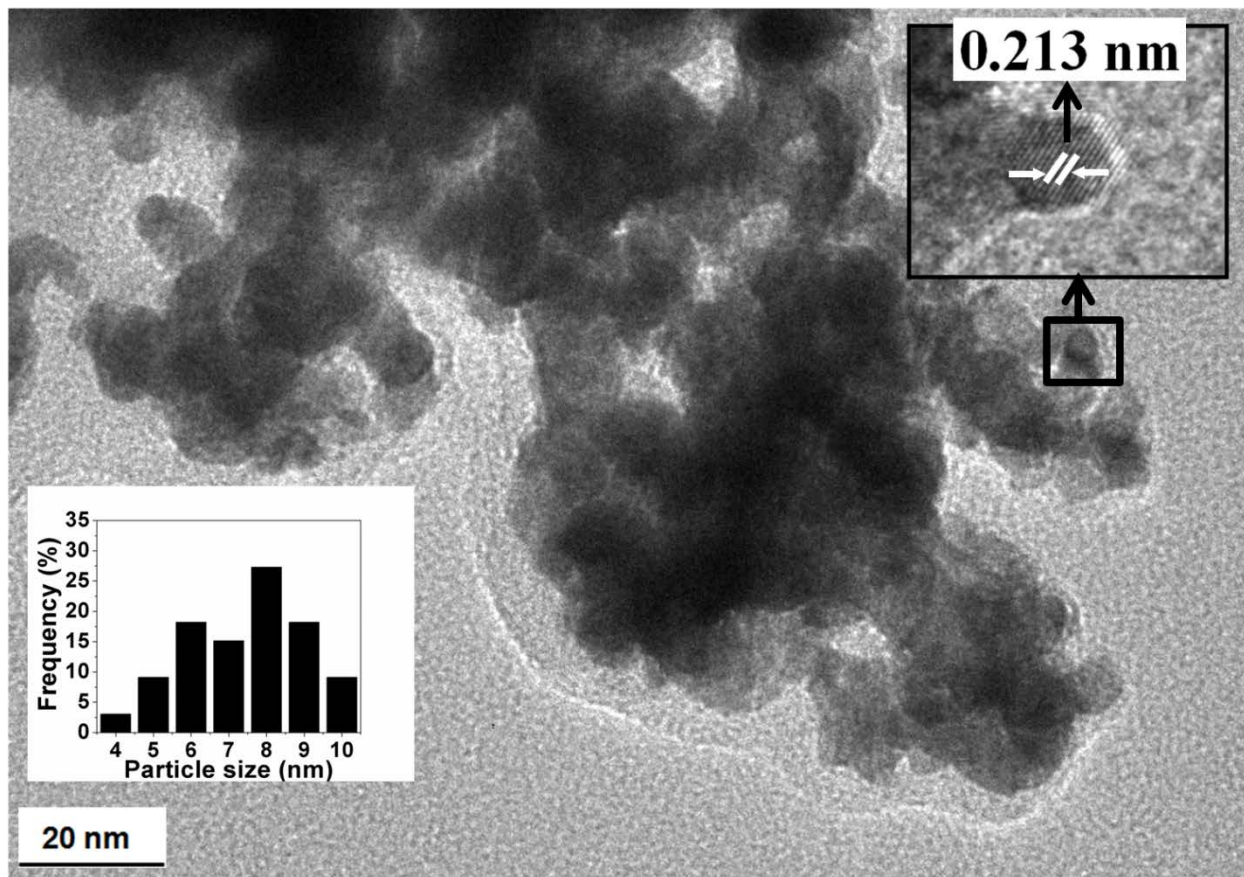


Figure 78: The bright field TEM image of $\text{Co}_{0.7}(\text{Ir}_{0.3})$ shows the presence of fine nanoparticles ($\sim 5\text{-}9$ nm) with HRTEM image showing lattice fringes with a spacing of ~ 0.213 nm

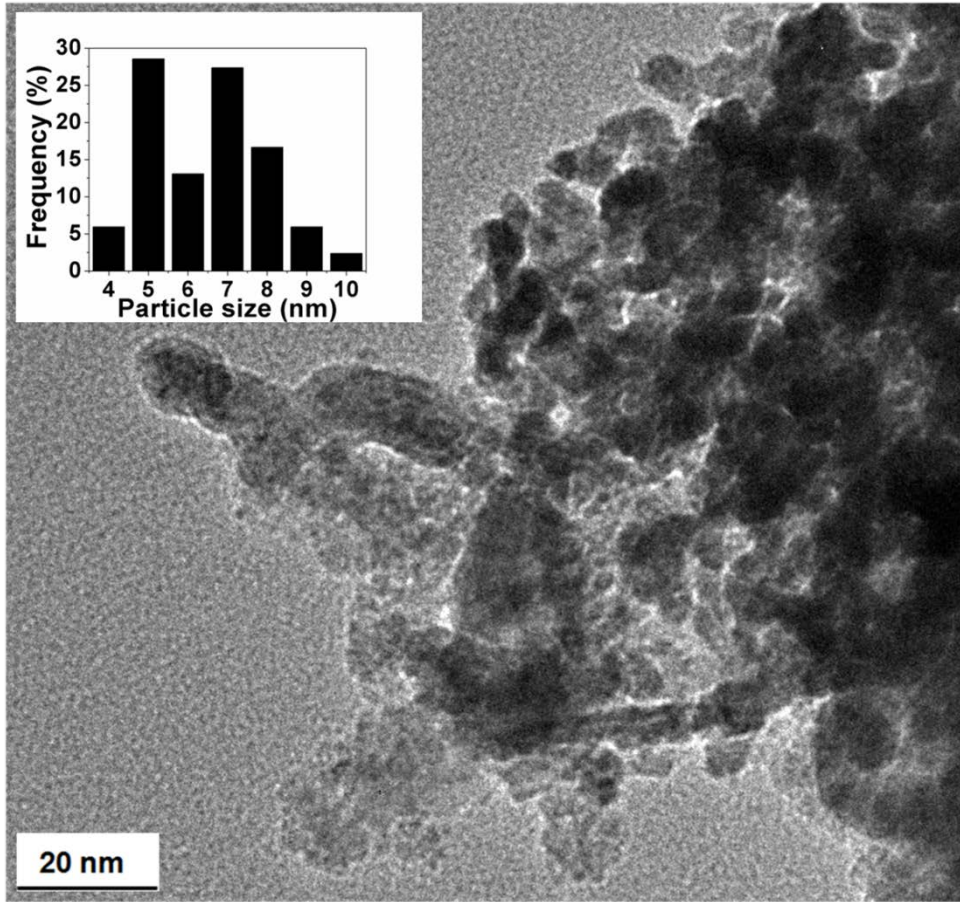


Figure 79: The bright field TEM image of $\text{Co}_{0.6}\text{Ir}_{0.4}$ shows the presence of fine nanoparticles ($\sim 4\text{-}7$ nm)

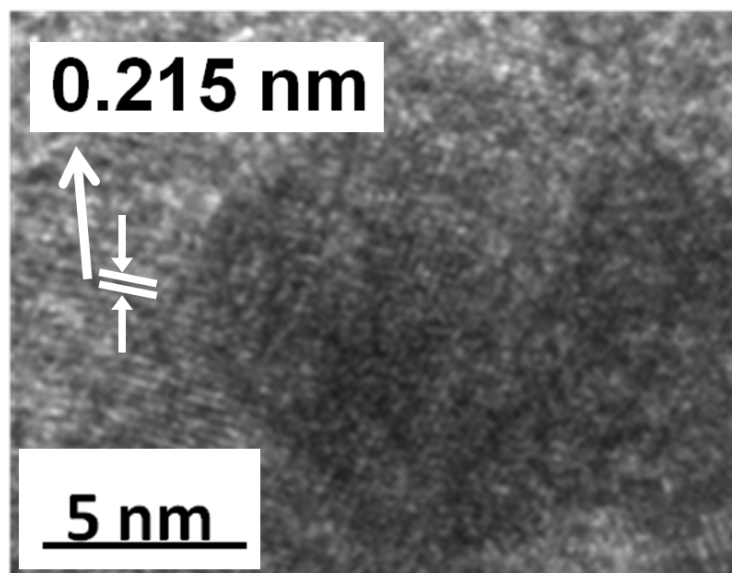


Figure 80: The HRTEM image of Co_{0.6}(Ir_{0.4}) shows lattice fringes with a spacing of ~0.215 nm

SEM/EDX study

The SEM image along with EDAX pattern of a representative composition Co_{0.6}(Ir_{0.4}), collected in **Figure 81**, shows the presence of Co and Ir. Quantitative elemental composition analysis of the Co_{1-x}(Ir_x) electro-catalyst of different compositions obtained by EDX confirmed that the measured elemental compositions of Co and Ir are in close agreement to the nominal composition (**Table 13**). Chlorine and carbon peaks could not be detected in the EDX spectra of all compositions, which indicate that complete removal of chloride ions and carbon (*viz.* stabilizer) has been achieved in the final powder. The elemental x-ray mapping of Co and Ir of Co_{0.6}(Ir_{0.4}) (**Figure 81**) confirms that Co and Ir are homogeneously distributed within the particles.

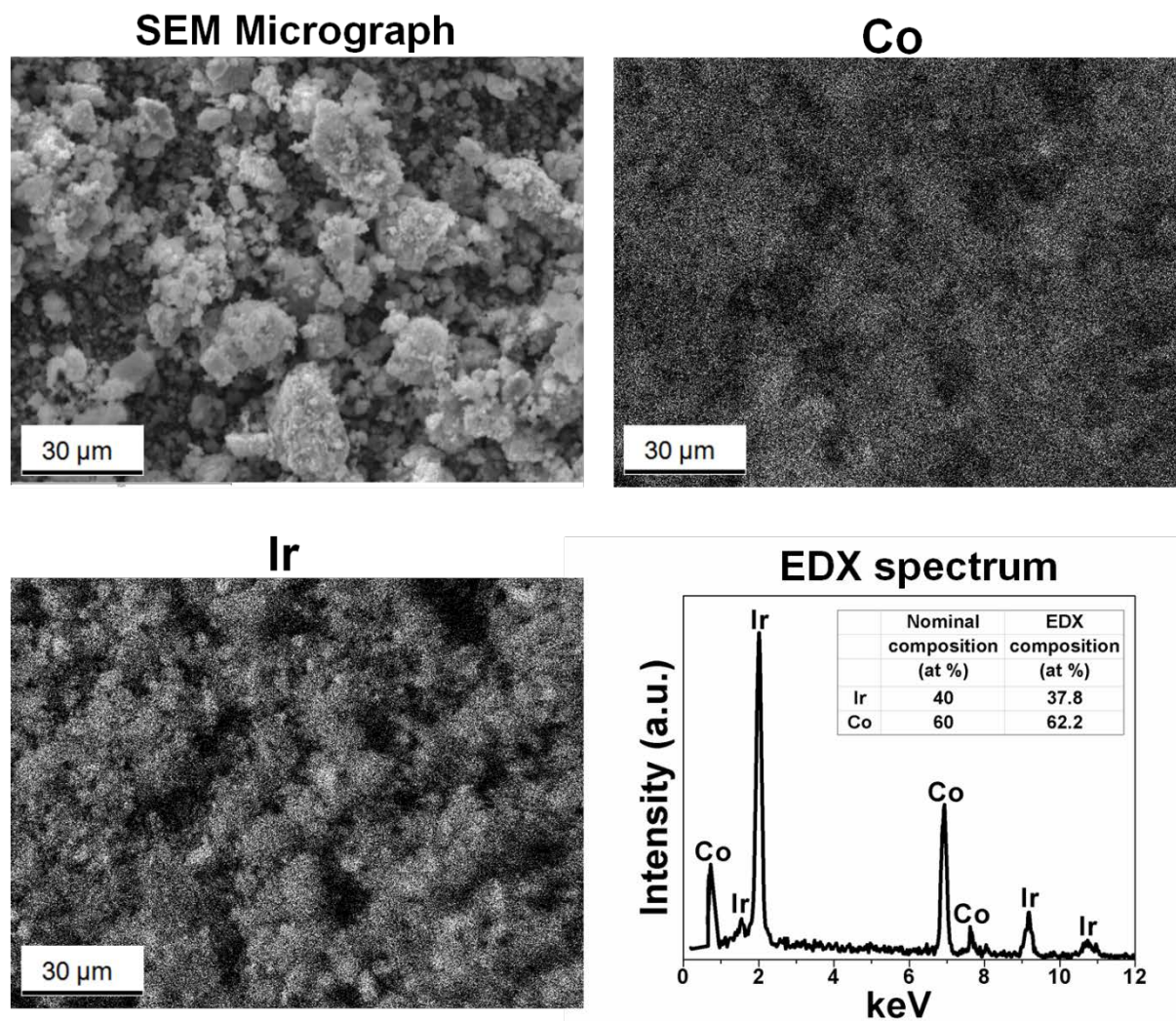


Figure 81: SEM micrograph with x-ray maps of Co and Ir and EDX spectrum of $\text{Co}_{0.6}(\text{Ir}_{0.4})$

X-ray photoelectron spectroscopy study (XPS)

XPS was conducted on the $\text{Co}_{1-x}(\text{Ir}_x)$ electro-catalyst to determine the surface composition and the chemical oxidation states of Co and Ir in the alloyed compositions. The XPS spectra of Ir and Co of $\text{Co}_{1-x}(\text{Ir}_x)$ ($x = 0.2, 0.3, 0.4, 1$) are shown in **Figure 82** and **Figure 83**, respectively. The XPS spectrum for pure Ir shows the presence of Ir $4f_{5/2}$ and $4f_{7/2}$ peaks corresponding to the

zero oxidation state of Ir centered at ~ 63.8 eV and ~ 60.8 eV, which is consistent with the values observed in bulk Ir.²⁶⁷ For $\text{Co}_{1-x}(\text{Ir}_x)$ ($x=0.2, 0.3$ and 0.4), a shift in the Ir $4f_{5/2}$ peak maxima by ~ 0.33 eV, ~ 0.24 eV and ~ 0.22 eV to lower binding energy is observed, which suggests a modification in the electronic structure of Ir.^{268, 269} Similarly, the peak maxima of Ir $4f_{7/2}$ peak is also shifted by ~ 0.28 eV, ~ 0.24 eV and ~ 0.07 eV to lower binding energy for $\text{Co}_{1-x}(\text{Ir}_x)$ ($x=0.2, 0.3$ and 0.4), respectively, which also indicates a modification in the electronic structure of Ir in the alloyed structure referring to the ability of electron transitions to occur in Ir in the alloyed structure.²⁷⁰⁻²⁷²

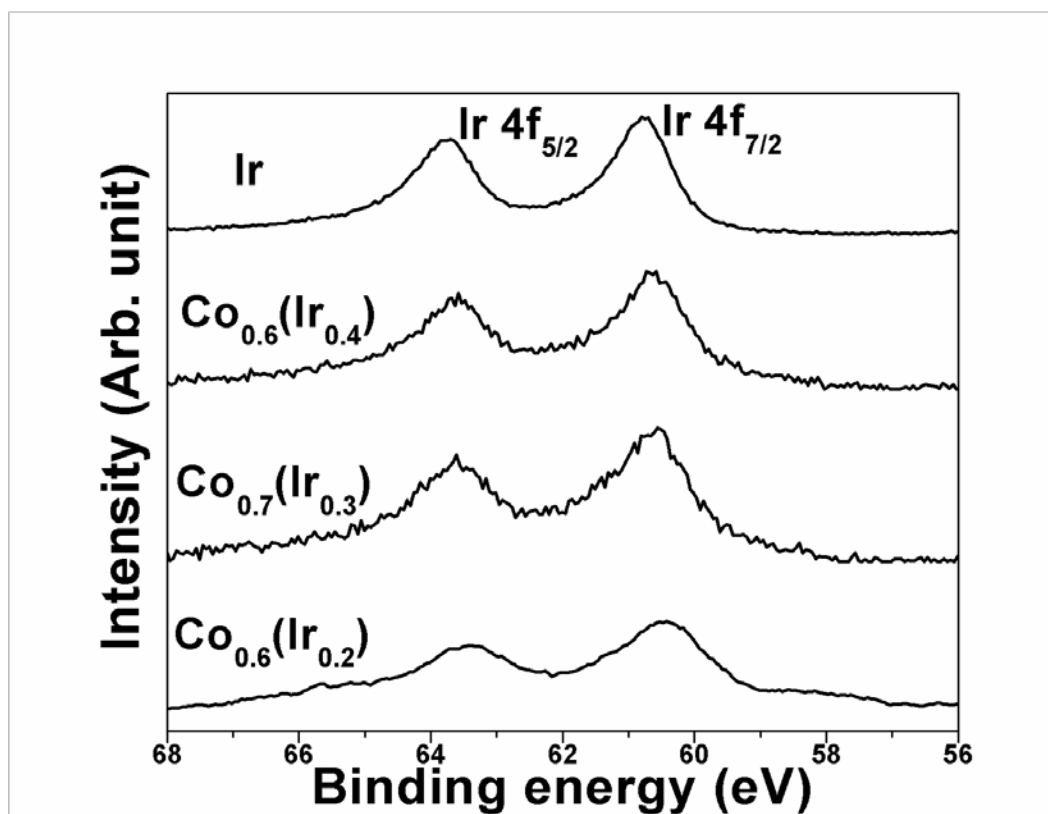


Figure 82: The XPS spectra of $\text{Co}_{1-x}(\text{Ir}_x)$ ($x=0.2, 0.3, 0.4, 1$) showing (a) Ir $4f_{5/2}$ and $4f_{7/2}$ doublet

Additionally, the XPS spectrum of pure Co portrayed in **Figure 83**, shows the presence of Co 2p_{1/2} and 2p_{3/2} peaks at ~793.25 eV and ~777.74 eV, corresponding to the zero oxidation state of Co. In the case of Co_{1-x}(Ir_x) (x=0.2), the Co maxima are shifted by ~0.05 eV and ~0.06 eV to slightly lower binding energy than that of pure Co,²⁷³ again suggesting a modification of the electronic structure of cobalt referring to the possible ease of electron transitions occurring in these systems. Similarly, shift in the Co 2p_{1/2} peak by ~0.1 eV and ~0.2 eV to lower binding energy is observed for Co_{1-x}(Ir_x) (x=0.3 and 0.4), respectively. The maxima of Co 2p_{3/2} peak is also shifted to slightly lower binding energy by ~0.15 eV and ~0.2 eV for Co_{1-x}(Ir_x) (x=0.3 and 0.4), respectively, which suggests modification in electronic structure of Co and the possible ease of electronic transitions in these newly formed alloys.^{268, 269} Furthermore, the surface atomic ratio of Ir/Co and composition, determined by XPS, is 1.57 (39at.% Co-61at.% Ir), 1.95 (34at.% Co-66at.% Ir) and 2.2 (31at.% Co-69at. %Ir) for Co_{1-x}(Ir_x) (x=0.2, 0.3, 0.4), respectively, which suggests a significant solute (Ir) segregation on the surface of the alloy nanoparticles. The surface composition of Co_{1-x}(Ir_x) determined from XPS analysis is tabulated in **Table 13**. The enrichment of iridium on the surface of the nanocrystalline Co_{1-x}(Ir_x) metal catalyst over cobalt is a result of heat treatment of all the synthesized alloy catalysts in (Ar+6.5% H₂) atmosphere at 200^oC. This can be attributed to higher adsorption enthalpy of hydrogen on Ir than Co which facilitate segregation of iridium on the catalyst surface.²⁷⁴⁻²⁷⁶ Similar results have been reported for carbon supported Pd-Co core-shell nanoparticles, where surface segregation was observed in which Pd migrated from the bulk to the surface forming a thin over-layer, due to heat treatment in H₂ atmosphere.²⁷⁷ This rearrangement of Pd and Co was attributed to the higher adsorption

enthalpy of hydrogen and consequently, stronger affinity of hydrogen on Pd than Co. Similar phenomena can therefore be expected to occur in the case of the Co-Ir alloys discussed herein.

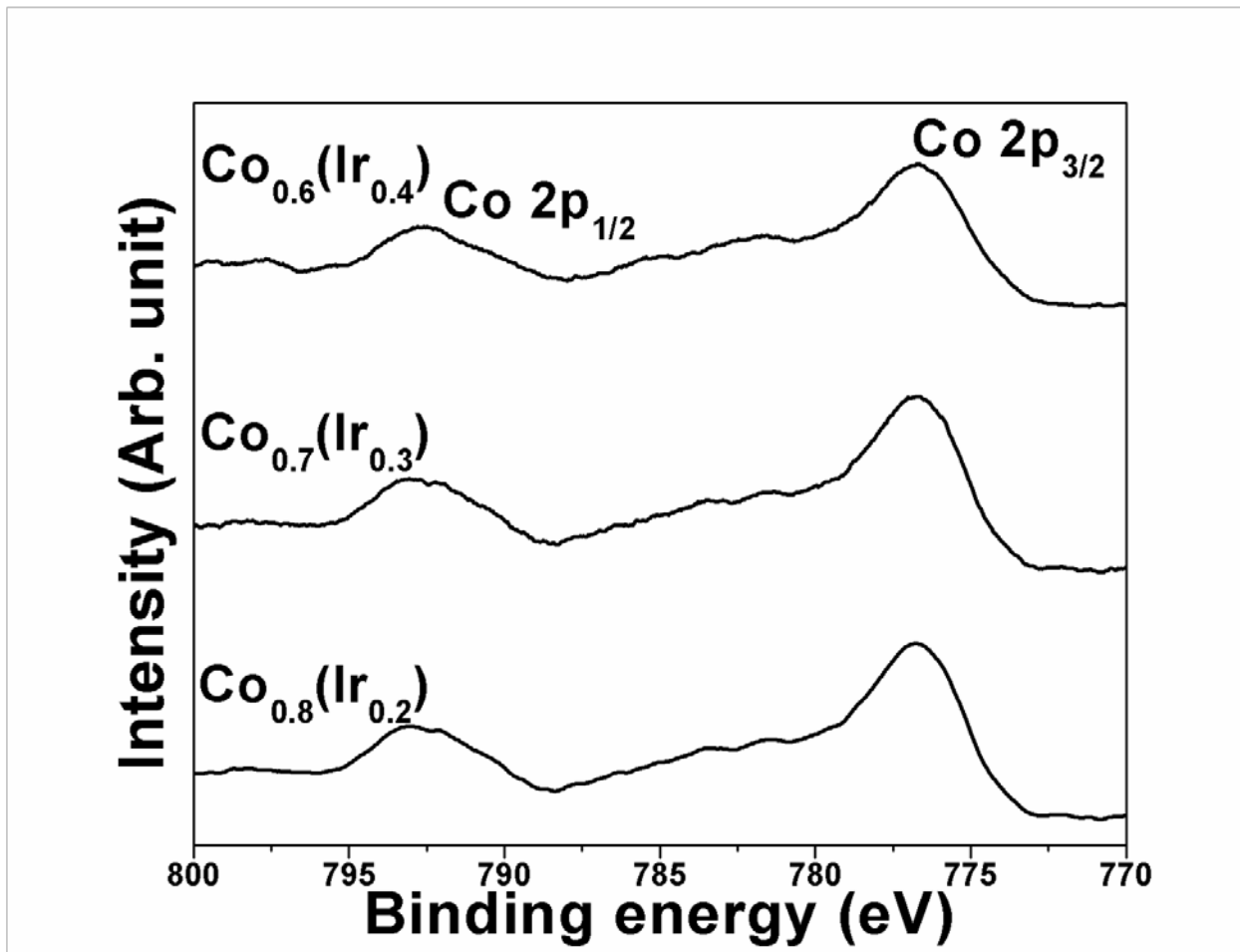


Figure 83: The XPS spectra of Co_{1-x}(Ir_x) (x=0.2, 0.3, 0.4) showing (b) Co 2p_{1/2} and 2p_{3/2} doublet

5.4.2 ELECTROCHEMICAL CHARACTERIZATION OF Co_{1-x}(Ir_x) FOR H₂ PRODUCTION FROM ELECTROLYTIC WATER SPLITTING

Electrochemical activity for HER in electrolytic water splitting

The electrochemical activity of Co_{1-x}(Ir_x) has been studied using linear scan voltammetry in 0.5 M H₂SO₄ electrolyte solution at 26°C. The iR_{Ω} corrected linear scan voltammogram (LSV) curves of Co_{1-x}(Ir_x) (x=0, 0.2, 0.3, 0.4, 1), Ti foil (current collector) and Pt/C are shown in **Figure 84**. The values of the onset overpotential and overpotential required to reach 10 mA/cm², 20 mA/cm² and 100 mA/cm² and current density at (-0.05 V vs RHE) for Co_{1-x}(Ir_x) (x=0, 0.2, 0.3, 0.4, 1) and Pt/C in iR_{Ω} corrected LSV plots, are given in **Table 14**. As shown in **Figure 84**, Ti foil shows poor current density, suggesting that there is no contribution by Ti foil to the current density obtained for the other active electro-catalysts rendering it almost inactive in the voltage range for HER. Pure Co NPs exhibit an onset overpotential of ~0.2 V (vs RHE) and poor current density at (-0.05 V vs RHE) (~27 μ A/cm²), significantly lower than that of Pt/C (~17.6 mA/cm²). This suggests poor electrochemical activity of pure Co NPs for HER.

Table 14: Results of electrochemical characterization for HER of Co_{1-x}(Ir_x) and Pt/C in 0.5 M H₂SO₄ at 26°C

Electro-catalyst, Co _{1-x} (Ir _x)	Onset overpotential (mV, RHE)	Overpotential (mV, RHE) to reach			Current density at (-0.05V vs RHE) (mA/cm ²)
		10 mA/cm ²	20 mA/cm ²	100 mA/cm ²	
x=0.2	10	67	96	310	5.5
x=0.3	10	41	49	83	22
x=0.4	10	39	46	69	29
Ir (x=1)	50	335	470	>700	0.4
Pt/C	10	43	51	95	17.6

The onset overpotential of pure Ir is ~50 mV (vs RHE), which is higher than that of Pt/C (~10 mV) (**Figure 84** and **Table 14**). Also, the current density of Ir NPs (~0.4 mA/cm²) at (-0.05 V vs RHE) is ~98% lower than Pt/C (~17.6 mA/cm²), which can be due to ~40 mV higher onset overpotential of Ir NPs than Pt/C (**Table 14**). The overpotential required for Ir NPs to reach 100 mA/cm² is (~>700 mV) (vs RHE), which is significantly higher than that for Pt/C, which requires an overpotential of ~95 mV (vs RHE; similar to earlier reports^{138, 144, 196-202}) to reach 100 mA/cm², respectively. These results show poor electrochemical activity of pure Co and Ir NPs for HER mainly due to higher onset overpotential and the corresponding overpotential required to obtain higher current density suggesting poor reaction kinetics (discussed later) for

HER, in comparison to Pt/C. The poor electrochemical activity of pure Co and Ir NPs can be due to ΔG_{H^*} of Co and Ir NPs being more negative (-0.24 eV for Co NPs) and positive (0.07 eV for Ir NPs) than 0 eV leading to stronger and weaker Co-H and Ir-H interactions, respectively which is discussed in detail later in the theoretical analysis of $\text{Co}_{1-x}(\text{Ir}_x)$ solid solution system examined in the present study (**Section A.3**).

$\text{Co}_{1-x}(\text{Ir}_x)$ alloys correspondingly show superior electrochemical activity for HER than pure Co NPs and Ir NPs, with an onset overpotential of ~ 10 mV (*vs* RHE), which is similar to that of Pt/C (**Figure 84** and **Table 14**). The overpotential required for $\text{Co}_{1-x}(\text{Ir}_x)$ ($x=0.2$) to reach 100 mA/cm^2 is ~ 310 mV (*vs* RHE), which is higher than that of Pt/C (**Table 14**). Though the onset overpotential of $\text{Co}_{1-x}(\text{Ir}_x)$ ($x=0.2$) is similar to that of Pt/C, $\sim 69\%$ lower current density for $\text{Co}_{1-x}(\text{Ir}_x)$ ($x=0.2$) ($\sim 5.5 \text{ mA/cm}^2$ at -0.05 V vs RHE) and higher overpotential required to reach 100 mA/cm^2 than that of Pt/C ($\sim 17.6 \text{ mA/cm}^2$ at -0.05 V vs RHE) indicates the poor reaction kinetics for the $\text{Co}_{1-x}(\text{Ir}_x)$ ($x=0.2$) alloy compared to that of Pt/C (discussed later).

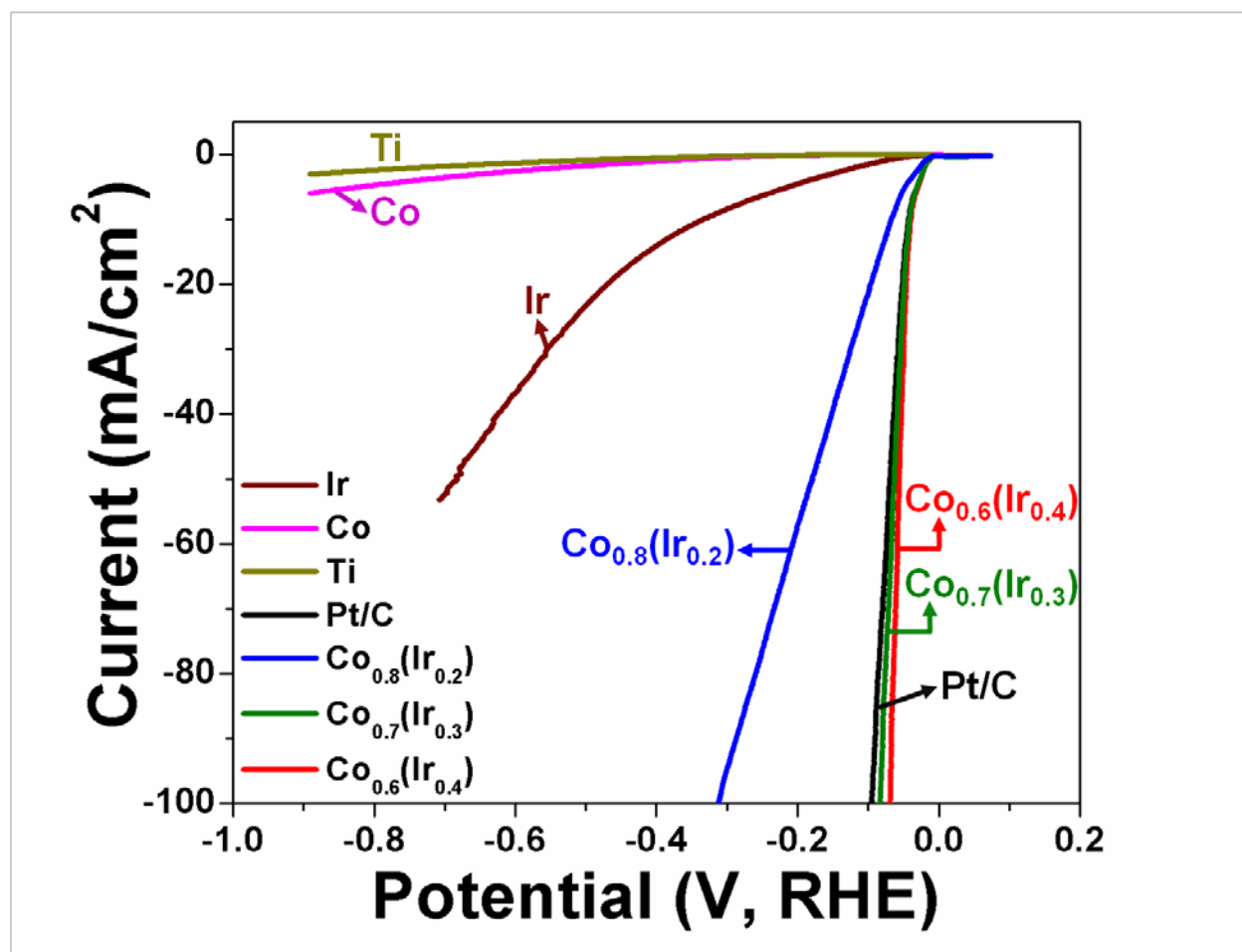


Figure 84: The iR_{Ω} corrected linear scan voltammogram (LSV) curves for HER of $\text{Co}_{1-x}(\text{Ir}_x)$ ($x=0.2, 0.3, 0.4$) and Pt/C, measured in 0.5 M H_2SO_4 at 26 $^{\circ}\text{C}$ at scan rate of 1 mV/sec

$\text{Co}_{1-x}(\text{Ir}_x)$ ($x=0.3$) shows even more superior electrochemical activity for HER than $\text{Co}_{1-x}(\text{Ir}_x)$ ($x=0.2$) and Pt/C exhibiting an overpotential of ~ 83 mV (*vs* RHE) to reach 100 mA/cm^2 , which is lower than that of Pt/C (Table 14). $\text{Co}_{1-x}(\text{Ir}_x)$ ($x=0.4$) also shows excellent electrochemical performance for HER with a reduced overpotential of ~ 69 mV (*vs* RHE) to reach 100 mA/cm^2 , much lower than that of $\text{Co}_{1-x}(\text{Ir}_x)$ ($x=0.2, 0.3$) and Pt/C (Table 14). Also, the values of current density of $\text{Co}_{1-x}(\text{Ir}_x)$ ($x=0.2, 0.3, 0.4$) at (-0.05 V *vs* RHE) are ~ 5.5 mA/cm^2 ,

~ 22 mA/cm² and ~ 29 mA/cm², respectively, which are $\sim 31\%$, $\sim 125\%$ and $\sim 165\%$ of that of Pt/C (~ 17.6 mA/cm²). Additionally, the corresponding current density of the alloys are ~ 14 , ~ 55 and ~ 73 fold higher than that of pure Ir-NPs (~ 0.4 mA/cm²) and significantly higher than that of pure Co NPs (~ 27 μ A/cm²) (**Table 14**). Thus, the current density at (-0.05 V vs RHE) for Co_{1-x}(Ir_x) (x=0.2, 0.3, 0.4) increases with Ir content, which suggests improvement in the reaction kinetics with increase in the Ir content in the solid solution system. The excellent electrochemical activity of Co_{1-x}(Ir_x) (x= 0.3, 0.4) compared to Co NPs, Ir NPs and Pt/C, can be attributed to the lower overpotential required for the solid solution electro-catalysts to reach 100 mA/cm² and overall improved reaction kinetics, which are superior than that of Co NPs, Ir NPs and Pt/C (discussed later). The superior electrochemical activity of the solid solution alloys, Co_{1-x}(Ir_x) (x=0.2, 0.3, 0.4) compared to pure Co and Ir NPs can be due to ΔG_{H^*} of Co_{1-x}(Ir_x) lying between that of pure Co and Ir, resulting in facile adsorption and desorption kinetics of hydrogen from the electro-catalyst surface sites and thus resulting in superior electrochemical activity, as discussed later in the theoretical analysis studies section (**Section A.3**).

Though the onset overpotential of Co_{1-x}(Ir_x) (x= 0.2, 0.3, 0.4) and Pt/C are almost similar, the current density of Co_{1-x}(Ir_x) (x=0.4) is higher than Co_{1-x}(Ir_x) (x= 0.2, 0.3) and Pt/C, as shown in **Table 14**. This suggests faster reaction kinetics on Co_{1-x}(Ir_x) (x=0.4) than those on Co_{1-x}(Ir_x) (x=0.2, 0.3) and Pt/C electro-catalysts. The improvement in reaction kinetics of the solid solution electro-catalysts, Co_{1-x}(Ir_x) is important to achieve the superior electrochemical activity compared to that of Pt/C. Hence, electrochemical impedance spectroscopy (EIS) has been carried out to further study the reaction kinetics to determine the charge transfer resistance (R_{ct}) for all the electro-catalysts studied in this work.

Electrochemical Impedance spectroscopy (EIS)

To understand the reaction kinetics of HER on $\text{Co}_{1-x}(\text{Ir}_x)$ ($x=0, 0.2, 0.3, 0.4, 1$), EIS was conducted to study the charge transfer resistance (R_{ct}) at the electro-catalyst/electrolyte interface in acidic medium using 0.5 M H_2SO_4 as electrolyte solution at 26°C at (-0.05V vs RHE) . The EIS study has also been used to determine the ohmic resistance (R_Ω) of $\text{Co}_{1-x}(\text{Ir}_x)$ ($x=0, 0.2, 0.3, 0.4, 1$) and Pt/C, which was further used for iR_Ω correction in LSV plots of all electro-catalysts in this study. R_Ω and R_{ct} of $\text{Co}_{1-x}(\text{Ir}_x)$ and Pt/C are obtained by fitting the experimental data with an equivalent circuit model $R_\Omega(R_{ct}Q_1)$, where R_Ω is the resistance contributed by components such as the wiring, electrolyte, electro-catalyst and electrode^{247, 278}; R_{ct} is charge transfer resistance; Q_1 is the constant phase element representing contribution from the capacitance behavior of the catalyst surface.^{114, 159, 160} The values of R_Ω and R_{ct} obtained after fitting the experimental data with the equivalent circuit model $R_\Omega(R_{ct}Q_1)$ are given in **Table 15**. **Figure 85** and **Figure 86** shows the EIS plots of $\text{Co}_{1-x}(\text{Ir}_x)$ ($x = 0.2, 0.3, 0.4$) along with pure Co NPs, Ir NPs and Pt/C. The EIS plots show a well-formed semicircular arc for all the electro-catalysts. The charge transfer resistance (R_{ct}) is determined from the diameter of the semicircular arc in the EIS plot and given in **Table 15**.

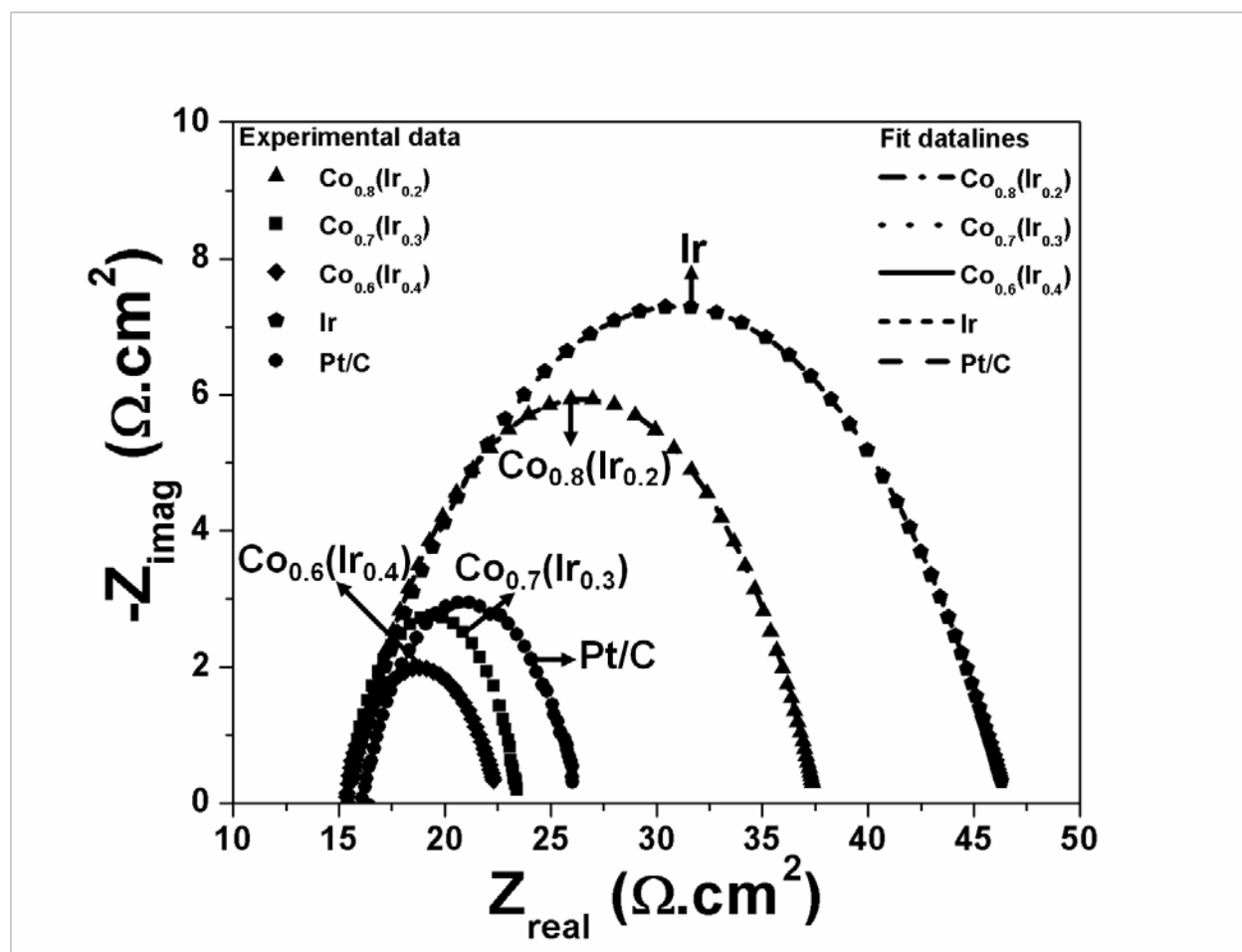


Figure 85: EIS spectra of $Co_{1-x}(Ir_x)$ ($x=0.2, 0.3, 0.4$), Ir-NPs and Pt/C obtained at (-0.05V vs RHE) in 0.5 M H_2SO_4 at 26^oC in the frequency range of 100 mHz to 100 kHz

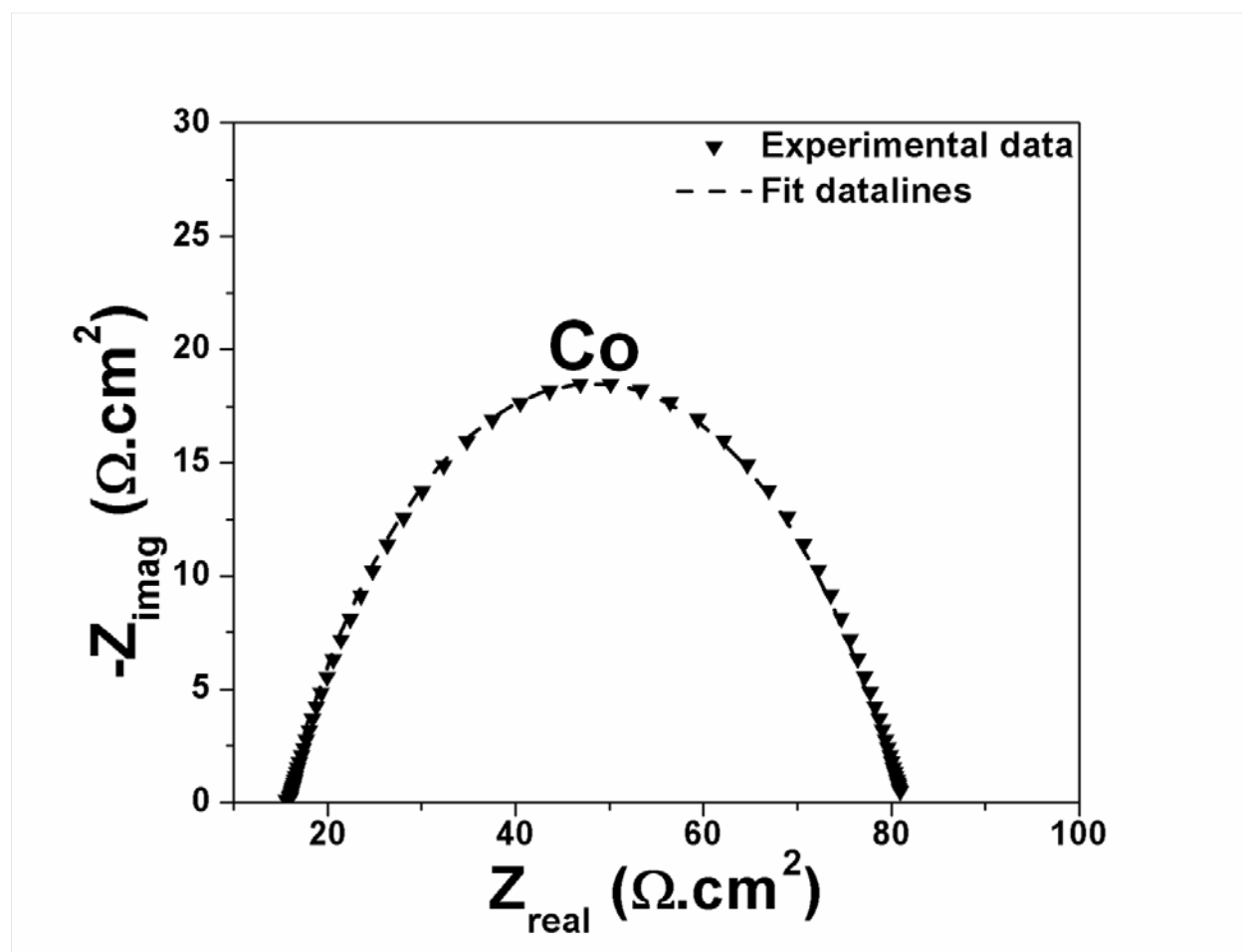


Figure 86: EIS spectra of pure Co NPs obtained at (-0.05V vs RHE) in 0.5 M H₂SO₄ at 26^oC in the frequency range of 100 mHz to 100 kHz

The R_{ct} of pure Co ($\sim 65.4 \Omega \cdot \text{cm}^2$) is higher than that of pure Ir NPs ($\sim 30.91 \Omega \cdot \text{cm}^2$) and Pt/C ($\sim 10.8 \Omega \cdot \text{cm}^2$) (Table 15). These results thus show the poor reaction kinetics and thus, poor electrochemical activity of pure Co and Ir NPs compared to that of Pt/C. Solid solution electro-catalysts Co_{1-x}(Ir_x) ($x=0.2, 0.3, 0.4$) show lower R_{ct} and thus, improved electrochemical activity, in comparison to pure Co and Ir NPs, suggesting synergistic effect of alloying of Co and Ir in improving the reaction kinetics of the solid solution electro-catalysts, compared to pure Ir and Co

NPs (**Table 15**). The R_{ct} for $Co_{1-x}(Ir_x)$ ($x=0.2, 0.3, 0.4$) decreases with increase in iridium content suggesting enhancement in charge-transfer kinetics with increase in iridium content attaining a minimum R_{ct} value for $Co_{0.6}(Ir_{0.4})$ ($\sim 7.39 \Omega.cm^2$). R_{ct} of $Co_{0.7}(Ir_{0.3})$ ($\sim 8.2 \Omega.cm^2$) and $Co_{0.6}(Ir_{0.4})$ ($\sim 7.39 \Omega.cm^2$) is lower than $Co_{0.8}(Ir_{0.2})$ ($\sim 22.4 \Omega.cm^2$) and Pt/C ($\sim 10.8 \Omega.cm^2$) suggesting improved reaction kinetics and hence, superior electrochemical activity of the two specific alloys, $Co_{1-x}(Ir_x)$ ($x=0.3, 0.4$) compared to $Co_{1-x}(Ir_x)$ ($x=0.2$) and Pt/C.

Table 15: Results of EIS analysis of $Co_{1-x}(Ir_x)$ and Pt/C, carried out at (-0.05 V vs RHE) in frequency range of 100mHz-100kHz in 0.5 M H_2SO_4 at 26⁰C and Tafel plot analysis

Electro-catalyst, $Co_{1-x}(Ir_x)$	R_{ct} ($\Omega.cm^2$)	Tafel slope (mV/dec)	Exchange current density, i_0 (mA/cm ²)
Co ($x=0$)	65.4	114	0.08
$x=0.2$	22.4	37	0.22
$x=0.3$	8.2	30.7	0.4
$x=0.4$	7.39	30	0.43
Ir ($x=1$)	30.91	63	0.2
Pt/C	10.8	31.6	0.38

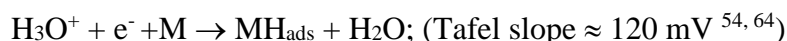
Possible mechanism of HER on $Co_{1-x}(Ir_x)$ ($x=0.2, 0.3, 0.4$) electro-catalysts

The Tafel slope is an important parameter characterizing the activity of electro-catalysts, related to the possible elementary steps involved in HER inherent to the catalyst material. HER is

known to occur on the electro-catalyst surface by two possible mechanisms, i.e., Volmer- Heyrovsky mechanism or Volmer- Tafel mechanism, each containing two reaction steps^{54, 64}:

Volmer- Heyrovsky HER mechanism:

Volmer reaction:



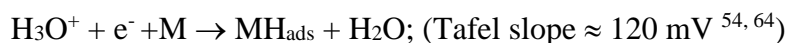
Heyrovsky reaction:



or

Volmer- Tafel HER mechanism:

Volmer reaction:



Tafel reaction:



The values of Tafel slope and exchange current density (i_0) (which give information about the inherent kinetics) determined from the Tafel plots for all the electro-catalysts, are given in **Table 15**. The Tafel slope of $\text{Co}_{1-x}(\text{Ir}_x)$ ($x=0.2, 0.3, 0.4$), Pt/C, pure Co and pure Ir, calculated from the iR_Ω corrected Tafel plots (in 0.5 M H_2SO_4), are ~ 114 mV/dec, ~ 37 mV/dec, ~ 30.7 mV/dec, ~ 30 mV/dec, ~ 63 mV/dec and ~ 31.6 mV/dec (similar to earlier reports^{144, 196, 198, 201, 279}), respectively, as shown in **Figure 87**, **Figure 88** and **Figure 89**, respectively. The decrease in Tafel slope with increase in Ir content for $\text{Co}_{1-x}(\text{Ir}_x)$ shows improvement in electrochemical activity with increase in Ir content for $\text{Co}_{1-x}(\text{Ir}_x)$. The lower Tafel slope of $\text{Co}_{1-x}(\text{Ir}_x)$ ($x=0.3, 0.4$) contrasted to $\text{Co}_{1-x}(\text{Ir}_x)$ ($x=0.2$), pure Co, pure Ir and Pt/C suggests the superior electrochemical activity of $\text{Co}_{1-x}(\text{Ir}_x)$ ($x=0.3, 0.4$) for HER than $\text{Co}_{1-x}(\text{Ir}_x)$ ($x=0.2$), pure Co, pure Ir and Pt/C. The

Tafel slope of $\text{Co}_{1-x}(\text{Ir}_x)$ ($x= 0.3, 0.4$) shows that the HER proceeds through Volmer-Tafel reaction, which is also the same for Pt/C^{64, 144}. The exchange current density (i_0) for electrocatalyst materials is determined by extrapolating the Tafel plots^{144, 199}. Accordingly, the value of i_0 for $\text{Co}_{1-x}(\text{Ir}_x)$ ($x= 0.2, 0.3, 0.4$) increases with increase in Ir content, suggesting the enhancement in electrochemical activity with increase in Ir content (**Table 15**).

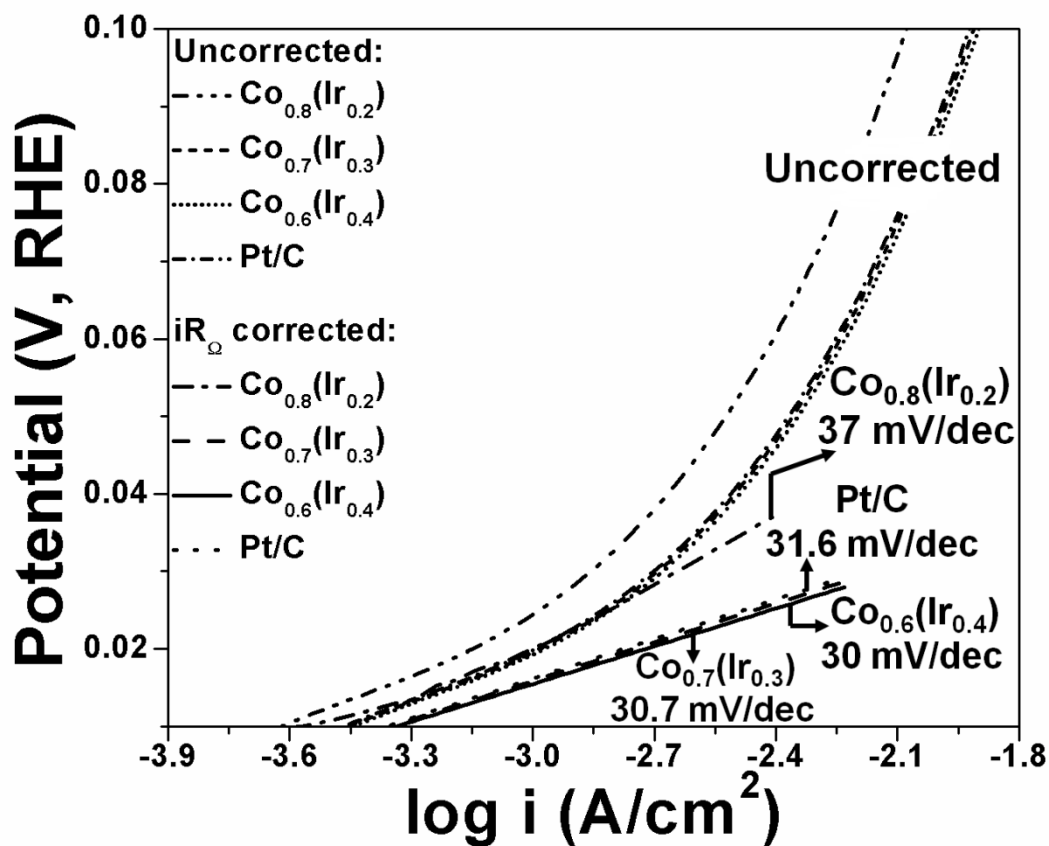


Figure 87: Tafel plot of $\text{Co}_{1-x}(\text{Ir}_x)$ ($x=0.2, 0.3, 0.4$) and Pt/C, before and after iR_{Ω} correction (in 0.5 M H_2SO_4)

It is also noteworthy to observe that i_0 for $\text{Co}_{1-x}(\text{Ir}_x)$ ($x= 0.3, 0.4$) corresponding to ~ 0.4 mA/cm^2 and ~ 0.43 mA/cm^2 are $\sim 6\%$ and $\sim 14\%$ higher than that of Pt/C (~ 0.38 mA/cm^2 similar to earlier reports^{199, 201, 202}), respectively suggesting the excellent inherent electrochemical reaction kinetics of the $\text{Co}_{1-x}(\text{Ir}_x)$ ($x= 0.3, 0.4$) alloys reflecting their superior response than that of Pt/C. $\text{Co}_{1-x}(\text{Ir}_x)$ ($x=0.4$) exhibited the lowest Tafel slope and the highest exchange current density in acidic media compared to other reported non-noble metals based HER electrocatalysts to date, to the best of our knowledge^{132, 200, 280, 281}. The lower Tafel slope and higher i_0 of $\text{Co}_{1-x}(\text{Ir}_x)$ ($x= 0.3, 0.4$) compared to pure Co and pure Ir suggests the synergistic effect of alloying of Ir with Co aiding in the modification of the electronic structure of Co which is also seen in the XPS analysis (**Figure 82** and **Figure 83**) exhibiting the excellent electrochemical activity compared to pure Co and pure Ir. These results thus suggest the excellent electrochemical activity of $\text{Co}_{1-x}(\text{Ir}_x)$ ($x= 0.3, 0.4$), indicating their superior electrochemical response for HER compared to Pt/C.

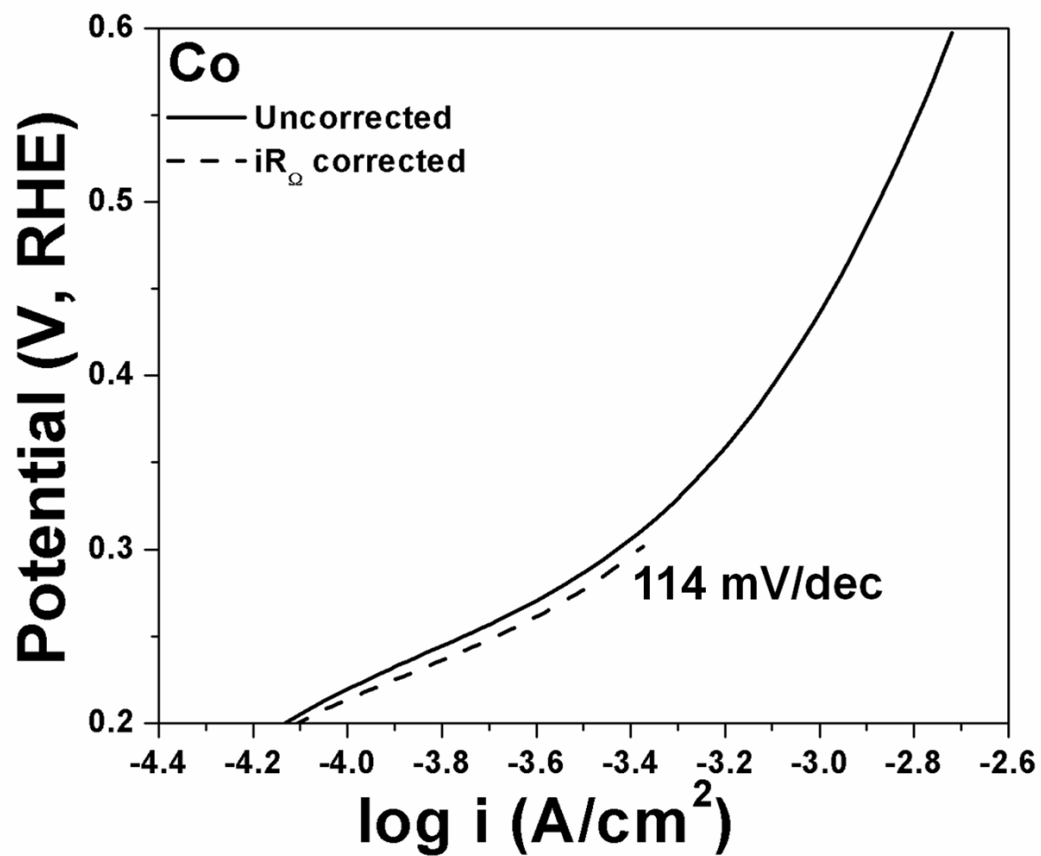


Figure 88: Tafel plot of Co-NPs, before and after iR_{Ω} correction (in 0.5 M H_2SO_4)

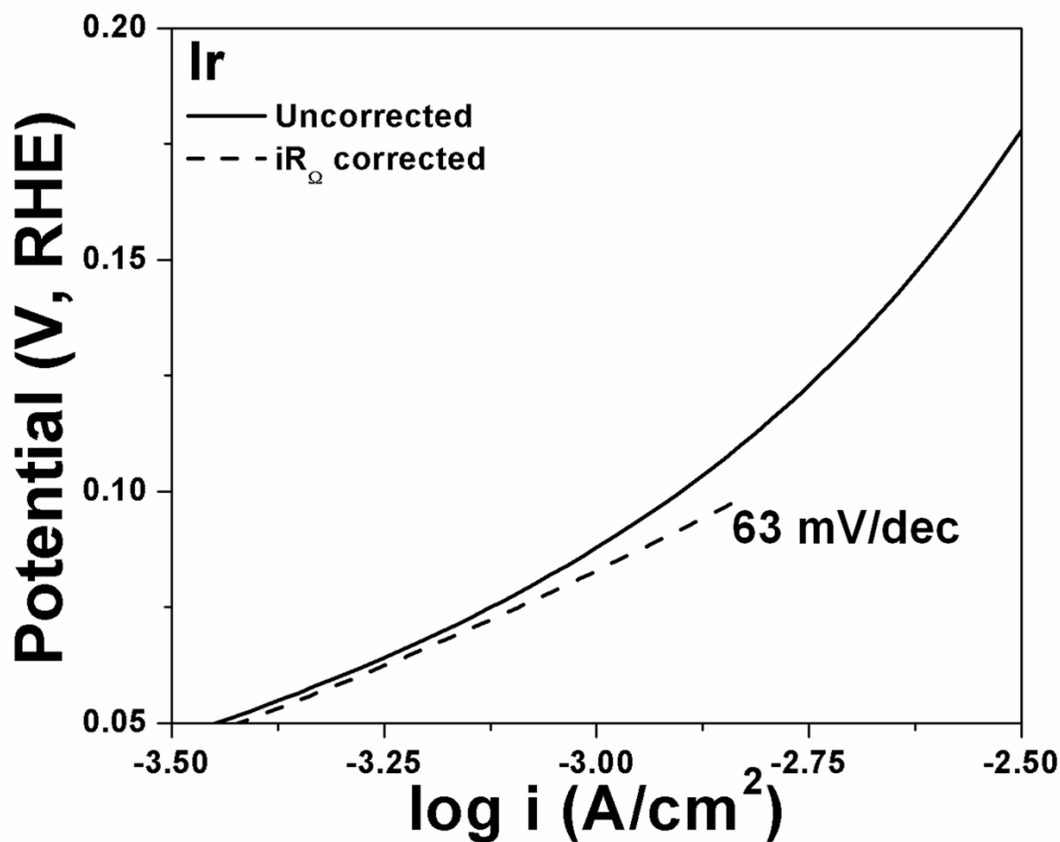


Figure 89: Tafel plot of Ir-NPs, before and after iR_{Ω} correction (in 0.5 M H_2SO_4)

Electrochemical stability test

The electrochemical stability of $Co_{1-x}(Ir_x)$ ($x=0.3, 0.4$) electro-catalysts was studied by conducting chronoamperometry (CA) test for 24 h at a constant potential of (-0.05 V vs RHE). The CA curves of $Co_{1-x}(Ir_x)$ ($x=0.3, 0.4$) are shown in **Figure 90**, alongside that of Pt/C. A negligible loss in current density is observed for the two specific alloys, $Co_{1-x}(Ir_x)$ ($x=0.3, 0.4$), as well as, Pt/C, suggesting the superior electrochemical stability of $Co_{1-x}(Ir_x)$ ($x=0.3, 0.4$), similar to that of Pt/C. and also to Ni_2P (reported in ¹³⁷) which has been recently identified as a

promising HER electro-catalyst as replacement of Pt with its superior electrochemical activity and long term stability in highly aggressive acidic conditions ^{136, 137}. The ICP analysis of electrolyte solution collected after 24 h of electrochemical testing does not indicate any Ir to have leached out from the electro-catalyst, whereas minimal (~0.01 ppm) Co was detected in the electrolyte solution for both $\text{Co}_{1-x}(\text{Ir}_x)$ ($x=0.3, 0.4$) alloys. These results thus show the excellent electrochemical stability of the $\text{Co}_{1-x}(\text{Ir}_x)$ ($x=0.3, 0.4$) alloys similar to that of Pt/C.

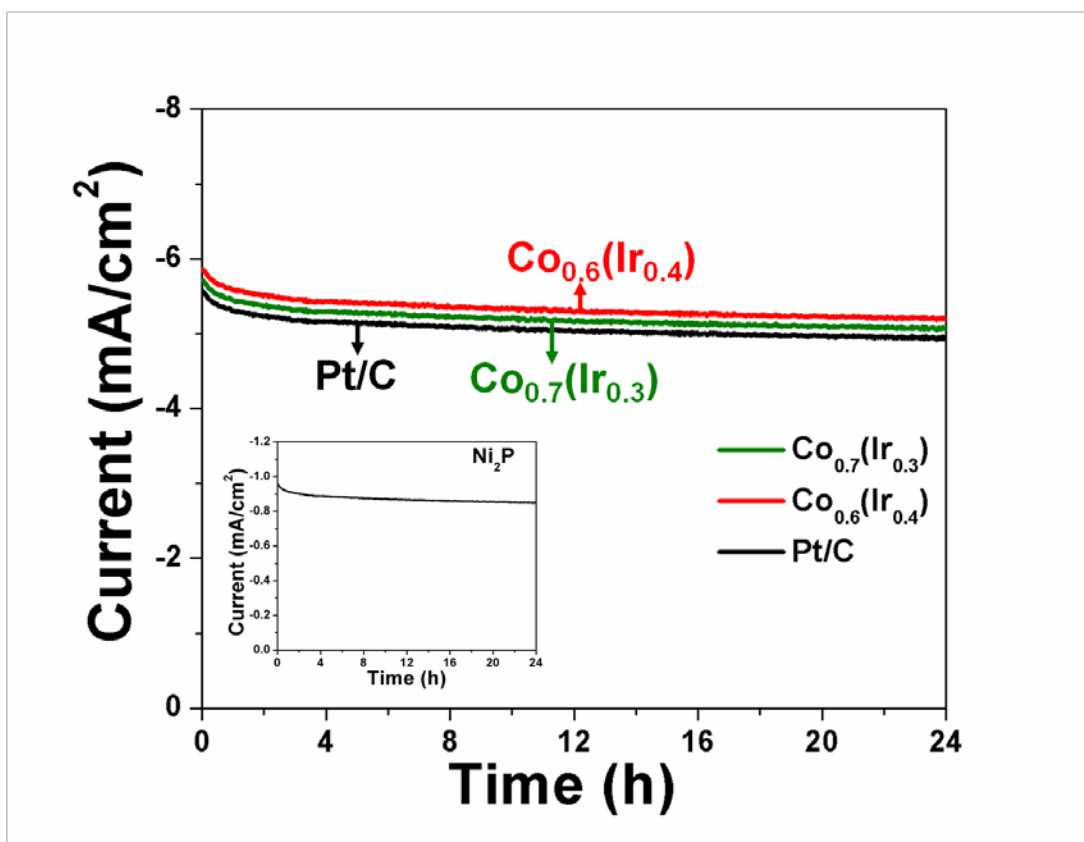


Figure 90: The variation of current vs time in the chronoamperometry test of $\text{Co}_{1-x}(\text{Ir}_x)$ ($x=0.3, 0.4$) and Pt/C, performed in a 0.5 M H_2SO_4 solution under a constant potential of (-0.05V vs RHE) at 26°C for 24 h

5.4.3 ELECTROCHEMICAL CHARACTERIZATION OF $\text{Co}_{1-x}(\text{Ir}_x)$ ($x=0.3, 0.4$) IN PEC WATER SPLITTING CELL

Following the excellent electrochemical activity exhibited by $\text{Co}_{1-x}(\text{Ir}_x)$ ($x=0.3, 0.4$) for HER superior to that of the state of the art Pt/C in electrolytic water splitting, the solid solution electro-catalysts have also been studied as electro-catalyst for HER in photoelectrochemical water splitting system, using $(\text{Sn}_{0.95}\text{Nb}_{0.05})\text{O}_2\text{:N-600}$ NTs as photoanode/working electrode based on our earlier studies ⁷⁶. As mentioned earlier, in the previous study on $(\text{Sn}_{0.95}\text{Nb}_{0.05})\text{O}_2\text{:N-600}$ NTs as photoanode, a maximum applied bias photon-to-current efficiency (ABPE) of $\sim 4.1\%$ was obtained at applied potential of $\sim 0.75\text{V}$ (*vs* RHE) using Pt wire as the counter electrode. Hence, in this study, chronoamperometry was conducted for $(\text{Sn}_{0.95}\text{Nb}_{0.05})\text{O}_2\text{:N-600}$ NTs (working electrode/photoanode) under illumination (100 mW/cm^2) by applying a constant potential of $\sim 0.75\text{V}$ (*vs* RHE) for an extended period of time (24 h) using $\text{Co}_{1-x}(\text{Ir}_x)$ ($x=0.3, 0.4$) as the cathode electro-catalysts. After each 1 h interval, the amount of generated H_2 gas (at cathode) was measured by using a gas chromatograph (helium as the carrier gas, Agilent 7820A), which was further used for determination of ABPE. For comparison, ABPE was also determined for Pt/C as the cathode electro-catalyst, using same protocol followed for $\text{Co}_{1-x}(\text{Ir}_x)$ ($x=0.3, 0.4$).

The amount of H_2 obtained as a function of irradiation time using $\text{Co}_{1-x}(\text{Ir}_x)$ ($x=0.3, 0.4$) alloys and Pt/C, as cathode electro-catalysts, are shown in **Figure 91**, respectively. At the end of 24 h, the amount of H_2 gas generated for $\text{Co}_{1-x}(\text{Ir}_x)$ ($x=0.3, 0.4$) is $\sim 210\text{ }\mu\text{mol/h/cm}^2$ and $\sim 291\text{ }\mu\text{mol/h/cm}^2$, respectively, which is correspondingly $\sim 40\%$ and $\sim 93\%$ higher than that of Pt/C

($\sim 151 \mu\text{mol/h/cm}^2$). The higher yield of H_2 gas generated by using $\text{Co}_{1-x}(\text{Ir}_x)$ ($x=0.3, 0.4$) alloys compared to Pt/C can be attributed to the improved reaction kinetics, as seen in the EIS analysis (Figure 85 and Table 15), Tafel analysis (Figure 87 and Table 15) and thus, excellent electrochemical activity for HER.

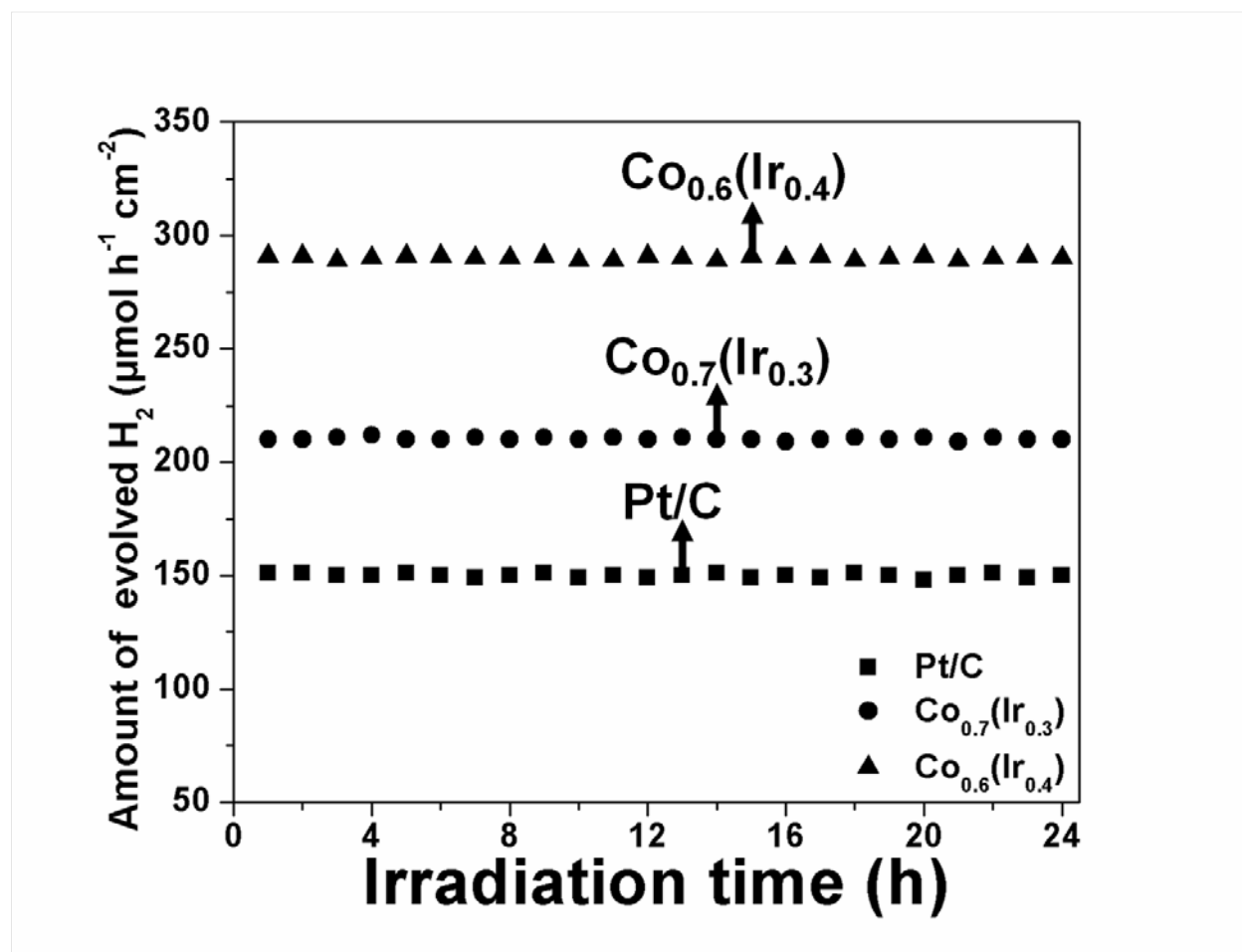


Figure 91: Amount of H_2 evolved as a function of irradiation time for $\text{Co}_{1-x}(\text{Ir}_x)$ ($x=0.3, 0.4$) and Pt/C as cathode electro-catalyst for HER and $(\text{Sn}_{0.95}\text{Nb}_{0.05})\text{O}_2\text{:N-600}$ NTs as photoanode/working electrode, obtained in $0.5 \text{ M H}_2\text{SO}_4$ solution at 26°C under illumination (100 mW/cm^2)

The applied bias photon-to-current efficiency (ABPE) was determined using the equation^{75, 77-79}:

$$ABPE = \frac{\Delta G^{\circ} \cdot n_{H_2} - V \cdot I}{P \cdot A} \times 100$$

where, n_{H_2} = H₂ evolution rate (mol/sec)

ΔG° = Gibbs free energy for generating one mole of H₂ from water (237130 J/mol)

P = Total incident power (W/cm²)

A = Area irradiated by incident light (cm²)

I = Photocurrent (A)

V = Bias voltage applied (0.75 V vs RHE) to (Sn_{0.95}Nb_{0.05})O₂:N-600 NTs (photoanode)

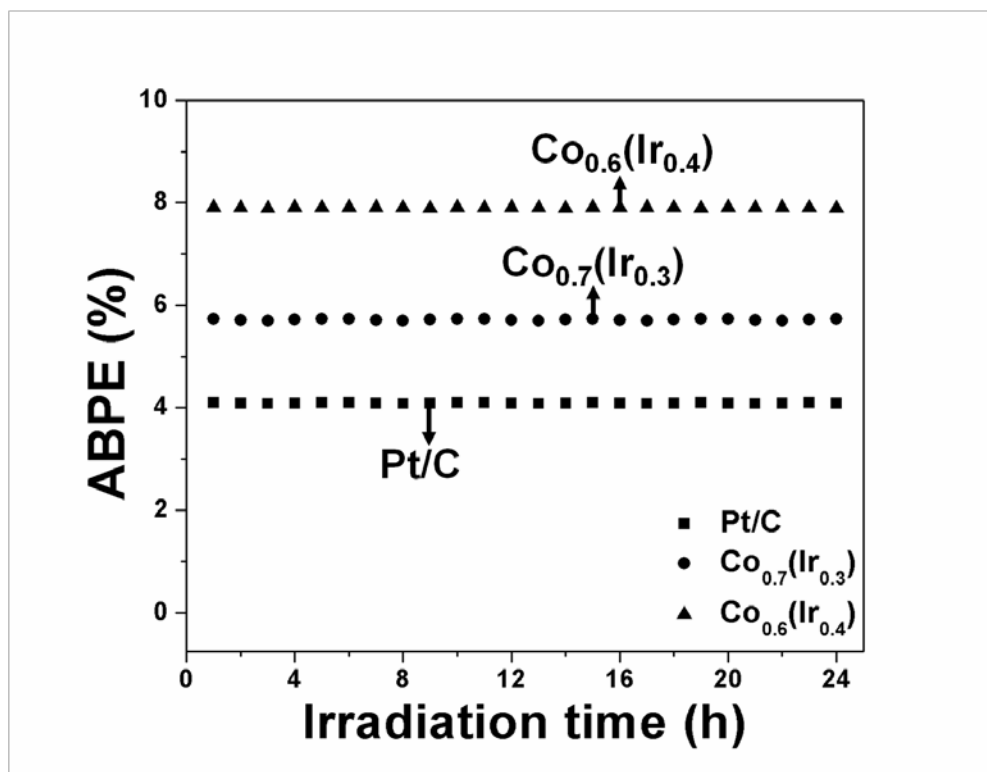


Figure 92: Applied bias photon-to-current efficiency (ABPE) as a function of irradiation time for $\text{Co}_{1-x}(\text{Ir}_x)$ ($x=0.3, 0.4$) and Pt/C as cathode electro-catalyst for HER and $(\text{Sn}_{0.95}\text{Nb}_{0.05})\text{O}_2\text{:N-600}$ NTs as photoanode/working electrode, obtained in 0.5 M H_2SO_4 solution at 26°C under illumination (100 mW/cm^2)

The plot of ABPE as function of irradiation time is shown in **Figure 92**. At the end of 24 h, the ABPE obtained using $\text{Co}_{1-x}(\text{Ir}_x)$ ($x=0.3, 0.4$) is ~5.74% and ~7.92%, which is ~40% and ~93% higher than that of Pt/C (~4.1%), respectively. This increased ABPE achieved for $\text{Co}_{1-x}(\text{Ir}_x)$ ($x=0.3, 0.4$) can be attributed to improved reaction kinetics and superior electrochemical activity leading to a higher H_2 yield, than that of Pt/C. Also, it is important to note that the ABPE of ~5.74% and ~7.92% obtained using $\text{Co}_{1-x}(\text{Ir}_x)$ ($x= 0.3, 0.4$) as cathode electro-catalyst and $(\text{Sn}_{0.95}\text{Nb}_{0.05})\text{O}_2\text{:N-600}$ NTs as the photoanode in a H-type PEC water splitting cell is the highest

ABPE obtained so far to the best of our knowledge of the reported literature to date, compared to other semiconductor materials studied as photoanode for PEC water splitting based on TiO_2 , ZnO and Fe_2O_3 .^{64, 114, 176-178} These excellent results thus show the potential of the reduced noble metal containing electro-catalysts, $\text{Co}_{1-x}(\text{Ir}_x)$ ($x= 0.3, 0.4$), for hydrogen production from photoelectrochemical water splitting, which can be indeed attributed to its unique electronic structure obtained by alloying of Co with Ir to form the Co(Ir) solid solution, which exhibits excellent reaction kinetics with low polarization resistance and superior electrochemical activity (as seen in LSV curves, EIS and Tafel plot analysis displayed in **Figure 84**, **Figure 85**, **Figure 87**, **Table 14** and **Table 15**).

Conclusions:

The present study demonstrates single phase solid solution of $\text{Co}_{1-x}(\text{Ir}_x)$ ($x=0.3, 0.4$) possessing the fcc-structure exhibiting superior reaction kinetics and excellent electrochemical activity for HER with onset overpotential of 10 mV (*vs* RHE), identical to that of Pt/C and lower overpotential to reach current density of 10 mA/cm^2 , 20 mA/cm^2 and 100 mA/cm^2 than that of Pt/C in acidic media which is in fact the lowest obtained so far compared to other reported non-noble metals based HER electro-catalysts, to the best of our knowledge.. The $\text{Co}_{1-x}(\text{Ir}_x)$ alloys correspondingly also exhibit excellent electro-catalytic performance as cathode electro-catalyst for HER in photo-electrochemical water splitting system using $(\text{Sn}_{0.95}\text{Nb}_{0.05})\text{O}_2\text{:N-600}$ NTs as photoanode. The ABPE obtained using $\text{Co}_{1-x}(\text{Ir}_x)$ ($x=0.3, 0.4$) is $\sim 5.74\%$ and $\sim 7.92\%$, which is $\sim 40\%$ and $\sim 93\%$ higher than that of Pt/C ($\sim 4.1\%$) at the end of 24 h, respectively. Moreover, the ABPE of $\sim 7.92\%$ obtained using $\text{Co}_{1-x}(\text{Ir}_x)$ ($x=0.4$) is the highest ABPE attained so far compared to other semiconductor materials studied as photoanode for PEC water splitting, related to TiO_2 ,

ZnO and Fe₂O₃, to the best of our knowledge of the known literature. Co_{1-x}(Ir_x) (x=0.3, 0.4) also display excellent long term electrochemical stability in acidic media, similar to Pt/C. Hence, the present study demonstrates Co_{1-x}(Ir_x) (x=0.3, 0.4) solid solution electro-catalysts as potential candidates for replacement of Pt/C for H₂ production from electrolytic and photoelectrochemical water splitting reactions, due to their excellent electrochemical performance and stability. Consequently, we believe the results of these studies will go a long way in the ultimate aim of achieving efficient and economic hydrogen generation to address the global energy crisis.

5.5 (Cu_{0.83}Co_{0.17})₃P:S HER ELECTRO-CATALYST FOR CATHODE

5.5.1 STRUCTURAL CHARACTERIZATION OF PURE Cu₃P NANOPARTICLES

(NPs), (Cu_{0.83}Co_{0.17})₃P NPs AND (Cu_{0.83}Co_{0.17})₃P:x at.% S NPs (X=10, 20, 30)

X-ray diffraction (XRD) study

The XRD pattern of the pure Cu₃P NPs (**Figure 93**) synthesized by heat treatment of CuCl₂.2H₂O and NaH₂PO₂.xH₂O in UHP-argon atmosphere at 250°C and subsequent water-wash shows a hexagonal structure (JCPDS card no: 71-2261) with lattice parameters, $a=b=0.6959$ nm, $c=0.7413$ nm and a molar volume (V_m) ~ 31.2 cm³ mol⁻¹, which is in good agreement with the literature value.²⁸² The XRD patterns of (Cu_{0.83}Co_{0.17})₃P NPs and (Cu_{0.83}Co_{0.17})₃P:S NPs of different S concentration, shown in **Figure 93**, show peaks corresponding to single phase hexagonal structure similar to that of Cu₃P without any other peaks of undesired secondary phase. This suggests incorporation of Co and S in lattice of Cu₃P for (Cu_{0.83}Co_{0.17})₃P:S NPs of different composition. The lattice parameters and molar volume of (Cu_{0.83}Co_{0.17})₃P NPs and (Cu_{0.83}Co_{0.17})₃P:S NPs of different S concentration (calculated using the least square refinement technique) are given in **Table 16**.

The lattice parameters and molar volume of (Cu_{0.83}Co_{0.17})₃P NPs are slightly lower than that of pure Cu₃P NPs which can be due to the smaller ionic radius of cobalt ion than that of copper ion.¹⁶⁸ However, there is a slight increase in the lattice parameters and molar volume of (Cu_{0.83}Co_{0.17})₃P:S NPs in comparison to pure Cu₃P NPs and (Cu_{0.83}Co_{0.17})₃P NPs. The lattice parameters and molar volume of (Cu_{0.83}Co_{0.17})₃P:S NPs increase slightly with increase in S concentrations indicating the slight lattice expansion upon incorporation of S which is similar to

earlier reports.^{283, 284} The TEM bright field image of $(\text{Cu}_{0.83}\text{Co}_{0.17})_3\text{P}:30\text{S}$ NPs, shown in **Figure 94**, shows nanoparticles in the range ~7-10 nm.

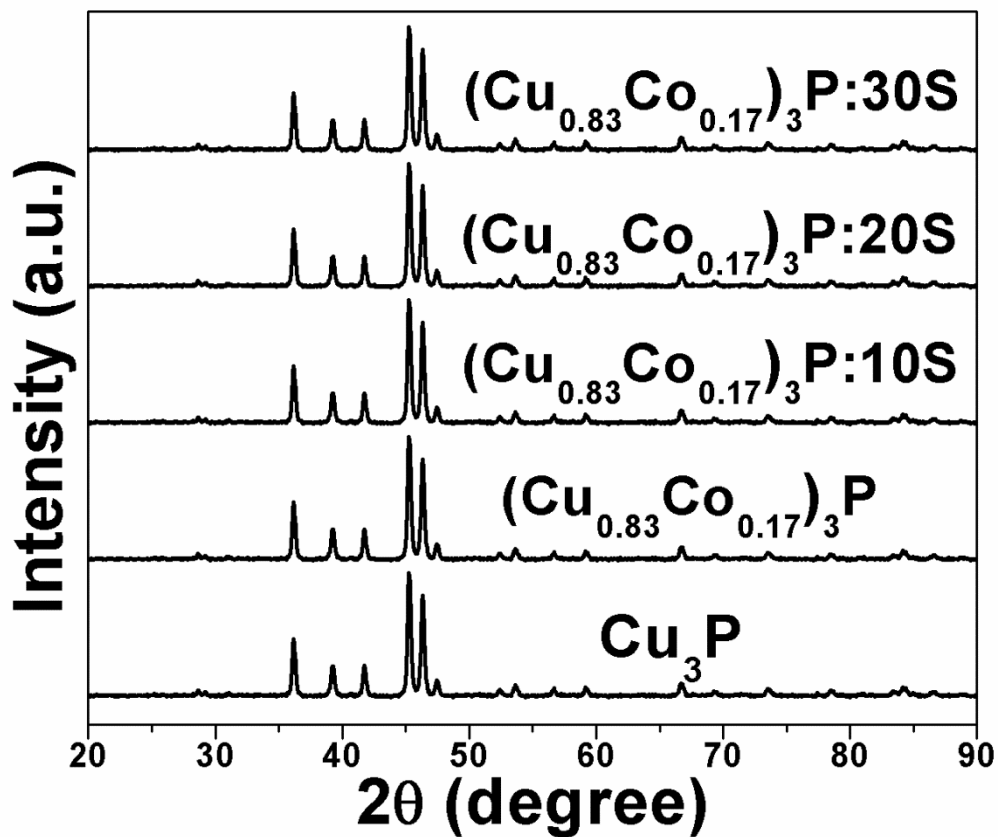


Figure 93: The XRD patterns of pure Cu_3P nanoparticles (NPs), $(\text{Cu}_{0.83}\text{Co}_{0.17})_3\text{P}$ NPs and $(\text{Cu}_{0.83}\text{Co}_{0.17})_3\text{P}:\text{S}$ NPs of different S concentration in wide angle 2θ scan

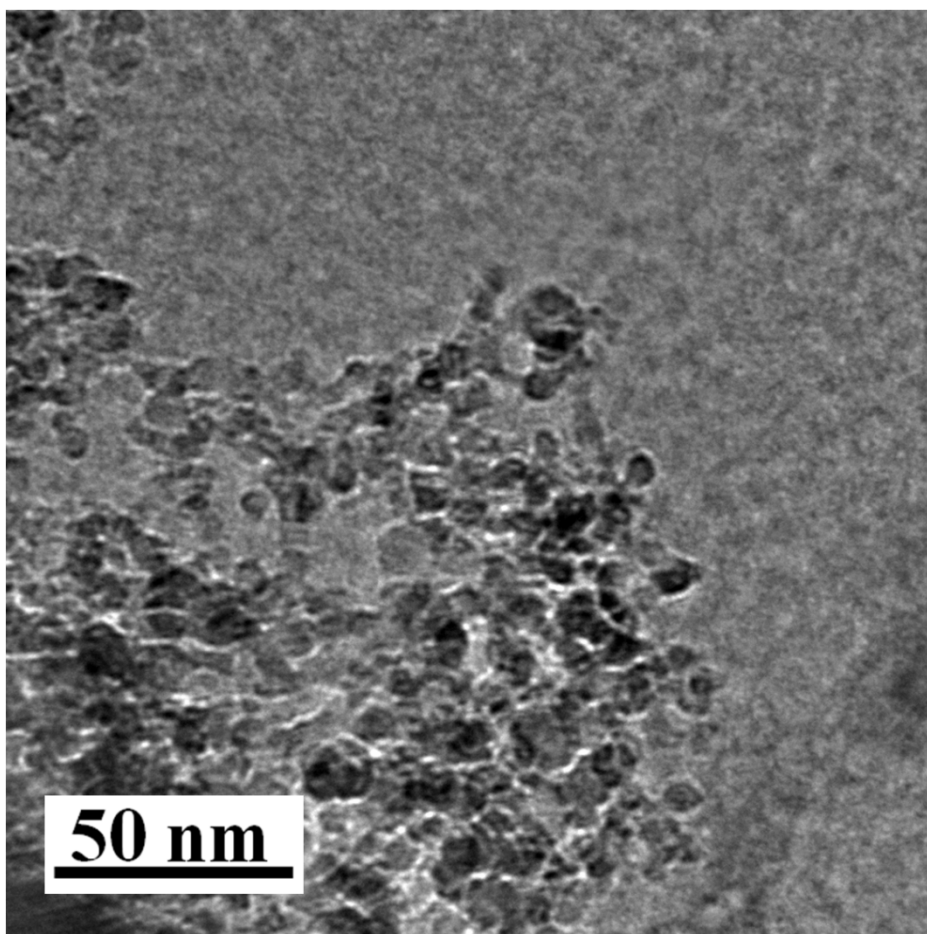


Figure 94: The bright field TEM image of $(\text{Cu}_{0.83}\text{Co}_{0.17})_3\text{P}:30\text{S}$ NPs

SEM/EDX study

The SEM image along with the EDX pattern of the same representative composition $(\text{Cu}_{0.83}\text{Co}_{0.17})_3\text{P}:30\text{S}$ NPs, is shown in **Figure 95**. The EDX pattern confirms the presence of Cu, Co, S and P in $(\text{Cu}_{0.83}\text{Co}_{0.17})_3\text{P}:30\text{S}$ NPs (**Figure 95**). The quantitative elemental composition analysis (from EDX) of $(\text{Cu}_{0.83}\text{Co}_{0.17})_3\text{P}:30\text{S}$ NPs shows the measured elemental composition of Cu, Co, S and P to be close to the nominal composition (**Figure 95**). Elemental x-ray maps of Cu, Co, S and P, shown in **Figure 96**, indicates a homogeneous distribution of elements in the

representative composition of $(\text{Cu}_{0.83}\text{Co}_{0.17})_3\text{P}:30\text{S}$ NPs with no evidence of of any segregation at any specific site.

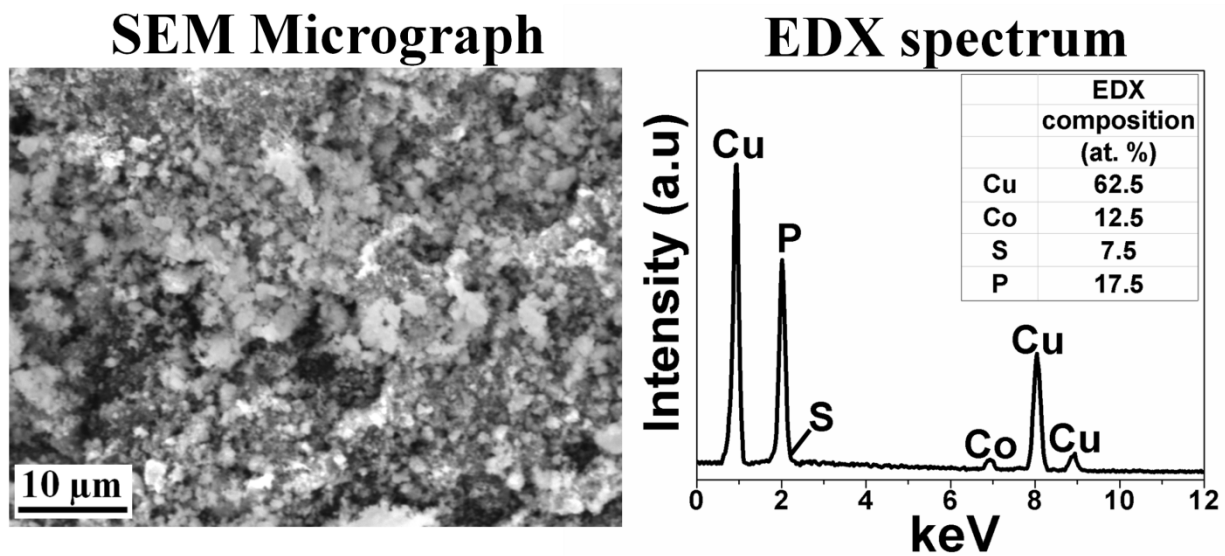


Figure 95: SEM micrograph with EDX spectrum of $(\text{Cu}_{0.83}\text{Co}_{0.17})_3\text{P}:30\text{S}$ NPs

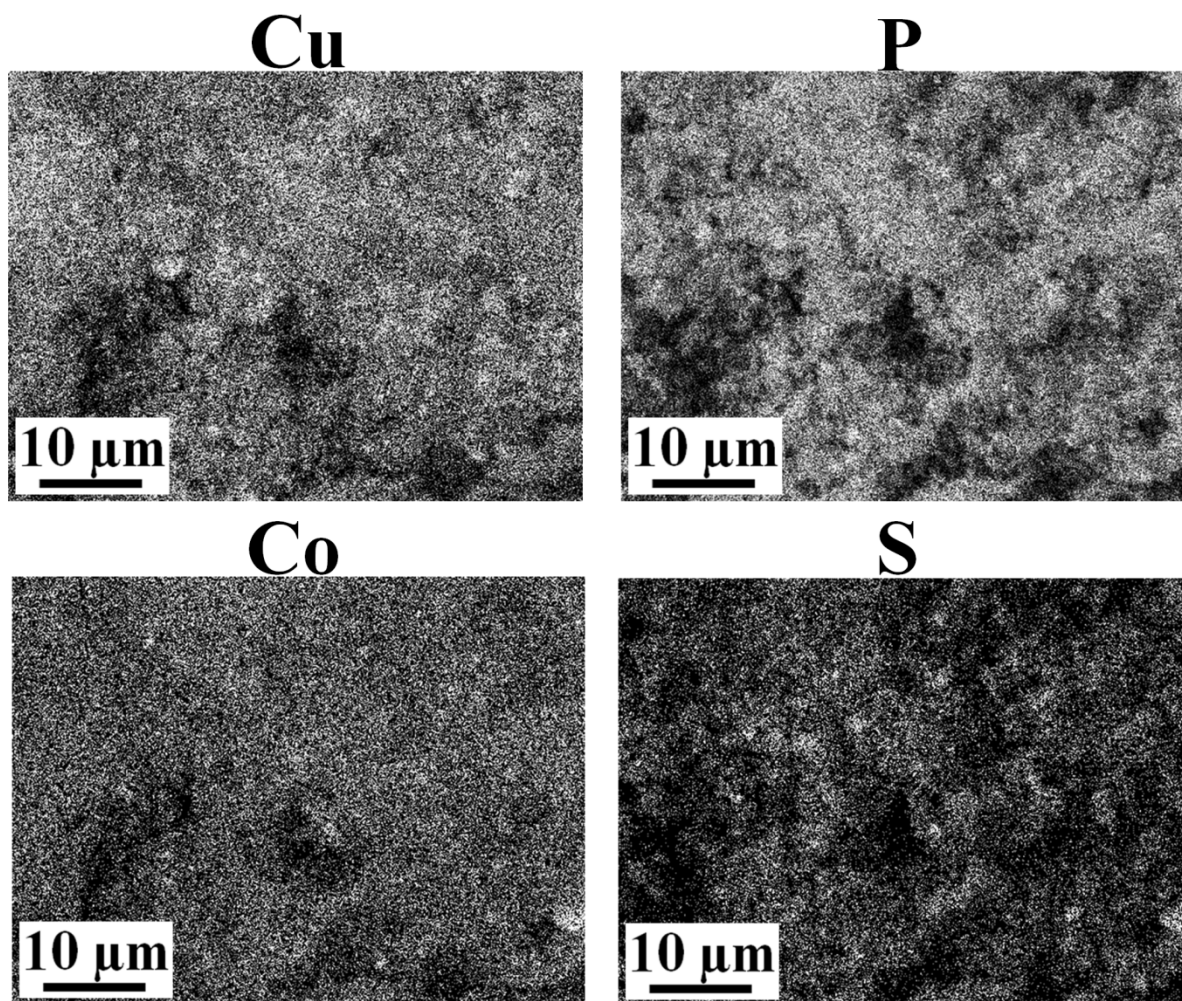


Figure 96: Elemental x-ray maps of $(\text{Cu}_{0.83}\text{Co}_{0.17})_3\text{P}:30\text{S}$ NPs

X-ray photoelectron spectroscopy (XPS)

Chemical oxidation states of Cu, Co, S and P were also studied using x-ray photoelectron spectroscopy (XPS) analysis performed on NPs of pure Cu_3P and $(\text{Cu}_{0.83}\text{Co}_{0.17})_3\text{P}:30\text{S}$ NPs, respectively. The XPS spectrum in the Cu $2p_{3/2}$ region for pure Cu_3P NPs shows a peak ~ 932.9 eV (**Figure 97**), which is similar to earlier report.¹⁶⁸ The XPS spectrum in the P 2p region for pure Cu_3P NPs, shown in **Figure 98**, shows two peaks at ~ 129.5 eV and ~ 133.8 eV. The peak at

~932.9 eV in the Cu 2p_{3/2} region and the peak at ~129.5 eV correspond to binding energies of Cu and P in pure Cu₃P NPs.^{168, 285} The peak at ~133.8 eV in the P 2p region corresponds to oxidation of P related to presence of (PO₄³⁻) forming possibly owing to air exposure during handling of pure Cu₃P NPs (**Figure 98**).²¹ It is noteworthy to note that the peak at ~932.9 eV in the Cu 2p_{3/2} region of pure Cu₃P NPs reflects higher binding energies than that of metallic Cu (~932.6 eV)²⁸⁶ and the peak at ~129.5 eV in P 2p region of pure Cu₃P NPs is at a lower binding energies than that of elemental P (~130.2 eV)²⁸⁵, respectively. This indicates presence of Cu (metal centers) with positive partial charge (δ^+) and P (pendant bases) with negative partial charge (δ^-) close to metal center and thus, suggesting transfer of electrons from Cu to P and modification of the charge density of Cu and P in pure Cu₃P NPs.¹³⁸ There is also a positive shift of ~0.5 eV seen in peak in the Cu 2p_{3/2} region for (Cu_{0.83}Co_{0.17})₃P:30S NPs, which can possibly be due to transfer of electrons from Cu to S and correspondingly, modification of the charge density of phosphosulfide (**Figure 97**).²⁸⁴ The XPS spectrum of (Cu_{0.83}Co_{0.17})₃P:30S NPs in the P 2p region shows only one peak at ~129.5 eV corresponding to P in Cu₃P²⁸⁵ or CoP²⁸⁷ (**Figure 98**). However, the peak corresponding to oxidized P (at ~133.8 eV which is seen for pure Cu₃P as discussed earlier) arising due to air exposure of the phosphide material during handling is absent for (Cu_{0.83}Co_{0.17})₃P:30S NPs (**Figure 98**) which can be due to likely stabilization of phosphide towards oxidation following the incorporation of S in the phosphide (as also seen earlier^{21, 287}). The exact reason is unknown at present warranting further study.

The XPS spectrum in the Co 2p_{3/2} region for (Cu_{0.83}Co_{0.17})₃P:30S NPs, shown in **Figure 99**, shows a peak at ~779.5 eV (which corresponds to Co in CoP¹⁴¹) is shifted by ~0.3 eV to higher binding energy than that of the typical peak (at ~779.2 eV) in the Co 2p_{3/2} region of CoP¹⁴¹, which can be due to transfer of electrons from Co to S.²⁸⁴ The peak at ~779.5 eV in Co

$2p_{3/2}$ region of $(\text{Cu}_{0.83}\text{Co}_{0.17})_3\text{P}:3\text{O}$ NPs (**Figure 99**) is also at higher binding energies than that of metallic Co (~ 778.4 eV)¹⁴¹ and the peak at ~ 129.5 eV in the P 2p region of $(\text{Cu}_{0.83}\text{Co}_{0.17})_3\text{P}:3\text{O}$ NPs (**Figure 98**) is at lower binding energies than that of elemental P (~ 130.2 eV)²⁸⁵, respectively. Similar to the discussion above for pure Cu_3P NPs, this also suggests the presence of Co (metal centers) with positive partial charge (δ^+) and P and S (pendant bases) with negative partial charge (δ^-) close to metal center and thus, implying transfer of electrons from Co to P and S in $(\text{Cu}_{0.83}\text{Co}_{0.17})_3\text{P}:3\text{O}$ NPs and possible modification of the resulting charge density.

The XPS spectrum of $(\text{Cu}_{0.83}\text{Co}_{0.17})_3\text{P}:3\text{O}$ NPs in the S 2p region (**Figure 100**) shows one peak at ~ 161 eV corresponding to the sulfide (S^{2-}) showing no presence of any oxidized sulfur species such as sulfate (whose peak appears in S $2p_{3/2}$ region at ~ 168 eV).^{288, 289} The proton relays are incorporated in a metal complex electro-catalyst for HER arising from the pendant acid-base groups which are present close to the metal center where the HER is known to occur.^{138, 290, 291} The active sites for metal complex hydrogenase enzyme also have pendant bases which are close to the metal centers.^{138, 292} The $(\text{Cu}_{0.83}\text{Co}_{0.17})_3\text{P}:3\text{O}$ NPs considered in this study exhibit metal centers Cu, Co (δ^+) and pendant bases P, S (δ^-) positioned close to the metal centers.¹³⁸ Thus, $(\text{Cu}_{0.83}\text{Co}_{0.17})_3\text{P}:3\text{O}$ NPs considered herein is expected to exhibit hydrogen evolution mechanism for HER similar to that of the metal complex hydrogenase enzyme reported.¹³⁸ Accordingly, Cu, Co and P, S in $(\text{Cu}_{0.83}\text{Co}_{0.17})_3\text{P}:3\text{O}$ NPs can offer hydride-acceptor and proton-acceptor centers, respectively.¹³⁸ These results collectively thus, show modification of the electronic structure of Cu_3P due to incorporation of Co and S into the lattice of the parent phosphide, Cu_3P which can likely result in a more catalytically active phase offering superior electrochemical response compared to that of pure Cu_3P NPs.

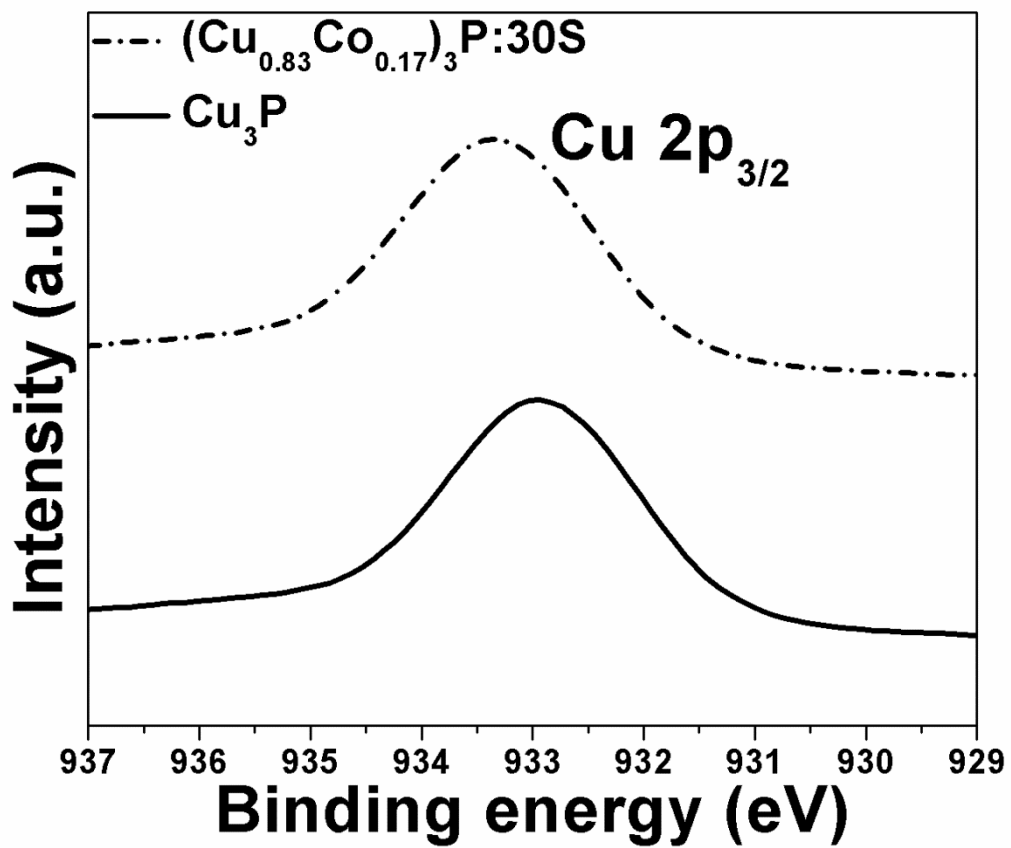


Figure 97: The XPS spectra of pure Cu_3P NPs and $(\text{Cu}_{0.83}\text{Co}_{0.17})_3\text{P}:30\text{S}$ NPs in the $\text{Cu } 2p_{3/2}$ region

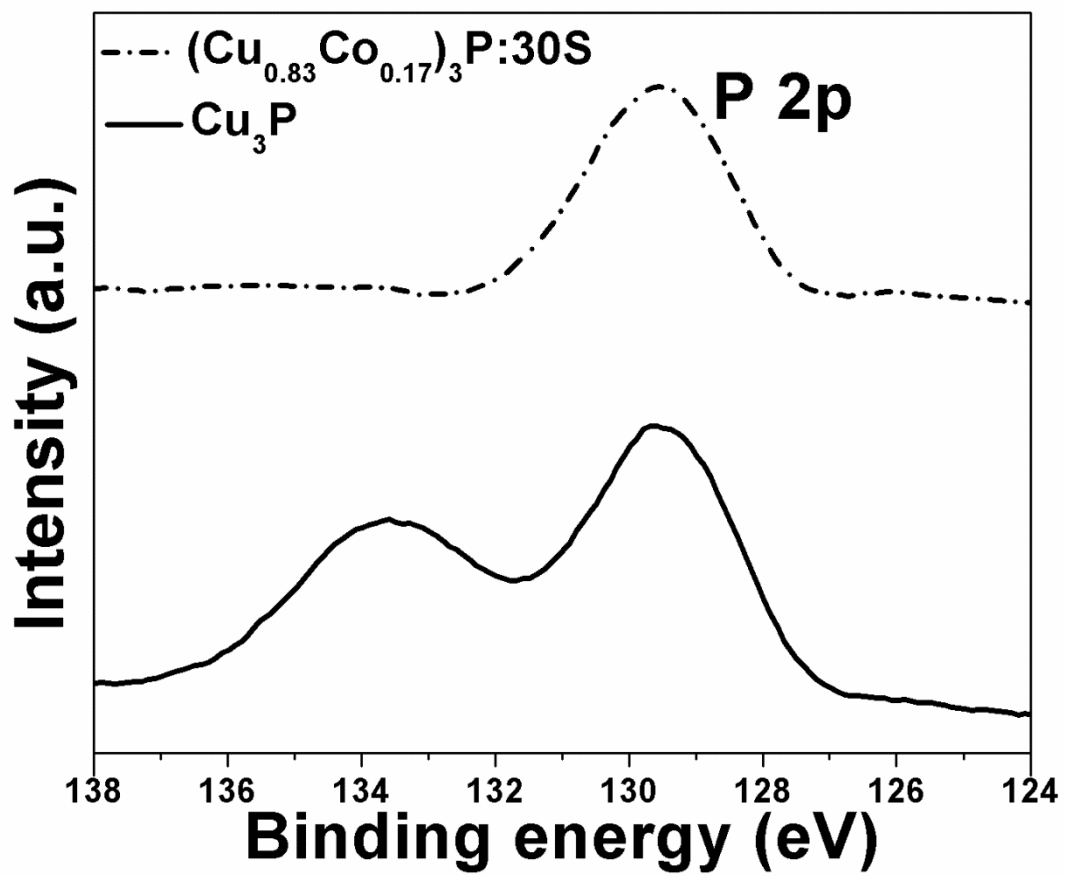


Figure 98: The XPS spectra of pure Cu_3P NPs and $(\text{Cu}_{0.83}\text{Co}_{0.17})_3\text{P}:30\text{S}$ NPs in the P 2p region

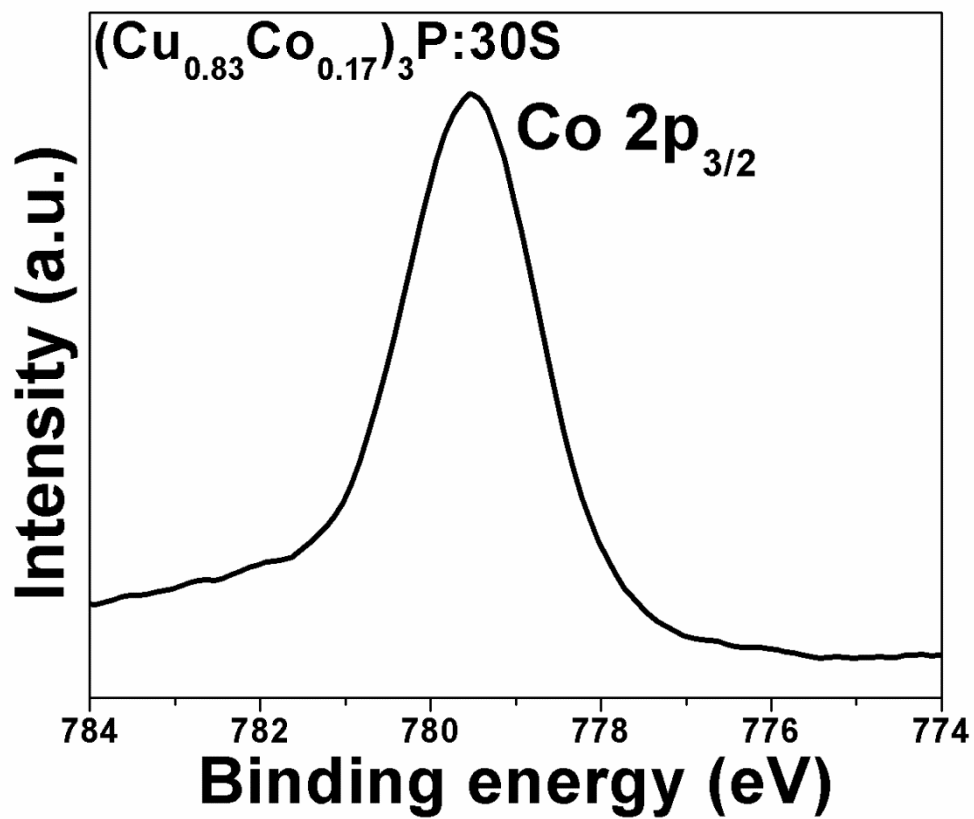


Figure 99: The XPS spectra of pure Cu_3P NPs and $(\text{Cu}_{0.83}\text{Co}_{0.17})_3\text{P}:30\text{S}$ NPs in the Co 2p_{3/2} region

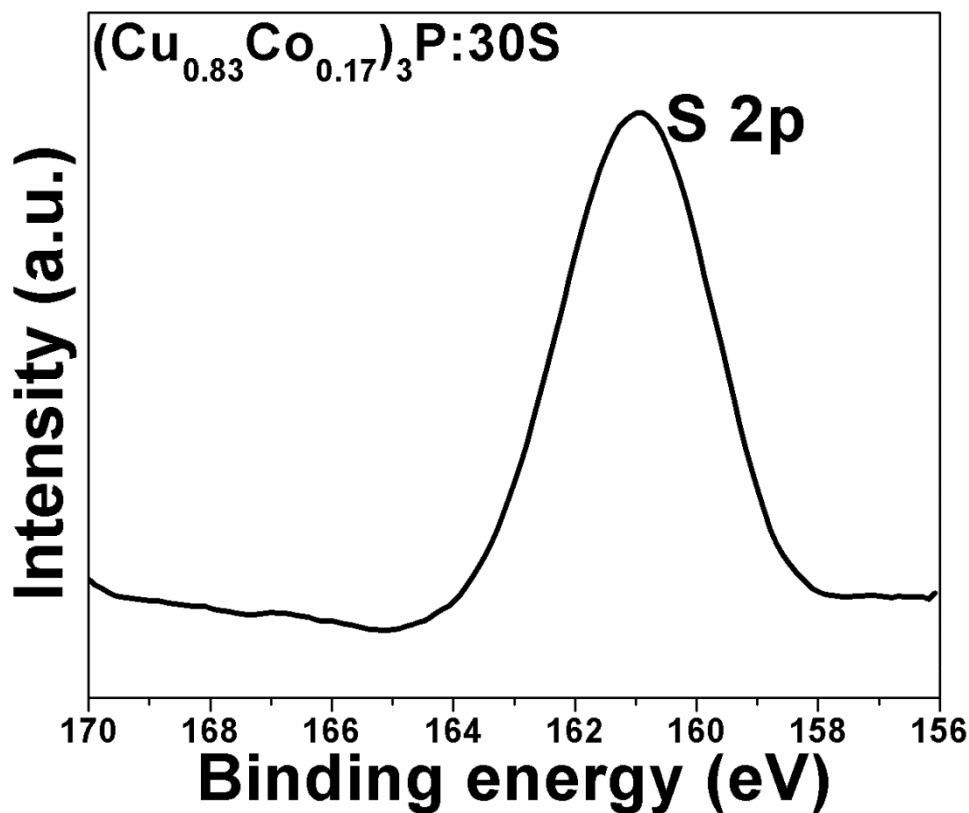


Figure 100: The XPS spectra of pure Cu_3P NPs and $(\text{Cu}_{0.83}\text{Co}_{0.17})_3\text{P}:30\text{S}$ NPs in the S 2p region

5.5.2 ELECTROCHEMICAL CHARACTERIZATION OF $(\text{Cu}_{0.83}\text{Co}_{0.17})_3\text{P}$ NPs AND $(\text{Cu}_{0.83}\text{Co}_{0.17})_3\text{P}:x$ at.% S NPs (X=10, 20, 30) COMPOSITIONS FOR HER IN ELECTROLYTIC WATER SPLITTING

The electrochemical activity of Cu_3P , $(\text{Cu}_{0.83}\text{Co}_{0.17})_3\text{P}$ and $(\text{Cu}_{0.83}\text{Co}_{0.17})_3\text{P}:S$ NPs of different S concentration has been studied by performing linear scan voltammetry in 0.5 M

H_2SO_4 electrolyte solution at 26°C using a total loading of 0.7 mg cm^{-2} . The iR_Ω corrected LSV curves of commercial Pt/C (Pt loading= $0.4 \text{ mg}_{\text{Pt}} \text{ cm}^{-2}$) and Ti foil (current collector) are shown in **Figure 101**. The Ti foil (current collector) as expected shows very poor electrochemical activity for HER and thus, has minimal contribution to the current density obtained in comparison to other active electro-catalysts used in this study.

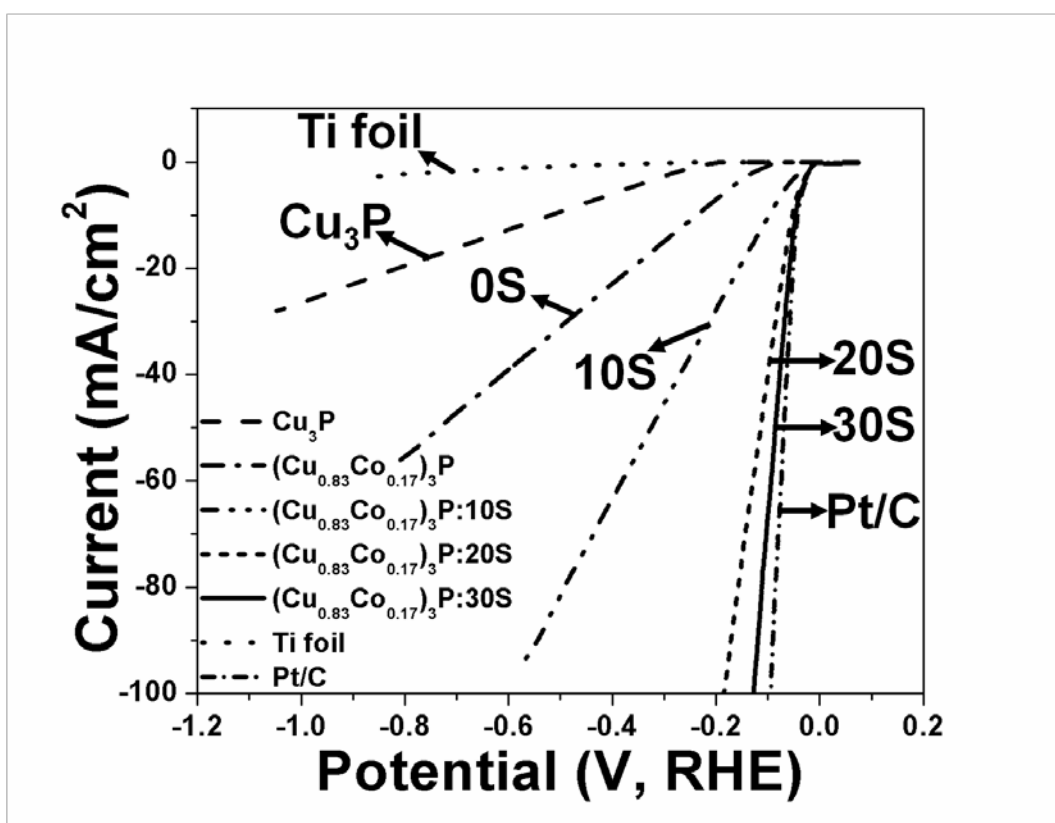


Figure 101: The iR_Ω corrected linear scan voltammogram (LSV) curves for HER of pure Cu_3P NPs (total loading= 0.7 mg/cm^2), $(\text{Cu}_{0.83}\text{Co}_{0.17})_3\text{P}$ NPs (total loading= 0.7 mg/cm^2), $(\text{Cu}_{0.83}\text{Co}_{0.17})_3\text{P:S}$ NPs of different S concentration (total loading= 0.7 mg/cm^2), Ti foil (current collector) and commercial Pt/C (Pt loading= $0.4 \text{ mg}_{\text{Pt}}/\text{cm}^2$), obtained in $0.5 \text{ M H}_2\text{SO}_4$ electrolyte solution at 26°C using scan rate of 1 mV/sec

The onset of HER starts at ~ 80 mV (*vs* RHE) for $(\text{Cu}_{0.83}\text{Co}_{0.17})_3\text{P}$ NPs which is lower than that of pure Cu_3P NPs (~ 190 mV *vs* RHE that is similar to earlier report¹⁶⁸) (**Table 16**). This clearly suggests a reduction in the reaction polarization^{159, 293} due to the incorporation of cobalt into the Cu_3P lattice which is in agreement with the results of theoretical study discussed later (**Section A.4** $(\text{Cu}_{0.83}\text{Co}_{0.17})_3\text{P}:\text{S}$ HER ELECTRO-CATALYST FOR CATHODE). Following incorporation of sulfur for all the compositions considered in the current study, the NPs of the $(\text{Cu}_{0.83}\text{Co}_{0.17})_3\text{P}:\text{S}$ system all show excellent performance for HER with an onset overpotential of ~ 10 mV (*vs* RHE). This response is not only similar to that of commercial Pt/C (**Figure 101** and **Table 16**) but also significantly lower than that of pure Cu_3P NPs (~ 190 mV *vs* RHE). Thus, simultaneous incorporation of S and Co into the Cu_3P lattice offers significant reduction in the onset overpotential of HER to the extent of ~ 180 mV (significantly reduced reaction polarization) and also offers reaction polarization similar to that of commercial Pt/C (similar onset overpotential). These results correlate well with results of theoretical study (discussed earlier) which predicts a minimum reaction polarization for $(\text{Cu}_{0.83}\text{Co}_{0.17})_3\text{P}:\text{S}$ than that of pure Cu_3P , due to the modification of the electronic structure following the simultaneous incorporation of Co and S into the Cu_3P lattice. It is also important to note that the onset overpotential for HER (~ 10 mV *vs* HER) obtained in this study for $(\text{Cu}_{0.83}\text{Co}_{0.17})_3\text{P}:\text{30S}$ NPs is the lowest onset overpotential obtained for HER thus far in the published open literature to date, compared to other reported non-noble metals based HER electro-catalysts, to the best of our knowledge (**Table 17**). This shows the excellent promise of Co and S acting as effective dopants in improving the electrochemical activity of the parent phosphide, Cu_3P .

Table 16: Results of structural and electrochemical characterization for HER of pure Cu₃P NPs (total loading=0.7 mg/cm²), (Cu_{0.83}Co_{0.17})₃P NPs (total loading=0.7 mg/cm²), (Cu_{0.83}Co_{0.17})₃P:S NPs (total loading=0.7 mg/cm²) and Pt/C (Pt loading=0.4 mg_{Pt}/cm²) in 0.5 M H₂SO₄ electrolyte solution at 26^oC

Electro-catalyst	Lattice parameter (nm)	Molar volume (cm ³ /mol)	Onset potential (mV, RHE)	Overpotential (mV, RHE) to reach			Current density at (-0.05V) (mA/cm ²)	R _{ct} (Ω.cm ²)
				10 mA/cm ²	20 mA/cm ²	100 mA/cm ²		
Cu ₃ P	a=b=0.6959, c=0.7413	31.20	190	519	813	>1048	0.01	65.29
(Cu _{0.83} Co _{0.17}) ₃ P	a=b=0.6958, c=0.7411	31.19	80	237	363	>809	0.085	31.3
(Cu _{0.83} Co _{0.17}) ₃ P:1 OS	a=b=0.696, c=0.7414	31.22	10	97	155	>567	3.19	21.29
(Cu _{0.83} Co _{0.17}) ₃ P:2 OS	a=b=0.6962, c=0.7415	31.24	10	52	70	185	8.67	10.31
(Cu _{0.83} Co _{0.17}) ₃ P:3 OS	a=b=0.6963, c=0.7417	31.26	10	46	58	115	17.2	7.00
Pt/C	-	-	10	43	51	95	17.6	6.32

Nanoparticles (NP) of $(\text{Cu}_{0.83}\text{Co}_{0.17})_3\text{P}$ exhibit current density of $\sim 0.085 \text{ mA cm}^{-2}$ at (-0.05 V vs RHE) , which is a finite potential required to overcome overpotential losses near 0V , standard potential of HER), the standard representative potential selected following literature reports for measuring electrochemical activity for HER^{138, 144, 179, 196-202}, which is eight-fold higher than that of pure Cu_3P NPs ($\sim 0.01 \text{ mA cm}^{-2}$) (**Figure 101** and **Table 16**). Additionally, $(\text{Cu}_{0.83}\text{Co}_{0.17})_3\text{P}$ NPs show an overpotential of $(>809 \text{ mV})$ (*vs RHE*) to reach a current density of 100 mA cm^{-2} which is lower than that of pure Cu_3P NPs showing an overpotential of $(>1048 \text{ mV})$ (*vs RHE*) to reach the current density of 100 mA cm^{-2} , respectively (**Figure 101** and **Table 16**). This improvement in overpotential is mainly due to $\sim 110 \text{ mV}$ lower onset overpotential (lower reaction polarization) and improved reaction kinetics (lower activation polarization^{159, 293}, also confirmed by the Electrochemical Impedance Spectroscopy (EIS) analysis discussed later) of $(\text{Cu}_{0.83}\text{Co}_{0.17})_3\text{P}$ NPs (onset overpotential $\sim 80 \text{ mV vs RHE}$) than that of pure Cu_3P NPs (onset overpotential $\sim 190 \text{ mV vs RHE}$) (**Figure 101** and **Table 16**). However, despite this improvement, the current density of the $(\text{Cu}_{0.83}\text{Co}_{0.17})_3\text{P}$ NPs at (-0.05 V vs RHE) ($\sim 0.085 \text{ mA cm}^{-2}$) is $\sim 99.5\%$ lower than that of Pt/C ($\sim 17.6 \text{ mA cm}^{-2}$) and correspondingly, the overpotential required to reach the current density of 100 mA cm^{-2} is higher than that of commercial Pt/C which shows an overpotential of $\sim 95 \text{ mV}$ (*vs RHE*, similar to earlier reports^{138, 144, 196-202}) to reach the identical current density of 100 mA cm^{-2} , respectively (**Figure 101** and **Table 16**). This is mainly due to $\sim 70 \text{ mV}$ higher onset overpotential (higher reaction polarization) and poor reaction kinetics (higher activation polarization, also confirmed further similarly, by EIS analysis discussed later) of $(\text{Cu}_{0.83}\text{Co}_{0.17})_3\text{P}$ NPs than that of commercial Pt/C (**Figure 101** and **Table 16**).

It is also important to note that the NPs in the $(\text{Cu}_{0.83}\text{Co}_{0.17})_3\text{P}:\text{S}$ system exhibit almost two-orders of magnitude higher current density at (-0.05 V vs RHE) than that of pure Cu_3P NPs and the Co doped phosphide, $(\text{Cu}_{0.83}\text{Co}_{0.17})_3\text{P}$ NPs (**Figure 101** and **Table 16**). This result is indeed in agreement with the results of the theoretical study (as discussed later in (**Section A.4**) and is a reflection of the significant reduction in reaction polarization (lower onset overpotential) and possibly lower activation polarization (improved reaction kinetics, again similarly confirmed by EIS analysis discussed later) for $(\text{Cu}_{0.83}\text{Co}_{0.17})_3\text{P}:\text{S}$ than that of pure Cu_3P . The current density at (-0.05 V vs RHE) for the NPs of the $(\text{Cu}_{0.83}\text{Co}_{0.17})_3\text{P}:\text{S}$ system increases with increase in S dopant concentration with the highest current density value obtained for $(\text{Cu}_{0.83}\text{Co}_{0.17})_3\text{P}:\text{30S}$ NPs ($\sim 17.2\text{ mA cm}^{-2}$) (**Figure 101** and **Table 16**). In addition, the overpotential required to reach the current density of 100 mA cm^{-2} for all of the sulfur doped $(\text{Cu}_{0.83}\text{Co}_{0.17})_3\text{P}:\text{S}$ NPs decreases with increase in S concentration with the lowest value of 105 mV obtained for $(\text{Cu}_{0.83}\text{Co}_{0.17})_3\text{P}:\text{30S}$ NPs (**Figure 101** and **Table 16**). Thus, despite the onset overpotential of $(\text{Cu}_{0.83}\text{Co}_{0.17})_3\text{P}:\text{S}$ NPs of different S concentration being same ($\sim 10\text{ mV vs RHE}$), the increase in electrochemical activity of the sulfur doped $(\text{Cu}_{0.83}\text{Co}_{0.17})_3\text{P}:\text{S}$ NPs with increase in S concentration with the highest activity displayed by $(\text{Cu}_{0.83}\text{Co}_{0.17})_3\text{P}:\text{30S}$ NPs indicates improvement in reaction kinetics (decrease in activation polarization) with increase in S concentration with the highest (lowest activation polarization) obtained for $(\text{Cu}_{0.83}\text{Co}_{0.17})_3\text{P}:\text{30S}$ NPs (which is confirmed using EIS analysis discussed later). The sulfur doped composition of $(\text{Cu}_{0.83}\text{Co}_{0.17})_3\text{P}:\text{30S}$ NPs show a current density of $\sim 17.2\text{ mA cm}^{-2}$ at (-0.05 V vs RHE) and overpotential of $\sim 105\text{ mV (vs RHE)}$ to reach the current density of 100 mA cm^{-2} , which is almost comparable to that of Pt/C (**Figure 101** and **Table 16**). Thus, the sulfur doped composition of $(\text{Cu}_{0.83}\text{Co}_{0.17})_3\text{P}:\text{30S}$ NPs display outstanding electrochemical performance for HER, almost

comparable to that of commercial Pt/C (**Figure 101** and **Table 16**) which is due to similar reaction polarization (similar onset overpotential) and similar activation polarization (similar reaction kinetics, confirmed by EIS analysis discussed later) for $(\text{Cu}_{0.83}\text{Co}_{0.17})_3\text{P}:\text{30S}$ NPs and commercial Pt/C. It is noteworthy that the overpotential of ~ 105 mV (vs RHE) shown by $(\text{Cu}_{0.83}\text{Co}_{0.17})_3\text{P}:\text{30S}$ NPs to reach current density of 100 mA cm^{-2} in acidic media in this study is the lowest obtained so far compared to other reported non-noble metals based HER electro-catalysts, to the best of our knowledge (**Table 17**).

The above results clearly suggest that the introduction of Co and S as co-dopants in the Cu_3P lattice offer a synergistic alteration of the electronic, atomic/molecular structure (which is in agreement with results of the theoretical study) leading to excellent electrochemical performance for HER, almost comparable to that of commercial Pt/C.

Table 17: Comparison of HER performance of $(\text{Cu}_{0.83}\text{Co}_{0.17})_3\text{P}:\text{30S}$ NPs with other reported non-noble metals based HER electro-catalysts in acidic media

Electro-catalyst	Condition	Onset potential, η (mV, RHE)	Tafel slope (mV dec⁻¹)	Current density (j, mA cm⁻²)	η at the corresponding j (mV)	Ref.
Double-gyroid MoS_2/FTO	0.5M H_2SO_4	150-	50	2	190	294
		200		10	230	
CoSe_2 NP/CP	0.5M H_2SO_4	-	42.1	10	139	131

Table 17 (continued)				100	184	
MoS ₃ particles	1M H ₂ SO ₄	100	54	2	190	295
MoS ₃ /FTO	1M H ₂ SO ₄	120	40	2	170	296
Defect rich MoS ₂	0.5M H ₂ SO ₄	120	50	13	200	297
MoO ₃ -MoS ₂ /FTO	0.5M H ₂ SO ₄	150- 200	50-60	10	310	247
MoS ₂ nanosheets	0.5M H ₂ SO ₄	200	54	10	195	298
Mo ₂ C nanowires	0.5M H ₂ SO ₄	70	53	60	200	299
MoN/C	0.1M HClO ₄	157	54.5	2	290	300
NiMoN _x /C	0.1M HClO ₄	78	35.9	2	170	300
CoSe ₂ nanobelts	0.5M H ₂ SO ₄	50	48	-	-	301
WS ₂ nanosheets	0.1M H ₂ SO ₄	80-100	60	-	-	302
WS ₂ /RGO	0.5M H ₂ SO ₄	150- 200	58	23	300	303
Ni ₂ P	0.5M H ₂ SO ₄	-	46	10	116	136
				100	180	
FeP	0.5M H ₂ SO ₄	100	67	10	~240	304
Bulk Mo ₂ C	0.1M HClO ₄	-	87.6	1	204	305
Mo ₂ C/CNT	0.1M HClO ₄	-	55.2	10	152	305
Oxygen- incorporated MoS ₂	0.5M H ₂ SO ₄	120	55	126.5	300	306
MoS ₂ /graphene/Ni	0.5M H ₂ SO ₄	-	42.8	10	141	307

Table 17 (continued)				100	263	
Co-NRCNTs	0.5M H ₂ SO ₄	50	69	1	140	308
				10	260	
CoP/CC (carbon cloth)	0.5M H ₂ SO ₄	38	51	10	67	138
				20	100	
				100	204	
MoB	1M H ₂ SO ₄	≥100	55	20	210-240	309
Mo ₂ C	1M H ₂ SO ₄	≥100	56	20	210-240	309
Co-MoS ₃ /FTO	pH 0	-	43	-	-	169
Ni ₂ P nanoparticles	1M H ₂ SO ₄	50	87	20	140	137
MoS ₂ /RGO	0.5M H ₂ SO ₄	100	41	20	170	61
Amorphous WP	0.5M H ₂ SO ₄	-	-	10	120	310
				20	140	
Crystalline WP	0.5M H ₂ SO ₄	-	-	10	200	310
				20	223	
MoP	0.5M H ₂ SO ₄	50	54	30	180	142
CoP	0.5M H ₂ SO ₄	-	50	20	85	311
MoP-graphite nanosheets	0.5M H ₂ SO ₄	320V vs. Ag/Ag Cl	63	10	460	312

Table 17 (continued)						
Cu ₃ P NWs	0.5M H ₂ SO ₄	62	67	1	79	168
				10	143	
				100	276	
CoP NWs	0.5M H ₂ SO ₄	40	54			141
				2	70	
				10	122	
CoP film	0.5M H ₂ SO ₄	25	50	10	85	313
Cu ₃ P NWs/CF	0.5M H ₂ SO ₄	62	67	1	79	314
				10	143	
				100	276	
FeP NPs	0.5M H ₂ SO ₄	50	37			143
				10	50	
				20	61	
MoP S	0.5M H ₂ SO ₄	-	50	10	64	21
				20	78	
				100	120	
WP ₂ SMPs	0.5M H ₂ SO ₄	54	57	2	115	146
				10	161	

Table 17 (continued)						
WP ₂ nanorods (NRs)	0.5M H ₂ SO ₄	56	52	2	101	315
				10	148	
CoP branched nanostructure	0.5M H ₂ SO ₄	-	48	20	117	139
CoP nanoparticles	0.5M H ₂ SO ₄	-	-	20	100	139
P-WN/rGO	0.5M H ₂ SO ₄	46	54	10	85	200
Cu ₃ P NWs/CF	0.5M H ₂ SO ₄	62	67	10	143	314
Ni-Mo nanopowder	0.5M H ₂ SO ₄	-	-	20	80	316
Co _{0.6} Mo _{1.4} N ₂	0.1M HClO ₄	-	-	10	190	132
(Cu_{0.83}Co_{0.17})₃P:30 S	0.5M H₂SO₄	10	32	10	46	Current work

Electrochemical impedance spectroscopy and Tafel slope

Based on the above, the reaction kinetics of HER for NPs of Cu₃P, (Cu_{0.83}Co_{0.17})₃P, and for the various sulfur doped NPs in the (Cu_{0.83}Co_{0.17})₃P:S system including commercial Pt/C were studied using electrochemical impedance spectroscopy (EIS). Accordingly, EIS was carried out to determine the charge transfer resistance (R_{ct}) in 0.5 M H₂SO₄ electrolyte solution (pH~0) at (-0.05 V vs RHE) in the frequency range of 100 mHz-100 kHz at 26°C at an amplitude of 10 mV, using the circuit model $R_{\Omega}(R_{ct}Q_1)$ for fitting the experimental data, where R_{Ω} is the ohmic

resistance, which includes contribution mainly from electrolyte and electrode. Similarly, R_{ct} is charge transfer resistance and Q_1 is the constant phase element representing the contribution from the capacitance behavior of the electro-catalyst surface.

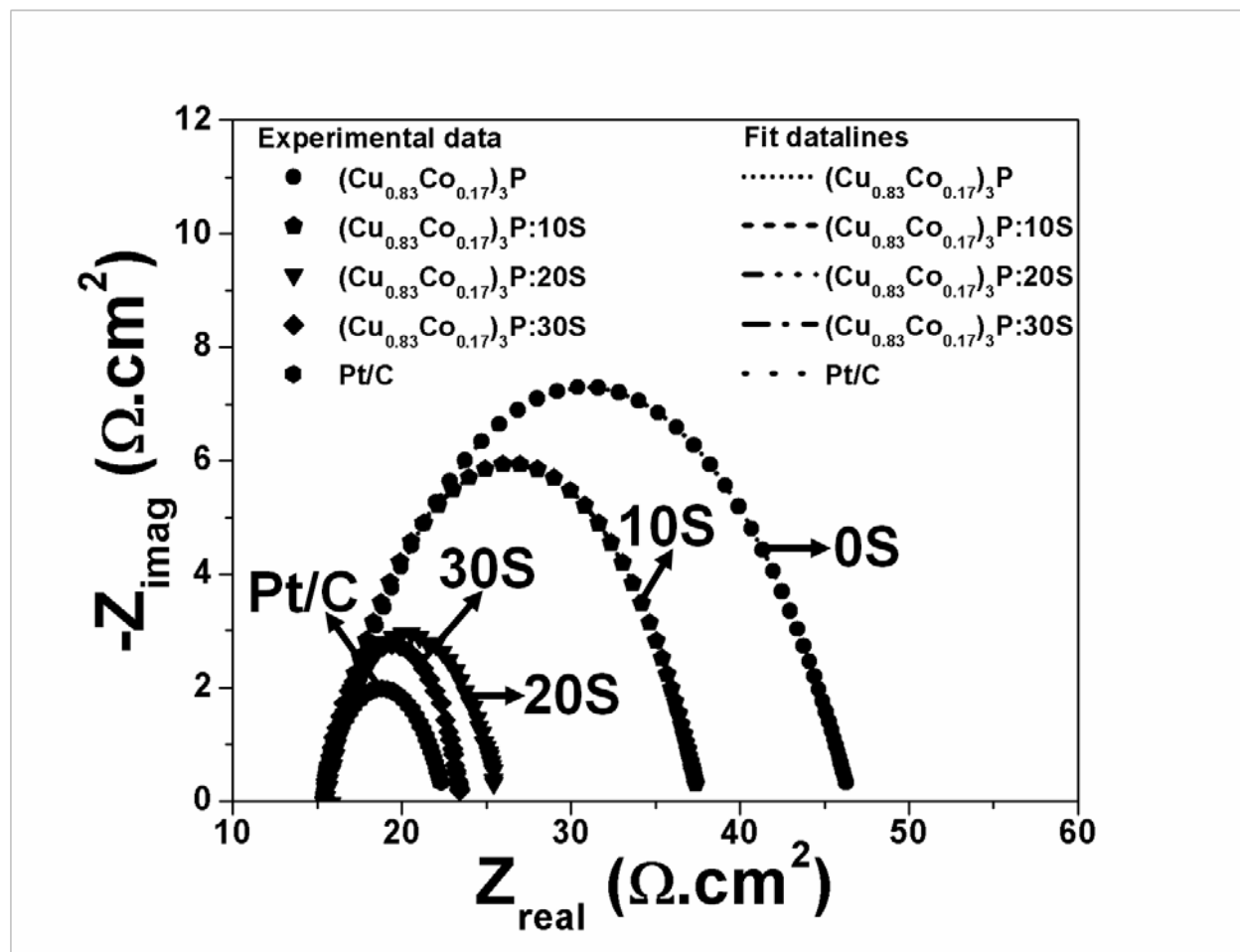


Figure 102: EIS spectra of $(\text{Cu}_{0.83}\text{Co}_{0.17})_3\text{P}$ NPs (total loading=0.7 mg/cm²), $(\text{Cu}_{0.83}\text{Co}_{0.17})_3\text{P}:\text{S}$ NPs of different S concentration (total loading=0.7 mg/cm²) and commercial Pt/C (Pt loading=0.4 mg_{Pt}/cm²) obtained at (-0.1 V vs RHE) in 0.5 M H₂SO₄ electrolyte solution at 26^oC in the frequency range of 100 mHz to 100 kHz (Amplitude=10 mV)

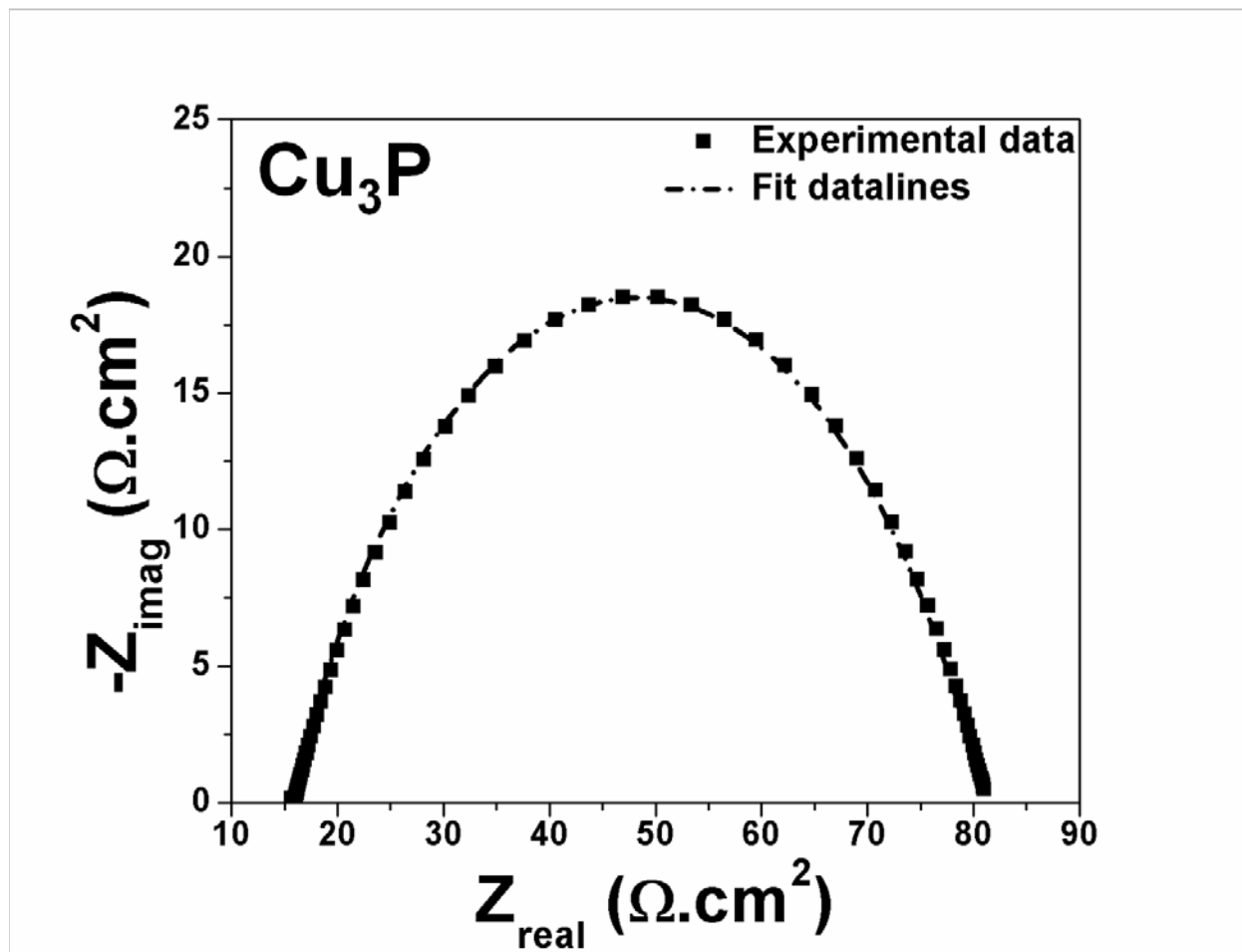


Figure 103: EIS spectrum of Cu₃P NPs (total loading=0.7 mg/cm²) obtained at (-0.05 V vs RHE) in 0.5 M H₂SO₄ electrolyte solution at 26^oC in the frequency range of 100 mHz to 100 kHz (Amplitude=10 mV)

The EIS plot of the electro-catalysts show a well-formed semicircular arc (**Figure 102** and **Figure 103**). The diameter of semi-circular arc is used to determine the charge transfer resistance (R_{ct}). The R_{ct} for all the NPs of the (Cu_{0.83}Co_{0.17})₃P: S system is significantly lower than that of (Cu_{0.83}Co_{0.17})₃P NPs and pure Cu₃P NPs (**Figure 102, Figure 103** and **Table 16**) clearly reflecting significant improvements in the kinetics of HER (significant decrease in

activation polarization) upon the incorporation of the dual dopants, Co and S into the Cu₃P lattice resulting in superior electrochemical activity for HER of all the NPs in the (Cu_{0.83}Co_{0.17})₃P:S system contrasted to that of (Cu_{0.83}Co_{0.17})₃P NPs and pure Cu₃P NPs, respectively. Correspondingly, the R_{ct} for all the NPs of the (Cu_{0.83}Co_{0.17})₃P:S system decreases with increase in S concentration with the lowest value of R_{ct} obtained for (Cu_{0.83}Co_{0.17})₃P:30S NPs (~7 Ω.cm²), suggesting improvement in reaction kinetics (decrease in activation polarization) and thus, improved electrochemical activity, with increase in S concentration with the highest current value of 17.2 mA cm⁻² at -0.05V vs RHE obtained for (Cu_{0.83}Co_{0.17})₃P:30S NPs (exhibiting lowest activation polarization in this study) (**Figure 102, Figure 103 and Table 16**). It should also be noted that R_{ct} for (Cu_{0.83}Co_{0.17})₃P:30S NPs (~7 Ω.cm²) is nine-fold lower than that of Cu₃P NPs (~65.29 Ω.cm²), five-fold lower than that of (Cu_{0.83}Co_{0.17})₃P NPs (~31.3 Ω.cm²) and almost comparable to commercial Pt/C (~6.32 Ω.cm²) (**Figure 102, Figure 103 and Table 16**). Thus, (Cu_{0.83}Co_{0.17})₃P:30S NPs shows outstanding electrochemical performance for HER with the reaction kinetics (activation polarization) being almost similar to that of Pt/C.

The Tafel slope of pure Cu₃P NPs, (Cu_{0.83}Co_{0.17})₃P NPs, (Cu_{0.83}Co_{0.17})₃P:10S NPs, (Cu_{0.83}Co_{0.17})₃P:20S NPs and (Cu_{0.83}Co_{0.17})₃P:30S NPs and commercial Pt/C, calculated from iR_Ω corrected Tafel plots (in 0.5 M H₂SO₄), are 96 mV dec⁻¹, 55 mV dec⁻¹, 50 dec⁻¹, 40 mV dec⁻¹, 32 mV dec⁻¹ and 31.6 mV dec⁻¹ (similar to earlier reports ^{144, 196, 198, 201, 279}), respectively (**Figure 104, Figure 105 and Figure 106**). The lower Tafel slopes for all the NPs of the (Cu_{0.83}Co_{0.17})₃P:S system corresponding to different S concentrations compared to that of pure Cu₃P NPs and (Cu_{0.83}Co_{0.17})₃P NPs is again a reflection of the superior reaction kinetics of all the NPs of the (Cu_{0.83}Co_{0.17})₃P: S system than that of pure Cu₃P NPs and (Cu_{0.83}Co_{0.17})₃P NPs which is also seen in EIS analysis (**Figure 102 and Figure 103**). The Tafel slope for (Cu_{0.83}Co_{0.17})₃P: S NPs

decreases with increase in S concentration with the lowest value obtained for $(\text{Cu}_{0.83}\text{Co}_{0.17})_3\text{P}:30\text{S}$ NPs (32 mV dec^{-1}), suggesting clearly an enhancement in the reaction kinetics (increase in number of electrons involved in HER) resulting in superior electrochemical activity for HER, which increases with increase in S concentration with the highest electrochemical response of 17.2 mA cm^{-2} at -0.05V vs RHE obtained for $(\text{Cu}_{0.83}\text{Co}_{0.17})_3\text{P}:30\text{S}$ NPs (**Figure 104**, **Figure 105** and **Figure 106**). It is again of interest to note that the Tafel slope of $(\text{Cu}_{0.83}\text{Co}_{0.17})_3\text{P}:30\text{S}$ NPs (32 mV dec^{-1}) is almost similar to that of commercial Pt/C (31.6 mV dec^{-1}) indicating almost similar reaction kinetics and thus, similar electrochemical activity of $(\text{Cu}_{0.83}\text{Co}_{0.17})_3\text{P}:30\text{S}$ NPs and commercial Pt/C (**Figure 104**, **Figure 105** and **Figure 106**) for HER which is known to primarily proceed through the Volmer-Tafel mechanism for both $(\text{Cu}_{0.83}\text{Co}_{0.17})_3\text{P}:30\text{S}$ NPs and commercial Pt/C.^{64, 144} The Tafel slope of $(\text{Cu}_{0.83}\text{Co}_{0.17})_3\text{P}:30\text{S}$ NPs (32 mV dec^{-1}) is the lowest Tafel slope obtained so far compared to other reported non-noble metals based HER electro-catalysts published in the open literature, to the best of our knowledge (**Table 17**). These results collectively taken again show that the incorporation of dual dopants, Co and S into the Cu_3P lattice offers unique modification of the electronic structure (as predicted by first principles ab-initio studies discussed before and also seen in XPS analysis) exhibiting significantly lower reaction polarization (lower onset overpotential) and lower activation polarization (improved reaction kinetics) than that of Cu_3P , resulting in excellent electrochemical activity with the highest electrochemical activity of 17.2 mA cm^{-2} current density at -0.05V vs RHE obtained for $(\text{Cu}_{0.83}\text{Co}_{0.17})_3\text{P}:30\text{S}$ NPs, which is almost similar to that of Pt/C ($\sim 17.6 \text{ mA cm}^{-2}$).

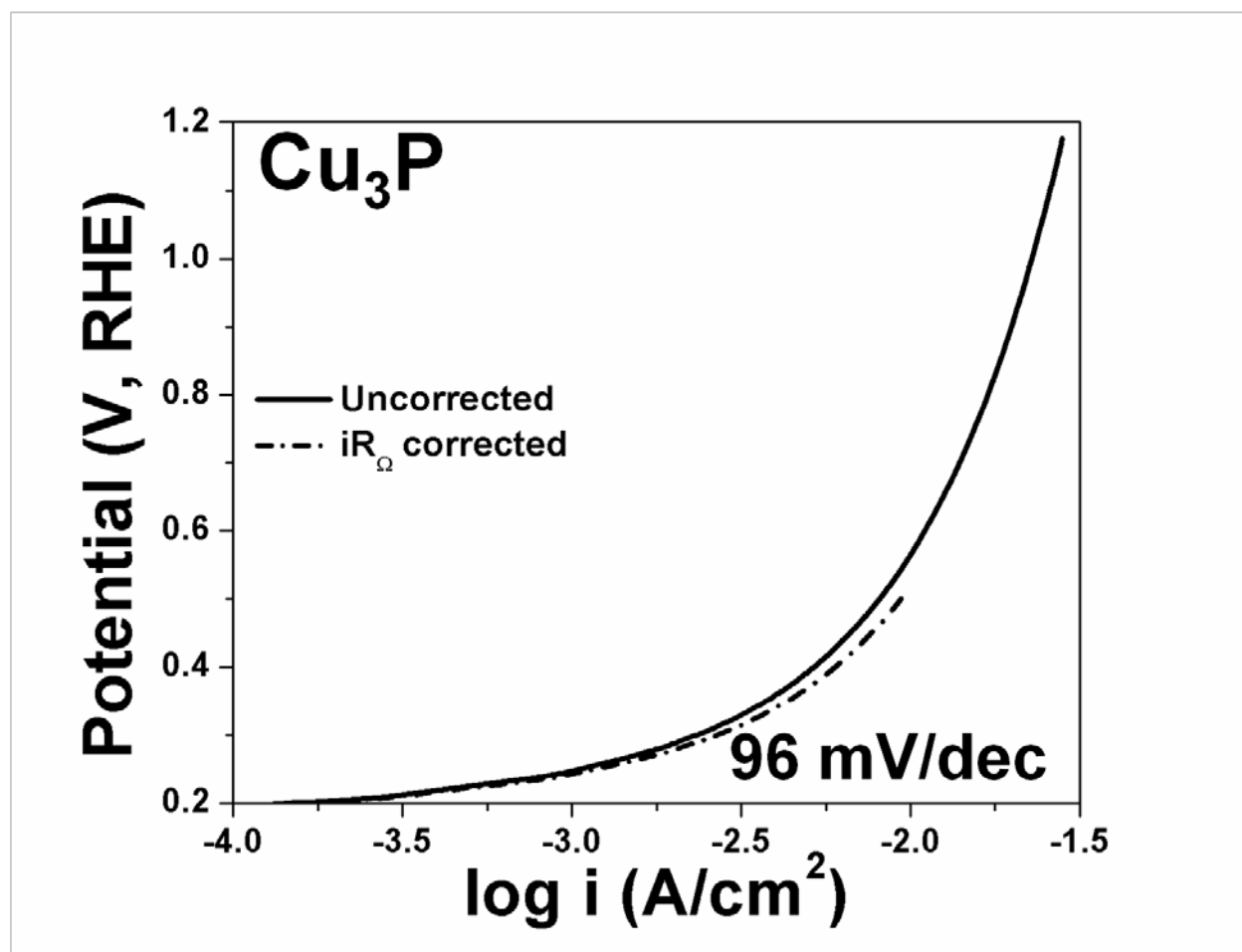


Figure 104: Tafel plot of pure Cu_3P NPs (in 0.5 M H_2SO_4 electrolyte solution)

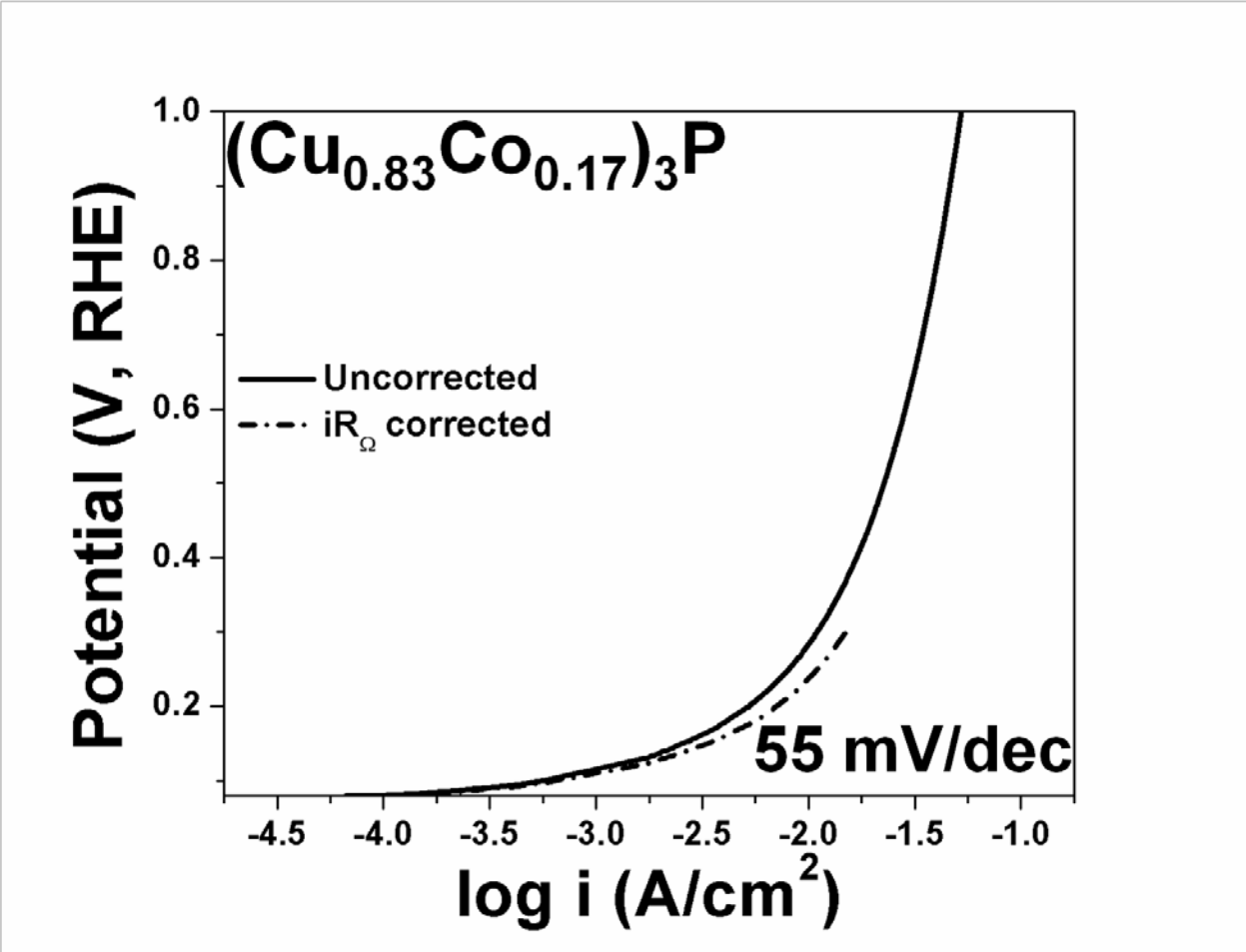


Figure 105: Tafel plot of $(\text{Cu}_{0.83}\text{Co}_{0.17})_3\text{P}$ NPs (in 0.5 M H_2SO_4 electrolyte solution)

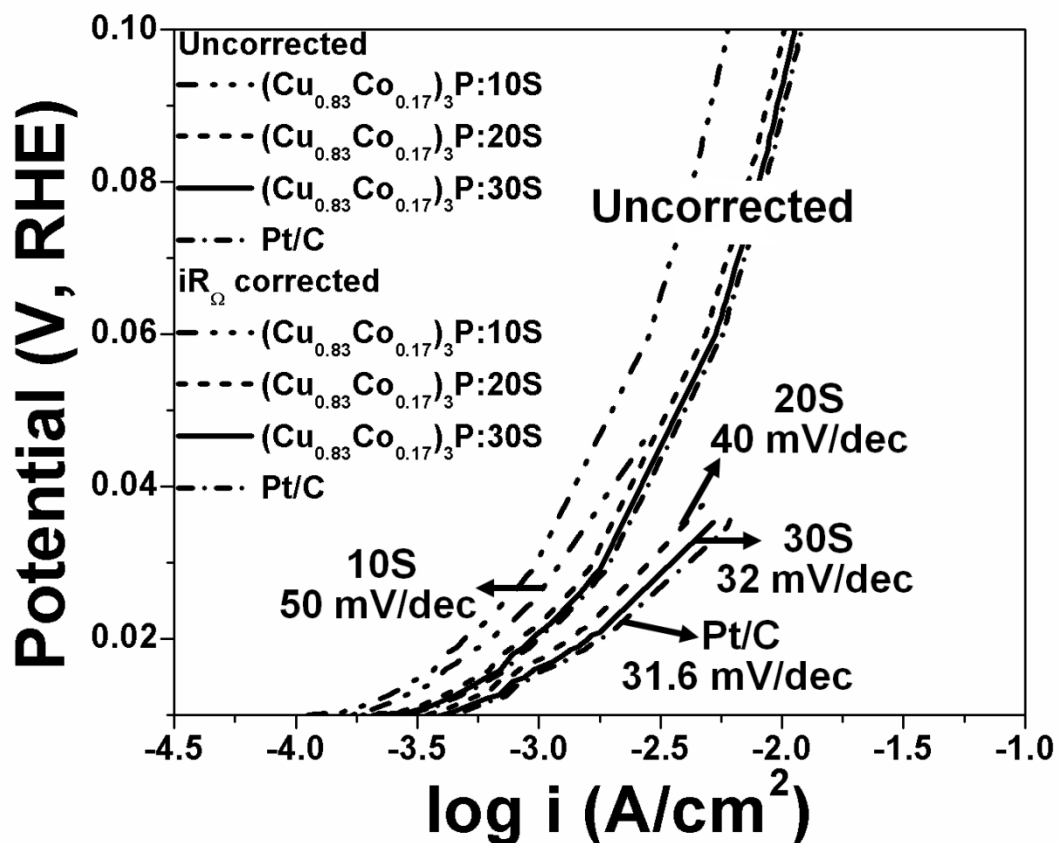


Figure 106: Tafel plot of $(\text{Cu}_{0.83}\text{Co}_{0.17})_3\text{P}:\text{S}$ NPs of different S concentration (total loading=0.7 mg/cm²) and commercial Pt/C (Pt loading=0.4 mg_{Pt}/cm²) (in 0.5 M H₂SO₄ electrolyte solution)

Electrochemical stability test

The long term electrochemical stability of $(\text{Cu}_{0.83}\text{Co}_{0.17})_3\text{P}:\text{30S}$ NPs is studied by performing chronoamperometry (CA) test wherein the electrode was maintained at constant potential of (-0.05 V vs RHE) and the loss in current density (i.e., electrochemical activity) is studied for the period of 24 h. The CA curve of $(\text{Cu}_{0.83}\text{Co}_{0.17})_3\text{P}:\text{30S}$ NPs, shown in **Figure 107**,

alongside that of commercial Pt/C, depicts negligible loss in current density ($\sim 1.6\%$) at the end of 24 h which is similar to that of commercial Pt/C ($\sim 1.5\%$). The LSV curve obtained after 24 h of exposure of the $(\text{Cu}_{0.83}\text{Co}_{0.17})_3\text{P:30S}$ NPs to the CA test (**Figure 108**) clearly depicts negligible loss in electrochemical activity. The inductively coupled plasma optical emission spectroscopy (ICP-OES) analysis of electrolyte solution ($0.5 \text{ M H}_2\text{SO}_4$) collected after 24 h of CA test of $(\text{Cu}_{0.83}\text{Co}_{0.17})_3\text{P:30S}$ NPs indicates very minimal amount of elements ($\sim 0 \text{ ppm}$) having leached out from electrode in the electrolyte solution (**Table 18**). These results show excellent long term electrochemical stability of $(\text{Cu}_{0.83}\text{Co}_{0.17})_3\text{P:30S}$ NPs, under HER operating conditions similar to that of Pt/C.

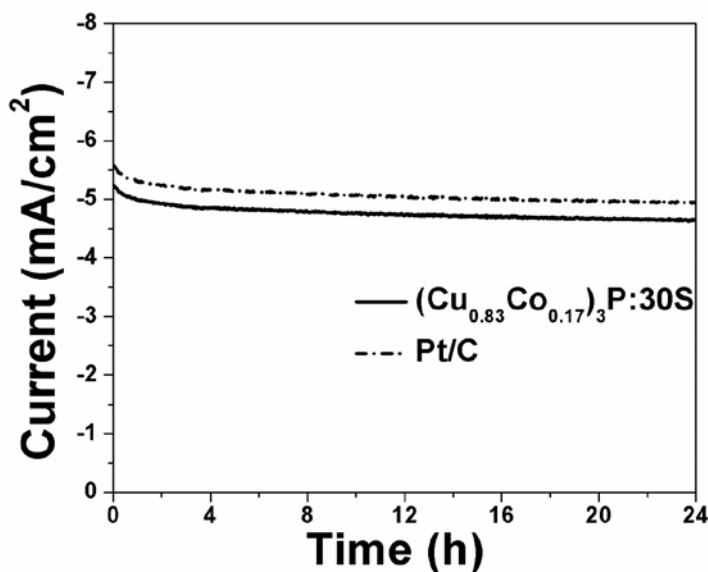


Figure 107: The variation of current vs time in the chronoamperometry (CA) test of $(\text{Cu}_{0.83}\text{Co}_{0.17})_3\text{P:30S}$ NPs (total loading= 0.7 mg/cm^2) and commercial Pt/C (Pt loading= 0.4 mgPt/cm^2), performed in $0.5 \text{ M H}_2\text{SO}_4$ electrolyte solution at a constant potential of (-0.05 V vs RHE) at 26°C for 24 h

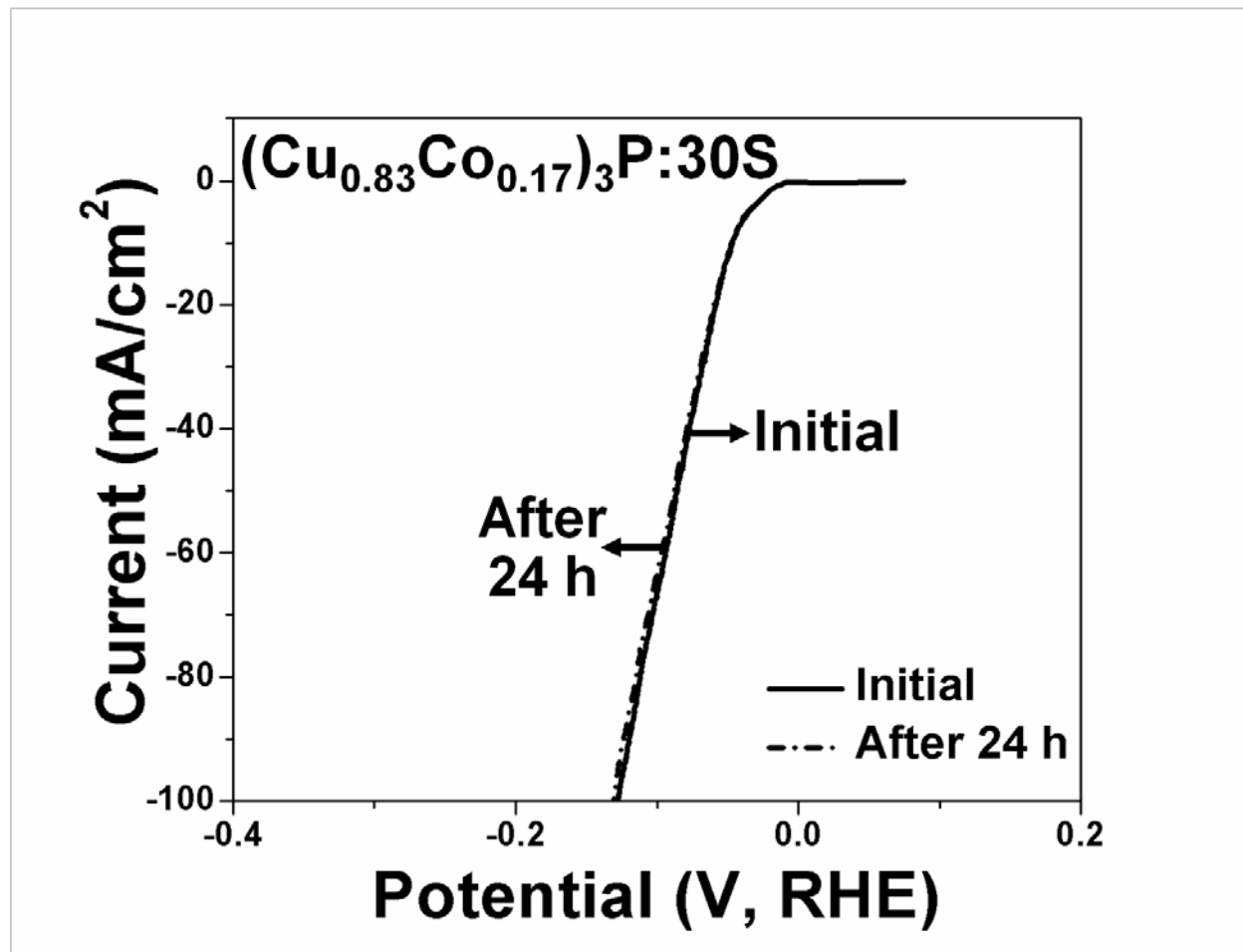


Figure 108: The iR_{Ω} corrected linear scan voltammogram (LSV) curve for HER of $(\text{Cu}_{0.83}\text{Co}_{0.17})_3\text{P:30S}$ NPs (total loading= $0.7 \text{ mg}/\text{cm}^2$), obtained in $0.5 \text{ M H}_2\text{SO}_4$ electrolyte solution at 26°C using scan rate of $1 \text{ mV}/\text{sec}$, after 24 h of CA test

Table 18: Results of ICP analysis on 0.5 M H₂SO₄ solution after chronoamperometry test of (Cu_{0.83}Co_{0.17})₃P:30S NPs

Elements	<u>Concentration (ppm)</u>
Cu	$9.4 \times 10^{-3} \pm 0.001$
Co	$8.2 \times 10^{-3} \pm 0.0002$
S	$7.1 \times 10^{-3} \pm 0.001$
P	$6.6 \times 10^{-3} \pm 0.002$

5.5.3 ELECTROCHEMICAL CHARACTERIZATION OF (Cu_{0.83}Co_{0.17})₃P:30S NPs AS HER ELECTRO-CATALYST IN H-TYPE PHOTOELECTROCHEMICAL WATER SPLITTING CELL

The NPs containing 30 at. % S, namely (Cu_{0.83}Co_{0.17})₃P:30S NPs is studied as electro-catalyst for HER in H-type PEC water splitting cell using (Sn_{0.95}Nb_{0.05})O₂:N-600 nanotubes (NTs) as the photoanode/working electrode. The photoanode and cathode compartments were separated by Nafion 115 membrane in H-type cell.⁷⁶ Chronoamperometry (CA) test was conducted for (Sn_{0.95}Nb_{0.05})O₂:N-600 NTs (photoanode) under illumination (100 mW cm⁻²) by applying a constant potential of ~0.75 V (*vs* RHE) for 24 h using (Cu_{0.83}Co_{0.17})₃P:30S NPs (total loading=0.7 mg cm⁻²) as the cathode electro-catalyst for HER in 0.5 M H₂SO₄ electrolyte solution (pH~0) at 26°C. It should be mentioned that 0.75 V (*vs* RHE) is chosen for the CA test, since a maximum ABPE of ~4.1% was obtained using (Sn_{0.95}Nb_{0.05})O₂:N-600 nanotubes (NTs) as semiconductor material for photoanode as mentioned earlier, and Pt as cathode electro-

catalyst for HER, as well as reported by us in an earlier publication ⁷⁶). During the CA test, the amount of H₂ gas (generated at the cathode) was measured after each 1 h interval using a gas chromatograph (helium as the carrier gas, Agilent 7820A) and further used for the determination of the applied bias photon-to-current efficiency (ABPE). For comparison, the ABPE was also determined using Pt/C (Pt loading=0.4 mg_{Pt} cm⁻²) as the cathode electro-catalyst, using similar procedure followed for (Cu_{0.83}Co_{0.17})₃P:30S NPs.

The amount of H₂ generated at the cathode as a function of irradiation time for (Cu_{0.83}Co_{0.17})₃P:30S NPs and Pt/C used as the cathode electro-catalyst, is shown in **Figure 109**. It is noteworthy to see that the amount of H₂ evolved at the cathode using the 30 at. % S containing NPs of (Cu_{0.83}Co_{0.17})₃P:30S as electro-catalyst is almost similar to that of commercial Pt/C. This can again be considered to be due to similar reaction polarization (similar onset overpotential) and similar activation polarization (similar reaction kinetics) for both (Cu_{0.83}Co_{0.17})₃P:30S NPs and commercial Pt/C, as discussed earlier in the LSV studies (**Figure 101** and **Table 16**) and EIS analysis (**Figure 102**, **Figure 103** and **Table 16**).

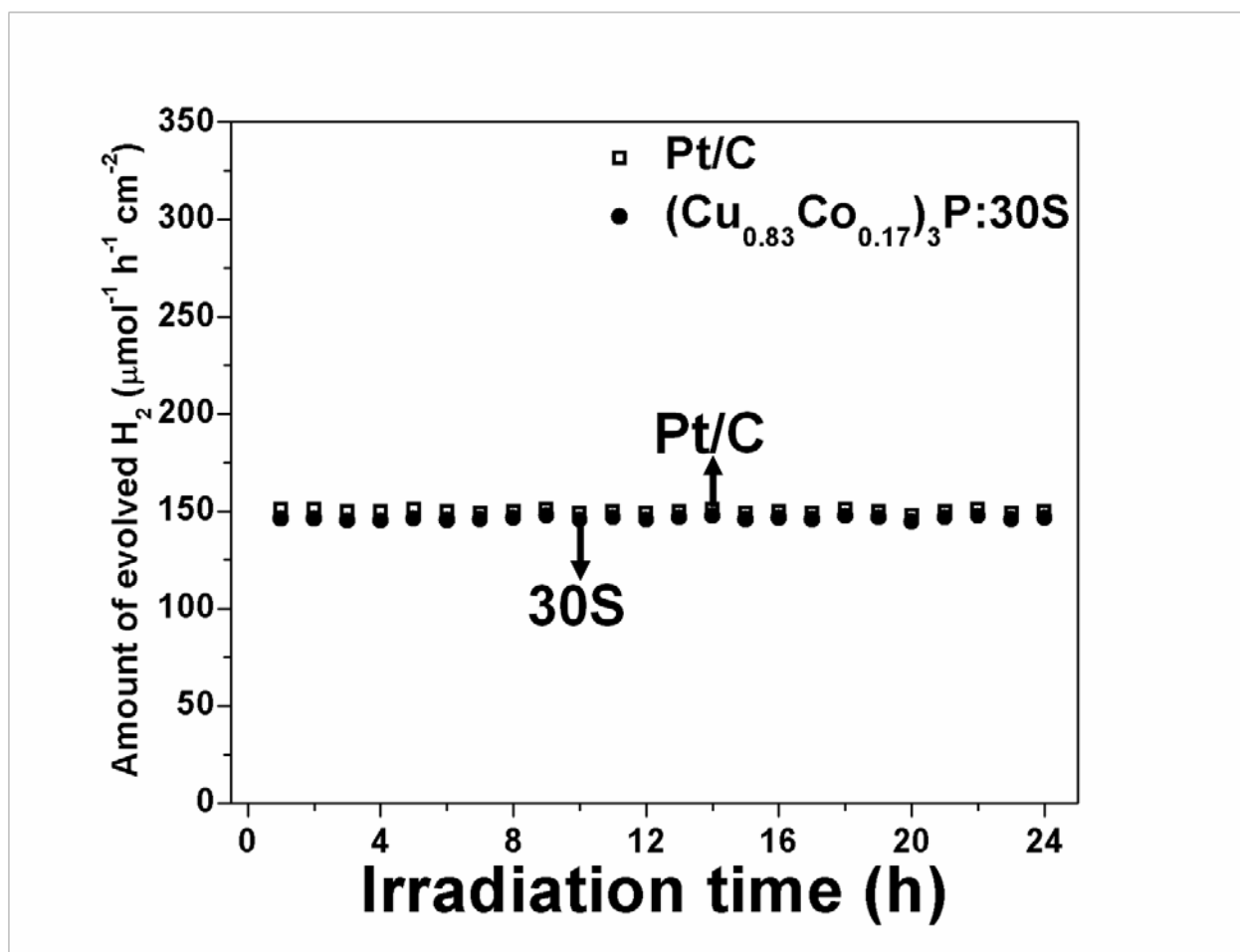


Figure 109: Amount of H₂ evolved at cathode as a function of irradiation time for (Cu_{0.83}Co_{0.17})₃P:30S NPs (total loading=0.7 mg/cm²) and Pt/C (Pt loading=0.4 mg_{Pt}/cm²) as cathode electro-catalyst for HER

Correspondingly, the ABPE is determined using the equation^{75, 77-79}:

$$ABPE = \frac{\Delta G^{\circ} \cdot n_{H_2} - V \cdot I}{P \cdot A} \times 100$$

where, n_{H_2} = H₂ evolution rate (mol sec⁻¹)

ΔG° =Gibbs free energy for generating one mole of H₂ from water (237130 J mol⁻¹)

P = Total incident power (W cm^{-2})

A = Area irradiated by incident light (cm^2)

I = Photocurrent (A)

V = Bias voltage applied (0.75 V vs RHE) to $(\text{Sn}_{0.95}\text{Nb}_{0.05})\text{O}_2\text{:N-600}$ NTs (photoanode/working electrode)

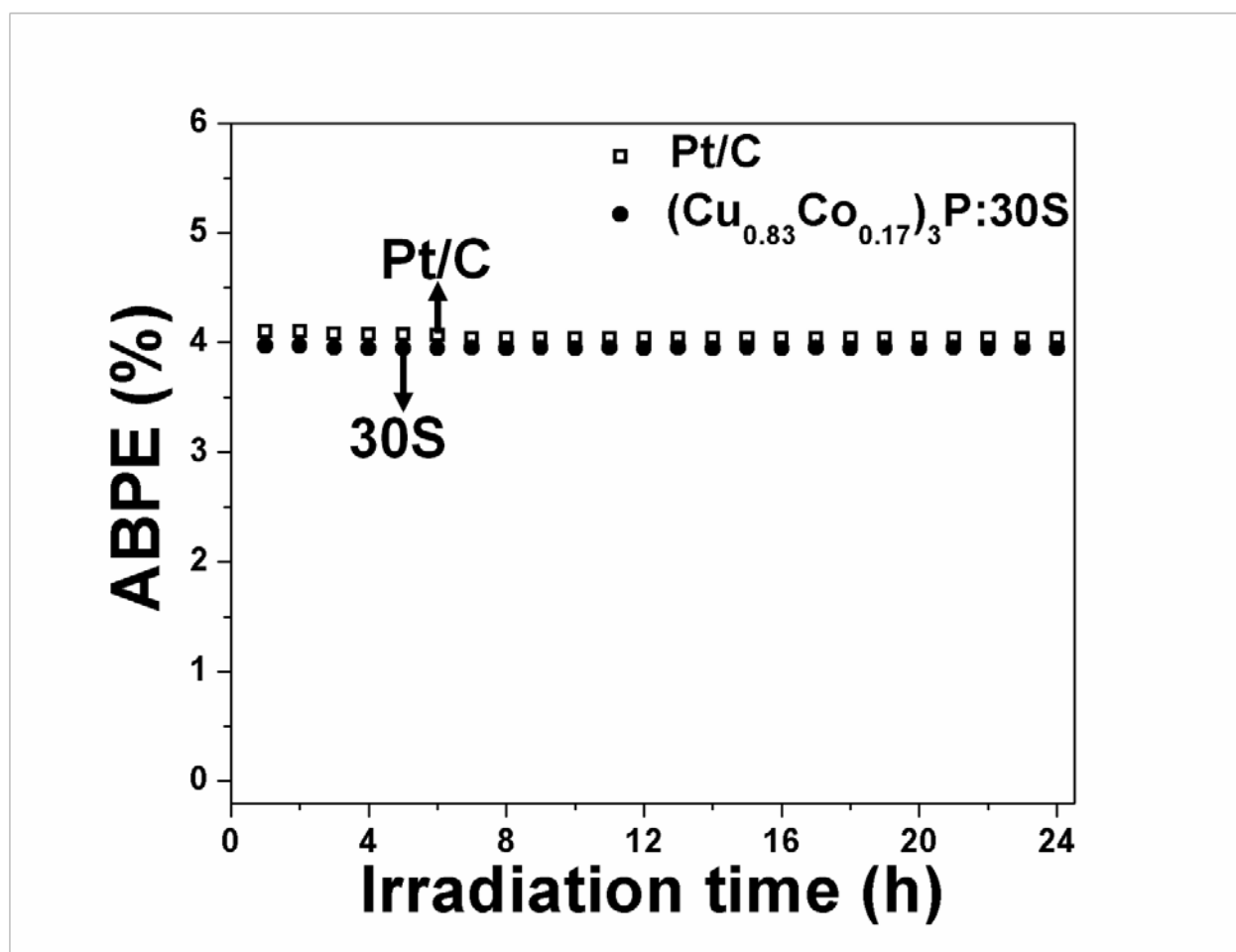


Figure 110: ABPE as a function of irradiation time for $(\text{Cu}_{0.83}\text{Co}_{0.17})_3\text{P:30S}$ NPs (total loading= 0.7 mg/cm^2) and Pt/C (Pt loading= $0.4 \text{ mg}_{\text{Pt}}/\text{cm}^2$) as cathode electro-catalyst for

HER

The plot of ABPE as function of irradiation time is shown in **Figure 110**. The ABPE obtained using $(\text{Cu}_{0.83}\text{Co}_{0.17})_3\text{P}:3\text{OS}$ NPs ($\sim 4\%$) is almost similar to that obtained using commercial Pt/C as cathode electro-catalyst for HER ($\sim 4.1\%$). Also, it should be noted that the ABPE of $\sim 4\%$ is obtained using materials (for both, the cathode and the photoanode) completely devoid of any precious metals (*e.g.* Pt) in this study. Furthermore, the ABPE of $\sim 4\%$ obtained using $(\text{Cu}_{0.83}\text{Co}_{0.17})_3\text{P}:3\text{OS}$ NPs as HER electro-catalyst and $(\text{Sn}_{0.95}\text{Nb}_{0.05})\text{O}_2:\text{N}-600$ NTs as photoanode in H-type PEC water splitting cell is the highest ABPE obtained thus far in the open published literature compared to other semiconductor materials studied as photoanode for PEC water splitting based on TiO_2 , ZnO and Fe_2O_3 to the best of our knowledge.^{64, 76, 114, 176-178} In addition, the minimal loss in ABPE ($\sim 1.8\%$) for $(\text{Cu}_{0.83}\text{Co}_{0.17})_3\text{P}:3\text{OS}$ NPs at the end of 24 h of irradiation shows excellent electrochemical stability of $(\text{Cu}_{0.83}\text{Co}_{0.17})_3\text{P}:3\text{OS}$ NPs similar to that of Pt/C ($\sim 1.7\%$ loss in ABPE at the end of 24 h) for continuous H_2 production in the PEC water splitting cell used in the current study for both the $(\text{Cu}_{0.83}\text{Co}_{0.17})_3\text{P}:3\text{OS}$ NPs and Pt/C system using $(\text{Sn}_{0.95}\text{Nb}_{0.05})\text{O}_2:\text{N}-600$ NTs as the photoanode.

The present theoretical and experimental study demonstrates excellent electrochemical performance of $(\text{Cu}_{0.83}\text{Co}_{0.17})_3\text{P}:3\text{OS}$ NPs, almost similar to that of commercial Pt/C in acidic media. This can be attributed to the introduction of Co and S in the Cu_3P lattice, resulting in novel and unique modification of the electronic structure, as indicated by the first principle studies discussd later (**Section A.4** $(\text{Cu}_{0.83}\text{Co}_{0.17})_3\text{P}:\text{S}$ HER ELECTRO-CATALYST FOR CATHODE) and confirmed by XPS analysis (**Figure 97, Figure 98, Figure 99** and **Figure 100**). The system correspondingly exhibits onset overpotential as seen in LSV plot (**Figure 101** and **Table 16**), reaction kinetics (charge transfer resistance) as studied in EIS analysis (**Figure 102,**

Figure 103 and **Table 16**) and Tafel slope (**Figure 104, Figure 105, Figure 106** and **Table 2**), electrochemical activity in PEC water splitting cell in acidic media (H_2 yield and ABPE) (**Figure 109** and **Figure 110**), almost similar to that of commercial Pt/C. These results collectively thus, demonstrate the potential of $(Cu_{0.83}Co_{0.17})_3P:30S$ NPs clearly as a replacement of the state of the art commercial Pt/C and with further system modification it is possible that the system can achieve even superior electrochemical activity for HER than that of Pt/C. The present report of its excellent electrochemical performance and stability for HER in both electrolytic water splitting (i.e., water electrolysis) and PEC water splitting indeed is a testimonial of a hallmark breakthrough achieved in the pursuit of identification and development of low cost, highly active and robust non-noble metals based electro-catalyst for HER for replacing the expensive state of the art commercial Pt/C electro-catalyst used at present.

Conclusions:

The present study shows that the sulfur and cobalt doped $(Cu_{0.83}Co_{0.17})_3P: S$ nanoparticles (NPs) system serves as a potential cathode electro-catalyst for HER. The system was identified using theoretical first principles studies. The XRD patterns of the synthesized $(Cu_{0.83}Co_{0.17})_3P:S$ NPs clearly indicate the formation of single phase with hexagonal structure (similar to that of Cu_3P). The XPS analysis conducted also showed modification in the electronic structure upon incorporation of Co and S into the Cu_3P lattice, leading to superior electrochemical activity for HER. The present study thus clearly demonstrates $(Cu_{0.83}Co_{0.17})_3P:S$ NPs of different S concentration exhibiting excellent electrochemical activity for HER with onset overpotential of ~ 10 mV (*vs* RHE) which is similar to that of commercial Pt/C in acidic media and is indeed the lowest obtained so far compared to other reported non-noble metals based HER electro-catalysts

in the open literature. The highest electrochemical performance is obtained for $(\text{Cu}_{0.83}\text{Co}_{0.17})_3\text{P}:30\text{S}$ NPs, which showed overpotential to reach current density of 100 mA cm^{-2} , almost similar to that of commercial Pt/C in acidic media and lower than other reported non-noble metals based HER electro-catalysts. These results bode well with the results of the theoretical study. Additionally, the $(\text{Cu}_{0.83}\text{Co}_{0.17})_3\text{P}:30\text{S}$ NPs showed excellent electrochemical activity for HER as cathode electro-catalyst in PEC water splitting system using $(\text{Sn}_{0.95}\text{Nb}_{0.05})\text{O}_2:\text{N}-600$ nanotubes (NTs) as photoanode in acidic media. An ABPE of $\sim 4\%$ obtained using $(\text{Cu}_{0.83}\text{Co}_{0.17})_3\text{P}:30\text{S}$ NPs is almost similar to that of commercial Pt/C as cathode electro-catalyst for HER ($\sim 4.1\%$) and the highest obtained so far using completely non-noble metals based materials (for cathode and photoanodes based on literature reports for TiO_2 , ZnO and Fe_2O_3), to the best of our knowledge. Furthermore, the $(\text{Cu}_{0.83}\text{Co}_{0.17})_3\text{P}:30\text{S}$ NPs exhibit excellent long term electrochemical stability for HER in acidic media similar to that of Pt/C in both water electrolysis and PEC water splitting cell. Hence, the present study demonstrates $(\text{Cu}_{0.83}\text{Co}_{0.17})_3\text{P}:30\text{S}$ NPs as potential electro-catalyst for replacing Pt/C for HER in electrolytic and photoelectrochemical water splitting system due to its excellent electrochemical performance and stability. The results reported here is anticipated to offer significant reduction in the capital cost of electrolytic and PEC water splitting systems for achieving efficient and economic hydrogen generation to address the global energy crisis. It is also likely that this system will ensure sustainable development of modern society utilizing clean non-carbonaceous fuels leading to an energy efficient economy.

6.0 SUMMARY

Vertically aligned 1-D semiconductor photoelectro-catalyst nanomaterials [for oxygen evolution reaction (OER) at photoanode] and nanostructured ultra-low noble metal containing solid solution electro-catalysts as well as noble metal-free electro-catalysts [for hydrogen evolution reaction (HER) at cathode] have been chemically synthesized, characterized and developed for use in solar energy driven water splitting, i.e., photoelectrochemical water splitting. The experimental work in this thesis was primarily targeted towards the accomplishment of superior efficiency and durability of the catalyst materials.

Semiconductor nanomaterials with significantly improved optoelectronic properties and excellent photoelectrochemical performance were obtained for the photoanodes using simple and economical liquid phase deposition method. The strategies involved comprised the following: (i) systematic band gap engineering using co-doping strategy for ZnO and SnO₂ to improve electron mobility compared to other well-studied semiconductor photoanodes and (ii) development of bilayered composite nanomaterials of Nb and N co-doped SnO₂ and WO₃ to achieve facile separation and transport of photogenerated carriers, thereby, achieving superior solar-to-hydrogen efficiency (STH) with minimum to no applied bias in addition to solar energy. The PEC activity of semiconductor materials was studied by analyzing the following: (i) incident photon-to-current efficiency (IPCE) obtained by using different optical band-pass filters to obtain information about the number of incident photons converted to photocurrent density in the

photoanode half-cell; (ii) Applied bias photon-to-current efficiency (ABPE) to study the utilization of the incident photons and the applied bias in initiating the water splitting reaction at the photoanode half-cell; (iii) solar-to-hydrogen efficiency (STH) to study the full-cell efficiency giving vital information about the incident photons at the photoanode which are further converted to hydrogen fuel at the cathode of the PEC water splitting cell in the absence of any bias. Thus, STH is ideally extremely important for the identification of efficient semiconductor materials that could essentially drive both OER and HER without the need of any co-catalysts and externally applied bias. The semiconductor nanomaterials currently studied in this thesis portend to be potentially preferred for use as a photoanode OER material in PEC water splitting. The results however, provide a path forward for potentially identifying novel photoanode materials that could likely attain higher STH values in the future.

Similarly, different electro-catalyst systems were chosen systematically for HER at cathodes of PEC water splitting in order to achieve excellent electrochemical activity and superior long term stability with the aim of replacing state of the art expensive and precious platinum electro-catalyst. The corresponding strategies involved synergistic Co-Ir alloying and thus, achieving improved chemical and catalytic properties compared to pure Co and pure Ir. Accordingly, Co(Ir) solid solution powders of different compositions were chemically synthesized. The strategy of Co(Ir) offered significantly improved electrochemical performance and efficiency not only compared to pure Co and pure Ir but also Pt/C electro-catalyst in electrolytic as well as PEC water splitting cells. In addition, the strategy for development of completely noble metal-free electro-catalyst involved Co and S co-doping strategy in Cu_3P for achieving beneficial modification of the electronic structure and thus, obtaining highly active surface phase for HER. The co-doping strategy offered excellent electrochemical performance of

chemically synthesized $(\text{Cu,Co})_3\text{P:S}$ nanoparticles for HER in electrolytic and PEC water splitting cells, similar to that of Pt/C.

Systematic structural and electrochemical characterization was conducted in this thesis to understand the relation between the catalyst structure and the electrochemical behavior.

6.1 1-D SEMICONDUCTOR PHOTOELECTRO-CATALYSTS FOR PHOTOANODES

1-D nanostructures of Co and N co-doped ZnO nanowires (NWs) and Nb and N co-doped SnO_2 nanotubes (NTs) have been synthesized on FTO substrate using simple liquid phase deposition method followed by heat treatment in ammonia atmosphere at different temperatures (400°C , 500°C and 600°C). No phase separation or any extra peak was observed for dopants used in the current thesis studies. Detailed characterization and photoelectrochemical studies were conducted to confirm the potential of photoelectro-catalysts as an OER photoanode for PEC water splitting. The study of co-doped ZnO NWs and SnO_2 NTs has been discussed in **Section 5.1** and **Section 5.2**, respectively. These results establish the potential of co-doping strategy in significantly improving optoelectronic properties and photoelectrochemical performance of ZnO and SnO_2 semiconductor systems. The co-doping strategy modified the electronic structure of ZnO and SnO_2 leading to significant band gap reduction offering superior visible light absorption, $\sim 4\text{-}5$ order of magnitude improved carrier density and facile electrochemical charge transfer compared to pure ZnO NWs and SnO_2 NTs.

The modified optoelectronic and charge transport properties of co-doped ZnO and SnO_2 (used as photoanode) aid in achieving superior PEC activity and applied bias photon-to-current

efficiency (ABPE) compared to pure ZnO and SnO₂. In fact, an η of 1.39% for (Zn_{0.95}Co_{0.05})O:N-600 NWs, the highest reported thus far, to the best of the literature values known is obtained for ZnO based nanostructures. Furthermore, an η of 4.1% is obtained for (Sn_{0.95}Nb_{0.05})O₂:N-600 NTs, which is even higher than that of hitherto studied TiO₂, ZnO, α -Fe₂O₃ systems following careful assessment of the dated reported literature. Additionally, (Zn_{0.95}Co_{0.05})O:N-600 NWs and (Sn_{0.95}Nb_{0.05})O₂:N-600 NTs exhibit excellent long term PEC stability in the electrolyte solution under illumination. These results gave the motivation for further system modification of (Sn_{0.95}Nb_{0.05})O₂:N-600 NTs with the aim of achieving- (i) excellent separation of photogenerated electron-hole pairs resulting in longer carrier lifetime, (ii) superior STH under illumination at zero applied bias.

Consequently, bilayered semiconductor photoanodes comprising (Sn_{0.95}Nb_{0.05})O₂:N-600 and WO₃ were synthesized using wet impregnation method and liquid phase deposition approach followed by heat treatment in ammonia atmosphere at 600°C. Extensive structural analysis utilizing x-ray diffraction (XRD), scanning electron microscopy (SEM), energy dispersive x-ray spectroscopy (EDX), transmission electron microscopy (TEM) and x-ray photoelectron microscopy (XPS) was performed for the synthesized semiconductor nanomaterials. Detailed results of structural analysis and photoelectrochemical characterization have been described in **Section 5.3**. Coupling nanolayers of (Sn_{0.95}Nb_{0.05})O₂:N-600 and WO₃ semiconductor materials offered modified optoelectronic properties, improved charge transport and excellent separation of photogenerated electron-hole pairs with minimum recombination under illumination, thereby, resulting in an hallmark ~20 fold improvement at (-0.2 V vs RHE, which is near zero bias and selected following the earlier reports in the literature^{65, 105, 218, 256-260}) in carrier lifetime compared to (Sn_{0.95}Nb_{0.05})O₂:N-600 NTs.

The bilayer semiconductor nanostructures of $[\text{WO}_3-(\text{Sn}_{0.95}\text{Nb}_{0.05})\text{O}_2:\text{N}-600]-2$ NTs showed excellent photoelectrochemical activity and superior long term photoelectrochemical stability in the acidic electrolyte solution under illumination. In fact, $[\text{WO}_3-(\text{Sn}_{0.95}\text{Nb}_{0.05})\text{O}_2:\text{N}-600]-2$ NTs showed a remarkable STH of $\sim 3.83\%$ (with no external potential applied) and ABPE of $\sim 5.1\%$ (at 0.6V vs RHE), which is the highest STH/ABPE reported thus far compared to other reported photoanode materials such as ZnO, Fe_2O_3 and TiO_2 , to the best of our knowledge.

The significantly improved optoelectronic properties and facile electrochemical charge transfer for 1-D semiconductor nanostructures developed and studied in this thesis suggest their potential as an OER photoanode for PEC water splitting and also opens up new avenues for these materials to be likely used in different solar energy based applications. For photoanodes, light absorption losses, recombination losses and polarization losses mainly limit STH/ABPE and electricity cost for the bilayer system. As discussed in **Section 5.3**, recombination losses decrease by a commendable $\sim 12\%$ for $[\text{WO}_3-(\text{Sn}_{0.95}\text{Nb}_{0.05})\text{O}_2:\text{N}-600]-2$ NTs under the applied bias of $\sim 0.6\text{V}$ (vs RHE) compared to the no bias condition, suggesting promise of the composite bilayer-2 system. Despite these losses, $[\text{WO}_3-(\text{Sn}_{0.95}\text{Nb}_{0.05})\text{O}_2:\text{N}-600]-2$ NTs show excellent PEC performance under applied bias with a commendable ABPE of $\sim 5.1\%$ (at $\sim 0.6\text{V}$ vs RHE) and STH of $\sim 3.83\%$ (under no bias). Hence, $[\text{WO}_3-(\text{Sn}_{0.95}\text{Nb}_{0.05})\text{O}_2:\text{N}-600]-2$ NTs bilayer system is indeed promising and further electronic structural modification of bilayer system by changing band edge positions, which can be achieved by suitable materials and defects engineering by introducing suitable acceptor/donor levels (in the band gap), will help in lowering the above mentioned losses and thus, likely contribute to achieving high STH (at zero applied bias) and superior ABPE (under minimal applied bias).

6.2 NANOSTRUCTURED HER ELECTRO-CATALYSTS

The electro-catalytic materials based on Co(Ir) and (Cu,Co)₃P:S in 3D architectures of nanoparticles were synthesized to achieve the compositional homogeneity at atomic scale. Synthesis of the nanostructured electro-catalyst architectures was carried out to promote cooperative and sequential reaction steps along different catalytic domains of the nanoscale structures.

Co_{1-x}(Ir_x) (x=0, 0.2, 0.3, 0.4, 1) solid solution nanoparticles of different compositions were synthesized by the wet chemical reduction approach. Solid solution formation resulted in excellent electrochemical activity for HER with no compromise in stability. Detailed electrochemical experiments and kinetic studies, along with the long term structural stability tests and EIS studies were conducted as discussed in **Section 5.4**. The electrochemical and kinetic parameters of Co_{1-x}(Ir_x) (x=0.3, 0.4) were significantly superior than Pt/C in electrolytic and PEC water splitting cells, which was corroborated by other electrochemical tests such as polarization, EIS and chronoamperometry (CA). The excellent ABPE of ~5.74% and ~7.92% obtained using Co_{1-x}(Ir_x) (x=0.3, 0.4) [\sim 40% and \sim 93% higher than that of Pt/C (\sim 4.1%), respectively] portends \sim 60-70 mol.% reduction in noble metal content in HER electro-catalyst.

Nanoparticulate robust cobalt doped copper phosphofluoride, i.e., (Cu_{0.83}Co_{0.17})₃P:x at.% S (x=10, 20, 30) system of different composition was synthesized *via* wet chemical approach. Excellent electrochemical properties along with superior corrosion resistance and ABPE of \sim 4% [similar to that of Pt/C (\sim 4.1%)] were obtained for (Cu_{0.83}Co_{0.17})₃P:30 at. % S for HER [using (Sn_{0.95}Nb_{0.05})O₂:N-600 NTs as photoanode] and is discussed in **Section 5.5**. A thorough characterization utilizing a range of characterizing techniques of XRD, SEM, EDX, TEM and

XPS was carried out to complement the electrochemical results. This work shows a hallmark ~100 mol.% reduction in noble metal content in HER electro-catalyst without any compromise in electrochemical performance.

Identification and engineering of such non-noble metals based electro-catalyst material systems by further modification on atomic scale as well as nanoscale architectures will indeed yield comparable or even higher electrochemical performance than the gold Pt/C standard and would contribute immensely to reducing the overall capital costs of electrolytic and PEC water splitting cells. This result would thus likely help in the attainment of the targeted hydrogen production cost (< \$3.0/gallon gasoline equivalent delivered) comparable to conventional liquid fuels and thus, will aid in addressing the global energy crisis while ensuring sustainable development of modern society with clean non-carbonaceous fuels based economy.

The results detailed in this thesis provide a compilation of strategies to develop novel materials displaying excellent electrochemical and photoelectrochemical response to splitting of water under acidic and neutral pH conditions. Strategies identified and implemented offer a rational pathway to identification of new photoanode materials with the promise for splitting water without the inducement of any electrical bias. Similarly, strategies are outlined for the development of electrocatalysts with minimal or completely devoid of noble metals and precious metals indicating their prowess to generate hydrogen serving as efficient cathode electrocatalysts in PEC water splitting systems. It is anticipated that the work detailed herein would serve as a pathway for continued research to be conducted leading to the development of new and novel materials that will likely result in even higher STH reported in this thesis ultimately meeting or even exceeding the DOE required standards while also meeting the proven robustness, accepted stability and performance inclusive of both, electrochemical and photoelectrochemical response

matching and exceeding that of Pt/C under practical field scale applications. These continuing studies will be planned for in the future.

APPENDIX A

FIRST PRINCIPLES CALCULATIONS

All the first principle calculations reported herein have been conducted by *Dr. Oleg I. Velikokhatnyi*, a Research Assistant Professor in the Department of Bioengineering at the University of Pittsburgh (*Dr. Kumta's group*). The theoretical studies complement the experimental results described herein in this thesis and provide valuable supporting information contributing to the fundamental understanding of the electrochemical activity of all the electrocatalysts and photoelectrocatalysts considered in this thesis.

A.1 Co AND N CO-DOPED ZnO NANOWIRES (NWS) (PHOTOANODE)

A.1.1 COMPUTATIONAL METHODOLOGY

The overall photoelectro-catalytic performance of ZnO is expected to depend on various factors, one of which is the width of the electronic band gap between the valence and the conduction bands of the oxide, which has strong dependence on the electronic structure of the material. Thus, the main aim of the computational component of the present study is to

investigate and understand the effects of chemical compositions of ZnO-based oxides on the electronic structure and the photoelectro-catalytic activity from the theoretical considerations. The total energy, electronic and optimized crystal structures as well as the total and projected densities of electronic states of pure ZnO and doped with Co and N have been calculated using the first principles approach within the density functional theory (DFT).

At room temperature, it is known that ZnO adopts the wurtzite crystal structure with hexagonal symmetry $P6_3mc$ space group and having four atoms in the elementary unit cell. Experimentally determined lattice parameters are: $a = 3.253 \text{ \AA}$, and $c = 5.213 \text{ \AA}$. Zinc atoms occupy the special 2b Wyckoff positions $(1/3, 2/3, 0)$, while oxygen atoms also occupy 2b positions with coordinates $(1/3, 2/3, u)$, where $u = 0.3817$.³¹⁷ Each oxygen atom lies in a tetrahedral site surrounded by four zinc atoms located at the corners of the tetrahedron and vice versa, each zinc atom is surrounded by four oxygen atoms. This unit cell has thus been chosen as a basis for construction of $[2 \times 2 \times 2]$ 32-atom supercell allowing modeling of various compositions of Co- and N- co-doped ZnO. In particular, one out of 16 available Zn atoms could be replaced for Co resulting in the following formula unit $(\text{Zn}_{0.9375}\text{Co}_{0.0625})\text{O}$ corresponding to 6.25 at% of Co in the Co-doped ZnO. Similarly, replacement of one atom of oxygen for nitrogen corresponds to 6.25 at% of N. Accordingly, the substitution of two atoms of Zn or O corresponds to 12.5 at% of these elements.

The Vienna Ab-initio Simulation Package (VASP) was used within the projector-augmented wave³¹⁸ method³¹⁹⁻³²¹ to calculate the total energies, electronic structure and density of electronic states, while the generalized gradient approximation³²² was used for the exchange-correlation energy functional in a form suggested by Perdew and Wang³²³. This program calculates the electronic structure and *via* the Hellmann-Feynman theorem, the inter-atomic

forces are also determined from first-principles. Standard PAW potentials were employed for the Zn, Co, O, and N potentials containing twelve, nine, six, and five valence electrons, respectively.

It is known that Co-doped ZnO demonstrates ferromagnetic properties originating from d-electrons of Co^{2+} ions in the compound (see, for example³²⁴) and hence, the spin-polarized calculations of the total energy and the electronic structure have been performed for all the compositions containing Co-doping, namely $(\text{Zn}_{0.9375}\text{Co}_{0.0625})\text{O}$ as well as $(\text{Zn}_{0.9375}\text{Co}_{0.0625})\text{O}_{0.9375}\text{N}_{0.0625}$ and $(\text{Zn}_{0.9375}\text{Co}_{0.0625})\text{O}_{0.875}\text{N}_{0.125}$.

The plane wave cutoff energy of 520 eV has been chosen for all the materials considered to maintain a high accuracy of the total energy calculations. The lattice parameters and internal positions of atoms were fully optimized employing the double relaxation procedure, and consequently, the minima of the total energies with respect to the lattice parameters and internal ionic positions have been determined. This geometry optimization was obtained by minimizing the Hellman–Feynman forces via a conjugate gradient method, so that the net forces applied on every ion in the lattice are close to zero. The total electronic energies were converged within 10^{-5} eV/un.cell resulting in the residual force components on each atom lower than 0.01 eV/Å/atom, thus allowing for an accurate determination of the internal structural parameters for the oxide. The Monkhorst-Pack scheme was used to sample the Brillouin Zone (BZ) and generate the k -point grid for all the materials considered in the present study. A choice of the appropriate number of k -points in the irreducible part of the BZ was based on convergence of the total energy to 0.1 meV/atom.

A.1.2 RESULTS OF THE COMPUTATIONAL STUDY

Pure ZnO

It should be noted that there are several published theoretical studies dedicated to pure and doped ZnO and the electronic structure of the oxide has already been thoroughly discussed in the literature (see, for example,³²⁵⁻³²⁷). However, in the context of the current study it is logical and pertinent to describe the electronic structure of ZnO. In addition, pure ZnO will be used to illustrate the combined Co- and N-doping effects on the ZnO electronic structure.

The total and projected densities of electronic states calculated for pure ZnO are shown in **Figure 111**. The primary energy band structure of ZnO consists of three bands. The low energy band between -17 and -18 eV is composed of the 2s states of oxygen. The wide valence band within the energy interval from -6.1 to 0.0 eV consists of Zn 3d states located primarily between -6.1 and -4 eV and O 2p states located between -4 eV and the Fermi level. Finally, the conduction band consists mainly of hybridized Zn 4s and O 2p electronic states separated from the valence band by the energy gap E_{bg} of 0.89 eV. This value of the forbidden gap is underestimated substantially in comparison to the experimental value of 3.18 eV as seen in **Table 19**³²⁸, which is the well-known intrinsic characteristic limitation of DFT calculations arising from the self-interaction effects and derivative discontinuities of the exchange correlation energy. However, for the purposes of the present study, a precise calculation of the band gap is not essentially critical since the goal of the present work is to assess the overall effect of Co and N co-doping on the electronic structure of ZnO and hence, general trends of the electronic structure modifications during doping of ZnO is deemed sufficient. Hence, this disadvantage of DFT will not affect the results obtained and discussed in the current study. Furthermore, the

main parameters of the electronic structure for ZnO calculated in the present study do agree well with the results obtained from previously published theoretical calculations.^{325, 326, 329}

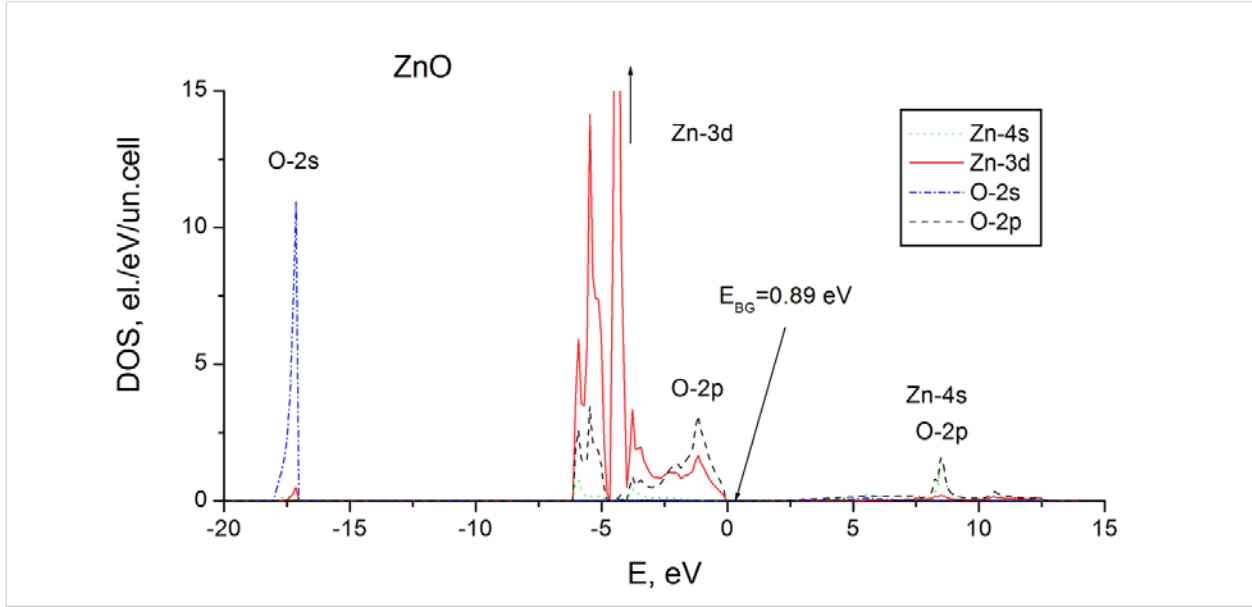


Figure 111: Projected density of states for pure ZnO. Fermi level is set for zero. Fermi level is set for zero

Table 19: Calculated and experimental optical band gaps E_{BG} for pure and doped ZnO

Composition	E_{BG} (eV) calc.	E_{BG} (eV) exp.
ZnO	0.89	3.18
$[Zn_{0.9375}Co_{0.0625}]O$	0.45	2.98
$Zn[O_{0.9375}N_{0.0625}]$	0.70	-
$[Zn_{0.9375}Co_{0.0625}][O_{0.9375}N_{0.0625}]$	0.34	2.31
$[Zn_{0.9375}Co_{0.0625}][O_{0.875}N_{0.125}]$	0.23	2.16

ZnO doped with Co and N

The calculated total and projected densities of the electronic states for $(\text{Zn}_{0.9375}\text{Co}_{0.0625})\text{O}$ oxide composition are shown in **Figure 114**. It can be seen that the main band structure of the Co-doped ZnO is similar to the undoped oxide. However, the main difference between the two is the appearance of the Co-3d electronic states within the Fermi level vicinity. A narrow Co-3d spin-up states located at the top of the valence band are strongly hybridized with O-2p electrons and separated from almost non-hybridized conduction Co-3d spin-down states by the energy gap of 0.45 eV. This optical band gap value is noticeably smaller than the E_{BG} calculated for the pure ZnO (0.89 eV) which agrees well with experimental observations (**Table 19**) demonstrating narrowing of the optical band gap following Co-doping of ZnO. Of course, both values are significantly underestimated due to the reasons discussed above. However the relative difference between these values is qualitatively the same as that observed experimentally. It should also be noted that since the impurity Co-3d states locate at the Fermi level, it clearly indicates that Co doped ZnO is n-type semiconductor. Additionally, the calculated electronic structure is very similar to other spin-polarized calculations reported in the literature³²⁴.

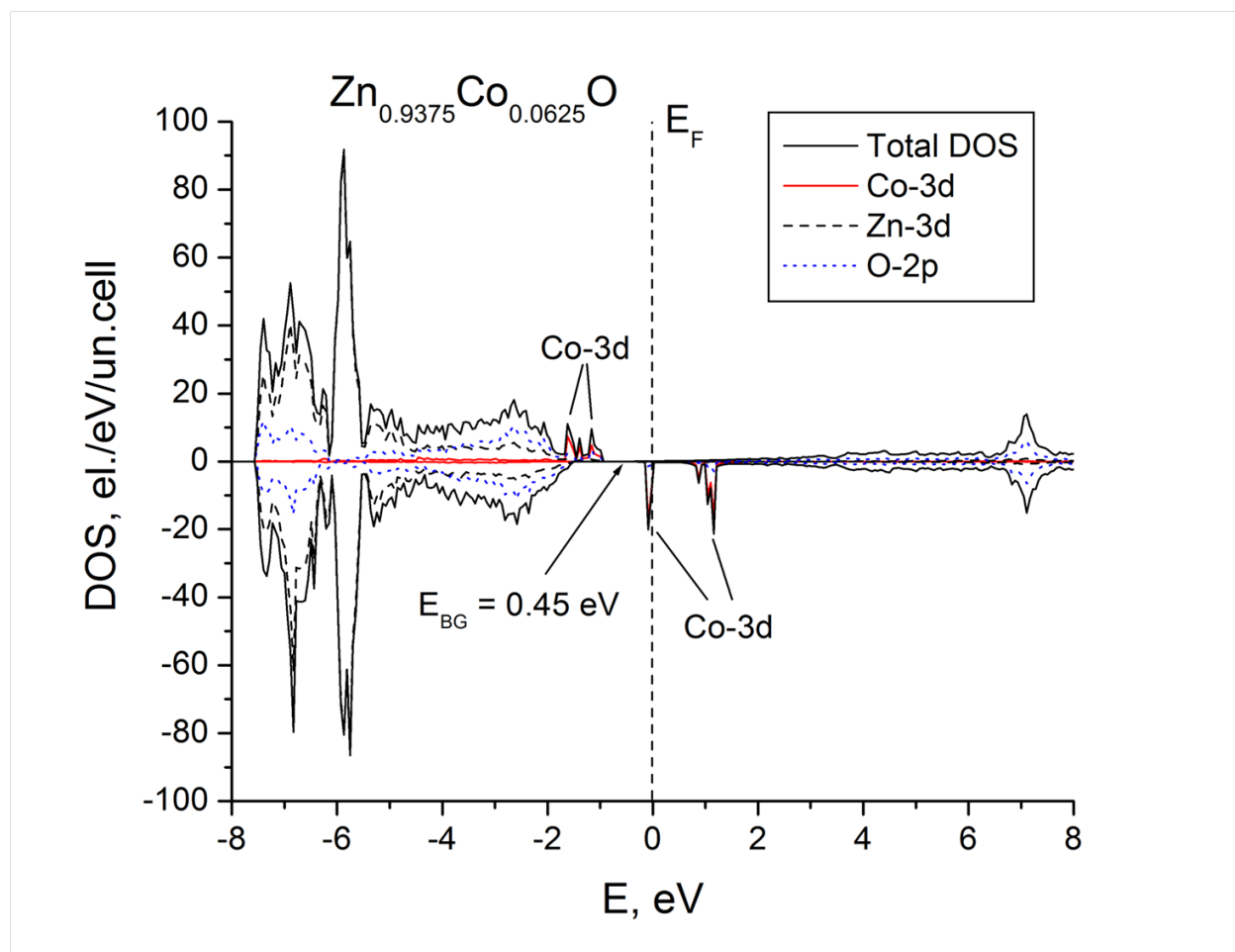


Figure 112: Total and projected density of states for ZnO doped with 6.25 at% of Co. Top panel is for spin-up, bottom panel is for spin-down. Fermi level is set for zero

To further elucidate the effects of nitrogen doping on the electronic structure of ZnO, $(\text{ZnO}_{0.9375})\text{:N}_{0.0625}$ has been considered as a representative composition. The projected density of electronic states for this composition is shown in **Figure 113**. As described above, it can be seen that the general picture is almost identical to that for pure ZnO. The only difference between pure and N-doped ZnO oxide is the appearance of N-2p impurity states at the top of the valence band. The calculated band gap E_{BG} is 0.7 eV which is noticeably narrower than the

corresponding band gap of 0.89 eV for pure ZnO. This trend also agrees well with calculations reported by Xu, Zong *et al.*³³⁰. Thus, the addition of N can help in decreasing the optical band gap further and extend the absorption of ZnO to the visible region.

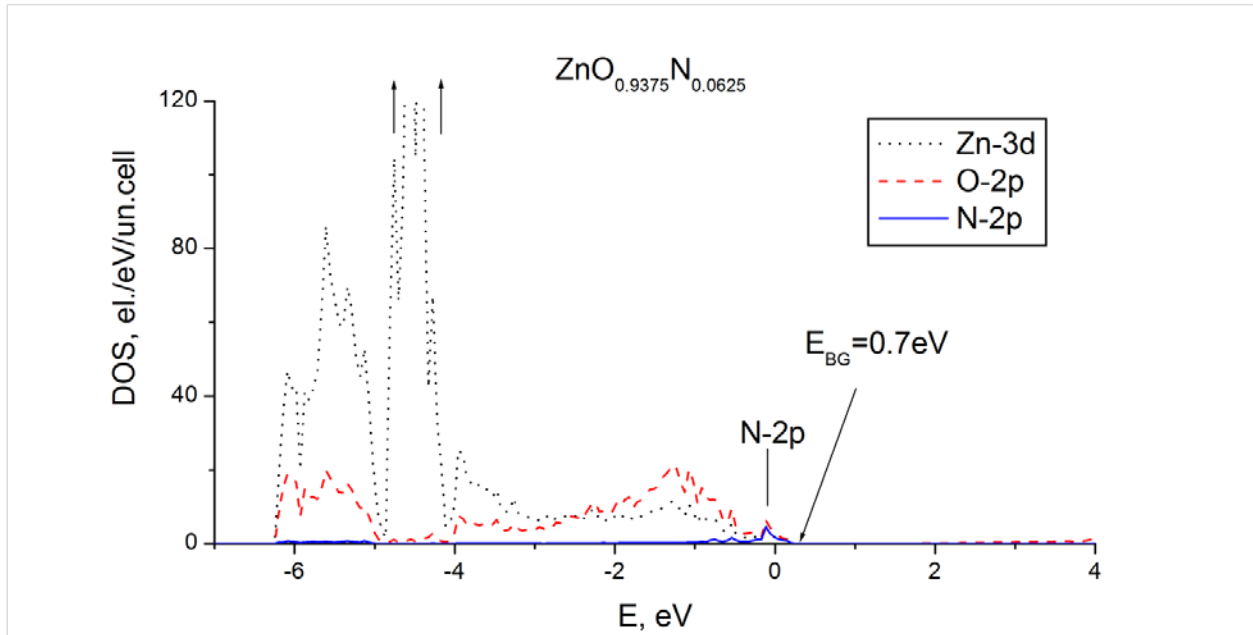


Figure 113: Projected density of states for ZnO doped with 6.25 at% of N. Fermi level is set for zero

Simultaneous co-doping of nitrogen together with cobalt into ZnO significantly influences the electronic structure of the system within the Fermi level vicinity (**Figure 114** and **Figure 115**) **Figure 114** and **Figure 115** show the calculated projected density of electronic states for $(Zn_{0.9375}Co_{0.0625})O_{0.9375}N_{0.0625}$ and $(Zn_{0.9375}Co_{0.0625})O_{0.875}N_{0.125}$ respectively. From **Figure 114**, it can be seen that there is a new impurity band originated from N-2p states located right in place of the optical band gap presented in Co-doped ZnO. Being strongly hybridized

with spin-down Co-3d states, this band closes completely the former optical band gap located below the Fermi level of Co-doped ZnO. However, new optical band gap opens above the Fermi level separating the spin-down filled and empty Co-3d states. Calculated value of this band gap is 0.34 eV. An increase in the N-content in the compound results in further narrowing of the optical band gap up to 0.23 eV as shown in **Table 19**. Otherwise, the overall electronic structure for 12.5 at% N remains identical to that of the previous case for 6.25 at% of N. Thus, the present computational study provides a qualitative agreement and validation of the experimental observations reflecting a general trend of narrowing the optical band gap obtained by Co and N co-doping of ZnO. The calculated and experimentally measured optical band gaps for all the materials considered in the present study are shown in **Table 19**.

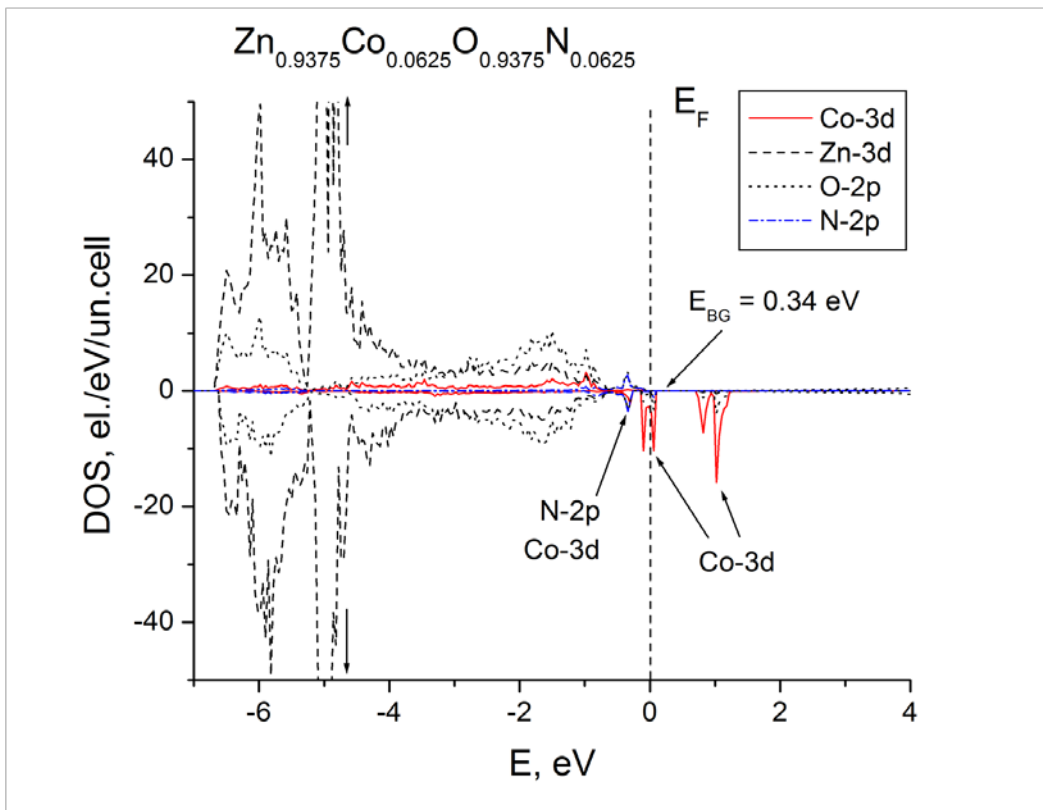


Figure 114: Projected density of states for ZnO doped with 6.25 at% of Co and 6.25 at% of N. Top panel is for spin-up, bottom panel is for spin-down. Fermi level is set for zero

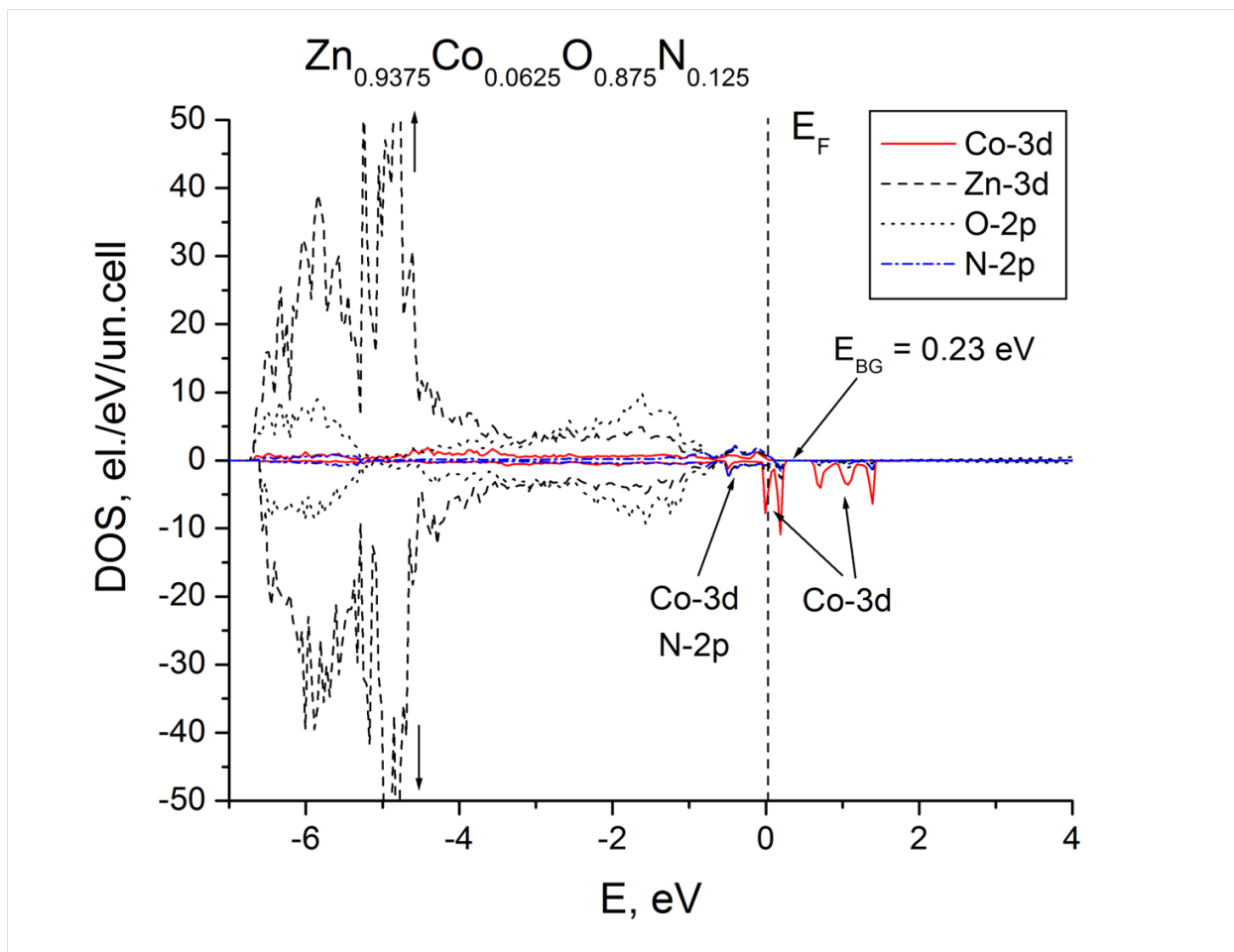


Figure 115: Projected density of states for ZnO doped with 6.25 at% of Co and 12.5 at% of N. Top panel is for spin-up, bottom panel is for spin-down. Fermi level is set for zero

A.2 Nb AND N CO-DOPED SnO₂ NANOTUBES (NTs) (PHOTOANODE)

A.2.1 COMPUTATIONAL METHODOLOGY

The overall photoelectro-catalytic performance of SnO₂ is expected to depend on various factors, an important component being the width of the electronic band gap between the valence and conduction bands of the oxide. Thus the main aim of the computational aspect of the present study is to investigate and understand effects of chemical compositions of SnO₂-based oxides on the electronic structure and the photo-electro-catalytic ³³¹ activity from theoretical considerations. The total energy, electronic and optimized crystal structures as well as the total and projected densities of electronic states for pure SnO₂ and SnO₂ doped with Nb and N have been calculated using the first principles approach within the density functional theory (DFT).

It is well known that SnO₂ adopts the rutile structure with a tetragonal unit cell and space group P42/mnm with lattice parameters: $a = b = 4.738 \text{ \AA}$, and $c = 3.187 \text{ \AA}$ (experimentally obtained as shown in **Table 5**). The unit cell contains six atoms, two tin atoms occupying the 2a Wyckoff positions: (0, 0, 0); (0.5, 0.5, 0.5) and four oxygen ions occupying the 4f positions: (u, u, 0); (-u, -u, 0); (0.5+u, 0.5-u, 0.5); (0.5-u, 0.5+u, 0.5), where $u = 0.307$.^{332, 333} Each unit cell consists of octahedra with tin atom at the center and six oxygen atoms located at the corners. This unit cell has been chosen as the basis for the construction of the 48-atom [2x2x2] supercell containing 16 atoms of Sn and 32 atoms of O allowing modeling of various compositions of the Nb- and N- doped SnO₂. In particular, one out of 16 available Sn atoms could be replaced for one Nb resulting in the following formula unit (Sn₁₅Nb₁)O₃₂ corresponding to 6.25 at% of Nb in the Nb-doped SnO₂. Similarly, replacement of one atom of oxygen for nitrogen will correspond to 3.125 at% of N. Accordingly, substitution of two and four atoms of O for N corresponds to

6.25 at% and 12.5 at% of N in the oxide compounds. Thus, based on this supercell the following compositions have been chosen for calculations of the electronic and structural properties: $\text{Sn}_{15}\text{Nb}_1\text{O}_{32}$, $\text{Sn}_{16}\text{O}_{31}\text{N}_1$, $\text{Sn}_{15}\text{Nb}_1\text{O}_{31}\text{N}_1$, $\text{Sn}_{15}\text{Nb}_1\text{O}_{30}\text{N}_2$, and $\text{Sn}_{15}\text{Nb}_1\text{O}_{28}\text{N}_4$, which correspond very closely to the chemical compositions actually used in the experimental aspect of the present study namely, $\text{Sn}_{0.95}\text{Nb}_{0.05}\text{O}_2$, $\text{Sn}_{0.95}\text{Nb}_{0.05}\text{O}_{1.97}\text{N}_{0.03}$, $\text{Sn}_{0.95}\text{Nb}_{0.05}\text{O}_{1.93}\text{N}_{0.07}$, and $\text{Sn}_{0.95}\text{Nb}_{0.05}\text{O}_{1.86}\text{N}_{0.14}$.

It should be noted, that for modeling oxides with randomly distributed doping elements, a very large crystal supercell is required to suppress effects of long-range order of the structure and mimic the disordered state of the lattice. However, since the goal of the present study is qualitative evaluation of the effects of Nb and N doping on electronic structure of SnO_2 , consideration of a single crystal in its ground state within 48-atom supercell is deemed sufficient.

Vienna Ab-initio Simulation Package (VASP) was utilized to calculate density of electronic states, electronic structure and total energies within the projector-augmented wave³¹⁸ method³¹⁹⁻³²¹ in a form reported earlier by Perdew and Wang³²³ using the generalized gradient approximation (GGA) for the exchange-correlation energy functional. This program calculates the electronic structure and the inter-atomic forces (identified from first-principles *via* the Hellmann-Feynman theorem). Standard PAW potentials were employed for the Sn, Nb, O, and N potentials containing four, eleven, six, and five valence electrons, respectively.

520 eV has been chosen as the plane wave cutoff energy in the case of all the materials considered in this study in order to maintain a high level of accuracy in total energy calculations. Double relaxation procedure was used to optimize lattice parameters and internal atomic positions. Thus, the minima of the total energies with respect to the lattice parameters and internal ionic positions have been calculated. This geometry optimization was obtained by

minimizing Hellman–Feynman forces (using a conjugate gradient method) in order to ensure that net forces applied on every ion in the lattice ~ 0 . The total electronic energies were converged within $\sim 10^{-5}$ eV/un.cell ensuring the residual force components < 0.01 eV/Å/atom. This allows for a high level of accuracy in determination of the oxide internal structural parameters. The Monkhorst-Pack scheme was used to sample the Brillouin Zone (BZ) and generate the k -point grid for all the materials considered in the present study. Number of k -points in the irreducible part of the BZ was chosen on the basis of convergence of total energy to 0.1 meV/atom. In order to minimize significant error in the calculations of the cohesive energy, a cubic box with edges of $15 \times 15 \times 15$ Å³ was chosen to eliminate any interatomic interaction caused by the periodic boundary conditions while calculating the total energy of isolated atoms of all the elements comprising the materials considered.

A.2.2 RESULTS OF THE COMPUTATIONAL STUDY

Pure SnO₂

It should be noted that the electronic structure of pure SnO₂ is ubiquitously discussed in the literature³³⁴⁻³³⁶ from a theoretical perspective. Nevertheless, in the context of the present work it is logical to describe the electronic structure of SnO₂. In addition the electronic structure of pure SnO₂ will be used for illustrating the combined Nb- and N-doping effects on the SnO₂ electronic structure.

The total and projected densities of electronic states calculated for pure SnO₂ are thus shown in **Figure 116**. The main energy band structure of SnO₂ consists of three bands, low energy oxygen 2s states (~ -18.9 to -16.4 eV), wide valence band (-7.9 to 0.0 eV) consisting of

hybridized O-2p – Sn-5s, -5p states (forming three sub-bands with O-2p – Sn-5s, O-2p – Sn-5p, and the non-hybridized O-2p states, respectively) and the conduction band consisting mainly of Sn-5s states (lower band) and Sn-5p states (upper band) with relatively small admixture of the oxygen 2s- and 2p- states. The energy gap separating the top of the valence band from the bottom of the conduction band of the Sn-5s character, is equal to 1.12 eV. Due to the well-known intrinsic characteristic limitation of DFT (on account of self-interaction effects and derivative discontinuities of the exchange correlation energy), the value of the forbidden gap is underestimated substantially in comparison to the experimental measured value of 3.53 eV (**Table 20**). Since the goal of the current study is to compare the general trends of the electronic structure modifications arising from the doping of SnO₂ (using Nb and N), a precise calculation of the band gap is however not critical. Hence this noted disadvantage of DFT will not significantly affect the results obtained and discussed in the current study. Furthermore, the main parameters of the electronic structure for SnO₂ calculated in the present study agree well with the results obtained from previously published theoretical calculations.³³⁴⁻³³⁶

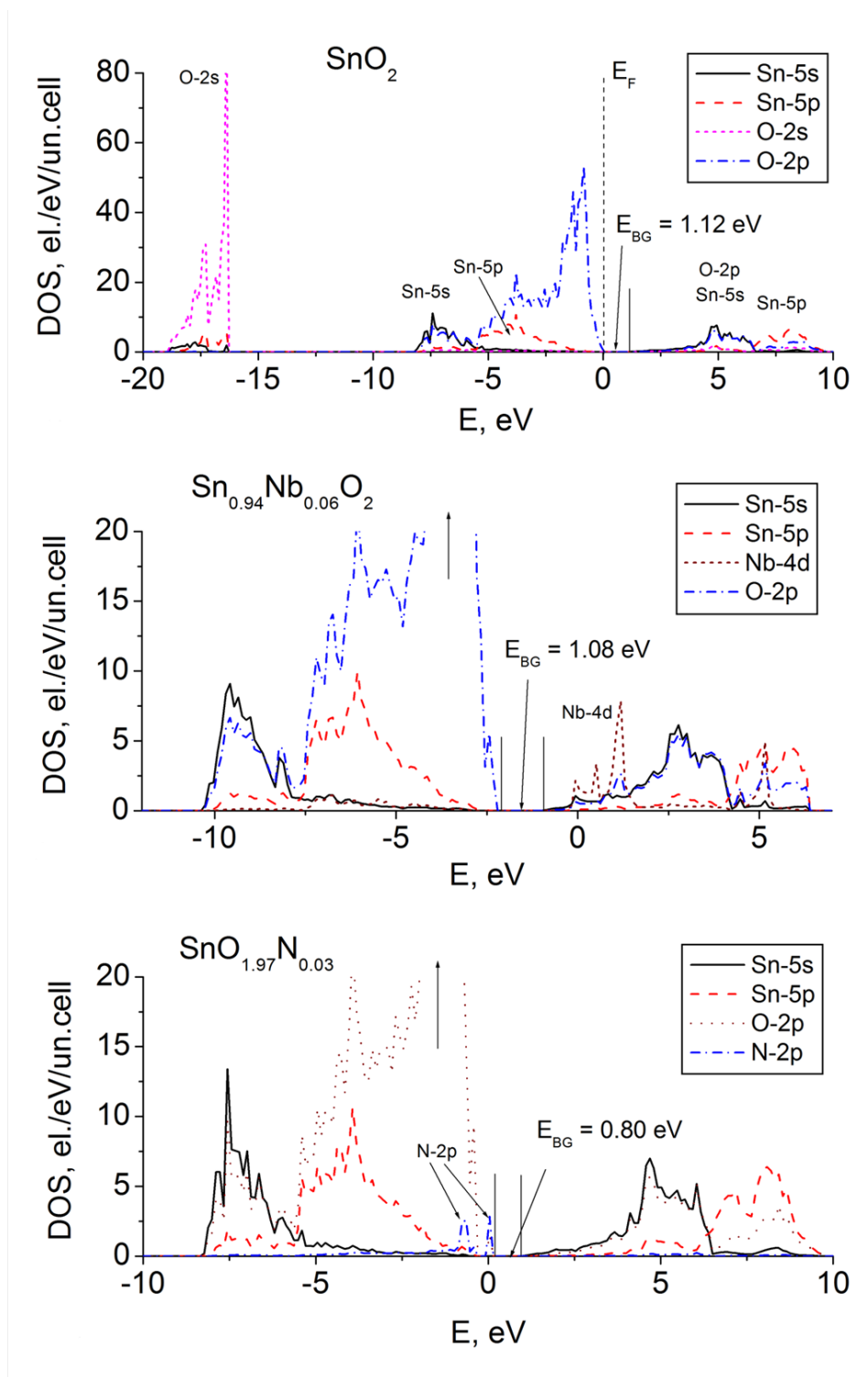


Figure 116: Projected density of states for pure SnO_2 , SnO_2 doped with 6.25 at% of Nb, SnO_2 doped with 3.125 at% of N. Fermi level is set for zero

Table 20: Calculated and experimental values of optical band gap (E_{BG}) of pure and doped**SnO₂**

Composition	Calculated E_{BG} (eV)	Experimental E_{BG} (eV)
SnO₂	1.12	3.53
(Sn_{0.94}Nb_{0.06})O₂	1.08	3.1
Sn(O_{1.97}N_{0.03})	0.80	-
(Sn_{0.94}Nb_{0.06})(O_{1.97}N_{0.03})	0.93	2.58
(Sn_{0.94}Nb_{0.06})(O_{1.94}N_{0.06})	0.91	2.38
(Sn_{0.94}Nb_{0.06})(O_{1.875}N_{0.125})	0.87	1.99

SnO₂ doped with Nb and N

The calculated total and projected densities of electronic states for (Sn_{0.94}Nb_{0.06})O₂ oxide composition are shown in **Figure 116**. One can see that the main band structure of the Nb-doped SnO₂ is similar to the undoped SnO₂. However, the main difference between the two is an appearance of the Nb-4d electronic states slightly hybridized with Sn-5s and O-2p states located at the bottom of the conduction band within the Fermi level vicinity. The valence band of Nb-doped SnO₂ remains virtually the same as that of pure SnO₂ and is separated from the hybridized conduction band by the energy gap of 1.08 eV. This optical band gap value is quite smaller than the E_{BG} calculated for the pure SnO₂ (1.12 eV) which agrees well with experimental observations demonstrating narrowing of the optical band gap observed with Nb-doping (**Table 20**). Of course, both values are significantly underestimated due to the limitation of DFT analysis (mentioned above). However the relative difference between these values is qualitatively the same as that experimentally observed. Since the impurity Nb-4d states locate at the Fermi level,

it clearly indicates that Nb-doped SnO₂ is a n-type semiconductor. Also, the calculated electronic structure is very similar to other calculations reported previously.³³⁶

To study effect of nitrogen doping on electronic structure of SnO₂ the composition SnO_{1.96875}N_{0.03125} has been considered. The projected density of electronic states for this composition is shown in **Figure 116**. One can see that the general picture is almost the same as for pure SnO₂. The only difference between pure and N-doped SnO₂ oxide is the appearance of N-2p impurity states at the top of the valence band. The calculated band gap E_{BG} is 0.8 eV (**Table 20**) which is noticeably narrower than the corresponding calculated band gap of pure SnO₂. Thus it can be seen that indeed the incorporation of N can help decrease the optical band gap and correspondingly extend the absorption of SnO₂ into the visible region.

Simultaneous co-doping of nitrogen together with niobium into SnO₂ significantly influences the electronic structure of the system within the Fermi level vicinity. **Figure 117** shows the calculated projected density of electronic states for (Sn_{0.94}Nb_{0.06})O_{1.97}N_{0.03}, (Sn_{0.94}Nb_{0.06})O_{1.94}N_{0.06}, and (Sn_{0.94}Nb_{0.06})O_{1.875}N_{0.125}, respectively. One can see that the overall electronic structure results from the combination of Nb-doped SnO₂ and N-doped SnO₂ considered above. Compared to pure SnO₂, there are N-2p electronic states located at the top of the valence band and Nb-4d electronic states located at the bottom of the conduction band, separated by the energy gap (E_{BG}). The value of this optical band gap gradually decreases with increase in the concentration of N in the compound (from 0.93 eV for 3 at% to 0.87 eV for 12.5 at% of N). Such a narrowing of the optical band gap originates from widening of the N-2p states at the top of the valence band with the corresponding increase in the N-concentration. Otherwise, the overall electronic structure is virtually the same for all the three different compositions containing 3, 6, and 12.5 at% of N shown in **Figure 117**. Thus, the present computational study

is in qualitative agreement with the experimental observations reflecting a general trend of narrowing the optical band gap with co-doping of Nb and N into SnO₂ structure. The calculated and experimentally measured optical band gaps for all the materials considered in the present study are shown in **Table 20**.

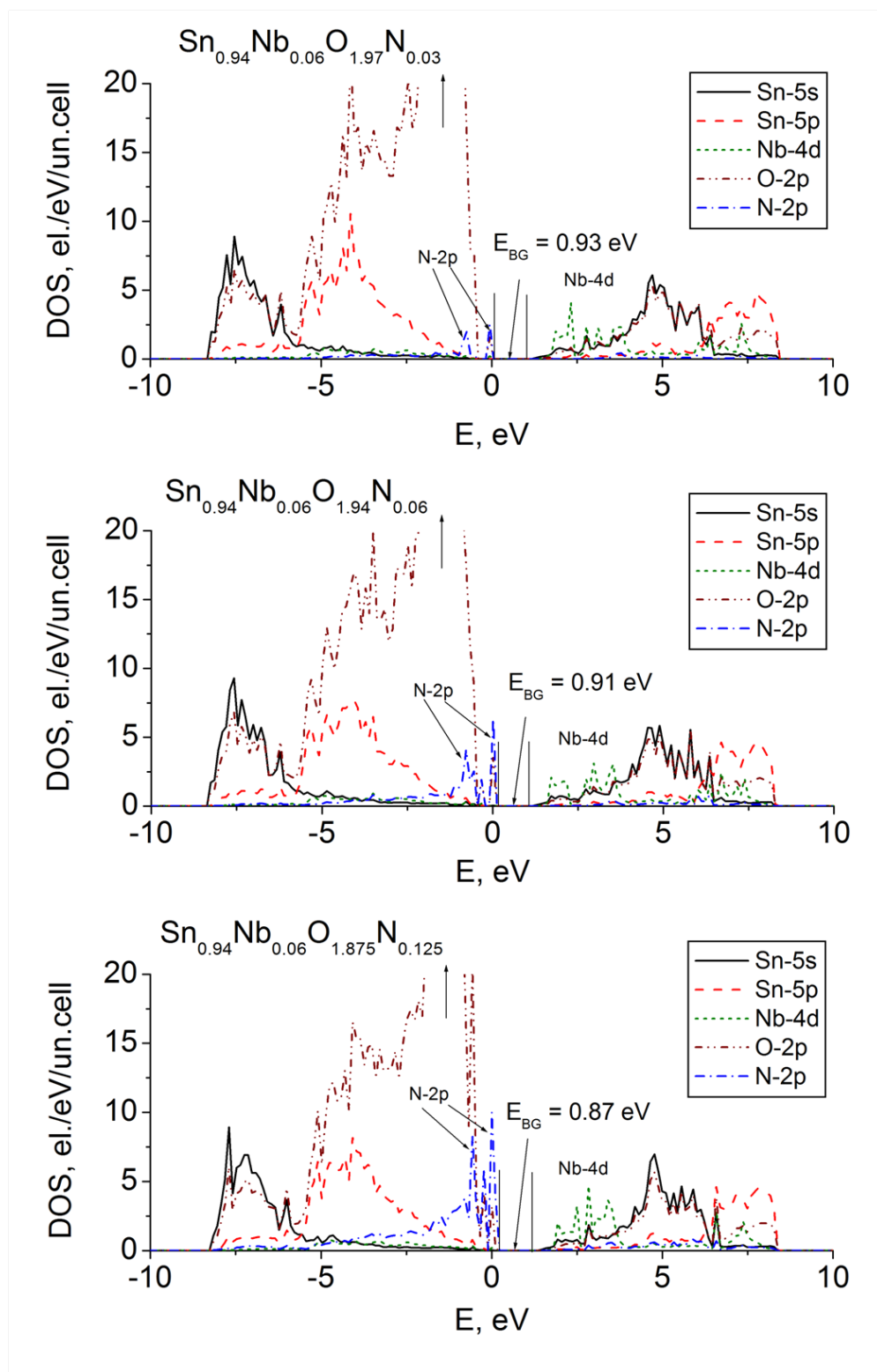


Figure 117: Projected density of states for $(\text{Sn}_{0.94}\text{Nb}_{0.06})(\text{O}_{1.97}\text{N}_{0.03})$, $(\text{Sn}_{0.94}\text{Nb}_{0.06})(\text{O}_{1.94}\text{N}_{0.06})$, $(\text{Sn}_{0.94}\text{Nb}_{0.06})(\text{O}_{1.875}\text{N}_{0.125})$. Fermi level is set for zero

A.3 Co(Ir) SOLID SOLUTION HER ELECTRO-CATALYST FOR CATHODE

A.3.1 COMPUTATIONAL METHODOLOGY

The catalytic activity of electro-catalyst can be described by a parameter, ΔG_{H^*} which is the free energy of the adsorbed H on the electro-catalyst surface. ΔG_{H^*} is desired to be close to 0 eV, which indicates easy adsorption and desorption of hydrogen atoms from the electro-catalyst surface.⁷²⁻⁷⁴ ΔG_{H^*} is represented by the following equation: $\Delta G_{H^*} = \Delta E_{H^*} + \Delta ZPE - T\Delta S$. The reaction energy, ΔE_{H^*} is calculated using DFT as follows:

$$\Delta E_{H^*} = E(\text{Me} + n\text{H}) - E(\text{Me} + (n-1)\text{H}) - 1/2 E(\text{H}_2)$$

where $E(\text{Me} + n\text{H})$ is the total energy of a metal surface slab with n hydrogen atoms adsorbed on surface, $E(\text{Me} + (n-1)\text{H})$ is the total energy of the corresponding metal surface slab with $(n-1)$ hydrogen atoms (after removal of one hydrogen atom from given site) and $E(\text{H}_2)$ is the total energy of hydrogen molecule in gas phase. In all the calculations, fcc sites have been considered as the active sites with 1 monolayer of H-coverage on the (111) fcc surface. The zero point energy correction ΔZPE minus the entropy term $T\Delta S$ has been taken equal to 0.24 eV, following the work of Nørskov et al.⁷⁴, for calculations of ΔG_{H^*} for all electro-catalysts considered in this study.

All the slabs consist of three *fcc* layers with fixed bottom and middle layers. A top layer was allowed to relax together with all the adsorbed hydrogen atoms on it. The free energy of the hydrogen adsorption has been directly calculated for pure Co, Ir and Pt metals as well as for $\text{Co}_{2/3}\text{Ir}_{1/3}$ alloy. For the pure metals, a [2x2] surface unit cell has been chosen similar to that suggested in⁷⁴, while for Co-Ir alloy a [2x3] unit cell with 2 Ir and 4 Co atoms on all the three layers has been used. The slab was separated from its image by a vacuum layer of ~ 17 Å. The

[2x3] surface unit cell denoted by the solid lines with 2 Ir and 4 Co atoms is shown in **Figure 118**. One can see that there are 6 *fcc* active sites with three different types of surroundings: 1) three Co atoms, 2) one Ir and two Co atoms, and 3) two Ir and one Co atoms. For all the three types of the sites, the free energy of the hydrogen adsorption has been calculated and an average ΔG_{H^*} has been obtained. In this model, we made an assumption that the overall catalytic activity in general, and ΔG_{H^*} in particular, will depend only on amount of specific active sites mentioned above, but not on their spatial distribution in the bulk and at the surface. It seems plausible, since the catalytic activity as a macroscopic quantity is expected to depend on ΔG_{H^*} averaged over the elementary unit cell of the surface slab. Another approximation of the model is to consider reconstruction of the surface only at the top layer leaving other two layers fixed. To validate correctness of these assumptions, there would be a need to conduct extensive and time consuming DFT calculations with numerous surfaces and bulk atomic configurations (planned for future studies to be included in a following submission). However, the aim of the proposed very simplified approach is a quick qualitative evaluation of the catalytic activity of various alloyed compositions without determining an exact composition for the most optimal material. The convenience of this approach is based on gaining knowledge of ΔG_{H^*} calculated only for very few different types of the active sites described later in this study.

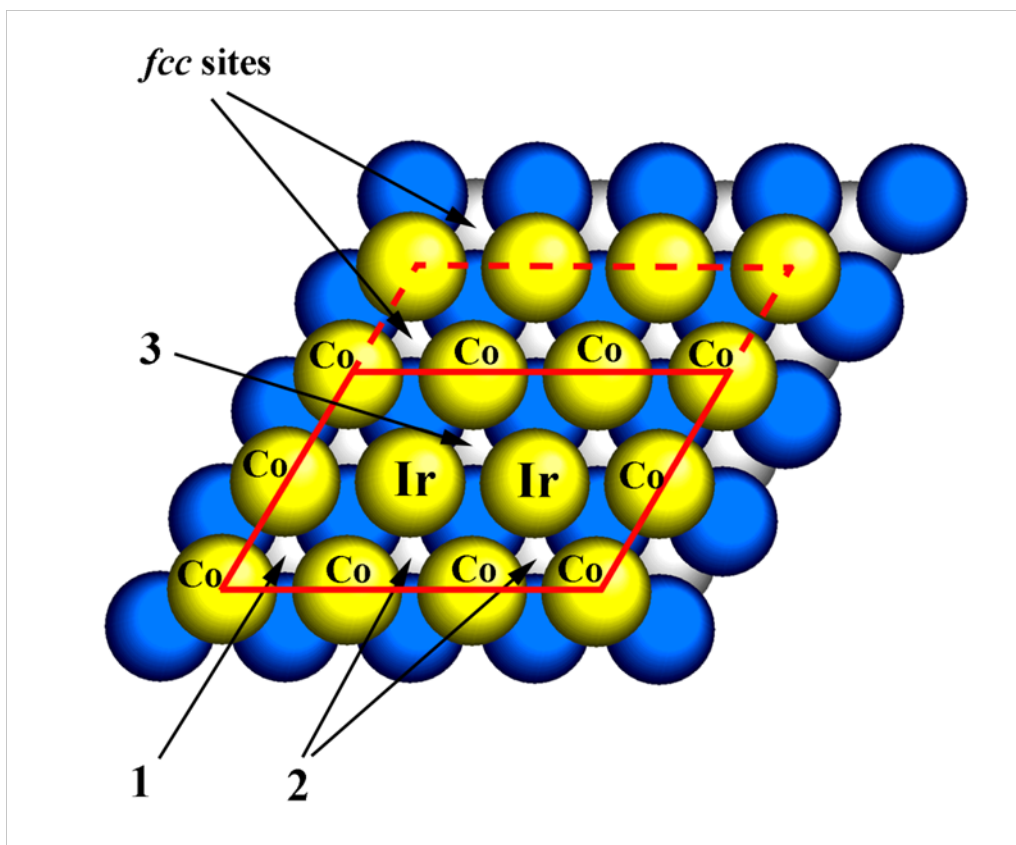


Figure 118: (111) fcc surface with [2x3] (solid lines) and [3x3] (extended with dashed lines) unit cell. Yellow balls – the top layer; blue balls – middle layer; light gray balls – the bottom layer. Arrows denote *fcc* active sites. Numbers 1, 2, and 3 denote sites with different surroundings

In the present study for all the DFT calculations, the Vienna Ab-initio Simulation Package (VASP) has been used within the projector-augmented wave³¹⁸ method³¹⁹⁻³²¹ and the generalized gradient approximation³²² for the exchange-correlation energy functional, in a form suggested by Perdew and Wang.³²³ This program calculates the electronic structure and *via* the Hellmann-Feynman theorem, the inter-atomic forces were determined from first-principles.

Standard PAW potentials were employed for the Ir, Co and Pt potentials containing nine, nine, and ten valence electrons, respectively.

For all the materials considered in this study, the plane wave cutoff energy of 520 eV has been chosen to maintain a high accuracy of the total energy calculations. The lattice parameters and internal positions of the atoms were fully optimized employing the double relaxation procedure and consequently, the minima of the total energies with respect to the lattice parameters and internal ionic positions have been determined. This geometry optimization was obtained by minimizing the Hellman–Feynman forces via a conjugate gradient method, so that the net forces applied on every ion in the lattice are close to zero. The total electronic energies were converged to within 10^{-5} eV/un.cell resulting in the residual force components on each atom to be lower than 0.01 eV/Å/atom, thus allowing for an accurate determination of the internal structural parameters for the material. The Monkhorst-Pack scheme was used to sample the Brillouin Zone (BZ) and generate the k -point grid for all the materials studied in the present research work.

A.3.2 RESULTS OF THE COMPUTATIONAL STUDY

Recent years has witnessed tremendous progress in the fundamental understanding of water splitting mechanisms occurring at the surfaces of metal and metal oxide electro-catalysts using modern theoretical approaches [in particular, Density Functional Theory (DFT)]. In particular, substantial efforts have been made by Prof. J. K. Nørskov and his group in identifying a parameter describing the catalytic activity of the given material ⁷²⁻⁷⁴. Specifically, for the hydrogen evolution reaction (HER), they demonstrated a strong correlation between the measured exchange current density (i_0) and calculated hydrogen binding energy (ΔG_{H^*}) to the

specific surface of electro-catalysts reported before ⁷⁴. Such dependence has a prominent maximum at $\Delta G_{\text{H}^*} \approx 0$ and bears the ubiquitous relation term called, “the volcano plot”. For a good HER electro-catalyst, therefore, there is a desire for the free energy of the adsorbed H to be close to 0 such that the hydrogen atoms would be able to spontaneously adsorb and desorb from the surface during the hydrogen evolution process. As expected, the top of the volcano is occupied by Pt which is the predominant gold standard electro-catalyst for HER with the calculated ΔG_{H^*} quite close to zero. Thus, the task of identifying good electro-catalyst materials for HER could partially be reduced to the calculation of the hydrogen binding energy to the catalytic surface, ΔG_{H^*} and ascertaining the position of this energy on the corresponding volcano plot. Modifying the electronic structure of the catalytic surface in such a way that the binding energy, ΔG_{H^*} becomes more optimal in terms of positioning the system on the volcano plot may also indeed substantially improve the electrochemical activity and thus aid in identifying the most optimal electro-catalyst for HER.

Accordingly, the computational component of the present study is thus an attempt to analyze the fundamental aspects underlying the high electrochemical activity of the Co-Ir alloys described in the experimental section of the current study. As it was shown in **Figure 84**, pure Co and pure Ir demonstrate lower electrochemical activity than their solid solution alloys containing 30-40 at% of Ir. For these purposes, the hydrogen binding free energy (ΔG_{H^*}) has been obtained from DFT calculations essentially by subtracting the free energy of the clean catalyst surface and a half of a hydrogen molecule in the gas phase from the corresponding free energy of the catalyst surface with hydrogen atom bonded to the site. The methodology is very similar to that presented by Nørskov *et al.* in their previous report ⁷⁴.

Table 21: ΔG_{H^*} in eV calculated for different materials and different types of the active sites

	From Ref. ⁷⁴	Present study
Pure Co	$-0.49+0.24 = -0.25$	$-0.48+0.24 = -0.24$
Pure Ir	$-0.16+0.24 = +0.08$	$-0.17+0.24 = +0.07$
Pure Pt	$-0.27+0.24 = -0.03$	$-0.29+0.24 = -0.05$
1. Ir _{0.33} Co _{0.67} [3Co]	-	$-0.46+0.24 = -0.22$
2. Ir _{0.33} Co _{0.67} [Ir-2Co]	-	$-0.37+0.24=-0.13$
3. Ir _{0.33} Co _{0.67} [2Ir-Co]	-	$-0.27+0.24=-0.03$

Table 21 collects the value of ΔG_{H^*} , calculated for pure Co, Ir, and Pt metals as well as for three different types of sites in Ir_{1/3}Co_{2/3} alloy within the unit cell shown in **Figure 118**. The corresponding ΔG_{H^*} calculated by Nørskov *et al.* in previous report ⁷⁴ are also presented for comparative purposes. One can see that for Ir_{1/3}Co_{2/3} alloy composition in the [2x3] unit cell, there is one site of the first type (3Co), four sites of the second type (1Ir-2Co), and one site of the third type (2Ir-1Co). An average value of ΔG_{H^*} calculated over all of the six sites is -0.128 eV collected in the corresponding column of **Table 22**.

Table 22: Average and interpolated ΔG_{H^*} for various Co-Ir alloys

Alloy	Unit cell	# of sites	Average ΔG_{H^*} (eV)	Interpolated ΔG_{H^*} (eV)
Ir_{0.44}Co_{0.56}	[3 x 3] 4Ir; 5Co	4[Ir-2Co] + 4[2Ir-Co]+1[3Co]	-0.096	
Ir_{0.4}Co_{0.6}	-	-	-	-0.109
Ir_{0.33}Co_{0.67}	[2 x 3] 2Ir; 4Co	4[Ir-2Co] + 1[3Co]+1[2Ir-Co]	-0.128	
Ir_{0.3}Co_{0.7}	-	-	-	-0.138
Ir_{0.22}Co_{0.78}	[3 x 3] 2Ir; 7Co	4[Ir-2Co] + 4[3Co]+1[2Ir-Co]	-0.159	
Ir_{0.2}Co_{0.8}	-	-	-	-0.165
Ir_{0.17}Co_{0.83}	[2 x 3] 1Ir; 5Co	3[Ir-2Co] + 3[3Co]	-0.175	

Knowing ΔG_{H^*} for these three types of sites, one can configure other chemical compositions using different sizes of the unit cell. For example, for the alloy Co_{0.78}(Ir_{0.22}) one can set up considering a [3x3] surface unit cell (in **Figure 118**, the cell is extended by dashed lines) with 2 Ir and 7 Co atoms on the surface. Corresponding number of different sites is indicated in the third column of **Table 22**. Similar constructions for other Ir-Co compositions have been made and the average adsorption hydrogen energies have been calculated and collected in **Table 22**. The last column of **Table 22** contains the interpolated ΔG_{H^*} for the experimental Co-Ir alloys of different composition synthesized in the present study. The interpolations have been made using a linear approximation of ΔG_{H^*} between the two neighbor compositions with calculated adsorption energies.

In addition to the hydrogen binding energy that was calculated outlined above, it is possible to create a graph showing the dependence of experimentally determined exchange

current density on the calculated values for ΔG_{H^*} for all the materials considered. This plot is shown in **Figure 119** which indeed exhibits the typical volcano plot shape with the prominent maximum corresponding to the $\text{Co}_{0.6}(\text{Ir}_{0.4})$ alloy and located at -0.109 eV. One can expect the position of the maximum around zero ΔG_{H^*} as it was established for many other systems (for example, [53]). This deviation can be attributed to the simplicity of the model used in the present study which may provide slightly underestimated values for calculated ΔG_{H^*} of binary Co-Ir alloys. Anyway, the hydrogen adsorption energies for Co-Ir alloys essentially lie in between ΔG_{H^*} for pure Co and Ir. It is obvious that the binding energies at the active sites containing both Co and Ir atoms are expected to be weaker than the ΔG_{H^*} for pure Co and correspondingly, stronger than the ΔG_{H^*} for pure Ir. Such a harmonization of the Co-H and Ir-H interactions due to the proper selection of the alloying composition within the Co-Ir alloy system thus renders the system comprising of two mediocre catalytic components to demonstrate excellent prowess for HER making them thus excellent electro-catalysts. This is essentially the reason contributing to the superior electrochemical activity of Co(Ir) solid solution electro-catalysts compared to pure Co and pure Ir, as discussed before (**Section 5.4.2** and **Figure 84**).

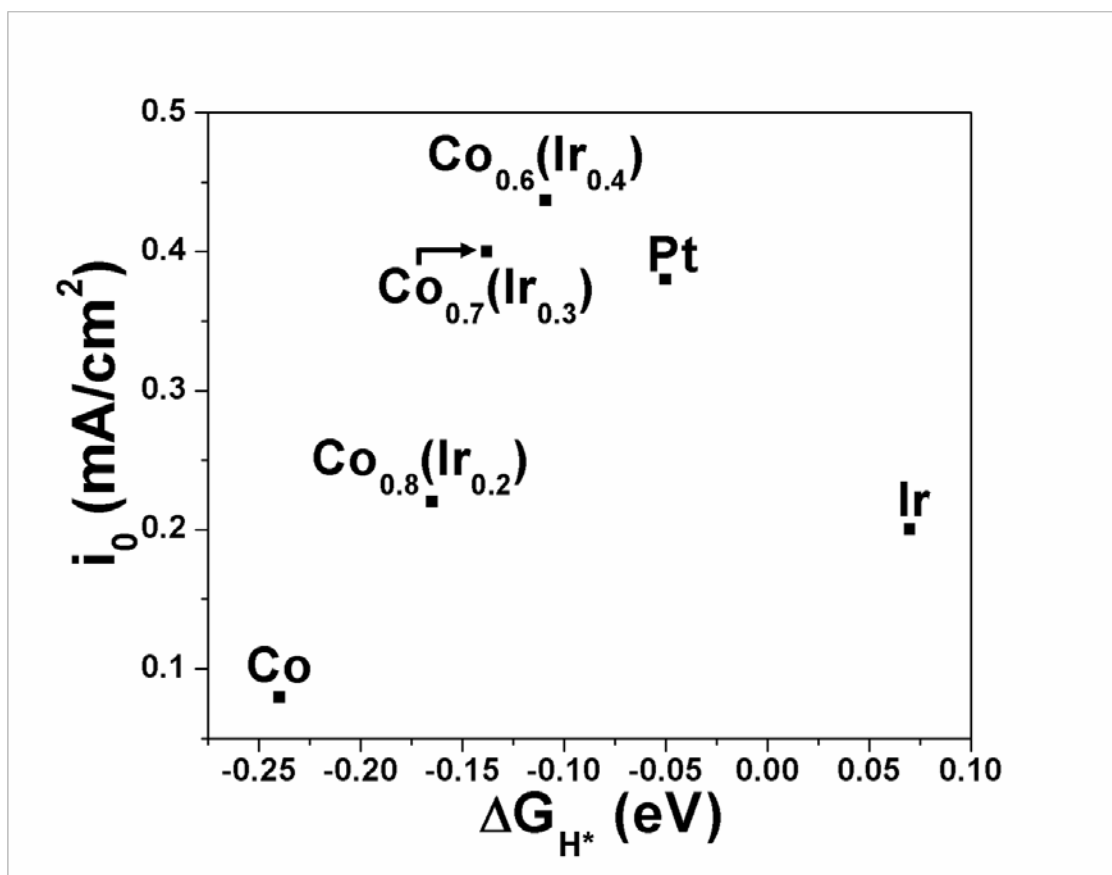


Figure 119: Experimentally measured exchange current density (i_0) as a function of calculated ΔG_{H^*} for pure Co, Ir, Pt and Co-Ir alloys

It is also important to note that the solid solution electro-catalyst $Co_{1-x}(Ir_x)$ ($x = 0.3, 0.4$) outperform even Pt/C in facilitating HER. All other metals and alloys fit well in the volcano plot clearly demonstrating the validity of the concept relating the hydrogen binding energy ΔG_{H^*} as a significant descriptor of the metal surface catalytic activity analogous to the familiar volcano plot. Also, this simplistic consideration of the HER helps in understanding synergistic effect of Co-Ir alloying in modification of the electronic structure of the surface and thus, in improving the overall electro-catalytic properties of the materials.

It should be noted that this computational study does not explain why $\text{Co}_{0.6}\text{(Ir}_{0.4})$ alloy demonstrates a higher catalytic activity than pure Pt. A thorough fundamental experimental and a more comprehensive study involving computations of the kinetic parameters of HER, such as the various activation barriers of all the elementary reactions steps during hydrogen evolution process will help in unraveling this aspect and also, to understand origin of improvement in electrochemical activity of Co(Ir) alloys of different compositions.

A.4 (Cu_{0.83}Co_{0.17})₃P:S HER ELECTRO-CATALYST FOR CATHODE

A.4.1 COMPUTATIONAL METHODOLOGY

The electro-catalytic activity of an electro-catalyst can be described by a parameter, ΔG_{H^*} which is the free energy of adsorbed hydrogen atom on the electro-catalyst surface. ΔG_{H^*} is desired to be close to 0 eV, which indicates the ease of adsorption and desorption of hydrogen atoms from the electro-catalyst surface.⁷²⁻⁷⁴ ΔG_{H^*} is represented by the following relation: $\Delta G_{H^*} = \Delta E_{H^*} + \Delta ZPE - T\Delta S$. The reaction energy ΔE_{H^*} is calculated using the density functional theory methodology (DFT) as following:

$$\Delta E_{H^*} = E(\text{Mat} + n\text{H}) - E(\text{Mat} + (n-1)\text{H}) - 1/2 E(\text{H}_2),$$

where $E(\text{Me} + n\text{H})$ is the total energy of a metal surface slab with the n hydrogen atoms adsorbed on the surface, $E(\text{Me} + (n-1)\text{H})$ is the total energy of the corresponding metal surface slab with $(n-1)$ hydrogen atoms (after removal of one hydrogen atom from the given site) and $E(\text{H}_2)$ is the total energy of the hydrogen molecule in the gas phase.

Cu₃P has a hexagonal crystal structure P6₃cm (group# 185) with 24 atoms in the unit cell with the following lattice parameters: $a=b=6.959\text{\AA}$ and $c=7.143\text{\AA}$.³³⁷ For estimation of ΔE_{H^*} , the crystallographic surface (0001) has been chosen with the active sites located above Cu 4b-type of the lattice sites as shown in **Figure 120**. Co and S atoms are also shown in this figure. In all the calculations, 1 monolayer of H-coverage of the (0001) surface has been considered. Also, the zero point energy correction ΔZPE minus the entropy term $T\Delta S$ has been taken equal to 0.24 eV, as it was used by Nørskov *et al.*⁷⁴, for calculations of ΔG_{H^*} for all materials considered in that study.

All the surface slabs consist of five copper and two phosphorus layers with fixed three lower copper and one phosphorus layers with the lattice parameters corresponding to the calculated bulk crystal structures. The remaining three top layers were allowed to relax together with all the adsorbed hydrogen atoms on the surface. The slab was separated from its image by a vacuum layer of ~ 20 Å. Since, the purpose of the present theoretical study is to bring to light the effects of Co and S elements on the overall catalytic activity of Cu_3P , only one composition of each dopant has been chosen for the calculation of ΔG_{H^*} and other properties of the corresponding compounds. Thus, accordingly, the free energies of hydrogen adsorption to the surface have been calculated for pure Cu_3P , $(\text{Co}_{0.17}\text{Cu}_{0.83})_3\text{P}$ and $(\text{Co}_{0.17}\text{Cu}_{0.83})_3\text{P}_{0.5}\text{S}_{0.5}$ compositions. These compositions have been chosen from the crystallographic consideration of the Cu_3P elementary unit cell.

In the present study for all the DFT calculations, the Vienna Ab-initio Simulation Package (VASP) has been used within the projector-augmented wave³¹⁸ method³¹⁹⁻³²¹ and the generalized gradient approximation for the exchange-correlation energy functional in a form suggested by Perdew and Wang.³²³ This program calculates the electronic structure and *via* the Hellmann-Feynman theorem, the inter-atomic forces are determined from first-principles. The standard PAW potentials were employed for the Cu, Co, P, and S potentials containing eleven, nine, five, and six valence electrons, respectively.

For all the materials considered in this study, the plane wave cutoff energy of 520 eV has been chosen to maintain a high accuracy of the total energy calculations. The lattice parameters and internal positions of atoms were fully optimized employing the double relaxation procedure and consequently, the minima of the total energies with respect to the lattice parameters and internal ionic positions have been determined. This geometry optimization was

obtained by minimizing the Hellman–Feynman forces via a conjugate gradient method, so that the net forces applied on every ion in the lattice are close to zero. The total electronic energies were converged to within 10^{-5} eV/un.cell resulting in the residual force components on each atom to be lower than 0.01 eV/Å/atom thus, allowing for an accurate determination of the internal structural parameters for the material. The Monkhorst-Pack scheme was used to sample the Brillouin Zone (BZ) and generate the k -point grid for all the materials considered in the present study.

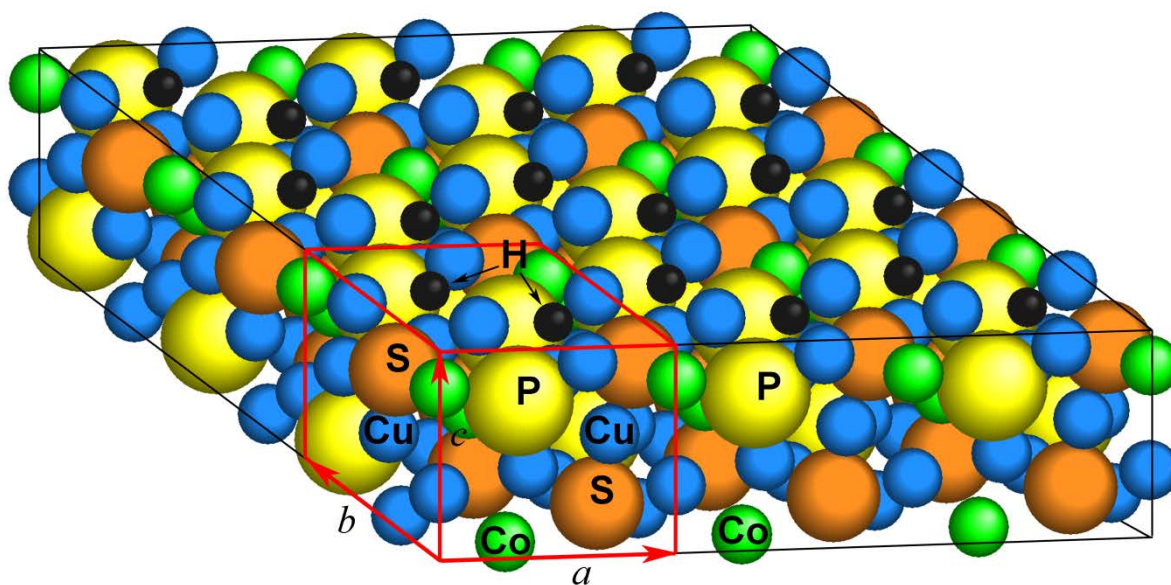


Figure 120: Surface slab of Cu_3P structure doped with Co and S. Red box is the unit cell used in all DFT calculations. Small blue balls – Cu, small green – Co, large yellow – P, large orange – S, the smallest black – hydrogen atoms attached to the surface on active sites.

Vectors a , b , and c correspond to the bulk crystal structure lattice parameters

A.4.2 RESULTS OF THE COMPUTATIONAL STUDY

The electro-catalytic activity of virtually any electro-catalyst is expected to depend on the electronic structure as well as the electronic conductivity, while the long term stability of the electro-catalyst is assumed to qualitatively depend on the cohesive energy of the system. The effect of compositions on the electronic and catalytic properties as well as the compositional effects on the structural stability of the material could be understood from the theoretical considerations.

As mentioned in earlier section of the study, the main purpose of the computational component of the present study is to explore the effects of Co and S dopants on the electro-catalytic activity as well as the structural and chemical stability of Cu_3P during HER. For these purposes the electronic structure, hydrogen adsorption free energies ΔG_{H^*} as well as the cohesive energies have been considered as a qualitative measure of the structural and chemical stability, and they have all been calculated for the different materials considered in the current study.

It should be noted that for a good HER electro-catalyst, it is essential that the free energy of adsorbed H (ΔG_{H^*}) should be close to 0 such that the hydrogen atoms would be able to easily adsorb and desorb from the surface during HER. Thus, the task of identifying a good electro-catalyst material for HER could partially be reduced to estimation of the free binding energy of the hydrogen to the electro-catalytic surface. Modification of the electro-catalytic surface electronic structure by changing the chemical composition in such a way that the resulting ΔG_{H^*} becomes close to zero, may also substantially improve the electro-catalytic activity of the material. For these purposes therefore, the hydrogen binding free energy (ΔG_{H^*}) has been obtained from DFT calculations by subtracting the free energy of the pristine electro-catalyst surface and a half of a hydrogen molecule in the gas phase from the corresponding free energy of

the electro-catalyst surface with hydrogen atom bonded to the site. The methodology is very similar to that presented by Nørskov et al. in previous report.⁷⁴

Table 23 shows a tabulation of the free energies ΔG_{H^*} , density of states at the Fermi level, and cohesive energies for all the different materials considered in the present study. One can see that the hydrogen adsorption to the surface of pure Cu_3P is too weak and quite far from the optimal value resulting in an inferior expected electro-catalytic activity for HER. It may be explained from the electronic structure consideration that since Cu-3d electrons locate relatively deep below the Fermi level the hybridization between these electrons and H-1s states located above the Fermi level becomes very weak thus, making adsorption of hydrogen atoms practically impossible (**Figure 121**).

An introduction of Co into the Cu_3P lattice substituting for Cu decreases ΔG_{H^*} noticeably bringing its value toward the more optimal energy value. In this case, new Co-3d electronic states are created locating in the vicinity of the Fermi level and hybridize with H-1s electrons more strongly resulting in stronger interaction between hydrogen atoms and the material's surface. Such a modification of the electronic structure is expected to improve the electro-catalytic activity of the electro-catalyst (**Figure 121**). Further substitution of phosphorus for sulfur in $(Cu,Co)_3P$ results in the hydrogen adsorption energy being even more close to the zero value of ~ 0.1 eV. This indicates a further increase in the strength of the hydrogen-surface interaction due to the stronger H-S bonds compared to the H-P bonds (bond dissociation energies for diatomic molecules are $353.6 \text{ kJ mol}^{-1}$ vs. $297.0 \text{ kJ mol}^{-1}$ respectively. This effect of the sulfur addition is expected to further improve the electro-catalytic activity of $(Cu,Co)_3P:S$ compound. Thus, using the concept of the free energy of the hydrogen adsorption to the electro-

catalytic surface, the present study has shown positive effect of introduction of Co and S on the expected catalytic activity of Cu₃P electrocatalyst for HER.

Another goal of the present study as outlined earlier is to investigate the effect of Co and S doping on the electronic conductivity of Cu₃P. Since, in general the metallic conductivity is proportional to the density of states at the Fermi level $N(E_F)$, it provides an opportunity to qualitatively estimate the influence of those dopants on the overall electronic conductivity of Cu₃P. The electronic structure of Cu₃P calculated in the present study demonstrates slight metal-type conductivity with non-zero density of the electronic states at the Fermi level (**Figure 121**) which is opposite to the experimental data indicating this material is a semiconductor with a narrow band gap ~ 0.8 eV between the valence and conduction electronic zones.³³⁸ This discrepancy with experimental data attributes to the inherent inability of the DFT methodology to reproduce correctly the band gaps of insulators and semiconductors with the well-known tendency of DFT to underestimate the corresponding band gap energy values on average by 30-50%. Also, some materials with narrow band gaps may very well be presented as metal-type conductors. Nevertheless, in the case of Cu₃P, the value of $N(E_F)$ is very small indicating poor electronic conductivity of the compound. The introduction of Co into the system however, changes the electronic structure in such a way that the presence of Co-3d electrons in the vicinity of the Fermi level increases the number of electrons and thus, improves the overall electronic conductivity of the material (**Figure 121**). An additional introduction of S into the (Cu,Co)₃P lattice by substituting for P atoms further improves the conductivity (**Figure 121**), since sulfur atoms bring additional valence electrons into the system, thus increasing the number of total charge carriers at the Fermi level as indicated in the **Figure 121**. Such an increase in the

electronic conductivity also positively contributes to the overall electro-catalytic activity of the material along with hydrogen adsorption energy to the surface.

The last aspect to be highlighted in the present theoretical study is the structural and electrochemical stability of the system for which the cohesive energy E_{coh} can be considered as a qualitative indicator. The higher the E_{coh} (the more negative value), the more durable is the electro-catalyst material and thus, can be expected to display long term stability and durability when considered over the entire duration of the long term HER electro-catalytic process. E_{coh} calculated for all the materials are collected in **Table 23**. One can see that an introduction of Co into the Cu_3P lattice substantially improves the overall stability of $(\text{Co}_{0.17}\text{Cu}_{0.83})_3\text{P}$ due to the presence of much stronger Co-P bonds in comparison to Cu-P [calculated E_{coh} for pure Cu_3P is -13.96 eV/f.u. vs. -14.94 eV/f.u. for $(\text{Co}_{0.17}\text{Cu}_{0.83})_3\text{P}$].¹⁶⁸ However, further introduction of S into the $(\text{Co}_{0.17}\text{Cu}_{0.83})_3\text{P}$ compound results in relative lowering of the cohesive energy that occurs mainly due to the lower ionic charge of S^{2-} vs. P^{3-} and thus, leads to significantly weakening the electrostatic component of Cu-S and Co-S bonds than those of Cu-P and Co-P ionic bonds. Nevertheless, even the relatively less stable $(\text{Co}_{0.17}\text{Cu}_{0.83})_3\text{P}_{0.5}\text{S}_{0.5}$ compound is more stable than pure Cu_3P , which makes this material likely more stable and capable of withstanding the harsh electrochemical conditions during HER.

Thus, based on results of the DFT study, $(\text{Cu,Co})_3\text{P:S}$ is expected to demonstrate improved electro-catalytic activity due to quite optimal hydrogen adsorption energy and high electronic conductivity together with good structural and chemical stability which altogether make this material a likely good candidate for demonstrating structural stability and high performance electro-catalytic response suitable for HER. The theoretical results presented here are accordingly experimentally verified by synthesizing and characterizing different

compositions of $(\text{Cu}_{0.83}\text{Co}_{0.17})_3\text{P}$: x at. % S (x=10, 20, 30) corresponding to different S concentrations to systematically study and illustrate the effect of different S concentrations on the electrochemical properties of $(\text{Cu}_{0.83}\text{Co}_{0.17})_3\text{P}:\text{S}$ that are further discussed in the following sections.

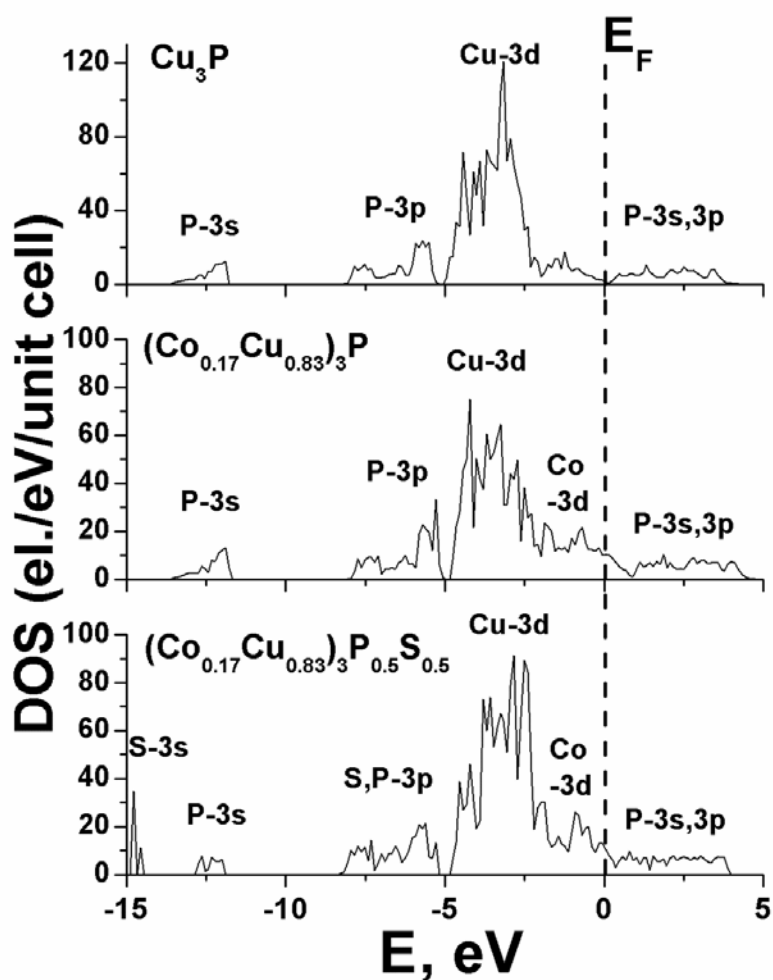


Figure 121: Calculated density of electronic states for pure Cu_3P , $(\text{Co}_{0.17}\text{Cu}_{0.87})_3\text{P}$ and $(\text{Co}_{0.17}\text{Cu}_{0.87})_3\text{P}_{0.5}\text{S}_{0.5}$; Fermi level corresponds to zero energy

Table 23: Calculated free energy of hydrogen adsorption ΔG_{H^*} , the electronic density of states at the Fermi level, and cohesive energy $-E_{coh}$ for all materials considered in the present study

Materials	ΔG_{H^*} (in eV)	$N(E_F)$ el./eV/unit cell	$-E_{coh}$ (in eV/f.unit)
Cu_3P	0.31	1.5	13.96
$(Co_{0.17}Cu_{0.83})_3P$	0.16	10.1	14.94
$(Co_{0.17}Cu_{0.83})_3P_{0.5}S_{0.5}$	0.10	11.7	14.48

APPENDIX B

PERMISSIONS

The thesis has text, figures and tables reprinted/reproduced with permission from several publishing companies and societies. All the journal papers listed here have been published in print and electronic form, wherein I (*Prasad Prakash Patel*) am a co-author.

The six journal papers listed below have been used in **Section 5.0** and **APPENDIX A**:

1. **P.P. Patel**, P.H. Jampani, O.I. Velikokhatnyi, M.K. Datta, D. Hong, B. Gattu, J. Poston, A. Manivannan, P.N. Kumta, “Nitrogen and cobalt co-doped zinc oxide nanowires–Viable photoanodes for hydrogen generation via photoelectrochemical water splitting”, *Journal of Power Sources*, 299 (2015) 11-24, Copyright © 2015, Reprinted with permission from Elsevier.
2. **P.P. Patel**, P.H. Jampani, O.I. Velikokhatnyi, M.K. Datta, B. Gattu, J. Poston, A. Manivannan, P.N. Kumta, “Vertically aligned nitrogen doped (Sn,Nb)O₂ nanotubes–Robust photoanodes for hydrogen generation by photoelectrochemical water splitting”, *Materials Science and Engineering B*, 208 (2016) 1-14, Copyright © 2016, Reprinted with permission from Elsevier

3. **P.P. Patel**, P.H. Jampani, M.K. Datta, O.I. Velikokhatnyi, D. Hong, J. Poston, A. Manivannan, P.N. Kumta, “Cobalt based nanostructured alloys: Versatile high performance hydrogen evolution reaction electro-catalysts for electrolytic and photo-electrochemical water splitting”, *International Journal of Hydrogen Energy*, 42 (2017) 17049-17062, Copyright © 2017, Reprinted with permission from Elsevier

BIBLIOGRAPHY

1. F. Umbach, *Energy Policy*, 2010, **38**, 1229-1240.
2. G. Resch, A. Held, T. Faber, C. Panzer, F. Toro and R. Haas, *Energy Policy*, 2008, **36**, 4048-4056.
3. M. G. Salameh, *Applied Energy*, 2003, **75**, 33-42.
4. J. R. Miller, *Science*, 2012, **335**, 1312-1313.
5. B. Peng and J. Chen, *Coordination Chemistry Reviews*, 2009, **253**, 2805-2813.
6. T. Bak, J. Nowotny, M. Rekas and C. Sorrell, *International journal of hydrogen energy*, 2002, **27**, 991-1022.
7. A. J. Bard and M. A. Fox, *Accounts of Chemical Research*, 1995, **28**, 141-145.
8. X. Chen, S. Shen, L. Guo and S. S. Mao, *Chemical Reviews*, 2010, **110**, 6503-6570.
9. G. W. Crabtree, M. S. Dresselhaus and M. V. Buchanan, *Physics Today*, 2004, **57**, 39-44.
10. M. G. Walter, E. L. Warren, J. R. McKone, S. W. Boettcher, Q. Mi, E. A. Santori and N. S. Lewis, *Chemical reviews*, 2010, **110**, 6446-6473.
11. Z. Zou, J. Ye, K. Sayama and H. Arakawa, *Nature*, 2001, **414**, 625-627.
12. M. Balat and M. Balat, *International journal of hydrogen energy*, 2009, **34**, 3589-3603.
13. J. A. Turner, *Science*, 1999, **285**, 687-689.
14. J. Suntivich, K. J. May, H. A. Gasteiger, J. B. Goodenough and Y. Shao-Horn, *Science*, 2011, **334**, 1383-1385.
15. K. Zeng and D. K. Zhang, *Prog. Energy Combust. Sci.*, 2010, **36**, 307-326.
16. M. Ball, M. Wietschel and O. Rentz, *International Journal of Hydrogen Energy*, 2007, **32**, 1355-1368.
17. G. Brumfiel, *Nature*, 2003, **422**, 104-104.

18. C.-J. Winter, *International Journal of Hydrogen Energy*, 2009, **34**, S1-S52.
19. C. Yang, P. Costamagna, S. Srinivasan, J. Benziger and A. B. Bocarsly, *Journal of Power Sources*, 2001, **103**, 1-9.
20. L. Barreto, A. Makihira and K. Riahi, *International Journal of Hydrogen Energy*, 2003, **28**, 267-284.
21. J. Kibsgaard and T. F. Jaramillo, *Angewandte Chemie International Edition*, 2014, **53**, 14433-14437.
22. M. K. Datta, K. Kadakia, O. I. Velikokhatnyi, P. H. Jampani, S. J. Chung, J. A. Poston, A. Manivannan and P. N. Kumta, *Journal of Materials Chemistry A*, 2013, **1**, 4026-4037.
23. H. Wang, D. Y. C. Leung and J. Xuan, *International Journal of Hydrogen Energy*, 2012, **37**, 10002-10009.
24. D. Aaron and C. Tsouris, *Separation Science and Technology*, 2005, **40**, 321-348.
25. R. Ribeiro, C. Grande and A. Rodrigues, *Separation Science and Technology*, 2014, **49**, 1985-2002.
26. C. Voss, *Adsorption*, 2014, **20**, 295-299.
27. P. A. Webley, *Adsorption*, 2014, **20**, 225-231.
28. J. Wilcox, R. Haghpanah, E. C. Rupp, J. He and K. Lee, *Annual review of chemical and biomolecular engineering*, 2014, **5**, 479-505.
29. M. Conte, F. Di Mario, A. Iacobazzi, A. Mattucci, A. Moreno and M. Ronchetti, *Energies*, 2009, **2**, 150-179.
30. R. H. Krishna, *European Journal of Biotechnology and Bioscience*, 2013, **1**, 84-93.
31. J. Liu, G. Cao, Z. Yang, D. Wang, D. Dubois, X. Zhou, G. L. Graff, L. R. Pederson and J.-G. Zhang, *ChemSusChem*, 2008, **1**, 676-697.
32. T. R. Cook, D. K. Dogutan, S. Y. Reece, Y. Surendranath, T. S. Teets and D. G. Nocera, *Chemical reviews*, 2010, **110**, 6474-6502.
33. H. Çakmak, E. Arslan, M. Rudziński, P. Demirel, H. Unalan, W. Strupiński, R. Turan, M. Öztürk and E. Özbay, *Journal of Materials Science: Materials in Electronics*, 2014, **25**, 3652-3658.
34. K. Maeda, *Physical Chemistry Chemical Physics*, 2013, **15**, 10537-10548.
35. J. D. Holladay, J. Hu, D. L. King and Y. Wang, *Catalysis Today*, 2009, **139**, 244-260.

36. J. Turner, G. Sverdrup, M. K. Mann, P. C. Maness, B. Kroposki, M. Ghirardi, R. J. Evans and D. Blake, *International Journal of Energy Research*, 2008, **32**, 379-407.
37. F. Barbir, *Sol. Energy*, 2005, **78**, 661-669.
38. C. P. De Pauli and S. Trasatti, *Journal of Electroanalytical Chemistry*, 1995, **396**, 161-168.
39. J. M. Hu, H. M. Meng, J. Q. Zhang and C. N. Cao, *Corrosion Science*, 2002, **44**, 1655-1668.
40. M. W. Kanan and D. G. Nocera, *Science*, 2008, **321**, 1072-1075.
41. A. T. Marshall, S. Sunde, M. Tsytkin and R. Tunold, *International Journal of Hydrogen Energy*, 2007, **32**, 2320-2324.
42. P. Millet, N. Mbemba, S. A. Grigoriev, V. N. Fateev, A. Aukauloo and C. Etiévant, *International Journal of Hydrogen Energy*, 2011, **36**, 4134-4142.
43. C.-J. Winter, *International Journal of Hydrogen Energy*, 2009, **34**, S1-S52.
44. X. Peng, C. He, X. Fan, Q. Liu, J. Zhang and H. Wang, *International Journal of Hydrogen Energy*, 2014, **39**, 14166-14171.
45. H.-S. Lee, W. F. J. Vermaas and B. E. Rittmann, *Trends in Biotechnology*, 2010, **28**, 262-271.
46. R. Sasikala, A. P. Gaikwad, V. Sudarsan, N. Gupta and S. R. Bharadwaj, *Applied Catalysis A: General*, 2013, **464-465**, 149-155.
47. R. Sasikala, A. Shirole, V. Sudarsan, C. Sudakar, R. Naik, R. Rao and S. Bharadwaj, *Applied Catalysis A: General*, 2010, **377**, 47-54.
48. F. E. Osterloh and B. A. Parkinson, *MRS bulletin*, 2011, **36**, 17-22.
49. A. Galinska and J. Walendziewski, *Energy & Fuels*, 2005, **19**, 1143-1147.
50. J.-P. Zou, L.-Z. Zhang, S.-L. Luo, L.-H. Leng, X.-B. Luo, M.-J. Zhang, Y. Luo and G.-C. Guo, *international journal of hydrogen energy*, 2012, **37**, 17068-17077.
51. L. J. Minggu, W. R. Wan Daud and M. B. Kassim, *International Journal of Hydrogen Energy*, 2010, **35**, 5233-5244.
52. A. Fujishima, *nature*, 1972, **238**, 37-38.
53. R. L. LeRoy, C. T. Bowen and D. J. LeRoy, *Journal of The Electrochemical Society*, 1980, **127**, 1954-1962.
54. B. E. Conway and B. V. Tilak, *Electrochimica Acta*, 2002, **47**, 3571-3594.

55. Y. Sun, Y. Dai, Y. Liu and S. Chen, *Physical Chemistry Chemical Physics*, 2012, **14**, 2278-2285.
56. J. Rossmeisl, Z. W. Qu, H. Zhu, G. J. Kroes and J. K. Nørskov, *Journal of Electroanalytical Chemistry*, 2007, **607**, 83-89.
57. K. Kadakia, M. K. Datta, O. I. Velikokhatnyi, P. Jampani, S. K. Park, S. J. Chung and P. N. Kumta, *Journal of Power Sources*, 2014, **245**, 362-370.
58. J. Rossmeisl, A. Logadottir and J. K. Nørskov, *Chemical Physics*, 2005, **319**, 178-184.
59. O. I. Velikokhatnyi, K. Kadakia, M. K. Datta and P. N. Kumta, *The Journal of Physical Chemistry C*, 2013, **117**, 20542-20547.
60. K. Kadakia, M. K. Datta, O. I. Velikokhatnyi, P. H. Jampani and P. N. Kumta, *International Journal of Hydrogen Energy*, 2014, **39**, 664-674.
61. Y. Li, H. Wang, L. Xie, Y. Liang, G. Hong and H. Dai, *Journal of the American Chemical Society*, 2011, **133**, 7296-7299.
62. E. Miller, N. Gaillard, J. Kaneshiro, A. DeAngelis and R. Garland, *International Journal of Energy Research*, 2010, **34**, 1215-1222.
63. Z. Zhang and J. T. Yates, *Chemical Reviews*, 2012, **112**, 5520-5551.
64. G. Wang, H. Wang, Y. Ling, Y. Tang, X. Yang, R. C. Fitzmorris, C. Wang, J. Z. Zhang and Y. Li, *Nano Letters*, 2011, **11**, 3026-3033.
65. A. Kushwaha and M. Aslam, *Electrochimica Acta*, 2014, **130**, 222-231.
66. R. Sasikala, A. Shirole, V. Sudarsan, T. Sakuntala, C. Sudakar, R. Naik and S. R. Bharadwaj, *International Journal of Hydrogen Energy*, 2009, **34**, 3621-3630.
67. C. W. Lai and S. Sreekantan, *Electrochimica Acta*, 2013, **87**, 294-302.
68. H. Han, S. Shin, J. Noh, I. Cho and K. Hong, *JOM*, 2014, **66**, 664-669.
69. C. W. Cheng, W. N. Ren and H. F. Zhang, *Nano Energy*, 2014, **5**, 132-138.
70. A. B. Laursen, S. Kegnaes, S. Dahl and I. Chorkendorff, *Energy & Environmental Science*, 2012, **5**, 5577-5591.
71. B. Hinnemann, P. G. Moses, J. Bonde, K. P. Jørgensen, J. H. Nielsen, S. Horch, I. Chorkendorff and J. K. Nørskov, *Journal of the American Chemical Society*, 2005, **127**, 5308-5309.
72. T. Bligaard and J. K. Nørskov, *Electrochimica Acta*, 2007, **52**, 5512-5516.
73. B. Hammer and J. K. Nørskov, *Advances in catalysis*, 2000, **45**, 71-129.

74. J. K. Nørskov, T. Bligaard, A. Logadottir, J. Kitchin, J. Chen, S. Pandelov and U. Stimming, *Journal of The Electrochemical Society*, 2005, **152**, J23-J26.
75. C.-H. Liao, C.-W. Huang and J. Wu, *Catalysts*, 2012, **2**, 490-516.
76. P. P. Patel, P. J. Hanumantha, O. I. Velikokhatnyi, M. K. Datta, B. Gattu, J. A. Poston, A. Manivannan and P. N. Kumta, *Materials Science and Engineering: B*, 2016, **208**, 1-14.
77. Z. Chen, T. F. Jaramillo, T. G. Deutsch, A. Kleiman-Shwarsstein, A. J. Forman, N. Gaillard, R. Garland, K. Takanahe, C. Heske and M. Sunkara, *Journal of Materials Research*, 2010, **25**, 3-16.
78. J. R. Bolton, *Solar Energy*, 1996, **57**, 37-50.
79. R. H. Coridan, A. C. Nielander, S. A. Francis, M. T. McDowell, V. Dix, S. M. Chatman and N. S. Lewis, *Energy & Environmental Science*, 2015, **8**, 2886-2901.
80. J. Li and N. Wu, *Catalysis Science & Technology*, 2015, **5**, 1360-1384.
81. S. Hernández, V. Cauda, A. Chiodoni, S. Dallorto, A. Sacco, D. Hidalgo, E. Celasco and C. F. Pirri, *ACS Applied Materials & Interfaces*, 2014, **6**, 12153-12167.
82. X. Zhang, Y. Liu and Z. Kang, *ACS applied materials & interfaces*, 2014, **6**, 4480-4489.
83. R. Dom, L. R. Baby, H. G. Kim and P. H. Borse, *International Journal of Photoenergy*, 2013, **2013**, 9.
84. M. Jakani, G. Campet, J. Claverie, D. Fichou, J. Pouliquen and J. Kossanyi, *Journal of Solid State Chemistry*, 1985, **56**, 269-277.
85. E. M. Kaidashev, M. Lorenz, H. von Wenckstern, A. Rahm, H.-C. Semmelhack, K.-H. Han, G. Benndorf, C. Bundesmann, H. Hochmuth and M. Grundmann, *Appl. Phys. Lett.*, 2003, **82**, 3901-3903.
86. P. Liao, M. C. Toroker and E. A. Carter, *Nano letters*, 2011, **11**, 1775-1781.
87. K. Sivula, F. Le Formal and M. Grätzel, *ChemSusChem*, 2011, **4**, 432-449.
88. Y. Wang, Q. Wang, X. Zhan, F. Wang, M. Safdar and J. He, *Nanoscale*, 2013, **5**, 8326-8339.
89. R. M. Navarro Yerga, M. C. Álvarez Galván, F. del Valle, J. A. Villoria de la Mano and J. L. G. Fierro, *ChemSusChem*, 2009, **2**, 471-485.
90. K. Maeda and K. Domen, *The Journal of Physical Chemistry C*, 2007, **111**, 7851-7861.
91. Z. Zhang, L. Zhang, M. N. Hedhili, H. Zhang and P. Wang, *Nano letters*, 2012, **13**, 14-20.

92. L. G. S. Pereira, V. A. Paganin and E. A. Ticianelli, *Electrochimica Acta*, 2009, **54**, 1992-1998.
93. Y. Dai, Y. Liu and S. Chen, *Electrochimica Acta*, 2013, **89**, 744-748.
94. M. Götz and H. Wendt, *Electrochimica Acta*, 1998, **43**, 3637-3644.
95. J. E. Hu, Z. Liu, B. W. Eichhorn and G. S. Jackson, *International Journal of Hydrogen Energy*, 2012, **37**, 11268-11275.
96. M. Nagarajan, G. Paruthimal kалаignan and G. A. Pathanjali, *International Journal of Hydrogen Energy*, 2011, **36**, 14829-14837.
97. D. Ham, S. Han, C. Pak, S. Ji, S.-A. Jin, H. Chang and J. Lee, *Top Catal*, 2012, **55**, 922-930.
98. D. M. F. Santos, B. Šljukić, C. A. C. Sequeira, D. Macciò, A. Saccone and J. L. Figueiredo, *Energy*, 2013, **50**, 486-492.
99. A. Kiani and S. Hatami, *International Journal of Hydrogen Energy*, 2010, **35**, 5202-5209.
100. M. Wu, P. K. Shen, Z. Wei, S. Song and M. Nie, *Journal of Power Sources*, 2007, **166**, 310-316.
101. F. T. da Silva, V. A. Dalmazzo, M. R. Becker, M. O. de Souza, R. F. de Souza and E. M. Martini, *Ionics*, 2014, **20**, 381-388.
102. M. P. Humbert, C. A. Menning and J. G. Chen, *Journal of Catalysis*, 2010, **271**, 132-139.
103. R. M. Navarro Yerga, M. C. Álvarez Galván, F. Del Valle, J. A. Villoria de la Mano and J. L. Fierro, *ChemSusChem*, 2009, **2**, 471-485.
104. U. V. Desai, C. Xu, J. Wu and D. Gao, *The Journal of Physical Chemistry C*, 2013, **117**, 3232-3239.
105. Q. Kang, J. Cao, Y. Zhang, L. Liu, H. Xu and J. Ye, *Journal of Materials Chemistry A*, 2013, **1**, 5766-5774.
106. X. Yang, A. Wolcott, G. Wang, A. Sobo, R. C. Fitzmorris, F. Qian, J. Z. Zhang and Y. Li, *Nano Letters*, 2009, **9**, 2331-2336.
107. M. Zhong, Y. Ma, P. Oleynikov, K. Domen and J.-J. Delaunay, *Energy & Environmental Science*, 2014, **7**, 1693-1699.
108. Y. Tamaki, K. Hara, R. Katoh, M. Tachiya and A. Furube, *The Journal of Physical Chemistry C*, 2009, **113**, 11741-11746.
109. E. Ramasamy and J. Lee, *The Journal of Physical Chemistry C*, 2010, **114**, 22032-22037.

110. Y.-G. Lin, Y.-K. Hsu, Y.-C. Chen, L.-C. Chen, S.-Y. Chen and K.-H. Chen, *Nanoscale*, 2012, **4**, 6515-6519.
111. M. A. Mayer, K. M. Yu, D. T. Speaks, J. D. Denlinger, L. A. Reichertz, J. W. Beeman, E. E. Haller and W. Walukiewicz, *Journal of Physical Chemistry C*, 2012, **116**, 15281-15289.
112. S. Shet, K.-S. Ahn, R. Nuggehalli, Y. Yan, J. Turner and M. Al-Jassim, *Thin Solid Films*, 2011, **519**, 5983-5987.
113. M. Yousefi, M. Amiri, R. Azimirad and A. Moshfegh, *Journal of Electroanalytical Chemistry*, 2011, **661**, 106-112.
114. P. P. Patel, P. J. Hanumantha, O. I. Velikokhatnyi, M. K. Datta, D. Hong, B. Gattu, J. A. Poston, A. Manivannan and P. N. Kumta, *Journal of Power Sources*, 2015, **299**, 11-24.
115. R. Asahi, T. Morikawa, T. Ohwaki, K. Aoki and Y. Taga, *Science*, 2001, **293**, 269-271.
116. B. M. Rajbongshi and S. Samdarshi, *Materials Science and Engineering: B*, 2014, **182**, 21-28.
117. M. Assadi, Y. Zhang and S. Li, *Journal of Applied Physics*, 2009, **105**, 3906.
118. A. Fernández Guillermet, *Int J Thermophys*, 1987, **8**, 481-510.
119. S. Hoang, S. Guo, N. T. Hahn, A. J. Bard and C. B. Mullins, *Nano Letters*, 2011, **12**, 26-32.
120. M. Law, L. E. Greene, J. C. Johnson, R. Saykally and P. Yang, *Nature materials*, 2005, **4**, 455-459.
121. A. Kushwaha and M. Aslam, *Journal of Applied Physics*, 2012, **112**, 054316.
122. L. Mai, X. Tian, X. Xu, L. Chang and L. Xu, *Chemical reviews*, 2014, **114**, 11828-11862.
123. M. Pourbaix, Pergamon Press, Oxford, 1974.
124. Y. Wang, T. Brezesinski, M. Antonietti and B. Smarsly, *ACS nano*, 2009, **3**, 1373-1378.
125. V. Gokulakrishnan, S. Parthiban, K. Jeganathan and K. Ramamurthi, *J Mater Sci*, 2011, **46**, 5553-5558.
126. M. Stefik, M. Cornuz, N. Mathews, T. Hisatomi, S. Mhaisalkar and M. Grätzel, *Nano letters*, 2012, **12**, 5431-5435.
127. S.-i. Shamoto, T. Nakano, Y. Nozue and T. Kajitani, *Journal of Physics and Chemistry of Solids*, 2002, **63**, 1047-1050.

128. R. Katiyar, P. Dawson, M. Hargreave and G. Wilkinson, *Journal of Physics C: Solid State Physics*, 1971, **4**, 2421-2431.
129. L. Ma, X. Shen, H. Zhou, J. Zhu, C. Xi, Z. Ji and L. Kong, *RSC Advances*, 2016, **6**, 9672-9677.
130. G.-Q. Han, X. Shang, S.-S. Lu, B. Dong, X. Li, Y.-R. Liu, W.-H. Hu, J.-B. Zeng, Y.-M. Chai and C.-G. Liu, *International Journal of Hydrogen Energy*, 2017, **42**, 5132-5138.
131. D. Kong, H. Wang, Z. Lu and Y. Cui, *Journal of the American Chemical Society*, 2014, **136**, 4897-4900.
132. B. Cao, G. M. Veith, J. C. Neufeind, R. R. Adzic and P. G. Khalifah, *Journal of the American Chemical Society*, 2013, **135**, 19186-19192.
133. H. Tang, K. Dou, C.-C. Kaun, Q. Kuang and S. Yang, *Journal of Materials Chemistry A*, 2014, **2**, 360-364.
134. W.-F. Chen, K. Sasaki, C. Ma, A. I. Frenkel, N. Marinkovic, J. T. Muckerman, Y. Zhu and R. R. Adzic, *Angewandte Chemie*, 2012, **124**, 6235-6239.
135. J. Yang, D. Voiry, S. J. Ahn, D. Kang, A. Y. Kim, M. Chhowalla and H. S. Shin, *Angewandte Chemie*, 2013, **125**, 13996-13999.
136. E. J. Popczun, J. R. McKone, C. G. Read, A. J. Biacchi, A. M. Wiltrout, N. S. Lewis and R. E. Schaak, *Journal of the American Chemical Society*, 2013, **135**, 9267-9270.
137. L. Feng, H. Vrabel, M. Bensimon and X. Hu, *Physical Chemistry Chemical Physics*, 2014, **16**, 5917-5921.
138. J. Tian, Q. Liu, A. M. Asiri and X. Sun, *Journal of the American Chemical Society*, 2014, **136**, 7587-7590.
139. E. J. Popczun, C. W. Roske, C. G. Read, J. C. Crompton, J. M. McEnaney, J. F. Callejas, N. S. Lewis and R. E. Schaak, *Journal of Materials Chemistry A*, 2015, **3**, 5420-5425.
140. E. J. Popczun, C. G. Read, C. W. Roske, N. S. Lewis and R. E. Schaak, *Angewandte Chemie*, 2014, **126**, 5531-5534.
141. P. Jiang, Q. Liu, C. Ge, W. Cui, Z. Pu, A. M. Asiri and X. Sun, *Journal of Materials Chemistry A*, 2014, **2**, 14634-14640.
142. P. Xiao, M. A. Sk, L. Thia, X. Ge, R. J. Lim, J.-Y. Wang, K. H. Lim and X. Wang, *Energy & Environmental Science*, 2014, **7**, 2624-2629.
143. J. F. Callejas, J. M. McEnaney, C. G. Read, J. C. Crompton, A. J. Biacchi, E. J. Popczun, T. R. Gordon, N. S. Lewis and R. E. Schaak, *ACS nano*, 2014, **8**, 11101-11107.

144. J. Tian, Q. Liu, Y. Liang, Z. Xing, A. M. Asiri and X. Sun, *ACS applied materials & interfaces*, 2014, **6**, 20579-20584.
145. J. M. McEnaney, J. C. Crompton, J. F. Callejas, E. J. Popczun, C. G. Read, N. S. Lewis and R. E. Schaak, *Chemical Communications*, 2014, **50**, 11026-11028.
146. Z. Xing, Q. Liu, A. M. Asiri and X. Sun, *ACS Catalysis*, 2014, **5**, 145-149.
147. A. Laursen, K. Patraju, M. Whitaker, M. Retuerto, T. Sarkar, N. Yao, K. Ramanujachary, M. Greenblatt and G. Dismukes, *Energy & Environmental Science*, 2015, **8**, 1027-1034.
148. Y. Yang, F. Li, W. Li, W. Gao, H. Wen, J. Li, Y. Hu, Y. Luo and R. Li, *International Journal of Hydrogen Energy*, 2017, **42**, 6665-6673.
149. C. Tang, L. Gan, R. Zhang, W. Lu, X. Jiang, A. M. Asiri, X. Sun, J. Wang and L. Chen, *Nano Letters*, 2016, **16**, 6617-6621.
150. X. Xia, Z. Zheng, Y. Zhang, X. Zhao and C. Wang, *International Journal of Hydrogen Energy*, 2014, **39**, 9638-9650.
151. F. Rosalbino, D. Macciò, A. Saccone, E. Angelini and S. Delfino, *International Journal of Hydrogen Energy*, 2011, **36**, 1965-1973.
152. Z. Zheng, N. Li, C.-Q. Wang, D.-Y. Li, Y.-M. Zhu and G. Wu, *international journal of hydrogen energy*, 2012, **37**, 13921-13932.
153. X. Zou and Y. Zhang, *Chemical Society Reviews*, 2015, **44**, 5148-5180.
154. J. Tayal, B. Rawat and S. Basu, *International Journal of Hydrogen Energy*, 2011, **36**, 14884-14897.
155. J. Xu, X. Liu, Y. Chen, Y. Zhou, T. Lu and Y. Tang, *Journal of Materials Chemistry*, 2012, **22**, 23659-23667.
156. M. K. Jeon and P. J. McGinn, *Journal of Power Sources*, 2010, **195**, 2664-2668.
157. M. K. Jeon and P. J. McGinn, *Journal of Power Sources*, 2009, **188**, 427-432.
158. R. S. Amin, R. M. Abdel Hameed, K. M. El-Khatib, H. El-Abd and E. R. Souaya, *International Journal of Hydrogen Energy*, 2012, **37**, 18870-18881.
159. P. P. Patel, M. K. Datta, O. I. Velikokhatnyi, P. Jampani, D. Hong, J. A. Poston, A. Manivannan and P. N. Kumta, *Journal of Materials Chemistry A*, 2015, **3**, 14015-14032.
160. P. P. Patel, M. K. Datta, P. H. Jampani, D. Hong, J. A. Poston, A. Manivannan and P. N. Kumta, *Journal of Power Sources*, 2015, **293**, 437-446.
161. L. Cao, G. Sun, H. Li and Q. Xin, *Electrochemistry Communications*, 2007, **9**, 2541-2546.

162. X. Wang, Y. Tang, Y. Gao and T. Lu, *Journal of Power Sources*, 2008, **175**, 784-788.
163. Y. Takasu, N. Yoshinaga and W. Sugimoto, *Electrochemistry Communications*, 2008, **10**, 668-672.
164. S. T. Oyama, T. Gott, H. Zhao and Y.-K. Lee, *Catalysis Today*, 2009, **143**, 94-107.
165. S. Carenco, D. Portehault, C. Boissière, N. Mézailles and C. Sanchez, *Chemical Reviews*, 2013, **113**, 7981-8065.
166. R. Prins and M. Bussell, *Catal Lett*, 2012, **142**, 1413-1436.
167. S. Carenco, D. Portehault, C. Boissiere, N. Mezailles and C. Sanchez, *Chemical reviews*, 2013, **113**, 7981-8065.
168. J. Tian, Q. Liu, N. Cheng, A. M. Asiri and X. Sun, *Angewandte Chemie International Edition*, 2014, **53**, 9577-9581.
169. D. Merki, H. Vrubel, L. Rovelli, S. Fierro and X. Hu, *Chemical Science*, 2012, **3**, 2515-2525.
170. J. Bonde, P. G. Moses, T. F. Jaramillo, J. K. Norskov and I. Chorkendorff, *Faraday Discussions*, 2009, **140**, 219-231.
171. Y. Okamoto, K. Tamura and T. Kubota, *Chemical Communications*, 2010, **46**, 2748-2750.
172. L. S. Byskov, J. K. Nørskov, B. S. Clausen and H. Topsøe, *Journal of Catalysis*, 1999, **187**, 109-122.
173. J. V. Lauritsen, S. Helveg, E. Lægsgaard, I. Stensgaard, B. S. Clausen, H. Topsøe and F. Besenbacher, *Journal of Catalysis*, 2001, **197**, 1-5.
174. Y. Shu and S. T. Oyama, *Carbon*, 2005, **43**, 1517-1532.
175. J. Bai, X. Li, A. Wang, R. Prins and Y. Wang, *Journal of Catalysis*, 2013, **300**, 197-200.
176. I. S. Cho, Z. Chen, A. J. Forman, D. R. Kim, P. M. Rao, T. F. Jaramillo and X. Zheng, *Nano Letters*, 2011, **11**, 4978-4984.
177. H. Dotan, K. Sivula, M. Gratzel, A. Rothschild and S. C. Warren, *Energy & Environmental Science*, 2011, **4**, 958-964.
178. Q. Liu, D. Ding, C. Ning and X. Wang, *International Journal of Hydrogen Energy*, 2015, **40**, 2107-2114.
179. P. P. Patel, P. J. Hanumantha, M. K. Datta, O. I. Velikokhatnyi, D. Hong, J. A. Poston, A. Manivannan and P. N. Kumta, *International Journal of Hydrogen Energy*, 2017, **42**, 17049-17062.

180. C. Xu, P. Shin, L. Cao and D. Gao, *The Journal of Physical Chemistry C*, 2009, **114**, 125-129.
181. U. V. Desai, C. Xu, J. Wu and D. Gao, *Nanotechnology*, 2012, **23**, 205401.
182. S. Deki, S. Iizuka, A. Horie, M. Mizuhata and A. Kajinami, *Chemistry of Materials*, 2004, **16**, 1747-1750.
183. J.-H. Lee, I.-C. Leu, M.-C. Hsu, Y.-W. Chung and M.-H. Hon, *The Journal of Physical Chemistry B*, 2005, **109**, 13056-13059.
184. M. Sadakane, K. Sasaki, H. Kunioku, B. Ohtani, R. Abe and W. Ueda, *Journal of Materials Chemistry*, 2010, **20**, 1811-1818.
185. T. H. de Keijser, J. I. Langford, E. J. Mittemeijer and A. B. P. Vogels, *Journal of Applied Crystallography*, 1982, **15**, 308-314.
186. P. P. Patel, P. H. Jampani, M. K. Datta, O. I. Velikokhatnyi, D. Hong, J. A. Poston, A. Manivannan and P. N. Kumta, *Journal of Materials Chemistry A*, 2015, **3**, 18296-18309.
187. P. P. Patel, M. K. Datta, O. I. Velikokhatnyi, R. Kuruba, K. Damodaran, P. Jampani, B. Gattu, P. M. Shanthi, S. S. Damle and P. N. Kumta, *Scientific Reports*, 2016, **6**, 28367.
188. P. P. Patel, O. I. Velikokhatnyi, S. D. Ghadge, P. H. Jampani, M. K. Datta, D. Hong, J. A. Poston, A. Manivannan and P. N. Kumta, *International Journal of Hydrogen Energy*, 2017, **42**, 24079-24089.
189. M. Chen and R. E. Blankenship, *Trends in Plant Science*, 2011, **16**, 427-431.
190. V. Kumar, N. Singh, V. Kumar, L. Purohit, A. Kapoor, O. M. Ntwaeaborwa and H. C. Swart, *Journal of Applied Physics*, 2013, **114**, 134506.
191. C. Yang, Z. Wang, T. Lin, H. Yin, X. Lü, D. Wan, T. Xu, C. Zheng, J. Lin, F. Huang, X. Xie and M. Jiang, *Journal of the American Chemical Society*, 2013, **135**, 17831-17838.
192. Y. Li, T. Takata, D. Cha, K. Takanabe, T. Minegishi, J. Kubota and K. Domen, *Advanced Materials*, 2013, **25**, 125-131.
193. M. Higashi, K. Domen and R. Abe, *Energy & Environmental Science*, 2011, **4**, 4138-4147.
194. P. P. Patel, P. J. Hanumantha, O. I. Velikokhatnyi, M. K. Datta, B. Gattu, J. A. Poston, A. Manivannan and P. N. Kumta, *Materials Science and Engineering: B*, 2016, **208**, 1-14.
195. B. AlOtaibi, H. P. T. Nguyen, S. Zhao, M. G. Kibria, S. Fan and Z. Mi, *Nano Letters*, 2013, **13**, 4356-4361.
196. M.-R. Gao, Z.-Y. Lin, T.-T. Zhuang, J. Jiang, Y.-F. Xu, Y.-R. Zheng and S.-H. Yu, *Journal of Materials Chemistry*, 2012, **22**, 13662-13668.

197. L. Feng, H. Vrubel, M. Bensimon and X. Hu, *Physical Chemistry Chemical Physics*, 2014, **16**, 5917-5921.
198. Z. Shi, Y. Wang, H. Lin, H. Zhang, M. Shen, S. Xie, Y. Zhang, Q. Gao and Y. Tang, *Journal of Materials Chemistry A*, 2016, **4**, 6006-6013.
199. J.-S. Li, Y. Wang, C.-H. Liu, S.-L. Li, Y.-G. Wang, L.-Z. Dong, Z.-H. Dai, Y.-F. Li and Y.-Q. Lan, *Nature Communications*, 2016, **7**.
200. H. Yan, C. Tian, L. Wang, A. Wu, M. Meng, L. Zhao and H. Fu, *Angewandte Chemie*, 2015, **127**, 6423-6427.
201. G.-R. Xu, J.-J. Hui, T. Huang, Y. Chen and J.-M. Lee, *Journal of Power Sources*, 2015, **285**, 393-399.
202. Y. J. Tang, M. R. Gao, C. H. Liu, S. L. Li, H. L. Jiang, Y. Q. Lan, M. Han and S. H. Yu, *Angewandte Chemie International Edition*, 2015, **54**, 12928-12932.
203. B. Yao, L. X. Guan, G. Z. Xing, Z. Z. Zhang, B. H. Li, Z. P. Wei, X. H. Wang, C. X. Cong, Y. P. Xie, Y. M. Lu and D. Z. Shen, *Journal of Luminescence*, 2007, **122-123**, 191-194.
204. J. Wang, D. N. Tafen, J. P. Lewis, Z. Hong, A. Manivannan, M. Zhi, M. Li and N. Wu, *Journal of the American Chemical Society*, 2009, **131**, 12290-12297.
205. J. Huang, Z. Ye, H. Chen, B. Zhao and L. Wang, *Journal of materials science letters*, 2003, **22**, 249-251.
206. M. Sathish, B. Viswanathan, R. P. Viswanath and C. S. Gopinath, *Chemistry of Materials*, 2005, **17**, 6349-6353.
207. Y. Qiu, K. Yan, H. Deng and S. Yang, *Nano letters*, 2011, **12**, 407-413.
208. J. P. Bonnelle, J. Grimblot and A. D'Huysser, *Journal of Electron Spectroscopy and Related Phenomena*, 1975, **7**, 151-162.
209. M. Oku and K. Hirokawa, *Journal of Electron Spectroscopy and Related Phenomena*, 1976, **8**, 475-481.
210. X. Wang, J. Xu, B. Zhang, H. Yu, J. Wang, X. Zhang, J. Yu and Q. Li, *Advanced Materials*, 2006, **18**, 2476-2480.
211. S. Bhattacharyya, S. Kurian, S. M. Shivaprasad and N. S. Gajbhiye, *J Nanopart Res*, 2010, **12**, 1107-1116.
212. Y. Lu, Y. Lin, D. Wang, L. Wang, T. Xie and T. Jiang, *Nano Res.*, 2011, **4**, 1144-1152.
213. I. Mora-Seró, F. Fabregat-Santiago, B. Denier, J. Bisquert, R. Tena-Zaera, J. Elias and C. Lévy-Clément, *Appl. Phys. Lett.*, 2006, **89**, -.

214. J. M. Bolts and M. S. Wrighton, *The Journal of Physical Chemistry*, 1976, **80**, 2641-2645.
215. H. M. Chen, C. K. Chen, Y.-C. Chang, C.-W. Tsai, R.-S. Liu, S.-F. Hu, W.-S. Chang and K.-H. Chen, *Angewandte Chemie*, 2010, **122**, 6102-6105.
216. J. Miao, H. B. Yang, S. Y. Khoo and B. Liu, *Nanoscale*, 2013, **5**, 11118-11124.
217. A. Sheikh, A. Yengantiwar, M. Deo, S. Kelkar and S. Ogale, *Small*, 2013, **9**, 2091-2096.
218. Q. Liu, H. Lu, Z. Shi, F. Wu, J. Guo, K. Deng and L. Li, *ACS applied materials & interfaces*, 2014, **6**, 17200-17207.
219. C.-H. Hsu and D.-H. Chen, *International Journal of Hydrogen Energy*, 2011, **36**, 15538-15547.
220. Y. Wei, L. Ke, J. Kong, H. Liu, Z. Jiao, X. Lu, H. Du and X. W. Sun, *Nanotechnology*, 2012, **23**, 235401.
221. M. Shi, X. Pan, W. Qiu, D. Zheng, M. Xu and H. Chen, *International Journal of Hydrogen Energy*, 2011, **36**, 15153-15159.
222. H. Kim, M. Seol, J. Lee and K. Yong, *The Journal of Physical Chemistry C*, 2011, **115**, 25429-25436.
223. J. Ji, W. Zhang, H. Zhang, Y. Qiu, Y. Wang, Y. Luo and L. Hu, *Journal of Materials Science: Materials in Electronics*, 2013, **24**, 3474-3480.
224. F. Su, T. Wang, R. Lv, J. Zhang, P. Zhang, J. Lu and J. Gong, *Nanoscale*, 2013, **5**, 9001-9009.
225. Y. Yang, X.-j. Li, J.-t. Chen and L.-y. Wang, *Journal of Photochemistry and Photobiology A: Chemistry*, 2004, **163**, 517-522.
226. A. Kudo and Y. Miseki, *Chemical Society Reviews*, 2009, **38**, 253-278.
227. M. S. Park, G. X. Wang, Y. M. Kang, D. Wexler, S. X. Dou and H. K. Liu, *Angewandte Chemie*, 2007, **119**, 764-767.
228. H. Wu and Z. Zhang, *International Journal of Hydrogen Energy*, 2011, **36**, 13481-13487.
229. J. Xu, Y. Ao, M. Chen and D. Fu, *Applied Surface Science*, 2010, **256**, 4397-4401.
230. W. K. Choi, H. J. Jung and S. K. Koh, *Journal of Vacuum Science & Technology A*, 1996, **14**, 359-366.
231. R. Ohnishi, M. Katayama, K. Takanabe, J. Kubota and K. Domen, *Electrochimica Acta*, 2010, **55**, 5393-5400.

232. M. Himmerlich, M. Koufaki, G. Ecke, C. Mauder, V. Cimalla, J. A. Schaefer, A. Kondilis, N. T. Pelekanos, M. Modreanu and S. Krischok, *ACS applied materials & interfaces*, 2009, **1**, 1451-1456.
233. D. D. Sarma and C. N. R. Rao, *Journal of Electron Spectroscopy and Related Phenomena*, 1980, **20**, 25-45.
234. J. Jouve, Y. Belkacem and C. Severac, *Thin Solid Films*, 1986, **139**, 67-75.
235. I. Bedja and P. V. Kamat, *The Journal of Physical Chemistry*, 1995, **99**, 9182-9188.
236. S. Luo, J. Fan, W. Liu, M. Zhang, Z. Song, C. Lin, X. Wu and P. K. Chu, *Nanotechnology*, 2006, **17**, 1695-1699.
237. B. Canava and D. Lincot, *J Appl Electrochem*, 2000, **30**, 711-716.
238. C.-M. Fan, Y. Peng, Q. Zhu, L. Lin, R.-X. Wang and A.-W. Xu, *The Journal of Physical Chemistry C*, 2013, **117**, 24157-24166.
239. T. Nishino and Y. Hamakawa, *Japanese Journal of Applied Physics*, 1970, **9**, 1085-1090.
240. D. M. Roessler and W. A. Albers Jr, *Journal of Physics and Chemistry of Solids*, 1972, **33**, 293-296.
241. J. M. D. Coey, A. P. Douvalis, C. B. Fitzgerald and M. Venkatesan, *Appl. Phys. Lett.*, 2004, **84**, 1332-1334.
242. S. Xie, X. Lu, T. Zhai, W. Li, M. Yu, C. Liang and Y. Tong, *Journal of Materials Chemistry*, 2012, **22**, 14272-14275.
243. Y.-Z. Zheng, H. Ding, X. Tao and J.-F. Chen, *Materials Research Bulletin*, 2014, **55**, 182-189.
244. G. Wang, Y. Ling and Y. Li, *Nanoscale*, 2012, **4**, 6682-6691.
245. C. Yang, Z. Wang, T. Lin, H. Yin, X. Lü, D. Wan, T. Xu, C. Zheng, J. Lin and F. Huang, *Journal of the American Chemical Society*, 2013, **135**, 17831-17838.
246. H. Cui, W. Zhao, C. Yang, H. Yin, T. Lin, Y. Shan, Y. Xie, H. Gu and F. Huang, *J. Mater. Chem. A*, 2014, **2**, 8612-8616.
247. Z. Chen, D. Cummins, B. N. Reinecke, E. Clark, M. K. Sunkara and T. F. Jaramillo, *Nano Letters*, 2011, **11**, 4168-4175.
248. C. Burda, Y. Lou, X. Chen, A. C. S. Samia, J. Stout and J. L. Gole, *Nano Letters*, 2003, **3**, 1049-1051.
249. R. Beranek, B. Neumann, S. Sakthivel, M. Janczarek, T. Dittrich, H. Tributsch and H. Kisch, *Chemical Physics*, 2007, **339**, 11-19.

250. J. Schrier, D. O. Demchenko, L.-W. Wang and A. P. Alivisatos, *Nano letters*, 2007, **7**, 2377-2382.
251. J. Zhou, H. Fang, J. Maley, J. Ko, M. Murphy, Y. Chu, R. Sammynaiken and T. Sham, *The Journal of Physical Chemistry C*, 2009, **113**, 6114-6117.
252. W. Li, J. Li, X. Wang, J. Ma and Q. Chen, *International Journal of Hydrogen Energy*, 2010, **35**, 13137-13145.
253. M. Yagi, S. Maruyama, K. Sone, K. Nagai and T. Norimatsu, *Journal of Solid State Chemistry*, 2008, **181**, 175-182.
254. G. Wang, X. Yang, F. Qian, J. Z. Zhang and Y. Li, *Nano letters*, 2010, **10**, 1088-1092.
255. I. H. Kwak, H. S. Im, D. M. Jang, Y. W. Kim, K. Park, Y. R. Lim, E. H. Cha and J. Park, *ACS Applied Materials & Interfaces*, 2016, **8**, 5327-5334.
256. H. S. Han, S. Shin, J. H. Noh, I. S. Cho and K. S. Hong, *JOM*, 2014, **66**, 664-669.
257. S. Hernández, V. Cauda, A. Chiodoni, S. Dallorto, A. Sacco, D. Hidalgo, E. Celasco and C. F. Pirri, *ACS applied materials & interfaces*, 2014, **6**, 12153-12167.
258. C. W. Lai and S. Sreekantan, *Electrochimica acta*, 2013, **87**, 294-302.
259. A. Zaban, M. Greenshtein and J. Bisquert, *ChemPhysChem*, 2003, **4**, 859-864.
260. K. Zhang, X.-J. Shi, J. K. Kim and J. H. Park, *Physical Chemistry Chemical Physics*, 2012, **14**, 11119-11124.
261. S. K. Pilli, T. E. Furtak, L. D. Brown, T. G. Deutsch, J. A. Turner and A. M. Herring, *Energy & Environmental Science*, 2011, **4**, 5028-5034.
262. S. K. Pilli, T. G. Deutsch, T. E. Furtak, J. A. Turner, L. D. Brown and A. M. Herring, *Physical Chemistry Chemical Physics*, 2012, **14**, 7032-7039.
263. D. G. Nocera, *Accounts of chemical research*, 2012, **45**, 767-776.
264. C. N. Singman, *Journal of Chemical Education*, 1984, **61**, 137-142.
265. B. S. Murty, M. K. Datta and S. K. Pabi, *Sadhana*, 2003, **28**, 23-45.
266. S. Ram, *Acta Materialia*, 2001, **49**, 2297-2307.
267. R. Nyholm, A. Berndtsson and N. Martensson, *Journal of Physics C: Solid State Physics*, 1980, **13**, L1091-L1096.
268. A. Arico, A. Shukla, H. Kim, S. Park, M. Min and V. Antonucci, *Applied Surface Science*, 2001, **172**, 33-40.

269. M. Wakisaka, S. Mitsui, Y. Hirose, K. Kawashima, H. Uchida and M. Watanabe, *The Journal of Physical Chemistry B*, 2006, **110**, 23489-23496.
270. W. Chen and S. Chen, *Journal of Materials Chemistry*, 2011, **21**, 9169-9178.
271. J.-H. Choi, K.-W. Park, B.-K. Kwon and Y.-E. Sung, *Journal of The Electrochemical Society*, 2003, **150**, A973-A978.
272. K.-W. Park, J.-H. Choi, B.-K. Kwon, S.-A. Lee, Y.-E. Sung, H.-Y. Ha, S.-A. Hong, H. Kim and A. Wieckowski, *The Journal of Physical Chemistry B*, 2002, **106**, 1869-1877.
273. A. Mandale, S. Badrinarayanan, S. Date and A. Sinha, *Journal of electron spectroscopy and related phenomena*, 1984, **33**, 61-72.
274. N. Popova and L. Babenkova, *Reaction Kinetics and Catalysis Letters*, 1979, **11**, 187-192.
275. H. Shi, O. Y. Gutiérrez, G. L. Haller, D. Mei, R. Rousseau and J. A. Lercher, *Journal of Catalysis*, 2013, **297**, 70-78.
276. M. Bridge, C. Comrie and R. Lambert, *Journal of Catalysis*, 1979, **58**, 28-33.
277. D. Wang, H. L. Xin, H. Wang, Y. Yu, E. Rus, D. A. Muller, F. J. DiSalvo and H. D. Abruña, *Chemistry of Materials*, 2012, **24**, 2274-2281.
278. M. S. Faber, M. A. Lukowski, Q. Ding, N. S. Kaiser and S. Jin, *The Journal of Physical Chemistry C*, 2014, **118**, 21347-21356.
279. J. A. Vigil and T. N. Lambert, *RSC Advances*, 2015, **5**, 105814-105819.
280. M. Sun, Y. Chen, G. Tian, A. Wu, H. Yan and H. Fu, *Electrochimica Acta*, 2016, **190**, 186-192.
281. D. Mukherjee, P. M. Austeria and S. Sampath, *ACS Energy Letters*, 2016, **1**, 367-372.
282. H. Pfeiffer, F. Tancret, M.-P. Bichat, L. Monconduit, F. Favier and T. Brousse, *Electrochemistry communications*, 2004, **6**, 263-267.
283. C.-M. Lin, H.-S. Sheu, M.-H. Tsai, B.-R. Wu and S.-R. Jian, *Solid State Communications*, 2009, **149**, 136-141.
284. Y. Teng, A. Wang, X. Li, J. Xie, Y. Wang and Y. Hu, *Journal of Catalysis*, 2009, **266**, 369-379.
285. H. Pfeiffer, F. Tancret and T. Brousse, *Electrochimica Acta*, 2005, **50**, 4763-4770.
286. C. Wagner, *Faraday Discussions of the Chemical Society*, 1975, **60**, 291-300.
287. I. I. Abu and K. J. Smith, *Journal of Catalysis*, 2006, **241**, 356-366.

288. C. Han, M. Pelaez, V. Likodimos, A. G. Kontos, P. Falaras, K. O'Shea and D. D. Dionysiou, *Applied Catalysis B: Environmental*, 2011, **107**, 77-87.
289. Y. Li, Y. Zhang, X. Zhu, Z. Wang, Z. Lü, X. Huang, Y. Zhou, L. Zhu and W. Jiang, *Journal of Power Sources*, 2015, **285**, 354-359.
290. A. D. Wilson, R. H. Newell, M. J. McNevin, J. T. Muckerman, M. Rakowski DuBois and D. L. DuBois, *Journal of the American Chemical Society*, 2006, **128**, 358-366.
291. A. D. Wilson, R. K. Shoemaker, A. Miedaner, J. T. Muckerman, D. L. DuBois and M. R. DuBois, *Proceedings of the National Academy of Sciences*, 2007, **104**, 6951-6956.
292. Y. Nicolet, A. L. de Lacey, X. Vernède, V. M. Fernandez, E. C. Hatchikian and J. C. Fontecilla-Camps, *Journal of the American Chemical Society*, 2001, **123**, 1596-1601.
293. P. P. Patel, M. K. Datta, O. I. Velikokhatnyi, R. Kuruba, K. Damodaran, P. Jampani, B. Gattu, P. M. Shanthi, S. S. Damle and P. N. Kumta, *Scientific Reports*, 2016, **6**.
294. J. Kibsgaard, Z. Chen, B. N. Reinecke and T. F. Jaramillo, *Nat Mater*, 2012, **11**, 963-969.
295. H. Vrubel, D. Merki and X. Hu, *Energy & Environmental Science*, 2012, **5**, 6136-6144.
296. D. Merki, S. Fierro, H. Vrubel and X. Hu, *Chemical Science*, 2011, **2**, 1262-1267.
297. J. Xie, H. Zhang, S. Li, R. Wang, X. Sun, M. Zhou, J. Zhou, X. W. Lou and Y. Xie, *Advanced Materials*, 2013, **25**, 5807-5813.
298. M. A. Lukowski, A. S. Daniel, F. Meng, A. Forticaux, L. Li and S. Jin, *Journal of the American Chemical Society*, 2013, **135**, 10274-10277.
299. L. Liao, S. Wang, J. Xiao, X. Bian, Y. Zhang, M. D. Scanlon, X. Hu, Y. Tang, B. Liu and H. H. Girault, *Energy & Environmental Science*, 2014, **7**, 387-392.
300. W.-F. Chen, K. Sasaki, C. Ma, A. I. Frenkel, N. Marinkovic, J. T. Muckerman, Y. Zhu and R. R. Adzic, *Angewandte Chemie International Edition*, 2012, **51**, 6131-6135.
301. Y.-F. Xu, M.-R. Gao, Y.-R. Zheng, J. Jiang and S.-H. Yu, *Angewandte Chemie International Edition*, 2013, **52**, 8546-8550.
302. D. Voiry, H. Yamaguchi, J. Li, R. Silva, D. C. B. Alves, T. Fujita, M. Chen, T. Asefa, V. B. Shenoy, G. Eda and M. Chhowalla, *Nat Mater*, 2013, **12**, 850-855.
303. J. Yang, D. Voiry, S. J. Ahn, D. Kang, A. Y. Kim, M. Chhowalla and H. S. Shin, *Angewandte Chemie International Edition*, 2013, **52**, 13751-13754.
304. Y. Xu, R. Wu, J. Zhang, Y. Shi and B. Zhang, *Chemical Communications*, 2013, **49**, 6656-6658.

305. W. F. Chen, C. H. Wang, K. Sasaki, N. Marinkovic, W. Xu, J. T. Muckerman, Y. Zhu and R. R. Adzic, *Energy & Environmental Science*, 2013, **6**, 943-951.
306. J. Xie, J. Zhang, S. Li, F. Grote, X. Zhang, H. Zhang, R. Wang, Y. Lei, B. Pan and Y. Xie, *Journal of the American Chemical Society*, 2013, **135**, 17881-17888.
307. Y.-H. Chang, C.-T. Lin, T.-Y. Chen, C.-L. Hsu, Y.-H. Lee, W. Zhang, K.-H. Wei and L.-J. Li, *Advanced Materials*, 2013, **25**, 756-760.
308. X. Zou, X. Huang, A. Goswami, R. Silva, B. R. Sathe, E. Mikmeková and T. Asefa, *Angewandte Chemie International Edition*, 2014, **53**, 4372-4376.
309. H. Vrubel and X. Hu, *Angewandte Chemie International Edition*, 2012, **51**, 12703-12706.
310. J. M. McEnaney, J. Chance Crompton, J. F. Callejas, E. J. Popczun, C. G. Read, N. S. Lewis and R. E. Schaak, *Chemical Communications*, 2014, **50**, 11026-11028.
311. E. J. Popczun, C. G. Read, C. W. Roske, N. S. Lewis and R. E. Schaak, *Angewandte Chemie International Edition*, 2014, **53**, 5427-5430.
312. S. J. Aravind, K. Ramanujachary, A. Mugweru and T. D. Vaden, *Applied Catalysis A: General*, 2015, **490**, 101-107.
313. F. H. Saadi, A. I. Carim, E. Verlage, J. C. Hemminger, N. S. Lewis and M. P. Soriaga, *The Journal of Physical Chemistry C*, 2014, **118**, 29294-29300.
314. J. Tian, Q. Liu, N. Cheng, A. M. Asiri and X. Sun, *Angewandte Chemie International Edition*, 2014, **53**, 9577-9581.
315. H. Du, S. Gu, R. Liu and C. M. Li, *Journal of Power Sources*, 2015, **278**, 540-545.
316. J. R. McKone, B. F. Sadler, C. A. Werlang, N. S. Lewis and H. B. Gray, *ACS Catalysis*, 2012, **3**, 166-169.
317. E. H. Kisi and M. M. Elcombe, *Acta Crystallographica Section C: Crystal Structure Communications*, 1989, **45**, 1867-1870.
318. P. J. Kulesza, I. S. Pieta, I. A. Rutkowska, A. Wadas, D. Marks, K. Klak, L. Stobinski and J. A. Cox, *Electrochimica acta*, 2013, **110**, 474-483.
319. G. Kresse and J. Furthmüller, *Computational Materials Science*, 1996, **6**, 15-50.
320. G. Kresse and J. Furthmüller, *Physical Review B*, 1996, **54**, 11169-11186.
321. G. Kresse and D. Joubert, *Physical Review B*, 1999, **59**, 1758-1775.
322. B. Wang, J. Iqbal, X. Shan, G. Huang, H. Fu, R. Yu and D. Yu, *Materials Chemistry and Physics*, 2009, **113**, 103-106.

323. J. P. Perdew and W. Yue, *Physical Review B*, 1986, **33**, 8800-8802.
324. B. U. Haq, A. Afaq, R. Ahmed and S. Naseem, *Chinese Physics B*, 2012, **21**, 097101.
325. L. Li, W. Wang, H. Liu, X. Liu, Q. Song and S. Ren, *The Journal of Physical Chemistry C*, 2009, **113**, 8460-8464.
326. P. Schröer, P. Krüger and J. Pollmann, *Physical Review B*, 1993, **47**, 6971-6980.
327. H. Morkoç and Ü. Özgür, *Zinc oxide: fundamentals, materials and device technology*, John Wiley & Sons, 2008.
328. A. Ohtomo, M. Kawasaki, I. Ohkubo, H. Koinuma, T. Yasuda and Y. Segawa, *Applied physics letters*, 1999, **75**, 980-982.
329. C.-Y. Ren, S.-H. Chiou and C.-S. Hsue, *Physica B: Condensed Matter*, 2004, **349**, 136-142.
330. X. Zong, C. Sun, H. Yu, Z. G. Chen, Z. Xing, D. Ye, G. Q. Lu, X. Li and L. Wang, *The Journal of Physical Chemistry C*, 2013, **117**, 4937-4942.
331. B. Gottlieb, R. Koropecki, R. Arce, R. Crisalle and J. Ferron, *Thin Solid Films*, 1991, **199**, 13-21.
332. K. Ellmer, *Journal of Physics D: Applied Physics*, 2001, **34**, 3097.
333. G. J. McCarthy and J. M. Welton, *Powder Diffraction*, 1989, **4**, 156-159.
334. Y. Duan, *Physical Review B*, 2008, **77**, 045332.
335. M. A. Mäki-Jaskari and T. T. Rantala, *Physical Review B*, 2001, **64**, 075407.
336. J. Xu, S. Huang and Z. Wang, *Solid State Communications*, 2009, **149**, 527-531.
337. O. OLOFSSON, *Acta Chem Scand*, 1972, **26**, 2777-2787.
338. J. A. Aitken, V. Ganzha-Hazen and S. L. Brock, *Journal of Solid State Chemistry*, 2005, **178**, 970-975.